

© 2023 Simon Lin

ON CANONICAL PURIFICATION OF RANDOM TENSOR NETWORKS

BY

SIMON LIN

DISSERTATION

Submitted in partial fulfillment of the requirements
for the degree of Doctor of Philosophy in Physics
in the Graduate College of the
University of Illinois Urbana-Champaign, 2023

Urbana, Illinois

Doctoral Committee:

Professor Robert G. Leigh, Chair
Associate Professor Thomas Faulkner, Director of Research
Associate Professor Bryan K. Clark
Assistant Professor Jacob P. Covey

Abstract

Understanding the entanglement structure of holographic states has played a significant role in demystifying quantum gravity and the emergence of spacetime. The state of the art development in this field makes heavy use of ideas from quantum information and quantum error correction to explain various features of quantum gravity including the holographic principle, the quantum extremal surface formula and subregion-subregion duality. In particular, *random tensor networks (RTNs)*, a toy model for holography which is understood to model fixed-area states, has been demonstrated to effectively capture the aforementioned traits shared by holographic theories.

While calculations of the entanglement entropy have led to most of the insight into holography and RTNs, it is useful to consider other quantum information quantities in order to give a more complete picture of the emergence of spacetime from entanglement. Among these, the *canonical purification*, along with its associated quantum information measure known as the *reflected entropy*, is of special interest in the pursuit of such new measures. The reflected entropy is closely related to the quantification of tripartite entanglement of a quantum state and enjoys a bulk geometric dual in terms of the area of entanglement wedge cross-section.

In this dissertation, we study the entanglement structure of the canonical purification of states built from holographic RTNs. For simple networks made from a single or a pair of random tensors, we analytically compute the entanglement spectra of the canonically purified density matrix. We found that the spectra effectively decomposes into different super-selection sectors, each of which can be given a gravitational interpretation of semiclassical bulk saddles with different topology. We show that our formalism can be extended to incorporate the *West Coast Model*, a toy model for black hole evaporation. We find that the spectrum exhibits a similar form in terms of the super-selection sectors, but with a wider window of fluctuation compared to the RTN results.

For RTNs built from arbitrary networks, we prove that the problem of finding the integer Rényi reflected entropy is equivalent to finding an optimization program known as the *minimal triway cut* when the system is far away from phase transitions. Minimal triway cuts can be formulated as integer programs which cannot be relaxed to find a dual maximal flow description. This sheds light on the gap between the existence of tripartite entanglement in holographic states and the bipartite entanglement structure motivated by bit-threads. In particular we show that the Markov gap, defined as the difference between the reflected entropy and the mutual information, is lower bounded by the integrality gap of the program that computes the triway cut. We apply this result to prove a conjecture that relates entanglement of purification to minimal entanglement wedge cross-section on a large class of RTNs.

Acknowledgments

I am deeply indebted to my advisor, Thomas Faulkner, for his guidance, support, patience and collaboration throughout my graduate study. Tom's passion and acute sense for physics has deeply inspired me on what a good theoretical physicist should be like. I will continue to look up to him in the rest of my career.

I would like to thank Robert Leigh for being the chair for my doctoral committee, and for his excellent courses on holography and QFT. Thanks to Bryan Clark and Jacob Covey for being on my doctoral committee, and Lance Cooper for his kind encouragement and support.

I would like to extend my gratitude to my current and past collaborators: Chris Akers, Pratik Rath and Souvik Dutta – without you this work would not have been possible. Thanks to Pratik for being a great friend and an excellent collaborator from whom I have learnt a great deal of physics. Thanks to Chris for talking me through the hard times in my graduate study: without your support I might not be able to continue to walk down the path of becoming a physicist.

I am grateful for the HEPG group of UIUC for providing a vibrant research environment and setting the stage for stimulating discussions to take place. I would like to thank my colleagues: Fikret Çeyhan, Min Li, Pin-Chun Pai, Weizhen Jia, Samuel Goldman, Marc Klinger, Manthos Karydas, Akash Vijay, Xuchen Cao, Antony Speranza and Animik Ghosh. Thanks to Weizhen and Pratik for comments on an early version of this thesis. Thanks to Jingwei, Shiliang, Ding-Yang and Yidong for resolving my confusions when it comes to mathematics.

I am grateful for the town of Champaign-Urbana where I can continue to play Table Tennis during my graduate study. Special thanks to the Illini and Champaign County Table Tennis Club, and also to my friends in this part of my life: Jimmy, Darshan, Ha, Zihan, Jingwei, Yan and Fei. Big thanks to Bryant for his nice camp and excellent woodworking.

I would also like to thank my close friends in UIUC: Joshua and Sunny for always making me feel at home; Pin-Chun for being an excellent office mate and the various board games; Ming-Wei for the games of badminton; Jimmy and Pin-Yi for taking care of SUSY when I am away. And also to my undergrad friends from NTHU for always keeping me entertained through online chats: Hsiu-Chung, Yu-Heng, Yuan-Tang, Wei-Peng, Chia-Hung and Jyun-Kai.

Special thanks goes to my cat, SUSY, for always being cute and fluffy and keeping me company over the hauling and stressful times during my PhD. Also to my family, without whose support nothing would have been possible.

Table of contents

Chapter 1	Introduction	1
1.1	Outline of the thesis	3
Chapter 2	Preliminaries	6
2.1	Quantum information basics	6
2.2	Holographic entanglement entropy	8
2.3	Canonical purification and the reflected entropy	12
2.4	Random tensor networks	17
2.5	A first pass	20
Chapter 3	Single Random Tensor	25
3.1	Summary of results	25
3.2	Setup	27
3.3	General considerations	29
3.4	Phase diagram and Rényi reflected entropies	32
3.5	Schwinger-Dyson for entanglement entropy	35
3.6	Schwinger-Dyson for reflected entropy	39
3.7	Spectrum and reflected entropy	45
3.8	Effective description	47
3.9	Numerical results	50
3.10	Discussion	51
3.10.1	Effective description of canonical purification	51
3.10.2	Non-flat spectrum and building geometry from RTNs	53
Chapter 4	West Coast Model	55
4.1	Summary of results	55
4.2	The west coast model	57
4.3	Entanglement spectrum	59
4.3.1	Resolvent trick	59
4.3.2	Rényi entropy	62
4.4	Reflected entanglement spectrum	65
4.4.1	Resolvent trick	65
4.4.2	Spectrum and reflected entropy	67
4.4.3	Rényi Reflected Entropy	70
4.5	Discussion	71
Chapter 5	Double Random Tensors	73
5.1	Summary of results	74
5.2	Motivation: canonical purification in gravity	75
5.3	Setup	79
5.3.1	Replica trick for the 2TN model	79
5.3.2	Resolvent via the Temperley-Lieb algebra	82
5.4	Reflected entropy in 2TN	86
5.4.1	Finite χ	86
5.4.2	Large χ limit	89

5.4.2.1	Even integer m	89
5.4.2.2	Analytic continuation	93
5.4.3	Reflected spectrum and the effective description	95
5.4.4	Corrections to the spectrum	99
5.4.4.1	Eigenvalue shifts	99
5.4.4.2	Fluctuations in each sector	100
5.4.5	Numerical results	103
5.5	Discussion	104
5.5.1	General RTNs and multiboundary wormholes	107
5.5.2	Junctions for the cross-section	108
5.5.3	Emergent von Neumann algebras	109
Chapter 6	Generic Tensor Networks	111
6.1	Summary of results	111
6.2	Setup	116
6.3	Preliminaries	122
6.3.1	Min cuts and Max flows	122
6.3.2	Permutations, Partitions and Boolean variables	125
6.4	Proof of the main theorem	130
6.4.1	From permutations to partitions	131
6.4.2	From partitions to integer program	134
6.4.3	From integer program to multiway cuts	135
6.4.4	Uniqueness theorem	138
6.5	Continuation in m	142
6.6	Hyperbolic RTNs	146
6.7	Discussion	150
Chapter 7	Holographic Entanglement of Purification in RTNs	154
7.1	Preliminary	154
7.1.1	Entanglement of purification	154
7.1.2	Reflected entropy from modular operator	155
7.1.3	A lower bound	156
7.2	Entanglement of purification on RTNs	157
7.2.1	Examples	158
7.3	Discussion	159
Chapter 8	Outlook	161
Appendix A	Symmetric Group and Set Partitions	163
A.1	Cayley distance	163
A.2	Non-crossing permutations	164
A.3	Set partitions	167
A.4	Annular non-crossing and topology	169
Appendix B	Temperley-Lieb Algebra	172
B.1	Basic definitions	172
B.2	The standard module	176
Appendix C	Supplement to Chapter 3	180
C.1	Proof of 1TN phase diagram	180
C.1.1	Simpler proof at $m = 2$	184
C.2	Reflected resolvent via direct group summation	184
C.2.1	Minimal elements in a fixed sector	185
C.2.2	Generating functions	191
C.2.3	Reflected resolvent	192
C.3	Full solution to $k = 2$ SD equation	193

Appendix D Supplement to Chapter 5	196
D.1 Multiboundary wormholes	196
D.2 Finite χ corrections	198
D.2.1 Corrections to orthogonality condition	198
D.2.2 Corrections from subleading TL diagrams	201
D.2.3 Explicit form for $k = 0$ and $k = 1$	206
D.3 Asymptotic behavior of $p_k(s)$	208
D.4 Proofs	214
D.4.1 Proof of Proposition 5.1	214
D.4.2 Proof of Proposition 5.2	217
D.4.3 Proof of Proposition 5.4	218
Appendix E Supplement to Chapter 6	220
E.1 Proof of Lemma 6.18: Structure of optimal ρ, σ	220
E.2 Proof of Lemma 6.19: An intersecting cut problem	229
E.3 Proof of Lemma 6.25: Probabilistic convergence for S_R	237
E.4 Proof of Eq. (6.166)	242
Appendix F Supplement to Chapter 7	245
F.1 Non-maximally entangled RTNs	245
References	247

Chapter 1

Introduction

The study of quantum entanglement has played a pivotal role in the advancement of our understanding of nature. Theoretical understanding of entanglement has led us to stimulating discoveries in various fields of physics. Examples of these discoveries include but are not limited to: The classification of topological phases [1–3], approximation of ground state wavefunction with tensor networks [4, 5], proof of c - and a -theorems under renormalization group (RG) flows [6–8], and the proof of averaged null energy conditions (ANEC) and quantum null energy conditions (QNEC) in QFT [9, 10], etc.

More importantly, time and again, lessons from quantum entanglement and quantum information have shed light on our everlasting pursuit towards a complete theory of quantum gravity – from the early days when Bekenstein-Hawking first conceived the formula of black hole entropy [11, 12], all the way to the recent calculation of the Page curve in an evaporating black hole [13–15], ideas from quantum entanglement have either directly or indirectly inspired critical breakthroughs in the field of quantum gravity.

Perhaps the most fruitful, yet surprising, connection between quantum entanglement and quantum gravity lies in what is now known as *AdS/CFT correspondence* [16, 17]. Also more colloquially known as *holography*, it states that a theory of quantum gravity in a hyperbolic anti-de Sitter (AdS) spacetime (commonly referred to as the *bulk*) is dual to a conformal field theory (CFT) that lives at the asymptotic boundary (commonly referred to as the *boundary*) of the spacetime. Originating from the top-down approach of superstring theory [18, 19], it is now believed that any consistent theory of quantum gravity must exhibit such a bulk to boundary duality. This viewpoint is known as the *holographic principle* [20, 21], which has led to numerous bottom-up approaches to AdS/CFT [22–25].

In the landmark work of Ryu-Takayanagi [26, 27], it was shown that the entanglement entropy (a measure of bipartite entanglement) of a region of the boundary CFT is equivalent to the minimal surface area of a volume homologous to the said boundary region in bulk spacetime, normalized in Plank units. This idea was soon generalized to include time dependence [28] and quantum corrections [29, 30]. Together, it was suggested that quantum entanglement is the fundamental property from which the fabric of spacetime we commonly know of emerges from. Subsequent works have shown that the bulk gravitational dynamics can be derived from boundary entanglement properties [31, 32].

In particular, the bulk volume enclosed by the minimal surface of Ryu-Takayanagi, called the *entanglement wedge (EW)* [33], is itself dual to the related region on the boundary. This property is an illustration of *subregion-subregion duality* [34–36], which is the statement that a boundary region contains complete information about its bulk entanglement wedge. In this regard, the holographic dictionary can itself be

viewed as a *quantum error-correcting code*, whose code subspace is the space where the bulk admits a semiclassical description, and physical subspace is the space of all possible CFT states. It can be shown that a Ryu-Takayanagi formula follows directly from the structure of any quantum error-correcting codes [37].

The various traits mentioned above were originally thought to be unique to AdS/CFT. However, it was soon discovered that there are other physical systems that exhibit strikingly similar phenomena. One class of such models is known as the *holographic tensor networks* [38–40]. Tensor networks (TN) are methods for building up many-body wave functions by contracting a collection of simple tensors [41, 42]. As toy models for AdS/CFT, they are known for possessing key signatures shared by holographic theories, such as Ryu-Takayanagi formulae [39, 40], subregion-subregion duality and quantum error-correction [39, 43], holographic renormalization groups [38, 44], and even non-perturbative gravitational effects [15, 45].

The main advantage of TNs over conventional AdS/CFT models lies in their ability to capture many desirable features of holography while remaining analytically tractable. In this regard, TN models help bridge the gap between quantum information theory and the AdS/CFT correspondence by providing a playground and tool for studying new ideas in quantum gravity. Understanding these systems can teach us valuable lessons about the fundamentals of the holographic principle. For example, TN models have been used to support/refute various conjectures that relate boundary entanglement measures to bulk surfaces [46–48].

Thus far, most of the insight into AdS/CFT and TN have come from calculations of entanglement entropy and related quantities. It is nonetheless useful to consider other quantum information quantities in order to give a more complete picture of spacetime from entanglement. For example, entanglement entropy based quantities cannot discriminate between different kinds of multi-partite entanglement [49]. In addition, the entanglement entropy is generically not well defined in continuum systems without imposing an artificial cutoff [50, 51]. This divergence issue has been identified as a signature of the underlying operator algebra of the theory, which is a universal feature across systems with large degrees of freedom [51–55].

In this thesis, we study a particular construction called the *canonical purification*, along with its associated quantum information measure known as the *reflected entropy* [56]. Reflected entropy is a quantity defined on a bipartite mixed state (or equivalently on a tripartite pure state). As opposed to the entanglement entropy, it is intrinsically well defined in the ultraviolet, thus circumventing the divergence issue that plagues entanglement entropy. Information theoretically, the difference of the reflected entropy and mutual information characterizes a particular type of tri-partite entanglement [57].

Reflected entropy is also of special interest in holographic theories, since it can be given a geometrical meaning of (twice) the area of the *entanglement wedge cross-section (EWCS)* [56], the minimal surface that divides the bulk entanglement wedge into two parts. As such, this relation behaves like a generalization of Ryu-Takayanagi, which relates a hard-to-compute boundary entanglement quantity to the area of a bulk surface. This has already given new insights to AdS/CFT, by demonstrating holographic CFT states have large tri-partite entanglement [58], in contrast to the previous conjecture that their entanglement is mostly bi-partite [59, 60].

It is known that the entanglement wedge can undergo a discontinuous jump when one smoothly varies the boundary regions [33]. In such a scenario one also expects the reflected entropy to acquire a jump transition of order $1/G_N$. This jump is discontinuous in contrast with that of the “Page curve” of entanglement entropy in which the transition is continuous [61]. However, we do expect non-perturbative phenomena would arise to smooth out the sharp discontinuity at the phase transition [15, 62, 63]. This is analogous to the corrections to the Page curve found in [15, 62, 63].

The aim of this thesis is to provide a systematic examination of the canonical purification and reflected

entropy in a subclass of TN models called *random tensor network (RTN)* [40]. Working in RTN allows us to study the intricate non-perturbative physics of phase transition of reflected entropy analytically in great detail. At the same time, we aim to test the assumptions that led to the reflected entropy/EWCS duality, which has been known to be intricate due to a problem in the analytic continuation of Rényi indices [56]. By studying the entanglement spectrum, we find effective descriptions of the canonical purification as a classical mixture of TN states, which can be matched directly into sub-leading saddles in gravitational path integrals in holography.

Quantum informatically, by working in RTN we show that reflected entropy naturally gives rise to a program that quantifies the amount of tripartite entanglement in holographic states. In particular, we find that the problem of calculating the reflected entropy in general RTNs can be translated to a problem in integer linear programming [64]. The solution to this integer program problem has deep implications on the non-trivial tripartite entanglement in holography. This is in contrast to the bit-thread program [65, 66] arising from the calculation of entanglement entropy, which suggests that the entanglement of such states are mostly bipartite [59, 60]. Our results suggests a new way to think about multi-partite entanglement in AdS/CFT.

1.1 Outline of the thesis

This dissertation is organized as follows:

- Chapter 2 reviews the necessary ingredients in quantum information theory and random tensor networks in order to set up our calculations in later chapters. After formalizing the basics of holographic entanglement entropy, we establish the definition of the canonical purification and reflected entropy. We then review the fundamentals of random tensor networks, focusing on the effective statistical mechanical model that reproduces a version of Ryu-Takayanagi formula. We conclude this chapter by giving a first pass on setting up the reflected entropy replica trick on RTNs, the naïve saddle solutions, and their gravitational interpretations.
- Chapter 3 studies the canonical purification of a single tri-partite random tensor, which we will refer to as the *1TN model*. Holographically, this setup corresponds to a coarse-grained version of three-boundary wormhole. We start by studying the reflected entropy phase diagram of the 1TN model. In particular, we show that there is no problem of analytic continuation if one is careful when picking the dominant saddles. We continue our journey by presenting a computation of the reflected spectrum (the entanglement spectrum of the canonical purification) by solving a set of matrix recursion relations. We obtain, analytically, the leading order corrections contributing to the reflected entropy phase transition and verify our finding with explicit numerics. The spectrum we obtained is not flat, as opposed to the usual Rényi spectrum for these networks. We propose an effective description for the 1TN models as a summation over two super-selection sectors with different area operator and discuss the gravitational interpretation of them. Lastly, we note that the calculation of reflected spectrum can also be computed directly by summing over a large class of group permutations.
- Chapter 4 switches focus from RTNs and present a parallel analysis of the canonical purification in the *west coast model*, a model of black hole evaporation consisting of Jackiw-Teitelboim (JT) gravity coupled to end-of-the-world branes. The west coast model can be thought of as a generalization of RTN states in a canonical ensemble. By performing the gravitational path integral, we show that the

reflected spectrum of this model can be extracted analytically by solving a similar matrix recursion relation as in the 1TN analysis. In short we find a similar story: the spectra consists of a sum over two super-selection sectors, which can be interpreted as a direct sum of geometries, a connected one and a disconnected one in a closed universe. We find that area fluctuations that spread out the reflected entropy phase transition is larger than the corresponding one in 1TN. transition. We compute the Renyi generalization of the reflected entropy and show that the location of the phase transition varies as a function of the Renyi parameter.

- Chapter 5 builds upon our 1TN results by studying a pair of tripartite random tensors contracted by an internal bond, which we will refer to as the *2TN model*. This corresponds to a coarse-grained version of a multi-boundary wormhole with the topology of two pairs of pants sewn together. Motivated by holography, we restrict our analysis to the limit where the external bond dimensions are much greater than the internal one. Under this limit, the spectrum of the 2TN model factorizes nicely into irreducible representations of an algebraic object known as the *Temperley-Lieb algebra*. The effective description now consists of an infinite tower of super-selection sectors. These sectors have the nice interpretation of a series of bulk solution of four-boundary wormholes with an increasing number of genus. Similar to the case of the 1TN model, we find important non-perturbative effects that contribute near the entanglement wedge phase transition. We give an expression for the reflected spectrum up to second order in terms of the internal bond dimension and compare it with numerical results. Finally, we conjecture that an emergent type-II₁ von Neumann algebra will arise on a modular flowed version of the canonical purification of the 2TN model.
- Chapter 6 examines generic random tensor networks and study the properties of their canonical purification. In contrast to our previous simple tensor models, it is not possible to perform an exact analysis on the spectrum of a generic RTN at any given point in the parameter space. However, we will make progress by limiting our attention to the case where the system is far from the phase transitions. Using techniques from linear programming theory, we relate the problem of computing integer Rényi reflected entropies to the problem of finding minimal triway cuts through the network. More precisely, we prove that the integer Rényi entropy of generic RTN states converges to the one given by the triway cut in large bond dimensions. Minimal multiway cuts can be formulated as integer programs which cannot be relaxed to a dual maximal flow problem. This is in contrast to the bit-thread formalism of entanglement entropy where such duality is present, with the implication that the bulk entanglement structure is dominantly bipartite (which is now known to be false). We show that the Markov gap (difference between reflected entropy and mutual information) that measures tripartite entanglement, is lower bounded by the *integrality gap* of the integer program that computes the triway cut. We demonstrate our result on RTN defined on hyperbolic graphs, giving an expression of the reflected entropy and the effective description in terms of a superposition over different RTNs.
- Chapter 7 uses the results we obtained for generic RTNs to prove a conjecture related to the entanglement of purification in holographic RTNs. The entanglement of purification has been conjectured to also be dual to EWCS in holographic theories. However, it is generally intractable to compute the entanglement of purification due to the required optimization over all possible purifications. We will show that our result in Chapter 6 allow us to prove this conjecture on a wide class (a codimension-0 subset in the parameter space) of generic RTNs.
- Chapter 8 wraps up this thesis with some discussions and future outlooks.

Several long technical reviews, calculations and proofs of this thesis are relegated to the appendices. The results presented in this dissertation is sourced mostly from the joint research works [48, 67–70] with the author’s advisor Thomas Faulkner, and collaborators Chris Akers and Pratik Rath.

Chapter 2

Preliminaries

2.1 Quantum information basics

Let ρ be a density operator on a bipartite quantum system with corresponding Hilbert space $\mathcal{H} = \mathcal{H}_A \otimes \mathcal{H}_B$. We say that ρ is *separable* if there exists a decomposition of ρ_{AB} into a sum of tensor products

$$\rho = \sum_i \lambda_i \rho_A^i \otimes \rho_B^i \quad (2.1)$$

for some ρ_A^i supported on \mathcal{H}_A and ρ_B^j supported on \mathcal{H}_B . We say ρ is *entangled* if it is not separable. We define the *reduced density matrix* on system A by tracing out all the degree of freedoms on the complement system B :

$$\rho_A = \text{Tr}_B \rho. \quad (2.2)$$

The *entanglement entropy* of subsystem A is defined as the von Neumann entropy of the reduced density matrix ρ_A :

$$S(A)_\rho \equiv S_{\text{vN}}(\rho_A) = -\text{Tr}_A \rho_A \ln \rho_A. \quad (2.3)$$

We have the bound $0 \leq S_\rho(A) \leq \ln(\dim \mathcal{H}_A)$ for any finite dimensional quantum system. In the case where $\rho = |\Psi\rangle\langle\Psi|$ is a pure state, we have $S(A)_\rho = S(B)_\rho$ and the entanglement entropy quantifies the amount of entanglement between subsystems A and B . That is, $S_\rho(A) = 0$ if and only if ρ is separable. ρ is said to be *maximally entangled* if its entanglement entropy saturates the upper bound, i.e. $S(A)_\rho = \ln(\dim \mathcal{H}_A)$.

Operationally, the entanglement entropy quantifies the amount of *distillable entanglement*: Let's say Alice and Bob has n copies of the pure state $\rho_{AB}^{\otimes n}$. Then $S(A)_\rho = S(B)_\rho$ measures the asymptotic rate where Alice and Bob can produce Bell pairs using only *Local Operations and Classical Communications (LOCC)* as $n \rightarrow \infty$. In other words, it measures the maximum amount of maximally entangled pairs that can be distilled out of a bipartite pure state.

The *mutual information* of a bipartite state ρ , denoted by $I(A : B)$, is defined as

$$I(A : B) = S(A)_\rho + S(B)_\rho - S(AB)_\rho. \quad (2.4)$$

The mutual information measures the correlation (both quantum and classical) between subsystems A and B and $I(A : B) = 0$ implies the state is factorizable, i.e. $\rho = \rho_A \otimes \rho_B$. In the case where ρ is pure, $I(A : B)$ is

equal to twice of the entanglement entropy. The mutual information is always semi-positive, $I(A : B) \geq 0$. When translated into the entanglement entropies this means

$$S(A)_\rho + S(B)_\rho \geq S(AB)_\rho. \quad (2.5)$$

This property is known as the *subadditivity* of the von Neumann entropy.

We will also consider a family of entropies called the *Rényi entropies*, which are defined in terms of the moments of the density operator ρ :

$$S_n(\rho) = \frac{1}{1-n} \ln \text{Tr} \rho^n. \quad (2.6)$$

The canonical definition here requires n to be a integer, but in various places it is useful to consider the analytical continuation of the Rényi index n into positive real numbers. In particular, the limit $n \rightarrow 1$ reproduces the von Neumann entropy

$$S_{\text{vN}}(\rho) = \lim_{n \rightarrow 1} S_n(\rho) = - \lim_{n \rightarrow 1} \frac{\partial}{\partial n} \ln \text{Tr} \rho^n. \quad (2.7)$$

Other notable cases are $S_0(\rho) = \ln \text{Rank}(\rho)$ and $S_\infty(\rho) = - \ln \lambda_{\text{max}}$, the largest eigenvalue of ρ . The Rényi entropies are non-increasing in its indices

$$S_n(\rho) \geq S_m(\rho), \quad n \geq m \geq 0, \quad (2.8)$$

which may come handy in proving various bounds in quantum information.

Our main interest of Rényi entropies is that they can be used as a means for calculating the von Neumann entropy. When the exact form of the density matrix is not known (e.g. as an disordered average) or hard to write down (e.g. for gravitational path integrals), it is not possible to compute the von Neumann entropy directly. Even if one does have a density matrix, a direction computation of the logarithm in S_{vN} requires exact diagonalization for the density matrix, which is in many cases not feasible. Instead, suppose that one knows the Rényi entropies for all integers. If one can “analytically continue” the Rényi entropies near $n = 1$, then Eq. (2.7) gives the value of the von Neumann entropy. This procedure is known as the *replica trick* [71].

Suppose that we start from a pure state $|\psi\rangle$ on a bipartite system AB and we form the reduced density matrix $\rho_A = \text{Tr}_B |\psi\rangle \langle\psi|$ by tracing out subsystem B . It is useful to introduce the tensor network diagrammatic notation here: To express the reduced density matrix we use the following diagram

$$\rho_{AB} = \begin{array}{c} \text{A} \quad \text{B} \\ | \quad | \\ \text{---} \text{---} \\ | \quad | \\ \text{---} \text{---} \\ | \quad | \end{array}, \quad \rho_A = \text{tr}_B \rho_{AB} = \begin{array}{c} \text{A} \quad \text{B} \\ | \quad | \\ \text{---} \text{---} \\ | \quad | \\ \text{---} \text{---} \\ | \quad | \end{array}, \quad (2.9)$$

where we have expressed the state $|\psi\rangle$ as a triangle and used lines to denote the Hilbert space corresponding to subsystems AB . An upward open line indicates basis in Hilbert space and downward open line indicates the dual Hilbert space, although for finite dimensional systems they are isomorphic and we will not care about the orientation of the diagram in general. A closed line indicates contraction in the Hilbert space along the common basis. Here we see that the partial trace can be simply expressed as a closed loop (self-contraction) around system B .

The trace of the n -th power of the reduced density matrix ρ_A^n can be expressed as, e.g.

$$\text{tr}_A \rho_A^4 = \text{Diagram}, \quad (2.10)$$

where we have rearranged the density matrices ρ_A in a to lay on a circle. It is clear from that the contraction pattern respects cyclic symmetry τ_n whose action permutes different copies of density matrix cyclically (which is realized as a rotational symmetry in Eq. (2.10)). This symmetry is known as the *replica symmetry*.

In general we can write the moment of ρ_A as some expectation value of the n -th tensor power of the original density matrix ρ :

$$\text{Tr}_A \rho_A^n = \text{Tr}(\Sigma_A(\sigma_A)\Sigma_B(\sigma_B)\rho_{AB}^{\otimes n}) = \langle \psi |^{\otimes n} \Sigma_A(\sigma_A)\Sigma_B(\sigma_B) | \psi \rangle^{\otimes n}, \quad (2.11)$$

where Σ_A and Σ_B acts on the tensor product Hilbert space $\mathcal{H}_{AB}^{\otimes n}$ by permuting the bases of different replicas on subregion A and B respectively. They are known as the *twist operators*. The action for Σ_A and Σ_B are characterized by a group element in the discrete permutation group $\sigma_A, \sigma_B \in S_n$. In the Rényi entropy case they can be simply read out from Eq. (2.10) to be

$$\sigma_A = \tau_n, \quad \sigma_B = e, \quad (2.12)$$

where $\tau_n = (12 \cdots n)$ is the maximal cyclic permutation of S_n and e is the identity permutation. Note that $\Sigma_B(e) = \mathbf{1}_{AB}$, the identity operator on \mathcal{H}_{AB} , so we can omit it in Eq. (2.11) and write the Rényi entropy as

$$S_n(A) = \frac{1}{1-n} \ln \langle \psi |^{\otimes n} \Sigma_A(\tau_n) | \psi \rangle^{\otimes n}. \quad (2.13)$$

2.2 Holographic entanglement entropy

We give a brief introduction of AdS/CFT and holographic entanglement in this section. The field of holographic entanglement has grown tremendously in the recent years, which we will not be able to do it justice in one single section. For more complete reviews on standard AdS/CFT dictionary we refer the reader to [72–75]. For reviews on the entanglement and quantum information methods in QFT and holography we refer the reader to the excellent book of Ragamani-Takayanagi [76], as well as TASI lecture notes [77, 78].

First, we give a lightening introduction to the AdS/CFT correspondence. AdS/CFT is a duality statement between quantum gravity and strongly coupled field theories. In its most common settings, it posits that a theory of quantum gravity (formulated in terms of string theory or M-theory) in the background of a $d + 1$ -dimensional asymptotic Anti-de Sitter (AdS) space is dual to a conformal field theory (CFT) that lives on its d -dimensional conformal boundary. More concretely, the AdS_{d+1} space can be parameterized by the following metric in the Poincaré patch:

$$ds^2 = \frac{1}{z^2}(dz^2 + \eta_{\mu\nu}dx^\mu dx^\nu), \quad \mu, \nu = 0, \dots, d-1. \quad (2.14)$$

The metric diverges as $z \rightarrow 0$. Its conformal boundary can be obtained by a scale transformation $x \rightarrow x/z$ and then sending $z \rightarrow 0$:

$$ds^2 = \eta_{\mu\nu} dx^\mu dx^\nu, \quad (2.15)$$

which is the usual metric of Minkowski space in d dimensions. If one approaches the boundary at different rates $z \sim \epsilon f(z, x^\mu)$, the resulting metric attains a Weyl factor

$$ds^2 = f^2(z, x^\mu) \eta_{\mu\nu} dx^\mu dx^\nu, \quad (2.16)$$

which is conformally equivalent to the previous metric. Thus the field theory living on the boundary must be invariant under a conformal transformation. Different choices of functions correspond to different symmetry transformations which must be respected by both sides of theories. In the case of AdS_{d+1} , the full isometry group is $SO(d, 2)$, which is the same as the group of conformal isometry on d dimensions for $d > 2$.¹

The duality statement in AdS/CFT is usually phrased in terms of *holographic dictionaries*. They consist of a set of relations between semiclassical fields in the bulk gravity theory and operators as well as a rule to match different computable objects on both sides. The two commonly used holographic dictionaries are the GPKW dictionary [16, 17], which state the equivalence of partition functions:

$$Z_{\text{grav}}[\phi] = Z_{\text{CFT}}[\phi] \quad (2.17)$$

And the extrapolate dictionary [80], which states the equivalence of correlation functions:

$$\langle O_1(x_1) \cdots O_n(x_n) \rangle_{\text{CFT}} = \lim_{z \rightarrow 0} z^{-\sum_i \Delta_i} \langle O_1(x_1, z) \cdots O_n(x_n, z) \rangle_{\text{grav}}, \quad (2.18)$$

where Δ_i is the scaling dimension of the operator O_i .

We now list a few pairs of well-known field theories and their corresponding gravity duals. The superstring theory is 10-dimensional in nature, hence the topology of the dual gravity theory generally has the topology of $AdS_d \times M$ with M a compactified manifold.

- $\mathcal{N} = 4$ 4d super Yang-Mills theory/ IIB superstring theory on $AdS_5 \times S^5$. This is the first discovered example of AdS/CFT [18, 19] and one of the best understood one. The field theory side is controlled by the coupling constant g_{YM} and the number of gauge fields N . In the limit $N \rightarrow \infty$ and holding the 't Hooft coupling $\lambda = g_{\text{YM}}^2 N$ fixed, the bulk dual is IIB superstring theory on $AdS_5 \times S^5$. If one further takes $\lambda \rightarrow \infty$, the bulk dynamics truncates to type IIB supergravity on the same background.
- 2d CFTs with large central charge $c \gg 1$ / classical gravity in AdS_3 . The details of the gravity side depends on the particular 2d CFT (which may not have a Einstein-Hilbert dual). However such duality is generally believed to hold true and is often used as a bottom-up approach. Models with precise duals do exist. A particular construction is $(4, 0)_{2d}$ Superconformal Field Theory (SCFT) and classical gravity on $AdS_3 \times S^2 \times X_4$, where X_4 can be either $K3$ or T^4 , see e.g. [81].
- Sachdev-Ye-Kitaev (SYK) model / Jackiw-Teitelboim (JT) gravity. SYK model is a quantum mechanical system of N interacting Majorana fermions with random interactions [23, 82, 83]. In the large N limit, the low energy sector of SYK model has been shown to be closely related to JT gravity, a 2d gravity

¹For $d = 2$ one must raise the bulk isometry group $SO(2, 2)$ as a projective representation of the classical Poisson bracket. Doing so introduces a central charge to the Lie algebra, which is isomorphic to the Virasoro algebra, the local symmetry group of 2d CFTs. [79]

theory with a dilaton. For this reason this particular pair is usually referred to as a $\text{AdS}_2/\text{CFT}_1$ duality. It has been used as a toy model to study various properties of holographic black holes [84, 85] and as a model for discrete bulk spacetime [86].

We will be mostly interested in the case where the CFT is strongly interacting with a large degree of freedom. It is in this limit that the dual bulk theory is semi-classical, i.e. weak-gravitating with a small Newton's constant and a large AdS radius compared to the string scale. This choice suppresses the stringy effects and allows us to work with classical geometry (plus perturbative corrections) in the bulk, which is crucial for making a precise proposal of holographic entanglement.

We now review the key developments in holographic entanglement. A central player in this field is the Ryu-Takayanagi formula [26, 27]. It has far-reaching implications in our modern understanding of the holographic duality, such as bulk reconstruction, subregion-subregion duality [34–36], and the corresponding quantum error correction picture [37], all of which we will review shortly below. A version of the RT formula has recently enabled us, for the first time ever since the black hole information paradox was proposed [87], formulate a purely semi-classical calculation of the Page curve for unitary black hole evaporation process [13].

The proposal of both holographic dictionaries (Eq. (2.17) and Eq. (2.18)) are concerned with mapping between the field/operator content of the duality. The RT formula proposes a dictionary of a different kind – by directly relating a geometrical object in the bulk theory to measures of entanglement on the boundary. This proposition is remarkable in both directions: First, it is a duality statement directly about the bulk geometry, which lies at the heart of the classical gravity theory. Second, it gives the entanglement entropy, a rather abstract information measure on the boundary CFT, a clear geometrical meaning. The original RT formula states that in a time reflection symmetric solution, the boundary entanglement entropy on a subregion A is equivalent to the area of a bulk codimension-2 minimal surface γ_A homologous to A ²:

$$S(A) = \min_{\gamma_A} \frac{\text{Area}(\gamma_A)}{4G_N} + O(G_N^0). \quad (2.19)$$

The minimal surface γ_A is usually called the RT surface of A . See Fig. (2.1) for an illustration. The fully covariant generalization was established by Hubeny-Ragamani-Takayanagi (HRT) [28], which replaces the minimal surface on a time reflection-symmetric Cauchy slice by an extremal surface in the full spacetime. An equivalent covariant formulation was given later by Wall [35] in terms of a maxmin prescription. A perturbative quantum correction (the $O(G_N^0)$ term) was found later by Faulkner-Lewkowycz-Maldacena (FLM) [29].

Some clarification is needed here. Both sides of Eq. (2.19) are divergent in nature: The area of minimal surface is divergent since the AdS metric is singular at its asymptotic boundary; whereas the entanglement entropy of a subregion in QFT is inherently divergent due to short range modes [50, 51]. To properly define Eq. (2.19) we must regularize both theories by imposing a IR cutoff in the bulk and a UV cutoff on the boundary. This kind of UV-IR correspondence is a common occurrence in holography, which is a manifestation of holographic renormalization groups [88–91].

As a simple example, let's take region A to be a single interval of length ℓ on a 2D CFT in Minkowski space. The entanglement entropy of the vacuum state in 2D CFT is uniquely determined by its central charge c [92]:

$$S(A) = \frac{c}{3} \ln(\ell/\epsilon), \quad (2.20)$$

²Homologous here means that the boundary of γ_A the same as A , i.e. $\partial\gamma_A = A$.

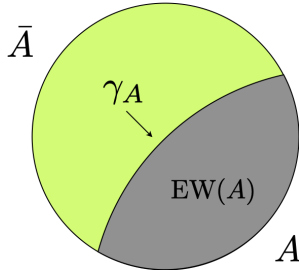


Figure 2.1: A spatial slice of the bulk AdS space with boundary region A and its complement \bar{A} . The figure shows the entanglement wedge of A (gray), the RT surface γ_A and the entanglement wedge $\text{EW}(A)$.

where ϵ is a short distance cutoff. The holographic counterpart in AdS_3 is given by the minimal surface \mathcal{A} with (renormalized) boundary length ℓ . The area (which is the same as its geodesic length) of this surface can be easily obtained from Eq. (2.14). It reads

$$\frac{\text{Area}(\gamma_A)}{4G_N} = \frac{1}{2G_N} \sinh^{-1}(\ell/2\delta) \underset{\delta \rightarrow 0}{=} \frac{1}{2G_N} \ln(\ell/\delta) \quad (2.21)$$

where δ is the bulk IR cutoff. We take $\delta \rightarrow 0$ since the asymptotic boundary of the Poincare patch lies at $z = 0$. The holographic dictionary between $\text{AdS}_3/\text{CFT}_2$ states that the bulk Newton's constant is related to the boundary central charge by $c = 3/2G_N$.³ We see that the RT formula holds true under this identification.

A important advancement in holographic entanglement took place when Engelhardt and Wall proposed a generalization of RT known as the *Quantum extremal surface* (QES) formula [30]. The QES formula proposes that, if one takes quantum correction at any given order into account, then the RT formula must be revised to minimize the *generalized entropy* S_{gen} :

$$S(A) = \min_{\gamma_A^Q} (S_{\text{gen}}(\gamma_A^Q)) \equiv \min_{\gamma_A^Q} \left(\frac{\text{Area}(\gamma_A^Q)}{4G_N} + S_{\text{bulk}}(\text{EW}(A)) \right) \quad (2.22)$$

where $S_{\text{bulk}}(\text{EW}(A))$ is the bulk entanglement entropy of the *entanglement wedge* of A , the codimension-1 volume⁴ enclosed by γ_A^Q and A . The minimization is carried over all possible quantum extremal surfaces γ_A^Q homologous to A . See Fig. (2.1) for an example. The implications of the QES formula is way more far-reaching a mere quantum correction to the RT proposal: It implies that the area of minimal surface and bulk entanglement are merely two faces of a single coin and must be treated on equal footing. In particular, it was recognized that the renormalization procedure needed for the minimal surface area and the bulk entanglement entropy cancels with each other, which allows one to give a UV-finite formulation of entanglement entropy in quantum gravity. This idea was recently rigorously formalized in the language of operator algebra in various semi-classical gravity systems [93–95].

The entanglement wedge (EW) of region A , defined as the region enclosed by the quantum extremal surface, is of special importance in the program of *bulk reconstruction*. It was proposed to be the dual bulk prescription of the reduced boundary density matrix ρ_A in boundary CFT [34–36]. This implies that all the information in the entanglement wedge can be reconstructed from the boundary theory given full knowledge

³We have normalized the AdS characteristic length ℓ_{AdS} to be 1 here.

⁴The entanglement wedge also refers to the causal development of the region, which is a bulk codimension-0 object. Since we are restricting to time-reflection symmetric situations with a preferred choice of Cauchy slice we will be agnostic to the differences.

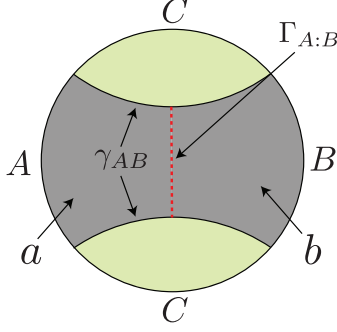


Figure 2.2: A spatial slice of the bulk AdS space with A and B chosen to be two disconnected intervals on the boundary. The figure depicts the entanglement wedge of AB (gray), the entanglement wedge of C (green), the RT surface γ_{AB} and the entanglement wedge cross-section $\Gamma_{A:B}$.

of the reduced density ρ_A . This property is known as the *subregion-subregion duality* of holography.

The idea of bulk reconstruction and subregion-subregion duality strongly suggests that the holography map between the boundary and the bulk should really be thought of as a realization of *quantum error-correction* (QEC) codes [24]. The code associated to holography is a special kind of QEC code with the property of *complementary recovery*. Consider the boundary region A along with its complement \bar{A} and denote their corresponding entanglement wedges $\text{EW}(A)$ and $\text{EW}(\bar{A})$. The holographic map can be viewed as isometry V that maps the boundary Hilbert space (the code subspace $\mathcal{H}_{\text{code}}$) to the semiclassical bulk states (the physical subspace $\mathcal{H}_{\text{phys}}$). The recovery map inverts the map V by embedding the code subspace back into the physical subspace, protecting against the error of the action of any operators in its complement, i.e. for any state $|\psi\rangle \in \mathcal{H}_{\text{phys}}$ and any Hermitian $O_A \in \text{End}(\mathcal{H}_A)$, $O_{\bar{A}} \in \text{End}(\mathcal{H}_{\bar{A}})$ there exists Hermitian operators $O_{\text{EW}} \in \text{End}(\mathcal{H}_{\text{EW}(A)})$, $O_{\overline{\text{EW}}} \in \mathcal{H}_{\text{EW}(\bar{A})}$ such that they satisfies the complementary recovery condition

$$VO_A |\psi\rangle = O_{\text{EW}}V |\psi\rangle, \quad VO_{\bar{A}} |\psi\rangle = O_{\overline{\text{EW}}}V |\psi\rangle. \quad (2.23)$$

The connection between QEC and the RT formula was first realized by Harlow [37], where he showed that the complementary recovery condition is equivalent to the existence of an area operator \mathcal{L}_A and an entropy formula that mimics RT:

$$S(\rho_A) = \text{Tr}(\rho \mathcal{L}_A) + S(\rho, \text{EW}(A)) \quad (2.24)$$

In particular, the area operator factorizes in terms of the centralizer of the underlying operator algebra $\mathcal{L}_A = \bigoplus_{\alpha} \mathcal{A}_{\alpha} \mathbb{1}_{\text{EW}(A), \text{EW}(\bar{A})}$, which correspond to different *superselection sectors*⁵ that has physical interpretation of *fixed area states* [96–98] which possess flat entanglement spectra. We will see that these fixed area states are precisely the proposed dual of RTNs when we review the basics of RTN later in this chapter.

2.3 Canonical purification and the reflected entropy

In this section we introduce the definition of the canonical purification and reflected entropy. We review various properties of the reflected entropy, focusing on the holography proposal that related reflected entropy to entanglement wedge cross-sections (EWCS). We then introduce the Rényi generalization and the replica trick for the reflected entropy.

⁵These are also sometimes referred to as α -blocks or α -sectors.

Let ρ_{AB} be a density matrix on a bipartite quantum system AB with Hilbert space $\mathcal{H}_{AB} = \mathcal{H}_A \otimes \mathcal{H}_B$.⁶ A *purification* for ρ_{AB} is an extended density operator ρ_{ABC} on a larger Hilbert space \mathcal{H}_{ABC} such that

$$\text{Tr}_C \rho_{ABC} = \rho_{AB}, \quad (2.25)$$

and that ρ_{ABC} is a pure state.

Given any ρ there will in general be many different choices of purifications. However there is a standard choice on the “doubled” Hilbert space: The space of linear maps $\text{End}(\mathcal{H})$ acting on \mathcal{H} itself forms a Hilbert space with inner product $\langle X|Y \rangle = \text{Tr}(X^\dagger Y)$ with the trace taken in the original Hilbert space. In general $\text{End}(\mathcal{H})$ is isomorphic to the tensor product $\mathcal{H} \otimes \mathcal{H}^*$, where \mathcal{H}^* is the dual Hilbert space of \mathcal{H} . For the density matrix ρ_{AB} introduced above, we define the *canonical purification* for ρ_{AB} to be the state

$$|\sqrt{\rho_{AB}}\rangle \in \text{End}(\mathcal{H}_A) \otimes \text{End}(\mathcal{H}_B) = (\mathcal{H}_A \otimes \mathcal{H}_A^*) \otimes (\mathcal{H}_B \otimes \mathcal{H}_B^*), \quad (2.26)$$

In other words, define $|\sqrt{\rho_{AB}}\rangle$ by finding the unique positive matrix square root of ρ_{AB} , regarding the result as a state in $\text{End}(\mathcal{H}_A \otimes \mathcal{H}_B)$. It is normalized since $\langle \sqrt{\rho_{AB}} | \sqrt{\rho_{AB}} \rangle = \text{tr}(\rho_{AB}) = 1$. To see that it is really a purification, write $\rho_{AB} = \sum_i \lambda_i |i\rangle_{AB} \langle i|_{AB}$ in eigenbasis and we can compute

$$\begin{aligned} \text{Tr}_{A^*B^*} |\sqrt{\rho_{AB}}\rangle \langle \sqrt{\rho_{AB}}| &= \sum_{ij} \lambda_i \text{Tr}_{A^*B^*} |i\rangle_{AB} \langle i'|_{A^*B^*} \langle j|_{AB} \langle j'|_{A^*B^*} \\ &= \sum_{k'} \sum_{ij} \lambda_i |i\rangle_{AB} \langle j|_{AB} \langle k'|_{A^*B^*} \langle j'|_{A^*B^*} \\ &= \sum_i \lambda_i |i\rangle_{AB} \langle i|_{AB} = \rho_{AB}, \end{aligned} \quad (2.27)$$

where $|i'\rangle_{A^*B^*}$ is the dual eigenbasis for ρ_{AB} .

In the case where $\rho_{th} = \sum_n e^{-\beta E_n} |E_n\rangle \langle E_n|$ is a thermal density matrix, the canonical purification is known as the *thermal field double (TFD)* [99]

$$|\sqrt{\rho_{th}}\rangle = |\text{TFD}\rangle = \sum_n e^{-\beta E_n/2} |E_n\rangle |E_n^*\rangle, \quad (2.28)$$

which has been widely adopted in holography to as the boundary dual of two-sided eternal black holes [100]. Therefore, physically one can think of the canonical purification as a generalization of TFD states to arbitrary density matrices.

The *reflected entropy* of a bipartite density matrix ρ_{AB} , is defined as the entanglement entropy on region AA^* (or equivalently BB^*) of the canonical purification [56]:

$$S_R(A : B) = S(AA^*)_{|\sqrt{\rho_{AB}}\rangle} = \text{Tr}(\rho_{AA^*} \ln \rho_{AA^*}), \quad \rho_{AA^*} = \text{Tr}_{BB^*} |\sqrt{\rho_{AB}}\rangle \langle \sqrt{\rho_{AB}}|. \quad (2.29)$$

We have $S_R(A : B) = 2S(A)$ if ρ_{AB} is pure and $S_R(A : B) = 0$ if $\rho_{AB} = \rho_A \otimes \rho_B$ is factorized. In general S_R satisfies the following inequality:

$$I(A : B) \leq S_R \leq 2 \min(S_A, S_B). \quad (2.30)$$

⁶We will mostly work with factorizable finite dimensional quantum in this thesis, although both canonical purification and the reflected entropy is well defined in continuum. We will come back to this issue later.

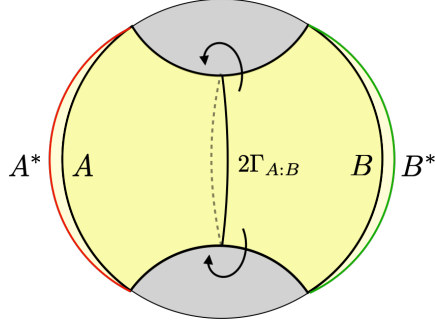


Figure 2.3: A sketch depicting the argument of the reflected entropy/EWCS duality. The entanglement wedge of AB (shown in yellow) is glued with its CPT dual, which acts like a mirror reflection of AB into A^*B^* , along their common RT surface. The end result creates a cylinder-like geometry. With the RT dictionary, the minimal surface of AA^* falls into the bulk which is then identified with twice of the EWCS $2\Gamma_{A:B}$.

In particular, the difference between mutual information and the reflected entropy,

$$MG(A : B) = S_R(A : B) - I(A : B) \geq 0, \quad (2.31)$$

called the *Markov gap* [101], is a useful measure of tri-partite entanglement. If ρ_{AB} comes from tracing out a tri-partite pure state $|\psi\rangle_{ABC}$, then $MG(A : B)$ is zero if and only if it can be written as a linear sum of *triangle states* [57], whose entanglement profiles are purely bipartite. Note that $S_R = 0$ is only a necessary condition of the state having only bipartite entanglement. For example the reflected entropy vanishes for GHZ states.

Holographically, the reflected entropy on the boundary CFT is conjectured to be dual to the twice the area of the *entanglement wedge cross-section (EWCS)*, normalized in Plank units [56]. EWCS is the minimal area surface Γ in the bulk geometric that divides the bulk EW into two regions, one containing region A the other containing B . See Fig. (2.2) for an example. More concretely, split the boundary into three regions ABC and for a reduced density matrix ρ_{AB} on CFT obtained by tracing out the degree freedom on region C we have

$$S_R(A : B) = 2EW(A : B) \equiv 2 \min_{\Gamma} \frac{\text{Area}(\Gamma)}{4G_N} + O(1), \quad (2.32)$$

where the minimization Γ is taken over all possible cross-sections that splits $A : B$. When the entanglement wedge is disconnected, we define the area of EWCS to be zero. Note that we have assumed a classical, time symmetric bulk solution in above. This proposal of reflected entropy-EWCS has been generalized to include time-dependent bulk configurations, where one adopts a maxmin recipe [102–104], and quantum corrections, where there is an additional term similar to that of the generalized entropy [103]. There are also proposal for generalizations to include multiple ($n > 3$) regions [105].

Ref. [56] establishes the duality Eq. (2.32) based on a holographic construction of the canonical purification whose holographic entropy can be related to the EWCS. We quickly sketch their arguments here: As shown in Fig. (2.3), by subregion-subregion duality, the reduced density matrix ρ_{AB} is dual to the EW of AB . The holographic construction of the canonical purification can be identified with taking the EW and glue it with its CPT dual along their common minimal surfaces. This construction has the property that these gluing surfaces acts like a “mirror” that reflects the EW into its CPT dual. Using the RT dictionary, the entropy of the boundary region AA^* should be identified with the minimal area surface that is homologous to AA^* , which can be shown to be equal to twice of the EW cross-section.

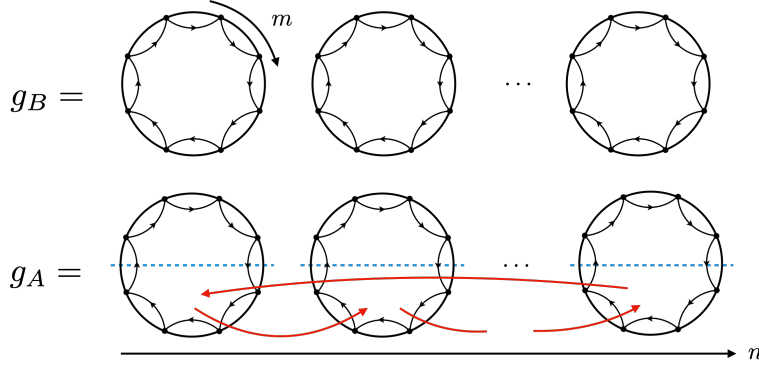


Figure 2.4: A graphical representation of g_A and g_B . We use the same replica ordering as in Eq. (2.37): The individual circles each represents the m replicas of the original tensor and each of the circles is further replicated n times. Going clockwise in each circle increases the m replica number and going to the next circle on the right increases the n replica number. A cycle of the permutation is represented by a closed directed loop. The element g_A can be thought of as cutting open the m -circles of g_B from the middle, shifting the bottom half cyclically in the n direction (as the red arrows) and then gluing them back together.

a dot on the circles – there will be m dots on the circle. The action of $g \in S_{mn}$ is represented by drawing directed closed loops corresponding to the cycle decomposition of g . For each circle we denote the upper half to be the $\beta = 1, \dots, m/2$ replicas of the column and the lower half to be $\beta = m/2 + 1, \dots, m$. The action of conjugation by γ_τ is simply cutting open each circle along its middle line, making a cyclic permutation on the lower halves, and then gluing back together.

2.4 Random tensor networks

Here we quickly review random tensor networks (RTNs). The entanglement profile of RTNs have been known to satisfy a generalized area law [107, 108]. In addition, RTNs have been shown to give rise to a bi-directional quantum error-correcting code and a two-point correlation function that matches expected holographic behavior [40], which makes them excellent candidates of a model of holographic duality. However in contrast to generic states obtained from gravitational path integral, RTN states have flat entanglement spectra. For this reason it was argued that they correspond to a special class of holographic states called the *fixed area states* [96–98]. There has been proposals to generalize RTN models to include gauge symmetry [109] and non-flat spectra [110]. For our purpose we will restrict our attention to the most basic formulation of RTNs, closely following the treatment in [40].

Consider a weighted graph $G = \{V, E\}$ with a edge weight function $\chi : E \rightarrow \mathbb{R}_+$. For each vertex $v \in V$ we assign a rank- k tensor $T_{v, \mu_1 \mu_2 \dots \mu_k}$, where the indices μ_i label the edges e_i connecting the vertex v . Thinking of each connecting edge as a Hilbert space \mathcal{H}_i spanned by basis vectors $|\mu_i\rangle$, the tensor T_v defines a state

$$|T_x\rangle = T_{x, \mu_1 \mu_2 \dots \mu_k} |\mu_1\rangle |\mu_2\rangle \dots |\mu_k\rangle \quad (2.43)$$

on the product Hilbert space of each edge $H^v \equiv \bigotimes_i \mathcal{H}_i$. The dimension of the respective Hilbert space is identified with the weight $\chi(e_i)$, called the *bond dimension* of the edge. In this thesis we will mostly work in the limit where all the bond dimensions are large, i.e. $\chi(e_i) \gg 1$. The idea is to contract all the adjacent

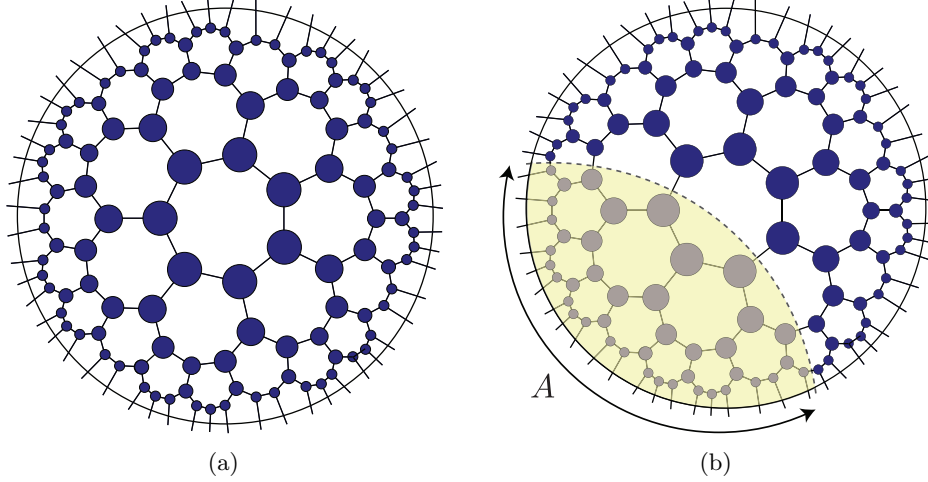


Figure 2.5: (a) We tile the hyperbolic disk isometrically by a graph. Each blue circle represents a random tensor and the connecting edges indicates contraction of the tensors. This tensor network defines a state on the Hilbert space spanned by the dangling legs on the boundary. (b) The Ising domain wall that arises in the calculation of Rényi entropies of region A in the RTN. Minimizing the length of the domain wall gives rise to an entropy formula that corresponds to the RT formula in AdS/CFT.

vertices among their shared common edges

$$\left(\bigotimes_{\{xy\} \in E} \langle xy| \right) \left(\bigotimes_{v \in V} |T_v\rangle \right). \quad (2.44)$$

Here $|xy\rangle = \delta_{\mu_i \mu'_j} |\mu_i\rangle |\mu'_j\rangle$ is an un-normalized maximally entangled state defined on the doubled Hilbert space of the edge $\{x, y\}$ where the i -th index of tensor x is contracted with the j -th index of tensor y . This defines a c -number for the network once one specifies the collection of tensors T_v associate to the graph G .

To define a tensor network state, we mark special boundary vertices $\partial \subset V$ and we leave the boundary vertices un-contracted. The resulting network now defines a pure state in the boundary Hilbert space $\mathcal{H}_\partial = \bigotimes_{v \in \partial} \mathcal{H}^v$ associated to the “dangling legs”:

$$|\Psi\rangle = \left(\bigotimes_{\{xy\} \in E} \langle xy| \right) \left(\bigotimes_{v \in V \setminus \partial} |T_v\rangle \right) \in \mathcal{H}_\partial \quad (2.45)$$

While we can work with a general graph, we will often be interested in models of AdS/CFT, where it is natural to pick a triangulation of two dimensional hyperbolic space, thought to represent a fixed time slice of the AdS_3 spacetime, see Fig. (2.5) (a). We fix all of the bond dimensions on this network to be the same, denoted as χ . We pick the boundary vertices of the network to be at a cutoff region near the boundary of hyperbolic space.

For RTNs, we demand that the state $|T_v\rangle$ is sampled from a uniform random ensemble on the tensor Hilbert space. This can be achieved by acting with a unitary matrix U_v picked from a Haar-random measure on some fixed anchor state $|0_v\rangle$. Then the average over such a measure can be readily done using Schur’s Lemma [111]:

$$\overline{(|V_v\rangle \langle V_v|)^{\otimes n}} = \int [DU_v] (U_v |0_v\rangle \langle 0_v| U_v^\dagger)^{\otimes n} \propto \sum_{g_v \in S_n} g_v \quad (2.46)$$

where g_v is a element of the symmetry group S_m whose action is to permute the contraction edges of the n -replicas. The state $|\Psi\rangle$ is unnormalized. Normalization can be achieved “on average” by dividing by the average of the norm of $|\Psi\rangle$. At large bond dimension this procedure is sufficient for our purposes.

We now consider a factorization of the boundary Hilbert space as $\mathcal{H}_\partial = \mathcal{H}_A \otimes \mathcal{H}_{\bar{A}}$. The n -th Rényi entropy of subregion A can be written as the expectation value of a twist operator Σ_A which acts on the tensor product of n copies of \mathcal{H}_A . The twist operator cyclically permutes the different copies of \mathcal{H}_A and we label the operation by τ_n , the maximal cyclic permutation element in S_n . After averaging and normalizing as described above one finds at large bond dimensions the moments of the density matrix can be written as ⁸

$$Z_n(A) \equiv \overline{\text{Tr} \rho_A^n} = \overline{\langle \Psi |^{\otimes n} \Sigma_A(\tau_n) | \Psi \rangle^{\otimes n}} = \sum_{\{g_v \in S_n\}_{b.c.}} \exp \left[- \sum_{e=\{x,y\} \in E} d(g_x, g_y) \ln \chi(e) \right], \quad (2.47)$$

where $\Sigma_A(g_A)$ is the twist operator on subregion A . This expression can be viewed as the partition function for a classical Ising-like model with nearest neighbor interactions where each Ising “spin” takes value in the symmetry group S_n . The interaction strength is given by the Cayley distance ⁹

$$d(g, h) = n - \#(gh^{-1}) \quad (2.48)$$

where $\#(\cdot)$ is a function that counts the total number of cycles of a group element, including trivial cycles that map a given element to itself. Cayley distance is a metric on the symmetric group in the sense that it measures the abstract distance between two elements $g, h \in S_n$, symmetric, semi-positive and satisfies triangle inequality, and $d(g, h) = 0$ iff $g = h$. Hence the energy function of the Ising model favors group elements that are “close” to each other in group space. The boundary conditions on the sum $\{g_v \in S_n\}_{b.c.}$ are dictated by the presence of the twist operators, i.e. we impose $g = \tau_n$ on boundary region $A \subset \partial$ and $g = e$ on $\bar{A} = \partial \setminus A$. In the case of large bond dimension, the Ising model is in its low temperature limit and is localized to its ground state. The field configuration in this limit is given by domains of group elements τ_n and e , separated by a domain wall as shown in Fig. (2.5) (b). Minimizing the energy of this domain wall requires it to be a minimal surface, thus reproducing the usual RT formula.

The Rényi entropy for ρ_A can be written as

$$\overline{S_n(A)} = \frac{1}{1-n} \overline{\left(\ln \frac{\text{Tr} \rho_A^n}{(\text{Tr} \rho_A)^n} \right)} \approx \frac{1}{1-n} \ln \frac{\overline{\text{Tr} \rho_A^n}}{(\overline{\text{Tr} \rho_A})^n} = \frac{1}{1-n} \ln \frac{\overline{Z_n}}{(\overline{Z_1})^n}, \quad (2.49)$$

where we have replaced the average over the logarithm by the logarithm of the averages of the partition function. The fluctuations around the average can be shown to be suppressed exponentially in bound dimension χ at large bond dimensions. More specifically, the normalized variance of the partition function around its average is given by

$$\overline{\left(\frac{Z_n}{\overline{Z_n}} - 1 \right)^2} = \frac{\overline{Z_n^2}}{(\overline{Z_n})^2} - 1. \quad (2.50)$$

The squared partition function can be shown to be dual to an Ising model with spin taking values in S_{2n} using a very similar approach. The boundary condition on this new model is $g = \tau_n \times \tau_n$ on A and $g = e$

⁸we have ignored the proportionality factor in Eq. (2.46), since it cancels out after we divide by the normalization of density matrix.

⁹We summarize various useful results for the symmetric group in Appendix A.

on \bar{A} . At large bond dimension the value of the partition function is simply the square of the original one, plus corrections in $O(1/\chi)$. It then follows that the variance Eq. (2.50) vanishes as $\chi \rightarrow \infty$. Since this result holds for all integer $n > 0$ one can prove a similar convergence on the spectrum of the density matrix itself, i.e. the eigenvalues of the RTN states are narrowly peaked around their average value. These results are known as *measure concentration*, which are known to hold for large random matrices; see [112].

Note that the above calculation gives the same results for the Rényi entropies $S_n(A)$ for all $n \geq 0$. The entanglement spectrum for the RTN is therefore flat, which is clearly not true for generic holographic states. Instead, RTN have been interpreted as models of fixed-area states in such theories [96–98]. Generic holographic states can be obtained as a superposition of fixed-area states. We will see in the later chapters that such superpositions naturally arise from the canonical purification without adding this structure in by hand.

2.5 A first pass

To set up the calculation for reflected entropy, we now consider a RTN defined by graph G and divide the boundary into three different regions $\partial = A \sqcup B \sqcup C$. As a simple example, we take both A and B to be connected intervals and trace out C to get the reduced density matrix ρ_{AB} . We will make use of the reflected entropy replica trick described in Sec. (2.3). To recapitulate, we want to construct the canonical purified density matrix

$$\rho_{AB} \rightarrow |\sqrt{\rho_{AB}}\rangle \langle \sqrt{\rho_{AB}}| \equiv \rho_{ABA^*B^*}, \quad (2.51)$$

where the A^* (respectively B^*) is the canonical purified counterpart of the original region. We achieve this by first computing the (m, n) -Rényi reflected entropies defined in Eq. (2.34). This is possible using a similar Ising-like model, for integer $n \geq 1$ and even integer $m \geq 2$. Using the same procedure as in Sec. (2.4), including an appropriate normalization that works at large bond dimension, we find:

$$S_R^{(m,n)}(A : B) \approx \frac{1}{1-n} \ln \left(\frac{Z_{m,n}}{(Z_{m,1})^n} \right), \quad (2.52)$$

$$Z_{m,n}(A, B) = \overline{\langle \Psi |^{\otimes mn} \Sigma_A(g_A) \Sigma_B(g_B) | \Psi \rangle^{\otimes mn}}, \quad (2.53)$$

$$Z_{m,1}(A, B) = \overline{\langle \Psi |^{\otimes m} \Sigma_{AB}(\tau_m) | \Psi \rangle^{\otimes m}}. \quad (2.54)$$

The group actions of twist operators g_A and g_B is given by Eq. (2.40). The partition functions of the Ising model $Z_{m,n}$ given by the sum over permutation group elements

$$Z_{m,n} = \sum_{\{g_v \in S_{mn}\}_{b.c.}} \exp \left[- \sum_{e=\{x,y\} \in E} d(g_x, g_y) \ln \chi(e) \right]. \quad (2.55)$$

The new boundary condition on the sum, denoted *b.c.*, imposes $g_v = g_A$ for $x \in A$, $g_v = g_B$ for $x \in B$ and $g_v = e$ for $x \in C$.

We now consider two natural saddle points, i.e. domain wall configurations for the Ising problem that arose in computing the (m, n) -Rényi reflected entropy. These saddles are the tensor network analogs of the saddle points that were considered in Ref. [56] and used to prove the reflected entropy/EWCS correspondence. These were also interpreted as arising from the gluing construction of Refs. [113, 114], which has a natural analog

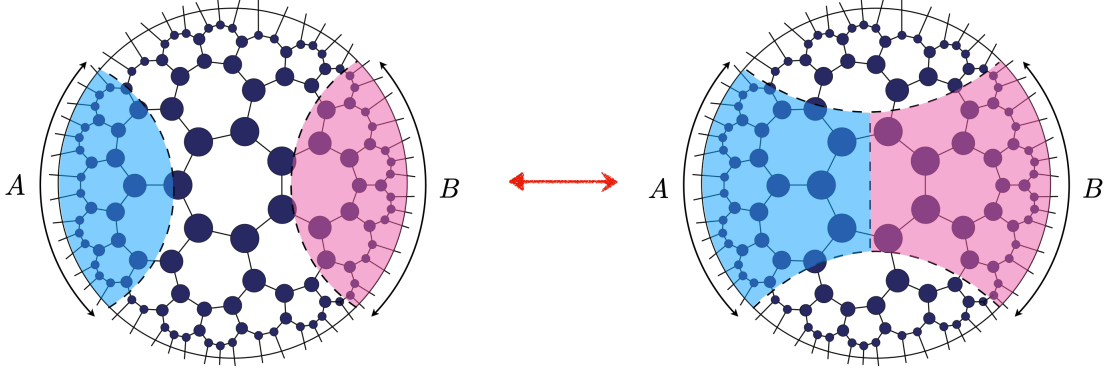


Figure 2.6: Two naive solutions for the spin Ising model for a RTN defined on a hyperbolic space. The domain for permutation group elements are indicated using different colors. The blue region indicates g_A , the red g_B , and white the identity permutation e . The left configuration is the naive disconnected saddle, and right configuration is the naive connected saddle.

in the tensor network case [115].¹⁰ In particular, these saddles are analogs of the Lewkowycz-Maldacena saddles [116] used to compute Rényi entropies in AdS/CFT.

With the above results at hand, we are now ready to make a first-pass calculation of the reflected entropy in RTN using the saddle-point approximation. The presentation in this section will be schematic and brief, merely touching on the issues that arise during the calculation. We return to those issues with more detailed treatments in Chapter 3 and Chapter 5, where we study the non-trivial corrections around the phase transition, and in Chapter 6, where we study the properties of saddles in generic RTNs using more advanced methods.

Imposing the boundary elements to be g_A on region A and g_B on region B and allowing the corresponding domains to propagate into the bulk, we immediately identify two possible geometrical saddles (see Fig. (2.6)). The first saddle is characterized by each region bounded by its minimal homology surface (we call this the *naive disconnected saddle*). The second saddle features a non-trivial entanglement wedge, with the minimal wedge cross-section marked as the domain wall for $g_A \leftrightarrow g_B$ (we call this the *naive connected saddle*). The tensions of these domain walls are found from the Cayley distances:

$$d(g_A, e) = d(g_B, e) = n(m - 1), \quad d(g_A, g_B) = 2(n - 1) \quad (2.56)$$

Assuming the naive disconnected saddle dominates and doing a simple analytic continuation to $(m, n) \rightarrow (1, 1)$ one finds that the reflected entropy vanishes, while a similar procedure for the naive connected saddles gives a reflected entropy proportional to the EW cross-section. It is then expected that as we vary the size of regions A, B , one of the two solutions gains dominance over the other, with a phase transition at some critical size. Furthermore, one can verify that the transition point occurs right at the point when the RT surface of $A \cup B$ jumps. Hence the conjecture “ $S_R(A : B) = 2EW(A : B)$ ” seems to be true in RTN.

We do expect that our construction of the two semi-classical saddles works well when the bulk is far from the transition point, where the sum in the partition function is strongly dominated by a single saddle. However there are several issues that arise from this proposal:

- This construction fails to correctly account for the n -Rényi reflected entropies at $m = 1$ even away from the phase transition. If we treat these saddles seriously for all (m, n) then we find the Rényi entropies

¹⁰This was one of several methods suggested for proving the correspondence in Ref. [56]. The other method is studying the modular flowed correlators, which doesn't obviously extend to the tensor network case.

for $n > 1$ at $m = 1$ are dominated (have smaller free energy) by the disconnected phase and thus vanish to leading order in $\ln \chi$. Taking the limit $n \rightarrow 1$ after setting $m = 1$ gives 0 for the reflected entropy even in the connected phase. In particular this indicates an order of limits issue that was first pointed out in Ref. [117]. This answer is not obviously inconsistent, however we will argue that it is nevertheless incorrect.

- While the two bulk solutions are legitimate saddles at integer $(m/2, n)$ and each carries physical significance, it is not obvious that other semi-classical bulk configurations do not dominate over these. There is ample reasoning to expect there would be other bulk solutions. First, the order of limits issue mentioned above suggests that the naive bulk solutions do not have nice analytical properties which may be resolved by inclusion of new saddles. Second, a similar situation happens for the negativity computations, where a series of non-trivial “replica symmetry breaking” elements are important in the semi-classical saddle solutions [118–120]. Indeed, we will show in the later chapters that there is such an element for reflected entropy as well, although the details differ significantly with negativity.
- At the EW phase transition there is considerable uncertainty with how to proceed. So far the calculations we discussed were based on some fixed integer replica number $n, m > 1$. To obtain the reflected entropy we need to analytically continue $n, m \rightarrow 1$. While the solutions we obtained above work independently, we need to include both of them to make a phase transition. However simply summing the two saddles is known to lead to incorrect results [121]. The simplest issue that arises is from the normalization. Sending $n \rightarrow 1$ we expect:

$$1 = \text{tr } \rho_{AA^*} = \text{tr} (\text{tr}_{BB^*} |\sqrt{\rho_{AB}}\rangle \langle \sqrt{\rho_{AB}}|) \quad (2.57)$$

However since we view the two bulk solutions as independent from one another, each of them contributes unity to the trace exactly at the phase transition. Adding those up we obtain a paradoxical result $\text{tr } \rho_{AA^*} = 2$. It is clear that we should somehow treat the two seemingly different saddles as limits of a more general class of solution.

- Indeed, around the phase transition point we expect there will be other previously sub-leading saddles that will smooth out the sharp transition. A notable example for such effect is the calculation of entanglement entropy for two disjoint regions [62, 63] (See also Ref. [15]), where a summation over a larger class of group elements called the non-crossing permutations is performed. In our case the problem is harder due to the appearance of the domain wall $g_A \leftrightarrow g_B$ in our bulk solution. However when we include a summation over a larger set of saddles, we also expect to find a smoothing out of the reflected entropy phase transition.

The above issues can be classified into two big categories:

1. The uncertainty of the dominant semi-classical saddles *away from* the phase transition.
2. The uncertainty of the sub-leading corrections *at the vicinity of* the phase transition.

These two problems are not independent of each other. For example understanding the first can help us determine what are the important saddles we should include to obtain the corrections in the second.

To answer the first problem, we will prove in the later chapters that there will be a new class of solutions featuring a new group element $X \in S_{mn}$ that can dominate the partition function. Using the notation

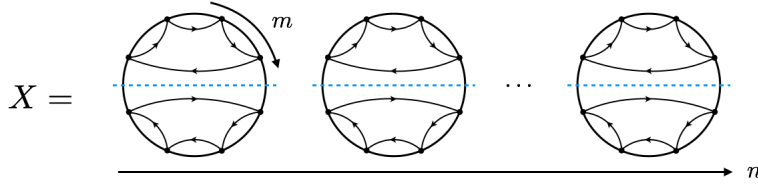


Figure 2.7: A graphical representation of X . It features maximal cyclic permutations in the upper and lower halves of each circle (separated by blue dashed lines).

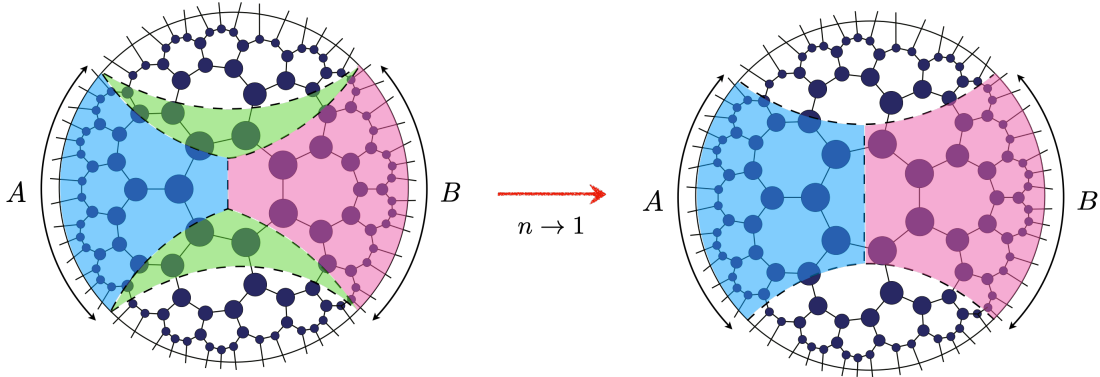


Figure 2.8: The bulk solution with the new element X (indicated as the green region). As $n \rightarrow 1$ the region disappears and we revert back to the naive connected saddle.

introduced in Sec. (2.3), the element X is given by

$$X = \prod_{j=1}^n (\tau_{m/2}^U \tau_{m/2}^D)^{[j]_n}, \quad \tau^U = (12 \cdots m/2), \quad \tau^D = (m/2 + 1 \cdots m), \quad (2.58)$$

where τ^U and τ^D are maximum cyclic permutations in the “upper” and “lower” m circles. A visualization of the actions of X is shown in Fig. (2.7). We will see that new element interacts with the existing solutions, and we will argue that phases involving X are the correct ones for computing the Rényi entropies at $m = 1$. Moreover, we prove rigorously in Chapter 6 that these are the *only* important saddles for RTNs defined on any graph, as long as one is only concerned with the parametric region away from phase transition. In short, the elements X “fill in” the spaces between the backreacted EW and the un-backreacted EW. As we continue $n \rightarrow 1$, the X regions slowly shrinks and give back the minimal cross-section solution, see Fig. (2.8).

The answer to the second problem is much more involved and intricate than the first one. The issues we list above suggest we need to sum over a larger set of non-trivial bulk saddles. For a generic RTN the bulk geometry is complicated, and it is not obvious how to construct these solutions a priori. However, we will show in later chapters that such summation is possible the case of a single tripartite random tensor (Chapter 3) and a pair of contracted random tensors (Chapter 5), see Fig. (2.9). That is, we are able to perform an analytic computation of the full entanglement spectrum of the canonical purified density matrix for these systems. Having the full eigenvalue spectrum is a very powerful result, as it allows us to construct effective descriptions of the canonical purification. We argue that these effective descriptions correspond to non-perturbative effects in the bulk as a genus expansion in the gravitational path integral. Although the answers we obtained for the second problem are limited only to the simplest networks, there is evidence that

EW phase transitions in general RTN and holography also follows a similar behavior, and we expect the lessons we learnt from these models hold generically true in other more complicated scenarios.

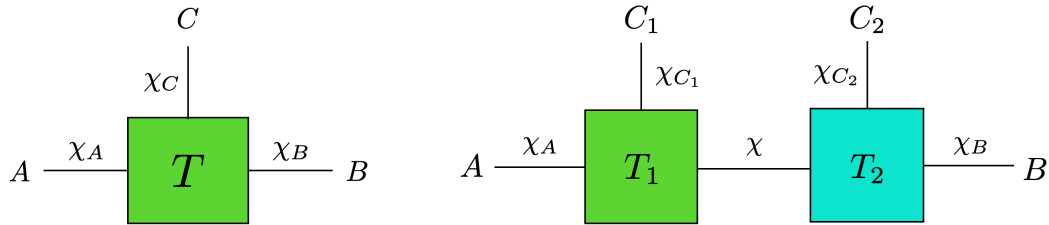


Figure 2.9: The simple tensor models for which we were able to extract analytical spectra of their canonical purifications. The left represents a tripartite single random tensor with bond dimensions $\chi_{A/B/C}$, which we study in detail in Chapter 3. The right represents a pair of random tensors contracted along a common internal bond χ , which we study in detail in Chapter 5.

Another advantage of working with simple tensors is that we are able to check our analytical answer directly with numerical simulations. Indeed we find that, in the case of both the 1TN and 2TN model, our analytical expressions for the reflected spectra match with the numerical results in the relevant large bond dimension limit, quantifying the corrections that smooth out the sharp jump of the reflected entropy around the phase transition.

Chapter 3

Single Random Tensor

In this chapter, we begin to explore the non-perturbative physics that describes the discontinuity of reflected entropy phase transition using a toy model of a single tripartite random tensor, which we refer to as *1TN*. The 1TN models a three-boundary wormhole with horizon areas fixed to a small window [96–98] and a large interior. This results in an EW phase transition as we tune the bond dimensions (the horizon areas). We compute the reflected entropy near such a phase transition, paying special attention to how non-perturbative effects smooth out the transition. We find a sharp, continuous transition analogous to the Page curve [61], which reproduces the expected discontinuous transition in the limit that the bond dimension goes to infinity.

The results presented in this chapter is mostly based on Ref. [48].

3.1 Summary of results

We now summarize some of the main points in this chapter:

- We prove some general results for the (m, n) -Rényi reflected entropy for 1TN, including various continuity arguments as a function of m which establishes independence of m away from the phase transition. These will serve as checks on our later computations, and help motivate the prescription we use to analytically continue in (m, n) . We then describe the phase diagram of dominant saddle points at integer $m/2, n$. See Sec. (3.3) and Sec. (3.4).
- We use a Schwinger-Dyson re-summation method similar to [15, 118] to compute the reflected spectrum for 1TN. We make an assumption about the class of diagrams that dominates, and prove this to be correct in various limits. The reflected spectrum thus obtained has two main components: A single eigenvalue representing the disconnected EW phase, and a broad peak with $\exp(2 \text{EW}(A : B))$ eigenvalues representing the connected EW phase. These two contributions are always present irrespective of the relevant phase, but their respective weights move around as we tune the bond dimensions in the tensor network. They make dominant contributions to the reflected entropy in their respective phases. We show a cartoon of the reflected spectrum for the single tensor model in Fig. (3.1). See Sec. (3.5) and Sec. (3.6).
- Based on the above we argue that near the phase transition both sets of eigenvalues contribute. In the

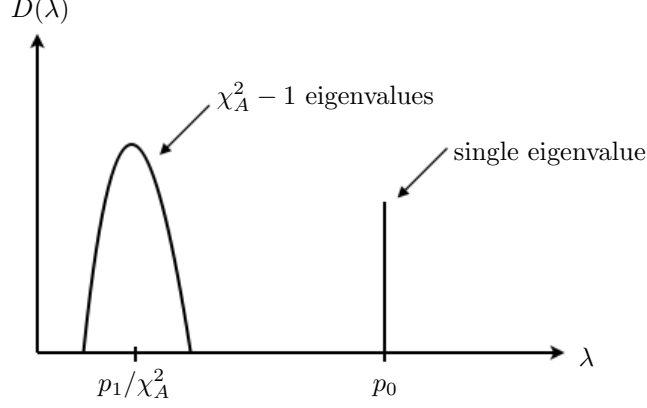


Figure 3.1: The reflected spectrum in the single tensor model has two superselection sectors corresponding to the disconnected and connected phase respectively.

single tensor, the reflected entropy takes the form:

$$S_R(A : B) = -p_0 \ln p_0 - p_1 \ln p_1 + p_1 \left(\ln \chi_A^2 - \frac{\chi_A^2}{2\chi_B^2} \right) + O(\chi_{A,B}^{-2}), \quad (3.1)$$

where $\chi_X \gg 1$ are the bond dimensions for $X = A, B, C$ and the classical probabilities are:

$$p_0 = \frac{\chi_C}{\chi_A \chi_B} {}_2F_1(1/2, -1/2; 2; \frac{\chi_C}{\chi_A \chi_B})^2, \quad p_1 + p_0 = 1, \quad (3.2)$$

At large bond dimensions this reproduces the characteristic jump in the reflected entropy, see Fig. (3.2). We argue that these results can be understood as arising from an effective description of the *entanglement structure* for the canonically purified state as a superposition of tensor networks states. Here, one state is described by a doubled random tensor network, representing the connected phase, while the other tensor network is trivially factorized:

$$\sqrt{\rho_{AB}} \sim \sqrt{p_1} \left(\begin{array}{c} A \\ \circ U \\ B \\ \circ U' \\ A^* \\ B^* \end{array} \right) + \sqrt{p_0} \left(\begin{array}{c} A \\ \left. \right) \\ A^* \\ \left. \right) \\ B^* \\ B \end{array} \right) \quad (3.3)$$

The two terms are weighted by the associated probabilities p_0 and $p_1 = 1 - p_0$. The reduced density matrices on AA^* are approximately orthogonal, so these represent (approximate) superselection sector with an associated area operator:

$$\mathcal{L}_{AA^*} = \bigoplus_{s=0,1} S_{vN}(\zeta_s) \quad (3.4)$$

where $\zeta_1 \approx 1_{AA^*}/\chi_A^2$ and $\zeta_0 = |1_A/\chi_A\rangle \langle 1_A/\chi_A|$. We also check the above results against numerics. See Sec. (3.7) and Sec. (3.9).

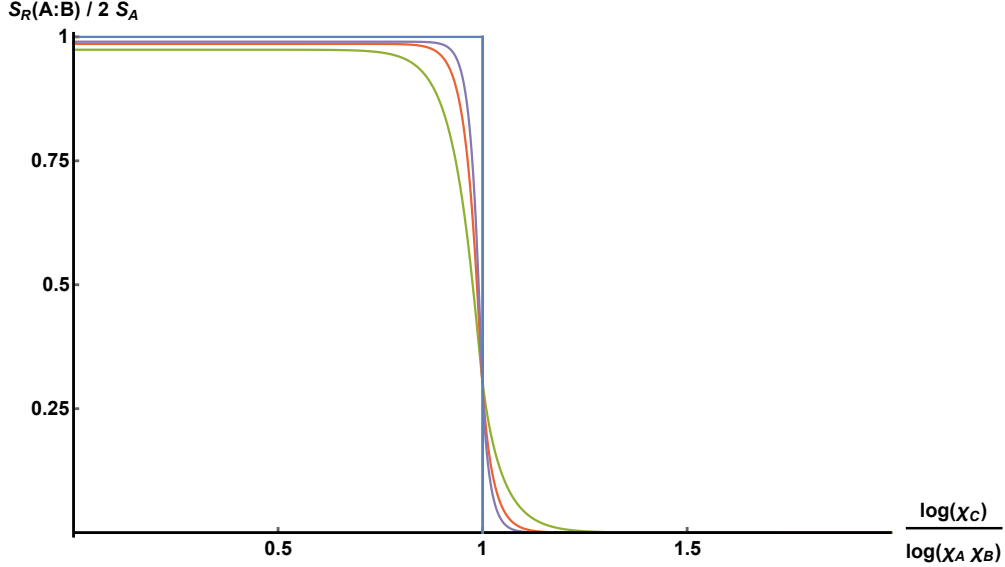


Figure 3.2: “Page curve” of the reflected entropy, for a single tripartite random tensor with bond dimensions χ_A, χ_B, χ_C . The blue curve corresponds to the infinite bond dimension limit, $\chi \rightarrow \infty$. The other curves correspond to large but finite bond dimension, correctly limiting to the blue curve as the bond dimension increases.

- Our results will resolve the order of limits issue pointed out in Ref. [117]. In particular if one applies the naive LM-like saddle point analysis in the limit $(m, n) \rightarrow (1, 1)$ then the “wrong” phase can dominate if one takes the limit $m \rightarrow 1$ first and then $n \rightarrow 1$, leading to a formula different from Eq. (2.32). This later formula fails several quantum information bounds, so one can rule out this order of limits on these grounds. However a better understanding of this issue and justification of the order of limit is desired. In fact we will show that no such order of limits issue occurs after we give a prescription for continuing the (m, n) -Rényi reflected entropies from $m \geq 2$ to $m = 1$. We will give evidence for this prescription based on the single random tensor, and show how it is consistent with a more general set of QI bounds.

Several appendices support our calculations, most notably Appendix C.1 where we give a proof of the phase diagram for the single network case.

3.2 Setup

Consider a single tripartite random tensor T with bond dimensions χ_A, χ_B and χ_C that prepares a state $|\psi\rangle_{ABC}$ on the Hilbert space \mathcal{H}_{ABC} . This setup can be thought of as a toy model for the holographic setting of a multiboundary wormhole with three asymptotic boundaries, where the area of the mouths $\mathcal{A}_{A,B,C}$ are related to the bond dimensions $\chi_{A,B,C}$ as

$$\log \chi_{A,B,C} = \frac{\mathcal{A}_{A,B,C}}{4G_N} \quad (3.5)$$

by the standard relation between the bulk spacetime and the tensor network that discretizes it [40, 122], as shown in Fig. (3.3). More so, when computing the Rényi entropy, there is an exact correspondence (including non-perturbative effects) between the single random tensor and the multiboundary wormhole when the

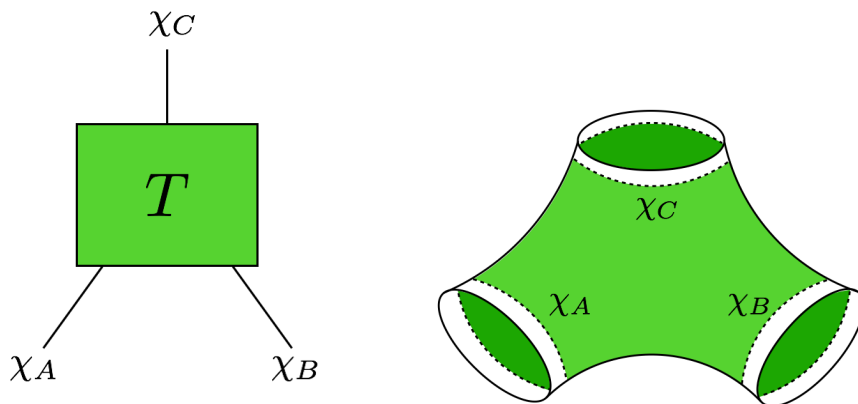


Figure 3.3: (left) A state on the Hilbert space \mathcal{H}_{ABC} is prepared by a single tripartite random tensor with bond dimensions χ_A , χ_B and χ_C . (right) The three-boundary wormhole solution, which is modeled by the single random tensor when its horizon areas are fixed to a small window. The horizon areas of the wormhole corresponds to the bond dimensions of the single tensor.

horizon areas are fixed to a parametrically small window [96–98].¹

Note that in order for the connection between the single tensor and the three boundary wormhole to be sharp, we require that the interior region is large enough that there are no other competing entanglement wedge cross sections except the horizons of A and B since there is no analog of such surfaces in the single tensor. It seems plausible that this can be arranged for by adding sufficient matter in the interior to support a long wormhole like in Ref. [123].

This setup is much more tractable than the general tensor network and allows us to understand phase transitions in the reflected entropy in detail. We will use the resolvent trick described in [15] to compute the exact entanglement spectrum of ρ_{AA^*} in the limit of large bond dimension. This allows us to compute the reflected entropy $S_R(A : B)$, along with other generalizations such as its Rényi versions, as a function of the bond dimensions. We will find a phase structure that is consistent with the holographic proposal [56] for the reflected entropy at least away from phase transitions, and the spectrum will smoothly interpolate between the different phases.

We summarize now the various parameter ranges we will be interested in, each some limit with $\chi_A, \chi_B, \chi_C \gg 1$. We consider the following fixed parameters as we take χ_i large:

$$x_A = \frac{\ln \chi_A}{\ln \chi_C} \quad x_B = \frac{\ln \chi_B}{\ln \chi_C} \quad (3.6)$$

with $0 < x_A, x_B < \infty$. The “entanglement wedge” phase transition, corresponding to the Page phase transition that we are mostly interested in, lives along the line $x_A + x_B = 1$. There are other phase boundaries along $x_A = 1 + x_B$ and $x_B = 1 + x_A$ where the derivative of the mutual information jumps. However, the reflected entropy $S_R(A : B)$ does not have interesting behavior here so we are less interested in them.

¹Note that by non-perturbative effects we mean effects of $O(e^{-1/G_N}) \sim \chi^k$ for some k , i.e., power law corrections in the bond dimension.

In terms of these parameters the mutual information approaches

$$\frac{I(A : B)}{\ln \chi_C} \rightarrow \begin{cases} 0, & x_A + x_B < 1 \\ x_A + x_B - 1, & x_A + x_B > 1 \ \& \ x_A - 1 < x_B < x_A + 1, \end{cases} \quad (3.7)$$

in the large bond dimensions limit. Also, as we will demonstrate below, the reflected entropy behaves like

$$\frac{S_R(A : B)}{\ln \chi_C} \rightarrow \begin{cases} 0, & x_A + x_B < 1 \\ 2 \min(x_A, x_B), & x_A + x_B > 1 \ \& \ x_A - 1 < x_B < x_A + 1. \end{cases} \quad (3.8)$$

Note the value of the reflected entropy in the connected phase matches the holographic expectation; it is the entanglement wedge cross-section in this single-tensor model. Our goal will be to compute this rigorously and to also study S_R near the phase boundaries.

Consider now the phase boundary near $x_A + x_B = 1$. Set:

$$q = \chi_A \chi_B / \chi_C, \quad y = \ln \chi_A / \ln \chi_B \quad (3.9)$$

We will explore the parameter range $0 < q < \infty$ and $0 < y < \infty$ fixed as we send $\chi_C \rightarrow \infty$. The mutual information is well studied in this limit as it can be computed from the entanglement entropies [61]. The behavior across the phase transition is generally referred to as the Page result/transition.

There is also another limit of interest at the edge of this phase boundary which lives near $x_B = 0$ and $x_A = 1$ where we fix $\chi_B \gg 1$ and send $\chi_C \rightarrow \infty$ holding $p = \chi_A / \chi_C$ fixed and χ_B fixed. This limit is mostly of interest because the analytic calculation is more tractable.

We start by proving certain results rigorously for the reflected entropy in different regimes of parameter space in Sec. (3.3). We then compute the phase diagram for the Rényi reflected entropy in the saddle point approximation in Sec. (3.4). We then analyze the phase transitions in reflected entropy by using the resolvent trick. Before doing so, in Sec. (3.5) we describe the phase transition in entanglement entropy which reproduces the Page curve as a warm up problem. This helps us establish the formalism and ingredients required to describe the reflected entropy phase transition in Sec. (3.6). We discuss the results of this calculation in Sec. (3.7) and check these against numerics in Sec. (3.9).

3.3 General considerations

Let us start by proving some rigorous results on reflected entropies and the Rényi generalizations in the large bond dimension limit. These results will help guide our way through the replica treatment of this problem.

The intuition behind the following result is that for a random state, the reduced density matrix ρ_{AB} has an approximately flat spectrum, implying it is approximately proportional to a projector at large bond dimension. This implies that the states $|\rho_{AB}^{m/2}\rangle$ for different m and after normalization, are close in the Hilbert space norm. This implies a certain continuity in m for the (m, n) -Rényi reflected entropies. While continuity results for Rényi entropies are weak, the states in question are sufficiently close at large bond dimension to imply a useful result. We prove the following lemma:

Lemma 3.1. *The (m, n) -Rényi reflected entropy for a tripartite random state with $\chi_C < \chi_A \chi_B$ satisfies a*

continuity bound as a function of m for $1 \leq m \leq 2$ and $n > 1$:

$$\left| \overline{S_R^{(1,n)}(A : B)} - \overline{S_R^{(m,n)}(A : B)} \right| \leq \frac{2n}{n-1} \left(\frac{(m-1)\chi_C}{\chi_A \chi_B} \right)^{1/2} \min\{\chi_A^{2(n-1)}, \chi_B^{2(n-1)}\} \quad (3.10)$$

Also the reflected entropy (at $n = 1$) satisfies:

$$\left| \overline{S_R(A : B)} - \overline{S_R^{(m,1)}(A : B)} \right| < 2 \left(\frac{(m-1)\chi_C}{\chi_A \chi_B} \right)^{1/2} \min\{\ln \chi_A, \ln \chi_B\} + \ln 2 \quad (3.11)$$

Proof. We will also need the continuity bound for reflected entropy [58], which follows from applying the Fannes-Audenaert inequality [124, 125] to the reflected entropy. In fact we will need a Rényi generalization of this inequality, which is usually considered to be a weak bound [126]:

$$\left| S_n(\rho_{AA^*}^{(1)}) - S_n(\rho_{AA^*}^{(m)}) \right| \leq \frac{\chi_A^{2(n-1)}}{n-1} (1 - (1-T)^n - (\chi_A^2 - 1)^{1-n} T^n) \quad n \geq 1 \quad (3.12)$$

$$\leq \frac{n\chi_A^{2(n-1)}}{n-1} T \quad (3.13)$$

where T is the trace distance:

$$T = \|\rho_{AA^*}^{(1)} - \rho_{AA^*}^{(m)}\|_1 \leq 2\sqrt{1 - |\langle \psi^{(1)} | \psi^{(m)} \rangle|^2} = 2\sqrt{1 - \frac{(\text{Tr} \rho_{AB}^{(1+m)/2})^2}{\text{Tr} \rho_{AB}^m}} \quad (3.14)$$

The later inequality follows from the bound of the trace norm by the fidelity, as well as monotonicity of the fidelity under tracing from ABA^*B^* to AA^* . The overlap $|\langle \psi^{(1)} | \psi^{(m)} \rangle|$ is the fidelity on ABA^*B^* . The last equality uses the Hilbert-Schmidt norm. We estimate:

$$\begin{aligned} T &\leq 2\sqrt{1 - \exp(-(m-1)(S_{(m+1)/2}(\rho_{AB}) - S_m(\rho_{AB})))} \\ &\leq 2((m-1))^{1/2} (S_{(m+1)/2}(\rho_{AB}) - S_m(\rho_{AB}))^{1/2} \\ &\leq 2((m-1))^{1/2} (\ln \chi_C - S_2(\rho_{AB}))^{1/2} \end{aligned} \quad (3.15)$$

where we used some elementary bounds and in the last line we used monotonicity of the Rényi entropies as a function of m : $S_m \geq S_2$ for $m \leq 2$. We also used $S_{(m+1)/2}(\rho_{AB}) \leq \ln \chi_C$ which follows from Schmidt rank and the assumption $\chi_C < \chi_A \chi_B$. Averaging over the Haar random unitaries we have:

$$\overline{T} \leq 2((m-1))^{1/2} \overline{(\ln \chi_C - S_2(\rho_{AB}))^{1/2}} \quad (3.16)$$

We now apply the Lubkin result [127], see Ref. [128]:

$$\overline{\langle S_2(\rho_{AB}) \rangle} \geq \ln \chi_C - \frac{\chi_C}{\chi_A \chi_B} \quad (3.17)$$

So we have:

$$\overline{(\ln \chi_C - S_2(\rho_{AB}))^{1/2}} \leq \left(\overline{\ln \chi_C - S_2(\rho_{AB})} \right)^{1/2} \leq \left(\frac{\chi_C}{\chi_A \chi_B} \right)^{1/2} \quad (3.18)$$

by Jensen and concavity of the square root. Putting all these inequalities together we find that:

$$\bar{T} \leq 2((m-1))^{1/2} \left(\frac{\chi_C}{\chi_A \chi_B} \right)^{1/2} \quad (3.19)$$

which gives Eq. (3.10) after using the symmetry between A and B . A similar analysis for the $n = 1$ case using now the Fannes continuity result and the bound on the Shannon correction term $-T \ln T - (1-T) \ln(1-T) \leq \ln 2$ gives Eq. (3.11). \square

While we focused on $1 \leq m \leq 2$ there is no obstruction to finding similar results for later $m > 2$, say by generalizing the Lubkin bound Eq. (3.17) for other integer Rényi entropies. The most efficient way to do this for general m would involve taking the large bond dimension limit, whereas the result above is for any bond dimensions. We expect the conclusions are the same for $m > 2$.

As an application of these results, consider sitting on the (x_A, x_B) phase diagram above $x_A + x_B \geq 1$ and assume that $x_A < x_B$. We see that there is always some window $1 \leq n \leq n_c$ where the leading large χ (m, n) -Rényi entropies are provably independent of m :

$$\overline{|S_n(\rho_{AA^*}^{(1)}) - S_n(\rho_{AA^*}^{(m)})|} \leq \frac{2n((m-1))^{1/2}}{n-1} \chi_C^{1/2(1-x_A-x_B)+2x_A(n-1)} \quad (3.20)$$

which implies that the change in the (m, n) -Rényi reflected entropy as a function of m is non-perturbatively small for $n > 1$ and $n < n_c$ where $n_c = 5/4 - (1-x_B)/(4x_A) \geq 1$. Additionally at $n = 1$ the shift as a function of m can be order 1. Based on explicit calculations we will argue that this is true for all $n > 1$, although these results will be less rigorous, relying on certain assumptions about the analytic continuation. In this way Lemma 3.1 will serve as a check on our method for analytic continuation.

We can make a similar argument for $\chi_A \chi_B \leq \chi_C$, but now we expect the reflected density matrix to be close to a factorized density matrix $\rho_{AB} \approx 1_A \otimes 1_B / (\chi_A \chi_B)$. This allows us to make a stronger statement since the reflected entropy of this density matrix vanishes.

Lemma 3.2. *For a tripartite random state with $\chi_A \chi_B \leq \chi_C$*

$$\overline{S_R^{(m,n)}(A : B)} \leq \frac{2n}{n-1} \left(\frac{\chi_A \chi_B}{\chi_C} \right)^{1/2} \min\{\chi_A^{2(n-1)}, \chi_B^{2(n-1)}\} \quad (3.21)$$

for $1 \leq m \leq 2$ and $n > 1$. Similarly for the entropy:

$$\overline{S_R^{(m,1)}(A : B)} \leq 2 \left(\frac{\chi_A \chi_B}{\chi_C} \right)^{1/2} \min\{\ln \chi_A, \ln \chi_B\} + \ln 2 \quad (3.22)$$

Proof. We use the same proof idea as in Lemma 3.1, except now one of our states in the Fannes-like inequalities is the reduced state $\tilde{\rho}_{AA^*}$ associated to the canonical purification for the maximally mixed state $\tilde{\rho}_{AB} = 1_{AB} / (\chi_A \chi_B)$. Of course the reflected entropy vanishes for this state, and thus $\tilde{\rho}_{AA^*}$ is a minimal projection. Again the trace distance can be estimated in terms of the overlap $|\langle \psi^{(m)} | \tilde{\rho}_{AB}^{1/2} \rangle|^2 = (\text{Tr} \rho_{AB}^{m/2})^2 / (\chi_A \chi_B \text{Tr} \rho_{AB}^m)$. For $1 \leq m \leq 2$ we apply monotonicity $S_{m/2} \geq S_2$ and $S_m \geq S_2$ and finally we use the Lubkin bound (for the case $\chi_A \chi_B > \chi_C$). This gives the stated results. \square

Note that if we simply set $m = 1$ we see this constrains the *answer* that we are interested in. Both the reflected entropy and the Rényi reflected entropies are provably non-perturbatively small, i.e. power law

suppressed in χ_C , for $x_A + x_B < 1$ and for $n > 1$ (using monotonicity with n).

3.4 Phase diagram and Rényi reflected entropies

In order to proceed we will use the replica trick at $(m/2, n)$ integer to evaluate the (m, n) -Rényi reflected entropy. We will find a phase diagram as a function of the bond dimensions and then give some arguments for how to analytically continue this phase diagram away from the integers.

The integer moments of the density matrix for the reflected entropy reads (up to the usual small corrections from the treatment of the normalization):

$$\overline{\text{Tr}(\rho_{AA^*}^{(m)})^n} = \frac{\sum_{g \in S_{mn}} \exp(-\ln \chi_C(x_A d(g, g_A) + x_B d(g, g_B) + d(g, e)))}{\left(\sum_{g \in S_m} \exp(-\ln \chi_C((x_A + x_B)d(g, \tau_m) + d(g, e)))\right)^n} \quad (3.23)$$

We now simply find the phase diagram (as a function of the various bond dimensions) at fixed integer $(m/2, n)$. At each point in the phase diagram some set of g dominates. We will find a picture of the phase diagram where at each point one of four possible elements dominates: e, g_A, g_B and a new element we call X .

To set the stage we are interested in minimizing the following free energy:

$$f(g) = x_A d(g, g_A) + x_B d(g, g_B) + d(g, e), \quad g \in S_{mn} \quad (3.24)$$

where we have factored out $\ln \chi_C$. Since f is a linear function of x_A and x_B , any region of the phase diagram in the $(x_A \geq 0, x_B \geq 0)$ plane must be convex.² The Cayley distance, as a metric on S_{mn} , satisfies the triangle inequality $d(g_1, g_2) + d(g_2, g_3) \geq d(g_1, g_3)$. It will be useful to introduce the geodesics in the Cayley that pass between two group elements g_1, g_2 as the set that saturates this inequality. We denote these elements using:

$$\Gamma(g_1, g_2) = \{g \in S_{mn} : d(g_1, g) + d(g, g_2) = d(g_1, g_2)\} \quad (3.25)$$

See Appendix A for a discussion of elements on this geodesic.

We now determine the two-dimensional phase diagram in terms of (x_A, x_B) . As a first step we proceed as follows. We solve for the dominating elements at various special points in the phase diagram. Then we fill in the undetermined regions by the convexity of the phase diagram. As a limiting case, it is easy to show that the identity element e dominates at $x_A = x_B = 0$ and $g_A(g_B)$ dominates at $x_A(x_B) \rightarrow \infty$. For the other regions:

- Along the line $x_A + x_B = 1$:

$$\begin{aligned} f &= x_A(d(g, g_A) + d(g, e)) + (1 - x_A)(d(g, g_B) + d(g, e)) \\ &\geq x_A d(g_A, e) + (1 - x_A) d(g_B, e) = n(m - 1) \end{aligned} \quad (3.26)$$

with saturation achieved for $g \in \Gamma(g_A, e) \cap \Gamma(g_B, e)$.

²See Lemma C.2 in Appendix C.1 for a proof.

- Along the line $x_A = x_B + 1$:

$$\begin{aligned} f &= x_B(d(g, g_A) + d(g, g_B)) + (d(g, g_A) + d(g, e)) \\ &\geq x_B d(g_A, g_B) + d(g_A, e) = 2(n-1)x_B + n(m-1) \end{aligned} \quad (3.27)$$

with saturation for $g = g_A$ since this is the single element in $\Gamma(g_A, g_B) \cap \Gamma(g_A, e)$.

- Along the line $x_B = x_A + 1$ is the same as above with $A \leftrightarrow B$.

After applying convexity to the above results the only region left is for $x_A + x_B > 1$ and $1 - x_B < x_A < 1 + x_B$. This is of course the main region of interest where the entanglement wedge is connected. Because there is no common geodesic element between all three elements (that is $\Gamma(g_A, e) \cap \Gamma(g_B, e) \cap \Gamma(g_A, g_B)$ is empty), there is no simple argument that determines the phase in this region.³ This is the main difference between our calculation and the negativity computations in [118–120]. Instead we must seek other methods for determining the phase in this region. Indeed, there exists a proof for this main region, providing a complete picture of the phase diagram. However, because the proof is relatively involved, we present it in Appendix C.1 for interested readers. For now we just summarize the results we find:

- There exists a new phase with a non-trivial element, which we denote X , in the triangular region $x_A + x_B \geq 1, x_A < 1 + x_B(1 - 2/n), x_B < 1 + x_A(1 - 2/n)$. X is a group element with the special property that it lies on the joint geodesic $\Gamma(g_A, e) \cap \Gamma(g_B, e)$ while being closest to g_A or g_B whose form is given in Sec. (2.5) which we replicate here:

$$X = \prod_{i=1}^n (\tau_{m/2}^U \tau_{m/2}^D)^{[j]_n} \quad (3.28)$$

where $\tau_{m/2}^U$ is the cyclic permutation that acts on the upper half of each *puddle* (that is it cyclically permutes elements $\beta = 1, \dots, m/2$ within each fixed puddle) and $\tau_{m/2}^D$ is the full cyclic permutation on the lower half (cyclically permuting elements $\beta = m/2 + 1, \dots, m$ within each fixed puddle). See the discussion in Sec. (2.3) to unpack this notation.

- The phase of $g = g_A$ smoothly extends into the main region and occupies the upper-diagonal wedge $x_A > x_B, x_A > 1 + x_B(1 - 2/n)$. The same is also true for g_B , where it occupies the lower-diagonal wedge. At the boundary where the two phases meet (i.e. $x_A = x_B$ and $x_A > n/2$) we have a large degeneracy shared by a complicated set of elements.⁴
- No other elements are dominant in the space between the co-existence boundaries.

We give an example of the phase diagram in Fig. (3.4).

We now extract the consequences for S_R and its Rényi versions. For the disconnected entanglement wedge with $x_A + x_B < 1$, there is only ever one phase for all (n, m) so it is reasonable that this remains the case upon analytic continuation. Indeed this always gives $S_R^{(m, n)} = 0$ upon correctly normalizing the free energy. This is of course consistent with Lemma 3.2.

³If there was a common geodesic element then this element would sit on all three edges of the region under consideration - so we could then fill the phase diagram inside the region with this common element using convexity.

⁴For detailed description of this set please see Appendix C.2.

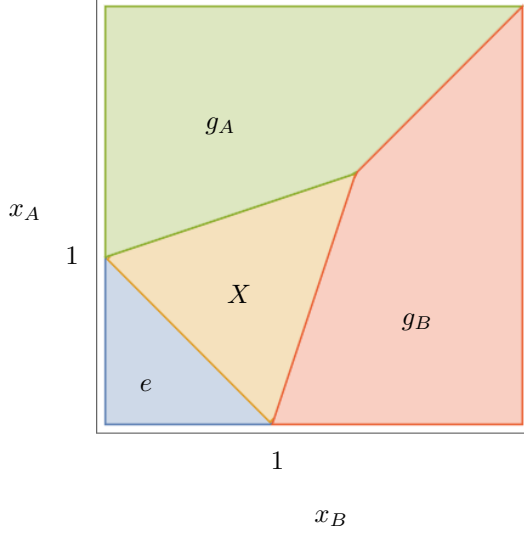


Figure 3.4: An example of the phase diagram of the single tripartite tensor. The tip of the X triangle lies at $(n/2, n/2)$.

From now on we consider only $x_A + x_B > 1$. The free energies of the four possible phases, including the normalization subtraction (which is different to the disconnected phase) are:

$$\begin{aligned}
 F(e)/\ln \chi_C &= (x_A + x_B - 1)(m - 1)n, & F(X)/\ln \chi_C &= -n + (x_A + x_B)n, \\
 F(g_A)/\ln \chi_C &= 2x_B(n - 1), & F(g_B)/\ln \chi_C &= 2x_A(n - 1)
 \end{aligned}
 \tag{3.29}$$

We make some observations. Firstly, at fixed (x_A, x_B) in certain regions of the phase diagram there is a new novel behavior where there is a phase transition as a function of n . This indicates that the entanglement spectrum is *not flat* for the reflected density matrix, as compared to the usual reduced density matrix of a random pure state. Secondly, if we do a very naive analytic continuation away from the integers, where we include all four phases and re-minimize at each (n, m) we arise at some puzzling results. For example at $m = 1$ and fixed $n > 1$ the e phase has minimal free energy and:

$$S_R^{(1,n)} \Big|_{\text{naive}} = 0, \quad n > 1
 \tag{3.30}$$

Which seems to imply that taking $\lim n \rightarrow 1$, $S_R(A : B) = 0$ for $x_A + x_B > 1$ which cannot be the case. In particular it violates the mutual information bound $S_R \geq I$. Previously this was attributed to an order of limits issue [117] where one must take $\lim_{m \rightarrow 1} \lim_{n \rightarrow 1}$ to get the right answer - indeed here that resolution does work. However this result gives a very puzzling set of Rényi entropies, which were naively still consistent. However we can now observe using Lemma 3.1 that they are in fact not consistent, since for $m = 2$, we see that either $F(X) = F(e)$ or $F(g_{A,B})$ dominates and neither gives the same reflected entropy as the naive $m = 1$ phase with $g = e$ given in Eq. (3.30). This is inconsistent with the continuity bounds of Lemma 3.1, at least in some window of parameters.

Note that one way to understand the origin of this latter issue is as follows. The Cayley distance between X and e reads

$$d(X, e) = n(m - 2)
 \tag{3.31}$$

For $m < 2$ this is negative. The effect of this negative tension is to exchange the two phases $e \leftrightarrow X$ in the phase diagram Fig. (3.4). This leads to the dominance of the e phase even deep in the phase diagram where the entanglement wedge is connected.

The resolution that we land on is to simply discard the $F(e)$ saddle for $x_A + x_B > 1$. This is reasonable since it never appears in the $x_A + x_B > 1$ part of the phase diagram for integer $(n, m/2)$. This will now give a different answer for the Rényi entropies as compared to the naive analysis. We motivate this prescription as follows. Rather than analytically continue the Rényi entropies we will analytically continue the *spectrum* of $\rho_{AA^*}^{(m)}$ from $m > 2$ down to $m = 1$. This has the same effect of discarding the e saddle. In fact the analytic continuation in m is trivial since there is simply no dependence on m in the free energies of X, g_A, g_B . This is now consistent with the bounds we derived in Lemma 3.1. The Rényi entropies read:

$$S_R^{(m,n)} = \ln \chi_C \times \min \left\{ 2x_B, 2x_A, \frac{n}{n-1}(x_B + x_A - 1) \right\} \quad n \geq 1 \quad (3.32)$$

and the entanglement spectrum defined via:

$$\text{Tr}(\rho_{AA^*}^{(m)})^n = \int d\lambda \lambda^n D(\lambda) \quad (3.33)$$

is given by:

$$D(\lambda) = D_1 \delta(\lambda - \lambda_1) + \delta(\lambda - \lambda_0), \quad D_1 = \min\{\chi_C^{2x_A}, \chi_C^{2x_B}\} \quad (3.34)$$

where $\lambda_0 = \chi_C^{1-x_A-x_B}$ and $\lambda_1 = \max\{\chi_C^{-2x_A}, \chi_C^{-2x_B}, \lambda_0\}$.⁵

This is a crude approximation to the actual spectrum that we will compute in the next section. One obvious crude feature, for example, is that it has one more than the allowed number of non-zero eigenvalues, $\min\{\chi_A^2, \chi_B^2\}$, although this is clearly a small correction in the large χ_C limit.

We now turn to an examination of the phase transition near $x_A + x_B = 1$. This will give some further evidence for the prescription given above, and will also give a more complete picture of the reflected entropy and spectrum. It is clear from the above discussion that there are potentially many g elements that we need to sum up in order to compute the cross-over corrections. While we might attempt to directly sum over a class of g this approach turns out to be somewhat ad-hoc. The main difficulty is that certain classes of elements can be more important at different values of n , so the issue of which elements to include is mixed up with the question of how to analytically continue in n . This is in turn related to the fact that the spectrum itself does not have a uniform limit as $\chi \rightarrow \infty$, being made up of distinct contributions. Instead, in the next few sections, we will develop a diagrammatic approach that attempts to directly extract the spectrum. Having said this we briefly discuss an explicit sum over elements in Appendix C.2, where we do find consistent results.

3.5 Schwinger-Dyson for entanglement entropy

In this section we will present a standard diagrammatic technique for computing the entanglement spectrum of a Haar random pure state on a bipartite Hilbert space AB reduced to A [61]. This is of course the setting for the Page curve, so these results are very well known. We review it here just to setup notation used in the

⁵Note that for $x_A < x_B - 1$ then $n(x_B + x_A - 1) > 2nx_A > 2(n-1)x_A$ so the last possibility in Eq. (3.32) is never dominant for $n \geq 1$. We interpret this to say that the single eigenvalue λ_0 gets absorbed by the large set of D_1 eigenvalues at λ_1 in this particular part of the phase diagram. We have written the spectrum in a way that is consistent with this.

next section for the reflected entanglement spectrum problem.

The approach we present was first proposed by Ref. [129–131]. It was recently applied to find the entanglement entropy of JT gravity [15] and generic fixed area states [46]. Similar techniques were used to calculate the negativity [119, 132]. This powerful approach enables us to write down the Schwinger-Dyson equation for the *resolvent* of ρ_{AB} , which then gives full information about the entanglement spectrum.

A density matrix $|\psi\rangle\langle\psi|$ is represented as a four-legged tensor

$$|\psi\rangle\langle\psi| = \begin{array}{c} \blacktriangle \quad \blacktriangle \\ \text{A} \quad \text{B} \quad \text{B}^* \quad \text{A}^* \end{array} \quad (3.35)$$

where we use black (green) lines to represent the subspace associated to A (B). We can form the reduced density matrix by tracing over the B indices

$$\rho_A = \text{Tr}_B |\psi\rangle\langle\psi| = \begin{array}{c} \blacktriangle \quad \blacktriangle \\ \text{A} \quad \text{A} \end{array} \quad (3.36)$$

Averaging over random states is accomplished by means of pair contractions between bras and kets. In Sec. (2.4) we reviewed the fact that an average over (the m -th power of) a Haar random state can be recast as a summation over permutation group elements $g \in S_m$. In terms of diagrams these permutations become pairwise contractions between the bras and kets:

$$\overline{(|\psi\rangle\langle\psi|)^{\otimes m}} \propto \sum \begin{array}{c} \text{all possible contractions} \\ \blacktriangle \quad \blacktriangle \quad \blacktriangle \quad \dots \quad \blacktriangle \\ \text{A} \quad \text{B} \quad \text{A} \quad \dots \quad \text{B} \end{array} \quad (3.37)$$

A single pair contraction is defined by simply connecting the corresponding legs:

$$\begin{array}{c} \blacktriangle \quad \blacktriangle \\ \text{A} \quad \text{B} \end{array} \equiv \frac{1}{\chi_A \chi_B} \begin{array}{c} \text{---} \\ \text{---} \\ \text{---} \end{array} \quad (3.38)$$

A solid black (green) line represents the Kronecker delta. The purpose of the $(\chi_A \chi_B)^{-1}$ factor associated to each contraction is to maintain the correct normalization of the density matrix. The element $g \in S_m$ is recovered by tracing out the contractions from bras to kets. This allows one to recover the Haar averaged expression Eq. (2.47).

As a simple example, let us compute the second Rényi entropy (purity) of the reduced state using this

method. Connecting the lower legs appropriately we have

$$\begin{aligned} \overline{\text{Tr}\rho_A^2} &= \text{Diagram 1} + \text{Diagram 2} \\ &= \frac{1}{\chi_A} + \frac{1}{\chi_B} \end{aligned} \tag{3.39}$$

where we have used the fact that a full contraction of black (green) loop gives a factor of χ_A (χ_B), the corresponding Hilbert space dimension.

To get the full eigenvalue distribution of ρ_A we will make use of the resolvent trick. The resolvent $R(\lambda)$ for the density matrix ρ_A is defined formally as

$$R(\lambda) = \text{tr} \left(\frac{1}{\lambda - \rho_A} \right) \tag{3.40}$$

from which one can extract the eigenvalue distribution function $D(\lambda)$ using

$$D(\lambda) = -\frac{1}{\pi} \lim_{\epsilon \rightarrow 0} \text{Im} R(\lambda + i\epsilon) \tag{3.41}$$

To evaluate $R(\lambda)$, we expand the matrix inverse around $\lambda = \infty$:

$$R_{ij}(\lambda) = \frac{\chi_A}{\lambda} \delta_{ij} + \sum_{m=1}^{\infty} \frac{(\rho_A^m)_{ij}}{\lambda^{m+1}}. \tag{3.42}$$

In terms of diagrams, this is

$$\text{Diagram } R = \frac{1}{\lambda} \text{Diagram 1} + \frac{1}{\lambda^2} \text{Diagram 2} + \frac{1}{\lambda^3} \text{Diagram 3} + \dots \tag{3.43}$$

where we have restricted our summation to planar diagrams only, or equivalently, over all the corresponding non-crossing permutations. The contribution of non-planar diagrams are always suppressed in the limit of the large bond dimension.

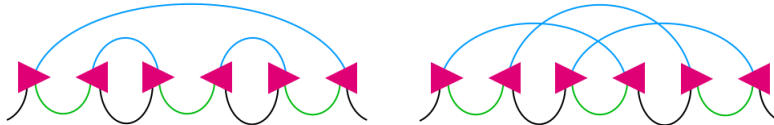


Figure 3.5: (left) An example of the planar diagram in the calculating ρ^3 , featuring a non-crossing permutation for the contraction. (right) An example of a non-planar diagram. The contribution is always suppressed by powers of χ .

Now denote $F_{ij}(\lambda)$ to be the connected part of the resolvent, defined by

$$\begin{aligned} \text{---} \bigcirc R \text{---} &= \frac{1}{\lambda} \text{---} + \frac{1}{\lambda^2} \text{---} \bigcirc F \text{---} + \frac{1}{\lambda^3} \text{---} \bigcirc F \text{---} \bigcirc F \text{---} + \dots \\ &= \frac{1}{\lambda - F} \end{aligned} \quad (3.44)$$

It allows us to write down a Schwinger-Dyson equation for $R_{ij}(\lambda)$ and $F_{ij}(\lambda)$:

$$\text{---} \bigcirc F \text{---} = \text{---} \bigcirc F \text{---} + \frac{1}{\lambda} \text{---} \bigcirc F \text{---} \bigcirc \lambda R \text{---} + \frac{1}{\lambda^2} \text{---} \bigcirc F \text{---} \bigcirc \lambda R \text{---} \bigcirc \lambda R \text{---} + \dots \quad (3.45)$$

which after taking the trace gives rise to the following algebraic equation

$$\text{tr } F_{ij}(\lambda) = 1 + \sum_{m=1}^{\infty} \frac{R(\lambda)^m}{(\chi_A \chi_B)^m} = \frac{1}{1 - \frac{R(\lambda)}{\chi_A \chi_B}} \quad (3.46)$$

Combining this with Eq. (3.44), and using the fact that both R and F are proportional to the identity matrix (as implied by contraction rules) we obtain a quadratic equation for $R(\lambda)$:

$$\frac{\lambda R^2(\lambda)}{\chi_A \chi_B} + \left(\frac{1}{\chi_A} - \frac{1}{\chi_B} - \lambda \right) R(\lambda) + \chi_A = 0 \quad (3.47)$$

Solving for $R(\lambda)$ and picking the square root sign by demanding the correct behavior at $\lambda \rightarrow \infty$ we find

$$R(\lambda) = \frac{\chi_A \chi_B}{2\lambda} \left(\lambda - \frac{1}{\chi_A} + \frac{1}{\chi_B} - \sqrt{(\lambda - \lambda_-)(\lambda - \lambda_+)} \right), \quad \lambda_{\pm} = \left(\frac{1}{\sqrt{\chi_A}} \pm \frac{1}{\sqrt{\chi_B}} \right)^2 \quad (3.48)$$

and

$$D(\lambda) = \frac{\chi_A \chi_B}{2\pi\lambda} \sqrt{(\lambda - \lambda_-)(\lambda_+ - \lambda)} + \delta(\lambda)(\chi_A - \chi_B)\theta(\chi_A - \chi_B). \quad (3.49)$$

Thus, we have found that the eigenvalue spectrum consists of a large peak within the range $[\lambda_-, \lambda_+]$ and a number of extra zero eigenvalues when $\chi_A > \chi_B$. This is the famous *Marchenko-Pastur (MP) distribution*. It describes the singular value distribution of a random $m \times n$ matrix when both $m, n \gg 1$. This result was first shown by Page [61]. Using the spectrum, the entanglement entropy is given by

$$S(A) = -\text{tr } \rho_A \ln \rho_A = \begin{cases} \log(\chi_A) - \frac{\chi_A}{2\chi_B}, & \chi_A < \chi_B \\ \log(\chi_B) - \frac{\chi_B}{2\chi_A}, & \chi_B < \chi_A. \end{cases} \quad (3.50)$$

up to an overall normalization factor that we will correct for later. In terms of diagrams, this is (e.g. for $m = 6$)

$$\begin{aligned}
 (\rho_{AB}^{m/2})^\Gamma &= \text{diagram 1}, & (\rho_{AB}^{m/2})^{\Gamma^*} &= \text{diagram 2}, \\
 \rho_{AA^*}^m &= \text{diagram 3}
 \end{aligned} \tag{3.56}$$

In the following calculations we will represent them diagrammatically using a short-hand:

$$\frac{1}{\sqrt{\lambda}} \text{diagram 4} = \text{diagram 5} \tag{3.57}$$

From these results we can infer an alternative expression for matrix $\mathbb{R}(\lambda)$:

$$\mathbb{R}(\lambda) = \sum_{n=0}^{\infty} \lambda^{-1-n} \begin{pmatrix} (\rho_{AA^*}^{(m)})^n & 0 \\ 0 & (\rho_{BB^*}^{(m)})^n \end{pmatrix} \tag{3.58}$$

$$+ \sum_{n=1}^{\infty} \lambda^{-1/2-n} \begin{pmatrix} 0 & (\rho_{AA^*}^{(m)})^{n-1} (\rho_{AB}^{m/2})^{\Gamma^\dagger} \\ (\rho_{BB^*}^{(m)})^{n-1} (\rho_{AB}^{m/2})^\Gamma & 0 \end{pmatrix}, \tag{3.59}$$

which diagrammatically looks like

$$\mathbb{R}(\lambda) = \frac{1}{\lambda} \left(\begin{array}{cc} \text{diagram 6} + \dots & \text{diagram 7} + \dots \\ \text{diagram 8} + \dots & \text{diagram 9} + \dots \end{array} \right). \tag{3.60}$$

Thus the actual resolvent we are interested in is

$$R(\lambda) = \text{Tr}_{AA^*}(\mathbb{R}_{11}(\lambda)). \tag{3.61}$$

Now, as in the calculation of the entanglement entropy, the Haar averaging over the states is done by summing over all possible pair contractions over bras and kets. We call each pattern of contractions a *diagram*. We call a single copy of $(\rho_{AB}^{m/2})^\Gamma$ a *puddle*. Each diagram corresponds to an element in $g \in S_{mk/2}$ where k is the total number of puddles. A sub-diagram is a subset of puddles and associated contractions that act

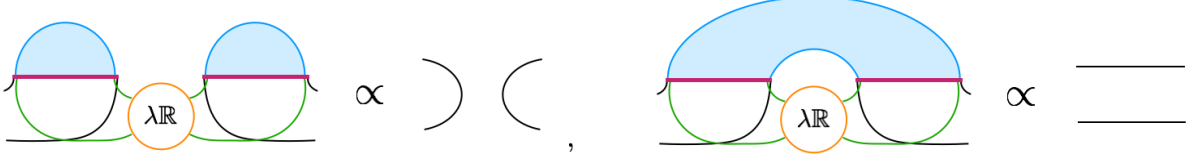


Figure 3.6: Example contractions of the diagram that give rise to the projector or the identity, where it should be clear that all the possible diagrams are either proportional to identity operator $1_{AA^*}, 1_{BB^*}$, or one of the four projectors $|\epsilon_{A,B}\rangle\langle\epsilon_{A,B}|$.

only inside this subset. We say a diagram is *connected* if the diagram cannot be split into more than one sub-diagrams each made up of a *contiguous* set of puddles. Otherwise the diagram is *disconnected*.

Consider the connected part of \mathbb{R} , which we call \mathbb{F} . This corresponds to a sum over a subset of diagrams which are connected. We have

$$\mathbb{R}(\lambda) = \frac{1}{\lambda} + \frac{\mathbb{F}}{\lambda^2} + \frac{\mathbb{F}^2}{\lambda^3} + \dots = \frac{1}{\lambda - \mathbb{F}} \quad (3.62)$$

Note that \mathbb{F} and \mathbb{R} are constrained to take the following form: (all possible contractions give rise to this form, for example see Fig. (3.6))

$$\mathbb{F}(\lambda) = \begin{pmatrix} G_{11}(1_{AA^*} - e_A) + F_{11}e_A & F_{12}|\epsilon_A\rangle\langle\epsilon_B| \\ F_{21}|\epsilon_B\rangle\langle\epsilon_A| & G_{22}(1_{BB^*} - e_B) + F_{22}e_B \end{pmatrix}, \quad (3.63)$$

where $|\epsilon_A\rangle = \chi_A^{-1/2}|1_A\rangle$ is the maximally mixed state on AA^* (same for $|\epsilon_B\rangle$), $e_A = |\epsilon_A\rangle\langle\epsilon_A|$ and $e_B = |\epsilon_B\rangle\langle\epsilon_B|$ are normalized minimal projectors and F is a 2×2 matrix of scalars (not to be confused with \mathbb{F}). Also 1_{AA^*} is the identity acting on \mathcal{H}_{AA^*} etc. A similar form applies to

$$\mathbb{R}(\lambda) = \begin{pmatrix} S_{11}(1_{AA^*} - e_A) + R_{11}e_A & R_{12}|\epsilon_A\rangle\langle\epsilon_B| \\ R_{21}|\epsilon_B\rangle\langle\epsilon_A| & S_{22}(1_{BB^*} - e_B) + R_{22}e_B \end{pmatrix}. \quad (3.64)$$

Meanwhile we must have $F_{12}^* = F_{21}$ and $R_{12}^* = R_{21}$ (for real λ). Then from Eq. (3.62) we obtain:

$$S_{11} = (\lambda - G_{11})^{-1}, \quad S_{22} = (\lambda - G_{22})^{-1}, \quad R_{ij} = (\lambda - F)_{ij}^{-1}, \quad (3.65)$$

and the resolvent of interest is

$$R(\lambda) = \text{tr } \mathbb{R}_{11} = (\chi_A^2 - 1)S_{11} + R_{11}. \quad (3.66)$$

We now seek a Schwinger-Dyson equation for $\mathbb{F}(\lambda)$. There will be many different diagrammatic contributions to \mathbb{F} . We can organize them by the number of \mathbb{R} insertions: $k - 1$ for $k = 1, 2, \dots$. That is $\mathbb{F} = \sum_k \mathbb{F}^{(k)}$. Note

that k is also the number of external puddles in each diagram:

$$\mathbb{F}(\lambda) = \lambda \left(\begin{array}{c} \text{conn.} \\ \text{conn.} \end{array} \right) \quad (3.67)$$

where we have used the shorthand *conn.* to indicate all the connected contractions.

The lowest order contribution ($k = 1$) for \mathbb{F} only features diagrams with a single disconnected puddle:

$$\mathbb{F}^{(1)} = D_m \sqrt{\lambda} \begin{pmatrix} 0 & |\epsilon_A\rangle \langle \epsilon_B| \\ |\epsilon_B\rangle \langle \epsilon_A| & 0 \end{pmatrix}, \quad (3.68)$$

where the number D_m is defined as

$$D_m = \frac{\sqrt{\lambda}}{\sqrt{\chi_A \chi_B}} \begin{array}{c} h \in S_{m/2} \\ \text{conn.} \end{array} = \sum_{h \in S_{m/2}} \chi_C^{\#(h) - m/2} (\chi_A \chi_B)^{\#(h^{-1} \tau_{m/2}) - (m+1)/2}. \quad (3.69)$$

At large χ , this sum is dominated by non-crossing permutations and we have $D_m \simeq \chi_C^{(m+1)/2} \sqrt{q} C_{m/2}(1/q) \sim O(\chi_C^{(m+1/2)})$. Using Eq. (3.65) we can find the lowest order solution for the matrix R :

$$R_{ij} = \frac{1}{\lambda - D_m^2} \begin{pmatrix} 1 & \lambda^{-1/2} D_m \\ \lambda^{-1/2} D_m & 1 \end{pmatrix}_{ij} + \dots \quad (3.70)$$

This represents the single eigenvalue contribution we had originally around Eq. (3.34) by summing elements. We will find significant corrections to this pole from the next order.

At the second order ($k = 2$), we have diagrams that contain exactly one \mathbb{R} insertion. Their contributions split into two parts according to the pattern of contractions between the first and last legs of each puddle. That is if we follow the contractions in the resulting diagram - following lines above and below puddles - the pattern of outer contractions tracks where the first and last legs connect to in the rest of the diagram.

For example, let's take a look at the diagonal component $\mathbb{F}_{11}^{(2)}$:

$$\frac{\mathbb{F}_{11}^{(2)}}{\lambda} = \begin{array}{c} \text{conn.} \\ \text{conn.} \end{array} = \begin{array}{c} \text{conn.} \\ \text{conn.} \end{array} + \begin{array}{c} \text{conn.} \\ \text{conn.} \end{array} \quad (3.71)$$

where the bold blue lines after the second equality represent the pattern/topology of outer contractions. By using this pattern to follow the green and black curves below the puddle, we can see if the contribution should be either proportional to the identity and thus contributing to (G_{11}) or a projector, contributing to (F_{11}) .

On the other hand, for the off-diagonal part of $\mathbb{F}^{(2)}$, both permutation types only contribute to the projector, e.g.,

$$\frac{\mathbb{F}_{12}^{(2)}}{\lambda} = \text{conn.} = \lambda R_{21} \left(\text{diagram 1} + \text{diagram 2} \right). \quad (3.72)$$

For both $\mathbb{F}_{11}^{(2)}$ and $\mathbb{F}_{12}^{(2)}$, the first diagram shown above necessarily involve elements $h \in S_m$ that are crossing or higher genus, so these are naturally suppressed by powers of external bond dimensions.

We can compute these diagrams to find $\mathbb{F}^{(2)}$ written as:

$$\begin{aligned} (\chi_A \chi_B)^2 G_{11}^{(2)} &= \lambda (S_{22}(\chi_B^2 - 1) + R_{22}) B_m, \\ (\chi_A \chi_B)^2 G_{22}^{(2)} &= \lambda (S_{11}(\chi_A^2 - 1) + R_{11}) B_m, \end{aligned} \quad (3.73)$$

$$\frac{(\chi_A \chi_B)^2}{\lambda} \begin{pmatrix} F_{11} & F_{12} \\ F_{21} & F_{22} \end{pmatrix}^{(2)} = \begin{pmatrix} R_{22} & R_{21} \\ R_{12} & R_{11} \end{pmatrix} E_m + \begin{pmatrix} S_{22}(\chi_B^2 - 1) & 0 \\ 0 & S_{11}(\chi_A^2 - 1) \end{pmatrix} B_m, \quad (3.74)$$

where the numbers B_m and E_m are defined by the following diagrams

$$B_m = \lambda \text{diagram 1}, \quad E_m = \lambda (\chi_A \chi_B) \text{diagram 2}. \quad (3.75)$$

More explicitly, we have

$$B_m = \frac{1}{(\chi_A \chi_B)^2 - 1} \left(-E_m + \sum_{h \in S_m \setminus S_{m/2} \times S_{m/2}} \chi_C^{\#(h)-m} (\chi_A \chi_B)^{\#(h^{-1}\tau_m)-m+2} \right) \quad (3.76)$$

$$E_m = \sum_{h \in S_m \setminus S_{m/2} \times S_{m/2}} \chi_C^{\#(h)-m} (\chi_A \chi_B)^{\#(h^{-1}\tau_{m/2} \times \tau_{m/2})-m+1}, \quad (3.77)$$

where we have used the identity

$$\begin{aligned} & \text{diagram 1} - \frac{1}{\chi_A \chi_B} \text{diagram 2} \\ &= \left(1 - \frac{1}{(\chi_A \chi_B)^2} \right) \text{diagram 1} \end{aligned}, \quad (3.78)$$

which follows from the fact that crossing permutations are projected out from the LHS.

We now conjecture that the main contribution to the matrix \mathbb{F} comes from lowest two orders in k , i.e.

$\mathbb{F} \simeq \mathbb{F}^{(1)} + \mathbb{F}^{(2)}$, in large bond dimensions. Unfortunately this truncation does not obviously follow from a genus counting argument. We base our conjecture on four pieces of evidence: First, we explicitly calculated the contribution from $k = 3$ and a special class of $k = 4$ diagrams and found that they only give corrections to higher orders of χ . Secondly we power counted a particular class of diagrams for general k (which we believe to be the dominant contributions for k) and find it to be suppressed by powers of χ . Thirdly, although our diagrammatic approach is not entirely the same as the direct summation of group elements in App. C.2, the two approaches give results that differ only by sub-leading χ corrections. Finally, we numerically evaluated the reflected entropy and eigenvalue spectrum for a Haar random state and we indeed find good match to the analytical results obtain from this truncation. The numerical results will be discussed in Sec. (3.9).

We rescale various quantities to restore the correct normalization from Eq. (3.52)

$$G \rightarrow GZ_1, \quad F \rightarrow FZ_1, \quad S \rightarrow S/Z_1, \quad R \rightarrow R/Z_1, \quad \lambda \rightarrow \lambda Z_1 \quad (3.79)$$

in which all the above equations take the same form but with $\widehat{B}_m = B_m/Z_1$, $\widehat{E}_m = E_m/Z_1$ and $\widehat{D}_m = D_m/Z_1^{1/2}$ and these hatted quantities are now all $\mathcal{O}(1)$ at large χ_C with q fixed. We have the sum rule:

$$\widehat{D}_m^2 + \left(1 - \frac{1}{(\chi_A \chi_B)^2}\right) \widehat{B}_m + \frac{1}{(\chi_A \chi_B)^2} \widehat{E}_m = 1 \quad (3.80)$$

We now attempt to solve for the system of matrix equations Eq. (3.65), Eq. (3.73)-Eq. (3.74). We can completely solve this system if we make one approximation, which we will later check is self-consistent. We will assume that we can drop the “back-reaction” of R on Eq. (3.73) that determined S_{11}, S_{22} . We have

$$(\chi_A \chi_B)^2 (\lambda - S_{11}^{-1}) = \lambda S_{22} (\chi_B^2 - 1) \widehat{B}_m, \quad (\chi_A \chi_B)^2 (\lambda - S_{22}^{-1}) = \lambda S_{11} (\chi_A^2 - 1) \widehat{B}_m \quad (3.81)$$

The solution is

$$(\chi_A^2 - 1) S_{11}, (\chi_B^2 - 1) S_{22} = \frac{\chi_A^2 \chi_B^2}{2 \widehat{B}_m \lambda} \left(\lambda - \sqrt{(\lambda - \lambda_+)(\lambda - \lambda_-)} \right) \pm \frac{\chi_A^2 - \chi_B^2}{2 \lambda} \quad (3.82)$$

where

$$\lambda_{\pm} = \frac{\widehat{B}_m}{\chi_A^2 \chi_B^2} \left(\chi_A^2 + \chi_B^2 - 2 \pm 2 \sqrt{(\chi_A^2 - 1)(\chi_B^2 - 1)} \right) \quad (3.83)$$

This is a Marchenko-Pastur distribution with support between $\lambda_{\pm} \simeq \widehat{B}_m (\chi_A^{-1} \pm \chi_B^{-1})^2$ and $\min(\chi_A^2 - 1, \chi_B^2 - 1)$ eigenvalues. We can check that our initial assumption for solving S_{11}, S_{22} is indeed valid since $R_{11} \sim \mathcal{O}(1)$ and $(\chi_A^2 - 1) S_{11} \sim \chi_B^2 \chi_A^2$. The validity of this assumption breaks down at $\lambda \gg \chi_A^{-2}, \chi_B^{-2}$, but as we have seen already, this is well outside the spectral weight of the MP distribution and so does not effect the spectrum that we find.

The second equation Eq. (3.74) determines correction to the leading order solution of matrix R_{ij} Eq. (3.70) we obtained earlier. Together with Eq. (3.65) and Eq. (3.68), this yields a quadratic equation of 2×2 matrices. We can solve this equation completely, although the algebra is a bit more involved and the it only features corrections of $\mathcal{O}(\chi^{-2})$ and higher orders. For this reason we only summarize our findings here:

1. The position of the single pole at $\lambda = \widehat{D}_m^2$ is now shifted to

$$\lambda = \widehat{D}_m^2 + \left(\frac{1}{\chi_A^2} + \frac{1}{\chi_B^2} \right) \widehat{B}_m + \mathcal{O}(\chi^{-4}) \quad (3.84)$$

2. The same pole is now resolved to a small peak of width

$$\delta\lambda \sim \frac{8\widehat{D}_m\sqrt{\widehat{E}_m}}{\chi_A\chi_B} + O(\chi^{-4}) \quad (3.85)$$

For the detailed form of R and its derivation please refer to appendix C.3. As a final remark, we stress here that the various techniques we used here, such as the truncation at $k = 2$ and various approximations we made to solve the SD equation, rely on the limit of large bond dimension $\chi_A, \chi_B, \chi_C \rightarrow \infty$. However we do not require all the external bond dimensions to be large for our analysis to work. In fact there are two interesting parameter ranges to take:

1. $\chi_A, \chi_B, \chi_C \rightarrow \infty$ with $q = \chi_A\chi_B/\chi_C$ and $r = \chi_A/\chi_B$ fixed:

This is the main parameter range of our interest in this chapter. The resolvent has two interesting regimes. For $\lambda \sim 1/\chi_C$ we simply find the MP distribution

$$R(\lambda) = \frac{(\chi_A\chi_B)^2}{2\widehat{B}_m\lambda} \left(\lambda - \sqrt{(\lambda - \lambda_+)(\lambda - \lambda_-)} \right) + \frac{\chi_A^2 - \chi_B^2}{2\lambda} \quad (3.86)$$

And for $\lambda = \widehat{D}_m \sim O(\chi_c^0)$ we find a simple pole. This pole is resolved into a mini-peak each with width $\delta\lambda \simeq 8\widehat{D}_m\sqrt{\widehat{E}_m}\chi_C^{-1}$ for finite χ_C .

2. $\chi_A, \chi_C \rightarrow \infty$ with χ_A/χ_C and χ_B fixed:

The main MP distribution becomes narrow, approximating a pole centered at $\lambda_{\pm} = \chi_B^{-2}$ with weight $\chi_B^2 - 1$. The other single pole is located at $\lambda = \widehat{B}_m\chi_B^{-2} + \widehat{D}_m^2$:

$$R(\lambda) = \frac{\chi_B^2 - 1}{\lambda - \widehat{B}_m\chi_B^{-2}} + \frac{1}{\lambda - \widehat{B}_m\chi_B^{-2} - \widehat{D}_m^2} \quad (3.87)$$

The first, smaller peak, is resolved into a peak with width $\delta\lambda \simeq 8\widehat{D}_m\sqrt{\widehat{E}_m}(\chi_A\chi_B)^{-1}$, and the larger peak is resolved into an MP distribution of width:

$$\delta\lambda = \frac{1}{\chi_A} \frac{2\widehat{B}_m\sqrt{\chi_B^2 - 1}}{\chi_B^2} \quad (3.88)$$

This regime is not relevant to the random tensor model we study in this chapter. However it will prove to be useful for a 2-site random tensor model that aims to better model the holographic phase transition, which we will aim to discuss in Chapter 5.

3.7 Spectrum and reflected entropy

We have seen how to use diagrammatic methods to construct the resolvent of the reflected entropy. We summarize what we have found here:

$$R(\lambda) = \frac{(\chi_A\chi_B)^2}{2\lambda} \left(\frac{\lambda}{\widehat{B}_m} + \left(\frac{1}{\chi_B^2} - \frac{1}{\chi_A^2} \right) - \sqrt{(\lambda/\widehat{B}_m - \lambda_+)(\lambda/\widehat{B}_m - \lambda_-)} \right) + \frac{1}{\lambda - \widehat{D}_m^2} \quad (3.89)$$

with

$$\lambda_{\pm} = \frac{1}{(\chi_A \chi_B)^2} \left(\sqrt{\chi_A^2 - 1} \pm \sqrt{\chi_B^2 - 1} \right)^2 \quad (3.90)$$

We have given evidence that this form is asymptotically correct under the limit $\chi_C \rightarrow \infty$ with $q = \chi_A \chi_B / \chi_C$ and $r = \chi_A / \chi_B$ fixed. For higher order corrections to the resolvent refer to the previous section and Appendix C.3. Under the limit of large bond dimension, the permutation sums \widehat{B}_m and \widehat{D}_m are dominated by non-crossing permutations and can be expressed in terms of q-Catalan numbers⁷.

$$\widehat{D}_m^2 \simeq \frac{C_{m/2}(q^{-1})^2}{C_m(q^{-1})} \equiv p_0, \quad \widehat{B}_m \simeq \frac{C_m(q^{-1}) - C_{m/2}(q^{-1})^2}{C_m(q^{-1})} \equiv p_1 \quad (3.91)$$

We now have the simplified sum rule:

$$p_0 + p_1 = 1 \quad (3.92)$$

We will see that these quantities act like classical probabilities, which control the phase transition between the connected and disconnected entanglement wedges, with q being the tuning parameter. We have the following asymptotic expressions:

$$(p_0, p_1) \sim \begin{cases} (1 - m^2 q/4, m^2 q/4), & q \ll 1 \\ (1/q, 1 - 1/q), & q \gg 1 \end{cases} \quad (3.93)$$

and around $q \sim 1$ the two probabilities are both order 1.

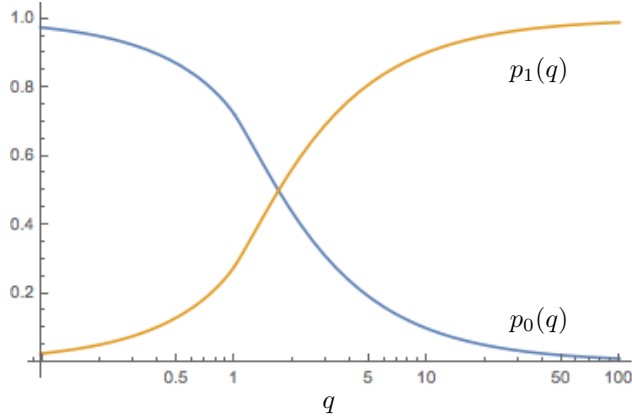


Figure 3.7: The plot showing the trend of $p_i(q)$. We have taken $m = 1$ here.

The reflected entropy that follows from this resolvent is given by (assuming $\chi_A < \chi_B$)

$$S_R = -p_0 \ln p_0 - p_1 \ln p_1 + p_1 \left(\ln \chi_A^2 - \frac{\chi_A^2}{2\chi_B^2} \right) + O(\chi^{-2}) \quad (3.94)$$

This is the main result of this section. Note that the entropy has a contribution from the classical Shannon entropy of a single bit p_i plus a term proportional to what seems to be the entropy of a Haar random state on AA^*BB^* reduced to AA^* (the standard Page result). This contribution however is multiplied by p_1 .

⁷The q-Catalan numbers generalize the Catalan numbers away from $q = 1$. They can be written in terms of Hypergeometric functions. For the complete definition see Appendix A.

We can better understand the physics by looking at the eigenvalue spectrum:

$$D(\lambda) = \frac{(\chi_A \chi_B)^2}{2\pi\lambda} \sqrt{(\lambda_+ - \lambda/p_1)(\lambda/p_1 - \lambda_-)} + \delta(\lambda)(\chi_A^2 - \chi_B^2)\theta(\chi_A^2 - \chi_B^2) + \delta(\lambda - p_0) \quad (3.95)$$

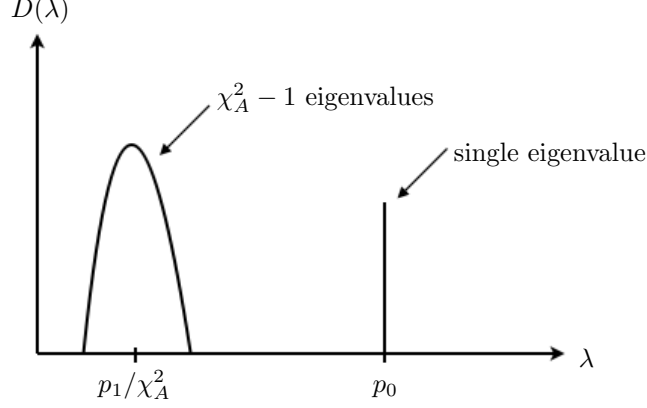


Figure 3.8: The spectrum obtained from the resolvent Eq. (3.95). We take $\chi_A < \chi_B$ here so the MP distribution has no zero eigenvalues.

We see that the spectrum is given by a shifted Marchenko-Pastur distribution with a total of $\min(\chi_A^2 - 1, \chi_B^2 - 1)$ eigenvalues, plus a single eigenvalue located at $\lambda = p_0$. The Rényi entropies can be reconstructed by the sum of the moments of the two pieces in resolvent

$$S_n(AA^*) = \frac{1}{1-n} \ln \left(p_0^n + \chi_A^{2(1-n)} r^{-2} C_n(r^2) p_1^n \right) \quad (3.96)$$

where $r = \chi_A^2/\chi_B^2$. Note that the (m, n) dependence has essentially factorized: the only m dependence is through the probabilities $p_0(m), p_1(m)$.

The Rényi entropies have three different approximate behaviors based on the relative ratio of the external bond dimensions. We have:

$$S_n(AA^*) \approx \begin{cases} \frac{n}{1-n} \ln p_0 \approx 0, & \chi_{AB} \ll \chi_C \\ \frac{n}{1-n} \ln p_0 \approx \frac{n}{n-1} \ln \frac{\chi_{AB}}{\chi_C}, & \chi_C \ll \chi_{AB} \ll \chi_C \chi_A^{\frac{2(n-1)}{n}} \\ \approx 2 \ln \chi_B, & \chi_{AB} \gg \chi_C \chi_B^{\frac{2(n-1)}{n}} \end{cases} \quad (3.97)$$

and we have assumed $\chi_A \leq \chi_B$ and $n > 1$. These three different behaviors exactly match the three phases we found in Sec. (3.4), and their transitions match the phase boundary lines in Fig. (3.4). As we take $n \rightarrow 1$ the middle regime vanishes and we get back the single transition in the reflected entropy as expected, as we move from disconnected to connected entanglement wedges.

3.8 Effective description

Based on the results of the previous subsection, we now give an alternative effective description of the canonically purified state and its m generalization: $|\rho_{AB}^{m/2}\rangle \langle \rho_{AB}^{m/2}|$. Consider the following pure state on the Hilbert space AA^*BB^* : a superposition of a factorized state (with probability p_0) plus a random maximally

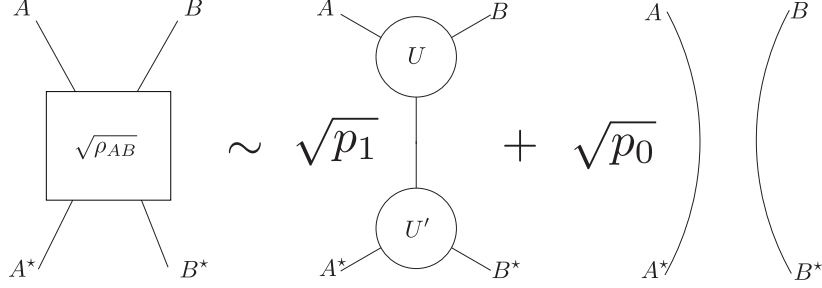


Figure 3.9: An illustration of Eq. (3.98). We argue that the canonical purification is effectively described by a sum over tensor network states. The first state comes from the natural doubling procedure outlined in Ref. [115] for the connected entanglement wedge of the original network in Fig. (3.3) and the second is the trivial factorized network which is obtained by doubling the trivial/disconnected entanglement wedge of the original network.

entangled state (with probability p_1):

$$|\psi_{\text{eff}}\rangle = p_0^{1/2} |\chi_0\rangle + p_1^{1/2} |\chi_1\rangle \quad (3.98)$$

Here $|\chi_0\rangle = |1_A/\chi_A\rangle_{AA^*} \otimes |1_B/\chi_B\rangle_{BB^*}$ is the factorized state and we construct $|\chi_1\rangle$ using a random tensor network state as follows. We use a new network geometry that comes from doubling across the connected entanglement wedge:

$$|\chi_1\rangle \propto \langle 1_C | U_{ABC} U'_{A^*B^*C^*} | 0 \rangle_{ABC} | 0 \rangle_{A^*B^*C^*} \quad (3.99)$$

where $|1_C\rangle$ is the (canonical) un-normalized maximally entangled state on the CC^* Hilbert space. It is natural to pick $U_{ABC} |0\rangle_{ABC}$ to be the same random state that we started with, but we choose $U'_{A^*B^*C^*}$ to be an independent Haar random unitary. We will comment on this choice further below. See Fig. (3.9) for a picture of these states.

Note that $|\chi_0\rangle$ is the canonical purification of a maximally mixed state $\rho_{AB} = 1_{AB}/(\chi_A\chi_B)$ - this is the density matrix ρ_{AB} that usually arises from a Haar random state reduced to AB when $\chi_C > \chi_A\chi_B$. And, $|\chi_1\rangle$ is the natural guess for the canonical purification of the original Haar random state reduced to AB when $\chi_C < \chi_A\chi_B$: that is, when the entanglement wedge is connected. The doubling procedure is motivated by the AdS/CFT discussion in [56].

The claim is that $|\psi_{\text{eff}}\rangle$ has the same entanglement structure as $|\rho_{AB}^{m/2}\rangle$, at large bond dimension and for all m (note that $p_{0,1}$ depend on m). In particular we will see that it has the same AA^* entanglement spectrum. Similarly, observe that the two states $|\chi_{0,1}\rangle$, when working in their respective phases, give the same expectation values for operators in AB as the original density matrix ρ_{AB} . Thus the entanglement structure for sub-regions of AB is also maintained, at least away from the phase transition. Since we think of the entanglement structure as being closely linked to the emergent bulk geometry, we can think of $|\psi_{\text{eff}}\rangle$ as capturing the effective geometry of the canonical purification.

Such superpositions Eq. (3.98) over different tensor networks, have been postulated as models of gravitational states in AdS/CFT [37, 96, 97, 133, 134], see also [135]. In particular these states allow for non-trivial fluctuations in the area of the RT surface, and do not suffer from the issue of a flat entanglement spectrum that is not expected in typical holographic states. Each wavefunction in the superposition is then thought of as a fixed area state, where the gravitational state is projected onto approximate eigenstates of the area operator.

More specifically, on the physical Hilbert space the reduced density matrices on AA^* will have approximately orthogonal support:

$$\text{supp}((\rho_0)_{AA^*}) \perp \text{supp}((\rho_1)_{AA^*}) \quad \text{supp}((\rho_0)_{BB^*}) \perp \text{supp}((\rho_1)_{BB^*}) \quad (3.100)$$

So the resulting states behave like approximate superselection sectors with respect to AA^* : the phase between the two components in the wavefunction is unobservable when restricting to AA^* or BB^* . This turns out to be approximately true for $|\chi_0\rangle, |\chi_1\rangle$, in particular because of how we chose $U'_{A^*B^*C^*}$ in Eq. (3.99): we picked an independent random unitary not equal to $(U_{ABC})^\dagger$. This latter choice might have seemed more natural, considering the $m = 2$ case $|\rho_{AB}\rangle$ exactly gives such a network, albeit without the disconnected wave-function $|\chi_0\rangle$. Note that the choice $U' = U^\dagger$ leads to correlations between different tensors in the doubled tensor network. Our claim here is that for the effective state, such correlations have already been taken into account by $|\chi_0\rangle$ so we should not double count this effect. This leads us to Eq. (3.99).

Given the discussion above, we can easily compute the entropy $S(AA^*)$ of $|\psi_{\text{eff}}\rangle$ and indeed it agrees with Eq. (3.94). Similarly the Rényi entropies also agree.

Let us push this interpretation a little further, and give an quantum error correction interpretation of this superposition of tensor networks states, and emergent area operator. For simplicity let us assume the density operators have exactly orthogonal support. We introduce an area operator that labels the different superselection sectors. The superselection sectors in this case are described by a single bit $s = 0, 1$. The area operator is:

$$\mathcal{L}_{AA^*} = \bigoplus_{s=0,1} \overline{S(\chi_s)} \quad (3.101)$$

accounting for the entropy of each sector. The two orthogonal subspaces, determined by projections π_0, π_1 , are defined using the supports:

$$\pi_0 = \text{supp}(\rho_{AA^*}^0) \otimes \text{supp}(\rho_{BB^*}^0) \quad (3.102)$$

and similarly for π_1 . Then:

$$\mathcal{L}_{AA^*} |\chi_s\rangle = \overline{S(\chi_s)} |\chi_s\rangle \quad (3.103)$$

In this case we can define a simple quantum/classical error correcting code, that protects a single classical bit from quantum errors. Define the code subspace as a single bit and the isometry $V = |\chi_0\rangle \langle 0| + |\chi_1\rangle \langle 1|$. This code protects from errors on either AA^* or BB^* , which can be confirmed by computing:

$$V^\dagger(1_{AA^*} \otimes \mathcal{O}_{BB^*})V = |0\rangle \langle 0| \langle \chi_0 | \mathcal{O}_{BB^*} | \chi_0\rangle + |1\rangle \langle 1| \langle \chi_1 | \mathcal{O}_{BB^*} | \chi_1\rangle \quad (3.104)$$

So the error, represented by an arbitrary operator on BB^* : \mathcal{O}_{BB^*} , does no damage to the classical information. This is the Knill-Laflamme condition stated for operator algebra error correction with complementary recovery and a center, see Refs. [37, 136] (in this case the center is everything in the code.)

We know how to compute the entropy for states on such a code, following [37] we find:

$$S_{\psi_{\text{eff}}}(AA^*) = -p_0 \ln p_0 - p_1 \ln p_1 + \langle \psi_{\text{eff}} | \mathcal{L}_{AA^*} | \psi_{\text{eff}} \rangle \quad (3.105)$$

as expected. Note that, in reality the supports of the reduced density matrices are not exactly orthogonal. This is because the error correcting code is not exact.

3.9 Numerical results

Our main result Eq. (3.94) corrects the naive holographic reflected entropy, from a step function to a smooth transition. In this subsection, we corroborate these corrections, comparing our answer to numerical results, showing they indeed capture the details of the phase transition. All numerical results are obtained by generating a random tripartite state of appropriate bond dimension and numerically computing its reflected entropy.

First, in Fig. (3.10) we plot a histogram of (the logarithm of the) eigenvalues of ρ_{AA^*} , corroborating Eq. (3.95) and Fig. (3.8). We choose bond dimensions $\chi := \chi_A = 23, \chi_B = 25, \chi_C = 11$, and 50 trials.

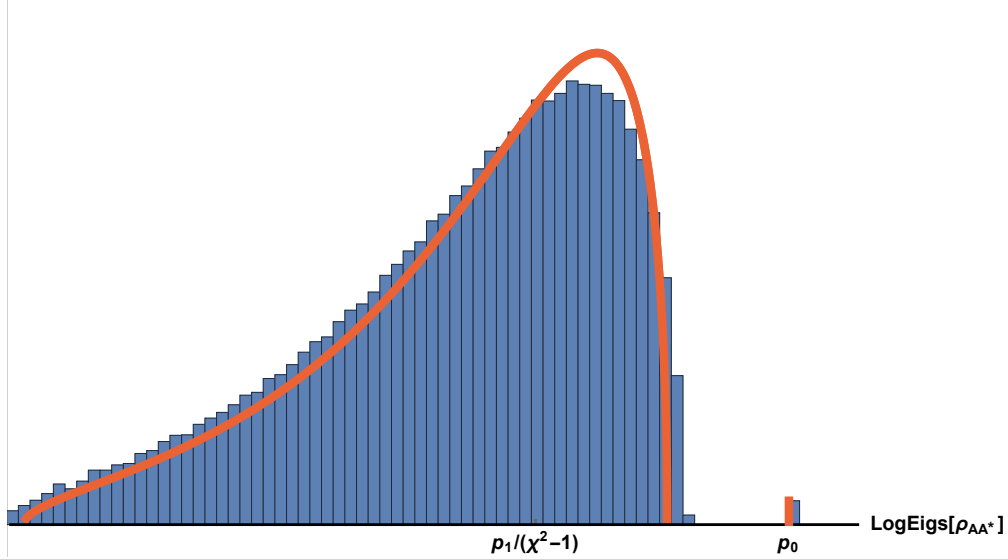


Figure 3.10: The blue histogram is a numerical plot of the spectrum of ρ_{AA^*} for a tripartite tensor. The orange curve is our analytic prediction for the spectrum Eq. (3.95). Note that the tick values on the x-axis are not exactly p_0 from Eq. (3.2), but instead include a small correction, replacing p_0 with its shifted version Eq. (C.79), differing only at $\mathcal{O}(\log(\chi)/\chi^2)$. This gives the value in the plot of $p_0 = 0.226$.

In Fig. (3.11), we present two plots of the “Page curve” for reflected entropy. Solid lines are analytic results Eq. (3.94). Dots are numerical results (only obtained for small bond dimension). All values are normalized by twice the entanglement entropy of A , the upper bound on $S_R(A : B)$. In the top figure, the blue step function is the large- χ limit, with $x_A + x_B = \log(\chi_A \chi_B) / \log(\chi_C)$ held fixed. The other dimensions are $\log_5 \chi_A = \log_5 \chi_B = x_A \log_5 \chi_C = \{16, 11, 6, 1\}$. The numerics agree, with larger deviation at large x_A . This is as expected, because large x_A at fixed χ_A means small χ_C , and Eq. (3.94) was derived in the large bond dimension limit. Besides illustrating that Eq. (3.94) agrees with small bond-dimension numerics and limits to the correct semiclassical answer in the limit $\chi \rightarrow \infty$, this plot also illustrates the novel prediction for $S_R(A : B)$ very near the phase transition.

Our results are depicted more precisely in the bottom figure: where we zoom into a narrower range of x_A around the phase transition point. The horizontal blue dashed line depicts the predicted value of $S_R(A : B) / 2S_A$ in the limit $\chi \rightarrow \infty$. To demonstrate agreement with numerics, we have included curves and numerics corresponding to smaller dimensions, $\chi_A = \chi_B = \chi_C^{x_A} = \{3, 4, 6, 7\}$. It is evidence that Eq. (3.94) is sufficient to capture many of the non-trivial features of the transition.

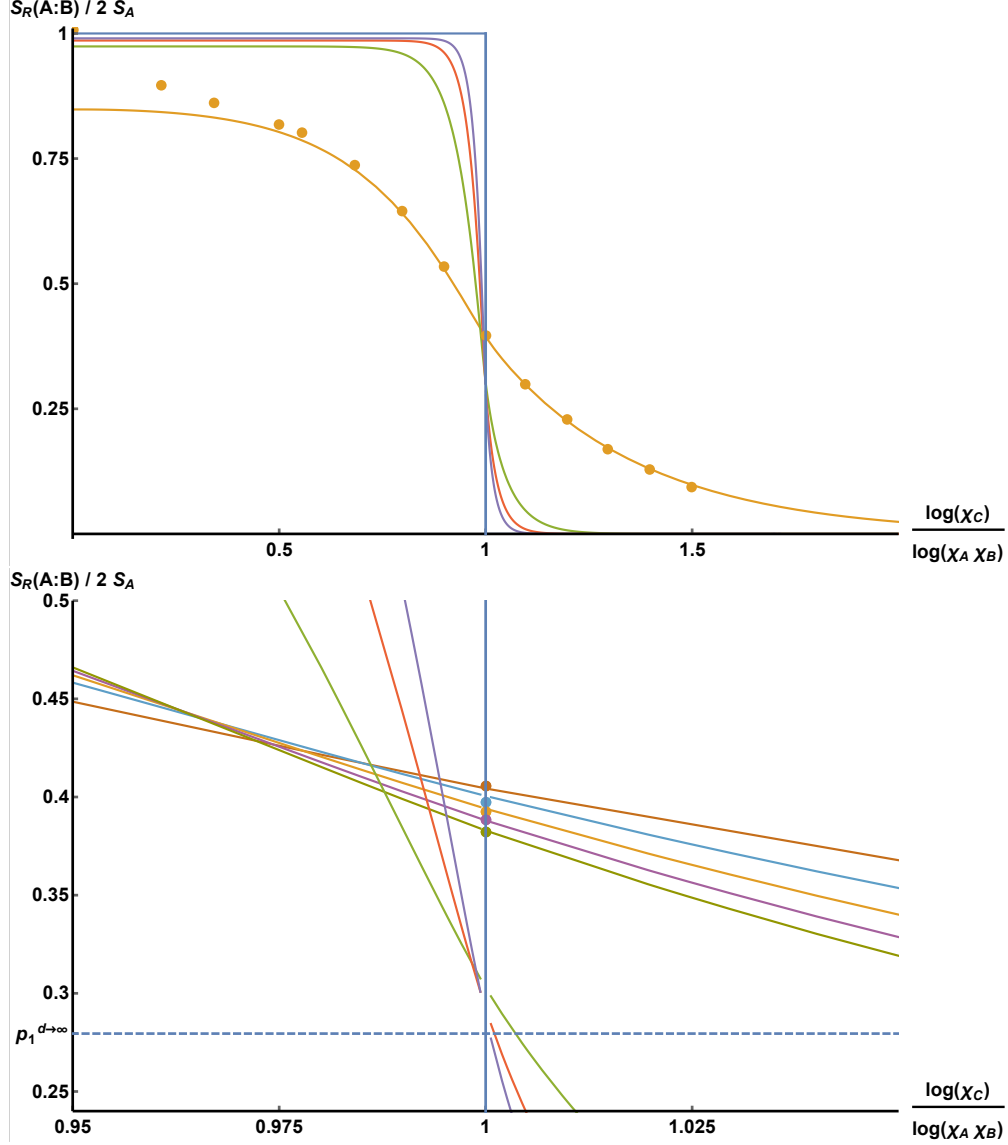


Figure 3.11: Plots of the “Page curve” for reflected entropy. Our results capture the phase transition and agree with numerics. The disagreement in the top figure at small χ_C is to be expected from Eq. (3.94) not being valid at small bond dimension. Note that the analytic functions plotted are not exactly Eq. (3.94), but instead include a small correction, replacing p_0 with its shifted version Eq. (C.79), differing only at $\mathcal{O}(\log(\chi)/\chi^2)$.

3.10 Discussion

3.10.1 Effective description of canonical purification

Given a state ρ_{AB} , we have suggested a recipe for computing the reflected entanglement spectrum in random tensor networks. First construct the canonical purification $|\sqrt{\rho_{AB}}\rangle_{AA^*BB^*}$ using a generalized gluing construction - allowing for a superposition of networks for different possible entanglement wedges. Then compute the spectrum of the density matrix on AA^* using the fact that the individual density matrices on AA^* are approximately orthogonal.

Let us comment in more detail how this relates to the gravitational gluing construction used in Ref. [56]. There, the canonical purification $|\sqrt{\rho_{AB}}\rangle_{AA^*BB^*}$ was described as dual to a particular bulk geometry, the one formed by gluing two copies of the AB entanglement wedge together. If we naively follow this procedure for a random tensor network we arrive at the following picture. Firstly the entanglement spectrum of ρ_{AB} is flat in this case, so up to normalization we can replace $\rho_{AB}^{1/2}$ by ρ_{AB} . Then seemingly the gluing procedure automatically follows, since we know there is an isometry from the bulk legs at the AB RT surface to the AB boundary legs and ρ_{AB} already contains two copies of the tensor network for the bra and the ket [115].

To see how this works, consider again the single tripartite tensor example. The canonical purification $|\sqrt{\rho_{AB}}\rangle_{AA^*BB^*}$ following this procedure corresponds to a tensor network with two tensors T_{ABC} and T_{ABC}^* contracted along leg C . This however is *not exactly* the analog of gluing two copies of the entanglement wedge together. The difference is that these two tensors are now correlated. Normal tensor network analogs of any given geometry discretize that geometry with a collection of tensors that are all chosen independently at random. Hence the random tensor network analogous to the glued entanglement wedges from gravity [56] would have completely uncorrelated tensors in the two copies!

How big is this difference? It is certainly somewhat important: while the network of two uncorrelated tensors would have a completely flat entanglement spectrum, the canonical purification does not. As computed in Sec. (3.7), the spectrum of AA^* involves two peaks. These two peaks can trade dominance as a function of Rényi parameter n . For example, when the entanglement wedge is in the connected phase, the single eigenvalue peak is subdominant, and the spectrum of AA^* is approximately that of two uncorrelated tensors—yet for large enough n , the single eigenvalue peak begins to dominate. This phase transition as a function of n is completely absent in two uncorrelated tensors. Hence the canonical purification in this tensor network example is not entirely described by the analog of gluing of two entanglement wedges.

That said, there is a simple fix, an updated effective description of the canonical purification that does capture this more complicated spectrum. As we described in Sec. 3.7, the spectrum of AA^* appears analogous to that obtained by summing, with appropriate weights, two tensor networks as in Eq. (3.3), one with two uncorrelated tensors and one with no tensors at all. And note, for the purposes of describing ρ_{AA^*} , this effective description is quite consistent with the original, naive gluing of the entanglement wedge, as long as we are far from any n -dependent phase transition, i.e. as long as one peak dominates and the other is an exponentially small correction to the state. Therefore this effective description is nice for at least two reasons: (1) it gives a good description of the reduced density matrix of AA^* , and (2) it clarifies the sense in which we should trust the doubled-and-glued description of the canonical purification.

How good is this effective description for more general purposes? Can we use it to compute things besides the Rényi entropies of AA^* , such as the spectrum of AB ? At least far from phase transitions, this seems roughly correct: as long as $|AB| \ll |C|$ or $|AB| \gg |C|$. In the former case, ρ_{AB} is approximately maximally mixed, which is indeed the density matrix in the effective description of that regime (AB maximally entangled with A^*B^*). In the latter case, ρ_{AB} is approximately maximally mixed on a random dimension $|C|$ subspace, which is indeed the density matrix of the effective description in that regime (two uncorrelated tensors contracted across a dimension $|C|$ leg). Hence this effective description seems valuable, capturing the far-from-transition physics as well as at least some of the physics near transitions.

We note one interesting subtlety: the two networks in the effective description Eq. (3.3) are not generally orthogonal. So while it is approximately correct for some purposes to view them as defining separate superselection sectors, their overlap is not always ignorable.

How does this effective description generalize beyond the single tensor example, to hyperbolic networks?

As we will describe in Chapter 6 (more specifically in Sec. (6.6)), the spectrum of AA^* is well-modeled by as a sum of many tensor networks, each formed by doubling and gluing the tensor network along a different, possibly kinked candidate entanglement wedge, with all tensors chosen independently at random. See Eq. (6.182).

What do these lessons say about reflected entropy in a gravitational theory? Because something is clearly missed in the random tensor network by the naive doubling and gluing of the entanglement wedges, we can expect that the same is true in gravity. Albeit we still expect the Reflected entropy/EW cross-section duality to hold, just not away from $n = 1$.

Likely there is some effective description that improves upon this naive doubling, analogous to the tensor network case sketched in Eq. (6.182). That said, it's not entirely clear how to interpret such an effective description in gravity. For example it is not obvious that the 'kinked' geometries in Eq. (6.182) correspond to any saddles in gravity. We leave a precise investigation of this question to future work.

3.10.2 Non-flat spectrum and building geometry from RTNs

This effective description offers an interesting possibility. Perhaps the canonical purification is a useful tool for constructing, out of tensor networks, a geometry with gravity-like area fluctuations.

To explain this, let us recall some background. While impressive in many ways, the precise relationship between random tensor networks and AdS/CFT is not yet fully understood. So far, the best understanding is that tensor networks resemble so-called fixed-area states, which have approximately flat Rényi spectra just like random tensor networks [96, 97]. This matching is quite good; both fixed-area states and random tensor networks have exactly the same non-perturbative corrections to the Rényi entropies [15].

However, it would be nice to have a random tensor network model of something more realistic than a fixed-area state. Our results suggest an interesting method for obtaining such a model. The procedure is as follows. First, start with some conventional random tensor network, say $|\psi\rangle_{ABC}$. Second, find the canonical purification $|\sqrt{\rho_{AB}}\rangle$. As we've shown, $\rho_{AA^*} = \text{tr}_{BB^*}(|\sqrt{\rho_{AB}}\rangle\langle\sqrt{\rho_{AB}}|)$ has a non-flat spectrum. That said, this is only a partial success. Not all factors of the canonical purification have a non-flat spectrum. In particular, ρ_{AB} is the same as in the original tensor network. To fix this we can iterate, now finding the canonical purification of the canonical purification, this time canonically purifying, say, ρ_{AA^*} . Then all factors have non-flat spectra. If we like, we can continue to iterate, building up increasingly sophisticated superpositions over tensor networks and associated spectrum. In this way we might even build up complicated tensor networks describing higher dimensional space times just starting from a single random tensor. This seems a bit like the Eguchi-Kawai mechanism which grows extra dimensions out of large- N matrices. See for example Ref. [137].

Having said this, this is not the only method for building up a tensor network with a non-flat spectrum. Another possibility is to simply add degrees of freedom to each of the legs connecting the tensors, as in [138]. This raises the question, is there any reason one might prefer this iterative canonical purification method for building a tensor network with a non-trivial entanglement spectrum?

Here's one possible reason. In conventional random tensor networks, even those with degrees of freedom on each of the links as in [138], the area operators associated to two crossing cuts commute. That is, if you consider one cut through the tensor network, and then a second cut that crosses it (but nowhere overlaps it), the 'areas' associated to those cuts can be simultaneously fixed. This cannot happen for overlapping cuts in AdS/CFT [133]. There, crossing areas do not commute because the area is conjugate to the boost angle across the surface, and fixing one area makes the geometry of the Cauchy surface highly uncertain. Hence

simply adding link degrees of freedom does not capture this subtle behavior seen in gravity.

Very speculatively, perhaps this *is* captured by the iterative canonical purification geometry. If so, this would be an interesting reason to take these seriously as toy models of holography. We leave such an investigation to future work.

Chapter 4

West Coast Model

In this chapter, we investigate the reflected entropy phase transition in the so-called *West Coast Model* (also known as the *Penington-Shenker-Stanford-Yang (PSSY)* model) [15]. The West Coast Model is a toy model consisting of Jackiw-Teitelboim (JT) gravity coupled to end-of-the-world (ETW) branes that was used to calculate the Page curve of black hole evaporation from semiclassical gravitational path integral. The model consists of two parameters: the horizon area S_{BH} and the number of ETW brane flavour indices k . Tuning these parameters simulates black hole evaporation, and one finds the entanglement entropy of the black hole radiation R to be

$$S(R) = \min(S_{BH}, \log k) \tag{4.1}$$

away from the Page time.

The west coast model can be thought of as a single random tensor in the canonical ensemble and they exhibit numerous common features. In particular, spectra of the reduced density matrices can be obtained using a similar resolvent trick as in the case of 1TN. This allows one to use the formalism we developed in Chapter 3 with only minor modifications to compute the reflected spectrum of the West Coast model in full detail. We will find that the reflected spectrum bears striking similarity to that of 1TN, composed from two super-selection sectors corresponding to a disconnected and connected bulk solution. The main difference is that there are additional $O(1/\sqrt{G_N})$ corrections resulting from thermal fluctuations in the horizon area near the phase transition. Such feature is absent in RTNs since they corresponding to fixed area states in which the horizon area cannot fluctuate.

The results presented in this chapter is based on Ref. [67].

4.1 Summary of results

We consider a natural generalization of the west coast model by splitting the radiation into two subsystems $R = R_1 \cup R_2$, each entangled to a ETW branes labeled by different sub-flavor indices k_1 and k_2 with $k_1 k_2 = k$, see Fig. (4.1). We analyze the reflected entropy between the radiation subsystems R_1 and R_2 . Simply applying Eq. (2.32) to the model leads to

$$S_R(R_1 : R_2) = \begin{cases} 0 & k < \exp(S_{BH}) \\ 2 \min(\log k_1, \log k_2) & k > \exp(S_{BH}) \end{cases} \tag{4.2}$$

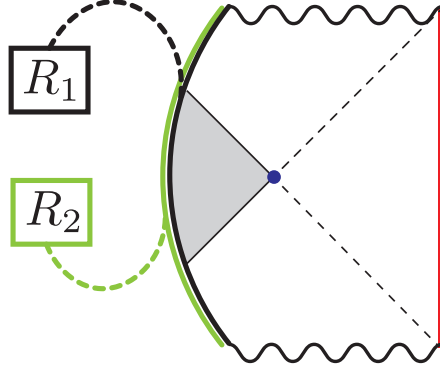


Figure 4.1: The Lorentzian description of the state we consider in the West Coast Model, a JT gravity black hole with an ETW brane. The ETW brane carries two sub-flavours, denoted black and green, that are entangled (dashed, coloured lines) with radiation systems R_1 and R_2 respectively. The extremal surface is denoted in purple and the island that dominates after the Page time is coloured gray.

This follows from the two possible saddles obtained upon canonical purification: the disconnected geometry and the connected geometry depicted in Fig. (4.2). We will compute the reflected entropy precisely, demonstrating the validity of the holographic formula away from phase transitions. The fact that the gravitational path integral can be performed exactly allows us to compute the detailed behaviour of $S_R(R_1 : R_2)$ including corrections to Eq. (2.32) near the phase transition.

We will compute the reflected entropy precisely, demonstrating the validity of the holographic formula away from phase transitions. The fact that the gravitational path integral can be performed exactly allows us to compute the detailed behaviour of $S_R(R_1 : R_2)$ including corrections to Eq. (4.2) near the phase transition. This is the main result of this chapter, summarized by Fig. (4.2).

In fact, we compute the entire reflected entanglement spectrum, which takes a very simple form: it consists of a mixture of two superselection sectors corresponding to the disconnected and connected geometries shown in Fig. (4.2). The probabilities p_d and p_c of the two sectors are computable functions, that vary as we change k , leading to the phase transition in Eq. (4.2). Moreover, we find corrections to Eq. (4.2) in a window of $\Delta \log k = O(\frac{1}{\sqrt{G_N}})$ near the phase transition that arise from fluctuations in the horizon area¹ (equivalently thermal fluctuations, in this model). This is analogous to a similar effect found in the entanglement entropy Page curve [15, 62, 63, 139, 140], and we expect it to be a universal feature of holographic reflected entropy.

We now give an outline of this chapter. In Sec. (4.2), we review the West Coast Model and set up the stage for our analysis. The proposed holographic answer arises from a leading saddle computation assuming replica symmetry. This calculation suffers from various issues, which motivates us to analyze the problem in more detail.

In Sec. (4.3), we review the computation of the entanglement spectrum in the West Coast Model. This serves as a warm-up for the resolvent trick which is used to obtain the spectrum in Sec. (4.3.1). We then use the spectrum to compute the Renyi entropies in this model in Sec. (4.3.2). Apart from being of interest on their own, the results for the Renyi entropies serve as an input for the reflected entropy calculation.

In Sec. (4.4), we analyze the reflected entanglement spectrum in the West Coast Model. We describe the resolvent trick in Sec. (4.4.1) to obtain a Schwinger-Dyson equation for the reflected entanglement spectrum. In Sec. (4.4.2), we solve this equation to obtain the spectrum and use it to analyze the reflected entropy. In Sec. (4.4.3), we go on to analyze a two-parameter Renyi generalization of the reflected entropy, called the

¹In JT gravity, this corresponds to the value of the dilaton at the bifurcation surface.

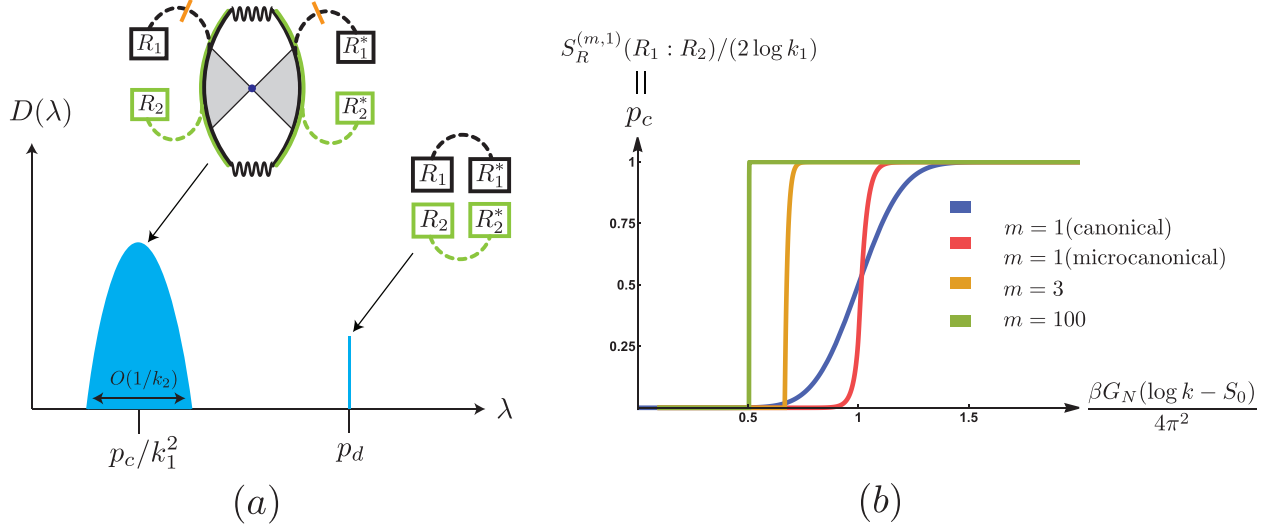


Figure 4.2: The main result: (a) The reflected entanglement spectrum of ρ_{AA^*} in the canonically purified state $|\sqrt{\rho_{AB}}\rangle$ is a mixture of two superselection sectors: a single pole of weight p_d corresponding to the disconnected purification, and a mound of approximately k_1^2 eigenvalues (assuming $k_1 < k_2$) with weight p_c corresponding to a connected purification involving a closed universe with the entanglement wedge cross section denoted in orange. (b) The probability of the connected purification p_c as we vary k across the Page transition. We show analytic plots for the microcanonical and canonical ensemble. The latter shows a spread in the phase transition of $O(\sqrt{G_N})$. We also show plots for p_c when considering the $(m, 1)$ -Renyi reflected entropy; these undergo sharp transitions at m -dependent locations in the canonical ensemble.

(m, n) -Renyi reflected entropies.

In Sec. (4.5), we discuss these results and future directions.

4.2 The west coast model

The West Coast Model is a toy model that was used to derive the Page curve of entanglement entropy. We briefly describe the model here, for more details refer to Ref. [15]. The model consists of JT gravity coupled to ETW branes. The action is given by

$$I = I_{JT} + \mu \int_{\text{brane}} ds \quad (4.3)$$

$$I_{JT} = -\frac{S_0}{2\pi} \left[\frac{1}{2} \int_{\mathcal{M}} \sqrt{g} R + \int_{\partial\mathcal{M}} \sqrt{h} K \right] - \left[\frac{1}{2} \int_{\mathcal{M}} \sqrt{g} \phi (R + 2) + \int_{\partial\mathcal{M}} \sqrt{h} \phi K \right], \quad (4.4)$$

where S_0 is the extremal entropy and μ is the mass of the brane. We will take both the above parameters to be large in our analysis. The ETW branes also possess a large number of flavours k , which we artificially divide into two sub-flavour indices that number k_1 and k_2 respectively.

We consider a state where the ETW brane is entangled with two radiation bath systems R_1 and R_2 as

$$|\Psi\rangle = \frac{1}{\sqrt{k}} \sum_{i=1}^{k_1} \sum_{j=1}^{k_2} |i\rangle_{R_1} |j\rangle_{R_2} |\psi_{ij}\rangle_B, \quad (4.5)$$

where $|\psi_{ij}\rangle_B$ is the state of the black hole system B with the ETW brane chosen to be of sub-flavours i and

corresponding to $|\psi^{(m)}\rangle$:

$$|\psi^{(m)}\rangle = \text{disconnected} \quad \text{or} \quad \text{connected} \quad (4.11)$$

We refer to these geometries as the disconnected and connected purifications respectively. Here, m is simply a parameter that fixes the area of the extremal surface and thus, the analytic continuation in m is straightforward. As $m \rightarrow 1$, these geometries can be interpreted as arising from gluing together two copies of the entanglement wedge of $R_1 \cup R_2$ [113, 114].³

Within the respective phases, we can apply the QES formula once we know the geometry corresponding to $|\psi^{(m)}\rangle$. For the disconnected saddle, the QES is trivial and thus, the reflected entropy vanishes. On the other hand, for the connected saddle we have two non-trivial candidate QESs represented by the pink and orange cuts in Eq. (4.11). This leads to the proposed formula

$$S_R(R_1 : R_2) = \begin{cases} 0 & k < \exp(S_{BH}) \\ 2 \min(\log k_1, \log k_2) & k > \exp(S_{BH}) \end{cases} \quad (4.12)$$

While this saddle point approximation is expected to work far away from the Page transition, there are various issues with this proposal which will require a more detailed analysis that we carry out in Sec. (4.4). In particular, the saddle point calculation suffers from an order of limits issue when analytically continuing $m, n \rightarrow 1$. Further, Eq. (4.12) has a discontinuous jump at the phase transition which is resolved by non-perturbative effects. Once these effects are included, we will find significant corrections to this formula near the phase transition.

4.3 Entanglement spectrum

Before we go to a more careful analysis of the reflected entropy, we first discuss the simpler case of entanglement entropy. In Sec. (4.3.1), we first review the resolvent trick that was used to compute the entanglement spectrum in Ref. [15]. This serves as a warm-up for the analogous calculation for the reflected spectrum. Further, we analyze the Renyi entropies in the West Coast Model in Sec. (4.3.2) which will be useful for our later calculations.

4.3.1 Resolvent trick

The technique we use here was presented in Ref. [15] (see also [46, 118, 119]). This powerful approach enables us to write down a Schwinger-Dyson equation for the *resolvent* of $\rho_{R_1 R_2}$, which then gives full information about the entanglement spectrum.

³See also Ref. [141] for a construction of the canonical purification of the black hole system in a model of JT gravity coupled to matter.

Consider the resolvent matrix $R_{ij}(\lambda)$ for the density matrix $\rho_{R_1 R_2}$ defined formally as

$$R_{ij}(\lambda) = \left(\frac{1}{\lambda - \rho_{R_1 R_2}} \right)_{ij}, \quad (4.13)$$

where the i, j indices run over both R_1 and R_2 labels and take values from 1 to $k = k_1 k_2$. We then define the resolvent as the trace $R(\lambda) = \text{tr} R_{ij}(\lambda)$. From the resolvent, we can obtain the density of eigenvalues $D(\lambda)$ using

$$D(\lambda) = -\frac{1}{\pi} \lim_{\epsilon \rightarrow 0} \text{Im} R(\lambda + i\epsilon). \quad (4.14)$$

To evaluate $R(\lambda)$, we expand the matrix inverse around $\lambda = \infty$ as

$$R(\lambda) = \frac{k}{\lambda} + \sum_{n=1}^{\infty} \frac{\text{tr}(\rho_{R_1 R_2}^n)}{\lambda^{n+1}}, \quad (4.15)$$

sum the series and then analytically continue to $\lambda \in [0, 1]$ on the real axis where $D(\lambda)$ is non-zero. In terms of diagrams, this leads to the boundary conditions:

$$\text{---} \circlearrowleft (R) \text{---} = \frac{1}{\lambda} \text{---} + \frac{1}{\lambda^2} \text{---} \text{---} \text{---} + \frac{1}{\lambda^3} \text{---} \text{---} \text{---} \text{---} + \dots, \quad (4.16)$$

where uncontracted indices have been used to represent a matrix equation for R_{ij} and each red line carries a power of $\frac{1}{kZ_1}$ for normalization. These boundary conditions are then filled in with planar disk geometries since crossing (higher genus) geometries are suppressed by powers of $\frac{1}{k}$ (e^{-S_0}).

Now denote $F_{ij}(\lambda)$ to be the connected part of the resolvent, defined by

$$\begin{aligned} \text{---} \circlearrowleft (R) \text{---} &= \frac{1}{\lambda} \text{---} + \frac{1}{\lambda^2} \text{---} \circlearrowleft (F) \text{---} + \frac{1}{\lambda^3} \text{---} \circlearrowleft (F) \text{---} \circlearrowleft (F) \text{---} + \dots \\ &= \frac{1}{\lambda - F} \end{aligned}, \quad (4.17)$$

where the last term denotes the matrix $(\lambda - F)^{-1}$. We can now write down a Schwinger-Dyson equation for $R_{ij}(\lambda)$ and $F_{ij}(\lambda)$:

$$\begin{aligned} \text{---} \circlearrowleft (F) \text{---} &= \text{---} \text{---} \text{---} + \frac{1}{\lambda} \text{---} \text{---} \text{---} \circlearrowleft (\lambda R) \text{---} \text{---} \text{---} \\ &+ \frac{1}{\lambda^2} \text{---} \text{---} \text{---} \circlearrowleft (\lambda R) \text{---} \text{---} \circlearrowleft (\lambda R) \text{---} \text{---} \text{---} + \dots \end{aligned}, \quad (4.18)$$

where we note that a self consistent solution is to consider every term to be proportional to δ_{ij} , and thus $F_{ij}(\lambda) = \frac{F(\lambda)}{k} \delta_{ij}$, where we have defined $F(\lambda) = \text{tr} F_{ij}(\lambda)$. After taking the trace of Eq. (4.18), we obtain the

following algebraic equation

$$F(\lambda) = \sum_{n=1}^{\infty} \frac{k Z_n R(\lambda)^{n-1}}{(k Z_1)^n}. \quad (4.19)$$

We could now consider boundary conditions that correspond to either the microcanonical or canonical ensemble. The microcanonical case is identical to 1TN and is discussed in detail in Chapter 3,⁴ so our primary focus here will be on the canonical ensemble. For this case, we can use an integral representation for the n -boundary partition function Z_n given by

$$Z_n = \int_0^{\infty} ds \rho(s) y(s)^n, \quad (4.20)$$

where $\rho(s)$ is the density of states, and $y(s)$ is the Boltzmann weight for the thermal spectrum given by

$$\rho(s) = \frac{e^{S_0} s \sinh 2\pi s}{2\pi^2} \quad (4.21)$$

$$y(s) = e^{-\frac{\beta s^2}{2}} 2^{1-2\mu} |\Gamma(\mu - \frac{1}{2} + is)|^2. \quad (4.22)$$

It is convenient to define the normalized Boltzmann weight $w(s) = \frac{y(s)}{Z_1}$. Using this representation in Eq. (4.19), we obtain

$$F(\lambda) = \int_0^{\infty} ds \frac{\rho(s) w(s)}{k - w(s) R}. \quad (4.23)$$

Finally, combining this with Eq. (3.44), we obtain an integral equation for $R(\lambda)$:

$$\lambda R = k + \int_0^{\infty} ds \frac{\rho(s) w(s) R}{k - w(s) R} \quad (4.24)$$

Solving this equation will give us the entanglement spectrum and corresponding entropies.

Approximate entanglement spectrum

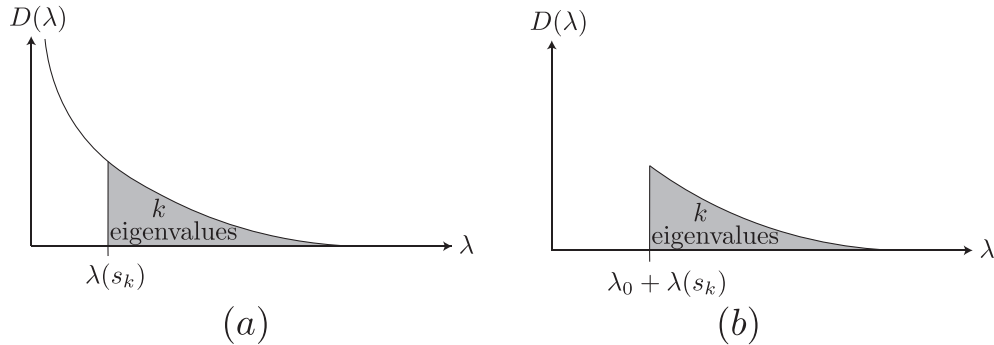


Figure 4.3: (a) The thermal spectrum of the JT black hole. (b) The approximate spectrum of $\rho_{R_1 R_2}$ is a cutoff thermal spectrum which is obtained by truncating the spectrum to the k largest eigenvalues and shifting it by λ_0 to make it normalized.

⁴In this model, fixing the energy is the same as fixing the area of the horizon in the semiclassical approximation. Thus, the calculations can be understood as related to those done in random tensor networks via the connection to fixed-area states [96–98]

The resolvent equation was solved approximately in Ref. [15] to obtain an approximate entanglement spectrum. It was shown that the spectrum of $\rho_{R_1 R_2}$ can be well approximated by a cutoff thermal spectrum (see Fig. (4.3)), i.e.,

$$D(\lambda) = \int_0^{s_k} ds \rho(s) \delta(\lambda - \lambda_0 - w(s)), \quad (4.25)$$

where the parameters s_k and λ_0 can be computed by

$$k = \int_0^{s_k} ds \rho(s) \quad (4.26)$$

$$\lambda_0 = \frac{1}{k} \int_{s_k}^{\infty} \rho(s) w(s). \quad (4.27)$$

For more details about the calculation, refer to Appendix F of Ref. [15]. Here, we will simply use the result and discuss the interpretation of this spectrum.

Intuitively, the thermal spectrum of the black hole is divided into two portions - a part that has already undergone the Page transition, and a part that hasn't. For states corresponding to sufficiently high energy in the thermal spectrum, the Page transition has still not occurred since they correspond to larger black holes. On the other hand, low energy states are past the Page transition and in this part of the wavefunction, the radiation system contains an island in the black hole interior. Thus, it is natural to expect that details of the spectrum such as the probability distribution of the horizon area should be observable. This natural ansatz is in fact a good approximation and leads to a cutoff thermal spectrum where s_k roughly corresponds to the threshold dividing the pre-Page and post-Page parts of the wavefunction. The post-Page portion of the spectrum is not normalized on its own and thus, λ_0 is the additive constant contributed by the pre-Page spectrum that shifts the spectrum of $\rho_{R_1 R_2}$ to make it appropriately normalized. Further, this ansatz captures the feature that the rank of $\rho_{R_1 R_2}$ cannot exceed k even far past the Page transition, since the dimension of the radiation Hilbert space is k .

4.3.2 Rényi entropy

Given this approximate description of the spectrum, we will now analyze the Rényi entropies in this model,

$$S_m(\rho_{R_1 R_2}) = -\frac{1}{m-1} \log(\text{tr}(\rho_{R_1 R_2}^m)) \quad (4.28)$$

for different values of m . To simplify the analysis, we choose $\mu \gg \frac{1}{\beta}$. In this limit, the μ -dependent terms drop out from $w(s)$. Further, we also work in the semiclassical limit $\beta \rightarrow 0$.⁵

Using Eq. (4.25), we obtain

$$\text{tr}(\rho_{R_1 R_2}^m) = \int_0^{s_k} \rho(s) (\lambda_0 + w(s))^m. \quad (4.29)$$

There are a few values of k near the phase transition, equivalently $s_k \approx \frac{\log k - S_0}{2\pi}$, that play an important role in this calculation. First, the location of the peak of $\rho(s)w(s)^m$ is $s_m = \frac{2\pi}{m\beta}$. Secondly, far from the phase transition the calculation of Rényi entropies is dominated by either of the two \mathbb{Z}_m symmetric saddles. The location at which they exchange dominance is denoted by $s_k^{(m)}$. Working in the saddle point approximation, we obtain the condition

$$\frac{1}{k^{m-1}} = \exp \left[(1-m)S_0 + \frac{2\pi^2}{\beta} \left(\frac{1}{m} - m \right) \right], \quad (4.30)$$

⁵Note that β should be replaced with βG_N to restore explicit dependence on the Newton constant.

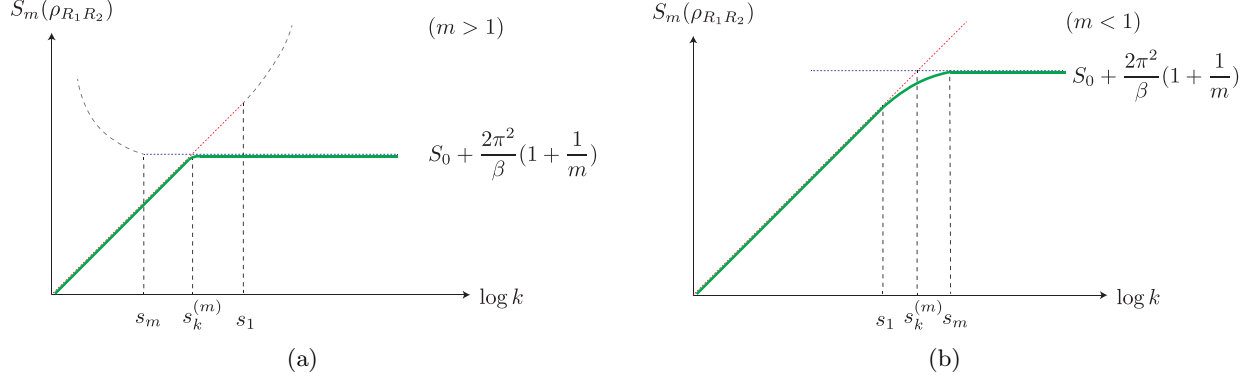


Figure 4.4: (a) For $m > 1$, the Renyi entropy (denoted by the green line) has a sharp transition at $s_k = s_k^{(m)}$ where the two replica symmetric saddle contributions (denoted by blue and red dotted lines) exchange dominance. Phase transitions in the two terms in Eq. (4.31) happen at $s_k = s_1, s_m$ (depicted with curved, gray dashed lines) and thus don't affect the Renyi entropies. (b) For $m < 1$, the Renyi entropy (denoted by the green line) has a transition in the range $s_k \in [s_1, s_m]$ whereas the two naive replica symmetric saddles (denoted by blue and red dotted lines) exchange dominance at $s_k = s_k^{(m)}$. Thus, the phase transition is over a large window of size $O(\frac{1}{\beta})$ and the Renyi entropy has $O(\frac{1}{\beta})$ corrections compared to a naive analytic continuation of the replica symmetric saddles.

which leads to $s_k^{(m)} \approx \frac{\pi}{\beta}(1 + \frac{1}{m})$. Lastly, from Eq. (4.27), we see that λ_0 has a phase transition at $s_k = s_1$.

With these ingredients in hand, we can now analyze Eq. (4.29). An important feature that appears in this model is that different Renyi entropies have transitions at different values of k . We will analyze them separately for $m > 1$, $m = 1$ and $m < 1$ since they have qualitatively different behaviour.

$m > 1$

For $m > 1$, we have $s_m < s_k^{(m)} < s_1$. This implies that $\lambda_0 \approx \frac{1}{k}$ for $s_k \approx s_k^{(m)}$. As a simple approximation, we can compute Eq. (4.29) by

$$\text{tr}(\rho_{R_1 R_2}^m) \approx \max \left[\int_0^{s_k} ds \rho(s) \lambda_0^m, \int_0^{s_k} ds \rho(s) w(s)^m \right]. \quad (4.31)$$

Since at the level of the saddle point approximation, this comparison is identical to Eq. (4.30), we see that $\text{tr}(\rho_{R_1 R_2}^m)$ has a phase transition at $s_k = s_k^{(m)}$. More so, the second term in Eq. (4.31) is the integral of a Gaussian with a width $\sigma_m = \frac{1}{\sqrt{m\beta}}$. Since $s_k^{(m)} - s_m \gg \sigma_m$, the second term is almost unchanging in this region. Thus, we see that for $m > 1$, $\text{tr}(\rho_{R_1 R_2}^m)$ has a rather sharp phase transition. The Renyi entropy takes the form

$$S_m(\rho_{R_1 R_2}) = \min \left[\log k, S_0 + \frac{2\pi^2}{\beta} \left(1 + \frac{1}{m}\right) \right], \quad (4.32)$$

as shown in Fig. (4.4).

$m = 1$

The case $m = 1$ corresponds to the entanglement entropy which was analyzed in detail in Ref. [15]. In this case, $s_m = s_k^{(m)} = s_1$ and thus, there isn't a sharp transition. Instead, one finds enhanced corrections of $O(\frac{1}{\sqrt{\beta}})$ in a window of size $\Delta \log k = O(\frac{1}{\sqrt{\beta}})$ near $s = s_1$. Again, we can use the approximate spectrum in

Eq. (4.25) to obtain

$$S(\rho_{R_1 R_2}) \approx - \int_0^{s_k} \rho(s) (\lambda_0 + w(s)) \log(\lambda_0 + w(s)). \quad (4.33)$$

$m < 1$

For $m < 1$, we instead have $s_m > s_k^{(m)} > s_1$. Thus, we see that the phase transition in $\text{tr}(\rho_{R_1 R_2}^m)$ starts happening at $s_k = s_1$ when λ_0 starts decaying. This is qualitatively different from the $m > 1$ case and will require a more careful analysis.⁶

In order to compute Eq. (4.29), we can use the following inequality on the integrand:

$$\max[\lambda_0^m, w(s)^m] \leq (\lambda_0 + w(s))^m \leq \lambda_0^m + w(s)^m, \quad (4.34)$$

where the lower bound follows from positivity, while the upper bound follows from concavity. Upon performing the integral for $s_k = s_1 - O(\frac{1}{\beta})$, since $\lambda_0 \gg w(s)$, we obtain

$$\text{tr}(\rho_{R_1 R_2}^m) \approx k \lambda_0^m \approx \frac{1}{k^{m-1}}, \quad (4.35)$$

since both the upper and lower bounds take the same value at leading order. In the regime $s_1 + O(\frac{1}{\beta}) < s_k < s_m - O(\frac{1}{\beta})$, both the terms are comparable. Thus, we obtain

$$\text{tr}(\rho_{R_1 R_2}^m) \approx \# \exp \left[2\pi s_k - \frac{m\beta s_k^2}{2} + (1-m)S_0 - \frac{2\pi^2 m}{\beta} \right], \quad (4.36)$$

where there is a potential $O(1)$ multiplicative uncertainty. Similarly in the regime $s_k = s_m + O(\frac{1}{\beta})$, the $w(s)$ term dominates over the λ_0 term giving us

$$\text{tr}(\rho_{R_1 R_2}^m) \approx \exp \left[(1-m)S_0 + \frac{2\pi^2}{\beta} \left(\frac{1}{m} - m \right) \right], \quad (4.37)$$

where we have used the saddle point approximation. Combining these results, we obtain

$$S_m(\rho_{R_1 R_2}) \approx \begin{cases} \log k & s_k < s_1 \\ \frac{2\pi s_k - \frac{m\beta s_k^2}{2} + (1-m)S_0 - \frac{2\pi^2}{m\beta}}{1-m} & s_1 < s_k < s_m \\ S_0 + \frac{2\pi^2}{\beta} \left(1 + \frac{1}{m} \right) & s_k > s_m \end{cases}, \quad (4.38)$$

where we have ignored subleading corrections at $s_k = s_1$ and $s_k = s_m$. The result is sketched in Fig. (4.4), along with the naive expectation from analytically continuing the results of the \mathbb{Z}_m symmetric saddles a la Lewkowycz-Maldacena [116, 142]. We see that there are in fact large $O(\frac{1}{\beta})$ corrections to the naive holographic answer for Renyi index $m < 1$. This is consistent with expectations, hinted at in Ref. [140], based on chaotic behaviour. As shown, the transition happens over a parametrically large window of $\Delta \log k \approx O(\frac{1}{\beta})$.

Before moving on, we analyze the problem a little more carefully in a window $s_k = s_1 \pm O(\frac{1}{\sqrt{\beta}})$ since this will be relevant for the reflected entropy transition. We can use the inequality in Eq. (4.34) and perform the integrals, which are simple Gaussian integrals. In fact, we will include one-loop effects to find the answer to

⁶Similar results have been discussed in Ref. [119]. We are very grateful to Sean McBride and Wayne Weng for discussions related to this topic.

greater accuracy. Computing the relevant quantities, we obtain

$$\begin{aligned}
Z_1 &\simeq \frac{e^{S_0+2\pi^2/\beta}}{\sqrt{2\pi\beta^3}} \\
k &\simeq e^{S_0} \frac{s_k e^{2\pi s_k}}{8\pi^3} \\
\lambda_0 &\simeq \frac{\operatorname{erfc}\left(\frac{\beta s_k - 2\pi}{\sqrt{2\beta}}\right)}{2k} \\
\int_0^{s_1} \rho(s) w(s)^m &\simeq \frac{\beta^{3m/2-1} e^{4\pi^2(1-m)/\beta}}{(1-m)(2\pi)^{m/2-2}},
\end{aligned} \tag{4.39}$$

where $\operatorname{erfc}(x) = \frac{2}{\sqrt{\pi}} \int_x^\infty e^{-x^2} dx$ is the error function. Thus, integrating Eq. (4.34) with the measure $\rho(s)$ and using Eq. (4.39), we obtain

$$\operatorname{tr}(\rho_{R_1 R_2}^m) \approx k \lambda_0^m, \tag{4.40}$$

where we have used the fact that the integral of $\rho(s)w(s)^m$ is suppressed by powers of β in the regime of interest.

4.4 Reflected entanglement spectrum

We now use a generalization of the resolvent trick in Sec. (4.4.1) to analyze the reflected entanglement spectrum. Solving the Schwinger-Dyson equation leads us to the spectrum and reflected entropy in Sec. (4.4.2). Finally, we analyze the (m, n) -Renyi reflected entropies in Sec. (4.4.3).

4.4.1 Resolvent trick

Our goal here is to find the resolvent for the reduced density matrix $\rho_{R_1 R_1^*}^{(m)}$ obtained from the Renyi generalization of the canonically purified state $|\psi^{(m)}\rangle$ defined in Eq. (2.33), i.e.,

$$R_m(\lambda) = \frac{k_1^2}{\lambda} + \sum_{n=1}^{\infty} \frac{\operatorname{tr}(\rho_{R_1 R_1^*}^{(m)})^n}{\lambda^{n+1}} \tag{4.41}$$

where the integer moments of the (normalized) density matrix can be computed using the replica trick on mn copies of the system [48, 56].

In order to do so, we first set up a slightly more general problem.⁷ Consider the following 2×2 “matrix” of resolvents:

$$\mathbb{R}(\lambda) = \sum_{k=0}^{\infty} \lambda^{-1-k/2} \begin{pmatrix} 0 & (\rho_{R_1 R_2}^{m/2})^{\Gamma^\dagger} \\ (\rho_{R_1 R_2}^{m/2})^\Gamma & 0 \end{pmatrix}^k, \tag{4.42}$$

where $\rho \rightarrow \rho^\Gamma$ is an involution defined to take a linear operator ρ on $\mathcal{H}_{R_1 R_2}$ to a linear operator from $\mathcal{H}_{R_1 R_1^*} \rightarrow \mathcal{H}_{R_2 R_2^*}$. It is defined by re-arranging the incoming/outgoing legs in the obvious (and canonical/basis independent) way. Each insertion of $(\rho_{R_1 R_2}^{m/2})^\Gamma$ (and $(\rho_{R_1 R_2}^{m/2})^{\Gamma^\dagger}$) has $m/2$ replicas of each of the bra and ket of the original state $|\psi\rangle$. These involuted density operators are related to the density matrices in the canonically purified state by

$$(\rho_{R_1 R_2}^{m/2})^{\Gamma^\dagger} (\rho_{R_1 R_2}^{m/2})^\Gamma = \rho_{R_1 R_1^*}^{(m)}, \quad (\rho_{R_1 R_2}^{m/2})^\Gamma (\rho_{R_1 R_2}^{m/2})^{\Gamma^\dagger} = \rho_{R_2 R_2^*}^{(m)}. \tag{4.43}$$

⁷This problem is analyzed in more detail in Chapter 3, here we attempt to be brief and focus on the main results.

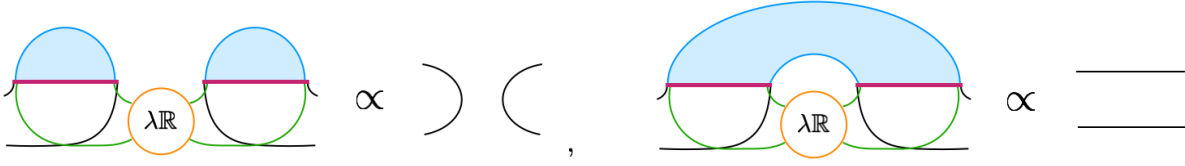


Figure 4.5: Example geometries that give rise to the projector or the identity. All possible contributions are either proportional to the identity operator $1_{R_1 R_1^*}, 1_{R_2 R_2^*}$, or one of the four projectors $|\epsilon_{R_1, R_2}\rangle \langle \epsilon_{R_1, R_2}|$.

Diagrammatically this is given by the following boundary conditions

$$(\rho_{R_1 R_2}^{m/2})^\Gamma = \text{diagram of a puddle with red wavy lines and arrows}, \quad (4.44)$$

where we have chosen $m = 6$ for example. As before, any calculation using the gravitational path integral in this model will amount to a sum over geometries of different topology connecting the various asymptotic boundaries, e.g, in computing Eq. (4.44) we get

$$(\rho_{R_1 R_2}^{m/2})^\Gamma = \sum_{\text{topologies}} \text{diagram of a puddle with a smaller puddle inside}, \quad (4.45)$$

For convenience, we will use a shorthand representation

$$\frac{1}{\sqrt{\lambda}} \text{diagram of a puddle with red wavy lines} = \text{diagram of a simple puddle}, \quad (4.46)$$

From these results we can infer an alternative expression for matrix $\mathbb{R}(\lambda)$:

$$\mathbb{R}(\lambda) = \sum_{n=0}^{\infty} \lambda^{-1-n} \begin{pmatrix} (\rho_{R_1 R_1^*}^{(m)})^n & 0 \\ 0 & (\rho_{R_2 R_2^*}^{(m)})^n \end{pmatrix} + \sum_{n=1}^{\infty} \lambda^{-1/2-n} \begin{pmatrix} 0 & \rho_{R_1 R_1^*}^{n-1} (\rho_{R_1 R_2}^{m/2})^{\Gamma^\dagger} \\ \rho_{R_2 R_2^*}^{n-1} (\rho_{R_1 R_2}^{m/2})^\Gamma & 0 \end{pmatrix}, \quad (4.47)$$

which diagrammatically looks like

$$\mathbb{R}(\lambda) = \frac{1}{\lambda} \left(\begin{array}{cc} \text{---} + \text{diagram of two puddles} + \dots & \text{diagram of one puddle} + \dots \\ \text{diagram of one puddle} + \dots & \text{---} + \text{diagram of two puddles} + \dots \end{array} \right). \quad (4.48)$$

The resolvent for system $R_1 \cup R_1^*$ in the state $|\rho_{R_1 R_2}^{m/2}\rangle$ is given by

$$R(\lambda) = \text{Tr}_{R_1 R_1^*}(\mathbb{R}_{11}(\lambda)) \quad (4.49)$$

A single copy of $(\rho_{R_1 R_2}^{m/2})^\Gamma$ is referred to as a *puddle* and given two contiguous sets of puddles, there are

two classes of diagrams, either *disconnected* or *connected*. As before, consider the connected part of \mathbb{R} that we call \mathbb{F} . This corresponds to a sum over the sub-diagrams over all connected contractions. We have

$$\mathbb{R}(\lambda) = \frac{1}{\lambda} + \frac{\mathbb{F}}{\lambda^2} + \frac{\mathbb{F}^2}{\lambda^3} + \dots = \frac{1}{\lambda - \mathbb{F}} \quad (4.50)$$

A useful fact is that all diagrams in \mathbb{F} and \mathbb{R} take the following form: (see Fig. (4.5))

$$\mathbb{F}(\lambda) = \begin{pmatrix} G_{11}(1_{R_1 R_1^*} - e_{R_1}) + F_{11}e_{R_1} & F_{12} |\epsilon_{R_1}\rangle \langle \epsilon_{R_2}| \\ F_{21} |\epsilon_{R_2}\rangle \langle \epsilon_{R_1}| & G_{22}(1_{R_2 R_2^*} - e_{R_2}) + F_{22}e_{R_2} \end{pmatrix}, \quad (4.51)$$

$$\mathbb{R}(\lambda) = \begin{pmatrix} S_{11}(1_{R_1 R_1^*} - e_{R_1}) + R_{11}e_{R_1} & R_{12} |\epsilon_{R_1}\rangle \langle \epsilon_{R_2}| \\ R_{21} |\epsilon_{R_2}\rangle \langle \epsilon_{R_1}| & S_{22}(1_{R_2 R_2^*} - e_{R_2}) + R_{22}e_{R_2} \end{pmatrix}, \quad (4.52)$$

where $|\epsilon_{R_1}\rangle = \frac{1}{\sqrt{k_1}} |1_{R_1}\rangle$ is the maximally mixed state on $R_1 R_1^*$ (same for $|\epsilon_{R_2}\rangle$), $e_{R_1} = |\epsilon_{R_1}\rangle \langle \epsilon_{R_1}|$ and $e_{R_2} = |\epsilon_{R_2}\rangle \langle \epsilon_{R_2}|$ are normalized minimal projectors and F is a 2×2 matrix of scalars (not to be confused with \mathbb{F}).

In order to write down a Schwinger-Dyson equation for $\mathbb{F}(\lambda)$, we can organize the different diagrammatic contributions to \mathbb{F} by the number of \mathbb{R} insertions, labelled $k - 1$, where k is the number of puddles in each diagram:

$$\mathbb{F}(\lambda) = \lambda \left(\begin{array}{c} \text{conn.} \\ \text{---} \lambda \mathbb{R} \text{---} \\ \text{---} \end{array} + \dots \quad \begin{array}{c} \text{---} \\ \text{---} \text{conn.} \text{---} \\ \text{---} \end{array} + \dots \\ \begin{array}{c} \text{---} \\ \text{---} \text{conn.} \text{---} \\ \text{---} \end{array} + \dots \quad \begin{array}{c} \text{---} \\ \text{---} \text{conn.} \text{---} \\ \text{---} \end{array} + \dots \end{array} \right) \quad (4.53)$$

where the shorthand *conn.* indicates connected contractions. In the above figure, the bubbles of $\lambda \mathbb{R}$ indicate insertions of the resolvent matrix given in Eq. (4.51) and the various components of the matrix are represented by coloured index lines. Thus, combining Eq. (4.53) and Eq. (4.50), we now have self-consistency equations that we can solve to obtain \mathbb{R} and \mathbb{F} , order by order in k .

4.4.2 Spectrum and reflected entropy

The solution to the Schwinger-Dyson equation is identical to that obtained in Chapter 3 for a random tripartite state. Thus, we only discuss the results here. The results follow from a conjecture that the important contributions to the matrix \mathbb{F} come from the lowest two orders in k , i.e. $\mathbb{F} \simeq \mathbb{F}^{(1)} + \mathbb{F}^{(2)}$, in the limit we are considering. Evidence for this conjecture in the case of the microcanonical ensemble is provided in Chapter 3, while here we simply apply the same conjecture, now to the case of the canonical ensemble, and obtain physically sensible results.

Since the solution to the Schwinger-Dyson equation is obtained by considering $k = 1$ and $k = 2$, the two

parameters that determine the spectrum turn out to be given by (e.g. for $m = 6$)

$$D_m = \frac{\sqrt{\lambda}}{\sqrt{k_1 k_2}} \text{ (arc) } = \frac{\sqrt{\lambda}}{\sqrt{k_1 k_2}} \sum_{\text{topologies}} \text{ (circle with regions) }, \quad (4.54)$$

$$B_m = \frac{\sqrt{\lambda}}{\sqrt{k_1 k_2}} \text{ (wide arc) } = \frac{\sqrt{\lambda}}{\sqrt{k_1 k_2}} \sum_{\text{connected topologies}} \text{ (circle with regions and dashed line) }, \quad (4.55)$$

where connected topologies are the ones which have geometries joining at least two asymptotic boundaries on either side of the vertical dashed line. We define the normalized quantities $\hat{B}_m = \frac{B_m}{Z_1}$ and $\hat{D}_m = \frac{D_m}{\sqrt{Z_1}}$. Further, these quantities are related by a sum rule:

$$\hat{D}_m^2 + \hat{B}_m = 1 \quad (4.56)$$

The solution to the resolvent is then given by

$$R(\lambda) \approx \frac{(\chi_A \chi_B)^2}{2\hat{B}_m \lambda} \left(\lambda + \hat{B}_m \left(\frac{1}{\chi_B^2} - \frac{1}{\chi_A^2} \right) - \sqrt{(\lambda - \lambda_+)(\lambda - \lambda_-)} \right) + \frac{1}{\lambda - \hat{D}_m^2} \quad (4.57)$$

with

$$\lambda_{\pm} = \frac{\hat{B}_m}{(k_1 k_2)^2} \left(\sqrt{k_1^2 - 1} \pm \sqrt{k_2^2 - 1} \right)^2 \quad (4.58)$$

The spectrum obtained from Eq. (4.57) takes a simple form (see Fig. (4.6)), with two superselection sectors: a single pole of weight $p_d = \hat{D}_m^2$ and a mound of eigenvalues with weight $p_c = \hat{B}_m$. The mound is a Marchenko-Pastur (MP) distribution with support between $\lambda_{\pm} \simeq \hat{B}_m (k_1^{-1} \pm k_2^{-1})^2$ and $\min(k_1^2 - 1, k_2^2 - 1)$ eigenvalues. I.e., the spectrum is given by

$$D(\lambda) = \frac{(k_1 k_2)^2}{2\pi p_c \lambda} \sqrt{(\lambda_+ - \lambda)(\lambda - \lambda_-)} + \delta(\lambda)(k_1^2 - k_2^2)\theta(k_1^2 - k_2^2) + \delta(\lambda - p_d), \quad (4.59)$$

where the sum rule then takes the form:

$$p_c + p_d = 1, \quad (4.60)$$

and thus we see that these quantities act like two ‘‘classical probabilities’’.

Using Eq. (4.54), we obtain

$$p_d = \frac{(\text{tr}(\rho_{R_1 R_2}^{m/2}))^2}{k \text{tr} \rho_{R_1 R_2}^m} \quad (4.61)$$

$$p_c = 1 - p_d. \quad (4.62)$$

we interpret these superselection sectors as corresponding to the two different geometries shown in Fig. (4.8),

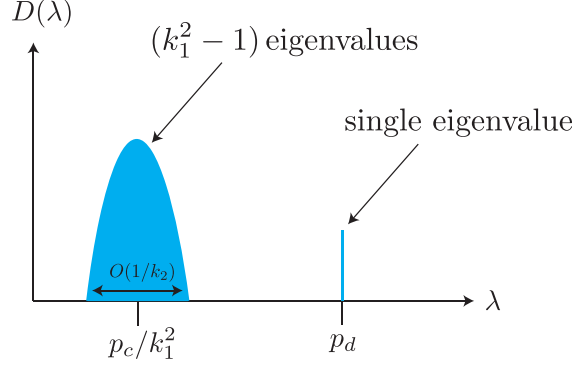


Figure 4.6: The spectrum obtained from the resolvent Eq. (3.89). We take $k_1 < k_2$ here so the MP distribution has no zero eigenvalues.

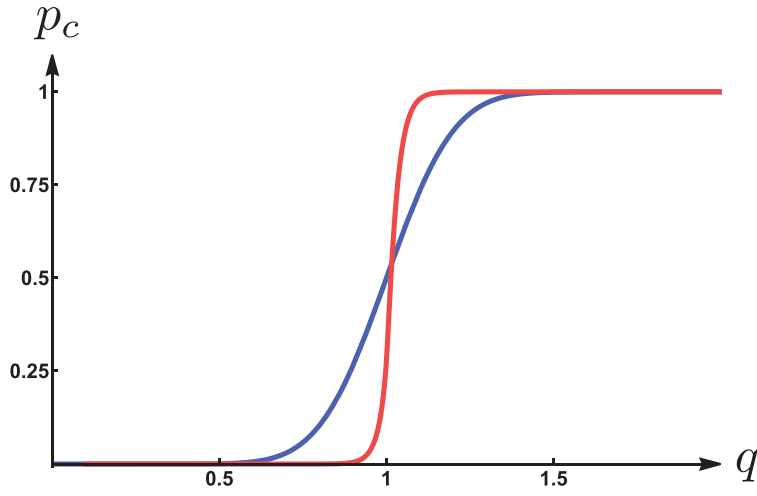


Figure 4.7: Plot of $p_c(q) \approx \frac{S_R(R_1:R_2)}{2 \min(S(R_1), S(R_2))}$ for $m = 1$ as a function of $q = \frac{\beta s_k}{2\pi}$, for $\beta = 1$, in the canonical ensemble (blue) and microcanonical ensemble (red). The phase transition in the canonical ensemble is spread out over a region of size $\Delta s = O(\frac{1}{\sqrt{\beta}})$ due to thermal fluctuations.

a disconnected and connected purification respectively. Thus, the reflected spectrum depends on the Renyi entropies of $\rho_{R_1 R_2}$, which we computed in Sec. (4.3.2). For $m = 1$, the physically most interesting case, we have from Eq. (4.61) and Eq. (4.40),

$$p_d \approx k \lambda_0 \approx \int_{s_k}^{\infty} ds \rho(s) w(s), \quad (4.63)$$

which can be interpreted as the Pre-Page probability as discussed earlier. Consequently, the connected probability p_c is interpreted as the Post-Page probability. We plot this result and compare the phase transitions in the canonical and microcanonical ensemble in Fig. (4.7). Due to thermal fluctuations, the phase transition is spread out over a range of parameter space of size $\Delta s = O(\frac{1}{\sqrt{\beta}})$.

The reflected entropy is given by (assuming $k_1 < k_2$)

$$S_R(R_1 : R_2) = \begin{cases} 0 & k < \exp(S_{BH}) \\ 2 \log k_1 & k > \exp(S_{BH}). \end{cases} \quad (4.64)$$

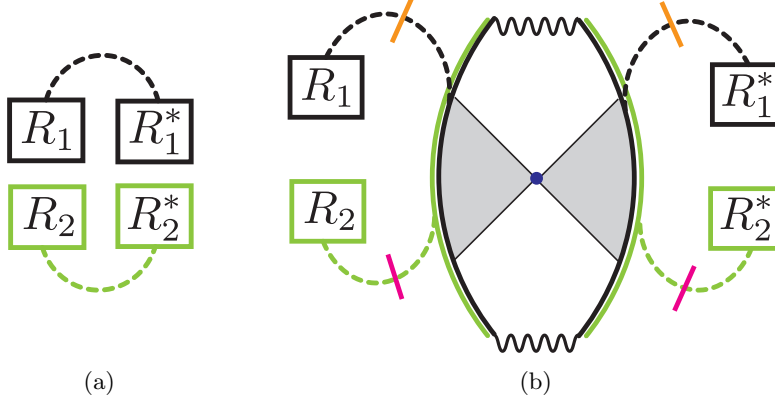


Figure 4.8: (a) The canonical purification in the disconnected phase has radiation systems purifying themselves. (b) The canonical purification in the connected phase has a state of radiation systems entangled via a closed universe. The two candidate RT surfaces are denoted orange and pink.

This is the main result of this chapter. The reflected entropy is given by:

$$S_R(R_1 : R_2) \approx p_c(2 \min(S(R_1), S(R_2))), \quad (4.65)$$

where we generally have the upper bound $S_R(R_1 : R_2) \leq 2 \min(S(R_1), S(R_2))$. Thus, Fig. (4.7) serves as an approximate plot of $S_R(R_1 : R_2)$ normalized by the upper bound.

4.4.3 Renyi Reflected Entropy

Having discussed the reflected entropy, we now analyze the (m, n) -Renyi reflected entropies. Since the spectrum is an analytic function of m , the Renyi entropies can be computed by using the sum of the moments of the two sectors in the spectrum

$$S_n(R_1 R_1^*) = \frac{1}{1-n} \ln \left(p_d^n + k_1^{2(1-n)} r^{-2} C_n(r^2) p_c^n \right) \quad (4.66)$$

where $r = k_1^2/k_2^2$ and $C_n(q)$ is the q -Catalan number defined by

$$C_n(q) = \sum_{k=0}^n q^k N(n, k), \quad (4.67)$$

where $N(n, k)$ is the Narayana number. Notably, the probabilities are the only source of m -dependence. Thus, we need to analyze the behaviour of $p_d(m)$ as we cross the Page transition using the analysis in Sec. (4.3.2).

For $m \geq 2$, we obtain

$$p_d \approx \begin{cases} 1 & s_k < s_k^{(m)} \\ \frac{\exp \left[(m-1)S_0 + (m-\frac{1}{m})\frac{2\pi^2}{\beta} \right]}{k^{m-1}} & s_k^{(m)} < s_k < s_k^{(m/2)} \\ \frac{\exp \left[S_0 + \frac{6\pi^2}{m\beta} \right]}{k} & s_k^{(m/2)} < s_k. \end{cases} \quad (4.68)$$

There are two continuous transitions in p_d and hence, also in the (m, n) -Renyi reflected entropy. However, the second transition is almost invisible since p_d is already non-perturbatively small at $s_k = s_k^{(m/2)}$ and the

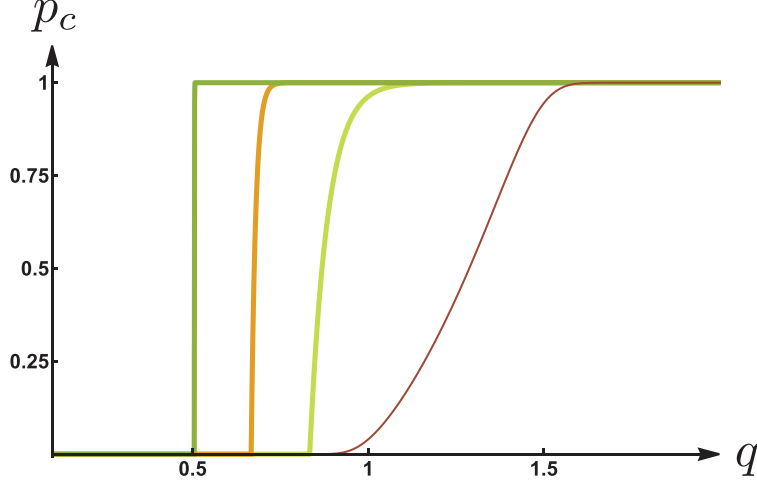


Figure 4.9: Analytic plot of $p_c(m, q)$ for $m = 1.5$ (yellow), $m = 3$ (orange) and $m = 100$ (green) and numerical plot for $m = 0.7$ (thin, brown) as a function of $q = \frac{\beta s_k}{2\pi}$ for $\beta = 1$. The locations at which the $(m, 1)$ Renyi reflected entropies undergo a transition changes as a function of m for $m > 1$.

reflected entropy is dominated by the connected entanglement wedge.

For $m \in (1, 2]$, the phase transition in p_d is largely determined by the phase transition in $\text{tr}(\rho_{R_1 R_2}^m)$ which occurs at $s_k = s_k^{(m)} < s_1$. Thus, we obtain

$$p_d \approx \begin{cases} 1 & s_k < s_k^{(m)} \\ \frac{\exp\left[(m-1)S_0 + (m-\frac{1}{m})\frac{2\pi^2}{\beta}\right]}{k^{m-1}} & s_k^{(m)} < s_k < s_1 \\ O(e^{-\frac{1}{\beta}}) & s_1 < s_k, \end{cases} \quad (4.69)$$

where the value in the last line is difficult to compute analytically, although it is non-perturbatively suppressed and has a negligible effect on the reflected entropy. We plot the behavior for $p_d(m)$ for different values of $m > 1$ in Fig. (4.9).

Finally, for the case $m < 1$, there is a multiplicative uncertainty in the calculation of $\text{tr}(\rho_{R_1 R_2}^m)$ which makes it difficult to compute $p_d(q)$ analytically. We provide a numerical plot instead in Fig. (4.9). Qualitatively, the transition happens over a large region in parameter space corresponding to $s_k \in [s_1, s_m]$.

To summarize, the phase transition in the (m, n) -Renyi reflected entropy comes from a shift in dominance between the two terms in Eq. (4.66). As $n \rightarrow 1$, the transition is dictated by the phase transition in p_d . This transition is qualitatively different for $m > 1$ and $m < 1$. For $m > 1$, it is a sharp transition at $s_k = s_k^{(m)}$ and for $m < 1$, it is spread out over $s_k \in [s_1, s_m]$.

4.5 Discussion

In this chapter we have analyzed the canonical purification and reflected entropy in the West Coast Model. We found that the holographic proposal is satisfied in the expected regimes: the canonical purification is related to a doubled spacetime, and the reflected entropy is related to the entanglement wedge cross section. Furthermore, by summing over the contributions from all relevant saddles, we have understood how the geometric picture evolves as we cross an entanglement phase transition. We now discuss certain interesting

aspects of our calculation and potential directions for future research.

Relation to Petz map

Consider a code subspace of bulk states encoded in the boundary Hilbert space. The Petz map provides an explicit realization in this setting of a reconstruction that maps a given bulk operator to a boundary operator [15, 143, 144]. In the West Coast Model, one can consider bulk operators that live on the ETW brane. Before the Page transition, they are reconstructable by the black hole B , whereas after the Page transition they are reconstructable by the radiation system R . More so, in Ref. [15], they computed the probability of the Petz map acting on the radiation to succeed. It turns out to be given by p_c , precisely the probability that showed up in our calculation of the reflected spectrum (regardless of the choice of how to split R into $R_1 R_2$). This is true in both the microcanonical ensemble and the canonical ensemble (see Fig. (4.7) for our p_c , which matches the Petz recovery probability computed in Ref. [15]).

This hints at a connection between the reflected entropy and the Petz map success probability. From one point of view, this seems completely sensible within the paradigm of entanglement wedge reconstruction. The reflected entropy $S_R(R_1 : R_2)$ is a sharp diagnostic of whether the entanglement wedge is connected, and only when it's connected does the entanglement wedge of $R_1 R_2$ include the black hole interior. Indeed, the probability p_c is simply the probability of measuring the canonical purification of $R_1 R_2$ in the connected phase. It will be interesting to investigate a possible deeper connection between the reflected entropy and reconstruction maps.

Area fluctuations

Here, we considered a holographic state in which the horizon area for B had area fluctuations. However, in order to do the calculation, we needed to consider a maximally entangled state between R and the ETW brane flavours. In the ER=EPR story, this can be interpreted as considering a three boundary wormhole with area fluctuations for the horizon of B but fixed area boundary conditions for the horizons of R_1 and R_2 respectively, see Fig. (4.10). It would be interesting in the future to understand how the area fluctuations of R_1 and R_2 affect the reflected entropy. Presumably, it will affect the spectrum on $R_1 R_1^*$ by including the effects of thermal fluctuations into the corresponding superselection sectors. One may attempt to analyze this using the techniques of the equilibrium approximation [145, 146].

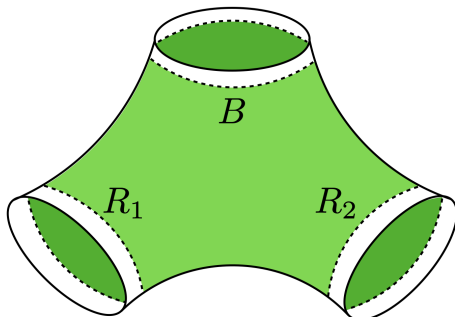


Figure 4.10: The three-boundary wormhole corresponding to our current setup.

Chapter 5

Double Random Tensors

In this chapter, we carry on with our analysis of reflected entropy in RTNs in the hope of finding other undiscovered aspects of the replica trick. We focus on an RTN consisting of two random tensors, which we refer to as *2TN*. 2TN can be interpreted as a model for a four-boundary wormhole as depicted in Fig. (5.1), where the areas of the labelled surfaces are fixed to a narrow window [96–98]. A key ingredient in our calculation is the use of *Temperley-Lieb (TL)* algebra and its representation theory. The appearance of the TL algebra has deep implications on the spectra of the 2TN model, and it hints an possible connection between our results and an emergent type-II von Neumann algebra.

More generally, we provide heuristic arguments that the calculations in 2TN are also useful for more general settings, e.g., the familiar setup of two intervals in vacuum AdS. Since the bulk geometry is coarse-grained down to just two tensors, the model cannot capture any of the local dynamics. However, it does capture general topological aspects of the gravitational calculation which turn out to be the relevant aspect for the reflected entropy, including near phase transition effects.

The results presented in this chapter is mostly based Ref. [68] as well as unpublished notes from the author.

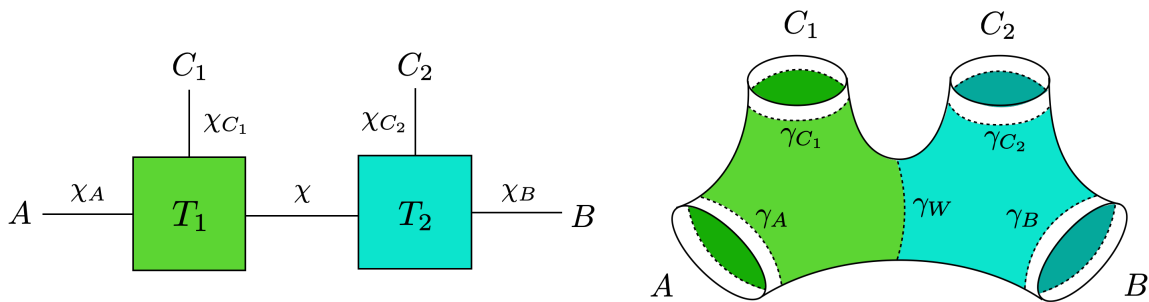


Figure 5.1: (left) The 2TN tensor network considered in this section is built from two random tensors T_1 and T_2 . The parameters are the boundary bond dimensions $\chi_A, \chi_B, \chi_{C_1}, \chi_{C_2}$ and the internal bond dimension χ . (right) The wormhole solution that is modeled by 2TN. The external bond dimensions corresponds to the three horizon areas and the internal bond dimension χ corresponds to the cross-section surface γ_W .

$$|\sqrt{\rho_{AB}}\rangle = \sqrt{p_0} \left(\begin{array}{c} A \\ \vdots \\ B \\ \hline A^* \quad B^* \end{array} \right) + \sqrt{p_1} \left(\begin{array}{c} A \quad B \\ \text{shaded region} \\ A^* \quad B^* \end{array} \right) + \sqrt{p_2} \left(\begin{array}{c} A \quad B \\ \text{shaded region} \\ A^* \quad B^* \end{array} \right) + \dots$$

Figure 5.2: The canonical purification $|\sqrt{\rho_{AB}}\rangle$ consists of a superposition of a one parameter family of geometries labelled by k . They are obtained by gluing together $2k$ copies of the shaded portion (see Fig. (5.1)) of the connected entanglement wedge of AB in the four boundary wormhole. The k -th geometry has $2k$ copies of the entanglement wedge cross section labelled EW .

5.1 Summary of results

In Sec. (5.2), we start by motivating the gravitational construction of novel, higher genus saddles that contribute to the canonical purification. We consider the gravitational state corresponding to the four boundary wormhole depicted in Fig. (5.1), prepared using a Euclidean path integral with fixed area boundary conditions. As discussed in Refs. [15, 46, 62, 63, 96–98], the replica trick for such fixed-area states is simplified by the fact that one can simply glue together multiple copies of the original bulk geometry without having to solve for a new backreacted geometry. Thus, we have control over the different saddles contributing to the canonical purification. By doing a replica trick to construct the state $|\rho_{AB}^{m/2}\rangle$ for even integer m [56], we find saddles labelled by a topological index $k \in \mathbb{Z}_{>0}$. They correspond to geometries with initial data slices obtained by gluing together $2k$ copies of the shaded region (see Fig. (5.1)) of the connected entanglement wedge of AB in the original state. Each such geometry contributes with an amplitude $\sqrt{p_k}$ computed from the path integral. The canonically purified state can then be obtained via analytic continuation to $m = 1$, and is approximately given by a superposition over such geometries as shown in Fig. (5.2). Thus, we obtain a family of geometries that contribute to the entanglement wedge gluing procedure dual to the canonical purification [56, 62, 113, 114]. Finally, computing the reflected entropy, we see that the geometry labelled by k contributes an amount $2k \frac{EW(A:B)}{4G}$ weighted by its probability.

Having motivated the existence of these higher genus geometries from the gravitational path integral, we set up the 2TN problem in Sec. (5.3) to get a better handle on such effects. The replica trick for reflected entropy, discussed in Sec. (5.3.1), involves computing the so called (m, n) -Rényi reflected entropy [56]. Here n is the usual Rényi entropy index and m labels the state $|\rho_{AB}^{m/2}\rangle$, a generalization of the canonical purification. For the reflected entropy, one needs to then analytically continue to $m, n \rightarrow 1$. Analyzing the (m, n) replica trick for the 2TN problem beyond the saddle point approximation requires a new tool, the Temperley-Lieb (TL) algebra [147], which we introduce in Sec. (5.3.2). Using the resolvent trick [15, 46, 48, 67, 118–120], we show that the reflected spectrum can be categorized into different sectors in terms of the irreducible representations of the TL algebra. These irreps are labeled by an index k which we call “topological” since it corresponds to the topology of the higher genus saddles in the gravitational path integral.

With the formalism for computing the reflected spectrum set up, we compute and analyze the 2TN reflected spectrum and entropy using the TL algebra in Sec. (5.4). As a proof of principle, we first solve for the spectrum at first few even integer values of m in Sec. (5.4.1). In order to then relate to the semiclassical limit in gravity, we take the limit where χ is large in Sec. (5.4.2). In this limit, we find the leading- χ contribution to reflected spectrum that can be analytically continued to $m = 1$. The spectrum exhibits an infinite sequence of delta function peaks, labelled by the index $k \in \mathbb{Z}_{\geq 0}$. Each peak consists of χ^{2k} eigenvalues, thus contributing

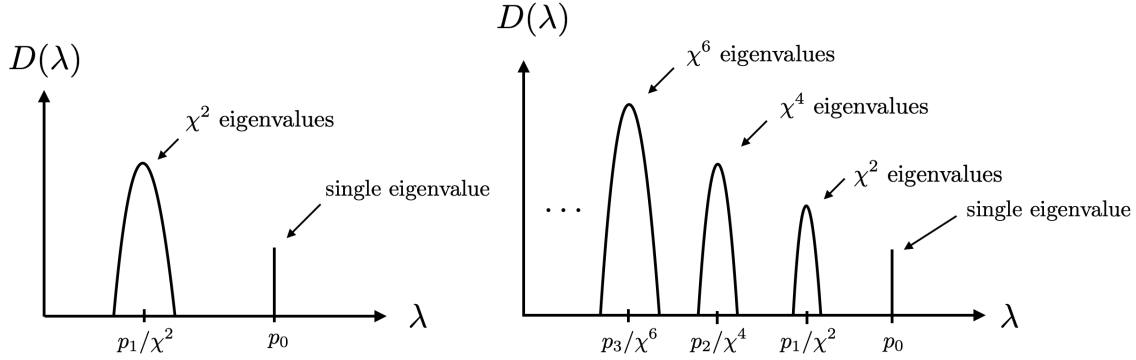


Figure 5.3: Sketch of spectrum of 1TN vs 2TN. While the 1TN model has two peaks corresponding to the connected and disconnected phases, the 2TN model has infinitely many peaks corresponding to the novel, higher-genus saddles discovered in Sec. (5.2).

to the reflected entropy by an amount $2kEW(A : B)$. This 2TN spectrum has a much richer structure than the single random tensor analyzed in Chapter 3, see comparison in Fig. (5.3). We analyze the properties of the 2TN spectrum and its relation to emergent superselection sectors and quantum error correction in Sec. (5.4.3). Using the reflected spectrum, we find consistency with the holographic proposal, Eq. (2.32), away from phase transitions where either $k = 0$ or $k = 1$ dominates. More so, the new sectors $k \geq 2$ become important near the phase transition and smooth out the discontinuity in the reflected entropy. In Sec. (5.4.4) we consider the leading corrections to the large χ limit. We find that these corrections shift the locations of the delta functions and spread them into peaks with finite width containing χ^{2k} eigenvalues. We give an estimate of the shift and relevant widths. Finally, we demonstrate the consistency of our calculations with numerical results in Sec. (5.4.5).

With this, we conclude in Sec. (5.5) with a discussion of how the results obtained here generalize to arbitrary RTNs which model multiboundary wormholes. We provide heuristic arguments that these additional sectors also contribute to the canonical purification in more general settings such as the two interval example in vacuum AdS. We also comment on the relation of our results to the emergence of non-trivial von Neumann algebras in gravitational theories. More specifically we speculate that signatures of a non-trivial von Neumann algebra, connected to the TL algebra, will emerge from a modular flowed version of reflected entropy.

We provide a short review on Temperley-Lieb algebra in Appendix B. Other supplementary materials of this chapter are provided in Appendix D: We review multiboundary wormholes in Appendix D.1. Calculations of the leading corrections to the large χ limit can be found in Appendix D.2. Proofs of various results used in Sec. (5.4) are available in Appendix D.4.

5.2 Motivation: canonical purification in gravity

Before analyzing the 2TN model in detail, we provide motivation for the anticipated results by constructing novel gravitational saddles that contribute to the canonical purification. We will discover new features from the gravitational path integral that will be mirrored by the 2TN model in Sec. (5.4). For simplicity, our discussion will focus on pure 3D gravity with a negative cosmological constant, where multiboundary wormholes are well understood [148–150]. In this context, we can make a direct connection between wormholes and RTNs, closely following and elaborating on the analysis in Ref. [122].

The 2TN model can be directly translated into a four-boundary wormhole with a hyperbolic metric as

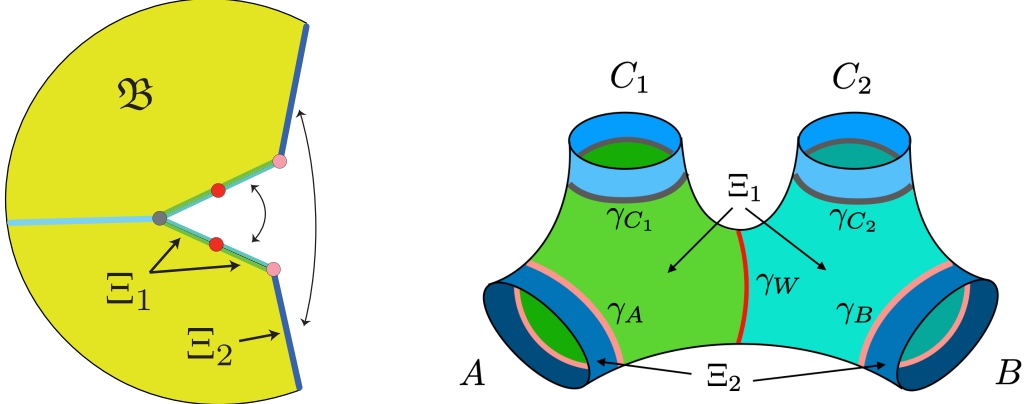


Figure 5.4: A fixed-area Euclidean saddle \mathfrak{B} (left) computing the norm of the state $|\psi\rangle$ representing a four boundary wormhole (right). Due to fixed-area boundary conditions at the relevant surfaces $\gamma_{A,B,C,W}$, generically the saddle consists of conical defects at these locations. The \mathbb{Z}_2 symmetric slice of the saddle is a Cauchy slice Ξ of the wormhole geometry with shaded regions and extremal surfaces represented on either side. The surfaces Ξ_1 (light and dark green) and Ξ_2 (dark blue) are identified as shown, but can be cut open to use as a building block for the replica trick.

shown in Fig. (5.1). First, it is useful to match the degrees of freedom on either side. The parameters in the tensor network are the bond dimensions. On the other hand, the moduli of the wormhole can be understood by a pair-of-pants decomposition of the hyperbolic geometry into two constituent three-boundary wormholes. For each three-boundary wormhole, the moduli are the three horizon areas. Gluing them together removes one degree of freedom due to identification and simultaneously introduces additional Dehn twist moduli. In order to have a reflection symmetric Cauchy slice and be able to apply the RT formula, we can set the twist to zero [122]. This leaves us with the areas of the labelled extremal surfaces, each corresponding to a bond in the tensor network. For the calculation of reflected entropy, these are the only surfaces that are relevant.¹ Thus, the 2TN model, despite being a rather coarse-grained description of the geometry, is sufficient to model the four-boundary wormhole accurately.

The construction of these wormhole geometries using a Euclidean path integral is also well understood (see Ref. [122] and references therein). Namely, given a spatial geometry Ξ , a corresponding Euclidean spacetime geometry that prepares such initial data is given by

$$ds^2 = l^2 (dt_E^2 + \cosh^2 t_E d\Xi^2), \quad (5.1)$$

where l is the AdS scale and t_E is the Euclidean time coordinate. However, since we are interested in preparing holographic states that are modelled by an RTN, it is important to fix the areas of the various surfaces that correspond to maximally entangled bonds [96–98]. Since these surfaces are all spacelike separated from each other, the areas can be simultaneously fixed. While the geometry in Eq. (5.1) is a valid Euclidean saddle for the fixed-area problem, other ways of preparing the same state would generically contain conical defects at the fixed-area surfaces as shown in Fig. (5.4). Moreover, Einstein’s equations require the conical defects to be located at extremal surfaces [98], and this is true by construction for the wormhole that we’re interested in.²

¹There are other possible cross-sections in the geometry which could be minimal. We discuss these in Appendix D.1 and for the comparison, one can restrict to a regime of parameters where the surface γ_W is indeed minimal.

²Note that despite the fact that Eq. (5.1) provides a valid saddle, there is no guarantee that it dominates and in general, it is not completely well understood which saddles dominate the path integral [151–153]. Our results should be understood to apply when such a dominant Euclidean saddle can be found.

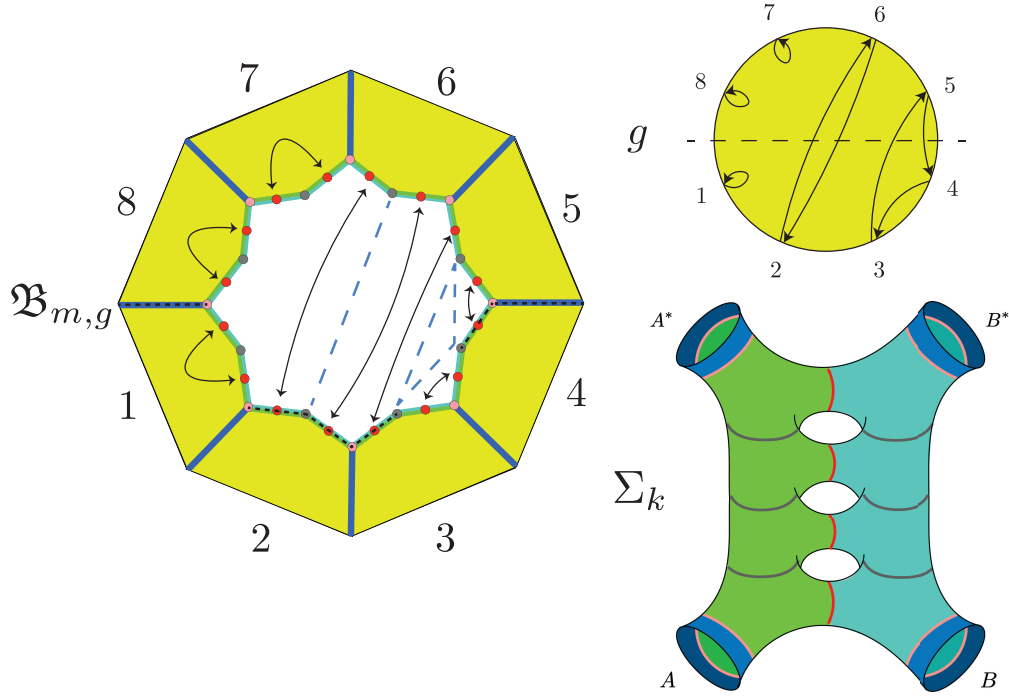


Figure 5.5: The computation of $\langle \rho_{AB}^{m/2} | \rho_{AB}^{m/2} \rangle = \text{tr}(\rho_{AB}^m)$ (e.g. $m = 8$) involves Euclidean saddles constructed by gluing m copies of the original fixed area saddle in different ways. E.g., a particular saddle $\mathfrak{B}_{m,g}$ is in a one-to-one correspondence to permutation g acting on m elements. Here, we depict one such example. The \mathbb{Z}_2 symmetric slice (black dotted) is then a Cauchy slice Σ_k for Lorentzian evolution and consists of $2k$ copies of the entanglement wedge, where k is the number of permutation cycles crossing the horizontal dotted line on the right (here $k = 2$).

Once we pick any such \mathbb{Z}_2 symmetric Euclidean geometry \mathfrak{B} , we can cut it open to obtain a preparation of the state $|\psi\rangle$ which has a spatial geometry Ξ . As usual, the norm of $|\psi\rangle$ is computed by \mathfrak{B} as depicted in Fig. (5.4). Moreover, the advantage of using fixed-area states is that we can find candidate geometries for computing $\text{tr}(\rho_{AB}^m)$ by using \mathfrak{B} as a building block. More specifically, we can cut open \mathfrak{B} in the region $\Xi_1 \cup \Xi_2$ such that $\partial\Xi_1 = \gamma_A \cup \gamma_B \cup \gamma_{C_1} \cup \gamma_{C_2}$ and $\partial\Xi_2 = A \cup B \cup \gamma_A \cup \gamma_B$. We can then glue together m copies cyclically in the region Ξ_2 as shown in Fig. (5.5). We are then left with picking a way to glue together the remaining section Ξ_1 . The different ways of gluing Ξ_1 are fixed by an element of the permutation group S_m . An example of this correspondence is demonstrated in Fig. (5.5).³ The fixed-area boundary condition ensures that all the contributing geometries solve Einstein's equations and satisfy the correct boundary conditions. Any such geometry $B_{m,g}$, obtained by gluing in a manner corresponding to a permutation g , contributes to the computation of $\text{tr}(\rho_{AB}^m)$. It is also easy to check that the Euclidean action agrees with the domain wall cost in the RTN [96]. Thus, it is clear that there is a direct correspondence between the RTN replica partition function and the gravitational path integral, which is a fact that has already been exploited in various calculations [46, 62, 63, 96, 97].

We can now look at $B_{m,g}$ for even integer m , and interpret it as computing the norm of the state $|\rho_{AB}^{m/2}\rangle$.

³In principle, we have two independent permutations on the two different portions separated by the fixed-area surface γ_W in correspondence with the two tensors in the RTN. However, saddles with different permutations are suppressed due to the cost of having a domain wall at γ_W .

It is well-known from the correspondence to the RTN that only the saddles corresponding to non-crossing permutations are important [15, 46, 62, 63], thus we will neglect all other permutations. Once we do so, it is useful to classify the non-crossing permutations by the number of cycles crossing the horizontal middle line, which is representative of the \mathbb{Z}_2 symmetric Cauchy slice of the geometry.⁴ For a crossing number k , it can be checked that the spatial geometry Σ_k is obtained by gluing together sections of $2k$ copies of the original Ξ at the horizons. We illustrate one such example in Fig. (5.5). As described before, these are also hyperbolic geometries with a different pair-of-pants decomposition and by construction are prepared by a Euclidean path integral which solves Einstein equations with fixed-area boundary conditions.⁵ Given the Cauchy data on Ξ that satisfies the constraint equations, one can then evolve it in Lorentzian time to find the full spacetime geometry.⁶

Since the spatial geometries on the \mathbb{Z}_2 symmetric slice are different for different values of k , the states are orthogonal in the gravitational path integral approximation. Thus, we can divide the path integral into a sum over the index k as

$$Z_m = \sum_{k=0}^{m/2} Z_{k,m}, \quad (5.2)$$

and for each value of k , we can write down

$$Z_{k,m} = \langle \psi_{k,m} | \psi_{k,m} \rangle. \quad (5.3)$$

The state $|\psi_{k,m}\rangle$ has an associated geometry Σ_k and can be written as a superposition over different half-permutations with appropriate weight-factors that contribute to its norm. For example, we have (for $m = 4$)

$$\begin{aligned} |\psi_{0,4}\rangle &= |\text{---}\rangle + |\text{---}\rangle \\ |\psi_{1,4}\rangle &= |\text{---}\rangle + |\text{---}\rangle + |\text{---}\rangle \\ |\psi_{2,4}\rangle &= |\text{---}\rangle \end{aligned}, \quad (5.4)$$

where the states written above are not normalized and the overlaps of these states can be computed by closing up the open ends of the permutation and computing the action of the corresponding Euclidean saddle. We will later see in Sec. (5.4.2) that the states $|\psi_{k,m}\rangle$ are naturally associated with specific states in the standard module of the Temperley-Lieb algebra that dominate in the large χ limit. Thus, we now have written the state $|\rho_{AB}^{m/2}\rangle$ in terms of a superposition of geometries with appropriate weights determined by the path integral.

The spatial geometry Σ_k consists of $2k$ copies of the surface γ_W , which is the entanglement wedge cross section in the connected phase. Now we can use the fact that the entropy of a superposition of a small number of fixed-area states behaves approximately linearly as argued in Refs. [46, 62, 135]. Thus, the analog

⁴The slice is only locally \mathbb{Z}_2 symmetric, but not globally so in general. The overall \mathbb{Z}_2 symmetry is restored by the sum over saddles.

⁵It is important to note that in general there are also perturbative corrections which have completely neglected in this analysis since there is no corresponding feature in the RTN. Thus, even at this level the RTN only captures certain topological aspects of the gravitational path integral, but they are usually the important non-perturbative corrections near phase transitions.

⁶Depending on how sharply the areas have been fixed, there may or may not exist a smooth spacetime to the future and past of these fixed-area surfaces (see Ref. [154] for more details).

of reflected entropy for the state $|\rho_{AB}^{m/2}\rangle$ is computed by averaging over the different sectors, i.e.,

$$\begin{aligned} S_R^{(m)}(A : B) &= S(\rho_{AA^*})_{|\rho_{AB}^{m/2}\rangle} \\ &= \sum_{k=0}^{m/2} p_k(m) (2kEW(A : B)) - p_k(m) \log p_k(m), \end{aligned} \quad (5.5)$$

where $EW(A : B)$ is used as a shorthand to represent the area of γ_W , independent of which phase dominates. The weights $p_k(m) = \langle \psi_{k,m} | \psi_{k,m} \rangle$ can be thought of as probability weights associated to the geometries Σ_k . We postpone the precise formulae for $p_k(m)$ to Sec. (5.4.2), but note for now that we will find a function that is analytic in m . By extending the sum in Eq. (5.5) to all integer k , we can thus analytically continue the answer away from even integer values of m . Doing so, we obtain an expression for the reflected entropy,

$$S_R(A : B) = \sum_{k=0}^{\infty} p_k(2kEW(A : B)) - p_k \log p_k, \quad (5.6)$$

where $p_k \equiv p_k(1)$. Thus, we have found that the canonical purification is given by a superposition of geometries obtained by gluing together multiple copies of the entanglement wedge of AB as demonstrated in Fig. (5.2). As we shall see later, the different geometries Σ_k obtained by this construction can equivalently be interpreted in terms of new RTNs which are obtained by gluing multiple copies of the network at different bonds, see Fig. (5.13). Thus, this provides a refined version of the effective description suggested in Sec. (3.8) for the canonical purification.

5.3 Setup

In this section, we set up the problem of finding the reflected entropy in our model of interest, the 2TN model. Sec. (5.3.1) describes the replica trick for reflected entropy, discussing the relevant saddle point configurations. Sec. (5.3.2) then sets up the problem of computing the resolvent for the reflected density matrix by introducing the Temperley-Lieb algebra.

5.3.1 Replica trick for the 2TN model

To recap, the replica trick for the reflected entropy involves computing the (m, n) Rényi reflected entropy defined as

$$S_R^{(m,n)}(A : B) = S_n(AA^*)_{|\rho_{AB}^{m/2}\rangle}, \quad (5.7)$$

which is the n th Rényi entropy of subregion AA^* in a state $|\rho_{AB}^{m/2}\rangle$ that generalizes the canonical purification.⁷ For integer n and $\frac{m}{2}$, Eq. (5.7) can be computed using correlation functions of appropriately defined twist

⁷Note that we ignored normalization factors in the state for simplicity of notation.

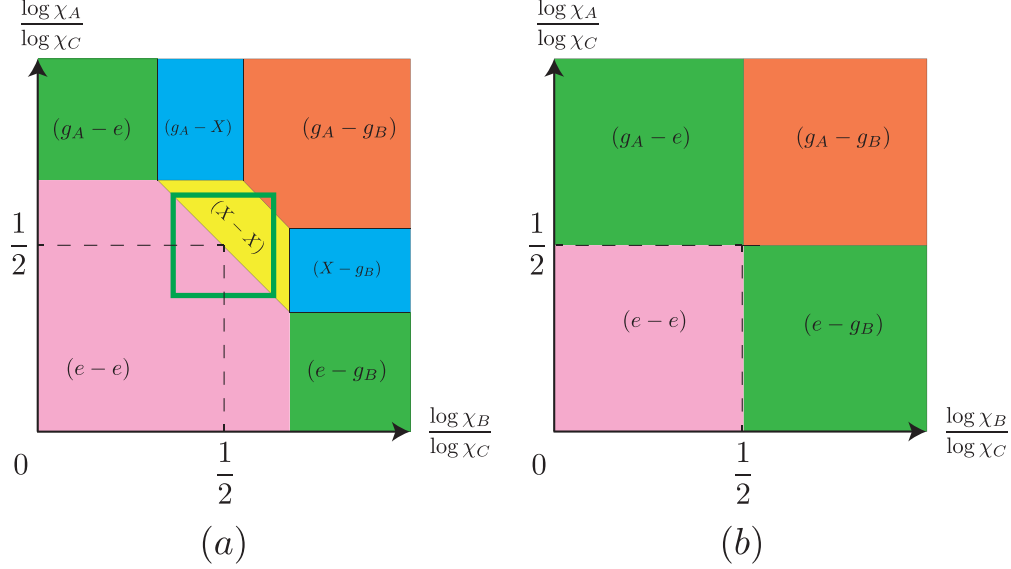


Figure 5.6: (a): An illustration of the phase diagram in the saddle point limit for 2TN for generic values of $m \geq 2, n \geq 1, \chi$ as a function of $\frac{\log \chi_A}{\log \chi_C}$ and $\frac{\log \chi_B}{\log \chi_C}$. The dominant elements in each phase are shown in a tuple as (g_1, g_2) . The green square roughly indicates the region of the phase diagram accessed by the TL limit. (b): As we take the limit $\frac{\log \chi}{\log \chi_C} \rightarrow 0$, the yellow and blue domains shrink in the phase diagram.

operators on mn copies of the system, i.e.,

$$\begin{aligned}
S_R^{(m,n)}(A : B) &= \frac{1}{1-n} \log \left(\frac{Z_{m,n}}{(Z_{m,1})^n} \right) \\
Z_{m,n} &= \langle \psi |^{\otimes mn} \Sigma_A(g_A) \Sigma_B(g_B) | \psi \rangle^{\otimes mn} \\
Z_{m,1} &= \langle \psi |^{\otimes m} \Sigma_{AB}(\tau_m) | \psi \rangle^{\otimes m},
\end{aligned} \tag{5.8}$$

where $\Sigma_R(g)$ implement the permutation g on subregion R .

We now specialize to the 2TN model, which is depicted in Fig. (5.1). It models a four-boundary wormhole with horizon areas \mathcal{A}_i which are related to the external bond dimensions $\chi_i = \exp[\frac{\mathcal{A}_i}{4G}]$, where $i \in \{A, B, C_1, C_2\}$. Moreover, the internal bond dimension χ is related to the area \mathcal{A}_W of the cross section surface γ_W in a similar fashion. For convenience, we denote $\chi_{C_1} \chi_{C_2} = \chi_C$, which is related to the total horizon area for region C .

When $\min(\mathcal{A}_A, \mathcal{A}_B) < \mathcal{A}_W$, the analysis is similar to that done for the single random tensor which was studied in detail in Chapter 3. Thus, here we will only be interested in the situation where the minimal entanglement wedge cross section $EW(A : B)$ is indeed given by \mathcal{A}_W in the connected phase. We will ensure this to be the case by picking \mathcal{A}_W to be parametrically smaller than $\mathcal{A}_{A/B/C}$.

For this problem, there are two limits of interest that we can discuss:

- The Temperley-Lieb (TL) limit: $q_A = \frac{\chi_A}{\chi_{C_1}}, q_B = \frac{\chi_B}{\chi_{C_2}}, \chi$ held finite while taking all external bond dimensions $\chi_{A/B/C_1/C_2} \rightarrow \infty$.
- The saddle point limit: $\frac{\log \chi_i}{\log \chi_C}$ is held finite while taking all bond dimensions $\chi_i \rightarrow \infty$.

While our calculations in this chapter will be in the TL limit, we briefly make a detour to discuss the phase diagram for the 2TN model in the saddle point limit. The saddle point limit is useful since it can be

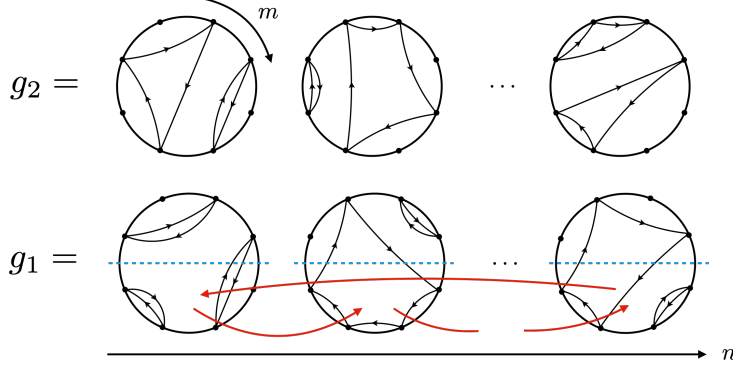


Figure 5.7: A graphical representation of the elements lying on the geodesics $\Gamma(g_A, e)$ and $\Gamma(g_B, e)$. An element $g_2 \in \Gamma(g_B, e)$ consists of products of non-crossing permutations acting within each circle; whereas an element $g_1 \in \Gamma(g_A, e)$ is similar to g_2 , but is additionally conjugated by the twist operator γ_τ .

shown that at every point in phase space, one only needs to optimize over the set $\{e, g_A, g_B, X\}$. We will prove this statement in Chapter 6.

For simplicity, we consider the phase diagram in the case $\chi_{C_1} = \chi_{C_2} = \sqrt{\chi_C}$. Doing so, we obtain the phase diagram shown in Fig. (5.6a) at generic values of $m \geq 2$ and $n \geq 1$. The first thing to note is that the phase diagram is convex as expected from the fact that the contributions of each possible permutation tuple is linear in $\log \chi_{A/B}$.

The TL limit approximately arises when we take the limit $\frac{\log \chi}{\log \chi_C} \rightarrow 0$ and zoom into a small, restricted region around $(\frac{1}{2}, \frac{1}{2})$. This follows from the fact that the ratios q_A and q_B are held finite. In the TL limit, the domains involving the X element shrink and we obtain the simpler phase diagram shown in Fig. (5.6b).

Returning to the calculation in Eq. (5.8) for the 2TN model, we have

$$\overline{Z}_{m,n} = \frac{1}{(\chi_A \chi_B \chi_{C_1} \chi_{C_2} \chi)^{mn}} \sum_{g_1, g_2 \in S_{mn}} \chi_A^{\#(g_1 g_A^{-1})} \chi_B^{\#(g_2 g_B^{-1})} \chi_{C_1}^{\#(g_1)} \chi_{C_2}^{\#(g_2)} \chi^{\#(g_1 g_2^{-1})}, \quad (5.9)$$

where $\#(g)$ counts the number of cycles in permutation g (including trivial ones) and we have used the relation $d(g, h) = nm - \#(gh^{-1})$. In the TL limit, the elements $g_{1/2}$ are then constrained to lie on the geodesics between $g_{A/B}$ and e , labelled by $\Gamma(g_{A/B}, e)$, since the contributions of all other elements are infinitely suppressed. The relevant geodesic condition reads

$$\#(g_1 g_A^{-1}) + \#(g_1) = n(m+1), \quad \#(g_2 g_B^{-1}) + \#(g_2) = n(m+1), \quad (5.10)$$

and the permutation elements that satisfy these conditions can be parameterized as:

$$g_1 = \gamma_\tau \left(\prod_{i=1}^n h_i \right) \gamma_\tau^{-1}, \quad g_2 = \prod_{i=1}^n k_i, \quad (5.11)$$

where h_i, k_i are permutations that act in a non-crossing fashion on the elements $m(i-1) + 1, \dots, mi$ and trivially on all other elements. γ_τ can be thought of as a “twist operator” that acts on the lower $m/2$ elements in each circle, cyclically permuting them as shown in Fig. (5.7). We refer the reader to Appendix A for more details on the geodesic elements and non-crossing permutations.

5.3.2 Resolvent via the Temperley-Lieb algebra

Now, restricting the sum to the permutations on the relevant geodesics, we can write Z_{mn} using the parametrization of Eq. (5.11) as

$$\overline{Z_{m,n}} = \left(\frac{\chi_A \chi_B}{\chi_C^m \chi^m} \right)^n \sum_{\{h_i, k_i\}} q_A^{-\sum_i \#(h_i)} q_B^{-\sum_i \#(k_i)} \chi^{\#(g_1 g_2^{-1})}. \quad (5.12)$$

To proceed, we must find a way to express $\#(g_1 g_2^{-1})$ solely in terms of h_i and k_i . To attack this problem we introduce the *Temperley-Lieb algebra*, denoted by TL_m .

The Temperley-Lieb (TL) algebra is an abstract algebra with basis vectors consisting of diagrams of non-crossing strands between $2m$ points arranged on two vertical lines as follows:

$$\text{TL}_m = \text{span} \left\{ \left[\begin{array}{c} | \\ | \\ | \\ | \end{array} \right], \left[\begin{array}{c} \cup \\ \cup \\ | \\ | \end{array} \right], \left[\begin{array}{c} \cup \\ \cup \\ \cup \\ | \\ | \end{array} \right], \left[\begin{array}{c} \cup \\ \cup \\ \cup \\ \cup \\ | \\ | \end{array} \right], \dots \right\}, \quad (5.13)$$

where each point necessarily has a strand emerging from it. This vector space is further endowed with a bilinear product given by concatenating two diagrams and replacing each closed loop by a power of χ . As an illustrative example, consider the following:

$$\left[\begin{array}{c} \cup \\ \cup \\ | \\ | \end{array} \right] \cdot \left[\begin{array}{c} \cup \\ \cup \\ | \\ | \end{array} \right] = \left[\begin{array}{c} \cup \\ \cup \\ \cup \\ \cup \\ | \\ | \end{array} \right] = \chi \left[\begin{array}{c} \cup \\ \cup \\ | \\ | \end{array} \right] \quad (5.14)$$

In our problem, the parameter χ in the algebra is chosen to be the same as the internal bond dimension in the 2TN model. For the interested reader, we present a short review of the TL algebra in Appendix B.

For our purposes, the important point is that there is a natural one-to-one correspondence between the set of non-crossing permutations NC_m and the elements of TL_m as shown pictorially in Fig. (5.8). We denote the element in TL_m corresponding to $h \in \text{NC}_m$ as $D(h)$. There is also a natural trace Tr_{TL_m} on TL_m , defined diagrammatically for basis elements by closing the strands on opposing ends and assigning the value $\chi^{\#\text{loops}}$, e.g.

$$\text{Tr}_{\text{TL}_m} \left(\left[\begin{array}{c} \cup \\ \cup \\ | \\ | \end{array} \right] \right) = \left[\begin{array}{c} \cup \\ \cup \\ \cup \\ \cup \\ | \\ | \end{array} \right] = \chi^3 \quad (5.15)$$

The trace is then linearly extended to the full algebra.

We now claim that

$$\chi^{\#(g_1 g_2^{-1})} = \text{Tr}_{\text{TL}_m} [D(h_1)^T D(k_1) D(h_2)^T D(k_2) \cdots D(h_n)^T D(k_n)], \quad (5.16)$$

where $D(h)^T$ denotes the transpose of $D(h)$, obtained by flipping the diagram across its central axis between two boundary lines. Instead of providing a formal proof, we demonstrate the above statement via pictures.

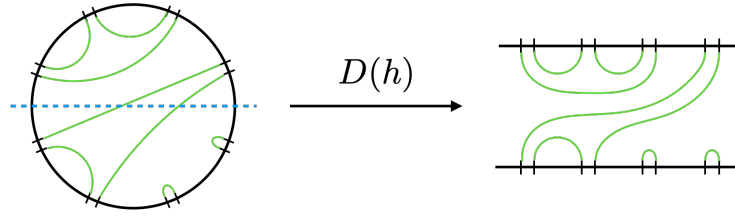


Figure 5.8: A non-crossing permutation is represented in double line notation, where there is an incoming and outgoing line at each vertex. The mapping from $h \in \text{NC}_m$ to $D(h) \in \text{TL}_m$ can be thought of as slicing the circle in half and straightening the two boundary arcs into lines while preserving the connections.

For example, for $(m, n) = (4, 2)$, we have

$$\#(g_1 g_2^{-1}) = \#(\gamma_\tau h_1 h_2 \gamma_\tau^{-1} k_2^{-1} k_1^{-1}). \quad (5.17)$$

Then, as a sample configuration consider:

$$\begin{array}{cc}
 D(h_1) = \begin{array}{c} \text{---} 1 \text{---} 2 \text{---} \\ | \quad | \\ | \quad | \\ \text{---} 3 \text{---} 4 \text{---} \end{array} & D(h_2) = \begin{array}{c} \text{---} \quad \text{---} \\ | \quad | \\ | \quad | \\ \text{---} \quad \text{---} \end{array} \\
 D(k_1) = \begin{array}{c} \text{---} \quad \text{---} \\ | \quad | \\ | \quad | \\ \text{---} \quad \text{---} \end{array} & D(k_2) = \begin{array}{c} \text{---} \quad \text{---} \\ | \quad | \\ | \quad | \\ \text{---} \quad \text{---} \end{array}
 \end{array} \quad (5.18)$$

For the above configuration, we have

$$\chi^{\#(g_1 g_2^{-1})} = \begin{array}{c} \text{---} 4 \text{---} 3 \text{---} \\ | \quad | \\ | \quad | \\ \text{---} 1 \text{---} 2 \text{---} \\ | \quad | \\ | \quad | \\ \text{---} 4 \text{---} 3 \text{---} \\ | \quad | \\ | \quad | \\ \text{---} 1 \text{---} 2 \text{---} \\ | \quad | \\ | \quad | \\ \text{---} 4 \text{---} 3 \text{---} \end{array} \begin{array}{l} D(h_1)^T \\ D(k_1) \\ D(h_2)^T \\ D(k_2) \end{array}, \quad (5.19)$$

as the reader can easily verify. This generalizes in a straightforward manner to arbitrary (m, n) .

Using this result we can then do the sum in Eq. (5.12):

$$\overline{Z}_{m,n} = \left(\frac{\chi_A \chi_B}{\chi_C \chi^m} \right)^n \text{Tr}_{\text{TL}_m} \left[\left(\sum_{h \in \text{NC}_m} D(h) q_A^{-\#(h)} \right) \left(\sum_{k \in \text{NC}_m} D(k) q_B^{-\#(k)} \right) \right]^n, \quad (5.20)$$

where we have used the fact that the h sum is invariant under $D(h) \rightarrow D(h)^T$ to drop the transpose.

We will now use Eq. (5.20) to obtain the reflected entanglement spectrum via the resolvent trick [48, 67]. The resolvent for the reflected density matrix $\rho_{AA^*}^{(m)}$ is defined as

$$R_m(\lambda) = \sum_{n=0}^{\infty} \frac{\overline{Z_{m,n}}}{\lambda^{1+n}} \quad (5.21)$$

where $Z_{m,0} = \chi_A^2$ and $Z_{m,1} = \text{Tr} \rho_{AB}^m$ (which can also be checked from Eq. (5.20)). Plugging Eq. (5.20) into Eq. (5.21) we obtain a formal expression for the resolvent:

$$R_m(\lambda) = \text{Tr}_{\text{TL}_m} \left[\lambda - \frac{\chi_{AXB}}{\chi_C^m \chi^m} \left(\sum_{h \in \text{NC}_m} D(h) q_A^{-\#(h)} \right) \left(\sum_{k \in \text{NC}_m} D(k) q_B^{-\#(k)} \right) \right]^{-1}. \quad (5.22)$$

Once we evaluate the resolvent, one can extract the eigenvalue spectrum $D_m(\lambda)$ of $\rho_{AA^*}^{(m)}$ from it using:

$$D_m(\lambda) = -\frac{1}{\pi} \lim_{\epsilon \rightarrow 0} \text{Im} R_m(\lambda + i\epsilon). \quad (5.23)$$

From the spectrum, one can obtain all the (m, n) -Rényi reflected entropies as well as the reflected entropy after analytically continuing to $m = 1$.

Now, in order to evaluate Eq. (5.22) we will pick a representation of TL_m . However, an arbitrary representation will not do the job for us. In particular, we must pick a representation such that the trace function on this representation correctly reproduces Tr_{TL_m} defined above. Such a representation will in general be decomposed into a direct sum of irreducible representations (irreps). Thus, we expect the reflected entanglement spectrum to be grouped into different “sectors” labeled by these irreps. This is precisely the form of spectrum we will find for the 2TN model.

There are many ways of classifying the irreps of the TL algebra. Here, we will make use of the *standard module* [155]. It is defined by considering vector spaces with basis vectors called *link states*, made by cutting the basis elements of the TL_m algebra into half. Cutting a diagram in half will always expose an even number of “defects” (since m is even in our case), which we label by $2k$ with $0 \leq k \leq m/2$. We call such a diagram with $2k$ defects a (m, k) -link state and the set of all (m, k) -link states $\mathcal{B}_k^{(m)}$. The vector space spanned by $\mathcal{B}_k^{(m)}$ is denoted by $\mathcal{V}_k^{(m)}$.

There is a natural action of TL diagrams on (m, k) -link states given by concatenating and replacing closed loops with powers of χ . Such a concatenation may result in a number of disconnected strands that decrease the number of defects. We will further require that the action maps the link state to zero whenever there are any disconnected strands after concatenation. For example:

$$\begin{aligned} \left(\begin{array}{c} | \\ | \\ | \\ | \\ | \\ | \\ | \\ | \\ | \\ | \end{array} \right) \cdot \left(\begin{array}{c} | \\ | \\ | \\ | \\ | \\ | \\ | \\ | \\ | \\ | \end{array} \right) &= \left(\begin{array}{c} | \\ | \\ | \\ | \\ | \\ | \\ | \\ | \\ | \\ | \end{array} \right) = \chi \left(\begin{array}{c} | \\ | \\ | \\ | \\ | \\ | \\ | \\ | \\ | \\ | \end{array} \right) \\ \left(\begin{array}{c} | \\ | \\ | \\ | \\ | \\ | \\ | \\ | \\ | \\ | \end{array} \right) \cdot \left(\begin{array}{c} | \\ | \\ | \\ | \\ | \\ | \\ | \\ | \\ | \\ | \end{array} \right) &= \left(\begin{array}{c} | \\ | \\ | \\ | \\ | \\ | \\ | \\ | \\ | \\ | \end{array} \right) = 0 \end{aligned} \quad (5.24)$$

This action then defines a representation of TL_m on $\mathcal{V}_k^{(m)}$, called the *standard module*. The usefulness of the standard modules comes from the fact that they classify all the finite dimensional irreducible representations of TL_m .⁸ We will denote $\pi_k^{(m)}(t)$ to be the matrix representation of $t \in \text{TL}_m$ associated with $\mathcal{V}_k^{(m)}$. For more details on the standard module, we refer the reader to Appendix B.

Our goal is to build a finite dimensional representation

$$\mathcal{V}^{(m)} = \bigoplus_{k=0,1,\dots,m/2} d_k^{(m)} \mathcal{V}_k^{(m)}, \quad (5.25)$$

where the coefficients $d_k^{(m)}$ represent the number of times the irrep $\mathcal{V}_k^{(m)}$ appears in $\mathcal{V}^{(m)}$. These coefficients are uniquely determined by demanding that the trace of $\mathcal{V}^{(m)}$ agree with the trace in the TL algebra Tr_{TL_m} . We will see that $d_k^{(m)}$ is in fact independent of m and thus, the superscript will be omitted from now on. The trace on TL_m then decomposes into the sum of matrix traces in each submodule, i.e.,

$$\text{Tr}_{\text{TL}_m}(t) = \sum_{k=0,1,\dots,m/2} d_k \text{tr}(\pi_k^{(m)}(t)), \quad \forall t \in \text{TL}_m. \quad (5.26)$$

Finally, in order to compute the resolvent, we are left with computing the matrix

$$M_k^{(m)}(q) = \sum_{h \in \text{NC}_m} q^{-\#(h)} \pi_k^{(m)}(D(h)). \quad (5.27)$$

for all k . From Eq. (5.22), we see that the spectrum of the product $M_k^{(m)}(q_A)M_k^{(m)}(q_B)$ determines the full spectrum of the reflected density matrix. In more detail, the resolvent is given by

$$R_m(\lambda) = \sum_{k,i} \frac{d_k}{\lambda - \frac{\chi A \chi B}{(\chi \chi C)^m} \lambda_{M_k^{(m)},i}}, \quad (5.28)$$

where $\lambda_{M_k^{(m)},i}$ are the eigenvalues of $M_k^{(m)}(q_A)M_k^{(m)}(q_B)$. Thus, we obtain the spectrum:

$$D(\lambda) = \sum_{k,i} d_k \delta \left(\lambda - \frac{\chi A \chi B}{(\chi \chi C)^m} \lambda_{M_k^{(m)},i} \right) = \sum_{k,i} d_k \delta \left(\lambda - \lambda_{k,i}^{(m)} \right), \quad (5.29)$$

where $\lambda_{k,i}^{(m)} \equiv \frac{\chi A \chi B}{(\chi \chi C)^m} \lambda_{M_k^{(m)},i}$. The spectrum takes the simple form of a sum over poles where the coefficients d_k determine the degeneracy, while the eigenvalues are given by $\chi A \chi B / (\chi \chi C)^m$ times the eigenvalues of $M_k^{(m)}(q_A)M_k^{(m)}(q_B)$.

We emphasize that, so far, our result is valid for large $\chi_{A/B/C} \gg 1$ with the ratios $q_A = \chi_A / \chi_{C_1}$, $q_B = \chi_B / \chi_{C_2}$ held fixed. The internal bond dimension is kept finite and thus, $\chi_{A/B/C} \gg \chi$. To match the gravitational saddles, we will eventually take the limit $\chi \gg 1$, but the more general result Eq. (5.29) is valid for *all* values of χ .

⁸There are certain values of χ where the standard modules are reducible. However those values are discrete and only exist for $\chi < 2$, thus, irrelevant for our problem of interest.

5.4 Reflected entropy in 2TN

Having set up the formalism for computing the reflected spectrum via the TL machinery, we will now compute and analyze the spectrum in this section. First, we demonstrate the formalism by performing the analysis at finite χ in Sec. (5.4.1), focusing on $m = 2, 4$ as illustrative examples. We will then analyze the large χ limit in Sec. (5.4.2). Working in this limit enables us to obtain the spectrum as an analytic function of m and thus, continue to $m = 1$. With the spectrum at hand, we compute the reflected entropy and discuss the interpretations in terms of superselection sectors in Sec. (5.4.3). We then analyze the leading effect of finite external bond dimensions in Sec. (5.4.4). We will see that they shift the locations and give rise to a width for each of the peaks in the spectrum. Finally, we demonstrate consistency of our analysis with numerics in Sec. (5.4.5).

5.4.1 Finite χ

The recipe outlined in Sec. (5.3.2) allows one to compute the spectrum exactly for arbitrary even integer m . In this subsection, we will work out the detailed spectrum for $m = 2$ and $m = 4$ following this recipe. The purpose of this analysis is twofold: First, it serves as a proof of principle for analyzing the spectrum of arbitrary even integer m . Note that in practice, such an analysis is not always feasible since the complexity of the calculation increases exponentially as m increases. Second, since we pose no restriction on χ here rather than $\chi_{A/B/C} \gg \chi$, we expect our result to hold even when χ is small. This particular small χ regime allows us to make non-trivial predictions for the Rényi reflected spectrum at even integer m . Such predictions can be checked numerically up to high accuracy, as opposed to the $\chi \rightarrow \infty$ results we will obtain in Sec. (5.4.2) and Sec. (5.4.3), where our numerics are limited by finite χ effects.

- $m = 2$

Let us begin with a trivial case. The diagrammatic basis of the TL_2 algebra is given by

$$\text{TL}_2 = \left\{ \begin{array}{c} | \text{---} | \\ | \text{---} | \end{array} , \begin{array}{c} | \text{---} | \\ | \text{---} | \end{array} \right\} \quad (5.30)$$

which we will refer to as $D(\tau_2)$ and $D(e)$ following the notation of NC_2 . There are two standard modules $\mathcal{V}_0^{(2)}$ and $\mathcal{V}_1^{(2)}$, each being one-dimensional:

$$\mathcal{V}_0^{(2)} = \left\{ \begin{array}{c} | \text{---} | \\ | \text{---} | \end{array} \right\}, \quad \mathcal{V}_1^{(2)} = \left\{ \begin{array}{c} | \text{---} | \\ | \text{---} | \end{array} \right\}, \quad (5.31)$$

where we remind the reader that the modules are labelled by half the number of open lines. Using the diagrammatic action described previously, we compute

$$\begin{aligned} \pi_0^{(2)}(D(\tau_2)) &= 1, & \pi_0^{(2)}(D(e)) &= \chi; \\ \pi_1^{(2)}(D(\tau_2)) &= 1, & \pi_1^{(2)}(D(e)) &= 0. \end{aligned} \quad (5.32)$$

To reproduce the TL trace, it is easy to check that we must pick $d_0 = 1$ and $d_1 = \chi^2 - 1$. Thus, the

matrices $M_k^{(2)}(q)$ (which are simply 1-dimensional here) are:

$$M_0^{(2)}(q) = \chi q^{-2} + q^{-1}, \quad M_1^{(2)}(q) = q^{-1} \quad (5.33)$$

Using Eq. (5.29), we find the spectrum to be a sum over two poles, which have degeneracies and eigenvalues summarized in Table 5.1.

sector	eigenvalue $\lambda_k^{(m)}$	multiplicity d_k
$k = 0$	$(q_A^{-1} + \chi^{-1})(q_B^{-1} + \chi^{-1})/\chi C$	1
$k = 1$	$1/(\chi^2 \chi C)$	$\chi^2 - 1$

Table 5.1: The list of eigenvalues and their degeneracies for the $m = 2$ reflected spectrum.

- $m = 4$

Moving on to a slightly more involved example, consider the TL_4 algebra which has 14 basis diagrams:

$$\text{TL}_4 = \left\{ \begin{array}{l} \left(\begin{array}{c} \text{Diagram 1} \\ \text{Diagram 2} \\ \text{Diagram 3} \\ \text{Diagram 4} \\ \text{Diagram 5} \\ \text{Diagram 6} \\ \text{Diagram 7} \\ \text{Diagram 8} \\ \text{Diagram 9} \\ \text{Diagram 10} \\ \text{Diagram 11} \\ \text{Diagram 12} \\ \text{Diagram 13} \\ \text{Diagram 14} \end{array} \right) \end{array} \right. \quad (5.34)$$

There are three standard modules now: $\mathcal{V}_0^{(4)}$, $\mathcal{V}_1^{(4)}$, $\mathcal{V}_2^{(4)}$ with dimensions 2, 3, 1 respectively:

$$\begin{aligned} \mathcal{V}_0^{(4)} &= \left\{ \begin{array}{c} \text{Diagram 1} \\ \text{Diagram 2} \end{array} \right\}, \\ \mathcal{V}_1^{(4)} &= \left\{ \begin{array}{c} \text{Diagram 3} \\ \text{Diagram 4} \\ \text{Diagram 5} \end{array} \right\}, \\ \mathcal{V}_2^{(4)} &= \left\{ \begin{array}{c} \text{Diagram 6} \end{array} \right\}. \end{aligned} \quad (5.35)$$

Note that any two of the (m, k) -link states with same k can be “paired up” to form a unique TL diagram with $2k$ crossing connections. In the case at hand the total number of diagrams that can be formed this way are $2^2 + 3^2 + 1^2 = 14$, i.e. such pairings generate the entire set of TL_4 basis diagrams. This pairing up action will be important in our large χ analysis in the next subsection.

Similar to the previous $m = 2$ calculation, the module is determined by the diagrammatic action of TL diagrams on link states. The matrix $M_k^{(4)}$ is then determined by a weighted sum over the module

representation of these diagrams. Since it is conceptually straightforward, albeit tedious, to carry out the analysis, we skip the details and present the results. They read:

$$M_0^{(4)}(q) = \begin{pmatrix} \chi^2 q^{-4} + 5\chi q^{-3} + 3q^{-2} & \chi^2 q^{-3} + 3\chi q^{-2} + q^{-1} \\ \chi^2 q^{-3} + \chi(q^{-4} + 2q^{-2}) + 4q^{-3} & \chi^2 q^{-2} + \chi(q^{-3} + q^{-1}) + 3q^{-2} \end{pmatrix} \quad (5.36)$$

$$M_1^{(4)}(q) = \begin{pmatrix} \chi q^{-3} + 2q^{-2} & \chi q^{-2} + 2q^{-3} & \chi q^{-3} + q^{-2} \\ \chi q^{-2} + q^{-1} & \chi q^{-1} + 3q^{-2} & \chi q^{-2} + q^{-1} \\ \chi q^{-3} + q^{-2} & \chi q^{-2} + 2q^{-3} & \chi q^{-3} + 2q^{-2} \end{pmatrix} \quad (5.37)$$

$$M_2^{(4)}(q) = q^{-2}. \quad (5.38)$$

Reproducing the TL trace requires us to pick $d_0 = 1$, $d_1 = \chi^2 - 1$ and $d_2 = \chi^4 - 3\chi^2 + 1$. The eigenvalues and their corresponding degeneracies are given in Table 5.2.

sector	eigenvalue $\lambda_k^{(m)}$	multiplicity d_k
$k = 0$	ℓ_+	1
$k = 0$	ℓ_-	1
$k = 1$	$(5q^{-1}\chi^{-1} + (2q^{-2} + 1))^2 / (\chi_C^3 \chi^2)$	$\chi^2 - 1$
$k = 1, 2$	$1 / (q^2 \chi_C^3 \chi^4)$	$\chi^4 - \chi^2 - 1$

Table 5.2: The list of eigenvalues and their degeneracies for the $m = 4$ reflected spectrum. We have set $q_A = q_B = q$ to simplify expressions.

Note that two eigenvalues of $M_2^{(4)}(q)$ turn out to coincide with the eigenvalue of $M_4^{(4)}(q)$. The $k = 0$ eigenvalues ℓ_{\pm} is complicated, arising from the eigenvalues of the matrix in Eq. (5.36):

$$\ell_{\pm} = \frac{1}{4q^6 \chi_C^3 \chi^4} \left((q^2 + 1)\chi^2 + (q^3 + 6q)\chi + 6q^2 \pm \sqrt{(q^2 + 1)^2 \chi^4 + (2q^5 + 10q^3 + 12q)\chi^3 + (q^6 + 20q^4 + 44q^2)\chi^2 + (8q^5 + 52q^3)\chi + 16q^4} \right)^2 \quad (5.39)$$

At large χ , the expressions simplify and we find

$$\ell_+ \approx \frac{(q^2 + 1)^2}{\chi_C^3 q^6}, \quad \ell_- \approx \frac{1}{\chi_C^3 \chi^2 (q^2 + 1)^2}. \quad (5.40)$$

We see that ℓ_+ scales as $O(\chi^0)$, while ℓ_- is suppressed by $O(\chi^{-2})$ and comes close to the eigenvalue of the $k = 1$ sector. However, since the multiplicity of $\lambda_1^{(4)}$ scales as $O(\chi^2)$ at large χ , λ_- can be ignored (at leading order in χ) when calculating the entropy. The same can also be said for the sub-leading eigenvalue of the $k = 1$ sector (they coincide with that of $k = 2$). At large χ the $k = 2$ sector multiplicity scales as $O(\chi^4)$ and it dominates over the subleading poles of the $k = 1$ sector.

We depict the spectra we found for $m = 2$ and $m = 4$ in Fig. (5.9). For higher m , similar calculations can be still be carried out, although the dimension of matrices $M_k^{(m)}(q)$ will be large and one has to revert back to numerical methods to find their eigenvalues. However, the lesson we learnt from studying $m = 2, 4$ modules still holds: In general there will be $m/2$ sectors, and the leading eigenvalue in each sector behaves as $O(\chi^{-2k})$ and with multiplicity $\sim \chi^{2k}$. This hierarchy structure is a general feature for the 2TN spectra and we will see that it persists through analytical continuation $m \rightarrow 1$.

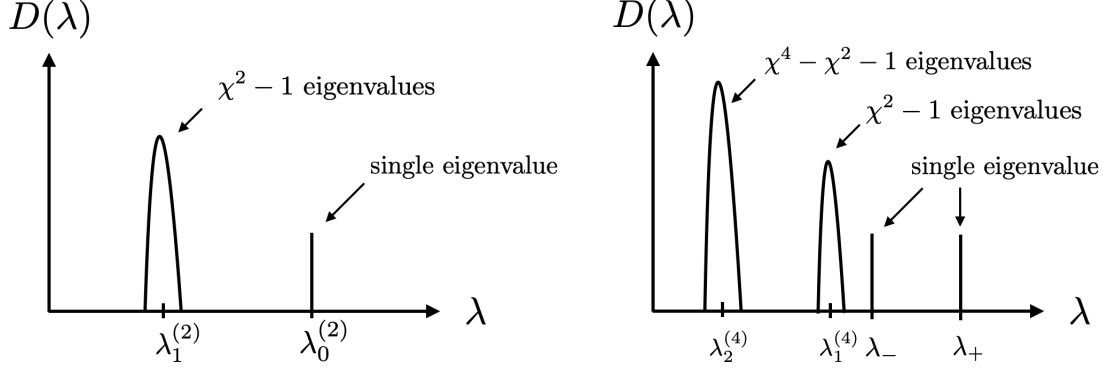


Figure 5.9: A sketch of the spectrum we obtained for $m = 2$ (left) and $m = 4$ (right). The eigenvalues of $k > 0$ sectors are depicted here as having a small width. This is found by including the finite external bond dimension effects, which we will study in Sec. (5.4.4)

5.4.2 Large χ limit

We have already seen how one can use the standard module of the TL algebra to extract the reflected spectrum of the 2TN at even integer m for arbitrary values of χ . In this subsection we will study this problem in the limit $\chi \rightarrow \infty$. This limit is physically relevant for comparison with holography since it corresponds to the $G \rightarrow 0$ limit in gravity. In Sec. (5.4.2.1) we obtain the leading χ behavior of the spectrum in this limit. Then we will analytically continue the spectrum in m in this limit in Sec. (5.4.2.2). This information will allow us to work at $m = 1$ to understand the reflected entropy, which is the main focus of Sec. (5.4.3).

5.4.2.1 Even integer m

We begin with a preliminary statement on the coefficients $d_k^{(m)}$ introduced previously.

Proposition 5.1. *The module multiplicity number $d_k^{(m)}$ satisfies the following properties:*

- $d_k^{(m)}$ is independent of m .
- As a function of χ , d_k is determined by

$$d_k = [2k + 1]_q, \quad (5.41)$$

where the q -number $[\cdot]_q$ is defined as

$$[k]_q = \frac{q^k - q^{-k}}{q - q^{-1}} = q^{k-1} + q^{k-3} + \dots + q^{-(k-3)} + q^{-(k-1)}. \quad (5.42)$$

χ and q are related by $\chi = [2]_q = q + q^{-1}$.

One can solve for q in terms of χ to obtain

$$d_k = \frac{1}{4^k} \sum_{n=1}^{k+1} \binom{2k+1}{2n-1} \chi^{2(k-n+1)} (\chi^2 - 4)^{n-1}, \quad (5.43)$$

so that d_k is a polynomial in χ . In fact one can show that the coefficients of this polynomial are integers. For

instance, the first few values of d_k are

$$\begin{aligned}
d_0 &= 1, \\
d_1 &= \chi^2 - 1, \\
d_2 &= \chi^4 - 3\chi^2 + 1, \\
d_3 &= \chi^6 - 5\chi^4 + 6\chi^2 - 1
\end{aligned}
\tag{5.44}$$

Although this result holds for all χ , we will mostly just need the large χ behavior of d_k , which is

$$d_k \approx \chi^{2k} + O(\chi^{2k-2}) \tag{5.45}$$

Proving this proposition requires some additional facts about the standard module. For this reason we present it in Appendix D.4.

Before moving on, let us introduce some useful notation. We define an inner product $\langle \cdot, \cdot \rangle$ on $\mathcal{V}_k^{(m)}$ as follows: If x, y are two link states, $\langle x, y \rangle$ is given by flipping x across the vertical axis, matching to y and assigning a power of χ for every closed loop. Furthermore, we define $\langle x, y \rangle$ to be nonzero only if every defect in x ends up being connected to a defect in y . A few examples should suffice to clarify the definition:

$$\left\langle \begin{array}{c} | \\ \text{---} \end{array}, \begin{array}{c} | \\ \text{---} \end{array} \right\rangle = \begin{array}{c} \text{---} \\ \text{---} \end{array} = \chi, \quad \left\langle \begin{array}{c} | \\ \text{---} \end{array}, \begin{array}{c} | \\ \text{---} \end{array} \right\rangle = \begin{array}{c} \text{---} \\ \text{---} \end{array} = 0 \tag{5.46}$$

Note that if x, y are two link states in $\mathcal{V}_k^{(m)}$, then

$$\langle x, y \rangle = \delta_{x,y} \chi^{m/2-k} + O(\chi^{m/2-k-1}), \tag{5.47}$$

where $\delta_{x,y} = 1$ if $x = y$ and 0 otherwise. In other words, the set of link states form an approximately orthogonal basis for $\mathcal{V}_k^{(m)}$ in the $\chi \rightarrow \infty$ limit. This fact will turn out to be useful later in this section, as well as in order to get a gravitational interpretation in Sec. (5.2).

We also define a bilinear map $|\cdot \cdot| : \mathcal{V}_k^{(m)} \times \mathcal{V}_k^{(m)} \rightarrow \text{TL}_m$, by flipping y across the vertical axis and ‘‘pairing up’’ with x to form a TL diagram. For instance,

$$\left| \begin{array}{c} | \\ \text{---} \end{array}, \begin{array}{c} | \\ \text{---} \end{array} \right| = \begin{array}{c} \text{---} \\ \text{---} \end{array} \tag{5.48}$$

This map has a nice property that for all $x, y, z \in \mathcal{V}_k^{(m)}$ we have

$$|x \ y| z = \langle y, z \rangle x. \tag{5.49}$$

The proof of this equality is provided in Appendix B.

Returning to our main problem of finding the leading χ behavior of $M_k^{(m)}$, we ask the following question: For any given link state $v \in \mathcal{B}_k^{(m)}$, which set of diagrams acting on v produce the dominant power of χ ? It turns out that, to produce the leading power of χ , the right half of the TL diagram must be exactly the mirror image of v , since this is the only way to get the maximum number of closed loops. Moreover, since

each closed loop contributes one power of χ , the overall contribution for such a diagram is $O(\chi^{m/2-k})$. This fact is illustrated in Fig. (5.10).

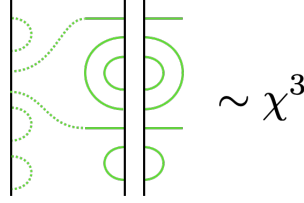


Figure 5.10: The leading contributions in $M_k^{(m)}$ come from the TL diagrams whose right half is a mirror image of the bases in $\mathcal{V}_k^{(m)}$. The contributing power is related to the number of defects by $\chi^{m/2-k}$. Here $m = 8$ and $k = 1$.

Using our previous notation, the set of all possibly dominant diagrams for a given vector $y \in \mathcal{V}_k^{(m)}$ is then all elements of the form $|x y\rangle \in \text{TL}_m$ where $x \in \mathcal{V}_k^{(m)}$. Note that every diagram in TL_m will be dominant in exactly one module $\mathcal{V}_k^{(m)}$. It is easy to write down the sum of such diagrams by making use of the bilinearity of $|\cdot\rangle\langle\cdot|$. For example:

$$\sum_{t \in \text{TL}_m} \pi_k^{(m)}(t) \approx \pi_k^{(m)} \left(\left| \sum_{x \in \mathcal{B}_k^{(m)}} x \quad \sum_{y \in \mathcal{B}_k^{(m)}} y \right. \right) + O(\chi^{m/2-k-1}), \quad (5.50)$$

To actually compute the matrix $M_k^{(m)}(q)$, we still need to weigh the sum by powers of $q^{-\#(h)}$. Given $h \in \text{NC}_m$, $\#(h)$ can be computed by considering a two-sided concatenation of $D(h)$ with a special link state that we call $e_0 \in \mathcal{V}_0^{(m)}$, given by the relation $D(e) = |e_0 \quad e_0\rangle$ where $e \in \text{NC}_m$ is the identity permutation. For example, if $h = (1456)(23) \in \text{NC}_6$, then we have

$$\#(h) = \#\text{loop} \left(\left| \begin{array}{c} \text{---} \\ \text{---} \\ \text{---} \\ \text{---} \\ \text{---} \\ \text{---} \end{array} \right. \right) = 2 \quad (5.51)$$

This facilitates the definition of the following linear functional $f_q : \mathcal{V}_k^{(m)} \rightarrow \mathbb{Z}[q^{-1}]$:

Definition 5.1. If v is a link state in $\mathcal{V}_k^{(m)}$, the value of $f_q(v)$ is given by concatenating the mirrored reflection of e_0 with v and assigning a factor of q^{-1} for every closed loop. The action of f_q on a general vector in $\mathcal{V}_k^{(m)}$ follows from the linearity of f_q .

We illustrate the definition with the following example:

$$f_q \left(\left| \begin{array}{c} \text{---} \\ \text{---} \\ \text{---} \\ \text{---} \\ \text{---} \\ \text{---} \end{array} \right. \right) = q^{-\#\text{loop}} \left(\left| \begin{array}{c} \text{---} \\ \text{---} \\ \text{---} \\ \text{---} \\ \text{---} \\ \text{---} \end{array} \right. \right) = q^{-1} \quad (5.52)$$

where we emphasize that only closed loops are counted, whereas open strands are ignored. Using the linear functional f_q , we can then write

$$q^{-\#(h)} = q^{-k} f_q(x) f_q(y) \quad (5.53)$$

for all $h \in \text{NC}_m$ with the decomposition $D(h) = |x \ y|$ and $x, y \in V_k^{(m)}$. It then follows that

$$M_k^{(m)}(q) = \sum_{h \in \text{NC}_m} q^{-\#(h)} D(h) \approx q^{-k} \left| \sum_{x \in \mathcal{B}_k^{(m)}} f_q(x)x \quad \sum_{y \in \mathcal{B}_k^{(m)}} f_q(y)y \right| + O(\chi^{m/2-k-1}) \quad (5.54)$$

when considered as a linear operator acting on $\mathcal{V}_k^{(m)}$.

For any $v \in V_k^{(m)}$ we can use Eq. (5.49) to write

$$\begin{aligned} & \left(\sum_{h \in \text{NC}_m} q_A^{-\#(h)} D(h) \right) \left(\sum_{k \in \text{NC}_m} q_B^{-\#(k)} D(k) \right) v \\ & \approx (q_{AB})^{-k} \sum_{x, y, z, w \in \mathcal{B}_k^{(m)}} f_{q_A}(x) f_{q_A}(y) f_{q_B}(z) f_{q_B}(w) \langle y, z \rangle \langle w, v \rangle x, \end{aligned} \quad (5.55)$$

where we use the shorthand $q_{AB} \equiv q_A q_B = \chi_A \chi_B / \chi_C$. It then follows that at large χ , the operator product $M_k^{(m)}(q_A) M_k^{(m)}(q_B)$ is of rank one with eigenvector $\sum_{x \in \mathcal{B}_k^{(m)}} f_{q_A}(x)x$ and eigenvalue

$$\lambda_{M_k^{(m)}} \approx (q_{AB})^{-k} \left(\sum_{x, y \in \mathcal{B}_k^{(m)}} f_{q_A}(x) f_{q_B}(y) \langle x, y \rangle \right)^2 \approx (q_{AB})^{-k} \chi^{m-2k} \left(\sum_{x \in \mathcal{B}_k^{(m)}} f_{q_A}(x) f_{q_B}(x) \right)^2, \quad (5.56)$$

where we have used Eq. (5.47) to arrive at the second expression. All other eigenvalues in the same sector are suppressed by $O(\chi^{-2})$ ⁹.

The sum in Eq. (5.56) is related to the generating function $G(q, r, z)$ of link states. This function can be computed in various ways. We present a diagrammatic derivation in Appendix D.4 and use the result here without proof.

Proposition 5.2. *The f_q -weighted generating function $G(q, r, z)$ for the (m, k) -link states is given by*

$$G(q, r, z) = \frac{1 - zC(q, z)}{1 - z(q + r) - zC(q, z)} \quad (5.57)$$

where $C(q, z) = \frac{1}{2z}(1 - z(q - 1) - \sqrt{(1 + z(q - 1))^2 - 4qz})$ is the generating function of q -Catalan numbers¹⁰. The argument r counts half the number of defects k and the argument z counts half the number of marked points $m/2$.

$G(q, r, z)$ has the following series expansion:

$$\begin{aligned} G(q, r, z) &= 1 + (q + r)z \\ &+ ((q + q^2) + (1 + 2q)r + r^2) z^2 \\ &+ ((q + 3q^2 + q^3) + (1 + 5q + 3q^2)r + (2 + 3q)r^2 + r^3) z^3 + \dots \end{aligned} \quad (5.58)$$

where the formal expression $G(q, r, z) = \sum_{\mu, k} g_{\mu, k}(q) z^\mu r^k$ allows us to compute the eigenvalues relevant for the reflected spectrum.

⁹Naively just from Eq. (5.56) it seems reasonable to assume that the subleading eigenvalue is suppressed by $O(\chi^{-1})$, rather than $O(\chi^{-2})$. We will prove that the first order correction to the subleading eigenvalue vanishes in Sec. (5.4.4).

¹⁰For more information on $C(q, z)$ please see the proof of Lemma B.1 in Appendix B.

Corollary 5.3. *The matrix $M_k^{(m)}(q_A)M_k^{(m)}(q_B)$ has a single nonzero eigenvalue at $\chi \rightarrow \infty$ given by*

$$\lambda_{M_k^{(m)}} = (q_{AB})^{-k} \chi^{m-2k} (g_{m/2,k}(q_{AB}^{-1}))^2 \quad (5.59)$$

with multiplicity χ^k .

To conclude, for each even m we identify $m/2$ eigenvalues given by Eq. (5.59), labeled by $k \in \{0, \dots, m/2\}$. At large χ the multiplicity of these eigenvalues goes as $d_k \approx \chi^{2k}$. All the other peaks found in Sec. (5.4.1) vanish in the limit.

5.4.2.2 Analytic continuation

Here, we will perform the analytic continuation away from even integer m to obtain the reflected spectrum at $m = 1$. This will be accomplished by analytically continuing the generating function coefficient to $g_{1/2,k}$. We have seen that for even integer m , only a finite number of eigenvalues are present, i.e., only the sectors labelled by even integer $k \in \{0, \dots, m/2\}$. However when taking the $m \rightarrow 1$ limit, we will see that all integer values of k contribute to the spectrum, forming an infinite tower of eigenvalues.

We start with Eq. (5.57). In particular, we need an analytic form for the coefficients in the series ¹¹

$$G(q, r, z) = \sum_{\mu, k=0}^{\infty} g_{\mu, k}(q) z^{\mu} r^k \quad (5.60)$$

The r expansion is easy to perform:

$$G(q, r, z) = \sum_{k=0}^{\infty} \frac{(1 - zC(q, z))z^k}{(1 - zq - zC(q, z))^{k+1}} r^k = \sum_{k=0}^{\infty} g_k(q, z) r^k \quad (5.61)$$

and thus, we identify

$$\begin{aligned} g_k(q, z) &= \frac{(1 - zC(q, z))z^k}{(1 - zq - zC(q, z))^{k+1}} \\ &= C(q, z)(C(q, z) - 1)^k q^{-k} \end{aligned} \quad (5.62)$$

where we have made use of Eq. (D.113) to arrive at the final expression. We then still need to expand this in terms of z and get a closed form for the coefficients. We will use a contour integral trick to pick out the appropriate coefficient, i.e.,

$$g_{\mu, k} = \frac{1}{2\pi i} \oint \frac{dz}{z^{\mu+1}} g_k(q, z) = \frac{1}{2\pi i} \oint \frac{dz}{z^{\mu+1}} C(q, z)(C(q, z) - 1)^k q^{-k} \quad (5.63)$$

Where the contour is chosen to enclose a neighborhood of $z = 0$. The function $C(q, z)$ has a branch cut running between

$$z_{\pm} = \frac{1}{(1 \mp \sqrt{q})^2}, \quad (5.64)$$

and there are no other poles or branch cuts on the complex plane ¹². We can then deform the contour to

¹¹We use the integer variable μ as the z exponent of the generating function $G(q, r, z)$, as opposed to the even integer valued m . The analytic continuation of $m \rightarrow 1$ is equivalent to continuing $\mu \rightarrow 1/2$.

¹²One must be careful about choosing the square root branch cut in $C(q, z)$. In particular if we want the function to behave nicely at $z \rightarrow \infty$ we have to use $C(q, z) = (1 - z(q-1) + |q-1|\sqrt{z-z_+}\sqrt{z-z_-})/(2z)$. This new $C(q, z)$ is equal to the original

enclose the branch cut running between (z_-, z_+) .

Now we would like to perform the analytic continuation for $\mu \rightarrow 1/2$. This introduces an extra branch cut emanating from $z = 0$, which does not affect our choice of contour. Since $C(q, z)$ has the property

$$\lim_{\text{Im } z \rightarrow 0^+} \text{Im}(C(q, z)) = - \lim_{\text{Im } z \rightarrow 0^-} \text{Im}(C(q, z)), \quad (5.65)$$

one can rewrite the integral as twice of the imaginary part of the UHP contour :

$$g_{1/2,k}(q) = \frac{1}{\pi} \text{Im} \int_{z_-}^{z_+} \frac{dz}{z^{3/2}} C(q, z) (C(q, z) - 1)^k q^{-k}. \quad (5.66)$$

For illustration, we evaluate the integral for the first few values of k :

- $k = 0$

We have

$$g_{1/2,0}(q) = \frac{1}{\pi} \text{Im} \int_{z_-}^{z_+} \frac{dz}{z^{3/2}} C(q, z) \quad (5.67)$$

This integral results in the analytic continuation of the q -Catalan numbers at $\mu = 1/2$,

$$g_{1/2,0}(q) = C_{1/2}(q). \quad (5.68)$$

$C_\mu(q)$ is a piecewise function depending on whether $q > 1$:

$$C_\mu(q) = \begin{cases} q {}_2F_1(1 - \mu, -\mu; 2; q), & q \leq 1, \\ q^\mu {}_2F_1(1 - \mu, -\mu; 2, q^{-1}), & q > 1 \end{cases}, \quad (5.69)$$

which will be important seeds for expressing the coefficients for all the subsequent k . The eigenvalue in this sector is

$$\lambda_0 = q_{AB} C_{1/2}(q_{AB}^{-1})^2 \quad (5.70)$$

with multiplicity 1.

- $k = 1$

The $k = 1$ integral reads

$$g_{1/2,1}(q) = \frac{1}{\pi} \text{Im} \int_{z_-}^{z_+} \frac{dz}{z^{3/2}} q^{-1} (C^2(q, z) - C(q, z)) \quad (5.71)$$

Using Eq. (D.113) it can be shown that $C(q, z)$ satisfies the quadratic equation

$$C^2(q, z) + \left(q - 1 - \frac{1}{z} \right) C(q, z) + \frac{1}{z} = 0, \quad (5.72)$$

so that one can write the integrand as a linear functional of $C(q, z)$:

$$\begin{aligned} g_{1/2,1}(q) &= \frac{1}{\pi} \text{Im} \int_{z_-}^{z_+} dz (q^{-1} z^{-5/2} - z^{-3/2}) C(q, z) \\ &= q^{-1} C_{3/2}(q) - C_{1/2}(q) \end{aligned} \quad (5.73)$$

definition in Proposition 5.2 near the $z = 0$ neighborhood and hence they have the same Taylor expansion.

The eigenvalue of this sector is given by

$$\lambda_1 = \chi^{-2}(q_{AB}C_{3/2}(q_{AB}^{-1}) - C_{1/2}(q_{AB}^{-1}))^2 \quad (5.74)$$

with multiplicity χ^2 .

- $k = 2$

We can use the same trick to reduce the integrand to be linear in $C(q, z)$:

$$\begin{aligned} g_{1/2,2}(q) &= \frac{1}{\pi} \operatorname{Im} \int_{z_-}^{z_+} \frac{dz}{z^{3/2}} q^{-2} C(q, z) (C(q, z) - 1)^2 \\ &= \frac{1}{\pi} \operatorname{Im} \int_{z_-}^{z_+} dz (q^{-2} z^{-7/2} - z^{-5/2} (2q^{-1} + q^{-2}) + z^{3/2}) C(q, z) \\ &= q^{-2} C_{5/2}(q) - (2q^{-1} + q^{-2}) C_{3/2}(q) + C_{1/2}(q) \end{aligned} \quad (5.75)$$

The eigenvalue of this sector is

$$\lambda_2 = q_{AB}^{-1} \chi^{-4} (q_{AB}^2 C_{5/2}(q_{AB}^{-1}) - (2q_{AB} + q_{AB}^2) C_{3/2}(q_{AB}^{-1}) + C_{1/2}(q_{AB}^{-1}))^2 \quad (5.76)$$

with multiplicity χ^4 .

Thus, we see a general pattern emerging. The integrand of $g_{1/2,k}$ is a polynomial of $C^k(q, z)$ and we can always reduce it to some linear functional $C(q, z)$ by repeated uses of Eq. (5.72). The outcome can in turn be expressed in terms of (half-integer valued) q -Catalan numbers. Therefore, we only need to find out how the reduction works for general k .

Proposition 5.4. *The generating function $G(q, r, z)$ in Proposition 5.2 can be alternatively resummed as*

$$G(q, r, z) = \frac{(r+q)C(q, z) - r/z}{r^2 + (q+1-1/z)r + q} \quad (5.77)$$

We present the proof of this statement in Appendix D.4. This result allows us to write down an explicit form of $g_k(q, z)$ as a linear functional of $C(q, z)$:

$$\begin{aligned} G(q, r, z) &= C(q, z) \left[1 + (q^{-1}z^{-1} - 1)r + (q^{-2}z^{-2} - (q^{-2} + 2q^{-1})z^{-1} + 1)r^2 \right. \\ &\quad \left. + (q^{-3}z^{-3} - (2q^{-3} + 3q^{-2})z^{-2} + (q^{-3} + 2q^{-2} + 3q^{-1})z^{-1} - 1)r^3 + \dots \right] \\ &\quad + \text{other terms...} \end{aligned} \quad (5.78)$$

The detailed expression of the remaining terms not proportional to $C(q, z)$ is irrelevant for determining the contour integral. From this expansion, one can read off the coefficients $g_{1/2,k}$ as linear combinations of q -Catalan numbers easily: A negative power of z^{-n} in the expansion coefficients becomes $C_{1/2+n}(q)$ after performing the contour integral.

5.4.3 Reflected spectrum and the effective description

In previous subsections, we have seen exact calculations of spectra for even integer m and arbitrary χ , as well as how the large χ limit allows us to extract analytic behavior of the eigenvalues in individual sectors. With

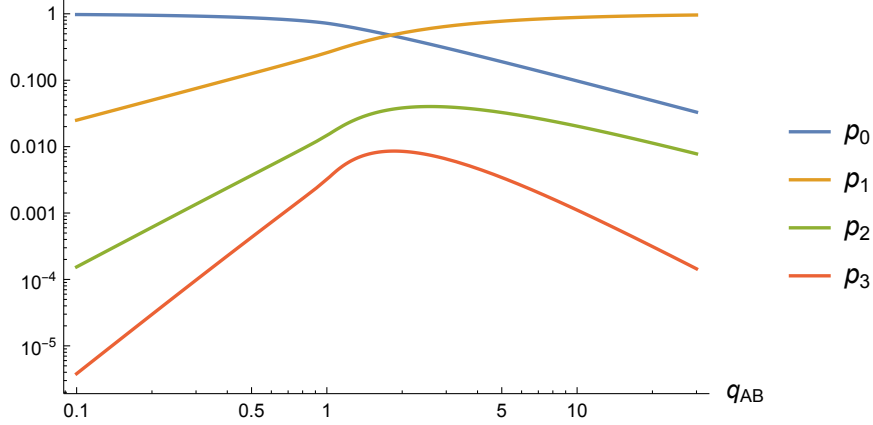


Figure 5.11: The plot showing the first few p_k 's as a function of q_{AB} . It is clear that at any point in parameter space, the dominant contribution comes from either p_0 (if $q_{AB} < 1$) or p_1 (if $q_{AB} > 1$).

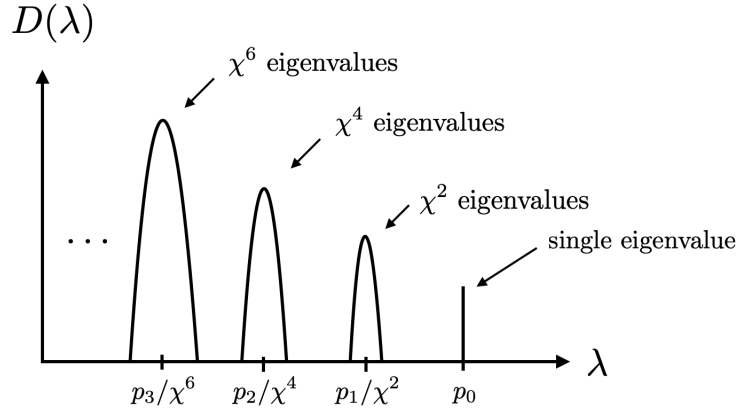


Figure 5.12: The sketch of the 2TN reflected spectrum at $m = 1$. It features an infinite tower of eigenvalues labeled by the sector number k . Note that the eigenvalues of the $k > 0$ sectors are drawn with a width here. This effect comes from taking the external bond dimensions $\chi_{A/B/C}$ large but finite, which we will investigate in detail in Sec. (5.4.4).

these results in hand, we are finally ready to tackle the problem of analyzing the reflected entropy for the 2TN model.

In the limit $\chi \rightarrow \infty$, the leading eigenvalue in each k sector is

$$\lambda_k = \chi^{-2k} q_{AB}^{1-k} (g_{1/2,k}(q_{AB}^{-1}))^2 \equiv \chi^{-2k} p_k \quad (5.79)$$

with multiplicity $d_k \approx \chi^{2k}$. The numbers p_k are independent of χ and satisfy $\sum_k p_k = 1$ from the normalization condition. We plot the first few p_k 's as a function of q_{AB} in Fig. (5.11). The spectrum in this limit is a sum of the eigenvalue over all k sectors:

$$D(\lambda) = \sum_{k=0}^{\infty} \chi^{2k} \delta(\lambda - \lambda_k) \quad (5.80)$$

We present a sketch of the full reflected spectrum in Fig. (5.12).

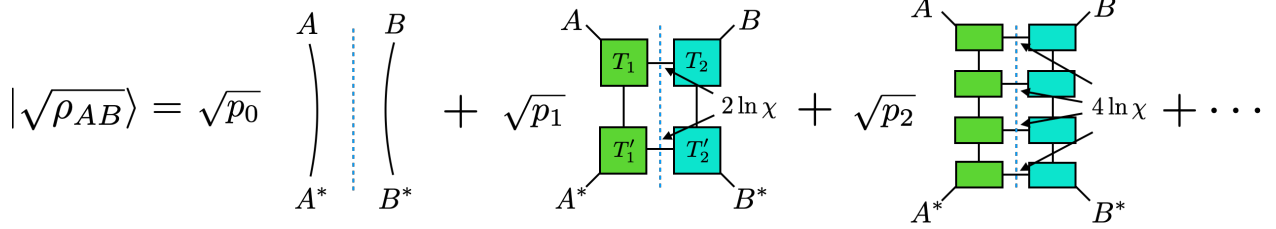


Figure 5.13: An illustration of Eq. (5.82). The canonical purification $|\rho_{AB}\rangle$ is effectively described by a superposition of tensor network states. For $k = 0$ we have the factorized state with zero cross-section. To form the $k > 0$ sectors we start from a simple network state made from two copies of the 2TN state. Then for each k we glue together k such states, resulting in a TN with total cross-sectional area $2k \ln \chi$, as indicated by the number of bonds cut by blue dashed lines. This figure should be compared to Fig. (5.2), where each effective TN corresponds to a genus- $(2k - 1)$ bulk solution of the replica boundary problem.

The reflected entropy obtained from this spectrum is given by

$$\begin{aligned}
 S_R(q_{AB}) &= - \sum_{k=0}^{\infty} \chi^{2k} p_k \ln p_k \\
 &= - \sum_{k=0}^{\infty} p_k \ln p_k + \sum_{k=0}^{\infty} p_k (2k \ln \chi)
 \end{aligned} \tag{5.81}$$

Eq. (5.81) is the main result of this chapter. There are two different contributions to the reflected entropy. There is a term from the classical Shannon entropy for the probabilities p_k , plus an infinite sum over terms proportional to $2k \ln \chi$, weighted by p_k . This should be compared with the result, Eq. (5.6) obtained from the gravitational path integral in Sec. (5.2). We can now interpret each k sector as a state with a effective tensor network configuration with different EW cross-sections.

Based on the gravitational calculation (Sec. (5.2)), the results on single random tensor (Chapter 3), and the analysis on finite external bond dimensions effects (Sec. (5.4.4)), we suggest that the effective TN states are built as follows: Consider the natural doubling procedure [115] for the canonical purification, by duplicating the 2TN state and gluing the two copies across the boundary of the bulk extremal surfaces (C_1 and C_2 in our case). Call such a state $|\psi_1\rangle$. Then, construct a series of wave functions $|\psi_k\rangle$ by further replicating $|\psi_1\rangle$ k times and gluing across the AA^*BB^* bonds. By construction $|\psi_k\rangle$ will have an entropy of $2k \ln \chi$ and we have the follow effective description

$$|\sqrt{\rho_{AB}}\rangle = \sqrt{p_0} |\psi_0\rangle + \sum_{k=1}^{\infty} \sqrt{p_k} |\psi_k\rangle, \tag{5.82}$$

where $|\psi_0\rangle$ is a factorized state across AA^* and BB^* . The states $|\psi_i\rangle$ are approximately orthogonal at large χ , i.e. $\langle \psi_i | \psi_j \rangle \sim \delta_{ij} + O(\chi^{-1})$. Calculating the entropy of Eq. (5.82) gives precisely Eq. (5.81) at $\chi \rightarrow \infty$. We give a diagrammatic illustration of Eq. (5.82) in Fig. (5.13).

Eq. (5.82) should be compared to the states prepared by a gravitational path integral in the sense of Eq. (5.4). There we have a superposition of bulk solutions of EW cross-section $2k \ln \chi$, whose reduced density matrices ρ_{k,AA^*} have approximately orthogonal support. One should think of the integer index k as capturing the *topology* of the effective description. By gluing together k copies of the state $|\psi_1\rangle$ we have created a bulk solution with genus $2k - 1$. From the entanglement structure we also identify emergent superselection sectors

labeled by the topological index $k \in \mathbb{Z}_{\geq 0}$. The area operator is:

$$\mathcal{L}_{AA^*} = \sum_k 2k \ln \chi \Pi_k, \quad (5.83)$$

where Π_k is the projection operator down to the orthogonal subspace of $|\psi_k\rangle$. Note that in real scenarios with finite bond dimensions, the aforementioned superselection sector is only approximate as supports of the density matrices are not exactly orthogonal.

As discussed in Ref. [37] there is a connection between the area law and quantum error correcting codes. Taking this seriously here we see that the effective description looks like an emergent error correcting code, with only a central degree of freedom. Hence it is perhaps better thought of as a classical error correcting code. Presumably including bulk degrees of freedom in the original network, before canonically purifying, will give rise to a genuinely quantum version of this code.

Returning to the calculation of the reflected entropy, the phase transition of $S_R(A : B)$ is controlled by the list of classical probabilities p_k as a function of q_{AB} . They can be shown to have the following asymptotic behaviors

$$(p_0, p_1, p_{k>1}) \sim \begin{cases} \left(q_{AB}^{-1}, 1 - \frac{5}{4}q_{AB}^{-1}, \frac{\Gamma(k-1/2)^2}{\pi\Gamma(k)^2}q_{AB}^{1-k} \right), & q_{AB} \gg 1, \\ \left(1 - \frac{1}{4}q_{AB}, \frac{1}{4}q_{AB}, \frac{\Gamma(k-1/2)^2}{\pi(2k)^2\Gamma(k)^2}q_{AB}^k \right), & q_{AB} \ll 1. \end{cases} \quad (5.84)$$

Away from phase transition, i.e., for $q_{AB} \ll 1$ ($q_{AB} \gg 1$), one can argue that either $k = 0$ ($k = 1$) is the dominant sector. The probabilities p_k of higher k sectors are always suppressed by factors of q (q^{-1}), as shown in Eq. (5.84) and Fig. (5.11). This matches our expectation, as in the limit $q_{AB} \ll 1$ the state $|\psi_0\rangle$ is dominant and we have $S_R(A : B) \sim O(1)$; whereas as $q_{AB} \gg 1$ the state $|\psi_1\rangle$ is dominant and we get the classical result $S_R(A : B) = 2 \ln \chi = 2EW(A : B)$. Near the vicinity of phase transition, i.e. $q_{AB} \approx 1$, all the k sectors become important in determining the entropy, as one can check numerically that the probabilities p_k for $k \geq 2$ are of comparable order of magnitude, although numerically smaller than $p_{0,1}$.

The $(1, n)$ -Rényi reflected entropies are given by the sum

$$S_R^{(1,n)} = \frac{1}{1-n} \ln \left(\sum_k \chi^{2k(1-n)} p_k^n \right). \quad (5.85)$$

In reality, only the first two terms $k = 0, 1$ can ever dominate the sum as long as $n > 1$. Therefore we found that $S_R^{(1,n)}$ has three different approximate behavior depending on the value of q_{AB} :

$$S_R^{(1,n)} \approx \begin{cases} \frac{1}{1-n} \ln p_0 \approx 0, & q_{AB} \ll 1, \\ \frac{1}{1-n} \ln p_0 \approx \frac{n}{n-1} \ln q_{AB}, & 1 \ll q_{AB} \ll \chi^{(2-2/n)}, \\ 2 \ln \chi, & q_{AB} \gg \chi^{(2-2/n)}, \end{cases} \quad (5.86)$$

which matches exactly the expected results from the phase diagram in Fig. (5.6) in the parameter regime where our analysis is valid. As we take $n \rightarrow 1$, the middle regime vanishes and we get back the single sharp phase transition of reflected entropy.

Interestingly, for $n < 1$, the $k > 2$ saddles can dominate. For sufficiently large χ , the term $\chi^{2k(1-n)}$ in Eq. (5.85) becomes increasingly important for larger k . For even integer m , this implies that the highest

sector, i.e., $k = \frac{m}{2}$, dominates. For m away from the even integers, this leads to a runoff to arbitrarily high k which leads to the entropy being infinite in our approximation. In practice, such calculations would receive large corrections from the finiteness of the external bond dimensions $\chi_{A/B/C}$ since there is a constraint on the rank of the reflected spectrum arising from $\min(\chi_A^2, \chi_B^2)$.

5.4.4 Corrections to the spectrum

In this subsection, we study the effect of having finite bond dimensions χ and χ_{A,B,C_1,C_2} . This is motivated by comparing to situations such as the four boundary wormholes with large but finite horizon areas and EW cross-section. Moreover, this allows us to make better comparison with numerics we obtained in Sec. (5.4.5).

Taking the internal/external bond dimensions finite alter the large χ spectrum in independent ways. In short, the leading effect of finite *internal* bond dimension χ is to shift the location of the poles in each sector. In contrast, the leading effect of finite *external* bond dimension χ_{A,B,C_1,C_2} is to spread out each pole into a narrow mound. In the following we will examine how these effects work together to create a consistent spectrum that matches our numerical data well and deepens our understanding of the effective description of the 2TN as a sum over superselection sectors. However, the calculation of the finite internal bond dimension χ corrections is rather technical and involved. For this purpose we present the full analysis in Appendix D.2 for interested readers.

5.4.4.1 Eigenvalue shifts

Here we give a qualitative summary of the effect of finite internal bond dimension χ . We identify two phenomena as we take χ finite: First, the orthogonality of link state basis $v \in \mathcal{B}_k^{(m)}$, i.e. Eq. (5.47), fails. Second, elements not of the form $\{|x y|; x, y \in \mathcal{B}_k^{(m)}\}$ in the sum $\sum \pi_k^{(m)}(D(h))$ will start to contribute. These two effects introduce $O(\chi^{-1})$ corrections to the leading eigenvalue in each sector λ_k . The latter effect also splits the degenerate zero eigenvalues in each sector. However, such corrections only appear at $O(\lambda_k \chi^{-2})$, so they do not affect the entropy at leading order. Note that $O(\lambda_k \chi^{-2})$ is also the order of the leading eigenvalue λ_{k+1} in sector $k + 1$. This is seen in our numerics from the fact that the number of eigenvalues in each mound is not exactly d_k , but has corrections suppressed by $O(\chi^{-2})$. We will refer to this as *sector mixing*, which should be understood as a signature that the wave functions in different superselection sectors acquire a non-zero overlap when χ is finite. Both effects are seen in our explicit examples of integer m (sector mixing is only visible in $m \geq 4$) in Sec. (5.4.1).

We conclude the brief discussion by giving expressions for the leading order correction to the eigenvalues λ_k for $k = 0$ and $k = 1$. We chose to do so since the shifts of these two eigenvalues completely characterizes the leading order correction to the reflected entropy for all q_{AB} . Corrections to other sectors are also obtainable via analytic continuation of the related generating function, but their contribution to the entropy is sub-leading. Please refer to Appendix D.2 for a detailed treatment.

$$\Delta\lambda_0 = \frac{q_A^{-1} + q_B^{-1}}{\chi} \left[C_{1/2}(q_{AB}^{-1}) \left((1 + q_{AB}^{-2})D_{3/2}(q_{AB}^{-1}) - 2(1 + q_{AB}^{-1})D_{5/2}(q_{AB}^{-1}) + D_{7/2}(q_{AB}^{-1}) \right) + (q_{AB}C_{3/2}(q_{AB}^{-1}) - C_{1/2}(q_{AB}^{-1}))^2 \right], \quad (5.87)$$

$$\Delta\lambda_1 = \frac{q_A^{-1} + q_B^{-1}}{\chi^3} \left[3 \left(C_{1/2}(q_{AB}^{-1}) - (2q_{AB} + q_{AB}^2)C_{3/2}(q_{AB}^{-1}) + q_{AB}^2 C_{5/2}(q_{AB}^{-1}) \right)^2 + (-C_{1/2}(q_{AB}^{-1}) + q_{AB}C_{3/2}(q_{AB}^{-1})) \times \left(-(q_{AB}^{-1} - 1)^2 D_{1/2}(q_{AB}^{-1}) + 2q_{AB}^{-1} D_{3/2}(q_{AB}^{-1}) + q_{AB}^2 D_{5/2}(q_{AB}^{-1}) - 2(q_{AB}^2 + q_{AB})D_{7/2}(q_{AB}^{-1}) + q_{AB}^2 D_{9/2}(q_{AB}^{-1}) \right) \right]. \quad (5.88)$$

where the function $D_\mu(q)$ is given by

$$D_\mu(q) = \begin{cases} {}_2F_1(1 - \mu, 1 - \mu; 1; q), & q \leq 1, \\ q^{\mu-1} {}_2F_1(1 - \mu, 1 - \mu; 1; q^{-1}), & q > 1. \end{cases} \quad (5.89)$$

5.4.4.2 Fluctuations in each sector

So far, the spectrum we have obtained consists of a bunch of poles, which in turn happened because we were working in the limit of large external bond dimensions. The leading effect of taking these dimensions finite will be to spread out each pole into a narrow mound, and the goal in this part will be to find a crude estimate for the width.

Based on the results obtained in the single random tensor, we conjecture that such spreading effects arise from including non-trivial permutations that act on the n -cycles. This motivates us to consider summing over a more general class of elements:

$$g_1 = \gamma_p \left(\prod_{i=1}^n h_i \right) \gamma_p^{-1}, \quad g_2 = \gamma_q \left(\prod_{j=1}^n k_j \right) \gamma_q^{-1} \quad (5.90)$$

where as before $h_i, k_j \in \text{NC}_m$ and additionally we pick $p, q \in \text{NC}_n$. γ_p stands for the n -twist operator associated to p applied to the lower half of the elements. This should be contrasted with Eq. (5.11) where we restricted to $\gamma_p = \gamma_\tau$ and $\gamma_q = e$. Note that these elements are only schematic since there is a possible overcounting when $h_i, k_j \in \text{NC}_{m/2} \times \text{NC}_{m/2}$, which will be accounted for later.

We remind the reader that in order to calculate the partition function Z_{mn} in Eq. (5.9), we need to evaluate $\#(g_1 g_A^{-1})$ and $\#(g_1 g_B^{-1})$. These numbers depend on whether $h_i, k_j \in \text{NC}_{m/2} \times \text{NC}_{m/2}$ (in which case we call these permutations *disconnected*) or not (in which case they are called *connected*). For the connected sector, we furthermore classify h_i and k_j based on the number of crossing connections when viewed as an element of TL_m : We say $h \in \text{NC}_{m,k}$ if $D(h) = |x y|$ for some $x, y \in \mathcal{B}_k^{(m)}$.

For now we restrict the sum to the set of h_i, k_j where all of the permutations are in the same subclass $\text{NC}_{m,k}$ but we allow k to vary. Using the formalism of annular non-crossing permutations (see Appendix A

for details) we get

$$\#(g_1 g_A^{-1}) = \begin{cases} \sum_i \#(h_i \tau_m^{-1}), & h_i \in \text{NC}_{m,0} \\ \sum_i \#(h_i \tau_m^{-1}) - 2(n - \#(p\tau_n^{-1})), & h_i \in \text{NC}_{m,k>0} \end{cases} \quad (5.91)$$

$$\#(g_2 g_B^{-1}) = \begin{cases} \sum_j \#(k_j \tau_m^{-1}), & k_j \in \text{NC}_{m,0} \\ \sum_j \#(k_j \tau_m^{-1}) - 2(n - \#(q)), & k_j \in \text{NC}_{m,k>0} \end{cases} \quad (5.92)$$

Note that it is possible to give a formula for an arbitrary mixture of two different values of k but those effects turn out to be subleading in determining the width, so we ignore them for now.

The partition function factorizes into different subclasses based on the number of crossings:

$$Z_{mn} \simeq Z_{mn}^{(0)} + Z_{mn}^{(1)} + Z_{mn}^{(2)} + \dots \quad (5.93)$$

where the disconnected sum is

$$Z_{mn}^{(0)} = \left(\frac{\chi_A \chi_B}{\chi_C^m \chi^m} \right)^n \sum_{h_i, k_j \in \text{NC}_{m,0}} q_A^{-\sum_i \#(h_i)} q_B^{-\sum_j \#(k_j)} \text{Tr}_{\text{TL}_m} (D(h_1) D(k_1) \dots D(h_n) D(k_n)) \quad (5.94)$$

The summation over p, q drops out since they all overcount the same set of permutations. Since its form receives no correction from the new p, q twist operators, we conclude that the single eigenvalue λ_0 remains unchanged in this approximation. We expect that by including the correction from mixed k contributions, λ_0 may be shifted by a small amount or spread out to a very narrow peak.

Moving on to the connected sectors, there is no overcounting and we get extra corrections from the cycles in p and q :

$$Z_{mn}^{(k)} = \left(\frac{1}{\chi_A \chi_B \chi_C^m \chi^m} \right)^n \sum_{p, q \in \text{NC}_n} \chi_A^{2\#(p\tau_n^{-1})} \chi_B^{2\#(q)} \sum_{h_i, k_j \in \text{NC}_{m,k}} q_A^{-\sum_i \#(h_i)} q_B^{-\sum_j \#(k_j)} \times \text{Tr}_{\text{TL}_m}^{pq^{-1}} (D(h_1) D(k_1) \dots D(h_n) D(k_n)), \quad (5.95)$$

where the trace pattern is determined by the partition pattern in pq^{-1} . For example,

$$\begin{aligned} & \text{Tr}_{\text{TL}_m}^{(12)(3)} (D(h_1) D(k_1) D(h_2) D(k_2) D(h_3) D(k_3)) \\ &= \text{Tr}_{\text{TL}_m} (D(h_1) D(k_1) D(h_2) D(k_2)) \times \text{Tr}_{\text{TL}_m} (D(h_3) D(k_3)) \end{aligned} \quad (5.96)$$

The dominant contribution in Eq. (5.95) comes from $p = \tau_n$, $q = e$, which gives the single eigenvalue identified in Sec. (5.4.1) and Sec. (5.4.2). The summation over p and q introduces nontrivial correlations in Z_n , which we now focus on analyzing.

Denoting $pq^{-1} = \prod_i c_i$ to be the individual cycle decomposition of pq^{-1} , we can write

$$\begin{aligned} & \sum_{h_i, k_j \in \text{NC}_{m,k}} q_A^{-\sum_i \#(h_i)} q_B^{-\sum_j \#(k_j)} \text{Tr}_{\text{TL}_m}^{pq^{-1}} (D(h_1) D(k_1) \dots D(h_n) D(k_n)) \\ &= \prod_{\{c_i\}} \text{Tr}_{\text{TL}_m} \left[\left(\sum_{h \in \text{NC}_{m,k}} q_A^{-\#(h)} D(h) \right) \left(\sum_{k \in \text{NC}_{m,k}} q_A^{-\#(k)} D(k) \right) \right]^{|c_i|}, \end{aligned} \quad (5.97)$$

where $|c_i|$ is the number of elements in a given cycle. Then, using the fact that the leading order result

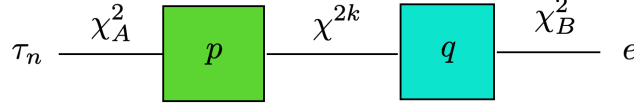


Figure 5.14: Calculating the partition function in the each k sector is equivalent to calculating the partition function for finding the n -th moment of an effective two-tensor model (up to a normalization factor) with two external bonds with bond dimensions χ_A^2 and χ_B^2 , along with an internal bond with dimension χ^{2k} .

$Z_n \approx \chi^{2k} \lambda_k^n$ in large χ limit for such sector, we have

$$Z_n^{(k)} \approx \left(\frac{\lambda_k}{\chi_A^2 \chi_B^2} \right)^n \sum_{p, q \in \text{NC}_n} \chi_A^{2\#(p\tau_n^{-1})} \chi_B^{2\#(q)} \chi^{2k\#(pq^{-1})}, \quad (5.98)$$

Interestingly, the partition function $Z_n^{(k)}$ is identical to the partition function of an equivalent tensor network (up to an overall normalization), see Fig. (5.14). One should view this effective network as an instantiation of the effective description of the k th superselection sector, in the sense that our result exposes the effective internal entanglement structure of a given sector. Note that the while the picture presented here is not the same as the one proposed in Fig. (5.13), they have the same entanglement spectrum up to leading order in $\chi_{A/B}^k$. We conjecture that by including the sum over different k sectors in the full partition function, one can restore the hidden internal structure of the effective description.

The normalized spectrum of the tensor network shown in Fig. (5.14) is the same as the spectrum of the product of two rectangular Ginibre matrices, which has been worked out in the large bond dimension limit [107, 156, 157] using techniques from free probability theory [158]. The resolvent for this network can be obtained through the following cubic algebraic equation

$$\lambda W(\lambda) = (1 + W(\lambda))(1 + c_A W(\lambda))(1 + c_B W(\lambda)) \quad (5.99)$$

where $c_A = \chi^{2k}/\chi_A^2$, $c_B = \chi^{2k}/\chi_B^2$ and $W(\lambda)$ is related to the resolvent by $\lambda R(\lambda) = (1 + W(\lambda))$. Working in the limit $c_A, c_B \ll 1$, we expand Eq. (5.99) to first order in $c_{A/B}$:

$$\lambda W(\lambda) \approx (1 + W(\lambda))(1 + (c_A + c_B)W(\lambda)), \quad (5.100)$$

whose solution gives a Marchenko-Pastur distribution [159] with parameter $c = c_A + c_B = \chi^{2k}(1/\chi_A^2 + 1/\chi_B^2)$. Putting back the correct normalization factors, we obtain an approximate spectrum for the k -th sector

$$D_k(\lambda) = \frac{1}{2\pi\lambda\lambda_k(\chi_A^{-2} + \chi_B^{-2})} \sqrt{(\lambda - \lambda_{k-})(\lambda_{k+} - \lambda)}, \quad \lambda_{k\pm} = \lambda_k \left(1 \pm \chi^k \sqrt{(\chi_A^{-2} + \chi_B^{-2})} \right)^2 \quad (5.101)$$

i.e. the single eigenvalue λ_k in each sector spreads out into a narrow peak with width $\sim 4\lambda_k\chi^k\sqrt{(\chi_A^{-2} + \chi_B^{-2})}$. Note that the approximation in Eq. (5.100) fails when χ^k and $\chi_{A/B}$ are of comparable size. This is the case in numerics when the number of eigenvalues in a higher k sector approaches the finite rank constraint $\min(\chi_A^2, \chi_B^2)$. In this case one should use the full solution to the cubic equation Eq. (5.99) instead.

Note that it is rather straightforward to adapt our calculation for arbitrary finite χ and finite integer m . First, one needs to replace the number of eigenvalues in each sector by $\chi^{2k} \rightarrow d_k$ in Eq. (5.98) to account for the finite χ effects. Further, our previous analysis in Sec. (5.4.1) shows that there are subleading eigenvalues in each sector that are suppressed by $O(\chi^{-2})$ compared to the leading one. Repeating the calculation, we

find that *every* eigenvalue in a sector will obtain a width, not just the leading one. Finally, for even integer m the normalization term $(Z_{m,1})^n$ in Eq. (5.8) can no longer be ignored. Far from the EW phase transition, $Z_{m,1}$ is sharply peaked around $\min(\chi_A\chi_B, \chi_C)^{m-1}$ and it merely restores the correct normalization for the spectrum. However around the transition, $Z_{m,1}$ has a large variance and it introduces extra fluctuations to the spectrum by spreading each mound further out in addition to the $Z_{m,n}$ effects computed here. While this is indeed a concern for our computation, we expect our result in this subsection to hold well when our system is far from the EW phase transition at $q_{AB} \sim 1$.

5.4.5 Numerical results

Throughout this section, we saw that the use of TL algebra is extremely powerful and enables us to extract various analytical properties for the 2TN reflected spectrum. To recapitulate, working in the limit $\chi_{A,B,C} \gg \chi$, it allows us to obtain χ -exact spectra for even integer m (Sec. (5.4.1)), leading (Sec. (5.4.2)) and sub-leading (Sec. (5.4.4.1), Appendix D.2) contributions to $m \rightarrow 1$ spectra, reflected entropy (Sec. (5.4.3)), as well as fluctuation effects (Sec. (5.4.4.2)). In this subsection we corroborate these analytical predictions by comparing to numerical results. All the numerical results presented here are obtained directly from simulating the 2TN state by contracting two random tensors along the internal bond and calculating its reflected spectrum using exact diagonalization.

First, in Fig. (5.15) we present the histogram of the reflected spectra for $m = 2$ and $m = 4$. The analytic predictions for the locations of the eigenvalues come from Table 5.1, 5.2, and the spreading within each sector is given by a modification of Eq. (5.101) to accommodate for finite- χ effects. The bond dimensions used in these plots are $\{\chi_A, \chi_B, \chi_{C_1}, \chi_{C_2}, \chi\} = \{40, 40, 80, 80, 3\}$. We remind our reader that the analytic results presented here are exact for arbitrary χ and when the system is sufficiently far from phase transition. Fig. (5.15) serves as an exceptional confirmation of our formalism in the regime of small internal bond dimension χ .

Moving on to the analytic continuation $m \rightarrow 1$ which is relevant to the canonical purification and reflected entropy, we present a similar histogram of the spectra for $m = 1$ in Fig. (5.16). The bond dimensions used here are $\{\chi_A, \chi_B, \chi_{C_1}, \chi_{C_2}, \chi\} = \{16, 16, 40, 40, 4\}$ (top) and $\{30, 30, 70, 70, 4\}$ (bottom). As opposed to the case of even integer m , here we only have analytic control of the spectra up to first order corrections in χ . The leading order analytic results of the eigenvalues are given by Eq. (5.79), and the first order corrections for λ_0 and λ_1 are given by Eq. (5.87) and Eq. (5.88). The corrections to higher λ_k 's are obtained via direct numerical contour integration to extract the relevant generating function coefficients, i.e. Eq. (D.20) and Eq. (D.42). The number of sectors that show up in the numerics abides the *rank constraint*, namely that the total number of eigenvalues cannot exceed the dimension of the matrix. Therefore, we expect to see higher k sectors materializing as $\chi_A\chi_B$ increases, which is indeed the case here: As we increase $\chi_A\chi_B$, we see an emergent fourth peak in the bottom plot compared to the top plot.

We also plot the transition of classical sector probability p_k in Fig. (5.17) as functions of q_{AB} , and likewise the normalized reflected entropy $S_R/2EW$ in Fig. (5.18). The bond dimensions used in these two plots are $\{\chi_A, \chi_B, \chi\} = \{25, 25, 5\}$ and we vary $\chi_{C_1} = \chi_{C_2}$ to obtain different values of q_{AB} . The colored dots indicate the numerical results. We present two different analytical predictions here: Solid lines are the ones that includes first order corrections (Eq. (5.87), Eq. (5.88), etc.), whereas dashed lines are the leading result (Eq. (5.79) for p_k and Eq. (5.81) for S_R), which is valid in the limit $\chi \rightarrow \infty$. It is evident that the first order corrections captures the non-trivial effects of small internal bond dimension surprisingly well.

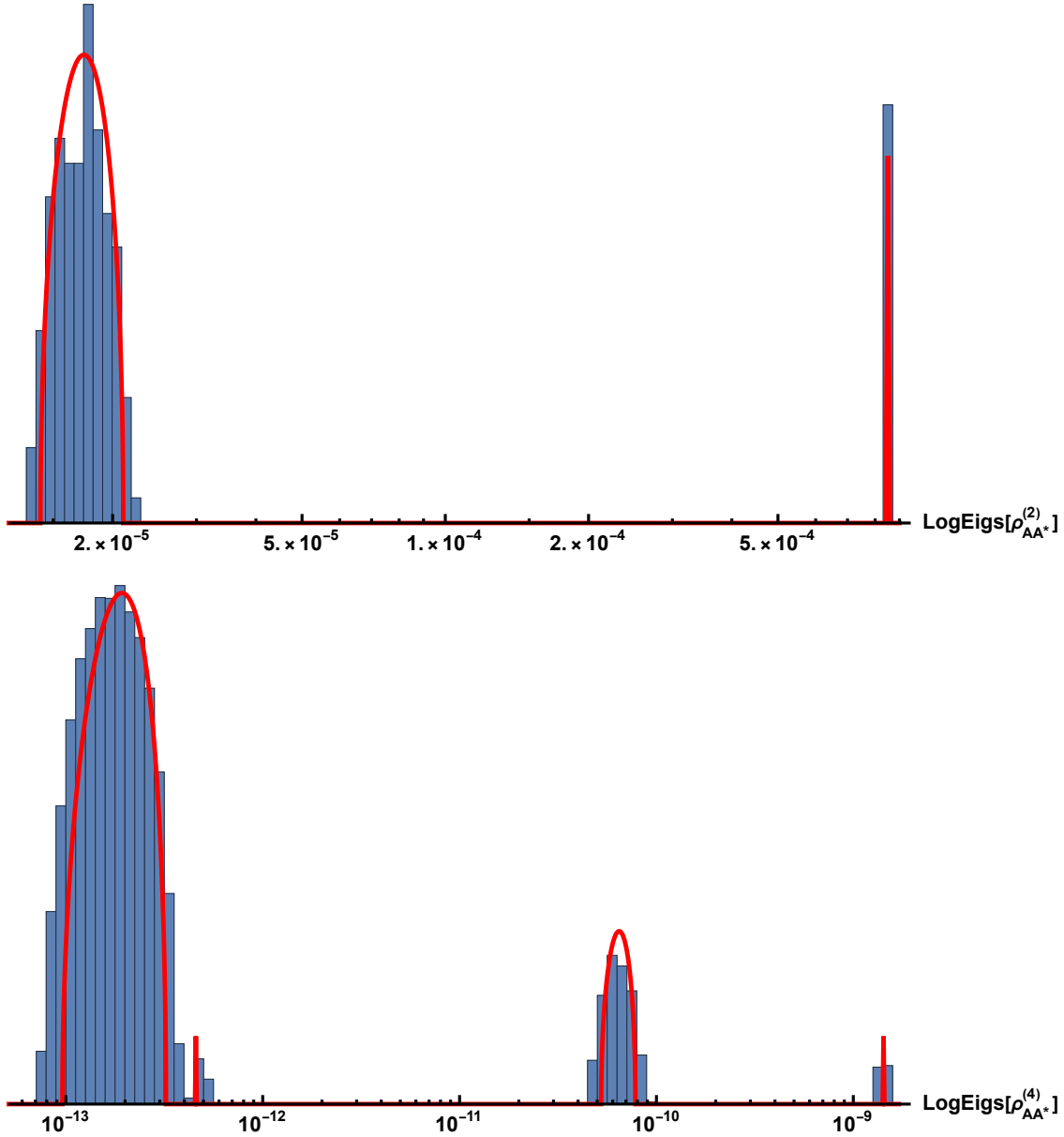


Figure 5.15: Plots of spectra of the (unnormalized) density matrix $\rho_{AB}^{(m)} \equiv \text{Tr}_{BB^*} |\rho_{AB}^{m/2}\rangle \langle \rho_{AB}^{m/2}|$ for $m = 2$ (top) and $m = 4$ (bottom), with the red lines being the analytic predictions. Note that in the case of $m = 4$ there is an additional eigenvalue that lies close to the leftmost peak. This is a finite χ effect that is not visible in our $m \rightarrow 1$ analytics. Nevertheless our results for even integer m are χ -exact which is well confirmed by these two plots.

5.5 Discussion

In this chapter we have continued the study of canonical purification and reflected entropy for random tensor networks. The picture developed in Ref. [48] for the tensor network version of the gravitational gluing construction persists to more complicated tensor networks. In particular we have found a detailed match between gravitational saddles that contribute to the canonical purification with higher genus equal time

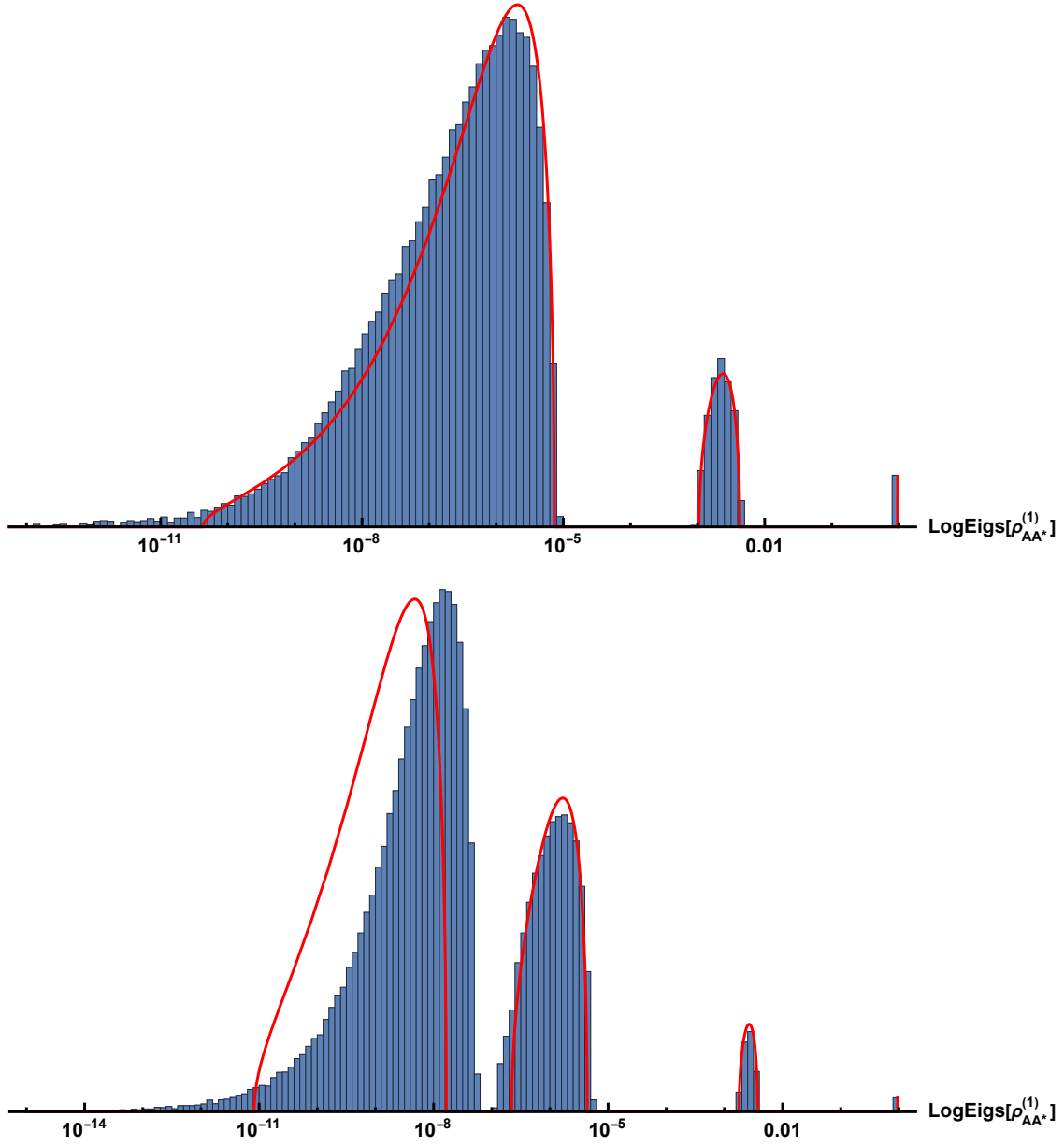


Figure 5.16: Plots of spectra of the $m = 1$ reflected density matrix $\rho_{AB}^{(1)} \equiv \text{Tr}_{BB^*} |\sqrt{\rho_{AB}}\rangle \langle \sqrt{\rho_{AB}}|$ for $\{\chi_A, \chi_B, \chi_{C_1}, \chi_{C_2}, \chi_f\} = \{16, 16, 40, 40, 4\}$ (top) and $\{30, 30, 70, 70, 4\}$ (bottom). The analytic predictions are shown as red lines. The mismatch of the $k = 3$ peak in the bottom plot is due to the fact that we can only work numerically in low bond dimension. As we scale up the bond dimensions in numerics, the agreement becomes better. We expect that it can also be resolved by improving the analytics, including subleading corrections to the eigenvalues beyond first order.

surfaces and certain saddles in the statistical mechanics model governing random tensor network calculations. Area fluctuations, probed using reflected entropy, are represented by the different topological sectors.

For the model at hand the topological sectors are governed mathematically by the Temperley-Lieb algebra. The representation theory of the TL algebra then gives a nice picture of the emergent superselection sectors that can be vividly seen in the numerics. The higher genus equal time surface arise from cutting open the TL

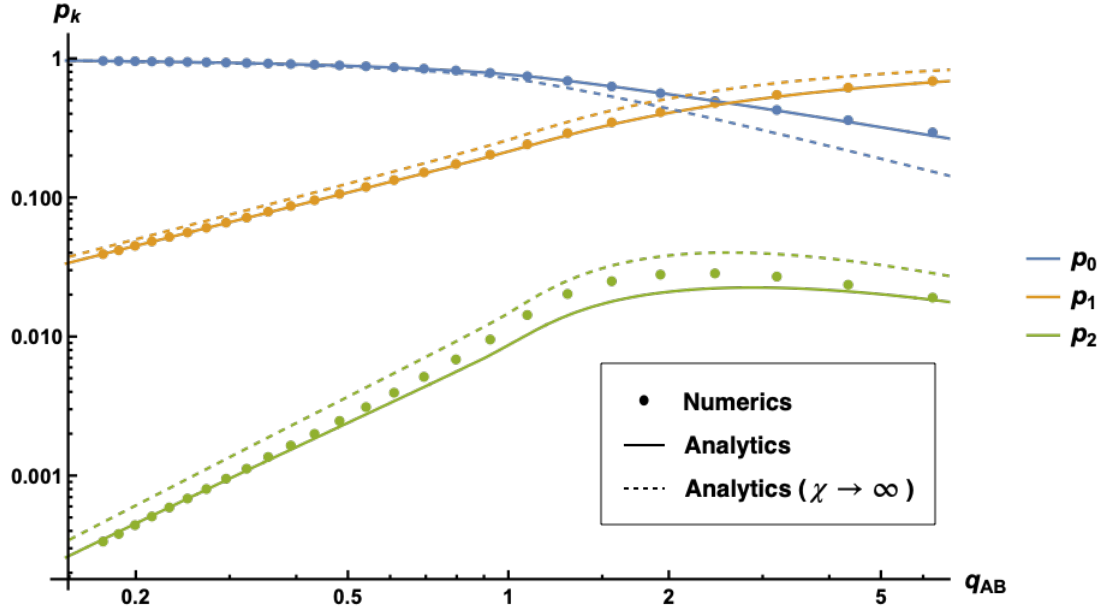


Figure 5.17: Plots of the sector probability p_k . The analytic result (solid lines) is obtained from the product of sector multiplicity d_k and eigenvalues λ_k . The d_k used here are the exact expressions in Eq. (5.43) and the λ_k used here includes the first order shifts. We also incorporated the exact expression of p_k at $\chi \rightarrow \infty$ (Eq. (5.79)) as dashed lines.

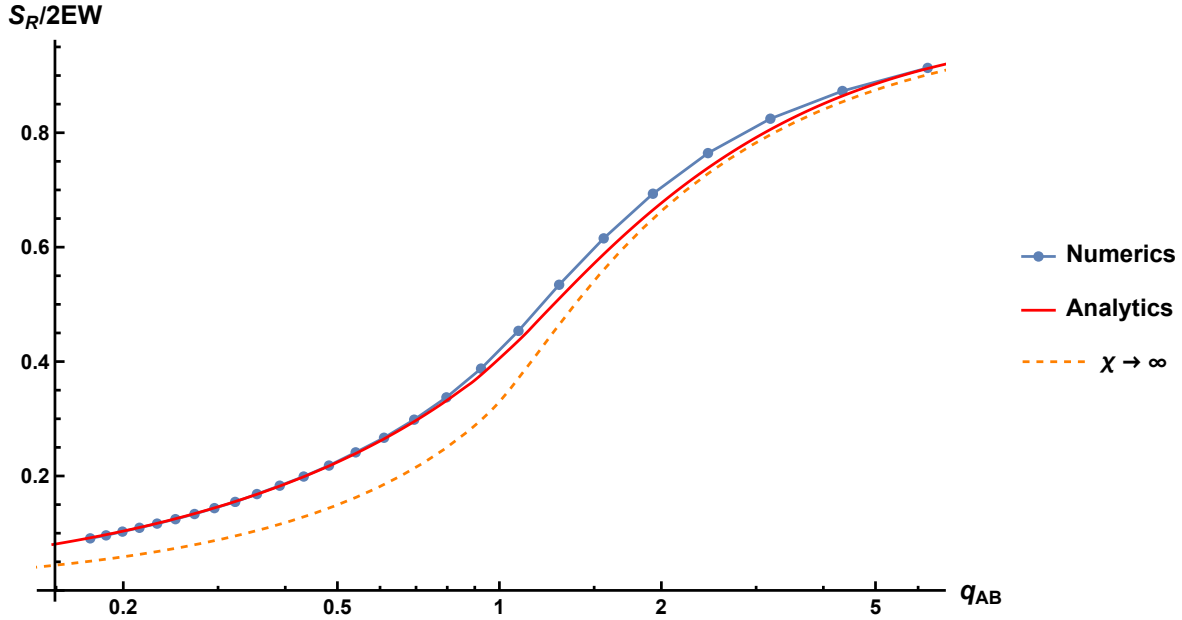


Figure 5.18: Plots of the reflected entropy, normalized by twice the EW cross-section $2 \ln \chi$. The analytic prediction (red) is obtained by summing over the eigenvalues in $k = 0, 1, 2$ sectors (these are the only available ones due to the rank constraint), including the first order corrections and the contribution from spreading (Eq. (5.101)). We have also included the form of S_R in the limit $\chi \rightarrow \infty$ shown as the orange dashed line for comparison.

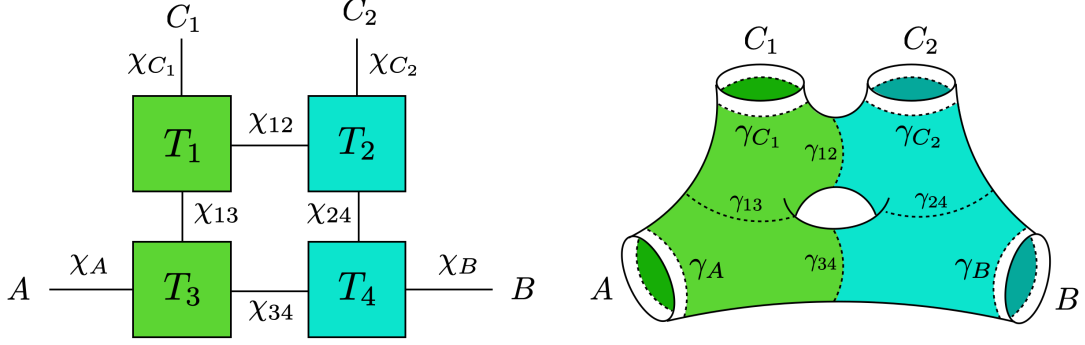


Figure 5.19: (left): The 4TN network consists of four internal vertices connected by internal bonds χ_{ij} . (right): It models a four-boundary wormhole with a handle.

diagrams. The genus, and hence topological index, is determined by the number of strands that are cut.

In the rest of the discussion section we summarize some possible avenues for future work and some intriguing speculative connections to the theory of emergent non-trivial von Neumann algebras.

5.5.1 General RTNs and multiboundary wormholes

Our analysis in this chapter was focused on the 2TN model, where we performed a concrete calculation using the TL algebra, and matched the results to those obtained from the gravitational path integral in Sec. (5.2). There is in fact a more general connection between RTNs and multiboundary wormholes [122]. In this section, we would like to make some comments on the presence of similar saddles for general multiboundary wormholes.

Consider an arbitrary RTN built out of constituent random tensors with three legs, an example is shown in Fig. (5.19). Such an RTN models a multiboundary wormhole where the tensors correspond to the constituent pair-of-pants decomposition of the spatial geometry. In general, there are multiple ways to decompose a hyperbolic geometry into pairs-of-pants. However, the RTN has fixed-area surfaces which pick a preferred pair-of-pants decomposition. The network is then interpreted as a coarse-grained descriptions of the given geometry. In Ref. [122], it was argued that this model captures the entanglement entropies of such multiboundary wormholes accurately. Our results here show that the same is true for the canonical purification and the reflected entropy, thus enlarging the scope of the random state model discussed in Ref. [122].

Firstly, note that the construction of geometries contributing to the canonical purification of a multi-boundary wormhole is similar to that discussed in Sec. (5.2). Since all the horizons have fixed areas, the saddles contributing to the path integral in Fig. (5.5) are identical, except that we now have more ways to glue together the fixed-area saddles. In terms of the Cauchy surface obtained on the \mathbb{Z}_2 -symmetric slice, the saddles can be classified by picking a particular choice of entanglement wedge and then gluing together multiple copies of the respective bulk regions.

In general, the TL algebra techniques can be applied to more general RTNs as well. For example, consider the 4TN network shown in Fig. (5.19). The computation of the average partition function $\overline{Z_{mn}}$ in this network includes a sum over independent permutations g_i on each of the tensors. As before, we can take the limit of external bond dimensions to be large. In addition, if we also take the internal vertical bonds to be large, it is easy to see that we can then restrict the sum to the non-crossing permutations $g_{1/3} \in \Gamma(g_A, e)$ and $g_{2/4} \in \Gamma(g_B, e)$ since the other permutations are suppressed. For each internal horizontal bond χ_{ij} , there is

a domain wall cost of the form $\chi_{ij}^{\#(g_i g_j^{-1})}$. As in Eq. (5.16), this can be done by introducing a TL algebra labelled by the bond dimension. Thus, $\overline{Z_{mn}}$ is computed by a product of TL traces, one for each horizontal bond. However, the analysis is complicated by the fact that the traces are coupled to each other. It would be interesting to analyze this using free probability theory techniques [110, 160] in the future.

5.5.2 Junctions for the cross-section

Our results in this chapter rigorously apply to situations where the entanglement wedge cross section is spacelike separated from all the external RT surfaces. This guarantees that we can simultaneously fix their areas and thus, model the holographic state by an RTN. Our TL algebra techniques can then be applied to such situations. However, we now argue that the TL algebra analysis can be useful for more generic situations in holography where all the surfaces are not necessarily spacelike separated.

For example, consider a three-boundary wormhole with horizons γ_i for $i = A, B, C$, each of the subregions being one asymptotic boundary. As discussed in Ref. [48], when the minimal entanglement wedge cross section is given by one of the external horizons, this situation is modelled by a single random tensor with three boundary legs, one for each subregion. However, in general there is a non-trivial cross section surface γ_W as shown in Fig. (5.20), which can be important for the reflected entropy. In fact, we show in Appendix D.1 that this is true for a large region in parameter space.

In such a situation, the TL algebra analysis cannot be applied directly since there is a codimension-3 junction where the surface γ_W meets γ_C . One can check that the areas of γ_C and γ_W can indeed be simultaneously fixed. This is manifest from the fact that the area of γ_W generates a kink transform [161–163], which preserves the minimal entanglement wedge cross section. Nevertheless, the RTN in fact fixes the areas of γ_{C_1} and γ_{C_2} as well, since they correspond to bonds in the network. It can be checked in various models [164] that these areas do not commute with γ_W .

Nevertheless, the saddles contributing to the gravitational path integral for $\text{tr}(\rho_{AB}^m)$ discussed in Sec. (5.2) are valid even if we don't fix the area of γ_W . Thus, for the state $|\rho_{AB}^{m/2}\rangle$, we still obtain the same geometries Σ_k , labelled by their genus. While, we cannot then use the TL algebra technology to compute the Rényi reflected entropies, we can gain some mileage from directly assuming that the RT formula can still be applied to each of these geometries. Since this is a superposition over a small number of geometries (not exponentially large in the entropy), we can use the expectations from Ref. [135] to argue that the (non-linear) entropy is given by the expectation value of the minimal area, a linear operator defined on the gravitational phase space. This expectation is clearly borne out in the situation where we could fix the area of γ_W as seen from Eq. (5.5). With this assumption, even in this situation, we expect to have an analog of Eq. (5.5). It would be interesting to generalize our TL algebra construction to include a non-flat spectrum which allows fluctuations for γ_W and make this heuristic argument more rigorous.

With the above heuristic understanding, our 2TN results also apply to a rather generic situation that arises for subregions in a CFT. In such a situation, the areas of the extremal surfaces or equivalently the external bond dimensions are IR divergent, whereas the cross section is finite. The external areas can be regularized by allowing for a small splitting between the regions. Having done so, the density matrix ρ_{AB} can in fact be defined rigorously by the split construction described in Ref. [56]. The regularization removes subtleties associated with fixing an IR divergent area. With this understanding, the analysis is similar to the heuristic argument described above for the three-boundary wormhole and thus, our results are rather generic.

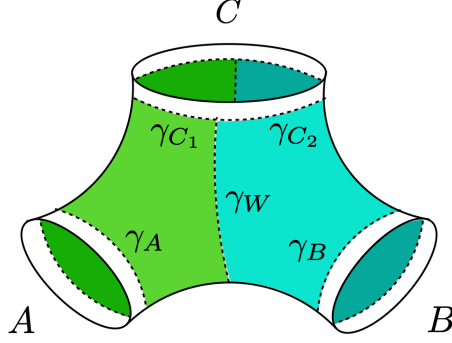


Figure 5.20: A three-boundary wormhole with horizons labeled as $\gamma_{A/B/C}$ and the non-trivial EW cross-section γ_W . While one cannot fix the individual area of γ_W and γ_{C_1/C_2} simultaneously, the area of γ_W and the sum $\gamma_C = \gamma_{C_1} + \gamma_{C_2}$ can be fixed simultaneously.

5.5.3 Emergent von Neumann algebras

Temperley-Lieb (TL) algebras play an important role in the study of type-II₁ subfactors, initiated by Jones. A subfactor is a subalgebra $\mathcal{B} \subset \mathcal{A}$ of von Neumann algebras both of which do not have centers. In this case the TL algebra emerges from a sequence of further subalgebras $\mathcal{B} \subset \mathcal{A} \subset \mathcal{A}_1 \subset \mathcal{A}_2 \dots$ constructed using the Jones basic construction [165]. Then the TL operators are generated by a sequence of projection operators that arise from the basic construction. The TL_m algebra for even m then appears in the relative commutants $\mathcal{A}_{i+m} \cap \mathcal{A}'_i$ of two of the algebras in this sequence. The algebra generated by all of these relative commutants would reproduce a type-II₁ algebra. We might then speculate that our model gives one more avenue [93, 94, 166] through which non-trivial von Neumann algebras can arise from gravitational like theories.

Comparing to the emergent TL algebras in our tensor network model the relevant inclusion involves decreasing the number of handles on the fixed time slice. To really see an emergent type-II₁ algebra we would need to move to high topological index. In particular $m \rightarrow \infty$ would be interpreted as giving rise to such a non-trivial von Neumann algebra. Interestingly by continuing m away from an even integer we have a mechanism by which arbitrarily high topological index can arise, unfortunately however these states become increasingly suppressed at high k by the sector probabilities. Near the phase transition all sectors are excited, however to really claim an emergent type-II₁ algebra we would need to somehow project to a high k sector so that p_k is peaked around k_0 which is then approaching ∞ . If we managed this then the leading reflected entropy $\approx k_0 \ln \chi$ is diverging with k_0 , a necessary condition for an emergent type-II₁ von Neumann algebra. Perhaps this can be achieved by perturbing the original density matrix by some $\chi_{A,B}$ dependent operator that excites the topological mode $k_0(\chi_{A,B})$, with $k_0 \rightarrow \infty$ as we send $\chi_{A,B} \rightarrow \infty$ while holding fixed χ . We certainly need to send the external bond dimensions to ∞ so that the rank condition does not come into play. A natural guess for such a perturbation is to apply ρ_{AB}^{is} (half sided) modular flow to the original state $|\rho_{AB}^{1/2}\rangle$. In fact one can show, using similar techniques to Section 5.4, that under modular flow the probabilities p_k get modified to

$$p_k(s) = q_{AB}^{1-k} g_{1/2+is,k}(q_{AB}^{-1}) g_{1/2-is,k}(q_{AB}^{-1}) \quad (5.102)$$

at leading order in χ . This change of $p_k(s)$ is seemingly consistent with the above requirements. We have confirmed this numerically (see Fig. (5.21)) and analytically using the method of asymptotic analysis (see Appendix D.3). We would then need to pick $s(\chi_A, \chi_B)$ diverging and one important question is can we control such a computation while taking s large? This would be an interesting avenue to pursue since it

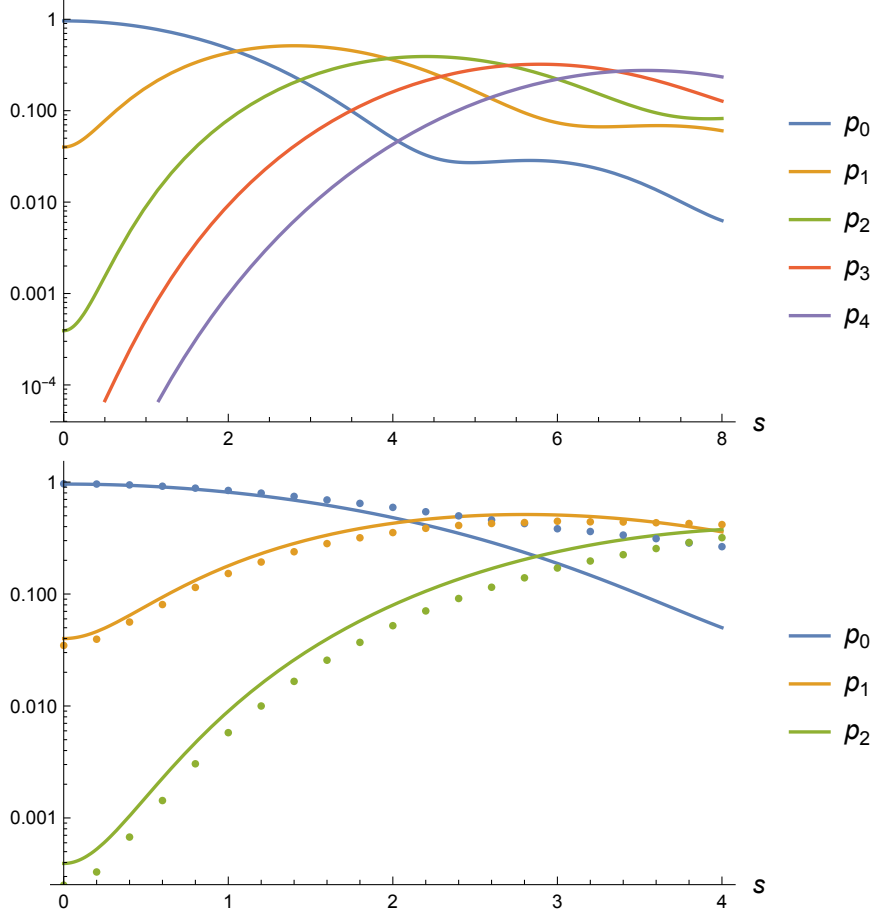


Figure 5.21: (Top) Sketch of the (χ -leading) modular flowed sector probability p_k as a function of modular parameter s . One can see the shift of dominance to higher k sectors as s increases. (Bottom) The numerical result of p_k for $k = 0, 1, 2$, shown as colored dots. The bond dimensions used in the numerics are $\{\chi_A, \chi_B, \chi_{C_1}, \chi_{C_2}, \chi\} = \{16, 16, 40, 40, 4\}$. One sees a good match with the analytical prediction at small s . To match the behavior at larger s one would need to access higher k sectors in the numerics.

would give rise to a computable model of topological gravitational like fluctuations. It is also important to understand the exact nature of the putative emergent type-II₁ von Neumann algebra other than simply via entropy computations.

There are also some superficial similarities to Ref. [86] that are worth exploring further. Ref. [86] gives a Hilbert space interpretation of the double scaled SYK model, for which a diagrammatic solution was given in Ref. [167]. These are the chord diagrams and the Hilbert space description is in terms of cutting open these chord diagrams, similar to the Temperley-Lieb Hilbert spaces. In this case an emergent type-II₁ von Neumann algebra naturally arises.

Chapter 6

Generic Tensor Networks

In this chapter we will examine canonical purification in RTNs defined on generic graphs. We will prove that at large bond dimension, the integer Rényi reflected entropies are determined by minimal triway cuts through the network when the system is sufficiently far away from phase transitions. Minimal triway cuts can be formulated as integer programs which cannot be relaxed to find a dual maximal flow/bit-thread description. We prove that the Markov gap that measures tripartite entanglement is lower bounded by the integrality gap of the integer program that computes the triway cut. To make connection with AdS/CFT, we apply this to the hyperbolic tensor networks and provide evidence for the $S_R = 2EW$ conjecture.

The results presented in this chapter are based on Refs. [48, 70].

6.1 Summary of results

In AdS/CFT, the RT formula relates the entanglement entropy of the boundary and areas of minimal surfaces in the bulk: a measure of bipartite entanglement in pure states. Minimal surfaces can be equivalently described by bit-threads [65, 66], maximal divergence free locally bounded flows between two boundary regions. Furthermore, these bit-threads give a vivid picture of bipartite entanglement in the boundary wavefunction, with a thread corresponding to a distillable EPR pair.

In RTN states, the bit-thread picture can be formulated more directly via the tool of linear programming and flow networks. For RTNs defined on a graph, the RT prescription can be formulated as an optimization program minimizing over all cuts that divides the vertices into two disjoint sets each containing the corresponding sets of boundary vertices whose entanglement entropy we wish to compute. Bit-threads correspond to dual maximal flows between the two sets of boundary vertices with flow capacities set by the bond dimensions. This correspondence is a version of the max-flow min-cut theorem that can be proven using strong duality theorems from the theory of linear/convex programs.

Bit-threads however tend to give a misleading picture of multipartite entanglement. For example, a bipartite dominance conjecture was formulated for three party holographic states based on the existence of such bit-thread configurations [59]. However, the conjecture of Ref. [59] contradicts other measures of tripartite entanglement beyond von Neumann entropies. For example, Ref. [58] argued using the reflected entropy that holographic states have large amounts of tripartite entanglement and thus, disproved a version of the bipartite dominance conjecture.

Generally, minimal areas are only a limited probe of the underlying geometry, and one might expect

other geometric objects – such as surfaces of various co-dimensions – to play an important role in a putative correspondence between geometry and quantum information. For example, computational complexity is believed to be associated to co-dimension 0 or 1 regions in spacetime [168, 169]. There are now also hints that a class of tripartite entanglement should be associated to spatial co-dimension 2 objects [101]. In this chapter we find further evidence for the latter by proving a correspondence between reflected entropy and a minimal triway cut. Triway cuts generalize the bipartite cuts described above, and are likely the closest graph analog of a co-dimension 2 object that is defined for any graph.¹

Triway cuts are integer optimization programs that cannot be dualized to a bit-thread description². Relaxing the integer constraint gives a linear program that underestimates the cut. The ratio between these values, the output of the integer program over that of the linear program, is generally a difficult quantity to compute, and is called the *integrality gap*. In fact, computing the integrality gap is an NP-complete problem [170].

We now introduce our main results in more detail. Recall that the reflected entropy S_R of a state ρ_{AB} is defined as the entropy of AA^* in the canonical purification $|\rho_{AB}^{1/2}\rangle \in \mathcal{H}_{AA^*BB^*}$. The Renyi generalization of S_R is a simple one parameter family of quantum information measures:

$$S_R^{(n)}(A : B) = -\frac{1}{n-1} \ln \text{Tr} \rho_{AA^*}^n \quad \rho_{AA^*} = \text{Tr}_{BB^*} |\rho_{AB}^{1/2}\rangle \langle \rho_{AB}^{1/2}| \quad (6.1)$$

We will prove:

Theorem 6.1. *For integer $n > 1$, the reflected entropy of a random tensor network state at large bond dimension, with a unique entanglement wedge for $AB : C$ and a unique triway cut for $A : B : C$ (with tensions specified below), satisfies:*

$$\lim_{\chi \rightarrow \infty} \frac{\overline{S_R^{(n)}(A : B)}}{\ln \chi} = \frac{1}{n-1} \mathcal{A}_{\mathbf{t}}(A : B : C) - \frac{n}{n-1} \mathcal{A}(AB : C), \quad (6.2)$$

where $\mathcal{A}_{\mathbf{t}}(A : B : C)$ is the area of a multiway cut with tensions $\mathbf{t} \equiv (t_{A:B}, t_{B:C}, t_{C:A}) = (2(n-1), n, n)$ ³ and $\mathcal{A}(AB : C)$ is the area of the minimal cut (with tension 1) for $AB : C$.

Averaging is taken with respect to the Haar measure over unitary matrices that are applied to vertex states in the graph. See Definition 6.1 (and also Sec. (2.4)) for the precise construction. The triway cut is defined in the same way as a cut: we split the vertices into three disjoint subsets containing respectively boundary vertices A, B, C . The area is then the sum over the edges e which intersect two of the three regions, weighted by the respective tensions and $w(e)$. See Definition 6.7 and Fig. (6.1).

The Markov gap is defined as [101]:

$$h(A : B) = S_R(A : B) - I(A : B) \geq 0, \quad (6.3)$$

where $I(A : B)$ is the mutual information. The Markov gap vanishes iff the three party state has a particular structure: a classical superposition of states with only bipartite entanglement between the three different

¹The cuts themselves are co-dimension 1, however the three cuts meet at some locus that might be considered co-dimension 2.

²What we mean here is that the (Lagrange) dual flow programs do not have the same optimal value, i.e. there is a *duality gap*. However it is possible to find a “dual” if one considers more exotic optimization problems. See Sec. (6.7) for more discussion on this topic.

³In this chapter we mostly consider triway cuts defined with this tension. For this reason we will often abbreviate the triway cuts simply as $\mathcal{A}(A : B : C)$ when it is unambiguous.

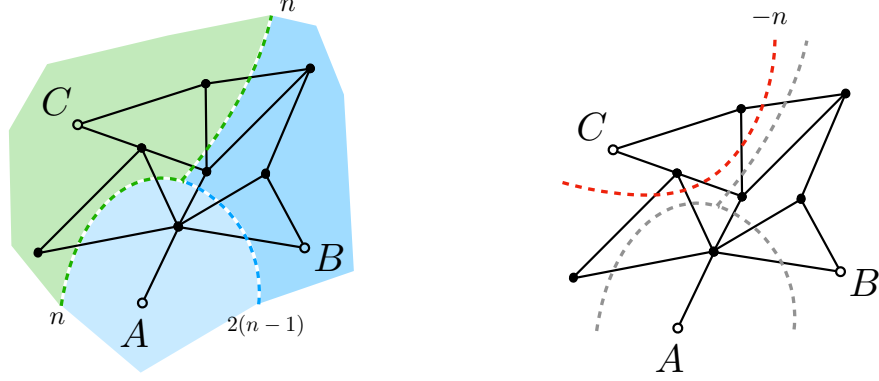


Figure 6.1: (*left*): A network with three boundary vertices (open dots) A, B, C , showing the definition of a triway cut, allowing for different domain wall tensions. This figure is schematic: edges in the graphs are weighted by some unspecified bond dimensions. (*right*): To compute the reflected entropy we must subtract the minimal cut for $AB : C$ which is always contained inside the C domain as shown. We should also divide the areas by $(n - 1)$.

parties [57]. The Markov gap thus detects a certain class of non-trivial tri-partite entanglement.⁴

In particular, we have the following lower bound:

Theorem 6.2. *Under the uniqueness assumption for $n = 2$ in Theorem 6.1, the (normalized) Markov gap (MG) of a random tensor network state at large bond dimension is lower bounded by:*

$$MG \equiv \lim_{\chi \rightarrow \infty} \frac{\overline{h(A, B)}}{\ln \chi} \geq 2\mathcal{A}_{\mathbf{s}}(A : B : C) - \mathcal{A}(A : BC) - \mathcal{A}(B : AC) - \mathcal{A}(C : AB), \quad (6.4)$$

where $\mathcal{A}_{\mathbf{s}}$ is the standard minimal triway cut with equal tensions $\mathbf{s} = (1, 1, 1)$.

Proof. This follows from $\partial_n S_R^{(n)} \leq 0$ and Theorem 6.1 applied at $n = 2$. □

We will show that the right hand side of Eq. (6.4) is determined by the integrality gap of the integer program [172]:

$$\begin{aligned} & \min_{\rho} \sum_e \rho(e) w(e) \\ & \forall L \in \mathcal{P}_{A, B} \cup \mathcal{P}_{A, C} \cup \mathcal{P}_{B, C} : \sum_{e \in L} \rho(e) \geq 1, \end{aligned} \quad (6.5)$$

where $\rho(e) \in \mathbb{Z}_{\geq 0}$ and $\mathcal{P}_{x, y}$ refers to all paths through the edges of the network connecting vertices x and y . The integrality gap IG is the ratio between the two optimal values of the program before and after relaxing the integer constraint on ρ , a standard concept in the theory of integer programming [64]. The original program computes $\mathcal{A}(A : B : C)$ with equal tensions, while the relaxed program allows the domain walls to split into pairs and form three minimal cuts with tensions $1/2$ (see Fig. (6.2)). The relaxed program is dual to the multicommodity flow problem [59] on three parties for which efficient algorithms exist. In this sense, we can interpret the integrality gap as an obstruction to obtaining a bit threads picture. Explicitly our bound

⁴ h vanishes on GHZ states, so it does not detect all kinds of tripartite entanglement [58]. A refined version, based on the entanglement of purification does better [33, 171]. This is generally harder to compute but the results of this chapter help compute it for a class of RTN states, as we will show in Chapter 7.

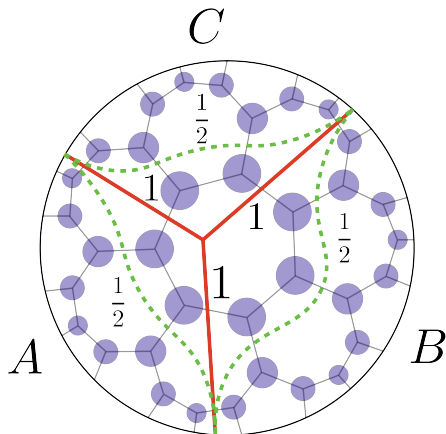


Figure 6.2: The optimal configuration for the integer program computing the triway cut at $n = 2$ involves domain walls (solid red) that indicate the location of $\rho(e) = 1$. The optimal configuration for the same program after removing the integer constraint has domain walls (dashed green) with $\rho(e) = \frac{1}{2}$, that relax to the minimal surfaces in contrast with the triway cut.

relates the two “gaps”:

$$MG \geq (IG - 1) \times (\mathcal{A}(A : BC) + \mathcal{A}(B : AC) + \mathcal{A}(C : AB)) \quad (6.6)$$

Roughly speaking $IG - 1 \geq 0$ measures how computationally hard the integer program is, and so this gives an intriguing link between the Markov gap and complexity.⁵

While an obvious and natural continuation in n away from the integers exists for the triway cut problem, we have not yet rigorously established that this still computes the n -Renyi reflected entropy. We have no reason to believe otherwise⁶, and so it is worth noting that the limit $n \rightarrow 1$ reproduces the entanglement wedge cross-section:

$$\lim_{n \rightarrow 1} \left(\frac{1}{n-1} \mathcal{A}(A : B : C) - \frac{n}{n-1} \mathcal{A}(AB : C) \right) = 2EW(A : B) \quad (6.7)$$

The calculation of reflected entropy in holography involves analytically continuing a two-parameter replica trick computation. It was shown in Ref. [117] that the continuation of the naive saddles proposed in Ref. [56] suffers from an order of limits issue, an analog of which exists for RTNs as well [48]. By incorporating new saddles, rigorously performing an analytic continuation in m and proposing an analytic continuation in n via the triway cut problem, we have resolved this issue in general RTNs. This motivates a similar prescription with the inclusion of new saddles even in AdS/CFT.

A summary of this chapter is as follows. In Sec. (6.2), we state our main theorems pertaining to the computation of Renyi reflected entropies for the state $|\rho_{AB}^{m/2}\rangle$ with $m \geq 2$ an even integer. In Sec. (6.3) we give some required background, including results on standard network flows, minimal cuts, and the mathematics of permutations and set partitions that make appearances in various statistical mechanics models that we consider. Sec. (6.4) proves that the optimal solution to the reflected entropy statistical mechanics model can be found in a series of coarser models, finally ending in the multiway cut problem. In Sec. (6.5) we continue

⁵Note that this is logically different from the computational complexity of the state often discussed in AdS/CFT [168, 169].

⁶Any lingering doubt might be used to challenge the conclusion [58] that the bipartite dominance conjecture [59] is false. However, independent of the EW duality, using Eq. (6.6) we have now rigorously proven the bipartite dominance conjecture false for any random tensor network with $IG \neq 1$ for the program Eq. (6.5).

the m parameter away from even integers to $m \rightarrow 1$, where we make contact with the reflected entropy. In this step we use the method of moments in conjunction with a weak form of measure concentration for random tensor network states. In Sec. (6.6), we apply our result to hyperbolic graphs and calculate the reflected entropy therein. In Sec. (6.7), we discuss various aspects of our work such as bit threads, the relation to entanglement of purification as well as generalization to hypergraphs. Several lengthy proofs are relegated to Appendix E.

We end this section with a list of common notations used in this chapter:

Table 6.1: Glossary of symbols and notations.

term	definition	first defined in
$G = \{E, V\}$	graph	Def. 6.1
$w(e)$	weight of an edge $e \in E$	after Def. 6.1
$E_G[V']$ or $E[V']$	set of edges that have some vertex in V'	before Def. 6.2
$V_G[E']$ or $V[E']$	set of vertices that lie in E'	before Def. 6.2
$\mathcal{P}_{A,B}$	set of paths from A to B	before Def. 6.2
$\widehat{\mathcal{P}}_{A,B}$	set of edge-disjoint paths from A to B	before Def. 6.2
r_A or $r_{A:B}$	cut region containing A or dividing $A : B$	before Eq. (6.30)
$\mu(r) \subset E$	cut surface of a region $r \subset V$	Eq. (6.30)
$\mathcal{A}(A : B)$	minimal cut for A and B	Def. 6.6
$\mathcal{A}(A : B : C)$	minimal triway cut among A, B and C	Def. 6.7
$\mathbf{1}_s(x)$	indicator function of the set s	after Eq. (6.40)
S_N	symmetric group of order N	before Eq. (6.13)
P_N	partitions of a set of order N	before Eq. (6.16)
B_N	set of string of N Boolean algebras	before Eq. (6.19)
$P(g)$	coarse graining $P : S_{mn} \rightarrow P_{mn}$	before Eq. (6.16)
$q_{g_0}(p)$	coarse graining $q_{g_0} : P_{mn} \rightarrow P_{\#(g_0)}$	Eq. (6.57)
$q_X(p)$	coarse graining $q_X : P_{mn} \rightarrow P_{2n}$	Eq. (6.16) and Eq. (6.57)
$s(q)$	coarse graining $s : P_{2n} \rightarrow s(P_{2n}) \simeq B_{2n}$	before Eq. (6.70)
$b^k(q)$	coarse graining $b^k : P_{2n} \rightarrow (B_{2n})^k \simeq \mathbb{Z}_2$	before Eq. (6.81)
u_k	largest partition with a singlet at location k	after Eq. (6.19)
$\#(x)$	cycle ($x \in S_N$) or block ($x \in P_N$) counting function	Eq. (6.13) and Eq. (6.17)
$\#_1(q)$	number of singlets in $q \in P_N$	before Eq. (6.70)
$a \wedge b$	meet of a and b	beginning of Sec. (6.3.2)
$a \vee b$	join of a and b	beginning of Sec. (6.3.2)
$d(g_1, g_2)$	($g_1, g_2 \in S_N$) Cayley distance in S_N	Eq. (6.13)
$d(q_1, q_2)$	($q_1, q_2 \in P_N$) distance on semimodular lattice P_N	Eq. (6.17) and Eq. (6.58)
$d_1(s_1, s_2)$	($s_i = s(p_i) : p_i \in P_N$) singlet distance on P_N	Eq. (6.70)
$d(b_1, b_2)$	($b_1, b_2 \in B_N$) Hamming distance on B_N	Eq. (6.20) and Eq. (6.81)
$d_\rho(x, y)$	($x, y \in E$) graph distance induced by $\rho : E \rightarrow \mathbb{R}$	Eq. (E.2)

Throughout this chapter we will define various distance functions on different sets. Most of these distances will be termed universally by $d(\cdot, \cdot)$, with an understanding that we use different definitions based on the set in context, as shown in Table 6.1. For a function $\rho(e)$ on the set of edges $\rho : E \rightarrow \mathbb{R}$ we will sometimes write $\rho(E') \equiv \sum_{e \in E'} \rho(e)$ for a subset $E' \subset E$.

Note: So far in this thesis we have been denoting the identity element in the group S_N to be $e \in S_N$. This unfortunately clashes with our notation for edges. Hence in this chapter we will use id to denote the identity element in S_N as well as the finest element of set partitions P_N . This will hopefully not cause confusion to our readers.

6.2 Setup

We summarize our key mathematical theorems that lead to our main result, setting up some of our notation at the same time. Our main results utilize the replica trick used to compute reflected entropy in random tensor networks (see Sec. 2.3-2.5). For definiteness we reiterate the constructions below:

Definition 6.1 (Random tensor network states). Consider an undirected graph $G = (V, E)$ where edges correspond to unordered pairs of vertices $e = \{v_1, v_2\}$ for $e \in E$ and $v_{1,2} \in V$. We mark special vertices $\partial \subset V$ as boundary vertices and the graph describes a pure state in the Hilbert space:

$$|\psi\rangle \in \bigotimes_{v \in \partial} \mathcal{H}^v, \quad \mathcal{H}^v = \bigotimes_{e \in E(v)} \mathcal{H}_{\chi(e)}^{(v)}, \quad (6.8)$$

where $E(v) := \{\{x, y\} \in E : x = v \text{ or } y = v\}$ are the subset of edges that contain v and $\chi(e)$ is the bond dimension of the edge. For a given vertex v not in the boundary, i.e. $v \in V \setminus \partial$, we pick random tensors $T(v) \in \mathcal{H}^v$ according to the Haar measure. Then the states in question are defined via:

$$|\psi\rangle \propto \left(\bigotimes_{v \in V \setminus \partial} \langle T(v) | \right) \left(\bigotimes_{e \in E} |\Psi_e\rangle \right), \quad (6.9)$$

where $|\Psi_e\rangle \in \mathcal{H}_{\chi(e)}^{(v_1)} \otimes \mathcal{H}_{\chi(e)}^{(v_2)}$ is a maximally entangled state between the vertex Hilbert spaces of $\{v_1, v_2\} = e$.

For convenience, on the graph we will use the rescaled weighting

$$w(e) = \frac{\ln \chi(e)}{\ln \chi}, \quad (6.10)$$

which we hold fixed as we send $\chi \rightarrow \infty$.

We will care about graphs with boundary $\partial = A \sqcup B \sqcup C$, and we are interested in using the replica trick to compute the averaged (m, n) -Renyi reflected entropy

$$S_R^{(m,n)}(A : B) = -\frac{1}{n-1} \ln \overline{\text{Tr}(\rho_{AA^*}^{(m)})^n}, \quad \rho_{AA^*}^{(m)} = \text{Tr}_{BB^*} \left| \rho_{AB}^{m/2} \right\rangle \left\langle \rho_{AB}^{m/2} \right|, \quad (6.11)$$

where $\rho_{AB} = \text{Tr}_C |\psi\rangle \langle \psi|$ and where $m \in 2\mathbb{Z}_{\geq 1}$. The n -th moment $\text{Tr}(\rho_{AA^*}^{(m)})^n$ contains nm copies of $|\psi\rangle \langle \psi|$, and the overline denotes that we compute the quantity in Eq. (6.11) averaged over the choice of $T(v)$ from the Haar ensemble. This calculation reduces to a statistical mechanics model with vertex-valued group elements

$g(v) \in S_{mn}$:

$$\overline{\text{Tr}(\rho_{AA^*}^{(m)})^n} = \frac{Z_{m,n}}{(Z_{m,1})^n}, \quad Z_{m,n} = \sum_{\{g(v)\}} \exp \left(- \sum_{e=\{x,y\} \in E} d(g(x), g(y)) \ln \chi(e) \right), \quad (6.12)$$

where $\sum_{\{g(v)\}}$ denotes a sum over all configurations of $g(v)$. We have denoted by $d(g_1, g_2)$ the Cayley distance in S_{mn} :

$$d(g_1, g_2) = mn - \#(g_1 g_2^{-1}), \quad (6.13)$$

where $\#(\cdot)$ is the cycle counting function. Note that we do not sum over permutations at boundary vertices; instead their permutations are fixed by the patterns of contractions that compute the moments in Eq. (6.11). We fix $g(v) = g_A$ for $v \in A$, $g(v) = g_B$ for $v \in B$, and $g(v) = \text{id}$ for $v \in C$ where id is the identity group element. For detailed for of the permutation elements g_A and g_B please refer to Sec. (2.3).

A particularly important group element that will arise in the optimal configuration $g(v)$ for Eq. (6.12) is the element X that has made numerous appearance in Chapter 3. It is uniquely defined as the element $X \in S_{mn}$ with the largest Cayley distance to the identity, $d(X, \text{id})$, that lies on the joint Cayley geodesics defined by: $d(g_A, X) + d(X, \text{id}) = d(g_A, \text{id})$ and $d(g_B, X) + d(X, \text{id}) = d(g_B, \text{id})$. See Sec. (2.3) and Sec. (2.5) for details on this element.

Exactly evaluating Eq. (6.12) for general graphs is difficult, but in the large χ limit we can often obtain a very good approximation by evaluating Eq. (6.12) at a saddle point, i.e., finding the configuration $\tilde{g}(v)$ that maximizes the exponential and dropping all other terms. Namely, we have

$$Z_{m,n} \approx \exp \left(- \sum_{e=\{x,y\} \in E} d(\tilde{g}(x), \tilde{g}(y)) \ln \chi(e) \right), \quad (6.14)$$

for $\tilde{g}(v)$ now the configuration minimizing the “free energy”

$$\sum_{e=\{x,y\} \in E} d(\tilde{g}(x), \tilde{g}(y)) \ln \chi(e). \quad (6.15)$$

The saddle point approximation is valid away from phase transitions and thus, in such generic situations, the problem of computing $S_R^{(m,n)}(A : B)$ reduces to the problem of finding the optimal configuration $\tilde{g}(v)$. It is this problem that we focus on in this chapter.

In order to find the optimal configuration $g(v)$, with minimal free energy, we will relate this statistical mechanics model to a sequence of increasingly coarse grained models where we throw out some information contained in $g(v)$. See Fig. (6.3). As a result the free energy can only decrease (as we prove rigorously), but then – crucially – we will prove that the minimal free energy in the most coarse-grained model *upperbounds* the free energy of the original model! This loop of inequalities allows us to use the tractable, most coarse-grained model to find the minimal free energy. This approach was inspired by the solution to the single tensor case studied earlier in Appendix C.1 where a similar sequence of steps was followed. Below we first describe the various coarse-grained variables, then we define the various stat mech/optimization problems we are interested in. An important ingredient is the theory of set partitions which form a lattice, in the sense of a partially ordered set, with binary operations \vee and \wedge . Boolean algebras will also make an appearance. We review the necessary background material in Sec. (6.3.2).

Given a permutation $g \in S_N$ we can associate a set partition $P(g) \in P_N$ by mapping the cycles to subsets

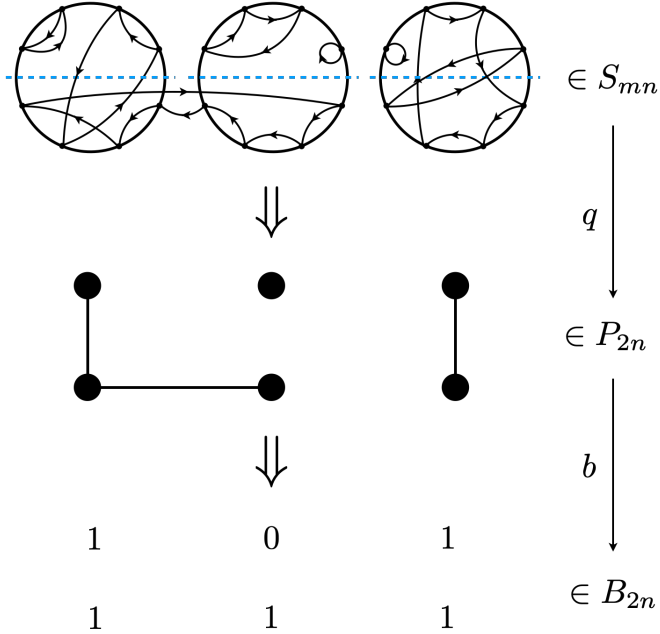


Figure 6.3: An illustration of the coarse-graining process used to establish our main result. We start from $g \in S_{mn}$ as shown at the top of the figure. For the convention used here to represent g : Each circle represents the m replica, and each circle is further replicated n times (here $m = 4$ and $n = 3$). The actions of g are represented as directed arrow connecting different replicas. See Sec. (2.3). To pass from S_{mn} to P_{2n} , we divide the mn elements into $2n$ blocks, each containing the $m/2$ elements in the corresponding half circle. We join two blocks if and only if any element in them can be reached by repeated actions of g . To pass from P_{2n} to B_{2n} , we simply label each block by a number in $\{0, 1\}$. That is, we label a block by 0 if it is not connected to any other block (such a block is called a *singlet*), and by 1 if otherwise. The result is a bit string of length $2n$.

of \mathbb{Z}_N , simply forgetting how elements within each cycle are permuted. In our case $N = nm$. We then further coarse-grain this set partition further by *blocking* $P(g)$ into partitions of the $2n$ blocks in $P(X)$. This reduction effectively removes dependence on m . More specifically for each $g \in S_{mn}$ we associate an element in P_{2n} via $q_X(g) : S_{mn} \rightarrow P_{2n}$ defined as:

$$q_X(g) \equiv (P(g) \vee P(X)) / \sim \quad x \sim y \text{ iff } \{x, y\} \vee P(X) = P(X), \quad (6.16)$$

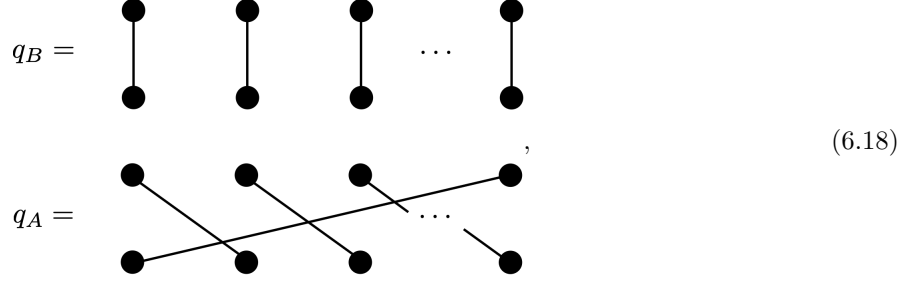
where \vee is the least upper bound operation on the lattice and the quotient is applied element wise to each element within the partition. We introduce a distance on set partitions⁷:

$$d(q_1, q_2) = \#(q_1) + \#(q_2) - 2\#(q_1 \vee q_2), \quad (6.17)$$

where $\#(\cdot)$ now counts the number of subsets in the partition. Note that $\#(g) = \#(P(g))$. This distance will replace the Cayley distance function in Eq. (6.12). For the problem in P_{2n} , the boundary elements will be

⁷See Sec. (6.3.2) for some properties of this metric. See Ref. [173] for some discussions of this metric.

fixed to partitions: $q_A = q_X(g_A)$ and $q_B = q_X(g_B)$ and $q_C = \text{id} \equiv q_X(\text{id})$. See:



where we have represented each dot as an element in \mathbb{Z}_{2n} , each corresponding to a cycle in the blocking permutation X , with position arranged in a similar fashion as in Fig. (6.3). We connect two dots by a line if they belongs to the same subset in the set partition. The partition distances are $d(q_A, q_B) = 2(n - 1)$ and $d(q_A, B, \text{id}) = n$.

At the next level we introduce Boolean variables $b = \{b^k\}_{k=1}^{2n} \in (\mathbb{Z}_2)^{\otimes 2n} \equiv B_{2n}$ that detect the presence of a singlet in $q \in P_{2n}$ (subsets with size 1). Define:

$$b^k(q) = 2 - \#(u_k \vee q), \quad (6.19)$$

where u_k for $k \in \{1, 2, \dots, 2n\}$, is the partition with a singlet at k plus a block of size $2n - 1$ containing with the rest of the elements. Thus $b^k = 0$ implies there is a singlet at location k ; otherwise $b^k = 1$. The distance between two Boolean strings $b_{1,2}$ is:

$$d(b_1, b_2) = \sum_{k=1}^{2n} |b_1^k - b_2^k|. \quad (6.20)$$

In this case the boundary conditions are $b_{AB} = 11 \dots 1$ and $b_C = 00 \dots 0$.

The set of walks/paths in a graph between v_1 and v_2 will be denoted \mathcal{P}_{v_1, v_2} , and consist of a sequence of edges $L \subset E$ that join at common vertices and start (end) at v_1 (v_2). The set of edge disjoint paths will be denoted $\widehat{\mathcal{P}}_{v_1, v_2}$ - these are paths with no repeated edges (vertices may be repeated). The vertices v_1 and v_2 may be replaced by sets of vertices with paths starting/ending on any vertex in the respective set. For a graph $G = \{V, E\}$ and a subset of edges $E' \subset E$, denote $V_G[E'] = \{v \in V : \{x, v\} \in E' \text{ or } \{v, y\} \in E'\}$ as the set of vertices that lie in E' . Similarly $E_G[V'] = \{\{x, y\} \in E : x \in V' \text{ or } y \in V'\}$ are the set of edges that have *some* vertex in $V' \subset V$. The subscript G in $E_G[\cdot]$ and $V_G[\cdot]$ shall often be omitted when the referencing graph is unambiguous. Lastly for a function on edges $\rho : E \rightarrow \mathbb{R}$ we define $\rho(E') = \sum_{e \in E'} \rho(e)$ for a subset $E' \subset E$.

Define the various optimization problems based on the refinements $g \rightarrow q \rightarrow b$:

Definition 6.2 (*Reflected entropy optimization*).

$$R = \min_g R(g), \quad R(g) \equiv \sum_{e=\{x,y\} \in E} w(e) d(g(x), g(y)), \quad (6.21)$$

where $g : V \rightarrow S_{mn}$ and such that $g(A) = g_A$, $g(B) = g_B$ and $g(C) = \text{id}$.

Definition 6.3 (*Set partition optimization*).

$$Q = \min_q Q(q), \quad Q(q) = \sum_{e=\{x,y\} \in E} w(e)d(q(x), q(y)), \quad (6.22)$$

where $q : V \rightarrow P_{2n}$ and such that $q(A) = q_A$ and $q(B) = q_B$ and $q(C) = \text{id}$.

Definition 6.4 (*Boolean optimization*).

$$B = \min_b B(b) \quad (6.23)$$

$$B(b) = \min_r \sum_{e \in E} w(e)r(e) \quad (6.24)$$

$$\text{subject to } \forall L \in \mathcal{P}_{A,B} : \sum_{e \in L} r(e) \in 2(n - \delta_{b_L, b_{AB}}) + 2\mathbb{Z}_{\geq 0} \quad (6.25)$$

$$\text{and } \forall e \in E : r(e) \geq \left\lceil \frac{1}{2}d(b(x), b(y)) \right\rceil, \quad (6.26)$$

where $r : E \rightarrow \mathbb{Z}_{\geq 0}$ and $b : V \rightarrow B_{2n}$ such that $b(A) = b(B) = b_{AB} \equiv 11 \dots 1$ and $b(C) = 00 \dots 0$, where $b_L \equiv \bigwedge_{v \in V[L]} b(v)$ denotes the piecewise *and* operation on Boolean algebra along the path L ⁸.

Definition 6.5 (*Integer program*).

$$I = \min_{\rho, \sigma} \sum_{e \in E} w(e)(\sigma(e) + \rho(e)) \quad (6.27)$$

$$\text{subject to } \forall L \in \mathcal{P}_{A,B} : \sum_{e \in L} (\sigma(e) + \rho(e)) \in 2(n - \delta_{\rho(L), 0}) + 2\mathbb{Z}_{\geq 0} \quad (6.28)$$

$$\text{and } \forall L \in \mathcal{P}_{AB,C} : \sum_{e \in L} \rho(e) \geq n, \quad (6.29)$$

where $\rho(L) \equiv \sum_{e \in L} \rho(e)$ and $\rho, \sigma : E \rightarrow \mathbb{Z}_{\geq 0}$.

Our main result is to prove that the optimal solution to these programs is given by a particular minimal and multiway cut program that we now define. A cut (or cut set) r for two vertices (or sets of vertices), $A : B$ is defined as a subset $r \subset V$ such that $A \subset r$ and $B \subset r^c$.⁹ A cut surface $\mu(r)$ for a given subset $r \subset V$ comprises the subset of edges that lie on the “boundary” of $r \leftrightarrow r^c$, in the sense that for all $e \in \mu(r)$ the pair $\{x, y\} = e$ satisfies $x \in r$ and $y \in r^c$ or vice-versa. In other words:

$$\mu(r) = E[r] \cap E[r^c] \quad (6.30)$$

Definition 6.6 (*Minimal cut*). The minimal cut for $A : B$ partitions two sets of boundary vertices $\partial = A \sqcup B$ and minimizes:

$$\begin{aligned} \mathcal{A}(A : B) &= \min_r \mathcal{A}(r) \\ \mathcal{A}(r) &= \sum_{e \in \mu(r)} w(e) \equiv w(\mu(r)) \end{aligned} \quad (6.31)$$

over all subsets $r \subset V$, such that the boundary vertices $A \subset r$ and $B \subset r^c$.

⁸That is for $L = \{\{v_0, v_1\}, \{v_1, v_2\}, \dots, \{v_{i-1}, v_i\}\}$: $b_L = b(v_1) \wedge b(v_2) \wedge \dots \wedge b(v_i)$ and $(b_1 \wedge b_2)^k \equiv b_1^k \wedge b_2^k$.

⁹We will sometimes denote a cut that divide boundary vertices $A : B$ as $r_{A,B}$, or simply as r_A when $B = A^c$.

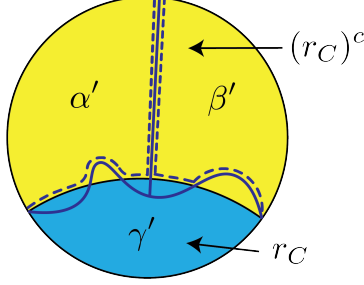


Figure 6.4: The entanglement wedge of C is denoted r_C (blue) and the complement is $(r_C)^c$ (yellow). For any triway cut configuration $(\alpha', \beta', \gamma')$ (demarcated by solid lines), we can construct a better triway cut (α, β, γ) (separated by dashed lines) such that $r_C \subset \gamma$.

Definition 6.7 (*Triway cut*). Fix some tensions $\mathbf{t} = \{t_{A:B}, t_{B:C}, t_{C:A}\}$ with $t_{A:B}, t_{B:C}, t_{C:A} > 0$ and boundary vertices $\partial = A \sqcup B \sqcup C$. The triway cut problem minimizes:

$$\begin{aligned} \mathcal{A}_{\mathbf{t}}(A : B : C) &= \min_{(\alpha, \beta, \gamma)} \mathcal{A}_{\mathbf{t}}(\alpha : \beta : \gamma) \\ \mathcal{A}_{\mathbf{t}}(\alpha : \beta : \gamma) &= t_{A:B} \sum_{e \in \mu(\alpha:\beta)} w(e) + t_{B:C} \sum_{e \in \mu(\beta:\gamma)} w(e) + t_{C:A} \sum_{e \in \mu(\gamma:\alpha)} w(e) \\ &= t_{A:B} w(\mu(\alpha : \beta)) + t_{B:C} w(\mu(\beta : \gamma)) + t_{A:C} w(\mu(\gamma : \alpha)) \end{aligned} \quad (6.32)$$

over all subsets (α, β, γ) such that $\alpha \sqcup \beta \sqcup \gamma = V$ with $A \subset \alpha, B \subset \beta, C \subset \gamma$ and where $\mu(r_1 : r_2) = E[r_1] \cap E[r_2]$.

Remark. The triway cut is a special case of a *multiway cut* and we will often refer to it as such. The equal tension case is the standard multiway cut problem, which arises here when $n = 2$ (see e.g. Ref. [170, 172]). In the context of AdS/CFT, multiway cuts have been studied previously in [174–176].

We note that minimal cuts must always lie inside some optimal multiway cut region:

Lemma 6.3. *Given an optimal solution to a minimal cut problem for $C : AB$, $r_C \subset V$ then there exists an optimal solution (α, β, γ) to the triway cut problem for (A, B, C) with $t_{A:C} = t_{B:C}$ and such that $r_C \subset \gamma$.*

Proof. Consider any optimal triway cut $(\alpha', \beta', \gamma')$. Construct $\alpha = \alpha' \cap (r_C)^c$, $\beta = \beta' \cap (r_C)^c$ and $\gamma = \gamma' \cup r_C$ (see Fig. (6.4)). We note:

$$\sum_{e \in \mu(\alpha:\beta)} w(e) \leq \sum_{e \in \mu(\alpha':\beta')} w(e) \quad (6.33)$$

since $\mu(\alpha : \beta) \supseteq \mu(\alpha' : \beta')$ by construction and $w(e) \geq 0$. Also,

$$\begin{aligned} \sum_{e \in \mu(\alpha:\gamma)} w(e) + \sum_{e \in \mu(\beta:\gamma)} w(e) &= w(\mu(\gamma)) \\ &= w(\mu(\gamma')) + w(\mu(r_C)) - w(\mu(\gamma \setminus r_C^c)) \leq w(\mu(\gamma')), \end{aligned} \quad (6.34)$$

where in the last inequality we used the fact that $\gamma \setminus r_C^c$ is a cut for $C : AB$ and that r_C is a minimal such cut. Putting these inequalities together we have:

$$\mathcal{A}(\alpha, \beta, \gamma) \leq \mathcal{A}(\alpha', \beta', \gamma'), \quad (6.35)$$

implying equality and that (α, β, γ) is a minimal triway cut satisfying the properties stated in the Lemma. \square

The main theorem of this chapter establishes:

Theorem 6.4. *The minimum of each of the programs defined above are determined by an optimal solution to the multiway cut problem with $\mathbf{t} = (t_{A:B}, t_{B:C}, t_{A:C}) = (2(n-1), n, n)$:*

$$R - \mathcal{A}(AB : C)n(m-2) = Q = B = I = \mathcal{A}_{\mathbf{t}}(A : B : C). \quad (6.36)$$

Proof. Consider some minimal cut r_C for $C : AB$. There is an optimal solution to the triway cut problem with $r_C \subset \gamma$ by Lemma 6.3. Set

$$g(x) = \begin{cases} g_A, & x \in \alpha \\ g_B, & x \in \beta \\ \text{id}, & x \in r_C \\ X, & x \in \gamma \setminus r_C \end{cases}. \quad (6.37)$$

We then estimate:

$$R \leq \mathcal{A}(AB : C)d(\text{id}, X) + \mathcal{A}_{\mathbf{t}}(A : B : C) \quad (6.38)$$

by direct computation and since $d(X, g_A) = d(X, g_B) = n$ and $d(g_A, g_B) = 2(n-1)$ give the correct tensions.

After this we prove a chain of inequalities in the other way, $R \geq \mathcal{A}(AB : C)d(\text{id}, X) + Q$ (Lemma 6.11 and Lemma 6.12), and $Q \geq B$ (Lemma 6.14 and Corollary 6.15), and $B \geq I$ (Lemma 6.16) and finally $I \geq \mathcal{A}_{\mathbf{t}}(A : B : C)$ (Theorem 6.17). Together with Eq. (6.38) this implies equality through the chain. \square

Theorem 6.4 only asserts that the optimal value of the program R are equivalent to that of the triway cut. It need not be the same as the one that was constructed above and there may be other degenerate solutions that achieve the minimum – Indeed one generally expects a huge degeneracy when a phase transition happens. Such phase transitions in tensor networks are usually signaled by a degenerate minimal surface. The following theorem states that the optimal solution constructed above is unique when the system is far away from such transitions.

Theorem 6.5. *Let $g : V \rightarrow S_{mn}$ be an optimal solution to the reflected entropy permutation group optimization problem R on graph G with a unique solution (α, β, γ) to the triway cut problem for (A, B, C) and a unique solution r_C to the minimal cut problem $C : AB$. Then g is unique and of the form as given in Eq. (6.37).*

We prove this theorem in Sec. (6.4.4) after we establish the necessary Lemmas that lead to Theorem 6.4.

6.3 Preliminaries

6.3.1 Min cuts and Max flows

We discuss a version of max-flow min-cut that is convenient here. Consider the undirected max flow problem written as a linear program and in terms of edge disjoint paths:

$$\max_c \sum_{L \in \hat{\mathcal{P}}_{A,B}} c(L) \quad (6.39)$$

$$\text{subject to: } \forall e \in E \quad \sum_{P \in \hat{\mathcal{P}}_{A,B}} c(L) \mathbf{1}_L(e) \leq w(e) \quad (6.40)$$

where $\mathbf{1}_L(e) = 1$ if $e \in L$ and 0 otherwise. and where $c : \widehat{\mathcal{P}}_{A,B} \rightarrow \mathbb{R}_{\geq 0}$ and we maximize over all such maps. Any $c(L)$ that satisfies the constraint above is called *feasible* while any feasible c that achieves the maximum is called *optimal*.

Let us derive the dual program. For each constraint we introduce a function $\rho : E \rightarrow \mathbb{R}_{\geq 0}$ and minimize over $\rho(e)$:

$$= \max_c \min_\rho \left(\sum_{L \in \widehat{\mathcal{P}}_{A,B}} c(L) + \sum_{e \in E} \rho(e) \left(w(e) - \sum_{P \in \widehat{\mathcal{P}}_{A,B}} c(L) \mathbf{1}_L(e) \right) \right) \quad (6.41)$$

The minimum is $-\infty$ with $\rho \rightarrow \infty$ for some e if c is not feasible. If c is feasible the minimum is $\rho(e) = 0$. Thus this gives back the original problem after maximizing over c . We can now exchange the maximum and the minimum since the function is linear in c at fixed ρ (and hence concave) and linear in ρ at fixed c (and hence convex), so we can use the von Neumann's minimax theorem:

$$= \min_\rho \max_c \left(\sum_{e \in E} \rho(e) w(e) + \sum_{L \in \widehat{\mathcal{P}}} c(L) (1 - \sum_{e \in L} \rho(e)) \right) \quad (6.42)$$

Maximizing over c gives $+\infty$ unless $\sum_{e \in P} \rho(e) \geq 1$ in which case we find $c(L) = 0$. Thus we can restrict to the set of *dual feasible* ρ satisfying this later constraint.

In summary the dual program is defined in terms of a map $\rho : E \rightarrow \mathbb{R}_{\geq 0}$:

$$\min_\rho \sum_{e \in E} \rho(e) w(e) \quad (6.43)$$

$$\text{subject to : } \forall L \in \widehat{\mathcal{P}}_{A,B} \quad \sum_{e \in L} \rho(e) \geq 1 \quad (6.44)$$

As we just derived, this problem satisfies strong duality.¹⁰ We can also impose the further constraints that all $L \in \mathcal{P}_{A,B}$ (not necessarily edge disjoint) also satisfy $\sum_{e \in L} \rho(e) \geq 1$ without changing the minimum, since it does not change the set of feasible ρ .

It is possible to show that this last problem is a min-cut problem. A proof of this fact can be found in standard references in linear programming, e.g. Ref. [64]. We will take a slightly different approach here. We consider the integer version of Eq. (6.44) where we further impose $\rho \in \mathbb{Z}_{\geq 0}$. This does indeed give the equivalent optimal value as Eq. (6.43), although this is not obvious and there could well have been an *integrality gap*. We will now demonstrate it is equivalent to the min-cut problem, or that the integrality gap vanishes for this problem. To construct the cut we consider an optimal ρ and define:

$$r_A = \{x : d_\rho(x, A) = 0\}, \quad (6.45)$$

where $d_\rho(x, y)$ is the graph distance induced by $\rho(e)$, which is the minimal distance between x and y as measured by the edge function $\rho(e)$. See Appendix E.1.

It is clear that

$$\rho(e) \geq \mathbf{1}_{\mu(r_A)}(e) \quad (6.46)$$

¹⁰Strong duality means that the optimal values of the original and dual program are equal.

by integrality. Then for any other feasible ρ' :

$$\sum_{e \in E} \rho'(e)w(e) \geq \sum_{e \in E} \rho(e)w(e) \geq w(\mu(r_A)) \quad (6.47)$$

Also any path from A to B must pass $\mu(r_A)$ so that $\rho'(e) = \mathbf{1}_{\mu(r_A)}(e)$ is feasible and we have the opposite inequality.

We now give a quick derivation of the RT formula for RTNs. We pick the cut $C : AB$, although this discussion is general. We compute the m th Renyi entropy for ρ_{AB} at large χ which involves finding the minimum of the free energy:

$$\min_g \sum_{e=\{x,y\} \in E} w(e)d(g(x), g(y)) \quad (6.48)$$

where $g : V \rightarrow S_m$ and $g(AB) = \tau_m = (12 \dots m)$ and $g(C) = \text{id}$. Use an optimal solution to the flow problem $c(L)$, inserting Eq. (6.40) into the objective function of Eq. (6.48):

$$\sum_{e=\{x,y\} \in E} w(e)d(g(x), g(y)) \geq \sum_{L \in \mathcal{P}_{AB:C}} c(L) \sum_{e=\{x,y\} \in L} d(g(x), g(y)) \quad (6.49)$$

$$\geq d(\tau_m, \text{id}) \sum_{L \in \mathcal{P}_{AB:C}} c(L) \quad (6.50)$$

$$= (m-1)\mathcal{A}(AB : C) \quad (6.51)$$

where in the first inequality we used the feasibility condition, and in the second we used the triangle inequality for the Cayley metric repeatedly along the path. The opposite inequality follows by considering $g(x) = \text{id}$ for $x \in r_{AB:C}^c$ and $g(x) = \tau_m$ for $x \in r_{AB:C}$. Thus Renyi entropies are all computed by the same minimal area cut. This is the well known result that the entanglement spectrum of random tensor networks is flat, and determined by minimal cuts.

We now give a proof that the integrality gap of Eq. (6.5) is determined by the ratio between $\mathcal{A}(A : B : C)$ and $\frac{1}{2}(\mathcal{A}(AB : C) + \mathcal{A}(B : AC) + \mathcal{A}(C : AB))$. First we show that the value of the following integer program

$$\begin{aligned} & \min_{\rho} \sum_{e \in E} \rho(e)w(e) \\ & \text{subject to : } \forall L \in \mathcal{P}_{A,B} \cup \mathcal{P}_{A,C} \cup \mathcal{P}_{B,C} : \sum_{e \in L} \rho(e) \geq 1 \end{aligned} \quad (6.52)$$

is given by the minimal triway cut. We restrict our discussion here to the case where every connected component of G is connected to at least one of A , B , or C , since any adding disconnected components to G does not change the area of an optimal triway cut.

Consider an optimal ρ and define $r_A = \{x \in V : d_{\rho}(x, A) = 0\}$ and similarly define r_B and r_C . (r_A, r_B, r_C) must be disjoint otherwise we violate the path constraint. Furthermore $r_A \cup r_B \cup r_C = V$: If otherwise define $r_D \equiv V \setminus r_A \setminus r_B \setminus r_C$. r_D must be connected to at least one of r_A, r_B or r_C , since otherwise r_D will be totally disconnected from the boundary. Without loss of generality suppose it is r_A . We have

$$\begin{aligned} \rho(e) & \geq (\mathbf{1}_{\mu(r_A:r_B)} + \mathbf{1}_{\mu(r_A:r_C)} + \mathbf{1}_{\mu(r_B:r_C)} + \mathbf{1}_{\mu(r_A:r_D)} + \mathbf{1}_{\mu(r_B:r_D)} + \mathbf{1}_{\mu(r_C:r_D)})(e) \\ & \geq (\mathbf{1}_{\mu(r'_A:r_B)} + \mathbf{1}_{\mu(r'_A:r_C)} + \mathbf{1}_{\mu(r_B:r_C)})(e) \equiv \rho'(e), \end{aligned} \quad (6.53)$$

where the first inequality follows from integrality. In the second line we defined $r'_A = r_A \cup r_D$ and this inequality is strict for $e \in \mu(r_A : r_D)$. $\rho'(e)$ is clearly feasible since any path from A to B must pass through $\mu(r'_A : r_B)$ and similarly for $B : C$ and $C : A$. Since $\mu(r_A : r_D) \neq \emptyset$ we have $\sum_e \rho(e)w(e) > \sum_e \rho'(e)w(e)$, which is a contradiction since we have assumed ρ to be optimal. Therefore $r_D = \emptyset$ and $r'_A = r_A$. Since ρ is optimal we must have

$$\min_{\rho} \sum_{e \in E} \rho(e)w(e) = \sum_{e \in E} \rho'(e)w(e) = \mathcal{A}(r_A : r_B : r_C) \geq \mathcal{A}(A : B : C). \quad (6.54)$$

On the other hand from any minimal triway cut (α, β, γ) we can construct $\rho''(e) = (\mathbf{1}_{\mu(\alpha:\beta)} + \mathbf{1}_{\mu(\alpha:\gamma)} + \mathbf{1}_{\mu(\beta:\gamma)})(e)$ which is clearly feasible. Hence $\mathcal{A}(A : B : C) \geq \sum_e \rho''(e)w(e)$ and the value of program is equivalent to minimal triway cut.

If one relaxes the integer constraint of ρ , then it allows us to construct a new solution from any optimal ρ :

$$\tilde{\rho}(e) = \frac{1}{2} \left(\mathbf{1}_{\mu(r_A:r_A^c)} + \mathbf{1}_{\mu(r_B:r_B^c)} + \mathbf{1}_{\mu(r_C:r_C^c)} \right) (e) \quad (6.55)$$

$\tilde{\rho}(e)$ violates the integer constraint but is still feasible. Using a similar argument as above one can show that in this scenario we get

$$\begin{aligned} \min_{\rho} \sum_{e \in E} \rho(e)w(e) &= \sum_{e \in E} \tilde{\rho}(e)w(e) = \frac{1}{2} (\mathcal{A}(r_A : r_A^c) + \mathcal{A}(r_B : r_B^c) + \mathcal{A}(r_C : r_C^c)) \\ &\geq \frac{1}{2} (\mathcal{A}(A : BC) + \mathcal{A}(B : AC) + \mathcal{A}(C : AB)), \end{aligned} \quad (6.56)$$

and the optimal value of the program is given by a sum of minimal cut areas. We have determined the optimal value of the program Eq. (6.5) before and after the linear relaxation, which agrees with the right hand side of Eq. (6.4).

6.3.2 Permutations, Partitions and Boolean variables

In Sec. (6.2) we introduced a coarse graining procedure which takes permutations to partitions. We further coarse grain our partitions by blocking them into partitions of the blocks in $P(X)$. We can apply this procedure given any fixed permutation g_0 , instead blocking with $P(g_0)$. We discuss this more general procedure here and prove some important bounds.

The collection of set partitions P_N admits a natural lattice structure. There is a partial order within P_N : Given two elements $p, q \in P_N$ we say $p \geq q$ if every subset of p can be expressed as the union of some subsets in q , or in other words, q is a “finer” version of p formed by further dividing blocks in p . The finest (smallest) element in P_N is the identity permutation $\text{id} \equiv \{\{1\}, \dots, \{N\}\}$, and the coarsest (largest) is $\{\mathbb{Z}_N\}$. The *join* of p and q , denoted by $p \vee q$, is defined to be the least upper bound of p and q , i.e. $p \vee q$ is the smallest element x such that $x \geq p$ and $x \geq q$. Conversely, the *meet* of p and q , denoted by $p \wedge q$, is defined to be greatest lower bound of p and q , i.e. $p \wedge q$ is the largest element y such that $y \leq p$ and $y \leq q$. In the lattice of P_N the meet is simply the set of non-empty pairwise intersections of p and q ; whereas the join can be thought of as the partition that arises from the connected orbits generated by p and q . For further information on the lattice of set partitions we refer the reader to Appendix A.

Given some element $g, g_0 \in S_N$ we define:

$$q_{g_0}(g) \equiv (P(g) \vee P(g_0)) / \sim \in P_{\#(g_0)} \quad (6.57)$$

where $/ \sim$ is the set quotient operation defined element wise on each block in the partition and using the equivalence $x \sim y$ if x, y are in the same block of $P(g_0)$.

Recall the distance measure on the set of partitions P_N :

$$d(p, p') \equiv \#(p) + \#(p') - 2\#(p \vee p') \quad (6.58)$$

We verify some properties.

Lemma 6.6. *The distance on set partitions $d(p, p')$ is a metric: it is positive, symmetric, vanishes iff $p = p'$ and satisfies the triangle inequality. Additionally:*

(a) *There is the estimate:*

$$d(p_1, p_2) \geq |\#(p_1) - \#(p_2)| \quad (6.59)$$

(b) *For all partitions r then:*

$$d(p_1, p_2) \geq d(p_1 \vee r, p_2 \vee r) \quad (6.60)$$

(c) *It bounds the Cayley distance by the associated set partitions $P(g)$, or coarse grained versions $q_{g_0}(g)$:*

$$\#(g) - \#(g \vee g') \geq \#(q_{g_0}(g)) - \#(q_{g_0}(g) \vee q_{g_0}(g')) \quad (6.61)$$

and

$$d(g, g') \geq d(P(g), P(g')) \geq d(q_{g_0}(g), q_{g_0}(g')) \quad (6.62)$$

Proof. Firstly the distance is positive since $\#(p) - \#(p \vee p') \geq 0$ and similarly for $p \leftrightarrow p'$. Equality implies that $\#(p') = \#(p) = \#(p \vee p')$ which is only possible if $p' \leq p$ and also $p' \geq p$ which implies equality of the partitions. We have the triangle inequality:

$$d(p, p') + d(p', p'') \geq d(p, p'') \quad (6.63)$$

which follows from semimodularity ¹¹:

$$\begin{aligned} & \#(p') - \#(p \vee p') - \#(p' \vee p'') + \#(p \vee p'') \\ & \geq \#((p' \vee p) \wedge (p' \vee p'')) - \#(p \vee p') - \#(p' \vee p'') + \#(p \vee p'' \vee p') \geq 0 \end{aligned} \quad (6.64)$$

where the first inequality follows simply from $p' \leq (p' \vee p) \wedge (p' \vee p'')$ and $p' \vee p'' \leq p \vee p'' \vee p'$.

(a) Using $\#(p_1 \vee p_2) \leq \#(p_1)$ or $\#(p_1 \vee p_2) \leq \#(p_2)$ we derive $d(p_1, p_2) \geq |\#(p_1) - \#(p_2)|$.

(b) For any $r \in P_N$:

$$\begin{aligned} & d(p_1, p_2) - d(p_1 \vee r, p_2 \vee r) \\ & = \#(p_1) + \#(p_2) - \#(p_1 \vee r) - \#(p_2 \vee r) + 2\#(p_1 \vee p_2 \vee r) - 2\#(p_1 \vee p_2) \\ & \geq \#(p_1) + \#(p_2) - \#((p_1 \vee p_2) \wedge (p_1 \vee r)) - \#((p_1 \vee p_2) \wedge (p_2 \vee r)) \geq 0 \end{aligned} \quad (6.65)$$

¹¹Semimodularity here means $\#(p_1 \wedge p_2) + \#(p_1 \vee p_2) \geq \#(p_1) + \#(p_2)$.

where we used semi-modularity in the first inequality¹² and we used $p_i \leq (p_1 \vee p_2) \wedge (p_i \vee r)$ in the second inequality.

(c) In general we start with some $g \in S_N$. Then we will remove fine-grained topological information (roughly speaking we lose information on the genus expansion) by moving to partitions. We can do this using the general bound:

$$\begin{aligned} d(g, g') &= -d(e, g) + d(e, g') + 2(\#(g') - \#(g' \vee g)) + 2G_{g'}(g) \\ &\geq \#(g) + \#(g') - 2\#(g \vee g') = d(P(g), P(g')) \end{aligned} \quad (6.66)$$

where $\#(g' \vee g) \equiv \#(P(g') \vee P(g))$ is the number of orbits generated by the joint action of g and g' , and $G_{g'}(g)$ is the genus of the admissible surface associated for g based over g' . The inequality then follows from the non-negativity of the genus. See Theorem A.5 of Appendix A.

Consider semimodularity applied to $p = P(g) \vee P(g_0)$ and $p' = P(g) \vee P(g')$ giving:

$$\#(P(g)) + \#(p \vee p') \geq \#(p \wedge p') + \#(p \vee p') \geq \#(p) + \#(p') = \#(q_{g_0}(g)) + \#(g \vee g') \quad (6.67)$$

where the first inequality follows since $P(g) \leq p$ and $P(g) \leq p'$ implying the same of the meet $p \wedge p'$. Note that $\#(p \vee p') = \#(q_{g_0}(g) \vee q_{g_0}(g'))$, $\#(p) = \#(q_{g_0}(g))$ and $\#(p') = \#(g \vee g')$. Thus we derived the bound:

$$\#(g) - \#(g \vee g') \geq \#(q_{g_0}(g)) - \#(q_{g_0}(g) \vee q_{g_0}(g')) \quad (6.68)$$

which implies:

$$d(P(g), P(g')) \geq d(q_{g_0}(g), q_{g_0}(g')) \quad (6.69)$$

□

Consider $q = q_X(g) \in P_{2n}$ for some $g \in S_{mn}$. We can further classify q by the singlets in q . A singlet is a block of size 1 so there are $2n$ possible singlets. We define $\#_1(q)$ as the number of singlets in a given partition. We define $s(q)$ as the (unique) largest partition with singlets in the same location as the singlets of q . That is $s(q) \geq q$ and $\#(s(q)) = \#_1(q) + 1 - \delta_{\#_1(q), 2n}$. Also $\#_1(q) = \#_1(s(q))$.

We define the *singlet distance* on the set of s as:

$$d_1(s_1, s_2) = \#_1(s_1) + \#_1(s_2) - 2\#_1(s_1 \vee s_2) \geq d(s_1, s_2), \quad (6.70)$$

where the later inequality is only not saturated if one of s_1 or s_2 is id (but not both.) We also have $d_1(s_1, s_2) \leq d(s_1, s_2) + 1$ with equality iff one and only one of s_1, s_2 is id.

We can bound the difference in q by s :

Lemma 6.7.

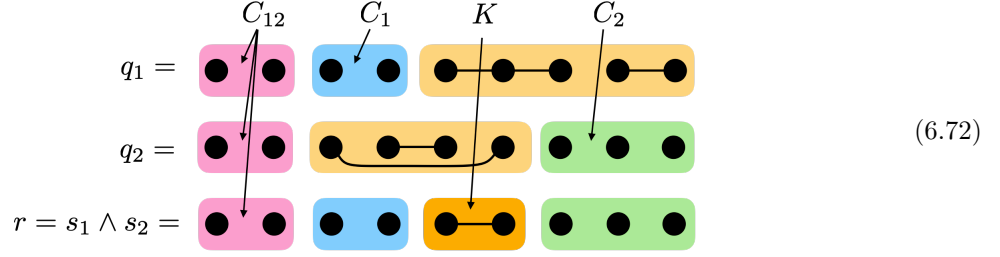
$$d(q_1, q_2) \geq \lceil d_1(s_1, s_2)/2 \rceil \geq d_1(s_1, s_2)/2, \quad (6.71)$$

where $s_i := s(q_i)$.

Proof. If q_1 and q_2 do not contain any singlet, then $s_1 = s_2 = \mathbb{Z}_{2n}$ and $d(s_1, s_2) = 0$ so the estimation is true. Now let C_{12} be the common singlets of q_1 and q_2 , C_1 be the singlets in q_1 that do not overlap with the singlets

¹²Specifically: $-\#(p_1 \vee p_2) - \#(p_1 \vee r) + \#(p_1 \vee p_2 \vee r) \geq -\#((p_1 \vee p_2) \wedge (p_1 \vee r))$ and $1 \leftrightarrow 2$.

in q_2 and similarly for C_2 . Note that $d(q_1, q_2) \geq d(q_1 \vee r, q_2 \vee r)$ from Eq. (6.60). We take $r = s_1 \vee s_2$. We can express r as the unique element that is fully connected in $K = \mathbb{Z}_{2n} \setminus C_1 \setminus C_2 \setminus C_{12}$ and singlets elsewhere. See:



We can compute

$$\begin{aligned} d(q_1 \vee r, q_2 \vee r) &= \#(q_1 \vee r) + \#(q_2 \vee r) - 2\#(q_1 \vee q_2 \vee r) \\ &= |C_1| + |C_2| + \#(q_1 \vee r)|_{K \cup C_2} + \#(q_2 \vee r)|_{K \cup C_1} - 2\#(q_1 \vee q_2 \vee r)|_{K \cup C_1 \cup C_2}, \end{aligned} \quad (6.73)$$

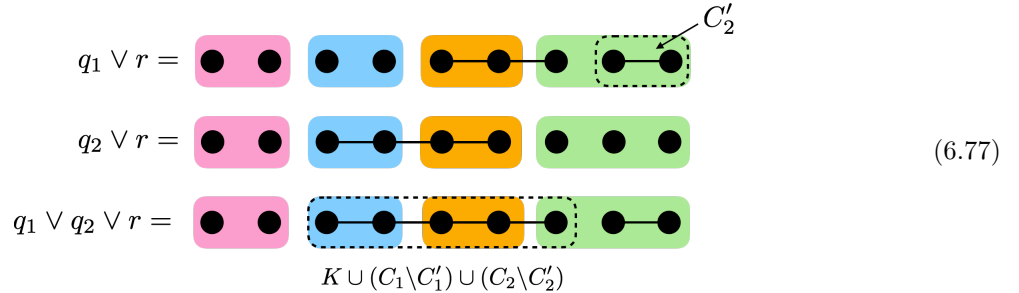
where we have used $\#(q)|_C$ to indicate the number of cycles of q when restricted to a subset of elements $C \subset \mathbb{Z}_{2n}$. Note that the common singlets $|C_{12}|$ cancels out in the calculation. To proceed further, we define $C'_1 \subset C_1$ to be the elements in C_1 that are not connected to K via $q_2 \vee r$ and similarly for C'_2 . Then we have

$$\#(q_1 \vee r)|_{K \cup C_2} = 1 + \#(q_1 \vee r)|_{C'_2} \quad (6.74)$$

$$\#(q_2 \vee r)|_{K \cup C_1} = 1 + \#(q_2 \vee r)|_{C'_1} \quad (6.75)$$

$$\#(q_1 \vee q_2 \vee r)|_{K \cup C_1 \cup C_2} = 1 + \#(q_1 \vee r)|_{C'_2} + \#(q_2 \vee r)|_{C'_1}, \quad (6.76)$$

which readily follows from the structure of $q_i \vee r$. See:



(In the example given here $C'_1 = \emptyset$) Hence,

$$d(q_1 \vee r, q_2 \vee r) = |C_1| + |C_2| - \#(q_1 \vee r)|_{C'_2} - \#(q_2 \vee r)|_{C'_1}. \quad (6.78)$$

Also note that $(q_2 \vee r)|_{C'_1}$ has no singlets so that $\#(q_2 \vee r)|_{C'_1} \leq \lfloor |C'_1|/2 \rfloor \leq \lfloor |C_1|/2 \rfloor$ since this number is maximized by forming the largest number of doublet blocks or doublet and a single triplet block in C'_1 (and similarly for $1 \leftrightarrow 2$.) This gives the estimate:

$$d(q_1, q_2) \geq \lceil |C_1|/2 \rceil + \lceil |C_2|/2 \rceil \geq \lceil (|C_1| + |C_2|)/2 \rceil. \quad (6.79)$$

Now $|C_1| + |C_2| = d_1(s_1, s_2)$ (see the proof of the Lemma following immediately after). \square

Note that the set of $s, s(P_{2n}) \subset P_{2n}$, forms a lattice (albeit not a sub-lattice of P_{2n} ¹³), under the new meet and join defined by $s_1 \wedge_B s_2 \equiv s_1 \wedge s_2$ and $s_1 \vee_B s_2 \equiv s(s_1 \vee s_2)$. Define the units $u_k \in s(P_{2n})$ to be the partition with one singlet at location k . That is, $u_k = \{\{k\}, \mathbb{Z}_{2n} \setminus \{k\}\}$. It then follows that every element in $s(P_{2n})$ (other than \mathbb{Z}_{2n}) can be expressed as the meet of a string of u^k 's, i.e. $s = u_{k_1} \wedge \cdots \wedge u_{k_i}$.

The lattice $(s(P_{2n}), \vee_B, \wedge_B)$ is isomorphic to Boolean algebra B_{2n} of bit-strings where singlets in s are 0's, and non-singlets are 1's. More specifically, identify s (and thus q) using a binary variable b^k for $k = 1, \dots, 2n$. That is:

$$b^k(q) = \#_1(s(q) \vee u_k) = \#_1(q \vee u_k), \quad (6.80)$$

so that $b^k(q) = 0$ if q has a singlet at the k -th element and $b^k(q) = 1$ otherwise. The bit-string $b = \{b^k\}_{k=1}^{2n}$ then forms a lattice where \vee is the pair-wise or operation and \wedge is the pair-wise and operation. Then the singlet distance on P_{2n} is simply the Hamming distance on bit-strings:

Lemma 6.8.

$$d(b_1, b_2) \equiv \sum_{k=1}^{2n} |b_1^k - b_2^k| = d_1(s_1, s_2), \quad (6.81)$$

where $b_{1,2}^k = b^k(s_{1,2})$.

Proof. Consider the k -th element in a partition of \mathbb{Z}_{2n} . Then $s_1 \vee s_2$ has a singlet at position k iff s_1 and s_2 both have a singlet at position k . Let S_i be the set of singlets in s_i , then we have

$$\begin{aligned} d_1(s_1, s_2) &= \#_1(s_1) + \#_1(s_2) - 2\#_1(s_1 \vee s_2) \\ &= |S_1| + |S_2| - 2|S_1 \cap S_2| = |C_1| + |C_2|, \end{aligned} \quad (6.82)$$

where C_1 are the elements in S_1 that are not contained in S_2 and likewise for C_2 . By definition $C_1 \cap C_2 = \emptyset$ and

$$|C_1| + |C_2| = |C_1 \cup C_2| = \sum_{k=1}^{2n} |b_1^k - b_2^k|, \quad (6.83)$$

since $|b_1^k - b_2^k| = 1$ signals $k \in C_1 \cup C_2$ and $|b_1^k - b_2^k| = 0$ otherwise. \square

Corollary 6.9.

$$d(q_1, q_2) \geq \lceil d(b_1, b_2)/2 \rceil \geq d(b_1, b_2)/2, \quad (6.84)$$

where $b_{1,2}^k = b^k(s_{1,2})$.

Proof. Substitute Eq. (6.81) into Lemma 6.7. \square

Remark. $d(b_1, b_2)$ clearly satisfies all the properties of a metric. We will also sometimes work with $\lceil d(b_1, b_2)/2 \rceil$ which also satisfies the properties of a metric, since $\lceil a \rceil + \lceil b \rceil \geq \lceil a + b \rceil$.

We need one final result, which generalizes the triangle inequality and was already proven in Appendix A.4.

Lemma 6.10. *Consider two partitions $t_A, t_B \in P_N$ and consider the bi-partite graph G formed from $\#(t_A)$ black vertices and $\#(t_B)$ white vertices joined with $t_A \wedge t_B = \text{id}$ edges for each block in t_A and t_B that intersect. If G is a cycle graph then:*

$$d(t_A, q) + d(q, t_B) \geq d(t_A, t_B) + 2(1 - \delta_{\#_1(q), 0}) \quad (6.85)$$

¹³Since $s(P_{2n})$ is not closed under \vee .

for any $q \in P_N$.

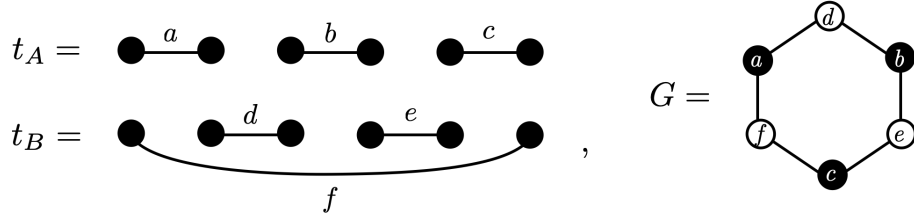


Figure 6.5: Two partitions $t_A, t_B \in P_N$ with $t_A \wedge t_B = \text{id}$ and the bi-partite graph G constructed from the subsets (labeled $\{a, b, \dots, f\}$) of t_A and t_B .

Proof. An example graph is shown in Fig. (6.5). Blocks in t_A can be found by combining the edges that intersect a fixed black vertex. From this figure it is clear that t_A and t_B are made of doublets. Because it has a single cycle t_A and t_B fail to be a modular pair¹⁴ by 1:

$$d(t_A, \text{id}) + d(t_B, \text{id}) - d(t_A, t_B) = 2(\#(t_A \vee t_B) + \#(t_A \wedge t_B) - \#(t_A) - \#(t_B)) = 2, \quad (6.86)$$

since $\#(t_A \vee t_B) = 1$. A modular pair (t'_A, t_B) is associated to a tree graph (c.f. Lemma A.4), and so any unit u_k will break a single edge $t'_A = t_A \wedge u_k$ of the cycle and produce a tree with:

$$d(t'_A, \text{id}) + d(t_B, \text{id}) - d(t'_A, t_B) = 2(\#(t'_A \vee t_B) + \#(t'_A \wedge t_B) - \#(t'_A) - \#(t_B)) = 0, \quad (6.87)$$

where we used the fact that $t'_A \wedge t_B = u_k \wedge \text{id} = \text{id}$. Thus if $q = q \wedge u_k$ then:

$$\begin{aligned} d(t_A, q) + d(t_B, q) &= d(t'_A, q) + d(t_B, q) \geq d(t'_A, t_B) = d(t'_A, \text{id}) + d(t_B, \text{id}) \\ &= d(t_A, \text{id}) + d(t_B, \text{id}) = d(t_A, t_B) + 2 \end{aligned} \quad (6.88)$$

Since this is true for any u_k it is true if $\#_1(q) \neq 0$ as required. \square

Remark. We will apply this Lemma to $t_A = q_A$ and $t_B = q_B$ where these partitions satisfy the required properties. While the above example only slightly generalizes the case of interest, it points towards the basic structure that makes our results work. In particular note that $\#_1(\text{id}) \neq 0$ and indeed the bound for $q = \text{id}$, Eq. (6.85), is saturated in this case. So the bounds we derive (here for partitions) are tight, which is important for the possibility of forming a collapsing chain in Theorem 6.4. It is also important that the pair (t_A, t_B) does not form a tree (they are not a modular pair) since otherwise we would not get minimal triway cuts – we would simply get minimal cuts.

6.4 Proof of the main theorem

In this section we establish our proof for the main results (Theorem 6.4 and Theorem 6.5) of this chapter. First, in Sec. (6.4.1) we show that the permutation group optimization problem R (Definition 6.2) can be coarse grained into a set partition optimization problem Q (Definition 6.3). Next, in Sec. (6.4.2) we bound Q by a mixed Boolean-integer program B (Definition 6.4), and then an integer program I (Definition 6.5). We these results at hand, we relate the value of I to multiway cuts in Sec. (6.4.3), thus proving the collapsing

¹⁴A modular pair saturates the semimodularity condition.

chain $R - \mathcal{A}(AB : C) \geq Q \geq B \geq I \geq \mathcal{A}(A : B : C)$ as required by Theorem 6.4. We prove the uniqueness of the solution in Sec. (6.4.4). Note that this section only establishes our results on even integer $m > 2$. We will deal with the problem of analytically continuing $m \rightarrow 1$ in Sec. (6.5).

6.4.1 From permutations to partitions

We seek:

$$R = \min_g R(g), \quad R(g) = \sum_{e=\{x,y\} \in E} w(e)d(g(x), g(y)) \quad (6.89)$$

Consider a minimal cut $r_{AB} \subset V$ associated to the division $AB : C$. Define $C' = \{x \in r_{AB}^c : \{x, y\} \in \mu(r_{AB})\}$ to be the vertices in r_{AB}^c that border r_{AB} . Define a new amputated graph $G' = (V', E') = (r_{AB} \cup C', E_G[r_{AB}])$. We can estimate R using a new model, written in terms of the coarse grained $q_X(g)$ with respect to element X , on this new graph:

Lemma 6.11. *We have the following estimate:*

$$R(g) \geq \mathcal{A}(AB : C)d(X, \text{id}) + Q'(q), \quad (6.90)$$

where $q : V' \rightarrow P_{2n}$ defined via $q(v) \equiv q_X(g(v))$ and where:

$$Q'(q) = \sum_{e=\{x,y\} \in E'} w(e)d(q(x), q(y)). \quad (6.91)$$

Remark. Minimizing over g gives $R \geq \mathcal{A}(r_{AB})d(X, \text{id}) + Q'$ with $Q' \equiv \min_q Q'(q)$, where the boundary conditions on q for this later model is such that vertices in $A(B)$ have a fixed permutation $q = q_A(q_B)$ and the permutations on C' are fixed as $q = \text{id}$. To pass from the program Q' (on the amputated graph G') to the program Q (on the original graph G), as required in Definition 6.3 and Theorem 6.4, we simply need to show that $Q' \geq Q$. This is proven in Lemma 6.12 after the proof of Lemma 6.11.

Proof. Given the minimal cut r_{AB} we can consider an optimal solution to the linear program $c(L)$ in Eq. (6.39) for edge-disjoint paths:

$$\mathcal{A}(r_{AB}) = \sum_{L \in \hat{\mathcal{P}}_{AB,C}} c(L), \quad (6.92)$$

where for all $e \in E$ then $w(e) \geq \sum_L c(L)\mathbf{1}_L(e)$. Consider a single such path $L \in \mathcal{P}_{AB,C}$. Such a path must pass through the minimal cut $\mu(r_{AB})$ at least one time. Denote the vertex ν to be the first vertex along L that connects r_{AB} to C' . That is for the first edge e in $L \cap \mu(r_{AB})$ we have $e = \{\nu', \nu\}$ where $\nu' \in C'$. Since C' lies on the minimal cut, this is guaranteed to exist, see Fig. (6.6). We split up $L = L_{AB} \sqcup L_C$ into two connecting paths at the common vertex ν , where $L_{AB} \in \hat{\mathcal{P}}_{AB,\nu}$ and $L_C \in \hat{\mathcal{P}}_{\nu,C}$. We estimate the contribution of L to be:

$$\sum_{e=\{x,y\} \in L} d(g(x), g(y)) = \sum_{e=\{x,y\} \in L_C} d(g(x), g(y)) + \sum_{e=\{x,y\} \in L_{AB}} d(g(x), g(y)) \quad (6.93)$$

$$\geq d(g(\nu), \text{id}) + \sum_{e=\{x,y\} \in L_{AB}} d(P(g(x)), P(g(y))) \quad (6.94)$$

To arrive at Eq. (6.94) we have used Eq. (6.62) for the part of the path that intersects r_{AB} and then repeated

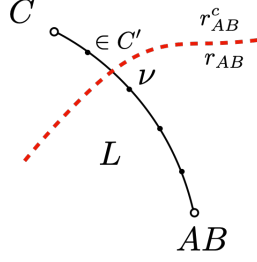


Figure 6.6: We split up a path $L \in \widehat{P}_{AB,C}$ at the cut surface $\mu(r_{AB})$, through a vertex $\nu \in r_{AB}$ that lies immediately inside r_{AB} .

uses of the (Cayley distance) triangle inequality in the complement.

We can re-arrange the sum:

$$\sum_{e=\{x,y\} \in L_{AB}} d(P(g(x)), P(g(y))) = \#(g_{A,B}) - 2\#(g_{A,B} \vee g(x_2)) + \#(g(\nu)) \quad (6.95)$$

$$+ \sum_{\alpha=2}^{|L_{AB}|} 2(\#(g(x_\alpha)) - \#(g(x_\alpha) \vee g(x_{\alpha+1}))), \quad (6.96)$$

where x_α is the sequence of vertices that connects the path L . With $x_1 \in AB$ and $x_{|L_{AB}|+1} = \nu$. Note that if there are no edges in L_{AB} then the sum Eq. (6.96) does not contribute. Now use the bound Eq. (6.61) along with the equality $\#(g_{A,B}) = \#(q_X(g_{A,B}))$ and $\#(g \vee g_{A,B}) = \#(q_X(g) \vee q_X(g_{A,B}))$, we turn all g 's in the sum of Eq. (6.96) into $q_X(g)$'s plus the remainder $\#(g(\nu)) - \#(q_X(g(\nu)))$. That is:

$$\sum_{e=\{x,y\} \in L_{AB}} d(P(g(x)), P(g(y))) \geq \#(g(\nu)) - \#(q(\nu)) + \sum_{e=\{x,y\} \in L_{AB}} d(q(x), q(y)) \quad (6.97)$$

(recall that $q_X(g(x)) \equiv q(x)$). Hence we have the following estimate:

$$\sum_{e=\{x,y\} \in L} d(g(x), g(y)) \geq d(\text{id}, X) + d(\text{id}, q(\nu)) + \sum_{e=\{x,y\} \in L_{AB}} d(q(x), q(y)), \quad (6.98)$$

where we have used the identity

$$d(\text{id}, g(\nu)) + \#(g(\nu)) - \#(q(\nu)) = nm - \#(q(\nu)) = d(\text{id}, X) + d(\text{id}, q(\nu)). \quad (6.99)$$

Now write:

$$R(g) = \sum_{e=\{x,y\}} \left(w(e) - \sum_L c(L) \mathbf{1}_L(e) \right) d(g(x), g(y)) + \sum_L c(L) \sum_{e=\{x,y\} \in L} d(g(x), g(y)) \quad (6.100)$$

$$\geq \sum_{e=\{x,y\} \subset r_{AB}} \left(w(e) - \sum_L c(L) \mathbf{1}_L(e) \right) d(q(x), q(y)) + \sum_L c(L) \left(d(\text{id}, X) + d(\text{id}, q(\nu)) + \sum_{e=\{x,y\} \in L_{AB}} d(q(x), q(y)) \right), \quad (6.101)$$

where we applied Eq. (6.98) to all paths weighted by $c(L)$ in the last term of Eq. (6.100), along with Eq. (6.62)

in the first term of Eq. (6.100) on the edges that are entirely inside r_{AB} and finally dropping all other edges in r_{AB}^c (note that the bracketed term in the first part of Eq. (6.100) is positive by feasibility of $c(L)$). Using:

$$\sum_L c(L)d(\text{id}, X) = \mathcal{A}(AB : C)d(\text{id}, X) \quad (6.102)$$

we arrive at Eq. (6.90). \square

Remark. We will make use of the saturation conditions for the inequality (6.90) in our proofs for uniqueness of the solution. It is useful to record them here for reference later. For edges e in r_{AB}^c the saturation of Eq. (6.100) requires:

$$\sum_{e=\{x,y\} \in r_{AB}^c} \left(w(e) - \sum_L c(L)\mathbf{1}_L(e) \right) d(g(x), g(y)) = 0. \quad (6.103)$$

We also have, from Eq. (6.94),

$$\sum_{e=\{x,y\} \in L_C} d(g(x), g(y)) = d(g(v), \text{id}), \quad (6.104)$$

where $L_C \in \mathcal{P}_{v,C}$ is a subpath of $L \in \mathcal{P}_{AB,C}$ with $c(L) > 0$. L_C connects a vertex v immediately inside r_{AB} to C . For the edges e in r_{AB} , saturation of Eq. (6.100) requires $\sum_{e \in r_{AB}} (w(e) - \sum_L c(L)\mathbf{1}_L(e)) d(g(x), g(y)) = \sum_{e \in r_{AB}} (w(e) - \sum_L c(L)\mathbf{1}_L(e)) d(q(x), q(y))$. Since $d(g(x), g(y)) \geq d(q(x), q(y)) \geq 0$ by Eq. (6.62), this condition holds locally, i.e.

$$d(g(x), g(y)) = d(q(x), q(y)) \quad (6.105)$$

for all edges $e = \{x, y\}$ where $w(e) - \sum_L c(L)\mathbf{1}_L(e) > 0$. If the minimal cut r_{AB} is unique then it holds for all e strictly inside r_{AB} .

Lemma 6.12. *Consider the program*

$$Q = \min_q Q(q), \quad (6.106)$$

on the original graph G , where we minimize over all $q : V \rightarrow P_{2n}$ with $q(A) = q_A, q(B) = q_B$ and $q_C = \text{id}$. Then we have

$$R \geq \mathcal{A}(AB : C)d(X, \text{id}) + Q. \quad (6.107)$$

Proof. Consider the program $Q' = \min_q Q'(q)$, as defined in Lemma 6.11 and Remark that follows immediately after. Let q' be an optimal solution to this problem. We construct from q' a feasible solution $q : V \rightarrow P_{2n}$ to the Q problem by

$$q(v) = \begin{cases} q'(v), & v \in V' \\ \text{id}, & v \in V \setminus V' \end{cases}. \quad (6.108)$$

It is clear that q satisfies all the boundary conditions and $Q(q) = Q'(q')$, since setting $q(v) = \text{id}$ on the new vertices does not increase the free energy. Minimizing over all $q : V \rightarrow P_{2n}$ we have $Q' > Q$. Then from Remark that follows immediately after Lemma 6.11 we have $R \geq \mathcal{A}(AB : C)d(X, \text{id}) + Q' \geq \mathcal{A}(AB : C)d(X, \text{id}) + Q$. \square

6.4.2 From partitions to integer program

In this section we move from partitions q , to Boolean variables b , to an integer program.

Lemma 6.13. *For all paths $L \in \mathcal{P}_{A,B}$ (not necessarily edge disjoint) we have the estimate:*

$$\sum_{e=\{x,y\} \in L} d(q(x), q(y)) \geq 2(n - \delta_{b_L, b_{AB}}), \quad \sum_{e=\{x,y\} \in L} d(q(x), q(y)) \in 2\mathbb{Z}, \quad (6.109)$$

where $b_{AB} = 11 \cdots 1 \in B_{2n}$ and

$$b_L = \bigwedge_{x \in V[L]} b(x), \quad (6.110)$$

and where $b : V \rightarrow B_{2n}$ is defined via $b(v)^k = b^k(q(v))$.

Proof. If $b_L = b_{AB}$ then we must have $b(x) = b_{AB} = 11 \cdots 1$ for the entire path, so that $\#_1(q(x)) = 0$ for all $x \in L$ (since singlets are preserved through the meet operation). We use the triangle inequality repeatedly to show:

$$\sum_{e=\{x,y\} \in L} d(q(x), q(y)) \geq d(q_A, q_B) = 2(n-1) \quad (6.111)$$

Conversely, if $b_L \neq b_{AB}$ then there must be some $x \in V$ along the path such that $\#_1(q(x)) \neq 0$. We apply the triangle inequality about this point:

$$\sum_{e=\{x,y\} \in L} d(q(x), q(y)) \geq d(q_A, q(x)) + d(q(x), q_B) \geq 2n \quad (6.112)$$

where we used the improved triangle inequality derived in Lemma 6.10, and which applies when $q(x)$ has a singlet somewhere.

More generally the deficit in the triangle inequality is always an even integer:

$$d(q_1, q_2) + d(q_2, q_3) - d(q_1, q_3) = 2(\#(q_2 \vee q_3) + \#(q_2) - \#(q_1 \vee q_2) - \#(q_2 \vee q_3)) \quad (6.113)$$

Thus the difference in the left and right hand side of the inequality in Eq. (6.109) must be an even integer. \square

We have the estimate in terms of an integer program:

Lemma 6.14. *Given some fixed $b : V \rightarrow B_{2n}$, define the integer program:*

$$\begin{aligned} B(b) &\equiv \min_r \sum_{e \in E} w(e)r(e) \\ &\text{subject to } \forall L \in \mathcal{P}_{A,B} : \sum_{e \in L} r(e) = 2(n - \delta_{b_L, b_{AB}}) + 2\mathbb{Z}_{\geq 0} \\ &\text{and } \forall e = \{x, y\} \in E : r(e) \geq \left\lceil \frac{1}{2}d(b(x), b(y)) \right\rceil \end{aligned} \quad (6.114)$$

where $r \in \mathbb{Z}_{\geq 0}$. Then for any $q : V \rightarrow P_{2n}$ satisfying the boundary condition $q(A) = q_A$, $q(B) = q_B$ and $q(C) = \text{id}$, we have the bound $Q(q) \geq B(b^k(q))$.

Proof. We simply consider $r(e) = d(q(x), q(y))$ for $e = \{x, y\}$. We use the bounds in Lemma 6.13 and Corollary 6.9 to check feasibility for the $B(b)$ problem. \square

Corollary 6.15. *Consider the program:*

$$B \equiv \min_b B(b), \quad (6.115)$$

where we now minimize over all $b : V \rightarrow B_{2n}$ with $b(A) = b(B) = b_{AB} = 11 \dots 1$ and $b(C) = 00 \dots 0$. Then we have $Q \geq B$.

Proof. Consider an optimal solution q to program Q . Then from Lemma 6.14 it is clear that $B(b^k(q)) \leq Q(q)$ is feasible. Minimizing over all b then gives $Q \geq B$. \square

We will now introduce an edge variable $\rho(e) = \lceil \frac{1}{2}d(b(x), b(y)) \rceil$ for $e = \{x, y\}$. We note that we can write:

$$\delta_{b_L, b_{AB}} = \delta_{\rho(L), 0}, \quad (6.116)$$

where we recall the shorthand notation $\rho(L) \equiv \sum_{e \in L} \rho(e)$. Thus we have the new integer program:

Lemma 6.16. *For integer $n \geq 2$, consider the integer non-linear program:*

$$\begin{aligned} I = \min_{\rho, \sigma} \sum_{e \in E} w(e)(\sigma(e) + \rho(e)) \\ \text{subject to } \forall L \in \mathcal{P}_{A,B} : \sum_{e \in L} (\sigma(e) + \rho(e)) \in 2(n - \delta_{\rho(L), 0}) + 2\mathbb{Z}_{\geq 0} \\ \text{and } \forall L \in \mathcal{P}_{AB,C} : \sum_{e \in L} \rho(e) \geq n \end{aligned} \quad (6.117)$$

for $\rho, \sigma \in \mathbb{Z}_{\geq 0}$. Then $\min_q Q(q) \geq \min_b B(b) \geq I$.

Proof. Again we just have to check feasibility with $\rho(e) = \lceil \frac{1}{2}d(b(x), b(y)) \rceil$ and $\sigma(e) = r(e) - \rho(e) \geq 0$, which again follows from Lemma 6.13, Lemma 6.7 and Eq. (6.116). We also need repeated use of the triangle inequality for the metric $\lceil \frac{1}{2}d(b_1, b_2) \rceil$:

$$\sum_{e \in L} \rho(e) \geq \left\lceil \frac{1}{2}d(b_{AB}, b_C) \right\rceil = n \quad (6.118)$$

for all $L \in \mathcal{P}_{AB,C}$. \square

Remark. In passing from the Boolean program B to the integer program I , we have split the integer variable $r(e)$ into two variables $\rho(e)$ and $\sigma(e)$. In particular, the region associated to $\rho = 0$ plays a special role in the program, as the constraint on a path is weaker if it stays entirely within the said region. It turns out that this region corresponds to the ‘‘squeezed entanglement wedge’’ (backreacted EW accommodating the non-zero tension $t_{A:B}$) in the solution to the reflected entropy optimization problem. The σ variable can be set to be non-zero only inside the $\rho = 0$ wedge, which sources a total of $2(n - 1)$ cuts separating A and B . We will see that these cut surfaces collapse to a single domain wall corresponding to the (squeezed) EW cross-section for an optimal solution.

6.4.3 From integer program to multiway cuts

The main theorem we would like to prove here is that the program Eq. (6.117) is equivalent to a multiway cut problem:

Theorem 6.17. *The minimum of the non-linear integer program Eq. (6.117) is achieved by an optimal solution to the multiway cut problem for $A : B : C$ with $t_{A:B} = 2(n-1)$ and $t_{A:C} = t_{B:C} = n$.*

We do this in two steps. In the first step we prove the existence of a subgraph $G' = (V', E')$ with $A, B \subset V'$ such that either (i) A and B are disconnected on V' and there is an optimal solution to Eq. (6.117) where $\rho(e) = \sigma(e) = 0$ for all $e \in V'$ or (ii) A and B are connected and there is an optimal solution (ρ, σ) to Eq. (6.117) where $\rho(e) = 0$ and σ can be described as a set of $2(n-1)$ cuts separating A, B for all $e \in V'$. These solutions then seed a multiboundary/intersecting cut problem in the remaining graph made from the remaining edges: $E^c = E \setminus E'$ and vertices $V^c \equiv (V \setminus V') \cup (AB)'$ where $(AB)' = \{x \in V' : x \in V_G[\mu(V')]\}$ are the vertices in G' that lie on the cut surface $\mu(V')$. Both cases (i) and (ii) will be treated together, using a vertex valued variable $k(x)$ instead of an edge variable. In the second step we solve this multiboundary cut problem.

More explicitly, the first step is the following Lemma:

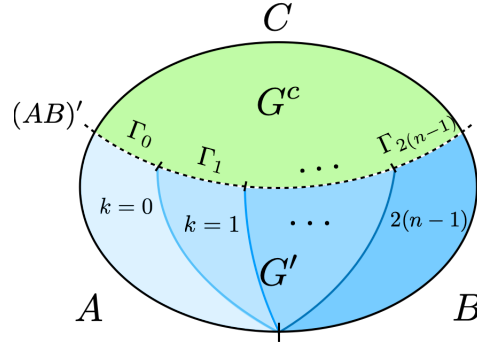


Figure 6.7: The original graph G is split into two subgraphs G' and G^c that share common vertices $(AB)'$ (dashed line). On G' we define a vertex variable k associated to σ , whose value on $(AB)'$ seeds an ℓ -intersecting cut problem on the complementary graph G' with boundary vertices Γ_k .

Lemma 6.18. *There exists a subgraph $G' = (V', E')$ of G where $A, B \subset V'$ such that there is an optimal solution (ρ, σ) to Eq. (6.117) where:*

1. *There exists a function $k : V' \rightarrow \mathbb{Z}_{\geq 0}$ with $k(x) \leq 2(n-1)$ such that: for all edges $e \in E'$ we have:*

$$\sigma(e) = |k(x) - k(y)|, \quad \rho(e) = 0, \quad (6.119)$$

where $k(x) = 0$ for $x \in A$ and $k(x) = 2(n-1)$ for $x \in B$.

2. *For the remaining edges we consider the ℓ -intersecting cut problem with $\ell = 2(n-1)$ (defined immediately below) on the complementary reduced subgraph $G^c = (V^c, E^c)$, with boundary vertices $\Gamma_k = \{x \in (AB)' : k(x) = k\}$ and C . Where the optimal minimum M of this later problem bounds:*

$$I \geq M + w(\mu(V')) + \sum_{e=\{x,y\} \in E'} w(e) |k(x) - k(y)| \quad (6.120)$$

See Fig. (6.7) for an exemplary configuration. We prove this in Appendix E.1. Recall the notation, used in Eq. (6.120), $f(E') = \sum_{e \in E'} f(e)$ for some function f on the edges and some subset $E' \subset E$.

Definition 6.8 (ℓ -intersecting cut problem). Given an integer $\ell \geq 1$ and weighted graph $G = (V, E)$ with $\ell + 2$ sets of boundary vertices $\{\Gamma_k; k = 0 \dots \ell\}$ and C , define the following k -intersecting cut problem:

$$\begin{aligned}
M &\equiv \min_{\varrho} M(\varrho) & M(\varrho) &= \sum_{e \in E} w(e) \varrho(e) \\
&\text{subject to} & \forall k, k' = 0, \dots, \ell & \forall L \in \mathcal{P}_{\Gamma_k, \Gamma_{k'}} : \varrho(L) \in |k - k'| + \mathbb{Z}_{\geq 0} \\
&\text{and} & \forall k = 0, \dots, \ell & \forall L \in \mathcal{P}_{\Gamma_k, C} : \varrho(L) \in \ell/2 + \mathbb{Z}_{\geq 0},
\end{aligned} \tag{6.121}$$

where $\varrho(e) \in \mathbb{Z}_{\geq 0}/2$.

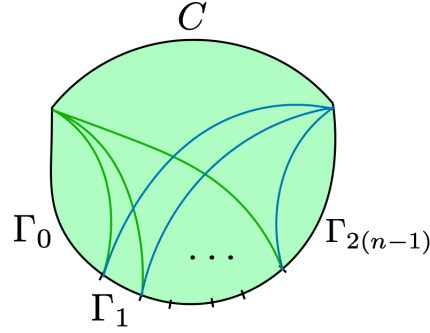


Figure 6.8: The solution to the ℓ -intersecting cut problem as described in Lemma 6.19. The dark green curves represent the cut surfaces of α_k and the dark blue curves represent the cut surfaces of β_k .

We solve this problem recursively in Appendix E.2. The result is:

Lemma 6.19. *The optimal value of the ℓ -intersecting cut problem is:*

$$M = \frac{1}{2} \sum_{k=0}^{\ell-1} (w(\mu(\alpha_k)) + w(\mu(\beta_k))), \tag{6.122}$$

where α_k is a minimal cut for $(\Gamma_0 \cup \dots \cup \Gamma_k) : (\Gamma_{k+1} \cup \dots \cup \Gamma_\ell \cup C)$ and β_k is a minimal cut for $(\Gamma_{k+1} \cup \dots \cup \Gamma_\ell) : (\Gamma_0 \cup \dots \cup \Gamma_k \cup C)$ and $\alpha_k \cap \beta_k = \emptyset$.

See Fig. (6.8) for an example. Given the above two Lemmas we now prove Theorem 6.17.

Proof of Theorem 6.17 and Theorem 6.4. Use the function $k(x)$ in Lemma 6.18 to define bulk regions:

$$\gamma_k = \{x \in V' : k(x) \leq k\} \tag{6.123}$$

for $k = 0, \dots, 2(n-1) - 1$ and such that:

$$\sum_{e=\{x,y\} \in E'} w(e) |k(x) - k(y)| = \sum_{k=0}^{2(n-1)-1} \sum_{e \in \mu_{G'}(\gamma_k)} w(e), \tag{6.124}$$

where $\mu_G(\cdot)$ denotes the edge cut function on some graph $G = \{V, E\}$, that is $\mu_G(r) \equiv E_G[r] \cap E_G[V \setminus r]$ for $r \subset V$.

The region γ_k contains A and shares vertices with α_k constructed from Lemma 6.19 on the subgraph G^c . Similarly $V' \setminus \gamma_k$ contains B and shares vertices with β_k . Thus we can combine them so that $A_k \equiv \gamma_k \cup \alpha_k$

forms a cut for $A : BC$ on the original graph G and $B_k \equiv (V' \setminus \gamma_k) \cup \beta_k$ forms a cut for $B : AC$. These cuts are non-intersecting but share edges in E' that are $\mu_G(\gamma_k)$. In particular:

$$\mu_G(A_k) = \mu_{G'}(\gamma_k) \cup \mu_{G^c}(\alpha_k) \quad (6.125)$$

and similarly for B_k .

We give an explicit proof of Eq. (6.125) for completeness. Recall that $(AB)' = V' \cap V^c$ and $E = E' \sqcup E^c$. We note that $(AB)' \cap \alpha_k = (AB)' \cap \gamma_k$ by the boundary conditions and this implies that $A_k \cap V' = \gamma_k$ and $A_k \cap V^c = \alpha_k$ further implying that $E_{G'}[A_k] = E_{G'}[\gamma_k]$ since all $\{x, y\} \in E'$ satisfy $\{x, y\} \subset V'$. Similarly $E_{G^c}[A_k] = E_{G^c}[\alpha_k]$. Also note that $V \setminus A_k = (V' \setminus \gamma_k) \cup (V^c \setminus \alpha_k)$. Putting this together:

$$\begin{aligned} \mu_G(A_k) &= E_G[A_k] \cap E_G[V \setminus A_k] \\ &= (E_{G'}[A_k] \cap E_{G'}[V \setminus A_k]) \cup (E_{G^c}[A_k] \cap E_{G^c}[V \setminus A_k]) \\ &= (E_{G'}[\gamma_k] \cap E_{G'}[V' \setminus \gamma_k]) \cup (E_{G^c}[\alpha_k] \cap E_{G^c}[V' \setminus \alpha_k]) \end{aligned} \quad (6.126)$$

as required. A similar argument applies to $\mu_G(B_k)$.

Thus we can write the estimate from Lemma 6.18 and using Eq. (6.124) as:

$$\begin{aligned} I &\geq \left(\frac{1}{2} \sum_{k=0}^{2(n-1)-1} w(\mu_G(A_k)) + w_G(\mu(B_k)) \right) + w(\mu_G(V')) \\ &\geq \min_k ((n-1)(w(\mu_G(A_k)) + w(\mu_G(B_k))) + w(\mu_G(V'))). \end{aligned} \quad (6.127)$$

The right hand side can be written as a sum of two triway cuts, with tensions as given in the statement of this theorem. That is:

$$\begin{aligned} I &\geq \min_k \left(\frac{(n-1)}{n} \mathcal{A}(A_k : B_k : (V \setminus (A_k \cup B_k))) + \frac{1}{n} \mathcal{A}(\gamma_k : (V' \setminus \gamma_k) : (V \setminus V')) \right) \\ &\geq \mathcal{A}(A : B : C) \end{aligned} \quad (6.128)$$

Equality follows from the collapsing chain mentioned in Theorem 6.4 that we have also now established. \square

The proofs we give for Lemma 6.18 and Lemma 6.19 are quite lengthy, so we present these in Appendix E.1 and Appendix E.2 respectively.

6.4.4 Uniqueness theorem

In this subsection we give a proof for Theorem 6.5, i.e. the solution to the permutation group optimization problem R (Definition 6.2) is the unique solution given by the triway cut if both the triway cut and the entanglement wedge of the graph are unique. Though this result may seem trivial, it lays the foundation for performing the analytic continuation $m \rightarrow 1$, the main result in Sec. (6.5).

We only consider the case where every connected component of the graph G is path connected to at least one boundary region. The reason is obvious – If such a disconnected region exists then one can always set the permutations on such region to be *any* fixed element on S_{mn} and we have a degeneracy of $|S_{mn}|$. In any case, such disconnected parts of the graph can be factored out of the computation of reflected entropy. We can thus deal with these trivially.

Lemma 6.20. *Let $g : V \rightarrow S_{mn}$ be an optimal solution to the permutation group program R . If the minimal cut r_{AB} for AB is unique, then $g(v) = \text{id}$ for all vertices $v \in r_{AB}^c$.*

Proof. We know from Theorem 6.4 that $R = \mathcal{A}(AB : C)d(\text{id}, X) + Q'$. We also have, from Lemma 6.11 that

$$R(g) \geq \mathcal{A}(AB : C)d(\text{id}, X) + Q'(q_X(g)). \quad (6.129)$$

If g is optimal, this inequality must be saturated since otherwise $Q'(q_X(g))$ has a smaller objective.

Consider an optimal solution $c : \mathcal{P}_{AB:C} \rightarrow \mathbb{R}_{\geq 0}$ to the dual max-flow problem Eq. (6.39). The saturation condition of Eq. (6.129) demands that (see the remark before Lemma 6.12)

$$\sum_{e=\{x,y\} \in L_C} d(g(x), g(y)) = d(g(v), \text{id}). \quad (6.130)$$

where L_C is the subpath of $L \in \mathcal{P}_{AB:C}$ such that $c(L) > 0$ and L_C connects C to the vertex v immediately inside r_{AB} (see Fig. (6.6)). In other words, it states that the elements along the path L_C must be on the group geodesic of id to $g(v)$. Another saturation condition demands that

$$\sum_{e=\{x,y\} \subset r_{AB}^c} \left(w(e) - \sum_{L \in \mathcal{P}_{AB,C}} c(L) \mathbf{1}_L(e) \right) d(g(x), g(y)) = 0. \quad (6.131)$$

where we sum over all the edges outside the entanglement wedge r_{AB} . Since both terms in the sum are semi-positive, for any $e = \{x, y\} \subset r_{AB}^c$ it must be that either

$$w(e) - \sum_{L \in \mathcal{P}_{AB,C}} c(L) \mathbf{1}_L(e) = 0, \quad \text{or} \quad d(g(x), g(y)) = 0. \quad (6.132)$$

Now pick any vertex $v \in r_{AB}^c$. We claim that there must exist a path $L' \in \mathcal{P}_{C,v}$ such that the $d(g(x), g(y)) = 0$ for all adjacent vertices x, y along the path. If this is true, the triangle inequalities along L' then require $d(g(v), \text{id}) = 0$ and thus $g(v) = \text{id}$. This holds true for any $v \in r_{AB}^c$ so we are done.

Suppose by contradiction that such a path does not exist. Define the region r_C to be the set of vertices that can be reached by some path with vanishing Cayley distance from C . It is clear that $g(x) = \text{id}$ for all $x \in r_C$ by a similar argument as above. r_C is a cut for C since any vertex in r_C is path connected to C . Consider now the cut surface $\mu(r_C)$. By definition, for all edges $\{x, y\} \in \mu(r_C)$ we must have $d(g(x), g(y)) > 0$, and thus $w(e) - \sum_L c(L) \mathbf{1}_L(e) = 0$ by Eq. (6.132). We compute

$$\sum_{e \in \mu(r_C)} w(e) = \sum_{L \in \mathcal{P}_{AB:C}} c(L) = \mathcal{A}(AB : C), \quad (6.133)$$

since all paths starting from C to AB must pass through $\mu(r_C)$. Moreover, any such path with $c(L) > 0$ can only intersect $\mu(r_C)$ once, since it cannot re-enter r_C once it has left the cut, as this will violate the geodesic condition Eq. (6.130). Hence $\mu(r_C)$ is a minimal surface and r_C is a minimal cut. It is different from r_{AB}^c since $v \in r_{AB}^c$ and $v \notin r_C$. This is a contradiction because we have assumed that the minimal cut is unique. \square

Lemma 6.21. *Let $q : V \rightarrow P_{2n}$ be an optimal solution to the set partition optimization problem Q on graph*

G with a unique triway cut. Then for any edge $e = \{x, y\} \in E$:

$$d(q(x), q(y)) = (2(n-1)\mathbf{1}_{\mu(r_A:r_B)} + n\mathbf{1}_{\mu(r_B:r_C)} + n\mathbf{1}_{\mu(r_A:r_C)})(e), \quad (6.134)$$

where (r_A, r_B, r_C) is the optimal triway cut for $(A : B : C)$.

Proof. Since q is optimal we know that the chain in Theorem 6.4 collapses, i.e.

$$Q(q) = B(\{b^k(q)\}, r) = I(\rho, \sigma), \quad (6.135)$$

are all optimal, where $r(e) = d(q(x), q(y))$, $\rho(e) = \lceil \frac{1}{2}d(b(x), b(y)) \rceil$ and $\sigma(e) = (r - \rho)(e)$ for $e = \{x, y\} \in E$. Since we have $r(e) = (\rho + \sigma)(e) = d(q(x), q(y))$, it suffices to prove Eq. (6.134) on $\rho + \sigma$ for an optimal solution (ρ, σ) of the integer program I . Now, from Lemma E.3 we know that for any optimal (ρ, σ) one can always construct a new optimal (ρ', σ') with $\rho + \sigma = \rho' + \sigma'$ that satisfies the conditions of Lemma 6.18. Now we write

$$I(\rho, \sigma) = \frac{1}{2} \sum_{k=0}^{2(n-1)-1} (w(\mu(A_k)) + w(\mu(B_k))) + w(\mu(V')) \quad (6.136)$$

$$= \sum_{k=0}^{2(n-1)-1} \left(\frac{n-1}{2n} \mathcal{A}(A_k : B_k : (V \setminus A_k \setminus B_k)) + \frac{1}{2n} \mathcal{A}(\gamma_k : (V' \setminus \gamma) : (V \setminus V')) \right) \quad (6.137)$$

$$= \mathcal{A}(A : B : C) \equiv \mathcal{A}(r_A : r_B : r_C), \quad (6.138)$$

where we have used Lemma 6.19 and replaced the bound by equality since (ρ, σ) is optimal. The cut surfaces A_k, B_k and γ_k are defined as in the proof of Theorem 6.17. Now since $\mathcal{A}(A : B : C)$ is the unique optimal triway cut, both terms in the sum of Eq. (6.137) must be equal to $\mathcal{A}(r_A : r_B : r_C)$ for all k . Hence we have

$$A_k = \gamma_k = r_A, \quad B_k = (V' \setminus \gamma_k) = r_B, \quad (V \setminus A_k \setminus B_k) = (V \setminus V') = r_C, \quad (6.139)$$

which implies that within V' ,

$$\rho'(e) = 0, \quad \sigma'(e) = 2(n-1)\mathbf{1}_{\mu(r_A:r_B)}(e) \quad (6.140)$$

and outside V' ,

$$(\rho' + \sigma')(e) = \mathbf{1}_{\mu(V')}(e) + (n-1)(\mathbf{1}_{\mu(\alpha_k)} + \mathbf{1}_{\mu(\beta_k)})(e) = n(\mathbf{1}_{\mu(r_A:r_C)} + \mathbf{1}_{\mu(r_B:r_C)})(e), \quad (6.141)$$

since any other configuration cannot reproduce an optimal value of M . Combining Eq. (6.140) and Eq. (6.141) together we have proven the Lemma. \square

Corollary 6.22. *Let $q : V \rightarrow P_{2n}$ be an optimal solution to the set partition optimization problem Q on graph G with a unique triway cut. Then for any vertex $v \in V$:*

$$q(v) = \begin{cases} q_A, & v \in r_A \\ q_B, & v \in r_B, \\ \text{id}, & v \in r_C \end{cases} \quad (6.142)$$

where (r_A, r_B, r_C) is the optimal triway cut for $(A : B : C)$.

Proof. Since (r_A, r_B, r_C) is an optimal triway cut, if $v \in r_A$ then it is connected to A by some path L in r_A . The reason is as follows: Suppose that there exists a region $r \subset r_A$ not connected to A . Then r must be connected to at least one of r_B or r_C otherwise r will be a totally disconnected region. Without loss of generality suppose it is B . We can then construct a new triway cut $(r_A \setminus r, r_B \cup r, r_C)$ whose weight is smaller than the original. This is a contradiction since we assumed (r_A, r_B, r_C) is optimal.

From Lemma 6.21 we know that $\sum_{\{x,y\} \in L} d(q(x), q(y)) = 0$ along the path L . Then by repeated use of triangle inequality we can show that $d(q(v), q_A) = 0$ and thus $q(v) = q_A$. Similar arguments also apply to subregion r_B and r_C . \square

We are now ready to complete the proof for our main result of this subsection. To begin with, we restate Theorem 6.5 in terms of the notations used here:

Theorem 6.23. *Let $g : V \rightarrow S_{mn}$ be an optimal solution to the reflected entropy permutation group optimization problem R on graph G with a unique triway cut (r_A, r_B, r_C) and a unique entanglement wedge r_{AB} . Then for any vertex $v \in V$:*

$$g(v) = \begin{cases} g_A, & v \in r_A \\ g_B, & v \in r_B \\ X, & v \in r_{AB} \setminus r_A \setminus r_B \equiv r_X \\ \text{id}, & v \in r_{AB}^c \end{cases} \quad (6.143)$$

Proof of Theorem 6.23 and Theorem 6.5. There are four regions that we need to take care of. It is immediate that the region r_{AB}^c follows trivially from Lemma 6.20. For the other regions: Note that since g is optimal for R , $q_X(g)$ must be optimal for Q , therefore $q_X(g)$ must coincide with Eq. (6.142). Moreover, the saturation conditions requires $d(g(x), g(y)) = d(P(g(x)), P(g(y))) = d(q(x), q(y))$ for all $e = \{x, y\}$ completely within r_{AB} (see the remark before Lemma 6.12).

Let's first consider r_A . There must be a path L completely within r_A such that $d(g(x), g(y)) = d(q(x), q(y)) = 0$ along adjacent vertices $\{x, y\} \in L$ (cf. the proof of Corollary 6.22). Applying triangle inequality along the path we see $d(g(v), g_A) = 0$ which implies $g(v) = g_A$. A similar argument holds for $v \in r_B$.

For the remaining region r_X , We split the contribution of $R(g)$ as

$$R(g) = \sum_{e \in E, e \subset r_{AB}} w(e) d(g(x), g(y)) + \sum_{v \in \partial r_{AB}} w(e) d(g(v), \text{id}), \quad (6.144)$$

where $\partial r_{AB} \equiv V[\mu(r_{AB})] \cap r_{AB}$ are the vertices on the cut surface $\mu(r_{AB})$ and within r_{AB} . We have used the fact that $g(v) = \text{id}$ for $v \in r_{AB}^c$. Since $q_X(g(v)) = \text{id}$ for $v \in r_{AB}$ we have $\#(g \vee X) = \#(g)$, and $P(g(v))$ lies on the geodesic between set partitions $P(X)$ and $P(\text{id})$ on P_{mn} :

$$d(P(X), P(g(v))) + d(P(g(v)), P(\text{id})) = \#(X) - 2\#(X \vee g(v)) + \#(\text{id}) = d(P(X), P(\text{id})) \quad (6.145)$$

We claim that this geodesic condition naturally extends to Cayley distances on S_{mn} . The reasoning is as follows: The region r_X must be path connected to either A or B , since if it is only connected to C then we know such region is subset of r_{AB}^c and thus must be empty. Now consider a connected component r_i of this region. Without loss of generality we may set $g = g_i$ for all $v \in r_i$. Consider an edge $\{x, y\}$ on the common

cut surface of r_A (or r_B respectively) and r_i such that $g(x) = g_i$ and $g(y) = g_{A/B}$. We know that since g is optimal and $x, y \in r_{AB}$,

$$d(g_i, g_{A/B}) = d(P(g_i), P(g_{A/B})) + 2G_{g_{A/B}}(g_i) = d(q_X(g_i), q_{A/B}), \quad (6.146)$$

which implies that the genus $G_{g_{A/B}}(g_i) = 0$. But since $P(g_{A/B}) \geq P(X)$ we have $G_{g_{A/B}}(g_i) \geq G_X(g_i)$ ¹⁵ and thus $G_X(g_i) = 0$. Also $G_{g_i}(\text{id}) = 0$ trivially. Thus $d(P(g_i), P(\text{id})) = d(g_i, \text{id})$ and $d(P(g_i), P(X)) = d(g_i, x)$ and we have

$$\begin{aligned} R(g) &= \sum_{e \in E, e \subset r_{AB}} w(e)d(g(x), g(y)) + \sum_{v \in \mu(r_{AB}) \cap r_{AB}} w(e)(d(X, \text{id}) - d(X, g(v))) \\ &= \sum_{e \in E, e \subset r_{AB}} w(e)d(g(x), g(y)) + \mathcal{A}(AB : C)d(X, \text{id}) - \sum_{v \in \partial r_{AB}} w(e)d(X, g(v)). \end{aligned} \quad (6.147)$$

Now since g is optimal we know $R(g) = Q(q_X(g)) + \mathcal{A}(AB : C)d(X, \text{id})$. Using $d(g(x), g(y)) = d(q(x), q(y))$ within r_{AB} we obtain

$$\sum_{v \in \partial r_{AB}} w(e)d(X, g(v)) = 0 \quad (6.148)$$

and thus $g(v) = X$ for $v \in r_{AB}$ on the cut surface $\mu(r_{AB})$. Since Cayley distance vanishes within r_X we must have $g(v) = X$ within the whole region. This completes our proof. \square

Remark. In general, when using the permutation optimization to determine the moments of the reflected density matrix, one must sum over all the configurations that minimizes the free energy functional, i.e. Eq. (6.12). Physically speaking, what we have proven here is that such minimum is unique as long as one is sufficiently far away from the phase transitions, which is signalled by a degenerate minimal surface. In fact, there are two different kinds of phase transitions in play here – one being the entanglement wedge phase transition, in which the reflected entropy suffers a discontinuous jump; and the other being the EW cross-section phase transition, in which there are two cross-sectional candidates with the same area. In the latter case the change of reflected entropy across the transition is still continuous. Our result here only applies when the system is far away from both kind of transitions.

However, based on various evidences, we conjecture that $S_R^{(n)}$ still converges as stated in Theorem 6.1 for the second kind of the transitions. In this case the multiplicity factor is no longer unity but some integer $d_m^{(n)} > 1$. We conjecture that $d_m^{(n)}$ is *independent* of m in this scenario. Therefore the techniques we will be using for analytic continuation still carries over. The multiplicity factor will introduce a $\ln d^{(n)} \sim O(\chi^0)$ correction to the entropy, which goes away as one takes $\chi \rightarrow \infty$. Our uniqueness assumption on the triway cut problem would then be unnecessary in Theorem 6.1.

6.5 Continuation in m

To finish the proof of Theorem 6.1, we need to “analytically continue” away from integer $m/2$. Since the answer we have for $R(g)$ only depends trivially on m through normalization (it is independent upon correctly normalizing the reflected density matrix), it seems like this task would be simple. For example one might expect a simple application of Carlson’s theorem. Unfortunately applying Carlson’s theorem after taking the

¹⁵This fact follows from the construction of admissible surfaces: Given an admissible surface of g_i based on g_A (or g_B) one can “pinch” the cycles of g_A (resp. g_B) to form cycles of X without destroying any connections. See Appendix A.4 for details.

limit $\chi \rightarrow \infty$ turns out to be rather difficult – a fact that is often not discussed in the AdS/CFT literature. The basic issue is that one does not know if the natural analytic continuation of $\text{Tr}(\sigma_{AA^*}^{(m)})^n$ in m remains an analytic function upon taking the limit $\chi \rightarrow \infty$. Compounding this difficulty is the need to divide the function one wishes to continue by the expected answer - this division is necessary for convergence, but will often introduce non-analytic dependence on m . Indeed it is well known that partition functions do not remain analytic in the thermodynamic limit due to phase transitions and the condensation of zeros. That said, such phase transitions in m are not present here since the expected answer has a simple analytic dependence on m . Even so, it is not obvious how to establish pointwise convergence of the sequence as $\chi \rightarrow \infty$ and this is necessary in order to establish analyticity of the limit.

Thus we follow a different approach here - that of the methods of moments. One immediate difficulty is that the quantity of interest $\text{Tr}(\sigma_{AA^*}^{(m)})^n$ is not obviously a moment for m (it is a moment for n , but here we are fixing n to be an integer.) However we can write it as a moment for some operator spectral measure:

$$\text{Tr}_{AA^*}(\sigma_{AA^*}^{(m)})^n = \langle 1_{AB}^{\otimes n} | \Sigma_A^\dagger \varrho^{m/2} \otimes \varrho^{m/2} \Sigma_A | 1_{AB}^{\otimes n} \rangle, \quad (6.149)$$

where $\varrho = \rho_{AB}^{\otimes n}$ and Σ_A is the usual n -twist operator. Consider the operator:

$$\mathcal{O} = \varrho \otimes \varrho \quad (6.150)$$

and the associated spectral measure E_λ from which we define a new measure $\mu_\Psi(\lambda) = \langle \Psi | E_\lambda | \Psi \rangle$ with $|\Psi\rangle = \Sigma_A | 1_{AB}^{\otimes n} \rangle$. More specifically we can write:

$$\mathcal{O} = \sum_i \lambda_i |v_i\rangle \langle v_i|, \quad (6.151)$$

and the measure for finite χ will have a discrete decomposition:

$$d\mu_\Psi(\lambda) = \sum_i |\langle \Psi | v_i \rangle|^2 \delta(\lambda - \lambda_i) d\lambda \quad (6.152)$$

We recover the quantity of interest:

$$\text{Tr}_{AA^*}(\sigma_{AA^*}^{(m)})^n = \int_0^\infty d\mu_\Psi(\lambda) \lambda^{m/2} \quad (6.153)$$

We have computed the moments for $m/2$ integer away from the phase transition, schematically:

$$\overline{\int_0^\infty d\mu_\Psi(\lambda) \lambda^{m/2}} \xrightarrow{\chi \rightarrow \infty} \chi^{-2(n-1)\mathcal{A}(A:B:C) + n(m-2)\mathcal{A}(AB:C)} \quad (6.154)$$

We have not computed the $m = 0$ moment. This makes the moment problem somewhat more involved since we have less control over the limit of the measure μ_Ψ near $\lambda = 0$. We will need to give an alternative estimate in this limit. We will show that, schematically:

$$\overline{\int_0^\infty d\mu_\Psi(\lambda) \lambda^{1/2} F(\lambda \chi^{2n\mathcal{A}(AB:C)})} \ll \overline{\int_0^\infty d\mu_\Psi(\lambda) \lambda^{1/2}} \quad (6.155)$$

for large χ and for a class of functions, specified in more detail later, which vanishes for $F(x) = 0 : x \geq 1$. This result follows from a weak form of measure concentration for general random tensor networks that works

as long as the entanglement wedge is appropriately unique:

Definition 6.9 (Unique entanglement wedge). Given a random tensor network with boundary $\partial = AB \sqcup C$ then the entanglement wedge r_{AB} is called *unique* if for any other $AB : C$ cut $r \neq r_{AB}$:

$$\mathcal{A}(AB : C) \leq \mathcal{A}(r : r^c) - g \quad (6.156)$$

for some non-zero gap $g > 0$.

Lemma 6.24 (Weak measure concentration). *1. Consider a density matrix ρ on a finite dimensional Hilbert space \mathcal{H} and supported on π_ρ with $\text{Tr}\pi_\rho \equiv \Lambda$ then for a real function $f \in C^\infty(\mathbb{R})$ such that $f(x) = 0$ for all $x \geq 0$ and such that f' is a rapidly decaying Schwartz function $f' \in \mathcal{S}(\mathbb{R})$, then:*

$$|\langle \eta_1 | f(\ln \rho + \ln \Lambda) | \eta_2 \rangle| \leq \|\mathfrak{F}(f')\|_{L^1} \|\rho - \pi_\rho / \Lambda\|_1, \quad (6.157)$$

with normalized $\eta_{1,2} \in \mathcal{H}$ and where \mathfrak{F} denotes the Fourier transform.

2. Consider a random tensor network state with boundary $\partial = AB \sqcup C$ and with a unique entanglement wedge for AB , then:

$$\overline{\|\rho_A - \pi_{\rho_{AB}} / \chi^{\mathcal{A}(AB:C)}\|_1} = \mathcal{O}(\chi^{-g/2}) \quad (6.158)$$

Remark. This might be called weak for two reasons. Firstly we are estimating matrix elements, and weak continuity of operators pertains to such matrix elements. However since the operators do not live in the same Hilbert space for different χ it is not exactly clear what you would call weak continuity. Secondly it is a much weaker bound than the standard measure concentration where the probability of finding a minimum non-zero eigenvalue away from the peak is exponentially small in $\chi^\#$. Such measure concentration results were proven for a single random tensor - multiple random tensors seem much harder to work with, hence we have not succeeded in deriving the much stronger result. This weaker result is however sufficient for our purposes.

Proof. (2) We start with a computation of the projected trace distance on the subspace $\pi_{\rho_{AB}} \mathcal{H}_{AB}$ where $\text{Tr}\pi_{\rho_{AB}} \leq \chi^{\mathcal{A}(AB)}$ for any tensor network state. Then from Hölder's inequality we have:

$$\begin{aligned} \left\| \rho_{AB} - \pi_{\rho_{AB}} / \chi^{\mathcal{A}(AB)} \right\|_1^2 &\leq \chi^{\mathcal{A}(AB)} \|\rho_{AB} - \pi_{\rho_{AB}} / \chi^{\mathcal{A}(AB)}\|_2^2 = \chi^{\mathcal{A}(AB)} \text{Tr}(\rho_{AB} - \pi_{\rho_{AB}} / \chi^{\mathcal{A}(AB)})^2 \\ &= \chi^{\mathcal{A}(AB)} \left(\text{Tr}\rho_{AB}^2 - 2/\chi^{\mathcal{A}(AB)} + \text{Tr}\pi_{\rho_{AB}} / \chi^{2\mathcal{A}(AB)} \right) \\ &\leq \chi^{\mathcal{A}(AB)} \text{Tr}\rho_{AB}^2 - 1. \end{aligned} \quad (6.159)$$

Averaging gives the required estimate:

$$\chi^{\mathcal{A}(AB)} \overline{\text{Tr}\rho_{AB}^2} - 1 = \mathcal{O}(\chi^{-g}) \quad (6.160)$$

by explicit computation of the replica statistical mechanics model, and application of the gap condition in Definition 6.9.

(1) Since ρ will have a minimum non-zero eigenvalue λ_{\min} we can cut off $f_a = f \circ w_a$ where $w_a \in C^\infty$ is a smooth cutoff function:

$$w_a(x) = w(x/a), \quad (6.161)$$

with $w(x) = 0$ for $x < -2$ and $w(x) = 1$ for $x > -1$ and generally $0 \leq w \leq 1$ and also $w' \in \mathcal{S}$. Choosing $a > -\ln \lambda_{\min} - \ln \Lambda \geq 0$ we can replace f with f_a . The result f_a is a smooth function of compact support so this has a Fourier transform. Thus:

$$f_a(\ln \rho + \ln \Lambda) = \int ds \mathfrak{F}(f_a)(s) \Lambda^{is} \rho^{is} \quad (6.162)$$

If ρ and ρ' commute then we can simultaneously diagonalize these and

$$|\langle \eta_1 | (\rho^{is} - (\rho')^{is}) | \eta_2 \rangle| = \left| \sum_i (\exp(-isE_i) - \exp(-isE'_i)) \langle \eta_1 | i \rangle \langle i | \eta_2 \rangle \right| \quad (6.163)$$

$$\leq \sum_i |1 - \exp(-is(E'_i - E_i))| \leq |s| \|\rho - \rho'\|_1, \quad (6.164)$$

where $E_i \equiv -\ln \lambda_i$, and the inequality follows from the bound $|\sin(x)| < |x|$. Thus:

$$|\langle \eta_1 | f(\ln \rho + \ln \Lambda) | \eta_2 \rangle - \langle \eta_1 | f(\ln \rho' + \ln \Lambda) | \eta_2 \rangle| \leq \|s \mathfrak{F}(f_a)(s)\|_{L_1} \|\rho - \rho'\|_1 \quad (6.165)$$

In Appendix E.4 we prove that we can remove the cutoff function w_a :

$$\lim_{a \rightarrow \infty} \|s \mathfrak{F}(f_a)(s)\|_{L_1} = \|\mathfrak{F}(f')(s)\|_{L_1} \quad (6.166)$$

for functions f and w that were specified in the statement and above. If we set $\rho' = \pi_\rho / \Lambda$ and use the properties of the function in the statement we find $f(\ln \rho' + \ln \Lambda) = 0$ away from the subspace of support of ρ . \square

To proceed, we define a specific form of convergence in probabilities as follows. We say that:

$$\alpha_\chi \xrightarrow{\text{Pr}} c \quad (6.167)$$

if for all ϵ :

$$\lim_{\chi \rightarrow \infty} \text{Pr}(|\alpha_\chi - c| \geq \epsilon) = 0, \quad (6.168)$$

where α_χ is a sequence of real valued random variables (on different probability spaces equipped with the Haar measure with dimension determined by χ) and c is simply a constant. We now state our main result of this section:

Lemma 6.25. *For integer n :*

$$S_R^{(n)}(A : B) - \ln \chi \left(\frac{1}{n-1} \mathcal{A}_t(A : B : C) - \frac{n}{n-1} \mathcal{A}(AB : C) \right) \xrightarrow{\text{Pr}} 0 \quad (6.169)$$

as $\chi \rightarrow \infty$.

The proof we give for Lemma 6.25 is rather lengthy and technical so we present it in Appendix E.3. We now use the above result to prove Theorem 6.1.

Proof of Theorem 6.1. The only thing remaining is to move from convergence in probability to convergence

in mean after dividing by $\ln \chi$. Certainly:

$$\frac{S_R^{(n)}(A : B)}{\ln \chi} - \left(\frac{1}{n-1} \mathcal{A}_t(A : B : C) - \frac{n}{n-1} \mathcal{A}(AB : C) \right) \xrightarrow{\text{Pr}} 0 \quad (6.170)$$

as $\chi \rightarrow \infty$, follows from Lemma 6.25. We now show that $\frac{S_R^{(n)}(A:B)}{\ln \chi}$ is a uniformly bounded random variable. We use monotonicity, established in Ref. [56] for integer $n \geq 2$:

$$S_R^{(n)}(A : B) = S_n(AA^*)_{\rho_{AB}^{1/2}} \leq S_n(AA^*)_{\rho_{ABC}^{1/2}} = S_R^{(n)}(A : BC) = 2S_n(A) \quad (6.171)$$

Using the Swingle bound gives:

$$\frac{S_R^{(n)}(A : B)}{\ln \chi} \leq 2\mathcal{A}(AB : C) \quad (6.172)$$

Both of these bounds apply to all instances of the ensemble. Convergence in probability for a bounded random variable, implies convergence in mean and so we are done. \square

6.6 Hyperbolic RTNs

So far in this chapter our focus has been on establishing general theorems for reflected entropy on arbitrary RTNs. In this section we make connection to holography by restricting our focus on RTNs defined on hyperbolic graphs motivated from AdS/CFT. We will revisit our initial the tensor network calculation for reflected entropy in Sec. (2.5) and see how the naive saddles gets modified to give a consistent picture. We focus on a regime away from the phase transition and does not investigate the phase transition itself.

To begin our discussion, recall that in Sec. (2.5) we identified two possible bulk solutions (Fig. (2.6)). We now understand that such picture is not correct and one must allow the possible appearance of new bulk regions associated to element X determined by the minimal triway cut. In continuum spaces, the minimal multiway cut problem naturally translates to the problem of finding a bulk partition whose surface area is minimized. For the equal tension case ($n = 2$ in our setup), this problem is a long studied problem in geometric measure theory with the conjectured solution termed the “double bubble”:

Conjecture 6.26 (Double bubble). *The least area connected partition of a manifold M into any number of regions consists of the union of minimal surfaces whose intersections in M are trivalent and equiangular.*

This conjecture has been proven for \mathbb{R}^3 [177] and the hyperbolic disk \mathbb{H}^2 [178] and is conjectured to hold true for all dimensions [179]. The case of weighted area was proven by Ref. [180]. With this in mind, we categorize different possible phases by the inclusion of an X -region. We consider four such possible saddles. We do not prove that these are the only saddles possible. However minimal multiway cut problem seems to We will simply assume this to be the case for now. The resulting physics we get from this assumption passes many tests, and so we strongly suspect these phases dominate in at least some finite window of parameter space.

Working with a connected entanglement wedge, with conformal cross ratio $x < 1/2$, we now show possible minimal solutions to the hyperbolic network model and list their normalized free energies. More specifically the (m, n) -Rényi Reflected entropies are $\ln \chi \times f$ for some minimal f . The candidate f 's arising from the phases in Fig. (6.9) are:

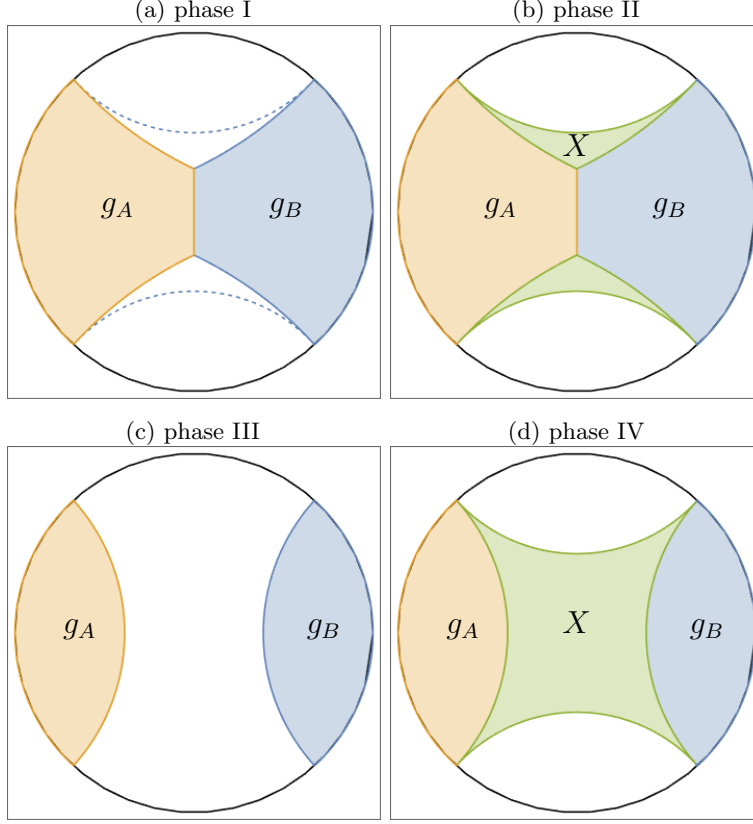


Figure 6.9: Different phases that can dominate in the reflected entropy bulk configuration.

- phase I

$$f_{\text{I}} = 4(n-1) \ln \frac{1 + \sqrt{1-x}}{\sqrt{x}} + 4n(m-1) (H(p_+, p_-) - \ln 2), \quad (6.173)$$

where $p_{\pm} = 1/2 \left(1 \pm \frac{(n-1)}{n(m-1)}\right)$ and $H(p_+, p_-) = -p_+ \ln p_+ - p_- \ln p_-$ is the Shannon entropy.

- phase II

$$f_{\text{II}} = 4(n-1) \ln \frac{1 + \sqrt{1-x}}{\sqrt{x}} + 4n \left(H \left(1 - \frac{1}{2n}, \frac{1}{2n} \right) - \ln 2 \right) \quad (6.174)$$

- phase III ¹⁶

$$f_{\text{III}} = 2n(m-1) \ln \frac{1-x}{x} \quad (6.175)$$

- phase IV

$$f_{\text{IV}} = 2n \ln \frac{1-x}{x} \quad (6.176)$$

Note that x is the conformal cross-ratio for end points of the intervals on the boundary, such that $0 \leq x \leq 1$ and $x \rightarrow 0$ gives the phase with a connected entanglement wedge. We have assumed that we can approximate the network geodesics by a continuum geometry where there is a conformal symmetry, this is a crude approximation that is sufficient for our purposes.

¹⁶For $x > 1/2$ we are always in the disconnected phase corresponding to phase III. The free energy for $x > 1/2$ differs by an amount $2n(m-1) \ln((1-x)/x)$ compared to that shown here, due to the phase transition in the normalization of the reflected Rényi entropies.

We now analytically continue in (n, m) . Our first approach is naive and will fail for $1 < m < 2$. We simply analytically continue the expressions in Eq. (6.173-6.176), and then compare all four free energies at each point in parameter space. For example, we plot the resulting phase diagram in the (m, n) plane for several different values of x in Figure 6.10. As we can see there is always a transition line at $m = 2$, and

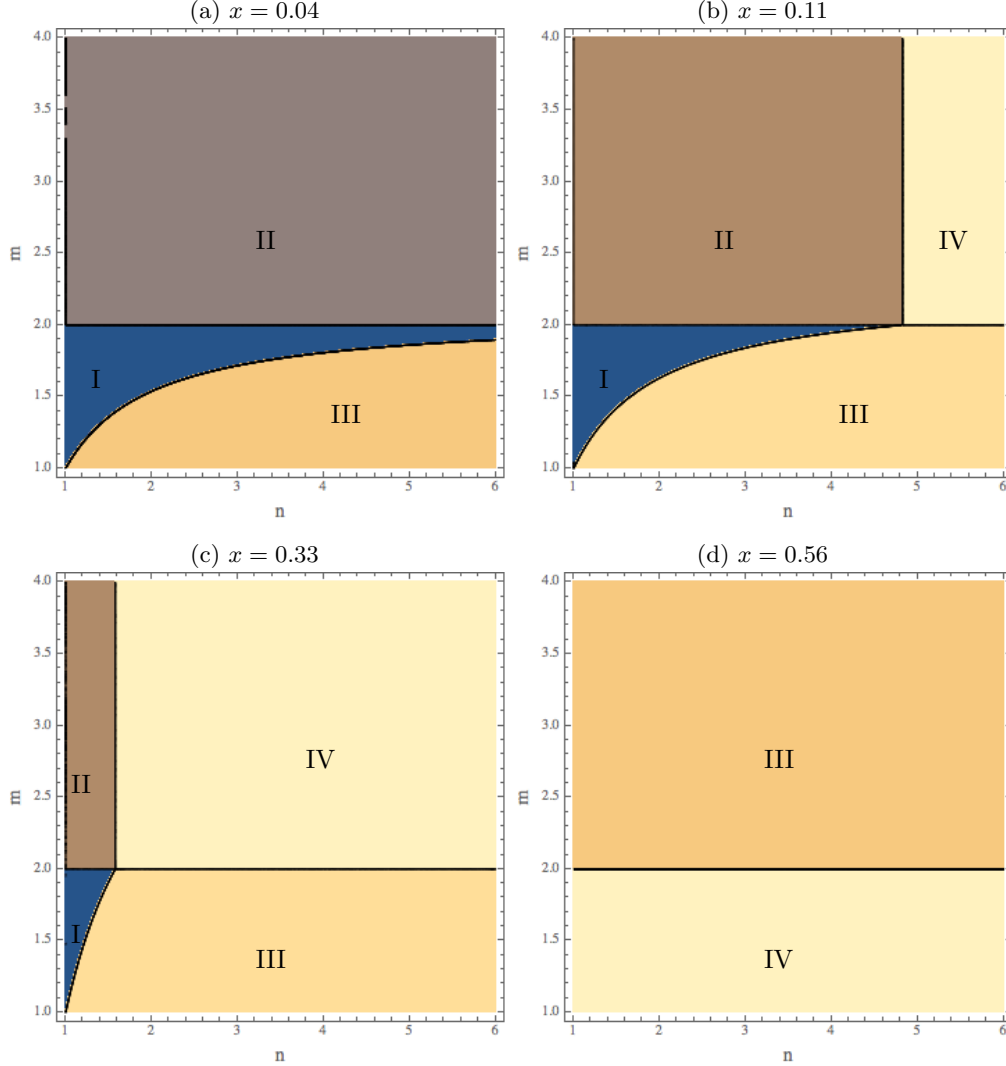


Figure 6.10: The phase diagrams for the four phases introduced above. The horizontal axis is n and the vertical is m . Note the flip in the two phases in the last diagram.

above the transition line the phases are independent of m . The reason for this transition is that the tension of the $X \leftrightarrow \text{id}$ domain wall $d(X, \text{id}) = n(m - 2)$ becomes negative. Indeed this was exactly the same as with the single tensor case. So rather than follow the above naive approach we apply our prescription from the single tensor case (which has already passed many checks) and this implies that the phase diagram in Fig. (6.10) is incorrect for $m < 2$. Instead we should analytically continue the phase transitions above $m \geq 2$ all the way to $m = 1$, without re-minimizing over the different phases. The resulting phase diagram is then independent of m for all $m \geq 1$.

We now compute the full entanglement spectrum for this model away from the phase transition point.

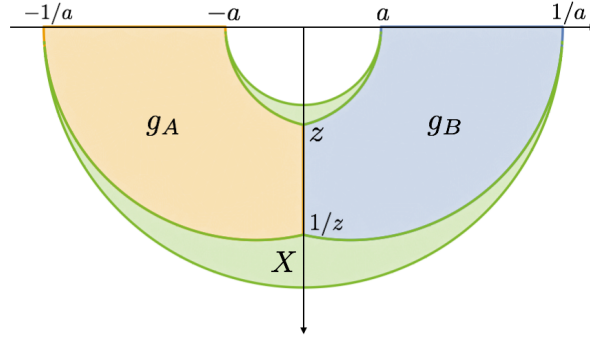


Figure 6.11: The bulk setup used to calculate Eq. (6.178). We work within Poincaré hyperbolic coordinate with moving downward as going deeper into the bulk. The position of various end points are shown in terms of a and z .

Analytically continuing from $m > 2$ gives for all m :

$$S_R = -\frac{1}{n-1} \begin{cases} 0, & x > 1/2 \\ \min\{f_{\text{II}}, f_{\text{IV}}\}, & x < 1/2 \end{cases} \quad (6.177)$$

While the expression in Eq. (6.174) seems rather complicated there is an interesting way to write f_{II} at large χ :

$$S_{R,\text{II}} = -\frac{1}{n-1} \ln \sum_{a < z < 1} \exp \left\{ -\ln \chi \left(-4(n-1) \ln z + 4n \ln \frac{1}{2} \left(\frac{a}{z} + \frac{z}{a} \right) \right) \right\} \quad (6.178)$$

where $a = \sqrt{x}/(1 + \sqrt{1-x})$ determines the un-pinned EW cross-section: $-2 \ln a$, and $-2 \ln z$ is the area of pinched cross-section, see Fig. (6.11).

We are being schematic about the sum. One is tempted to make this an integral, but recall that the network in question is really discrete and so there will indeed be a discrete set of cuts for the cross section. This form agrees with the previous one since we have to evaluate the sum in a saddle point approximation at large χ . In particular Fig. (6.11) represents how we computed Eq. (6.174) in the first place.

Following the discussion in Sec. (3.8) for the 1TN model and Sec. (5.4.3) for the 2TN model, we now interpret Eq. (6.177) as arising from an effective description of the canonical purification as a superposition of wavefunctions. These wavefunctions then live in approximate superselection sectors when reduced to AA^* . It is clear the different sectors are associated to tensor networks with different/pinched cross-sectional areas. We think of this pinching as being determined by an area operator that is now allowed to fluctuate. The area is $A(z) \equiv -2 \ln z$.

Given this discussion we can read off from Eq. (6.177) the probabilities of each sector arising:

$$P(A) = (\cosh((A - A_0)/2))^{-4 \ln \chi} \quad 0 \leq A \leq A_0, \quad (6.179)$$

where $A_0 = A(a) = -2 \ln a$, the un-pinned cross section. These probabilities are exponentially small except when $A = -2 \ln a$ where the probability goes to 1. In general, there will be some perturbative corrections that help maintain the normalization condition. Thus we write our effective model for the canonical purification

state using a new set of doubled and glued random tensor networks labelled by A :

$$|\rho_{AB}^{1/2}\rangle \sim \sum_A P(A)^{1/2} |\Psi(A)\rangle, \quad (6.180)$$

where $|\Psi(A)\rangle$ is defined as a random tensor network state as follows. Consider the pinched entanglement wedge consisting of the vertices with group elements g_A, g_B in Fig. (6.11). We construct a new tensor network by doubling and gluing along the $X \leftrightarrow g_A, g_B$ domain wall. This domain wall is slightly pinched relative to the original entanglement wedge. As before we can pick the random tensors on the AB entanglement wedge to match those of the original tensor network, while we pick the tensors on the $(AB)^*$ to be independent and random.

Note that $2A(z)$ will represent a true minimal cut, homologous to AA^* , through this new doubled network. In particular there is an associated AA^* entanglement wedge consisting of the region outside of this minimal cut/cross-section. Since the entanglement wedges for these random tensor networks associated to the boundary region AA^* are very different for different $A(z)$ we expect the density matrices reduced to AA^* to be approximately orthogonal. This is also true for BB^* .

It then follows that $\text{Tr}_{AA^*} |\Psi(A)\rangle \langle \Psi(A')| \propto \delta_{A,A'}$ and $\text{Tr}_{BB^*} |\Psi(A)\rangle \langle \Psi(A')| \propto \delta_{A,A'}$ up to small non-perturbative corrections, and our results now parallel the results discussed in Sec. (3.8) and Sec. (5.4.3). In particular an area operator on the physical Hilbert space emerges, by using the approximately orthogonal supports of $\rho_{AA^*}(A(z))$ and $\rho_{BB^*}(A(z))$. This area operator then determines the Rényi reflected entropy:

$$e^{-(n-1)S_{R,\Pi}} = \sum_A P(A)^n e^{-(n-1)A}, \quad (6.181)$$

which agrees with Eq. (6.178). Evaluating the sum in the saddle point leads back to Eq. (6.174). The dominant area A shifts as a function of n and in particular the $n \rightarrow 1$ limit gives back the entanglement wedge cross section since $P(A) \rightarrow 1$ in this limit.

For large enough n the dominant phase actually becomes the disconnected phase IV which is the same n dependent phase transition that occurred for the single random tensor model. The final effective description of the canonical purification, that captures all these effects, is shown pictorially here:

$$\sim \sum_i \sqrt{p_i} + \sqrt{p_0} \quad (6.182)$$

6.7 Discussion

In conclusion, we have demonstrated quite rigorously that the (m, n) -Rényi reflected entropies in random tensor networks are computed by dominant saddles involving triway cuts as shown in Fig. (6.1) for arbitrary m and integer n . Moreover, there is a natural analytic continuation of the triway cut problem for non-integer n which leads to the holographic proposal relating to the entanglement wedge cross section. It is then natural to guess that similar saddles, which are different from the naive saddles written down in Ref. [56], will also

play an important role in holography resolving the issues with analytic continuation found in Ref. [117]. We now comment on various aspects of our work.

Bit Threads

As discussed earlier, bit threads provide a vivid picture of the entanglement structure of holographic states. Based on the structure of bit thread configurations, Ref. [59] conjectured that the three party entanglement structure of holographic systems is dominated by bipartite entanglement. However, a version of this conjecture is in conflict with the $S_R = 2EW$ proposal [58], for which we have found further evidence. While this is conclusive, we would nevertheless like to discuss a way to see how one can get as close to bit threads as possible.

As reviewed in Sec. (6.3.1), the RT formula can be recast as a max flow problem by convex duality. Moreover, the natural form of the min-cut problem from the RTN perspective is an integer program where the optimization is over domain walls with integer energy costs, representing the different permutations that contribute to the free energy minimization problem. For the entanglement entropy, the problem can be relaxed to a linear program over the real numbers since there isn't an integrality gap for this problem. Once relaxed, convex duality naturally leads to a max-flow problem, i.e., bit threads.

In the context of reflected entropy however, we showed that the triway cut problem is equivalent to an integer program with a non-trivial integrality gap. While the Renyi reflected entropies are computed by triway cuts, which are related to the entanglement wedge cross section, the non-integer program allows relaxation to surfaces that are related to the original RT surfaces as shown in Fig. (6.2) (e.g. for $n = 2$). For RTNs, this is identical to the mutual information, as found from assuming the mostly bipartite conjecture. Thus, we can think of the relaxation of the integer program as the “incorrect” step that led to bit threads, as well as the mostly bipartite conjecture.

It has been conjectured that one can amend the mostly bipartite story from bit threads by considering a generalized “hyperthread” optimization program [181] (see also [182]). Hyperthreads are threads connecting between multiple ($k \geq 3$) boundary regions and it is conjectured that the optimal value of a k -thread program may be a measure of k -partite entanglement. In the case of 3-threads, the optimal configuration saturates a minimal triway cut. In this sense our results serve as a firsthand bridge that connects the 3-thread problem to a concrete quantum information measure. We think it should be possible to derive the hyperthread optimization as a dual problem of the various integer programs appearing in this chapter – indeed the triway cut does not admit a bit thread dual but it may still be able to be “dual” to a more exotic program such as the hyperthreads. On the other hand, reflected entropy can be naturally generalized to accommodate k -party systems [105]. It would be interesting to see if the formalism we developed in this chapter extends to such case and if there is possible connection to the k -thread programs. We leave these investigations to future works.

More General Tensor Networks

There are various aspects of RTNs that make them good models of holography such as their relation to fixed-area states [96–98]. However, there are other aspects that are missing such as the lack of mutual backreaction between domain walls, as well as the commutativity of area operators [133]. Thus, it is interesting to analyze the extent to which variants of random tensor networks can model holography.

For instance, the RT formula can be reproduced by choosing tensors that are 2-designs where the average

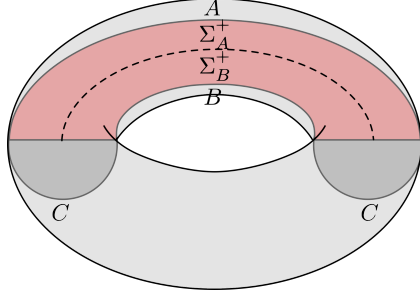


Figure 6.12: The purification for two intervals in the vacuum state at $m = 2$ is a BTZ geometry where fixing the area of the entanglement wedge cross section induces a conical defect (dotted line) at the BTZ horizon.

is the same as the Haar average up to the second moment [40]. Random stabilizer tensor networks are an example which form at most a projective 3-design [183–186]. However, they satisfy the bipartite dominance conjecture [60] and thus, do not accurately model the reflected entropy for holographic states. Our results certainly makes use of larger moments, so the discrepancy is no surprise. In fact our results suggest that the integrality gap would become visible to a projective 4-design, at least when computing the $(2, 2)$ Renyi reflected entropy (involving canonical purifications of the density matrix $\rho_{AB}^2/\text{Tr}\rho_{AB}^2$). The implications for the Renyi reflected entropy and the Markov gap are less clear, and we leave it as an important open question to understand at what level of k -design the Markov gaps becomes large, of order $\ln \chi$.

Another possible generalization of the RTN that can be considered is to use non-maximally entangled edge states [110]. In this case, the calculation for the (m, n) -Renyi reflected entropy is similar except the energy costs on the domain wall become functions of the entanglement spectrum of the edge states. In this case, it is harder to prove anything about the analytic continuation, but we expect similar saddles to play an important role.

Another generalization we can consider is that of hypergraph RTNs. Hypergraphs are a natural generalization of graphs where edges connecting 2 vertices are generalized to hyperedges potentially connecting more than 2 vertices. States satisfying the RT formula on hypergraphs were discussed in Refs. [187]. Such states have a natural construction in terms of the RTN where hyperedges are formed by projecting onto GHZ states coupling multiple vertex tensors [188]. One could then ask what the reflected entropy for such states is. While we do not have a proof analogous to the one for usual RTNs, assuming that triway cut like configurations dominate, we can compute the Renyi reflected entropy. The important ingredient is the generalization of the free energy optimization problem. The free energy cost of an edge in the RTN for vertex permutations g_1 and g_2 is weighted by $\#(g_2 g_1^{-1})$. It is easy to work out the generalization for hyperedges. For instance, for a 3-edge with vertex permutations g_1, g_2 and g_3 , the free energy cost is $\#(g_2 g_1^{-1} \vee g_3 g_1^{-1})$, which measures the number of orbits of the relevant elements.

Effective Description

In Sec. (6.6), we discussed an effective description of the canonical purification as a superposition over states with different values of area for the squeezed cross sections (e.g. Eq. (6.182)). It is natural to expect a generalization of this result to general RTNs where the squeezed cross sections are solutions to the triway cut problem at different values of n .

While this effective description was proposed in the context of RTNs, where there is no backreaction and the superposition is simply over different sets of vertices in the graph, it is natural to ask if it can be

understood in holographic systems as well. For the special case of two intervals in the vacuum state at $m = 2$, it was found in Refs. [189, 190] that the Renyi reflected entropies for arbitrary n can be computed by the torus partition function. This makes analytic continuation easy, and is related to the fact that for $m = 2$, there is no independent X element which we expect should play a role in holography more generally. The calculation of Renyi reflected entropy can then similarly be decomposed into fixed-area sectors of the entanglement wedge cross section, which correspond to different horizon areas in the BTZ saddle. It is then easy to see that the effective description with different squeezed cross sections is represented by these fixed-area states which induce varying conical defects at the horizon, which translate into the angle subtended at the triway cut at different values of n (see Fig. (6.12)).

Chapter 7

Holographic Entanglement of Purification in RTNs

In this chapter we apply the results we obtained in Chapter 6 to prove that the entanglement of purification E_p is equal to EWCS: $E_p(A : B) = \text{EW}(A : B)$ in holographic RTNs, a conjecture motivated from AdS/CFT [33, 171]. More specifically, we will prove a new inequality: $E_P(A : B) \geq \frac{1}{2} S_R^{(2)}(A : B)$. Using this, we compute $E_P(A : B)$ for a large class of RTNs at large bond dimension and show that it is equal to the EWCS.

This chapter is organized as follows: In Sec. (7.1) we review the necessary ingredients for proving the conjecture, including the entanglement of purification and a formulation of reflected entropy using Tomita-Takesaki theory. Armed with these results, we establish the necessary inequality that leads to the main theorem. In Sec. (7.2) we combine the results obtained in Sec. (7.1) and Chapter 6 to prove the $E_p = \text{EW}$ conjecture in a wide class of RTNs. We also showcase the validity of our results in terms of the phase diagrams of the 1TN and 2TN model obtained in Chapter 3 and 5. We summarize our findings and discuss possible future directions in Sec. (7.3).

The results presented in this chapter are based on Ref. [69].

7.1 Preliminary

7.1.1 Entanglement of purification

Given a bipartite density matrix ρ_{AB} , the entanglement of purification $E_P(A : B)$ is defined as [191]

$$E_P(A : B) = \min_{|\psi\rangle_{ABA'B'}} S(AA'), \quad (7.1)$$

where $S(R) = -\text{Tr}(\rho_R \log \rho_R)$ is the entanglement entropy. The minimization runs over all possible purifications of ρ_{AB} , i.e., $|\psi\rangle_{ABA'B'}$ such that $\text{tr}_{A'B'}(|\psi\rangle\langle\psi|) = \rho_{AB}$, and the $|\psi\rangle$ that achieves the minimum is called the optimal purification. $E_P(A : B)$ is a useful measure of correlations in a bipartite mixed state and is proven to be monotonic under local operations [191]. However, it is generally intractable to compute because of the optimization over all possible purifications ¹.

¹Exceptions to this include pure states like Bell pairs and classically correlated states like GHZ states, see Ref. [171] for details.

In the context of AdS/CFT ², it has been conjectured that for A, B subregions of the CFT, there is a simple geometric, AdS dual to $E_P(A : B)$. The entanglement wedge of subregion AB of the CFT is the bulk region between AB and the minimal surface γ_{AB} (also called the Ryu-Takayanagi (RT) surface [26]). This is, in appropriate settings, the bulk region reconstructable from the corresponding boundary subregion [36]. Based on this, Refs. [33, 171] conjectured that $E_P(A : B)$ is given by

$$E_P(A : B) = \text{EW}(A : B) \quad (7.2)$$

We compute E_P by using a known upper bound and deriving a new lower bound (Theorem 7.2), which we are able to argue matches the upper bound in certain RTNs. This argument relies on the results obtained previously in this thesis for the reflected entropy:

$$S_R(A : B) = 2 \text{EW}(A : B), \quad (7.3)$$

which has been proven rigorously for a large class of RTNs in Chapter 3,5 and 6. Moreover, as argued in [33], RTNs in general satisfy

$$E_P(A : B) \leq \text{EW}(A : B). \quad (7.4)$$

This places the upper bound $E_P \leq S_R/2$.

7.1.2 Reflected entropy from modular operator

The lower bound in Theorem 7.2 will require the following lemma that rewrites the Rényi reflected entropy using the formalism of modular operators appearing in Tomita-Takesaki theory ³. Consider a finite dimensional system with Hilbert space $\mathcal{H}_{AB} \otimes \mathcal{H}_C$, where subsystem C is completely general. Given a state $|\psi\rangle$ ⁴ and subsystem AB , the modular operator is defined as

$$\Delta_{AB,\psi} = \rho_{AB} \otimes \rho_C^{-1}, \quad (7.5)$$

where the inverse is defined to act only on the non-zero subspace of ρ_C and $\Delta_{AB,\psi}$ is defined to annihilate the orthogonal subspace.

Lemma 7.1. *For integer $n \geq 2$,*

$$S_R^{(n)}(A : B) = \frac{1}{1-n} \log \langle \psi^{\otimes n} | \Sigma_A \Delta_{AB^{\otimes n}, \psi^{\otimes n}}^{1/2} \Sigma_A^\dagger | \psi^{\otimes n} \rangle, \quad (7.6)$$

where $\Sigma_{A(A^*)}$ are twist operators that cyclically permute the n copies of $|\sqrt{\rho_{AB}}\rangle$ on subregion $A(A^*)$, $|\psi\rangle$ is an arbitrary purification of ρ_{AB} , and $\Delta_{AB^{\otimes n}, \psi^{\otimes n}} = \Delta_{AB,\psi}^{\otimes n}$.

Proof. The Rényi reflected entropy can be written as

$$S_R^{(n)}(A : B) = \frac{1}{1-n} \log \text{Tr}(\rho_{AA^*}^n) \quad (7.7)$$

$$\text{Tr}(\rho_{AA^*}^n) = \langle \sqrt{\rho_{AB}}^{\otimes n} | \Sigma_A \Sigma_{A^*} | \sqrt{\rho_{AB}}^{\otimes n} \rangle. \quad (7.8)$$

²See Ref. [78] for a review of the quantum information perspective on AdS/CFT.

³See Ref. [51] for a review.

⁴ $|\psi\rangle$ does not need to be cyclic and separating.

As described in Sec. (2.3), operators act on $\text{End}(\mathcal{H}_{AB})$ by left and right actions, i.e.,

$$O_{AB} |M_{AB}\rangle = |O_{AB} M_{AB}\rangle \quad (7.9)$$

$$O_{A^*B^*} |M_{AB}\rangle = |M_{AB} O_{AB}^\dagger\rangle, \quad (7.10)$$

and the inner product is defined by

$$\langle M|N\rangle = \text{Tr}(M^\dagger N). \quad (7.11)$$

Using this, one finds that Eq. (7.8) is given by

$$\text{tr}(\rho_{AA^*}^n) = \text{Tr}_{(AB)^{\otimes n}}(\sqrt{\rho_{AB}}^{\otimes n} \Sigma_A \sqrt{\rho_{AB}}^{\otimes n} \Sigma_A^\dagger). \quad (7.12)$$

To express Eq. (7.12) in terms of modular operators, we consider an arbitrary purification of ρ_{AB} denoted $|\psi\rangle$, giving

$$\begin{aligned} \text{Tr}(\rho_{AA^*}^n) &= \text{Tr}_{(AB)^{\otimes n}}(\sqrt{\rho_{AB}}^{\otimes n} \Sigma_A \sqrt{\rho_{AB}}^{\otimes n} \Sigma_A^\dagger) \\ &= \langle \psi^{\otimes n} | \Sigma_A \Delta_{AB^{\otimes n}, \psi^{\otimes n}}^{1/2} \Sigma_A^\dagger \Delta_{AB^{\otimes n}, \psi^{\otimes n}}^{-1/2} | \psi^{\otimes n} \rangle \\ &= \langle \psi^{\otimes n} | \Sigma_A \Delta_{AB^{\otimes n}, \psi^{\otimes n}}^{1/2} \Sigma_A^\dagger | \psi^{\otimes n} \rangle, \end{aligned}$$

where we have used the fact that the ρ_C dependence cancels out in the second line. For the last line, we have used $\Delta_{AB, \psi}^{-1/2} |\psi\rangle = |\psi\rangle$ which is easy to see by working in the Schmidt basis. \square

7.1.3 A lower bound

Theorem 7.2. For integer $n \geq 2$,

$$E_P(A : B) \geq S_R^{(n)}(A : B)/2. \quad (7.13)$$

Remark. In Ref. [56], it was proven that for integer $n \geq 2$, the Rényi reflected entropy is monotonic under partial trace, i.e., $S_R^{(n)}(A : BC) \geq S_R^{(n)}(A : B)$. This immediately implies Theorem 7.2 by the following argument. Let $|\psi\rangle_{ABA'B'}$ be the optimal purification. Then

$$2S(AA') \geq 2S_n(AA') = S_R^{(n)}(AA' : BB') \geq S_R^{(n)}(A : B), \quad (7.14)$$

where we have used the fact that $S_R^{(n)}(C : D) = 2S_n(C)$ for a pure state on CD . That said, we choose to present the proof below because it is self-contained and far simpler than the proof of monotonicity in Ref. [56].

Proof of Theorem 7.2. We first define the Rényi generalization of $E_P(A : B)$ as

$$E_P^{(n)}(A : B) = \min_{|\psi\rangle_{ABA'B'}} S_n(AA'). \quad (7.15)$$

Applying the monotonicity of Rényi entropy, i.e., $\partial_n S_n \leq 0$, for $n > 1$ we have

$$E_P(A : B) \geq E_P^{(n)}(A : B). \quad (7.16)$$

Now consider an arbitrary purification $|\psi\rangle_{ABA'B'}$. For integer $n \geq 2$, the Rényi entropy for subregion

AA' can be computed using twist operators in a fashion similar to Eqs. (7.7,7.8), i.e.,

$$S_n(AA') = \frac{1}{1-n} \log \text{Tr}(\rho_{AA'}^n) \quad (7.17)$$

$$\text{tr}(\rho_{AA'}^n) = \langle \psi^{\otimes n} | \Sigma_A \Sigma_{A'} | \psi^{\otimes n} \rangle. \quad (7.18)$$

Define the operators $\Pi_{AB,\psi}$ ($\Pi_{A'B',\psi}$) to be projectors onto the non-zero subspaces of the reduced density matrices on AB ($A'B'$). Then, using $\Pi_{AB,\psi} |\psi\rangle = \Pi_{A'B',\psi} |\psi\rangle = |\psi\rangle$, we can insert $\Pi_{AB,\psi}$ ($\Pi_{A'B',\psi}$) from the right (left) in Eq. (7.18) for each of the n copies of $|\psi\rangle$. Note that $\Pi_{AB}\Pi_{A'B'} = \Delta_{AB,\psi}^{1/4} \Delta_{AB,\psi}^{-1/4}$ as the inverse density matrices in the modular operators annihilate the orthogonal subspaces. We can use this fact to insert a pair of modular operators into Eq. (7.18) to get

$$\begin{aligned} \text{tr}(\rho_{AA'}^n) &= \langle \psi^{\otimes n} | \Sigma_A (\Delta_{AB,\psi}^{1/4} \Delta_{AB,\psi}^{-1/4})^{\otimes n} \Sigma_{A'} | \psi^{\otimes n} \rangle \\ &\leq \left(\langle \psi^{\otimes n} | \Sigma_A \Delta_{AB^{\otimes n},\psi^{\otimes n}}^{1/2} \Sigma_A^\dagger | \psi^{\otimes n} \rangle \langle \psi^{\otimes n} | \Sigma_{A'} \Delta_{AB^{\otimes n},\psi^{\otimes n}}^{-1/2} \Sigma_{A'}^\dagger | \psi^{\otimes n} \rangle \right)^{\frac{1}{2}}, \end{aligned} \quad (7.19)$$

where we have applied the Cauchy-Schwarz inequality between the modular operators.

Using $\Delta_{AB,\psi}^{-1} = \Delta_{A'B',\psi}$ and Eq. (7.13), the two terms in the last line of Eq. (7.19) can be related to Renyi reflected entropies on $A : B$ and $A' : B'$ respectively. Thus, we have

$$2 \frac{1}{1-n} \log \text{tr}(\rho_{AA'}^n) \geq S_R^{(n)}(A : B) + S_R^{(n)}(A' : B'). \quad (7.20)$$

Finally using the fact that $S_R^{(n)}(A' : B') \geq 0$, applying Eq. (7.20) to the optimal purification arising in the calculation of $E_P^{(n)}(A : B)$ and using Eq. (7.16), we have our desired inequality. \square

We will use the inequality at $n = 2$ since it is the strongest. It is important to note that this inequality was derived using twist operators which only exist at integer n . In the context of computing entanglement entropy, one usually analytically continues the answer obtained at integer n to non-integer values using Carlson's theorem. However, it is not necessarily possible to analytically continue an inequality. For example, the monotonicity of Renyi reflected entropy under partial trace, i.e., $S_R^{(n)}(A : BC) \geq S_R^{(n)}(A : B)$ was proved to be true at integer n [56], whereas counterexamples were found for non-integer n in Ref. [106].

7.2 Entanglement of purification on RTNs

We can now use these bounds to compute E_P in RTN states. We will consider RTNs in the simplifying limit where all bond dimensions χ_{xy} are large such that $\log \chi_{xy} \propto \log D$ and $D \rightarrow \infty$ ⁵.

It was proved in Chapter 6 that the optimal configuration involves four permutation elements $\{e, g_A, g_B, X\}$ and takes the general form shown in Fig. (7.1). In detail, we have

$$\lim_{D \rightarrow \infty} \frac{S_R^{(n)}(A : B)}{\log D} = 2\mathcal{A}_n(A : B : C) - \frac{n}{n-1} \mathcal{A}(AB : C), \quad (7.21)$$

where $\mathcal{A}_n(A : B : C)$ is the triway cut with tensions $t_{A:B} = 1$ and $t_{A:C} = t_{B:C} = \frac{n}{2(n-1)}$ (see Fig. (7.1)). $\mathcal{A}(AB : C)$ is the minimal cut separating AB from C .

⁵ $\log D \sim \frac{1}{4G_N}$ in AdS/CFT in units where $l_{AdS} = 1$.

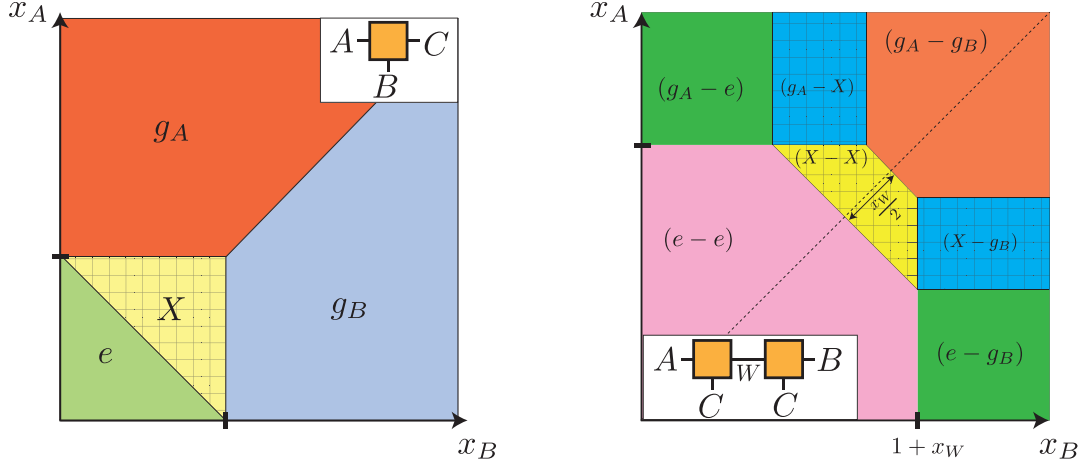


Figure 7.2: The phase diagram of the 1TN model (left) and the 2TN model (right), labeled by the dominant permutation element in each domain. We have proved $E_P(A: B) = EW(A: B)$ everywhere except the region marked with squares.

phase boundaries at $n = 2$ are represented as a function of $x_A = \frac{\log d_A}{\log d_C}$ and $x_B = \frac{\log d_B}{\log d_C}$. Apart from the shaded region marking the X domain, we have proved $E_P(A: B) = EW(A: B)$ everywhere else. It is also straightforward to read off the optimal purification since we already argued it is given by the geometric purification suggested in Ref. [33, 171].

One may consider a simple deformation of the above model, by changing the maximally entangled legs of the RTN to non-maximally entangled legs. Such states have also been useful to model holographic states [110]. In fact, the simplest situation where we add non-maximal entanglement to the C leg results in a state identical to the PSSY model of black hole evaporation [15]. We can thus use the results of Chapter 4 which computed the reflected entropy in this model. The phase diagram turns out to be similar to the 1TN phase diagram except the shaded region turns out to be larger. Thus, non-maximal links do not help in improving the applicability of our result. We provide some more details on this in Appendix F.1.

- **2TN**

The next simplest network to consider is one where we have two vertices connected by an internal bond. For simplicity, the external C bonds are chosen to have identical bond dimension. In general, we have the phase diagram shown in the right panel of Fig. (7.2). Again, we see a large codimension-0 region of parameter space where our proof applies. In fact, motivated by holography, Chapter 5 considered a limit where $x_W = \frac{\log d_W}{\log d_C} \rightarrow 0$. In this limit, the shaded domains containing the element X vanish at arbitrary n . Thus, our proof always applies in this limit.

7.3 Discussion

In this chapter we have proven $E_P = EW$ for a large class of RTNs. Our result relied on the inequality $E_P \geq \frac{1}{2}S_R^{(2)}$ proven as Theorem 7.2. Proving the stronger inequality $E_P \geq \frac{1}{2}S_R$ would prove $E_P = EW$ more generally, but this cannot be achieved with our proof technique. It would be interesting to check this numerically using the techniques of Ref. [192].

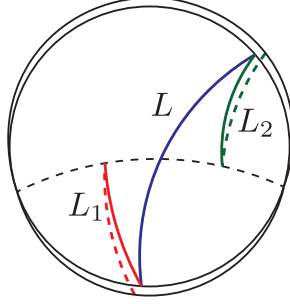


Figure 7.3: A correlation function computed by the geodesic of length L (solid blue) can be compared to the mirror correlation functions analogous to Eq. (7.19) computed by mirror geodesics (red and green) meeting the RT surface (dashed) orthogonally. Each of the mirror geodesics with length $L_{1,2}$ involves two copies (dashed and solid). It is then clear that $L \geq \frac{L_1+L_2}{2}$.

An inequality of the form of Eq. (7.19) can in fact be proved for heavy local operators in AdS/CFT by using the geodesic approximation and the techniques of computing mirror correlation functions [193] (see Fig. (7.3)). In AdS₃/CFT₂, twist operators are local and can be analytically continued to $n \approx 1$. Applying the inequality, we would then find $S(AA') \geq \frac{1}{2}S_R(A : B) + \frac{1}{2}S_R(A' : B')$ in any geometric purification. It would be interesting if this argument can be generalized to non-geometric states, so that we can minimize the LHS and find the strengthened inequality.

Chapter 8

Outlook

In this dissertation we carried out a thorough study of the entanglement properties of the canonical purification for random tensor network states. We conclude this dissertation by summarizing some interesting future research directions.

Analytic continuation of Rényi index $n \rightarrow 1$ on generic RTNs

Our main result in Chapter 6 pertains to the integer (m, n) -Rényi reflected entropy. We have performed the analytic continuation $m \rightarrow 1$ rigorously, but not for the $n \rightarrow 1$ required for the (von Neumann) reflected entropy. The main difficulty is that the reflected spectrum is not flat in n inherently, and thus we have less control over analytic continuation. This is in contrast to the simple tensor models in Chapter 3 and Chapter 5, where we know all the n -Rényi entropies exactly. One may be able to bound the difference by application of various bounds of Rényi entropy but so far we have not managed to do it. A successful implementation of this result would have profound implications on the entanglement structure of holographic RTNs. In particular it would push our result in Chapter 7 to cover the missing parameter spaces of RTN with large bond dimensions.

Entanglement measures beyond reflected entropy

As we have shown in this thesis, the study of canonical purification and reflected has led to new and profound insights in our understanding of the entanglement structure of holographic states and the emergence of spacetime. A natural question is that what can more general information measures can tell us about quantum gravity. Indeed the quantification of multipartite entanglement is known to be a very hard problem [49]. However, the methods we developed in this thesis provide a set of new lens which enable one to study these measures under a new perspective. In particular, our proof of $S_R = 2$ EW conjecture for generic RTNs makes heavy uses of lattice theory and convex optimization theory. In particular, lattice theory of the symmetry group provides a natural language for twist operators in calculating different entanglement measures. Such a approach has already been adopted in Refs. [174, 176] to construct new multi-partite quantum information measures.

On the other hand, the application of max flow-min cut theorem has led to the bit-thread picture for entanglement entropy [65, 66]. Naively, it suggests that the bulk entanglement is mostly bipartite [59]. On the contrary, our results in Chapter 6 shows that tripartite entanglement involves solving a minimal triway

cut problem, which has no dual flow/bit-thread picture. It has been conjectured that one can amend the mostly bipartite story from bit-threads by considering a generalized “hyperthread” optimization program [181] (see also [182]), which involves k -threads connecting between multiple boundary ($k \geq 3$) regions. Our results in this thesis specifically applies to $k = 3$ hyperthreads. It has been proposed that reflected entropy can be naturally generalized to accommodate k -party systems [105]. It would be interesting to see if the formalism we developed extends to such case and if there is possible connection to k -thread programs.

Better tensor network models for AdS/CFT

Another interesting future direction involves improving existing TN models for AdS/CFT. It is long known that random tensor networks possess flat entanglement spectra, which is not true for generic gravity states due to area fluctuations [96, 97]. There has been proposals to address this issue by substituting the maximally entangled state the at each bond dimension of the RTN by non-maximally entangled ones [110, 138]. However it does not seem to pose a solution to another issue with TN models, namely that the non-commutativity of minimal surfaces in quantum gravity. In RTN, the area operators obtained from two crossing minimal surfaces commute. This cannot happen for overlapping cuts in AdS/CFT [133].

Our construction for the canonical purification in RTNs marks a novel way to introduce area fluctuations via an effective superposition of different networks. In particular our construction seems to be able to naturally introduce both the fluctuations in the entanglement spectra as well as non-commuting area operators. The idea is that by repeated application of canonical purification, one should be able to build up increasing sophisticated networks describing the bulk geometry. For details see the discussion in Sec. (3.10).

Tensor networks and von Neumann algebra

A promising direction worth pursuing along the line is establishing the connection between tensor networks and operator algebras. In particular, the TL algebra we employed in solving the spectrum of 2TN (Chapter 5) plays an important role in the study of type-II von Neumann algebras, which has been shown to be the type of operator algebra in de Sitter space [94], (see also Refs. [93, 194]), double-scaled SYK model and JT gravity [86, 95]. There seems to be a deep connection between the emergent bulk geometry of TNs and this type-II subfactor generated by the TL algebra. In addition, the analysis of double-scaled SYK model makes heavy uses of the so-called “chord diagrams” [85, 86, 167], which bears striking resemblance to the TL diagrams used in our calculation in Sec. (5.4), suggesting that there may be deeper connections between RTN and the SYK model. Understanding this connection will give us better intuition about holography and quantum gravity.

Appendix A

Symmetric Group and Set Partitions

In this appendix, we will summarize certain aspects of the symmetric group S_N , the group of all permutations on N elements. These are closely related to set partitions P_N , the set of all partitions of N elements. We start with a quick review of some well-known theorems of non-crossing permutations NC_N . These theorems can be given a topological meaning via the relation to set partitions, which allows us to generalize the theory of non-crossing permutations to multiple disjoint boundaries. They will play an important role in the proof of the form of the phase diagram for reflected entropy.

A.1 Cayley distance

The Cayley distance $d(g, h)$ is a metric on S_N defined by the minimal number of transpositions, i.e., swaps of two elements, required to go from g to h . Any permutation can be decomposed into disjoint cycles, where a cycle of n elements is represented by the notation $(i_1 i_2 \dots i_n)$. We first note that conjugation of an element g by an element h results in an element hgh^{-1} with the same structure of cycles as g but with a relabelling of the entries in each cycle dictated by h as

$$(i_1 i_2 \dots i_n) \mapsto (h(i_1) h(i_2) \dots h(i_n)). \quad (\text{A.1})$$

Using this it is easy to show that the Cayley metric is both left and right invariant, i.e.,

$$d(g, h) = d(gx, hx) = d(xg, xh). \quad (\text{A.2})$$

The right invariance follows from the definition, while left invariance uses the fact that conjugation of a product of transpositions by x is still a product of transpositions.

In particular, this means we can reduce all calculations of distance between two elements to the distance of an element from the identity element e , i.e.,

$$d(g, h) = d(e, g^{-1}h) = d(e, hg^{-1}). \quad (\text{A.3})$$

A special example is a cycle of k elements for which the distance from e is simply $k - 1$, as can be seen by

constructing an optimal decomposition

$$(i_1 i_2 \dots i_N) = (i_n i_1) \dots (i_3 i_1)(i_2 i_1). \quad (\text{A.4})$$

Using the above fact and the decomposition of an arbitrary permutation g into k disjoint cycles of size n_k , we have

$$d(e, g) = \sum_k (n_k - 1) = N - \#(g), \quad (\text{A.5})$$

where we use the notation $\#(g) = k$ to denote the cycle counting function.¹ This makes it manifest that $d(e, g) = d(e, hgh^{-1})$, i.e., distance from the identity is invariant under conjugation.

A.2 Non-crossing permutations

The Cayley metric like any other metric satisfies a triangle inequality

$$d(g, h) + d(h, r) \geq d(g, r), \quad (\text{A.6})$$

where equality implies h lies on a geodesic between g and r , and the elements lying on the geodesic are collectively denoted $\Gamma(g, r)$. In the case where one of the elements is the identity, the set $\Gamma(g, e)$ can be easily classified using the theory of non-crossing permutations as we review below.

Definition A.1 (Non-crossing permutations). Let $g \in S_N$. Consider a disk with N cyclically ordered (say clockwise) marked points on its boundary and connect the points with directed lines according to the cycle decomposition of g . Then g is non-crossing if and only if every directed cycle are also clockwise oriented and can be drawn in the interior of the disk without ever crossing each other. The set of non-crossing permutations is denoted NC_N .

Theorem A.1. (Biane [195]) *An element g lies on the geodesic between e and maximal cyclic permutation $\tau \equiv (12 \dots N)$, i.e. , satisfies*

$$d(e, g) + d(g, \tau) = N - 1, \quad (\text{A.7})$$

or equivalently,

$$\#(g) + \#(\tau g^{-1}) = N + 1, \quad (\text{A.8})$$

if and only if it is a non-crossing permutation.

We need the following lemma.

Lemma A.2. *Suppose g is a permutation such that $\#(g) = k$ and σ is a transposition. Then $\#(g\sigma) = k + 1$ if and only if the elements exchanged by σ are in the same cycle of g , else $\#(g\sigma) = k - 1$.*

Proof. Suppose the elements transposed by σ , labelled i_1 and i_2 , are part of the same cycle in g , then $g\sigma$

¹Note that elements that map to themselves are counted as cycles of size 1.

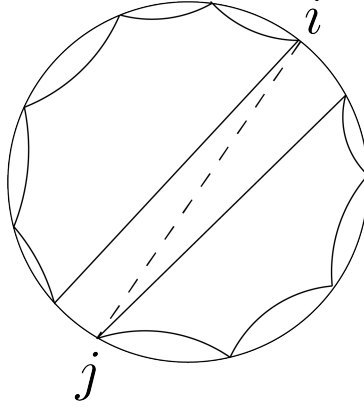


Figure A.1: The transposition (i, j) breaks the cyclic permutation τ into two cycles divided across the chord joining points i and j . In order to satisfy the geodesic condition, all further transpositions should act on elements within the given cycles. Thus, we end up with a non-crossing permutation.

splits into two cycles of the form

$$(i_1, g(i_2), \dots, g^{-1}(i_1))(i_2, g(i_1), \dots, g^{-1}(i_2)). \quad (\text{A.9})$$

On the other hand if i_1 and i_2 were not part of the same cycle in g , then $g\sigma$ couples them into a single cycle of the form

$$(i_1, g(i_2), \dots, i_2, g(i_1), \dots). \quad (\text{A.10})$$

□

Proof. (of Theorem A.1). Consider an element g such that $d(g, e) = k$ or $\#(g) = N - k$. Using Lemma A.2, we see that τg^{-1} has at most $k + 1$ cycles and this precisely happens when the transpositions generating g^{-1} break the cycles of τ at each step. The action of a transposition (i, j) is to break τ into cycles $(1, 2, \dots, i, j + 1, \dots, N)$ and $(i + 1, \dots, j)$. This can be represented on a disk as two cycles divided by the chord joining elements i and j as seen in Fig. (A.1). This process can be repeated k times, while ensuring that transpositions always act on elements within the same cycle. The figure makes it clear that the element τg^{-1} obtained this way is a non-crossing permutation.

To prove the other direction, it is useful to introduce a topological representation as shown in Fig. (A.2), where the green blocks represent the group action of g while the orange blocks represents the action of τg^{-1} . These blocks can never cross as implied from the non-crossing condition. Now reinterpreting the figure as a graph we identify $2N$ vertices, $3N$ edges and the faces represent a cycle of either g or τg^{-1} . Thus, using the Euler formula we have

$$V - E + F = \#(g) + \#(\tau g^{-1}) - N = 2 - 2G - B \quad (\text{A.11})$$

$$\implies \#(g) + \#(\tau g^{-1}) = N + 1 - 2G, \quad (\text{A.12})$$

where G is the genus of the Riemann surface and we have used $B = 1$ for the number of boundaries. Since the graph is planar, $G = 0$, and we find that the geodesic condition is satisfied for non-crossing permutations. □

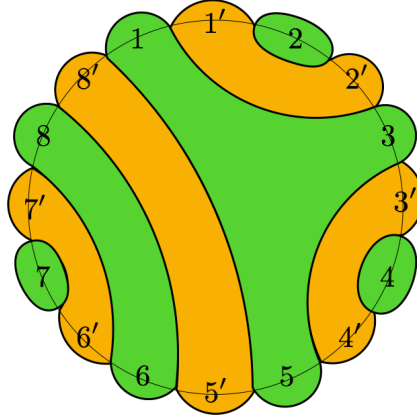


Figure A.2: The group action of a non-crossing permutation g is represented by its orbits (green) acting on the elements $i \in 1, 2, \dots, N$, where $N = 8$. The action of τg^{-1} is represented by its orbits (orange) acting on the same elements denoted i' for clarity.

We note a nice corollary of theorem A.1.

Corollary A.3. *Suppose g is a permutation with a decomposition into disjoint cycles B_1, B_2, \dots, B_k . Then an element h lies on the geodesic between e and g if and only if $\forall j$ B_j is a union of disjoint cycles of h , and h restricts to a non-crossing permutation on each B_j . In this case, non-crossing is defined with respect to the orientation of cycles of g .*

Proof. This follows from a simple application of Theorem A.1 for each B_j separately. \square

Remark. The topological representation (Fig. (A.2)) relates a permutation to a graph defined on $2N$ vertices. The converse is also true and there is a bijection between such graphs and permutation elements $g \in S_N$. However the corresponding graph is only planar iff $g \in NC_N$. In general one can think of embedding this graph onto some Riemann surface and make this statement much more refined by relating the genus directly to the failure to comply the geodesic condition, i.e. For $g, h \in S_N$,

$$d(e, g) + d(g, h) = d(e, h) + 2(C - B) + 2G \quad (\text{A.13})$$

where B is the number of boundaries in the graph which is set by $\#(h)$, C is the number of connected components of the graph and G is the genus of the surface.² For example when $h = \tau$, we have $B = C = 1$ and we recover the geodesic condition Eq. (A.7). This allows us to study the group geodesic in a more general setting and have a better handle on the resolvent calculation. We will give a proof for this proposition in appendix A.4.

In the calculation of various entropic quantities we will encounter group summations over non-crossing permutations, weighted by the individual cycle counts. The outcome of these summations can be expressed in terms of q -Catalan numbers.

Definition A.2 (q -Catalan numbers). Given any positive integer $n \in \mathbb{N}$ and $q \in \mathbb{C}$, the q -Catalan number

²The meaning of C and G is ambiguous at this point. In particular the genus of the embedding surface is not the same as the common definition of the genus of the graph itself since our surface has nontrivial boundaries. We will clarify what we mean by these numbers when we set out to prove this proposition.

$C_n(q)$ is defined by the following sum

$$C_n(q) = \sum_{g \in NC_n} q^{\#(g)} = \sum_{k=0}^n q^k N(n, k), \quad (\text{A.14})$$

where $N(n, k) = \binom{n}{p} \binom{n}{p-1}$ are called the *Narayama Numbers*.

$N(n, k)$ counts the number of distinct non-crossing permutations with exactly k cycles. Thus $C_n(q)$ is also the generating function for Narayama Numbers. The q -Catalan numbers can be expressed in terms of the Hypergeometric functions

$$C_n(q) = q {}_2F_1(1-n, -n; 2; q) \quad (\text{A.15})$$

For positive integer $n > 0$ we have the following relationship:

$$C_n(1/q) = q^{-n-1} C_n(q) \quad (\text{A.16})$$

This is not true for non-integer n . Because of the ambiguity in Hypergeometric function due to the branch cut at $q = 1$ we give the following analytic continuation in n at fixed q :

Definition A.3 (analytic continuation of q -Catalan numbers). For $n > 0$ and $q > 0$,

$$C_n(q) \equiv \begin{cases} q {}_2F_1(1-n, -n; 2; q), & q \leq 1 \\ q^n {}_2F_1(1-n, -n; 2; 1/q), & q > 1 \end{cases} \quad (\text{A.17})$$

A.3 Set partitions

We now establish the relation between symmetric group S_N and set partitions P_N . We then show that it is naturally equipped with a lattice structure which defines a way to compare elements in P_N .

A partition $p \in P_N$ is a disjoint set of subsets, or blocks, whose disjoint union is \mathbb{Z}_N . Given a $g \in S_N$ we can use the cycles to produce a partition $P : S_N \rightarrow P_N$. This map is surjective but not injective. For example, if $g = (132)(45) \in S_5$ then $P(g) = \{\{1, 2, 3\}, \{4, 5\}\}$. We can similarly define the counting function $\#(p)$ as the number of blocks in the partition. So $\#(g) = \#(P(g))$. We denote the finest partition by $e = \{\{1\}, \{2\}, \dots, \{N\}\}$ and the coarsest by $\{\mathbb{Z}_N\}$.

There is a natural partial order on such partitions given by a refinement of the partitions or sub-partitions. That is $p_1 \leq p_2$ if for every block $c \in p_2$ there is a subset of blocks in p_1 that forms a partition of c . It turns out P_N satisfies nicer properties that makes it a lattice. We review the definition and basic properties of lattices below.

Definition A.4 (Lattice). A lattice is a partially ordered set L in which each two elements $a, b \in L$ always have a meet and join, where:

Definition A.5 (Meet and Join). Let P be a partially ordered set and $a, b \in P$. The *join* of a and b , denoted $a \vee b$, is the least upper bound of a and b , i.e. $a \vee b \leq x$ for every x that simultaneously satisfies $x > a$ and $x > b$. Conversely, the *meet* of a and b , denoted $a \wedge b$, is the greatest lower bound of a and b , i.e. $a \wedge b \geq y$ for all y such that $y < a$ and $y < b$.

The join satisfies certain properties:

$$a \vee b = b \vee a \quad (\text{commutativity}) \quad (\text{A.18})$$

$$a \vee (b \vee c) = (a \vee b) \vee c \quad (\text{associativity}) \quad (\text{A.19})$$

$$a \vee a = a, \quad (\text{idempotent}) \quad (\text{A.20})$$

and similarly for the meet. If $a \leq b$ then $a \vee b = b$ and $a \wedge b = a$. They commute with the order, e.g. $a \leq b \implies a \vee c \leq b \vee c$. Note however in general they do not satisfy the distributive property that is familiar from set intersections and unions, i.e. $a \vee (b \wedge c) \neq (a \vee b) \wedge (a \vee c)$.

We now show that the set partition P_N is indeed a lattice by explicitly constructing $p_1 \vee p_2$ and $p_1 \wedge p_2$. The latter $p_1 \wedge p_2$ is simply the set of pairwise non-empty intersections taken over all blocks in p_1, p_2 . While the former can be found recursively via: $p_1 \vee p_2 = p_1 \vee (d_1) \vee (d_2) \dots$ where $p_2 = (d_1)(d_2) \dots$ is the block decomposition. Then for a single block: $q \vee (d_1)$ is simply $(\cup_{d_1 \cap c_i \neq \emptyset} c_i)q'$ with $(\cup_{d_1 \cap c_i \neq \emptyset} c_i) \equiv$ the single block formed by all q 's that intersect d_1 and $q' = \prod_{d_1 \cap c_i = \emptyset} (c_i)$ are the remaining blocks that do not.

It turns out this lattice is also graded and (upper) semimodular.

Definition A.6 (Grading of a lattice). A lattice L is *graded* if there exists a map $\rho : L \rightarrow \mathbb{N}$ such that for $a, b \in L$:

- It is compatible with the ordering of the lattice: we have $\rho(a) > \rho(b)$ when $a > b$.
- It is compatible with the covering condition: $\rho(a) = \rho(b) + 1$ iff a covers b (denoted $a :> b$), i.e. $a > b$ and there is no other $c \in L$ such that $a > c > b$.

The map ρ is called a *grading* of the lattice L .

For the lattice at hand the grading $\rho(q) = N - \#(q)$ satisfies these properties. We can check that ρ is graded by the fact that when $p_1 > p_2$ and there is no other p_3 such that $p_1 > p_3 > p_2$, then p_1 must to be formed from p_2 by merging two blocks implying that $\rho(p_1) = \rho(p_2) + 1$.

A graded lattice L is semimodular iff the grading ρ satisfies the following property: ³

$$\rho(a \vee b) + \rho(a \wedge b) \leq \rho(a) + \rho(b) \quad \forall a, b \in L \quad (\text{A.21})$$

We give a proof that set partitions satisfy this inequality.

Lemma A.4 (Semimodularity of P_N). *For all $p_1, p_2 \in P_N$ then:*

$$\#(p_1 \vee p_2) + \#(p_1 \wedge p_2) \geq \#(p_1) + \#(p_2) \quad (\text{A.22})$$

with equality iff the graph, formed by $\#(p_1) + \#(p_2)$ vertices, and connected via $\#(p_1 \wedge p_2)$ edges in the natural way, is a disconnected union of tree graphs.

Proof. Without loss of generality we can consider the case where $\#(p_1 \vee p_2) = 1$ since the different blocks in $p_1 \vee p_2$ contribute independently to the inequality. So the general case can be written as a sum over this case.

Consider a bi-partite graph formed by black vertices for each block in $c_1^i \in p_1$ and white vertices for each block in $c_2^j \in p_2$. Connect the vertices by edges for each non-trivial intersection $c_1^i \cap c_2^j \neq \emptyset$. There must be

³For a general lattice L the semimodular condition is that $\forall a, b \in L, a \wedge b < a$ implies $b < a \vee b$. The equivalence of two definitions can be found on standard textbooks on lattice theory, e.g. Birkoff [196].

exactly $E = \#(p_1 \wedge p_2)$ edges by definition. The graph must also be connected by $p_1 \vee p_2 = \mathbb{Z}_N$. A connected graph has the simple bound:

$$E \geq V - 1 \tag{A.23}$$

which is easy to prove by induction on the number of vertices. But $V = \#(p_1) + \#(p_2)$ and we are done. Saturation of the inequality implies the graph is a tree (with no cycles), and this follows from the induction proof mentioned above. \square

A.4 Annular non-crossing and topology

We now make precise the statement in (A.13) and provide a proof for it. In particular we will define what we mean by the embedding surface and various topological quantities associated to it. The statement of proposition gives rise to an inequality which is saturated when the genus $G = 0$. This marks the proposition as a generalization to the geodesic conditions of non-crossing permutations and we will denote the set of the elements that saturates the inequality as *multi-annular non-crossing permutations*.⁴

Fix a special element $g_0 \in S_N$ with cycle decomposition $g_0 = \prod_i c_i^0$. From corollary A.3 we know that geodesics to the identity $g \in \Gamma(e, g_0)$ are products of non-crossing permutations of length $|c_i^0|$ for each cycle. We will denote these simply as $NC_{g_0} \equiv NC_{|c_0^1|, |c_0^2|, \dots}$. There is a geometric picture of these elements as curves living on a disjoint union of $\#(g_0)$ disconnected discs.

Beyond non-crossing permutations we now discuss multi-annular non-crossing permutations that allow for connections between the different g_0 cycles but continue to have zero genus. We will need a way to describe how the different cycles in g_0 are connected through the action of g .

Definition A.7 (Connectedness). Given two elements $g, g_0 \in S_N$. We define the *connectedness* of g over g_0 , written as $q_{g_0}(g)$, to be the set quotient $(P(g) \vee P(g_0))/P(g_0)$, which is itself a partition $q_{g_0}(g) \in P_{\#(g_0)}$.

Note that the quotient is well defined since $P(g_0) \leq P(g) \vee P(g_0)$. We will often drop the subscript g_0 when it is clear which base permutation we refer to. The connectedness $q_{g_0}(g)$ measures how the different orbits of g_0 are joined by actions of g . Besides connectedness there is another quantity we can define that measures the number of connected components.

Definition A.8. Given $g, g_0 \in S_N$. We denote $\#(g \vee g_0)$ to be the number of orbits of where \mathbb{Z}_N is split under the joint action of g and g_0 . By the “joint action” we mean the action on \mathbb{Z}_N by the subgroup generated by $\langle g, g_0 \rangle$.

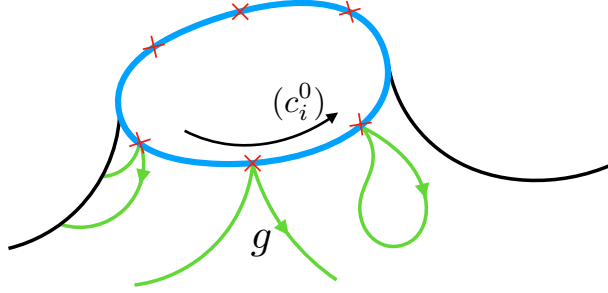
Note that $\#(g \vee g_0) = \#(P(g) \vee P(g_0)) = \#(q_{g_0}(g))$. This number equals $\#(g \vee g_0) = \#(g_0)$ for $g \in \Gamma(g_0, e)$. More generally, we have to discuss the topology of permutation elements.

Definition A.9. Given elements $g, g_0 \in S_N$ we define an *admissible surface* Σ for g (based over g_0) as a disjoint union of oriented two dimensional Riemann surfaces with a total of $\#(g_0)$ connected boundaries, and such that it is possible to decorate this surface as follows:

1. Each connected boundary has $|c_i^0|$ marked points where $i = 1, \dots, \#(g_0)$ labels the boundary. Each point is ordered and marked using an element from the cycle (c_i^0) . The orientation of the ordering is fixed by the orientation of the surface.

⁴This terminology comes from [197] who first studied the case of two boundaries, where the embedding surface of the graph is annular.

2. The permutations in g are represented by oriented curves on Σ that pass between two different marked points on the boundaries according to g . Each marked point has a curve entering and leaving, and we locally pick these in the same direction as the cycles in c_0 (see Figure below.)
3. The curves are all mutually *non-crossing*.



Theorem A.5. For all $g \in S_N$ write:

$$d(g_0, g) + d(g, e) = d(g_0, e) + 2(\#(g_0) - \#(g \vee g_0)) + 2G_{g_0}(g) \quad (\text{A.24})$$

then $G_{g_0}(g) \geq 0$. Furthermore there exists an admissible surface for g that has genus $G_{g_0}(g)$ and $\#(g \vee g_0)$ connected components. This is the minimal possible genus and maximal possible number of connected components.

Proof. It is clear we can always work with surfaces that have $\#(g \vee g_0)$ connected components and this is the maximal number. Without loss of generality we can now assume that $\#(g \vee g_0) = \#(q_{g_0}(g)) = 1$, since the more general case is then just a sum over the partitions in $q_{g_0}(g)$.

Firstly there always exists at least one *admissible* surface (not necessarily with minimal genus) since we can simply thicken the lines defined by g into tubes and connect these tubes onto $\#(g_0)$ disks near the marked points on the boundaries of the disk and according to g . Then each curve segment simply pass through their respective tubes and do not cross each other.

Consider some *admissible* surface Σ . Let $c_i \in g$ be a cycle. The corresponding line segments are \mathcal{L}_k^i where $k = 1, \dots, |c_i|$. Consider a closed curve C_i that hugs tightly to the line segments in this cycle - following the direction of the cycle and strictly “inside” the boundary anchored curve $\cup_k \mathcal{L}_k^i$. Locally “inside” is defined such that the curve does not intersect the boundary. It also does not intersect any of the g curves by the non-crossing condition. Perform surgery on this closed curve C_i . That is cut along the curve, and insert two disks to close up the surface along the cuts. Discard any boundaryless Riemann surface that gets disconnected under this process - by the non-crossing condition the result is a single surface with the original $\#(g_0)$ boundaries. There can only be one boundaryless surface \mathcal{B} that is discarded. This produces a new Riemann surface Σ' that is also *admissible*. The genus of this new surface must decrease:

$$G(\Sigma') \leq G(\Sigma) \quad (\text{A.25})$$

This is because the Euler character under connected sum must decrease by an amount corresponding to the Euler character of a sphere:

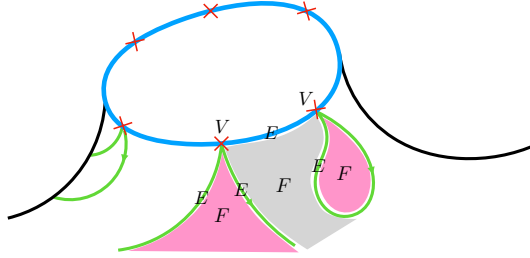
$$\chi(\Sigma) = \chi(\Sigma' \sqcup \mathcal{B}) - 2 \quad (\text{A.26})$$

The Euler character of \mathcal{B} is bounded above by 2 and contributes additively:

$$\chi(\Sigma) = \chi(\Sigma') + \chi(\mathcal{B}) - 2 \leq \chi(\Sigma') \quad (\text{A.27})$$

Since the number of simple boundaries in Σ and Σ' is the same we get Eq. (A.25). On Σ' the curve C_i is now contractible.

Continue this process for all cycles in g such that the corresponding curves $\cup_k \mathcal{L}_k^i$ for all i are contractible. Similarly by including line segments between adjacent marked points on the boundaries, oriented opposite to the c'_0 s, we can cut along closed cycles on the “outside” of the cycles. It is easy to see that these can be represented by the cycles in $(g_0)g^{-1}$. Applying surgery to all of these cycles gives the final surface that we call Σ_0 . We now give a triangulation of the surface Σ_0 . We have edges corresponding to the curves defined by g . There are N of these. There are also edges on the boundaries of Σ_0 between the marked points. There are also N of these. So we have $E = 2N$. The vertices have 4 lines meeting at the boundary for each marked point on the boundary. There are $V = N$ of these. See for example:



The faces are the interiors of the cycles in g and gg_0^{-1} so $F = \#(g) + \#(g_0)$. Thus:

$$\chi = 2 - 2G(\Sigma_0) - \#(g_0) \quad (\text{A.28})$$

$$= V - E + F = -N + \#(g) + \#(g_0) = N - d(g, e) - d(g, g_0) \quad (\text{A.29})$$

Thus:

$$2G(\Sigma_0) = 2 + d(g, e) + d(g, g_0) - d(g_0, e) - 2\#(g_0) \quad (\text{A.30})$$

Which gives $G(\Sigma) \geq G(\Sigma_0) = G_{g_0}(g)$. In particular this implies that Σ_0 has the minimal genus, since for any other valid surface $\tilde{\Sigma}$ with lower genus $G(\tilde{\Sigma}) < G_{g_0}(g)$ we run the above surgery argument and arrive at a contradiction: $G(\tilde{\Sigma}) \geq G_{g_0}(g)$. \square

Finally we give a definition of the multi-annular non-crossing permutations.

Definition A.10. A multi-annular non-crossing permutation g for g_0 with $\#(g_0) > 1$ is a group element with $G(g) = 0$ as defined in Eq. (A.24) and such that $\#(g \vee g_0) = 1$ (fully connected). We will denote these $ANC_{g_0} = ANC_{|c_0^1|, |c_0^2|, \dots}$.

Appendix B

Temperley-Lieb Algebra

In this appendix, we will summarize basic aspects of the Temperley-Lieb (TL) algebra and its representation theory. There are many different flavors of classifying the representations of TL algebra, with the two most prominent approaches being: 1. As a quotient of the Iwahori-Hecke algebra [198, 199], or 2. As an algebraic module acting on a specific class of “link diagrams”. We will take the second approach here, also known under the name of *standard module* [155, 200], or *cell modules* [201]. The goal of this appendix is to provide a pedagogical review on various properties of the TL algebra and the standard module used in our computations. Due to the length constraint we will omit the proof of many important theorems. Interested reader can refer to [155] for a more complete and rigorous treatment on this subject.

B.1 Basic definitions

First, we define, for any positive integer n , an n -*diagram*. It is constructed by first drawing two parallel lines, each with n marked points. Then, the set of $2n$ points are connected pairwise via n non-crossing strands that lies entirely within the space between two parallel lines. We also define a pairwise product of two n -diagrams by concatenating two diagrams side by side and replacing each closed loop by a factor of χ . For example, for $n = 4$ we write:

$$\text{Diagram 1} \cdot \text{Diagram 2} = \text{Diagram 3} = \chi \text{Diagram 4} \tag{B.1}$$

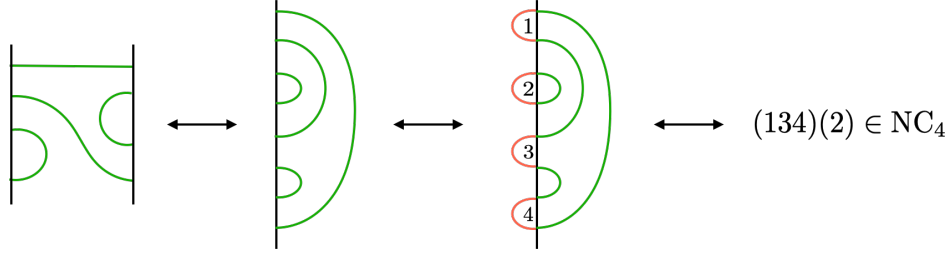
This product is associative by construction. Although the parameter χ is considered to be complex in more general settings, in what is relevant to this note we will assume $\chi \in \mathbb{R}_+$ and we will often consider the limiting case where $\chi \gg 1$.

Definition B.1 (Temperley-Lieb algebra). The Temperley-Lieb algebra TL_n for a positive integer n , is the (complex) vector space spanned by n -diagrams. This vector space is equipped with a pairwise product by taking the diagrammatic product from above and extend it to the whole vector space bilinearly.

Lemma B.1. *The dimension of TL_n vector space is equal to the n -th Catalan number C_n .*

Proof. To find the dimension of TL_n , we need to count the total number of distinct n -diagrams for given n . There is a bijection $D(\cdot)$ between n -diagrams and NC_n , the non-crossing permutations on n elements,

defined as follows. First, one deforms the n -diagram h by rotating the RHS of the diagram by 180 degrees and append it below the LHS. Having done so one now has a diagram with non-crossing strands connecting $2n$ marked points arranged on a single line. These diagrams are of one to one correspondence to the double line notations of non-crossing permutations on n elements. This fact can be made clear by concatenating the left of the diagram with n “caps” and assigning a number to each cap. After doing so, the diagram factors into a set of non-crossing closed blocks partitioning the set $\{1, \dots, n\}$, which can be further identified to the cycle decomposition of a non-crossing permutation $D(h) \in \text{NC}_n$. We give an example of the map D below.



The number of distinct non-crossing permutations on n elements is given by Catalan numbers C_n . The detailed form of C_n can be worked out using a simple generating function, but for reference here let us consider a slight generalization by weighing each cycle of $D(h)$ by a power of q . Define

$$\begin{aligned}
 C(q, z) &= \left| \begin{array}{l} +z \text{ (circle)} \\ +z^2 \left(\text{(S)} + \text{(O)} \right) \\ + \dots \end{array} \right. \quad \text{(B.2)} \\
 &= 1 + qz + (q + q^2)z^2 + \dots
 \end{aligned}$$

to be the q -weighted generating function for NC_n and $F(q, z)$ the generating function for connected diagrams, i.e.

$$C(q, z) = 1 + F(q, z) + F(q, z)^2 + \dots = \frac{1}{1 - F(q, z)} \quad \text{(B.3)}$$

$C(q, z)$ and $F(q, z)$ satisfies the following Schwinger-Dyson equation

$$\begin{aligned}
 F(q, z) &= z \text{ (circle)} + z^2 \text{ (S)} + z^3 \left(\text{(S)} + \text{(O)} \right) + \dots \\
 &= z \text{ (circle)} + z^2 \text{ (S)} + z^3 \text{ (S)} + \dots \quad \text{(B.4)}
 \end{aligned}$$

or

$$F(q, z) = \frac{qz}{1 - zC(q, z)} \quad \text{(B.5)}$$

which can be solved to give

$$C(q, z) = \frac{1 - z(q - 1) - \sqrt{(1 + z(q - 1))^2 - 4qz}}{2z} \quad \text{(B.6)}$$

The proof that the algebra generated from this definition is isomorphic to the diagrammatic one (Definition B.1) can be found in standard references of the subject.

We conclude this subsection by introducing a trace function on TL_n .

Definition B.3. For a positive integer n , $\text{Tr}_{\text{TL}_n} : \text{TL}_n \rightarrow \mathbb{C}$ is a cyclic linear function on TL_n . It is defined diagrammatically on an n -diagram by closing the strands on opposing marked points on two lines and assign a power of χ for each closed loop obtained this way. Tr_{TL_n} is cyclic from definition, and it is extended to the full algebra using linearity.

For example,

$$\text{Tr}_{\text{TL}_n} \left(\left(\begin{array}{c} | \quad | \\ \text{---} \\ | \quad | \end{array} \right) \right) = \left(\begin{array}{c} | \quad | \\ \text{---} \\ | \quad | \end{array} \right) = \chi^3. \quad (\text{B.15})$$

We also define a normalized version of this trace, denoted by $\text{Tr}_{\widehat{\text{TL}}} = \chi^{-n} \text{Tr}_{\text{TL}_n}$ ¹. This normalized trace is consistent with respect to all n and satisfies the following properties:

$$\text{Tr}_{\widehat{\text{TL}}}(\text{id}) = 1, \quad \text{Tr}_{\widehat{\text{TL}}}(h) = \chi \text{Tr}_{\widehat{\text{TL}}}(he_{n-1}) \quad (\text{B.16})$$

where $h \in \text{TL}_{n-1} \subset \text{TL}_n$ is an element in the subalgebra of TL_n consisting of elements such that the n -th marked point on both sides of its diagram are connected via a strand. This fact can be illustrated using the diagrams below.

$$\begin{aligned} \text{Tr}_{\text{TL}_n} \left(\left(\begin{array}{c} | \quad | \\ \text{---} \\ | \quad | \end{array} \right) \right) &= \left(\begin{array}{c} | \quad | \\ \text{---} \\ | \quad | \end{array} \right) = \left(\begin{array}{c} | \quad | \\ \text{---} \\ | \quad | \end{array} \right) = \text{Tr}_{\text{TL}_{n-1}} \left(\left(\begin{array}{c} | \quad | \\ \text{---} \\ | \quad | \end{array} \right) \right), \\ \text{Tr}_{\text{TL}_n} \left(\left(\begin{array}{c} | \quad | \\ \text{---} \\ | \quad | \end{array} \right) \right) &= \left(\begin{array}{c} | \quad | \\ \text{---} \\ | \quad | \end{array} \right) = \chi \text{Tr}_{\text{TL}_n} \left(\left(\begin{array}{c} | \quad | \\ \text{---} \\ | \quad | \end{array} \right) \right) \end{aligned} \quad (\text{B.17})$$

where we used colored blocks to indicate arbitrary connections in the region. After putting back the normalization factors one recovers Eq. (B.16). In fact the property Eq. (B.16) completely characterizes $\text{Tr}_{\widehat{\text{TL}}}$, as shown in the following lemma:

Lemma B.2. $\text{Tr}_{\widehat{\text{TL}}}$ is the unique linear function on TL_n that is cyclic ($\text{Tr}(ab) = \text{Tr}(ba)$) and such that Eq. (B.16) is true.

Proof. Every element $h \in \text{TL}_n$ can be written as a product of finitely many generators $h = e_{i_1} \cdots e_{i_k}$ where $i_k \in \{1, \dots, n-1\}$. The e_{i_j} 's in the string can be further made unique by using Eq. (B.14) to permute the list and eliminate any duplicates. To evaluate $\text{Tr}_{\widehat{\text{TL}}}(h) = \text{Tr}_{\widehat{\text{TL}}}(e_{i_1} \cdots e_{i_k})$, we use cyclicity of the trace to

¹This trace is usually referred to as the *Markov trace* in math literature.

cycle the possible e_{n-1} to the end of the list, and we pick up a factor of χ if there is one. Now since the new list of generators does not contain e_{n-1} , the new element h' obtained by multiplying the new list of generators is in the subalgebra $\text{TL}_{n-1} \subset \text{TL}_n$. Using Eq. (B.16) we see that $\text{Tr}_{\widehat{\text{TL}}}(h) = \chi^b \text{Tr}_{\widehat{\text{TL}}}(h')$ where $b = 0$ if there is no e_{n-1} in the generating string of h and $b = -1$ if there is one. Now by repeated iteration of this whole process $n - 1$ times, one can eliminate all the generators of h and obtain $\text{Tr}_{\widehat{\text{TL}}}(h) = \chi^{-k} \text{Tr}_{\widehat{\text{TL}}}(\text{id}) = \chi^{-k}$ where k is the length of the generating list $h = e_{i_1} \cdots e_{i_k}$ with non-duplicating generators. Thus the condition Eq. (B.14) uniquely fixes the action of $\text{Tr}_{\widehat{\text{TL}}}$ on every element in TL_n . \square

B.2 The standard module

To define an algebraic module, one must first form the vector space for the algebra to act on. In the standard module of Temperley-Lieb algebra such vector space is spanned by a collection of diagrams called *link states* (or *cup diagrams* in Westbury [200]).

An n -diagram can be cut in half across the middle line and expose a number of “defects”, each corresponding to a connection between a point in the left and another point in the right. The number of defects, denoted l , is always even if n is even and odd if n is odd, which we keep track of using an integer $k \in \mathbb{Z}_{\geq 0}$, by saying that $l = 2k$ when n is even and $l = 2k + 1$ when n is odd. We will call a half diagram obtained this way an (n, k) -link state.² A link state will be drawn with the lines on the left and any possible defects facing right, as shown in Fig. (B.1). We will refer to the set of all (n, k) -link states as $\mathcal{B}_k^{(n)}$.

$$\mathcal{B}_1^{(4)} = \left\{ \begin{array}{c} \text{---} \\ \text{---} \\ \text{---} \\ \text{---} \\ \text{---} \\ \text{---} \end{array} \begin{array}{c} \text{---} \\ \text{---} \\ \text{---} \\ \text{---} \\ \text{---} \\ \text{---} \end{array} \right\}$$

Figure B.1: All the possible $(4, 1)$ -link states.

Lemma B.3. For integer n and $k \leq \lfloor n/2 \rfloor$, the number of distinct (n, k) -link states is equal to the number of standard Young tableaux of shape $(\lfloor n/2 \rfloor + k, \lfloor n/2 \rfloor - k)$.

$$|\mathcal{B}_k^{(n)}| = \#\text{SYT} \left(\left\lfloor \frac{n}{2} \right\rfloor + k, \left\lfloor \frac{n}{2} \right\rfloor - k \right) \quad (\text{B.18})$$

Proof. Note that there is a bijection between a link state and a *lattice word* consisting of left and right brackets $\{[,]\}$ such that every prefix has more opening brackets than closing brackets. For example, $[[[[]]][]$ is a lattice word but $[[[]][[]]$ is not since the prefix $[[[]]$ has more $]$'s than $[$'s. To put it in another way, there can never be a closing bracket without a previous matched opening bracket, but a standalone opening bracket is allowed. To see that this is true, simply assign an opening-closing pair to a closed strand in the link state and any standalone opening brackets to defects, e.g.

$$\text{---} \longleftrightarrow \text{[[[[]]]} \quad (\text{B.19})$$

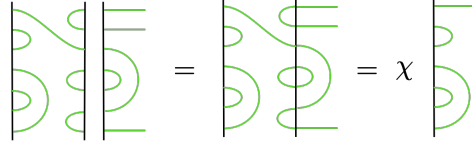
²Note that we label link states by k , (one half of) the number of *defects*, as opposed to the common practice of labeling by the number of *closed arcs* $p = \lfloor n/2 \rfloor - k$. The main advantage for this notation change is to make the various formulae regarding to different k sector in the main text cleaner.

where we have color coded the brackets to the matching strands. This correspondence works in either way so it is really a bijection. Now it is a standard result that the number of lattice words are counted by standard Young tableaux: Given a standard Young tableau of shape (p, q) , construct the following word (s_1, \dots, s_{p+q}) via

$$s_i = \begin{cases} [, & \text{if } i \text{ is in first row,} \\], & \text{if } i \text{ is in second row.} \end{cases} \quad (\text{B.20})$$

Then at any given point i there can never be more closing brackets than opening brackets since the tableau is standard. The number of total brackets are $p + q$ whereas the number of standalone opening brackets are $p - q$ from which one immediately sees that $p = \lceil n/2 \rceil + k$ and $q = \lfloor n/2 \rfloor - k$. \square

For a n -diagram $h \in \text{TL}_n$, we define a left action of h on a link state v in a similar fashion by concatenating h and v from left to right, removing any disconnected open strands and assign a factor of χ for each closed loop. We illustrate this definition with an example:



$$\text{Diagram} = \chi \text{Diagram} \quad (\text{B.21})$$

This action naturally defines an algebraic module (representation) on the vector space spanned by link states. We will refer to such module as the *link module*.

Definition B.4 (link module). For given integer n , the *link module*, denoted by $\mathcal{M}^{(n)}$, is a left TL_n -module on the collective vector space spanned by all link states whose action is given by the diagrammatic action above and is extended to the whole vector space through linearity.

Note that the number of defects is not necessarily conserved under the action. (Eq. (B.21) is an example where it decreases by two) However, it can only close defects in pairs, so k is always non-increasing under this action. Acknowledging this fact, one can identify TL_n -submodules $\mathcal{M}_k^{(n)} \subseteq \mathcal{M}^{(n)}$ spanned by all (n, k') -link states with $k' < k$. There is a natural chain of submodules

$$\mathcal{M}_0^{(n)} \subset \mathcal{M}_1^{(n)} \subset \dots \subset \mathcal{M}_{\lfloor n/2 \rfloor}^{(n)} = \mathcal{M}^{(n)} \quad (\text{B.22})$$

Consecutive quotients on this chain determines quotient TL_n -modules called *standard modules*:

Definition B.5 (The standard module). For integer n and $k < \lfloor n/2 \rfloor$, the (n, k) -*standard module*, denoted by $\mathcal{V}_k^{(n)}$, is the quotient module

$$\mathcal{V}_k^{(n)} = \frac{\mathcal{M}_{k+1}^{(n)}}{\mathcal{M}_k^{(n)}}. \quad (\text{B.23})$$

The standard module vector space (which we will also refer to as $\mathcal{V}_k^{(n)}$ by an abuse of notation) is the coset $[\mathcal{M}_{k+1}^{(n)} : \mathcal{M}_k^{(n)}]$, which is isomorphic to the vector space spanned by (n, k) -link states. In this regard, we will often talk about the action of (n, k) -standard module on (n, k) -link states directly, forgetting the fact that it is really the coset that $\mathcal{V}_k^{(n)}$ is acting on. Diagrammatically, the action of an n -diagram h on a (n, k) -link state v is given by the same action as in the link module, but with the further requirement that h maps v to zero whenever the number of defects k decreases under the action.

There is a natural inner product $\langle \cdot, \cdot \rangle$ on the vector space $\mathcal{V}_k^{(n)}$ defined as follows:

Definition B.6. For $x, y \in \mathcal{B}_k^{(n)}$, the inner product between x and y , denoted by $\langle x, y \rangle$, is obtained by first flipping x around the vertical axis and identifying it with the vertical border of y . Then, define $\langle x, y \rangle$ by assigning a factor of χ for every closed loop obtained this way. Furthermore, we require $\langle x, y \rangle$ to be nonzero only when every defect of x is connected to a defect of y . This product is extended to the full vector space $\mathcal{V}_k^{(n)}$ by requiring the form being linear in the y and anti-linear in x .

As an example, we have

$$\left\langle \begin{array}{|c|} \hline \text{---} \\ \hline \end{array}, \begin{array}{|c|} \hline \text{---} \\ \hline \end{array} \right\rangle = \begin{array}{|c|} \hline \text{---} \\ \hline \end{array} = \chi, \quad \left\langle \begin{array}{|c|} \hline \text{---} \\ \hline \end{array}, \begin{array}{|c|} \hline \text{---} \\ \hline \end{array} \right\rangle = \begin{array}{|c|} \hline \text{---} \\ \hline \end{array} = 0, \quad (\text{B.24})$$

Note that the link state basis $\mathcal{B}_k^{(n)}$ is *not* orthogonal under this inner product. However, they are approximate orthogonal at large χ , with corrections $\sim O(1/\chi)$. This inner product is invariant under the TL action.

Lemma B.4. For all $x, y \in \mathcal{V}_k^{(n)}$ and $h \in TL_n$,

$$\langle x, Uy \rangle = \langle U^\dagger x, y \rangle, \quad (\text{B.25})$$

where the “adjoint” U^\dagger is obtained by flipping the n -diagrams across horizontally and conjugating the complex coefficients.

Along with the inner product we define another sesquilinear form $|\cdot \cdot| : \mathcal{V}_k^{(n)} \times \mathcal{V}_k^{(n)} \rightarrow TL_n$ that takes two (n, k) -link states and form a n -diagram.

Definition B.7. For $x, y \in \mathcal{B}_k^{(n)}$, denote $|x y|$ to be the unique n -diagram formed by flipping y across the vertical axis and identifying its defects with the defects of x . This form is extended to the full vector space in the same way as in Definition B.6.

For example,

$$\left| \begin{array}{|c|} \hline \text{---} \\ \hline \end{array} \begin{array}{|c|} \hline \text{---} \\ \hline \end{array} \right| = \begin{array}{|c|} \hline \text{---} \\ \hline \end{array} \quad (\text{B.26})$$

The usefulness of Definition B.7 comes from the following lemma.

Lemma B.5. If $x, y, z \in \mathcal{V}_k^{(n)}$, then

$$|x y| z = \langle y, z \rangle x \quad (\text{B.27})$$

Proof. Without loss of generality we can consider the case where all of x, y, z are (n, k) -link states. If $|x y|$ decreases the number of defects in z , then the LHS of Eq. (B.27) vanishes. This is consistent with the RHS as since there must exist disconnected strands in $\langle y, z \rangle$ when such a pair of defect is closed, forcing $\langle y, z \rangle = 0$. It remains to check the case where no defects are closed. In this case the LHS of Eq. (B.27) will be proportional to x . The proportionality factor is given by $\chi^\#$, where $\#$ is the number of closed loops in the concatenation, which is the same as the number of closed loops in calculating $\langle y, z \rangle$. \square

It is sometimes useful to think of $|x y|$ as the outer product of link states xy^\dagger , with the adjoint $y^\dagger \in \bar{\mathcal{V}}_k^{(n)}$ in the dual module obtained by flipping y around its vertical axis. However such analogy is only true when all

of x, y, z lie in the same (n, k) -standard module. When it is not the case, say when $x, y \in V_k^{(n)}$ and $z \in V_{k'}^{(n)}$, then not only $\langle y, z \rangle$ is not defined, $|x y|z$ will not be proportional to x . For example,

(B.28)

In general, the standard module classify all the finite dimensional irreducible representations of TL_n for almost all values of χ , except for a discrete set of points when $\chi < 2$. The key to proving this proposition is by studying the degeneracy of the inner product $\langle \cdot, \cdot \rangle$ through its *Gram matrices* $G_k^{(n)}$. The idea is very similar to the process of determining the reducibility of Verma modules of Virasoro algebra in 2d CFT: $G_k^{(n)}$ being non-singular implies the irreducibility of $\mathcal{V}_k^{(n)}$. When $G_k^{(n)}$ is singular (i.e. $\det G_k^{(n)} = 0$), there will be additional null states that one needs to discard to obtain a irreducible representation.

To end this short review we quote an important theorem, first due to Jones [165] and studied in more detail by Westbury [200].

Theorem B.6 (Jones). *When $\chi \neq 2 \cos(m\pi/n)$ for some integer $m \geq 3$, the algebra TL_n is semisimple and the standard modules $\mathcal{V}_k^{(n)}$ form a complete set of finite dimensional irreducible non-isomorphic representations of TL_n .*

Due to the length constraint we will not present a proof for this theorem. Interested reader can refer to the various literature (e.g. Refs. [155, 200]) on this subject. Throughout this note we always work with integer $\chi \geq 2$, and we frequently consider the case $\chi \gg 1$. In this regime the standard modules are always irreducible.

Appendix C

Supplement to Chapter 3

C.1 Proof of 1TN phase diagram

In this appendix we give a proof for the single site phase diagram Fig. (3.4) appeared in Sec. (3.4). This proof draws heavily from the results in Appendix A, in particular the theorem given in Appendix A.4.

To set up the problem, we consider the group $S_N = S_{nm}$ and the elements g_A and g_B with n cycles each and defined as

$$g_B = (1 \dots m)(m + 1 \dots 2m) \dots (nm - m + 1 \dots nm) \quad (\text{C.1})$$

$$g_A = (m/2 + 1 \dots 3m/2)(3m/2 + 1 \dots 5m/2) \dots (nm - m/2 + 1 \dots m/2) \quad (\text{C.2})$$

where the cycles contain all element that appear in between the numbers shown and are cyclicly ordered. These are defined for $n \geq 1$ and $m/2 \geq 1$ integers. These have the property that $\Gamma(g_A, e) \cap \Gamma(g_B, e)$ is non-trivial (contains more than the identity), although the triple intersection $\Gamma(g_A, e) \cap \Gamma(g_B, e) \cap \Gamma(g_A, g_B) = \emptyset$. This is the main origin of “frustration” in the problem below, and distinguishes the reflected entropy from negativity. There is a unique element we call X that satisfies the property $X \in \Gamma(g_A, e) \cap \Gamma(g_B, e)$ and it minimizes $d(X, g_{A,B})$. It has $2n$ cycles:

$$X = (1 \dots m/2)(m/2 + 1 \dots m) \dots (nm - m/2 + 1 \dots nm) \quad (\text{C.3})$$

Note that $P(X) = P(g_A) \wedge P(g_B)$. If $m = 2$ then $X = e$.

The free energy function we wish to minimize is:

$$f(g) = x_A d(g, g_A) + x_B d(g, g_B) + d(g, e) \quad (\text{C.4})$$

for $x_{A,B} \geq 0$. We wish to prove:

Theorem C.1. *For all $x_A, x_B > 0$ then the following minimum is achieved on a simple four element subset:*

$$f_{\min} \equiv \min_{g \in S_{mn}} f(g) = \min_{g \in \{e, X, g_A, g_B\}} f(g) \quad (\text{C.5})$$

Remark. This theorem only states that the minimum of $f(g)$ can be achieved for $g \in e, X, g_A, g_B$, but does not exclude the possibility of other elements also saturating the minimum. In fact there exists other minimal

elements $g \in S_{mn}$ that lives at the phase boundaries of the phase diagram Fig. (3.4), and they are crucial for smoothing out the phase transition near $x_A + x_B = 1$. We will investigate the detailed form of these elements in Appendix C.2.

Preliminary. We firstly note there are regions in the phase diagram that are easy to deal with:

$$x_A + x_B < 1 : \quad f(g) \geq d(g, e)(1 - x_A - x_B) + f(e) \geq f(e) \quad (\text{C.6})$$

where we have used the triangle inequality: $d(g_{A,B}, g) + d(g, e) \geq d(e, g_{A,B})$. So we have equality iff $d(g, e) = 0$. For $x_A + x_B = 1$ then we have equality for $g \in \Gamma(g_A, e) \cup \Gamma(g_B, e)$. Similarly:

$$x_A > x_B + 1 : \quad f(g) \geq (x_A - x_B - 1)d(g, g_A) + f(g_A) \geq f(g_A) \quad (\text{C.7})$$

where we have used the triangle inequality: $d(g_A, g) + d(g, g_B) \geq d(g_A, g_B)$ and $d(g_A, g) + d(g, e) \geq d(e, g_A)$. Equality is achieved iff $g = g_A$. For $x_A = x_B + 1$ we still only have g_A as the minimal element since the intersection $\Gamma(g_A, g_B) \cup \Gamma(g_A, e) = \{g_A\}$. Similarly for $A \leftrightarrow B$. Thus the *non-trivial region* is $x_A + x_B > 1$, $x_A < x_B + 1$ and $x_B < x_A + 1$. Indeed the phase diagram is convex:

Lemma C.2. *If the minimum for $f(g)$ is achieved for some g_\star at two locations in the $(x_A, x_B)_{1,2}$ phase diagram then g_\star is also minimal at:*

$$(x_A, x_B)_\lambda = \lambda(x_A, x_B)_1 + (1 - \lambda)(x_A, x_B)_2 \quad 0 \leq \lambda \leq 1 \quad (\text{C.8})$$

Proof. Note that (in hopefully clear notation) for $g \in S_{mn}$:

$$f_\lambda(g) = \lambda f_1(g) + (1 - \lambda)f_2(g) \geq \lambda f_1(g_\star) + (1 - \lambda)f_2(g_\star) = f_\lambda(g_\star) \quad (\text{C.9})$$

□

Thus, for the general Theorem C.1 we can limit ourselves to the line $x_A = x_B > 1/2$. Convexity will do the rest, since all four elements $\{g_A, g_B, X, e\}$ are already represented somewhere on the phase diagram away from the *non-trivial region*. For $m = 2$ there is a much simpler proof than the proof discussed below, we present this in Appendix C.1.1.

Proof. (of Theorem C.1) As discussed above we need only consider $x_A = x_B = x \geq 1/2$. Consider the topological discussion of Appendix A.4 for $g_0 = X$. We classify all elements in S_{mn} using their connectedness $q_X(g)$ over X . Recall that $q_X(g) = (P(g) \vee P(X))/P(X)$. The quotient is a partition $q_X(g) \in P_{2n}$.

Set $q = q_X(g)$ and $n_1 = \#_1(q)$, where $\#_1(q)$ counts the number of length 1 blocks in q . It satisfies $0 \leq n_1 \leq 2n$. Now write:

$$f(g) = f(e) + (1 - 2x)d(e, X) + n - \lfloor n_1/2 \rfloor - 2x\delta_{n_1,0} \quad (\text{C.10})$$

$$+ 2x(G_A - G_X) + 2x(G_B - G_X) + 2(G_X) \quad (\text{C.11})$$

$$+ (2x - 1) \left(d(g, X) - 2n + \#(q) \right) \quad (\text{C.12})$$

$$+ 2x \left(\#(q) - \#(q \vee t_A) - \#(q \vee t_B) + \delta_{n_1,0} \right) \quad (\text{C.13})$$

$$+ \left(n + \lfloor n_1/2 \rfloor - \#(q) \right) \quad (\text{C.14})$$

where $\lfloor \cdot \rfloor$ is the floor function, $G_{A,B} \equiv G_{g_{A,B}}(g)$ and $G_X \equiv G_X(g)$ were defined in Lemma A.5. And $t_{A,B} = q(g_{A,B})$ or more specifically: $t_B = (12)(34) \dots (2n-1, 2n)$ and $t_A = (23)(34) \dots (2n, 1)$. To arrive at the formula above we have used:

$$\#(g_A \vee g) = \#(t_A \vee q(g)), \quad \#(g_B \vee g) = \#(t_B \vee q(g)) \quad (\text{C.15})$$

which follows from $\#(g_A \vee g) = \#(P(g_A) \vee P(g))$ and since $P(g_A) \geq P(X)$ this implies that $P(g_A) \vee P(g) \geq P(X)$ and so we can take the set quotient $(P(g_A) \vee P(g))/P(X) = (P(g_A) \vee (P(g) \vee P(X)))/P(X) = t_A \vee q(g)$. And the number of sets is the same under the quotient $\#(P(g_A) \vee P(g)) = \#(t_A \vee q(g))$. Similarly for $\#(g_B \vee g)$.

We aim to show that each bracketed terms in lines (C.11-C.14) are all positive. That is we wish to establish the estimate:

$$f(g) \geq f(e) + (1 - 2x)d(e, X) + (n - \lfloor n_1/2 \rfloor) - 2x\delta_{n_1,0} \quad (\text{C.16})$$

Assuming this is the case then:

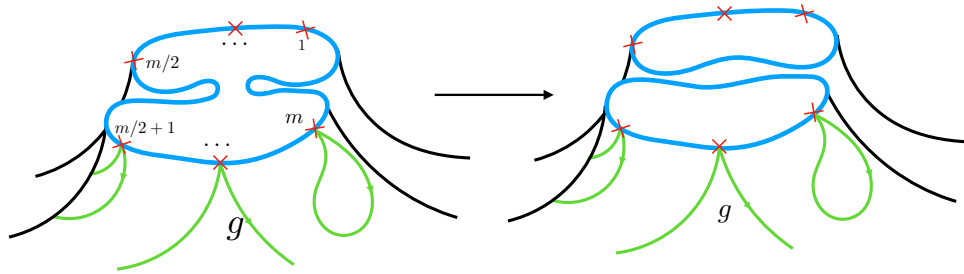
$$\min_{g \in S_{mn}} f(g) \geq f(e) + (1 - 2x)d(e, X) + \min_{0 \leq n_1 \leq 2n} ((n - \lfloor n_1/2 \rfloor) - 2x\delta_{n_1,0}) = \min_{g \in e, X, g_A, g_B} f(g) \quad (\text{C.17})$$

which ,together with:

$$\min_{g \in S_{mn}} f(g) \leq \min_{g \in e, X, g_A, g_B} f(g) \quad (\text{C.18})$$

proves the theorem. The last step in Eq. (C.17) is by direct computation. It also follows since the bounds (C.11-C.13) that we derive below are all tight for the elements $g = X, g_A, g_B$.

We need the bound $G_A \geq G_X$ in line Eq. (C.11). This follows from the construction of the genus. We use the surface Σ_0 for g based over g_A which has genus G_A . We then deform the n boundaries of this surface into $2n$ boundaries by pinching - dividing the m marked points into two sets of $m/2$ marked points on the new boundary (see figure below). This deformed Σ'_0 is an *admissible surface* of genus $G(\Sigma_0)$ for g based over X since we can do this deformation without touching any of the curves. By Theorem A.5 we must have $G_A = G(\Sigma_0) = G(\Sigma'_0) \geq G_X$. Similarly $G_B \geq G_X$ and $G_X \leq 0$ always.



Moving to the next line we also need the lower bound Eq. (C.12):

$$d(g, X) \geq (2n - \#(q_X(g))) \quad (\text{C.19})$$

Note that $q_X(X^{-1}g) = q_X(g)$ since $\langle X, g \rangle = \langle X, X^{-1}g \rangle$. So we can equivalently prove $d(g, e) \geq (2n - \#(q_X(g)))$ for all g . This follows from Lemma C.3 applied to $g_0 = X$ and $N = nm$.

We also need to bound Eq. (C.13):

$$\#(q) - \#(q \vee t_A) - \#(q \vee t_B) + \delta_{\#_1(q),0} \geq 0 \quad (\text{C.20})$$

To do this we use Lemma C.4, which simply follows from the semimodular condition Eq. (A.21). We apply this Lemma with $N = 2n$, $q = q$, $s = t_B$ and $t = t_A$, and use the fact that $t_A \vee t_B = (\mathbb{Z}_{2n})$ and $t_A \wedge t_B = e$, giving the estimate:

$$\#(q) - \#(q \vee t_A) - \#(q \vee t_B) + 1 \geq 0 \quad (\text{C.21})$$

We can improve this estimate as follows. If there is at least one block in q of length-1 then we remove one of the double blocks in t_B where this length-1 q -block would overlap. That is we split this double block into two single blocks to give a new $t'_B < t_B$. After doing this we still have:

$$t_A \vee t'_B = (\mathbb{Z}_{2n}) \quad t_A \wedge t'_B = e \quad \#(q \vee t'_B) = \#(q \vee t_B) + 1 \quad (\text{C.22})$$

such that $\#(q) - \#(q \vee t_A) - \#(q \vee t_B) \geq 0$. Together the final estimate is Eq. (C.20).

Finally line Eq. (C.14) is positive since $\#(q) \leq n + \lfloor \#_1(q)/2 \rfloor$ (the floor) which comes simply from maximizing $\#(q)$ by splitting the remaining non length 1 blocks into pairs if $\#_1$ is even, or pairs and a triplet if $\#_1$ is odd. □

Above we needed the following results:

Lemma C.3. *For all $g_0, g \in S_N$, then:*

$$d(g, e) \geq \#(g_0) - \#(g \vee g_0) \quad (\text{C.23})$$

Proof. Map to the set of partitions P_N and consider:

$$d(g, e) - (\#(g_0) - \#(g \vee g_0)) = N - \#(P(g)) - \#(P(g_0)) + \#(P(g) \vee P(g_0)) \quad (\text{C.24})$$

$$\geq \#(P(g) \wedge P(g_0)) - \#(P(g)) - \#(P(g_0)) + \#(P(g) \vee P(g_0)) \geq 0 \quad (\text{C.25})$$

where the first equality follows since for all partitions $\#(P) \leq N$ and the second inequality uses the semimodularity property of ρ on P_N . Saturation requires that $P(g) \wedge P(g_0) = e$ and also that for all $p \leq P(g_0)$ then:

$$P(g_0) \wedge (p \vee P(g)) = (P(g_0) \wedge P(g)) \vee p = p \quad (\text{C.26})$$

□

Lemma C.4. *Given three partitions $q, t, s \in P_N$ then:*

$$\#(q \vee (t \wedge s)) - \#(q \vee t) - \#(q \vee s) + \#(q \wedge (t \vee s)) \geq 0 \quad (\text{C.27})$$

Proof. Since set partitions form a ρ -graded semimodular lattice with: $\rho(q) = N - \#(q)$ we know that the grading satisfies:

$$\rho(q_1 \vee q_2) + \rho(q_1 \wedge q_2) \leq \rho(q_1) + \rho(q_2) \quad (\text{C.28})$$

Set $q_1 = q \vee t$ and $q_2 = q \vee s$, then $q_1 \vee q_2 = q \vee s \vee t$ and $q_1 \wedge q_2 \geq q \vee (t \wedge s)$ (since $t \geq t \wedge s$ implies that $q \vee t \geq q \vee (t \wedge s)$.) Thus:

$$\rho(q \vee s \vee t) + \rho(q \vee (t \wedge s)) \leq \rho(q_1 \vee q_2) + \rho(q_1 \wedge q_2) \leq \rho(q \vee t) + \rho(q \wedge s) \quad (\text{C.29})$$

as required. \square

C.1.1 Simpler proof at $m = 2$

There is an independent proof of Theorem C.1 for $m = 2$, where there is only a three element subset on the right hand side. A quick sketch:

Proof. (For $m = 2$.) Set $x_A = x_B = x > 1/2$. Write:

$$f_{\min} = \min_{g \in S_{2n}} f'(g) \quad f'(g) = f(g_A g) = x(d(g, g_A^{-1} g_B) + d(g, e)) + d(g, g_A^{-1}) \quad (\text{C.30})$$

where it is easy to see that $g_A^{-1} g_B$ is made of two cycles of length n . We have the more general bound

$$f'(g) \geq x(d(g_A^{-1} g_B, e) + 2(\#(g_A^{-1} g_B) - \#(g_A^{-1} g_B \vee g))) + d(g, g_A^{-1}) \quad (\text{C.31})$$

where recall $1 \leq \#(g_A^{-1} g_B \vee g) \leq \#(g_A^{-1} g_B) = 2$ is the number of connected components discussed above. We minimize over the partition of S_{mn} defined by the integer $\#(g_A^{-1} g_B \vee g) = 1, 2$:

$$f_{\min,1} = \min_{g \in S_{2n}: \#(g_A^{-1} g_B \vee g)=1} f'(g) \geq x(d(g_A^{-1} g_B, e) + 2) + d(g, g_A^{-1}) \geq x2n = f'(g_A^{-1}) \quad (\text{C.32})$$

with equality iff $g = g_A^{-1}$. And also

$$f_{\min,2} = \min_{g \in S_{2n}: \#(g_A^{-1} g_B \vee g)=2} f'(g) \geq xd(g_A^{-1} g_B, e) + d(g, g_A^{-1}) \quad (\text{C.33})$$

$$= xd(g_A^{-1} g_B, e) + (2n - \#(kq)) \geq f'(e) \quad (\text{C.34})$$

where we have used the fact that all elements with $\#(g_A^{-1} g_B \vee g) = 2$ must take the form $g = k_1 q_2$ where $k, q \in S_n$ and acts on the respective elements in the two cycles of $g_A^{-1} g_B$. The minimal is achieved for $f_{\min,2}$ iff $g \in \Gamma(g_A^{-1} g_B, e)$ and $k = q^{-1}$. Minimizing over the two different sets gives:

$$f_{\min} = \min_{g \in e, g_A, g_B} f(g) \quad (\text{C.35})$$

where the minimum is achieved iff $g \in \{g_A k_1 (k^{-1})_2 : k \in \Gamma(\tau_n, e)\} \subset \Gamma(g_A, g_B)$ or $g = e$. \square

C.2 Reflected resolvent via direct group summation

In this appendix we provide a parallel approach for finding the reflected entropy resolvent Eq. (3.89). We consider factorization of $g \in S_{mn}$ into different $q \equiv q_X(g)$ sectors. In each sector we will find conditions that must be satisfied for g that minimizes the free energy. By restricting the full permutation group to these special elements we are able to arrive at an expression of the reflected entropy resolvent that matches the form given in main text.

C.2.1 Minimal elements in a fixed sector

The problem of finding elements that minimizes the free energy function Eq. (C.4) factorizes into two parts. Firstly, we seek for minimal elements for a fixed $\#(q)$ sector that saturates the two conditions Eq. (C.13) and Eq. (C.14):

$$\#(q) - \#(q \vee t_A) - \#(q \vee t_B) + \delta_{n_1,0} = 0, \quad n + \lfloor n_1/2 \rfloor - \#(q) = 0 \quad (\text{C.36})$$

Secondly, for a fixed $q \in S_{2n}$, it should be possible to find all the minimal $g \in S_{mn}$ elements where:

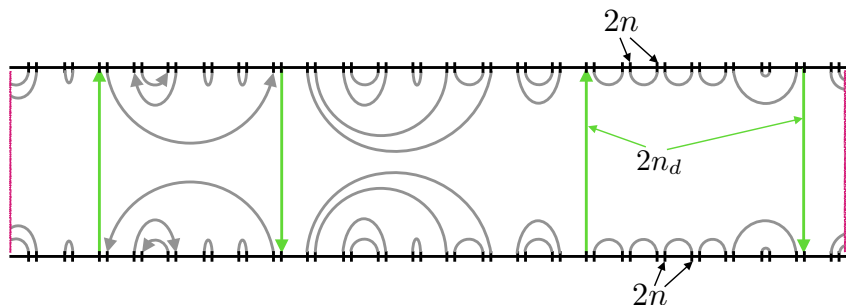
$$G_A = G_B = G_X = 0, \quad d(g, X) = 2n - \#(q) \quad (\text{C.37})$$

Note that at $x = 1/2$ (which is at the vicinity of reflected entropy phase transition at $n = 1$) we can drop the latter condition in which case the answer can be written in terms of multi-annular non-crossing elements. These elements marks the contribution of the new dominant saddles that smooth out the phases transition. We will return to this problem when we have a better handle on the minimal q elements discussed next.

Let's begin with the first minimization problem. We will look for minimal elements for fixed $\lfloor n_1/2 \rfloor = 0, \dots, n$ sector. Note that we have, somewhat arbitrarily chosen to fix the ceiling of $n_1(q)/2$ since this removes the odd case. ¹ That is fix $n_d = 0, 1 \dots, n$ then look for q 's such that:

$$\#_1(q) = 2n_d, \quad \#(q) = n + n_d, \quad \#(q \vee t_A) + \#(q \vee t_B) = n + n_d + \delta_{n_d,0} \quad (\text{C.38})$$

Theorem C.5. For fixed integer $0 \leq n_d \leq n$ all partitions which satisfy Eq. (C.38) take the form $q = P(\hat{h}g_B|_{m=2})$ where $\hat{h} \in S_{2n}$ and is best described as the following diagram:



In words, form the diagram by placing $2n$ points on the top (representing element $135 \dots (2n-1)$) and $2n$ points on the bottom (representing element $246 \dots (2n)$). The left and right ends of the strip are further identified (so it is really a annulus). $\hat{h} \in ANC_{n,n} \subset S_{2n}$ is then drawn by connecting the points pairwise without crossing as per the permutations in \hat{h} , where we split each of the $2n$ elements into two, each representing the incoming and outgoing lines of \hat{h} . Pick $2n_d$ vertically aligned defect elements that is unique up to cyclic translation. \hat{h} is then constrained to take the form that it directly connects the $2n_d$ pairs of vertical defects (one-way) and otherwise only connects within the top/bottom half strip as an inverse with respect to each other.

Proof. Fix $g_{A,B} = g_{A,B}|_{m=2}$ the $m = 2$ version of these group elements. That is $g_B = (12)(34) \dots (2n-1, 2n)$

¹Recall that the saturation of $\#(q) \leq n + \lfloor n_1/2 \rfloor$ enforces the non length-1 blocks of q into pairs if n_1 is even, or pairs and a triplet (which we do not have a good handle on) if n_1 is odd. If we instead fix the ceiling then one can show that the inequality will never be saturated when $\#_1(q)$ is odd. This will likely not change our conclusion of this section and we suspect that the effect of odd n_d sector will only serve as a correction to the resolvent.

and $g_A = (23)(34) \dots (2n, 1)$. The first two conditions Eq. (C.38) require q to be composed of pairs or singlets. In this case there is a canonical map to a permutation element $h_q \in S_{2n}$ since the order does not matter for cycles of length 2 or 1. Given this, we can easily compare $\#(h_q g_B)$ and $\#(q \vee t_B)$ since the latter is either made of “closed even blocks” (a block that does not include any singlets) or “ n_d blocks” that start and end on a singlet. The counting is doubled in $\#(h_q g_B)$ for the closed blocks in $\#(q \vee t_B)$ (since the block factors into an even and odd orbits under the action of $h_q g_B$) while it is not for the blocks containing singlets. Thus:

$$\#(h_q g_A) = 2\#(q \vee t_A) - n_d, \quad \#(h_q g_B) = 2\#(q \vee t_B) - n_d \quad (\text{C.39})$$

Substituting these relations into Eq. (C.38) and defining $\hat{h} = h_q g_B$ one can show that the conditions Eq. (C.38) are equivalent to

$$\#(\hat{h}) + \#(\hat{h} g_B g_A) = 2n + 2\delta_{n_d, 0}, \quad \#(\hat{h} g_B) = n + n_d, \quad \#_1(\hat{h} g_B) = 2n_d \quad (\text{C.40})$$

Define $\tau \equiv g_A g_B = (135 \dots 2n - 1)(246 \dots 2n)^{-1}$. We will use the notation $(k)_1(q)_2$ for $k, q \in S_n$ to mean permuting $(1, 3, 5 \dots 2n - 1)$ according to k and the elements $(2, 4, 6 \dots 2n)$ according to q . So $\tau = (\tau_n)_1(\tau_n^{-1})_2$. We then recognize the first condition in Eq. (C.40) as the problem of finding annular non-crossing permutations: $ANC_\tau = ANC_{n, n}$, i.e.

$$d(\hat{h}, e) + d(\hat{h}, \tau) = d(\tau, e) + 2(\#(\tau) - \#(\hat{h} \vee \tau)) \quad (\text{C.41})$$

which implies that the genus G_τ must be zero, see Definition A.10.

For $n_d = 0$ we can only have factorized $\hat{h} = (k)_1(k'^{-1})_2$ on the two cycles in $g_A g_B$ where $k, k' \in NC_n$ are non-crossing permutations. Now also $\#(h_q) = \#(\hat{h} g_B) = \#(kk'^{-1}) = 2n$ implying that $k = k'$. Thus:

$$q = P((k)_1(k^{-1})_2 g_B) \quad (\text{C.42})$$

For $n_d \neq 0$ we have annular non-crossing permutations. In particular we can only get one-cycles in $\hat{h} g_B$ iff there are *straight* crossings between the two sectors. Thus we are looking for a certain class of annular non-crossings with $2n_d$ straight crossings – where we count either direction of crossings.

Draw \hat{h} as shown in the diagram in the statement of the theorem. Such a diagram can be interpreted as an operator acting on the Hilbert space $(\mathcal{H}_\chi \otimes \mathcal{H}_\chi^*)^{\otimes n}$ of dimension χ^{2n} . We define this corresponding operator as $D(\hat{h})$:²

$$\left\langle e_{i_1 j_1} \otimes e_{i_2 j_2} \dots \otimes e_{i_n j_n} \left| D(\hat{h}) \right| e_{j_{2n} i_{2n}} \otimes e_{j_{2n-1} i_{2n-1}} \dots \otimes e_{j_{n+1} i_{n+1}} \right\rangle \equiv \prod_{k=1}^{2n} \left\langle i_k \left| j_{\hat{h}(k)} \right\rangle \quad (\text{C.43})$$

where $e_{ij} = |i\rangle \langle j|$ for some basis $|i\rangle$ on the \mathcal{H}_χ Hilbert space.

Given $\hat{h} \in ANC_\tau$ or it's corresponding $D(\hat{h})$, we can define $s(\hat{h})$ as the number of straight crossings and $t(\hat{h})$ as the total number of crossings. These are both even numbers. We can form \hat{h} by considering two non-crossing permutations $k_1, k_2 \in NC_{n+n_d}$ each with t defect elements placed cyclically together and such that k is constrained to connect all the n_d defect elements to and from other non-defect elements. The first defect is further constrained to connect the non-defect element directly next to it, as shown in Fig. (C.1).

²The relevant non-crossing diagrams can be understood as arising from the *affine Temperley-Lieb* (TL) algebra on $2n$ strands, which in turn has a representation acting on this Hilbert space. Indeed there is a well known correspondence between the annular non-crossing permutations and the affine TL algebra.

$\hat{h} \in ANC_{n,n}$ can be constructed by cutting open the connections at the defects of k_1 and $(k_2)^{-1}$ and glue the open connections in order, which we denote by $\hat{h} = k_1 \#_t k_2^{-1}$. We have the obvious bound $s(\hat{h}) \leq t(\hat{h})$.

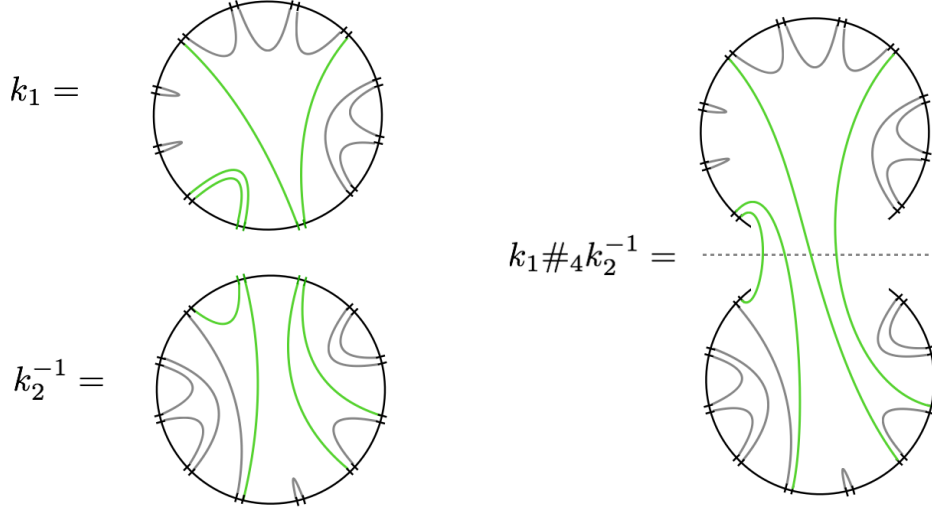


Figure C.1: The procedure for constructing $k_1 \#_t k_2^{-1}$. The green lines represent the would-be crossings.

Now we seek elements $\hat{h} \in ANC_\tau$, with $s(\hat{h}) = 2n_d$ such that

$$\chi^{\#(\hat{h}g_A)} = \text{Tr}_{\mathcal{H}_\chi^{\otimes 2n}} D(\hat{h}) = \chi^{n+n_d} \quad (\text{C.44})$$

In fact we have the following inequality:

$$\text{Tr}_{\mathcal{H}_\chi^{\otimes 2n}} D(\hat{h}) \leq \chi^{n+s(\hat{h})/2} \quad (\text{C.45})$$

and this is saturated iff $\hat{h} = k \#_t k^{-1}$ for some $k \in NC'_{n+t/2}$ in which case $s = t = 2n_d$. This proves the theorem (after applying an arbitrary rotation by conjugating by powers of to $(\tau_n)_1(\tau_n)_2$.) We prove Eq. (C.45) and the saturation condition just used in Lemma C.6. \square

Lemma C.6. *For any $\hat{h} \in NC_{2n}$ then we have the estimates:*

$$\text{Tr}_{\mathcal{H}_\chi^{\otimes 2n}} D(\hat{h}) \leq \chi^{n+s(\hat{h})-t(\hat{h})/2}, \quad \text{Tr}_{\mathcal{H}_\chi^{\otimes 2n}} D(\hat{h}) \leq \chi^{n+s(\hat{h})/2} \quad (\text{C.46})$$

Furthermore the later inequality is saturated iff $\hat{h} = k \#_t k^{-1}$ for some $k \in NC'_{n+t/2}$ where $t = t(\hat{h})$.

Proof. Note that:

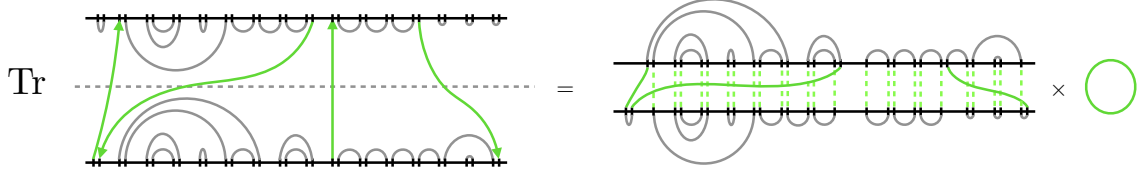
$$\text{Tr}_{\mathcal{H}_\chi^{\otimes 2n}} D(k \#_t k^{-1}) = \chi^{n+t/2} \quad (\text{C.47})$$

by direct computation.

Consider now the first inequality Eq. (C.46). We can remove any *straight crossings* since they factor out trivially from both sides of this inequality. So wlog consider only elements with $s(\hat{h}) = 0$. We can then write:

$$\text{Tr}_{\mathcal{H}_\chi^{\otimes 2n}} D(k_1 \#_t k_2^{-1}) = \langle k'_1 | \Sigma | k'_2 \rangle \quad k'_{1,2} \in NC_{n-t} \quad (\text{C.48})$$

defined as follows (see Figure below). Here $k'_{1,2}$ are constructed from k_1 and k_2 by removing the defects/crossing lines and considering the remaining elements as a non-crossing permutation on $n - t$ points. These can then be interpreted as pure states (non-normalized maximally entangled states) in the Hilbert space of dimension $\chi^{2(n-t)}$. Finally Σ is a unitary permutation on this Hilbert space formed by following crossing lines in $k_1 \#_t k_2^{-1}$ around the trace.



(where we have included a single straight crossing, that may be removed trivially.)

Then Cauchy-Schwarz gives:

$$|\text{Tr}_{\mathcal{H}_\chi^{\otimes 2n}} D(k_1 \#_t k_2^{-1})|^2 = |\langle k'_1 | \Sigma | k'_2 \rangle|^2 \leq \langle k'_1 | \Sigma^\dagger \Sigma | k'_1 \rangle \langle k'_2 | k'_2 \rangle \quad (\text{C.49})$$

$$= \langle k'_1 | k'_1 \rangle \langle k'_2 | k'_2 \rangle \quad (\text{C.50})$$

$$= \chi^{-2t} \text{Tr}_{\mathcal{H}_\chi^{\otimes 2n}} D(k_1 \#_t k_1^{-1}) \text{Tr}_{\mathcal{H}_\chi^{\otimes 2n}} D(k_2 \#_t k_2^{-1}) = \chi^{2n-t} \quad (\text{C.51})$$

as required. The second inequality in Eq. (C.46) is trivial now. Saturation of this later inequality requires $t(\hat{h}) = s(\hat{h})$ and saturation of the Cauchy-Schwarz inequality above (now with no Σ) requires $k'_1 = k'_2$ implying the correct condition. \square

We now consider the saturation condition for g in Eq. (C.37). To make progress we consider only the form of q given by Theorem C.5.

Theorem C.7. *Fix an n_d and a corresponding q satisfying Eq. (C.38). Then there is a unique $g \in S_{mn}$ that satisfies Eq. (C.37). This element is:*

$$g(q) = \iota(\hat{h})g_B \quad (\text{C.52})$$

where $\hat{h} \in S_{2n}$ is the unique element that satisfies $q = P(\hat{h}g_B|_{m=2})$ and where ι embeds the subgroup S_{2n} into S_{mn} . The subgroup acts only on elements $jm/2 + 1$ for $j = 0 \dots 2n - 1$ fixing all other elements.

If we relax the second condition in Eq. (C.37) then all the dominant elements are those satisfying $g' : P(g') \leq P(g(q))$ where $g(q)$ was defined above, and also $P(g') \not\leq P(g(q'))$ for any $q' < q$. There are:

$$(C_m - C_{m/2}^2)^{n-n_d} (C_{m/2}^2)^{n_d} \quad (\text{C.53})$$

of these, where C_m are the Catalan numbers.

Proof. We first consider the case where we ignore second part of Eq. (C.37). Given a connectivity fixed by q satisfying Eq. (C.38) first consider the blocks of length 1 in $a_i \in q$. These contribute to all G_X, G_A, G_B for a given g' independently, and so we have zero genus for g' restricted to these blocks, iff these g' forms a NC permutation within the corresponding $m/2$ block. We call these NC permutation $\alpha_i \in NC_{m/2}$. It is not hard to see that $\iota(\hat{h})g_A$ contains a cycle $\tau_{m/2}$ on this same $m/2$ block. Thus the statements of the theorem are true for the $2n_d$ unit blocks.

Now consider a block $b_i \in q$ of length 2. From the form of q given in Lemma C.5 we can see that such a block sits either in a closed block of $q \vee t_A$ or a closed block of $q \vee t_B$ (or both). Assume without loss of generality it is the former. Now recall the “pinching argument” in Theorem C.1. Start with the zero genus surface Σ_A describing g' with respect to g_A . Now pinch to form the surface with respect to X . Since $0 \leq G_X \leq G_A = 0$ the pinched surface must also be an admissible surface Σ_X for g' (with respect to X) that has minimal genus 0. Focus on the curves connecting the two $m/2$ boundaries on Σ_X associated to b_i that describe a disconnected genus 0 surface with two boundaries Σ_i . These must form an annular non-crossing permutations in $S_m \subset ANC_{m/2, m/2}$ that we call β_i . We now show that these must be a special subset of annular non-crossing permutations.

We will show that we can add to Σ_i a curve that starts between the marked points 1 and $m/2$ on the first boundary and ends between the marked points 1 and $m/2$ on the second boundary, and does not cross any other curves on Σ_i . We construct this as follows (see Figure below). Since we found Σ_X by pinching Σ_A between the marked points 1 and $m/2$ and $m/2 + 1$ and m on the boundaries of Σ_A , we can add *new* non-crossing curves to Σ_X that pass between pairs of boundaries described by the blocks in t_A that start and end between the 1 and $m/2$ marked points on each X boundary. On Σ_X shrink all boundaries except for the two described by b_i to arrive at Σ_i plus some bulk points where the boundaries shrunk, and non-crossing curves between the bulk points. Since $q \vee t_A$ contains the block b_i in a “closed block” we can find a curve on Σ_X that follows alternatively the *new* curves that we constructed using t_A and the curves in g' *not* associated to b_i . The result connects, via the bulk points, the two remaining boundaries as required.

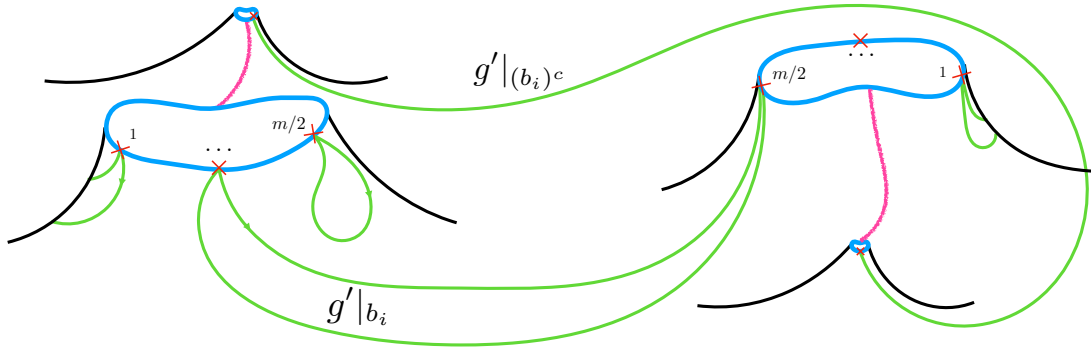


Figure C.2: The surface Σ_X is constructed from Σ_A in such way that we can insert non-crossing curves on Σ_X , shown in pink. These curves pass between the two boundaries associated to the blocks in t_A . We can use these curves and some other non-crossing curves, labelled $g'|_{b_i^c}$, to pass between the two boundaries associated to the block $b_i \in q$.

An annular non-crossing permutation ($ANC_{m/2, m/2}$) does not cross a line between the two boundaries iff it is a non-crossing permutation NC_m associated to the joined boundaries, where we join the boundaries through the non-crossing line. This is a special subset $NC_m \subset ANC_{m/2, m/2}$. It is not hard to see that in our case these are defined as non-crossing permutations with respect to the remaining cycles τ_m of length m in $g(q) \equiv \iota(\hat{h})g_B$. Thus we solve the condition $G_X = G_A = G_B = 0$ by demanding $P(g') \leq P(g(q))$ (such that the connectivity of g' is still described by q which requires that $P(g') \not\leq P(g(q'))$ for $q' < q$.)

For the first statement of the theorem (including the second condition in Eq. (C.37)), we now simply need

to compute the following for $g' \leq g(q)$:

$$d(X, g') = mn - \sum_i \#(\tau_{m/2}(\alpha_i)^{-1}) - \sum_j \#(\tau_{m/2} \times \tau_{m/2}(\beta_j)^{-1}) \quad (\text{C.54})$$

$$= mn - \sum (m/2 + 1 - \#(\alpha_i)) - \sum (m - \#(\beta_j)) \quad (\text{C.55})$$

$$= (n - n_d) + \sum (\#(\alpha_i) - 1) + \sum (\#(\beta_j) - 1) \quad (\text{C.56})$$

where $n - n_d = 2n - \#(q)$. So we get equality for the second part of Eq. (C.37) iff α_i and β_j have one cycle - namely they equal $\tau_{m/2}$ or τ_m within their respective blocks. Again it is not hard to check that the unique element that does the job is $g(q)$. \square

The surfaces that describe g' with respect to g_B , are disconnected $NC_{m/2}$ discs and, the k -fold branched coverings of the disk. We give some pictures to describe the dominant saddles.

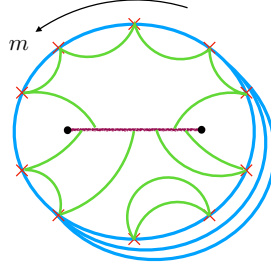


Figure C.3: A part of g' corresponding to single block in $\#(q \vee t_B)$ and represented as a surface with respect to g_B . The boundary represented by the cycles of g_B is shown in blue. The purple line can be thought of as a “twist operator” which relates the different branches of the block.

Lastly we mention how these elements make their appearances in the phase diagram. The minimal elements are constituted by $g(q) \in S_{mn}$ described in Theorem C.7 but also saturating Eq. (C.11), which in turn forces either $n_d = n$ or $n_d = 0$. They are:

$$\begin{cases} \{e\}, & x < 1/2, \\ \{g : P(g) \leq P(X)\} = \Gamma(g_A, e) \cap \Gamma(g_B, e), & x = 1/2, \\ \{X\}, & 1/2 < x \leq n/2, \\ \{k^{[1]_m} (k^{-1})^{[m/2+1]_m} g_B : k \in NC_n\} \subset \Gamma(g_A, g_B), & x \geq n/2, \end{cases} \quad (\text{C.57})$$

in terms of the notation of Sec. (2.3). We see that the X element comes from $n_d = n$, whereas the $x \geq n/2$ elements come from $n_d = 0$. Intuitively one can also regard the elements with $0 < n_d < n$ as smoothly interpolating between $\{X\}$ and $\{k^{[1]_m} (k^{-1})^{[m/2+1]_m} g_B\}$. They are essential around the reflected entropy phase transition $x = n/2 = 1/2$, where all the four regions in Eq. (C.57) come on top of each other. The fact that phase transition occurs at $x = 1/2$ also implies that we drop the second condition of Eq. (C.37), that is we must sum over all the elements prescribed in theorem C.7.

C.2.2 Generating functions

Let us compute the generating function for elements that saturate the q conditions in Eq. (C.38). Define:

$$Z(z, w, p) = \sum_{n=0}^{\infty} \sum_{n_d=0}^n w^{n_d} z^n \sum_{q \in P_{2n}: Eq. (C.38) \checkmark} p^{-\#(t_A \vee q) + \#(t_B \vee q)} \quad (\text{C.58})$$

where we *pick* the $n_d = n = 0$ term to equal p (which then violates the seeming $p \rightarrow 1/p$ symmetry.) We use the result in Lemma C.5. Let us separate out the $n_d = 0$ contribution. For $n = n_d$ we simply get the generating function of the q -Catalan numbers:

$$Z|_{n_d=0} = \sum_{n=0}^{\infty} \sum_{a \in NC_n} z^n p^{-2\#(a) + n + 1} \equiv C(z, p) = -\frac{\sqrt{(1-z/z_+)(1-z/z_-)}}{2z} + \frac{1}{2z} - \frac{1}{2\sqrt{z_+z_-}} \quad (\text{C.59})$$

where $z_{\pm} = p(1 \pm p)^{-2}$ and we pick the cut such that $\sqrt{z_+z_-} = p/(1-p^2)$ which is the term that violates the symmetry $p \rightarrow 1/p$. This function satisfies:

$$C(z, 1/p) = C(z, p) + (p^{-1} - p), \quad zC(z, p)C(z, 1/p) = C(z, p) - p \quad (\text{C.60})$$

Focus now on the rest. Consider the integer partition $n - n_d = \sum_{k=1}^{2n_d} \ell_k$ where $0 \leq \ell_k \leq n - n_d$, then diagram represented in Theorem C.5 is described by $2n_d$ group elements $b_k \in NC_{\ell_k}$ and is weighted in the partition function above by:

$$w^{n_d} z^n p^{\sum_k (-1)^k (2\#(b_k) - \ell_k - 3/2)} \quad (\text{C.61})$$

where we pick $\#(b_k) = 0$ for $\ell_k = 0$. We also need to account for translations of the diagram up to an amount of $1 + \ell_1 + \ell_2$. By cyclic symmetry we can pick any two ℓ 's and sum $(\sum_{k=1}^{2n_d} (1/2 + \ell_k))/n_d = n/n_d$. Thus we need to compute:

$$Z_{n_d \neq 0} = \sum_{n=1}^{\infty} \sum_{n_d=1}^n \frac{n}{n_d} \sum_{\{\ell_k=0, \dots, n-n_d\}_k} \sum_{\{b_k \in NC_{\ell_k}\}} \delta_{\sum_{k=1}^{2n_d} \ell_k, n-n_d} w^{n_d} z^n p^{\sum_k (-1)^k (2\#(b_k) - \ell_k)} \quad (\text{C.62})$$

We introduce a contour integral to extract the correct power of y :

$$\delta_{\sum_{k=1}^{2n_d} \ell_k, n-n_d} = \oint_C \frac{dy}{2\pi i y} y^{(n_d-n) + \sum_k \ell_k} \quad (\text{C.63})$$

where C encircles the origin $y = 0$. This also allows us to extend the sum $\sum_{\ell_k=0}^{2n_d} \rightarrow \sum_{\ell_k=0}^{\infty}$. Computing this:

$$Z_{n_d \neq 0} = z \partial_z \oint_C \frac{dy}{2\pi i y} \sum_{n=1}^{\infty} \sum_{n_d=1}^n \frac{1}{n_d} w^{n_d} z^n y^{(n_d-n)} (C(y, p)C(y, 1/p))^{n_d} \quad (\text{C.64})$$

Shifting the sums to $n_d = 1, \dots, \infty$ and $\tilde{n} = n - n_d = 0, \dots, \infty$ allows us to do the sums:

$$Z_{n_d \neq 0} = z \partial_z \oint_C \frac{dy}{2\pi i y} \frac{1}{(1-z/y)} \ln(1 - wzC(y, p)C(y, 1/p)) \quad (\text{C.65})$$

converging for small w, z . Then doing the contour integral to pickup the pole at $z = y$ (we can pick the contour C to be at sufficiently small y to avoid non-analyticities from the $C(y, p)$ terms above, but large

enough to encircle this pole):

$$Z_{n_d \neq 0} = z \frac{\partial}{\partial z} \ln(1 - wzC(z, p)C(z, 1/p)) \quad (\text{C.66})$$

while this derivation required small z, w we can then analytically continue this answer away from this regime.

Putting it together we find:

$$Z(z, w, p) = C(z, p) + \frac{z \partial_z C(z, p)}{C(z, p) - p - w^{-1}} \quad (\text{C.67})$$

Note that the second term has a pole at $z = \frac{pw}{(1+pw)(p+w)}$ with unit residue.

Now consider the problem of the minimal elements for $g \in S_{mn}$ in a fixed n_d sector, satisfying Eq. (C.37).

$$Z(z, w, p) = \sum_{n=0}^{\infty} \sum_{n_d=0}^n w^{n_d} z^n \sum_{g \in S_{mn}: \begin{cases} \text{Eq. (C.37)} \checkmark \\ \text{Eq. (C.38)}|_{q=q_g} \checkmark \end{cases}} p^{-\frac{1}{2}(\#(gg_A^{-1}) - \#(gg_B^{-1}))} \quad (\text{C.68})$$

and this gives the same generating function.

We finally drop the second condition in Eq. (C.37) such that we have a new degree of freedom. Motivating the more complicated generating function:

$$Y(z, w, p, r) = \sum_{n=0}^{\infty} \sum_{n_d=0}^n w^{n_d} z^n \sum_{g \in S_{mn}: \begin{cases} G_A = G_B = 0 \checkmark \\ \text{Eq. (C.38)}|_{q=q_g} \checkmark \end{cases}} r^{-\#(g)} p^{\frac{1}{2}(\#(gg_A^{-1}) - \#(gg_B^{-1}))} \quad (\text{C.69})$$

In a fixed q sector we have to sum over all elements $g \leq \iota(\hat{h}_q)g_A$ which simply gives:

$$\rho_1(r)^{n-n_d} \rho_0(r)^{n_d}, \quad \rho_1(r) = C_m(r^{-1}) - C_{m/2}(r^{-1})^2 \quad \rho_0(r) = C_{m/2}(r^{-1})^2 \quad (\text{C.70})$$

where $C_m(r) = \sum_{g \in NC_m} r^{\#(g)}$, with $C_1(r) = 1$. So that:

$$Y(z, w, p, r) = Z(\rho_1(r)z, \rho_0(r)\rho_1(r)^{-1}w, p) \quad (\text{C.71})$$

C.2.3 Reflected resolvent

The resolvent can be expressed using the generating functions we found in previous subsection. We set:

$$\chi_A = p^{1/2} q^{1/2} \chi^{1/2} \quad \chi_B = p^{-1/2} q^{1/2} \chi^{1/2} \quad \chi_C = \chi \quad (\text{C.72})$$

and take χ large. This zooms into the $x_A = x_B = 1/2$ part of the phase diagram.

$$R(\lambda) = \sum_{n=0}^{\infty} \lambda^{-n-1} \frac{\overline{\text{Tr} \sigma_{AA}^n}}{(\overline{\text{Tr} \rho_{AB}^n})} \approx \lambda^{-1} \hat{Y}((\lambda \chi q (\rho_1(q) + \rho_0(q)))^{-1}, \chi q, p, q) \quad (\text{C.73})$$

$$= \lambda^{-1} \hat{Z}((\lambda \chi q)^{-1} p_1(q), \chi q p_0(q) / p_1(q), p) \quad (\text{C.74})$$

Where $\hat{Y}(z, w, p, q) = (\chi q - 1)Y(z, 0, p, q) + Y(z, w, p, q)$ and similarly for \hat{Z} . We have defined:

$$p_{0,1}(q) = \frac{\rho_{0,1}(q)}{\rho_0(q) + \rho_1(q)} \quad (\text{C.75})$$

At large χ there are multiple scales in the resolvent, which makes it difficult to prove a clean statements on the large χ answer. We have the main part of the resolvent which describes the MP distribution given by:

$$R(\lambda)|_{\lambda \sim 1/\chi} = \lambda^{-1} \chi q C((\lambda \chi q)^{-1} p_1(q), p) \quad (\text{C.76})$$

$$= \chi^2 \left(-\frac{\sqrt{(\lambda \chi - z'/z_+)(\lambda \chi - z'/z_-)}}{2z' \lambda \chi} + \frac{1}{2z'} - \frac{1}{2\lambda \chi \sqrt{z_+ z_-}} \right) \quad (\text{C.77})$$

and is found near eigenvalues $\lambda \sim 1/\chi$ where we have defined $z' = p_1(q)/q$ and $z_{\pm} = z_{\pm}(p)$ was defined previously. Then there is a single pole approximately at $zw \approx 1$ (taking w large and zw held fixed.) That is $\lambda \approx p_0(q)$. For $\lambda \sim \mathcal{O}(1)$ we have z small so we can approximate $C(z, p) \approx p + z + \dots$

$$R(\lambda)|_{\lambda \sim 1} \approx \frac{1}{\lambda - p_0(q)} \quad (\text{C.78})$$

In particular the naively leading MP distribution is not relevant because it has zero imaginary part for this range of λ .

Note the general location of the pole is:

$$\lambda = p_0 \left(p + \frac{p_1}{p_0 \chi q} \right) \left(\frac{1}{p} + \frac{p_1}{p_0 \chi q} \right) = p_0 \left(1 + \frac{p_1}{p_0 \chi_A^2} \right) \left(1 + \frac{p_1}{p_0 \chi_B^2} \right) \quad (\text{C.79})$$

although there is no reason to expect there are not other $1/\chi$ corrections that possibly even compete with the corrections implied by the above formula. The more general resolvent that is represented by Eq. (C.69) is not accessible in this physical quantity since it lies outside of the domain of validity for the approximation that we are using. This is due to the large $w \sim \chi$ value that we must use in the generating function. In order to access this we need a way to hold fixed w without changing q or p .

C.3 Full solution to $k = 2$ SD equation

In section 3.6 we have the following set of matrix equations for the 2×2 matrix R which determines the resolvent at $\lambda \sim \mathcal{O}(\chi_C^0)$:

$$\begin{aligned} \begin{pmatrix} R_{11} & R_{12} \\ R_{21} & R_{22} \end{pmatrix} &= \begin{pmatrix} \lambda - F_{11} & -F_{12} \\ -F_{21} & \lambda - F_{22} \end{pmatrix}^{-1} \\ \begin{pmatrix} F_{11} & F_{12} \\ F_{21} & F_{22} \end{pmatrix} &= \sqrt{\lambda} \begin{pmatrix} 0 & \hat{D}_m \\ \hat{D}_m & 0 \end{pmatrix} + \frac{\lambda \hat{E}_m}{(\chi_A \chi_B)^2} \begin{pmatrix} R_{22} & R_{21} \\ R_{12} & R_{11} \end{pmatrix} + \frac{\lambda \hat{B}_m}{(\chi_A \chi_B)^2} \begin{pmatrix} S_{22}(\chi_B^2 - 1) & 0 \\ 0 & S_{11}(\chi_A^2 - 1) \end{pmatrix} \end{aligned} \quad (\text{C.80})$$

With S_{11} and S_{22} given by

$$(\chi_A^2 - 1)S_{11}, (\chi_B^2 - 1)S_{22} = \frac{\chi_A^2 \chi_B^2}{2\hat{B}_m \lambda} \left(\lambda - \sqrt{(\lambda - \lambda_+)(\lambda - \lambda_-)} \right) \pm \frac{\chi_A^2 - \chi_B^2}{2\lambda} \quad (\text{C.81})$$

We now attempt to find a complete solution for matrix R . Define

$$M = \begin{pmatrix} \lambda & -\sqrt{\lambda}\widehat{D}_m \\ -\sqrt{\lambda}\widehat{D}_m & \lambda \end{pmatrix} - \frac{\lambda\widehat{B}_m}{(\chi_A\chi_B)^2} \begin{pmatrix} S_{11}(\chi_A^2 - 1) & 0 \\ 0 & S_{22}(\chi_B^2 - 1) \end{pmatrix} \equiv \begin{pmatrix} M_{11} & M_{12} \\ M_{21} & M_{22} \end{pmatrix} \quad (\text{C.82})$$

Note that M is symmetric, $M_{12} = M_{21}$. We can write Eq. (C.80) as

$$T^{-1}RT = \left(M - \frac{\lambda\widehat{E}_m}{(\chi_A\chi_B)^2} R \right)^{-1} \quad (\text{C.83})$$

where

$$T = T^{-1} = \begin{pmatrix} 0 & 1 \\ 1 & 0 \end{pmatrix} \quad (\text{C.84})$$

is the $\chi_A \leftrightarrow \chi_B$ basis flip matrix. Multiply both sides by T from the left we obtain

$$RT = \left(MT - \frac{\lambda\widehat{E}_m}{(\chi_A\chi_B)^2} RT \right)^{-1} \quad (\text{C.85})$$

What we have shown is that RT and MT are simultaneously diagonalizable. Our strategy is then straightforward: we simply go to the basis where both matrices are diagonalized. Doing so allows us to solve for the eigenvalues of RT easily, then we transform back to the familiar basis and undo the effect of T . Start by diagonalizing MT :

$$\begin{aligned} MT &= \begin{pmatrix} M_{12} & M_{11} \\ M_{22} & M_{12} \end{pmatrix} = Q \begin{pmatrix} d_+ & 0 \\ 0 & d_- \end{pmatrix} Q^{-1} \\ &= \begin{pmatrix} \sqrt{M_{11}} & -\sqrt{M_{11}} \\ \sqrt{M_{22}} & \sqrt{M_{22}} \end{pmatrix} \begin{pmatrix} M_{12} + \sqrt{M_{11}M_{22}} & 0 \\ 0 & M_{12} - \sqrt{M_{11}M_{22}} \end{pmatrix} \begin{pmatrix} \sqrt{M_{11}} & -\sqrt{M_{11}} \\ \sqrt{M_{22}} & \sqrt{M_{22}} \end{pmatrix}^{-1} \end{aligned} \quad (\text{C.86})$$

We find that the eigenvalues of MT are

$$d_{\pm} = M_{12} \pm \sqrt{M_{11}M_{22}} \quad (\text{C.87})$$

so we have

$$\begin{aligned} R &= Q \begin{pmatrix} r_+ & 0 \\ 0 & r_- \end{pmatrix} Q^{-1}T \\ &= \frac{1}{2} \begin{pmatrix} \sqrt{\frac{M_{11}}{M_{22}}}(r_+ - r_-) & r_+ + r_- \\ r_+ + r_- & \sqrt{\frac{M_{22}}{M_{11}}}(r_+ - r_-) \end{pmatrix} \end{aligned} \quad (\text{C.88})$$

with r_{\pm} given by

$$r_{\pm} = \frac{(\chi_A\chi_B)^2}{2\lambda\widehat{E}_m} \left(d_{\pm} - \sqrt{d_{\pm}^2 - \frac{4\lambda\widehat{E}_m}{(\chi_A\chi_B)^2}} \right) \quad (\text{C.89})$$

In calculating the resolvent we only need the R_{11} component. It is

$$R_{11}(\lambda) = \sqrt{\frac{M_{11}}{M_{22}} \frac{(\chi_A \chi_B)^2}{4\lambda \widehat{E}_m}} \left(2\sqrt{M_{11}M_{22}} + \sqrt{(M_{12} - \sqrt{M_{11}M_{22}})^2 - \frac{4\lambda \widehat{E}_m}{(\chi_A \chi_B)^2}} - \sqrt{(M_{12} + \sqrt{M_{11}M_{22}})^2 - \frac{4\lambda \widehat{E}_m}{(\chi_A \chi_B)^2}} \right) \quad (\text{C.90})$$

The form of $R_{11}(\lambda)$ seems to predict two ‘‘mini-MP’’ peaks with width $\propto \sqrt{\widehat{E}_m}/(\chi_A \chi_B)$, centered at λ_* where the condition

$$M_{12} = \pm \sqrt{M_{11}M_{22}} \quad (\text{C.91})$$

is satisfied. However since $M_{12} \propto \sqrt{\lambda}$, from the branch cut of square root we see that solutions for these two equations lie immediately above and below real axis, respectively. In fact they represent the same peak, as we must have $R(\lambda + i\epsilon) = -R(\lambda - i\epsilon)$ for any resolvent $R(\lambda)$. Solving for λ_* gives

$$\begin{aligned} \lambda_* &= \frac{(\widehat{B}_m(1 - \chi_A^{-2})\chi_B^{-2} + \widehat{D}_m^2)(\widehat{B}_m(1 - \chi_B^{-2})\chi_A^{-2} + \widehat{D}_m^2)}{\widehat{D}_m^2} \\ &= \widehat{D}_m^2 + \left(\frac{1}{\chi_A^2} + \frac{1}{\chi_B^2} \right) \widehat{B}_m + O(\chi^{-4}) \end{aligned} \quad (\text{C.92})$$

We can calculate the width of this mini-MP peak via solving the relation

$$(M_{12} \pm \sqrt{M_{11}M_{22}})^2 = \frac{4\lambda \widehat{E}_m}{(\chi_A \chi_B)^2} \quad (\text{C.93})$$

We find

$$\begin{aligned} \delta\lambda &= \frac{8\widehat{D}_m \sqrt{\widehat{E}_m}}{\chi_A \chi_B} \left(1 + \frac{\widehat{B}_m^2 (\chi_A^2 - 1)(\chi_B^2 - 1)}{(4\widehat{E}_m - \widehat{D}_m^2 \chi_A^2 \chi_B^2)^2} \right) \\ &= \frac{8\widehat{D}_m \sqrt{\widehat{E}_m}}{\chi_A \chi_B} + O(\chi^{-4}) \end{aligned} \quad (\text{C.94})$$

Note that:

$$\lambda_* - \lambda_{\pm} = \left(\widehat{D}_m^2 \mp \widehat{B}_m \frac{(\chi_A^2 - 1)^{1/2} (\chi_B^2 - 1)^{1/2}}{(\chi_A \chi_B)^2} \right)^2 \quad (\text{C.95})$$

so the λ_* pole never reaches the main MP peak. It rather bounces when

$$\widehat{D}_m^2 = \widehat{B}_m \frac{(\chi_A^2 - 1)^{1/2} (\chi_B^2 - 1)^{1/2}}{(\chi_A \chi_B)^2} \quad (\text{C.96})$$

which is outside of the validity of our approximations.

Appendix D

Supplement to Chapter 5

D.1 Multiboundary wormholes

In this appendix, our primary goal is to analyze the extremal surfaces in a multiboundary wormhole. In particular, we are interested in understanding the competition between different candidates for the minimal entanglement wedge cross section.

The four boundary wormhole we are interested in can be decomposed into two pair-of-pants geometries (see Fig. (D.1)). Without loss of generality, consider one of the constituent geometries with extremal surfaces γ_i that have area L_i for $i = A, C_1, W$, corresponding to each of the asymptotic boundary regions as shown in Fig. (D.1). In this geometry, there are three potential candidates for the minimal entanglement wedge cross section for the region AB , i.e., γ_A and γ_W , which have obvious analogs in the 2TN model, as well as a non-trivial surface γ' , whose area L' is completely fixed in terms of the moduli L_i . In order for the tensor network to faithfully model this wormhole's minimal cross section, we need to ensure that $L_W < L'$.

To compute L' as a function of L_i , we can use the symmetries of the problem and identities from hyperbolic geometry (see Ref. [101] and references therein). In particular, an identity satisfied by right-angled pentagons in hyperbolic space is

$$\sinh(a) \sinh(b) = \cosh(c), \tag{D.1}$$

where a and b are the lengths of adjacent sides of the pentagon and c is the unique side not adjacent to either of them. Note that all lengths are measured in units of the AdS scale l . Suppose γ' splits γ_{C_1} into portions of length x and $L_{C_1} - x$, then we have

$$\begin{aligned} \sinh(x) \sinh\left(\frac{L'}{2}\right) &= \cosh\left(\frac{L_W}{2}\right), \\ \sinh\left(\frac{L_{C_1}}{2} - x\right) \sinh\left(\frac{L'}{2}\right) &= \cosh\left(\frac{L_A}{2}\right). \end{aligned} \tag{D.2}$$

Moreover, we are interested in a limit where $L_A, L_{C_1} \gg L_W$. Solving the above set of equations in this limit, we obtain

$$L' = 2 \sinh^{-1} \left(\sqrt{\exp(L_A - L_{C_1}) + 2 \exp\left(\frac{L_A - L_{C_1}}{2}\right) \cosh\left(\frac{L_W}{2}\right)} \right). \tag{D.3}$$

We can now compare L' to L_W either by plotting the function as in Fig. (D.2), or by comparing them in

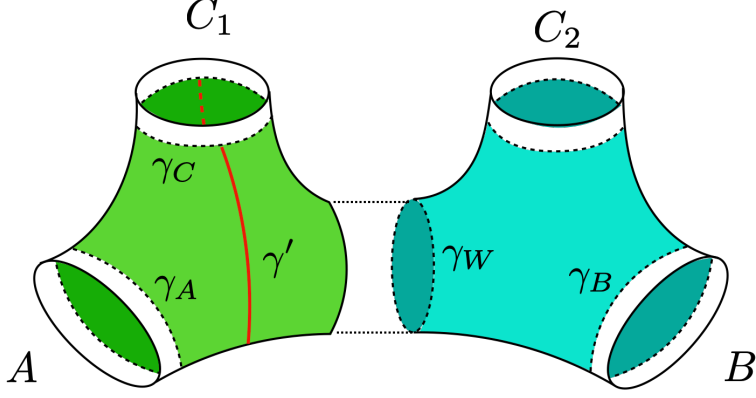


Figure D.1: A pair of pants decomposition of a four-boundary wormhole. The constituent three-boundary wormholes have horizons γ_i with area L_i . The surface γ_W was treated as the minimal entanglement wedge cross section in our analysis. However, another possible non-trivial entanglement wedge cross section surface γ' exists with an area L' that could be lesser in regions of parameter space.

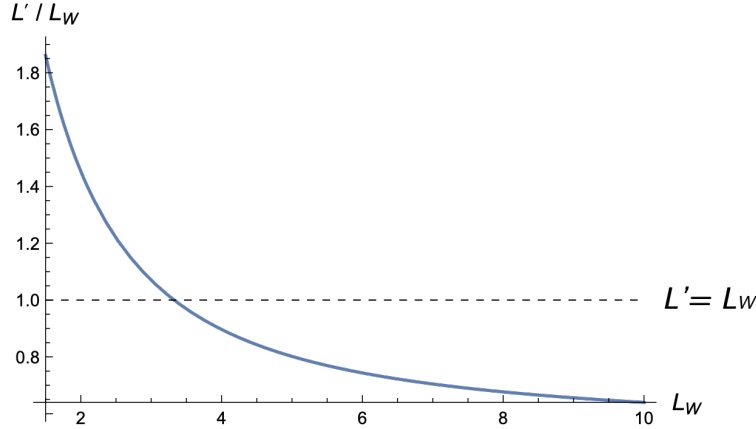


Figure D.2: A plot of L'/L_W as a function of L_W for fixed L_A and L_{C_1} . The dashed line labels the location where the shift of minimal cross-section happens.

various limits. When $L_A > L_{C_1}$, we find that $L' \gg L_W$ which means we can ignore the surface γ' for the cross section. On the other hand, for $L_A < L_{C_1}$, we find that $L' \ll L_W$ and thus, it is very important to consider γ' . This means that the 2TN approximation fails as we go far into the disconnected phase. However, for our calculations we were mostly interested in the region near phase transitions. Thus for simplicity, consider the case $L_A = L_{C_1}$. Then, for small L_W , we have $L' = 2 \sinh^{-1}(\sqrt{3}) \gg L_W$. For large L_W , we instead have $L' = \frac{L_W}{2} \ll L_W$. As seen from Fig. (D.2), there is a transition at an $O(1)$ value of L_W . Identical arguments can be applied to the other constituent pair-of-pants geometry. Thus, as long as we tune the moduli to such a regime, we find a wormhole whose minimal entanglement wedge cross section is indeed given by γ_W and is modelled well by the 2TN.

On the other hand, it isn't clear whether such saddles are dominant in the gravitational path integral. An analysis similar to Ref. [152] would be useful to determine if this is the case. Even if such a saddle is not dominant, we can consider a few alternate options: matter can be used to source a larger interior region in which case it is clear that $L' > \min(L_A, L_W)$. It may also be possible to simply choose to project on the relevant saddles [202].

D.2 Finite χ corrections

In this appendix we will study the effect of finite bond dimension χ . As opposed to the corrections from finite external bond dimensions $\chi_{A,B,C}$, the effect of finite χ acts only on eigenvalues within each k sectors by shifting them by a small amount. In the following we will give generating functions pertain to these eigenvalue shifts. Analytically continuing the coefficient of the relevant generating function gives the leading correction to the reflected spectrum. We give explicit formulae of such analytic continuation for $k = 0, 1$. The correction to these two sectors completely characterizes the leading order corrections to the reflected entropy in the finite χ limit, which matches well with our numerics (Sec. (5.4.5)). While the detailed effect of sector mixing is interesting on its own in that there seems to be an additional hierarchy structure from our TL numerics, its effect on the reflected entropy is to the order $O(\chi^{-2})$ which is outside the main interest of this note.

D.2.1 Corrections to orthogonality condition

We will find the first order χ corrections to Eq. (5.56). Denote the related generating function ¹

$$G(r, z) = \sum_{m \in 2\mathbb{Z}_+, k \in \mathbb{Z}_+} X_k^{(m)}(q_A, q_B, \chi) z^{m/2} r^k, \quad X_k^{(m)}(q_A, q_B, \chi) = \sum_{x, y \in \mathcal{B}_k^{(m)}} f_{q_A}(x) f_{q_B}(y) \langle x, y \rangle \quad (\text{D.4})$$

We write the function $X_k^{(m)}$ as a sum of diagrams:

$$X_k^{(m)} = \sum_{\substack{x, y \in \mathcal{B}_k^{(m)} \\ \langle x, y \rangle \neq 0}} \left[\text{Diagram with blue strands, red loops, and green loops} \right], \quad / = //, \quad (\text{D.5})$$

where we assign each closed red loop a factor of q_A , each closed green loop a factor of q_B and each closed black loop a factor of χ . Note that we work in the limit of large χ and $q_A, q_B \sim O(1)$. The contraction pattern of blue strands is determined by the link states x (on top) and y (on bottom) where we exclude all contractions in which $\langle x, y \rangle = 0$. The dominant contribution comes from $x = y$, reflecting the fact that the link states form a approximately orthogonal basis for $\mathcal{V}_k^{(m)}$. We now try to determine the first order correction to this result. Begin by splitting $G(r, z)$ in the following fashion

$$G(r, z) = G_0(r, z) + G_1(r, z), \quad (\text{D.6})$$

where $G_0(r, z)$ contains all the leading diagrams (that is with $x = y$). It is related to the link state generating function Eq. (5.57) by $G_0(r, z) = G(q_{AB}, r/\chi, z\chi)$. $G_1(r, z)$ contains all the next order corrections. Also denote $H(r, z)$ to be the generating function for 1PI diagrams and split it in a similar fashion

$$H(r, z) = H_0(r, z) + H_1(r, z) \quad (\text{D.7})$$

¹We will suppress the $q_{A,B}$ dependence in this section unless necessary to make our notation more clear.

$G(r, z)$ and $H(r, z)$ are related by

$$\begin{aligned}
\text{---} \circledast G \text{---} &= \underbrace{\text{---} + \text{---} \circledast H_0 \text{---} + \text{---} \circledast H_0 \text{---} \circledast H_0 \text{---} + \dots}_{G_0} \\
&+ \underbrace{\text{---} \circledast H_1 \text{---} + 2 \text{---} \circledast H_1 \text{---} \circledast H_0 \text{---} + 3 \text{---} \circledast H_1 \text{---} \circledast H_0 \text{---} \circledast H_0 \text{---} + \dots}_{G_1}
\end{aligned} \tag{D.8}$$

The weights in the sum of G_1 counts the number of permutations for the 1PI diagrams. Algebraically, Eq. (D.8) can be written as

$$\begin{aligned}
G_0(r, z) &= \sum_{n=0}^{\infty} H_0^n(r, z) = \frac{1}{1 - H_0(r, z)}, \\
G_1(r, z) &= H_1(r, z) \sum_{n=0}^{\infty} (n+1) H_0^n(r, z) = G_0^2(r, z) H_1(r, z)
\end{aligned} \tag{D.9}$$

An important seed for the generating function G is the special case $k = 0$, where the link states are non-crossing partitions $x, y \in NC_m$. Schematically the SD equation for H_1 and $k = 0$ is

$$\begin{aligned}
\text{---} \circledast H_1 \text{---} &= z^2 \text{---} \circledast G_1 \text{---} + 2z^3 \text{---} \circledast G_1 \text{---} \circledast G_0 \text{---} + \dots \\
&+ z^2 \text{---} \circledast G_0 \text{---} + 3z^3 \text{---} \circledast G_0 \text{---} \circledast G_0 \text{---} \\
&+ z^2 \text{---} \circledast G_0 \text{---} + 3z^3 \text{---} \circledast G_0 \text{---} \circledast G_0 \text{---}
\end{aligned} \tag{D.10}$$

For the diagrammatic notations used here: dashed circles indicate generating functions such as $G(r, z)$ and $H(r, z)$; and solid line circles indicate the generating functions for the $k = 0$ sector, i.e. $G(0, z)$ and $H(0, z)$. In the last two rows the blue connections feature non-crossing permutations (x, y) of the form $(\tau_n, \tau_n \sigma)$ or $(\tau_n \sigma, \tau_n)$, where σ is a simple transposition (permutation that swaps two elements and keeping all others invariant). The number of these permutations $\sigma \tau_n$ are $n(n-1)/2$. We get the following equation

$$\begin{aligned}
H_1(0, z) &= q_{AB} \chi^2 z^2 G_1(0, z) \sum_{n=0}^{\infty} (n+1) (\chi z G_0(0, z))^n \\
&+ q_{AB} (q_A + q_B) \sum_{n=0}^{\infty} \frac{n(n-1)}{2} z^n (\chi G_0(0, z))^{n-1} \\
&= q_{AB} \frac{\chi^2 z^2 G_1(0, z)}{(1 - \chi z G_0(0, z))^2} + q_{AB} (q_A + q_B) \frac{\chi z^2 G_0(0, z)}{(1 - \chi z G_0(0, z))^3}
\end{aligned} \tag{D.11}$$

This equation, together with Eq. (D.9) yields a linear equation for $G_1(0, z)$ in terms of $G_0(0, z)$. We get

$$G_1(0, z) = \frac{q_{AB} (q_A + q_B) \chi z^2 G_0^3(0, z)}{(\chi z G_0(0, z) - 1) (q_{AB} \chi^2 z^2 G_0^2(0, z) - (\chi z G_0(0, z) - 1)^2)} \tag{D.12}$$

This generating function characterizes the correction to the single pole $\lambda_{M_0^{(m)}}$ of the $k = 0$ sector.

For the $k > 0$ sectors we must include in our sum connections with open strands, but only such that each open strand on top is connected to an open strand in bottom, as required by the condition $\langle x, y \rangle \neq 0$. To better organize the SD equation we define an auxiliary matrix $\mathbb{F}_0(z)$

$$\begin{aligned} \mathbb{F}_0 &= \text{---} + z \text{---} \text{---} + z^2 \text{---} \text{---} + \dots \\ &= \frac{1}{1 - z\chi G_0(0, z)} \text{---} \end{aligned} \quad (\text{D.13})$$

$\mathbb{F}_0(z)$ can be thought of as an stripped down version of $H_0(z)$ in the sense of the following equality

$$\text{---} \text{---} = \mathbb{F}_0 \quad (\text{D.14})$$

Similarly we define the matrix $\mathbb{F}_1(z)$ that is comprised of the next order diagrams

$$\begin{aligned} \mathbb{F}_1 &= z \text{---} + 2z^2 \text{---} + 3z^3 \text{---} + \dots \\ &+ z^2 \text{---} + 3z^3 \text{---} \\ &+ z^2 \text{---} + 3z^3 \text{---} \\ &= \left(\frac{\chi z G_1(0, z)}{(1 - \chi z G_0(0, z))^2} + \frac{(q_A + q_B)\chi z^2 G_0(0, z)^2}{(1 - \chi z G_0(0, z))^3} \right) \text{---} \end{aligned} \quad (\text{D.15})$$

Note that despite the similarity, $\mathbb{F}_1(z)$ does not satisfy a simple relation to $H_1(z)$ like Eq. (D.14). The SD equation for the connected generating function $H(r, z)$ can then be formulated using these matrices

$$\text{---} \text{---} = \text{---} \text{---} + zr \text{---} \text{---} + z^2 r \left(\text{---} \text{---} \text{---} + \text{mirror diagrams} \right) \quad (\text{D.16})$$

As indicated there are three additional diagrams consists of vertical and horizontal reflections of the “zigzag” diagram. Since each “zigzag” decrease the power of χ by one, diagrams that with more than one “zigzags” only contribute at higher orders. Algebraically this equation is

$$H_1(r, z) = H_1(0, z) + zrF_1(z) + 2z^2r(q_A + q_B)F_0(z)^2G_0(z) \quad (\text{D.17})$$

where the non-bold version of \mathbb{F}_i denote the common prefactor of the respective matrix. Together with Eq. (D.9) this determines the form of $G_1(r, z)$ (since both $G_1(0, z)$ and $G_0(r, z)$ are known):

$$\begin{aligned} G_1(r, z) &= G_0(r, z)^2 \left(\frac{G_1(0, z)}{G_0(0, z)^2} + \frac{\chi z^2 r G_1(0, z)}{(1 - \chi z G_0(0, z))^2} + \frac{(q_A + q_B)\chi z^3 r G_0(0, z)^2}{(1 - \chi z G_0(0, z))^3} \right. \\ &\quad \left. + \frac{2z^2 r (q_A + q_B) G_0(0, z)}{(1 - \chi z G_0(0, z))^2} \right) \end{aligned} \quad (\text{D.18})$$

The $k = 0$ result Eq. (D.12) is recovered by taking $r = 0$. Denote formally the series coefficient of $G_1(r, z)$ by

$$G_1(r, z) = \sum_{\mu, k=0} g_{\mu, k}^{(1)}(q_A, q_B) z^\mu r^k \quad (\text{D.19})$$

The correction to the matrix eigenvalue $\lambda_{M_k^{(m)}}$ Eq. (5.56) from orthogonality is then

$$\Delta_1 \lambda_{M_k^{(m)}} = 2(q_{AB})^{-k} \chi^{m/2-k} g_{m/2, k}(q_{AB}^{-1}) g_{m/2, k}^{(1)}(q_A^{-1}, q_B^{-1}) + O(\chi^{m-2k-2}) \quad (\text{D.20})$$

where $g_{m/2, k}(q_{AB}^{-1})$ is the series coefficient of the link state generating function Eq. (5.57).

D.2.2 Corrections from subleading TL diagrams

We now write down the corrections from including the subleading TL diagrams in $M_k^{(m)}(q)$. We begin by splitting the sum

$$M_k^{(m)}(q) = \sum_{h \in \text{NC}_m} q^{-\#(h)} \pi_k^{(m)}(D(h)) = (M_0)_k^{(m)}(q) + \Delta M_k^{(m)}(q) \quad (\text{D.21})$$

where $(M_0)_k^{(m)} = \sum_{h \in \text{NC}_{m, k}} q^{-\#(h)} \pi_k^{(m)}(D(h))$ contains diagrams of the form $\{|x y|; x, y \in \mathcal{B}_k^{(m)}\}$ ² and $\Delta M_k^{(m)} = \sum_{h \in \text{NC}_m \setminus \text{NC}_{m, k}} q^{-\#(h)} \pi_k^{(m)}(D(h))$ contains the rest. Then we have

$$\Delta \left(M_k^{(m)}(q_A) M_k^{(m)}(q_B) \right) \approx \Delta M_k^{(m)}(q_A) (M_0)_k^{(m)}(q_B) + (M_0)_k^{(m)}(q_A) \Delta M_k^{(m)}(q_B) \quad (\text{D.22})$$

up to first order corrections. Our goal is to apply first order QM perturbation theory on the matrix $\Delta \left(M_k^{(m)}(q_A) M_k^{(m)}(q_B) \right)$. Since $M_k^{(m)}(q_A) M_k^{(m)}(q_B)$ is not Hermitian, we need a slightly modified version of usual first order perturbation theory.

- correction to leading eigenvalue

Denote $v_k^{(m)}(q) = \sum_{x \in \mathcal{B}_k^{(m)}} f_q(x) x$, we have $(M_0)_k^{(m)}(q) = q^{-k} |v_k^{(m)}(q)\rangle \langle v_k^{(m)}(q)|$ and the right (left) eigenvector of the unperturbed matrix $|v_k^{(m)}(q_A)\rangle \langle v_k^{(m)}(q_B)|$.³ The first order correction to the leading eigenvalue is

$$\begin{aligned} \Delta \lambda_{M_k^{(m)}} &= \frac{\langle v_k^{(m)}(q_B) | \Delta M_k^{(m)}(q_A) (M_0)_k^{(m)}(q_B) + (M_0)_k^{(m)}(q_A) \Delta M_k^{(m)}(q_B) | v_k^{(m)}(q_A) \rangle}{\langle v_k^{(m)}(q_B) | v_k^{(m)}(q_A) \rangle} \\ &= q_A^{-k} \langle v_k^{(m)}(q_A) | \Delta M_k^{(m)}(q_B) | v_k^{(m)}(q_A) \rangle + q_B^{-k} \langle v_k^{(m)}(q_B) | \Delta M_k^{(m)}(q_A) | v_k^{(m)}(q_B) \rangle \end{aligned} \quad (\text{D.23})$$

Hence we must evaluate the expectation values of the form

$$\langle v_k^{(m)}(q) | \Delta M_k^{(m)}(q') | v_k^{(m)}(q) \rangle = \sum_{x, y \in \mathcal{B}_k^{(m)}} f_q(x) f_q(y) \sum_{h \in \text{NC}_m \setminus \text{NC}_{m, k}} q'^{-\#(h)} \langle x | \pi_k^{(m)}(D(h)) | y \rangle \quad (\text{D.24})$$

²Certainly there are diagrams in M_0 that contribute at $O(\chi^{-1})$ but their effect is to alter the orthogonality condition Eq. (5.56), which we have already dealt with earlier.

³We will use v and $|v\rangle$ interchangeably as a vector in the module $\mathcal{V}_k^{(m)}$ and $\langle v|$ as the associated vector in the dual module $\mathcal{V}_k^{*(m)}$ defined from the inner product $\langle v| \equiv \langle \cdot, v \rangle$ to match the notation of QM perturbation theory. We hope the change of notation is not too confusing for the readers.

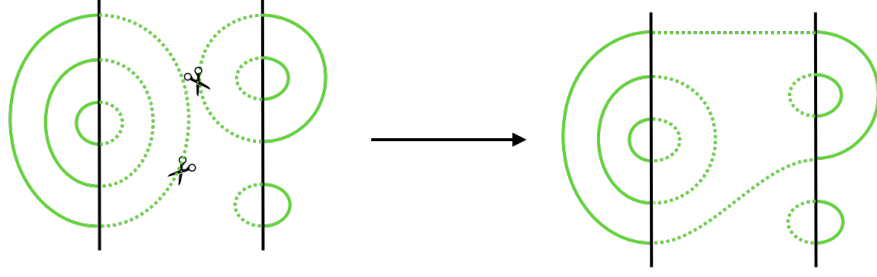


Figure D.3: The leading correction diagrams for $\langle x | D(h) | y \rangle$ in the $k = 0$ sector ($D(h)$ shown as dashed lines in the middle) is constructed by starting with mirroring the x and y link states (shown as solid lines on the left and right sides). Then an outer strand is cut on both mirrored link states before connecting them to form $D(h)$. This construction decreases the contribution of such diagram by one order of χ compared to $|x y\rangle$.

We can think of the sum $\sum_{h \in \text{NC}_m \setminus \text{NC}_{m,k}} \langle x | \pi_k^{(m)}(D(h)) | y \rangle$ as flipping the diagram of $|x\rangle$ horizontally and try to “fill in” the spaces between $|x\rangle$ and $|y\rangle$ by TL diagrams associated with $D(h)$. Every $D(h)$ contributes to this sum in different powers of χ and for our purpose here it suffices to find the diagrams that contribute at leading order.

Again an important seed is the $k = 0$ sector. For $k = 0$ the leading elements in the sum $\sum_{h \in \text{NC}_{m,k>0}} q^{-\#(h)} \langle x | \pi_k^{(m)}(D(h)) | y \rangle$ are elements such that $D(h) = |z w\rangle$ where $z, w \in \mathcal{B}_2^{(m)}$ in which they can be thought of as the “cut-open” versions of x and y , as shown in Fig. (D.3). For a link state $x \in \mathcal{B}_k^{(m)}$, denote $c(x)$ to be the number of outer strands it possesses, then the number of diagrams we should include to get the leading behavior of $\sum_h \langle x | D(h) | y \rangle$ is equal to $c(x)c(y)$. We have, up to leading order in χ :

$$\sum_{h \in \text{NC}_{m,k>0}} q^{-\#(h)} \langle x | \pi_k^{(m)}(D(h)) | y \rangle \approx \chi^{2m-1} q f_q(x) f_q(y) c(x) c(y), \quad x, y \in \mathcal{B}_0^{(m)} \quad (\text{D.25})$$

$c(x)$ is also equal to the number of connected components x contains, which can be counted using a modified generating function. Recall that $H(q, r = 0, z)$ Eq. (D.111) is the 1PI generating function of $k = 0$ link states. Instead of $G(q, r = 0, z) = 1/(1 - H(q, 0, z))$ we can additionally weigh the sum by the number of 1PI diagrams using

$$Y(q, z) = H(q, 0, z) + 2H^2(q, 0, z) + 3H^3(q, 0, z) + \dots = \frac{H(q, 0, z)}{(1 - H(q, 0, z))^2} \quad (\text{D.26})$$

Denote formally the expansion coefficient of Y by

$$Y(q, z) = \sum_{\mu=0}^{\infty} y_{\mu}(q) z^{\mu} \quad (\text{D.27})$$

Then one can write $\langle v_0^{(m)}(q) | \Delta M_0^{(m)}(q') | v_0^{(m)}(q) \rangle$ (up to leading order) as

$$\langle v_0^{(m)}(q) | \Delta M_0^{(m)}(q') | v_0^{(m)}(q) \rangle \approx q' y_{m/2}^2 ((q q')^{-1}) \chi^{m-1} + O(\chi^{m-2}) \quad (\text{D.28})$$

The additional factor of q' in front comes from the fact that the total number of loops decreases by one when performing the surgery shown in Fig. (D.3). Finally from Eq. (D.23) we obtain the first order

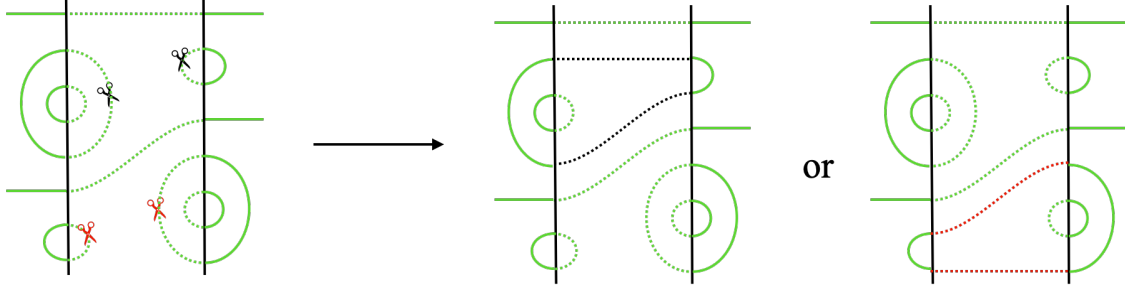


Figure D.4: The procedure of constructing leading diagrams for $\langle x | D(h) | y \rangle$ for the $k > 0$ sector. Starting with the diagram $|x y\rangle$, a similar procedure of cutting and gluing two outer strands are performed. However different to the $k = 0$ case, the two outer strands being cut must stay inside the same block. This is demonstrated using scissors with the same color in the above figure: The surgery on $|x y\rangle$ can be performed either on the strands with two black scissors (which produces the first diagram on RHS), or strands with two red scissors (which produces the second diagram on RHS), but performing surgery on a black-red scissor pair is prohibited.

correction to $\lambda_{M_0^{(m)}}$:

$$\Delta_2 \lambda_{M_0^{(m)}} \simeq (q_A + q_B) y_{m/2}^2 (q_{AB}^{-1}) \chi^{m-1} + O(\chi^{m-2}) \quad (\text{D.29})$$

For the $k > 0$ sectors one proceeds in a similar fashion but the rule is more complicated. As shown in Fig. (D.4), connecting the open strands dissects $|x y\rangle$ into different blocks. Due to the non-crossing nature of the TL diagram, we must only perform the surgery on outer strands within the same block. To do the required counting here we introduce the two-variable generating functions $\mathcal{G}(z, w)$ and $\mathcal{J}_0(r, z, w)$, defined as

$$\boxed{\mathcal{G}} = \begin{array}{c} | \\ | \\ \text{---} \\ | \\ | \\ | \end{array} = \begin{array}{c} | \\ | \\ \text{---} \\ | \\ | \\ | \end{array} \begin{array}{c} | \\ | \\ \text{---} \\ | \\ | \\ | \end{array} = C(q, z) C(q, w) \quad (\text{D.30})$$

and

$$\begin{aligned} \boxed{\mathcal{J}_0} &= zw \begin{array}{c} | \\ | \\ \text{---} \\ | \\ | \\ | \end{array} + z^2 w \begin{array}{c} | \\ | \\ \text{---} \\ | \\ | \\ | \end{array} + zw^2 \begin{array}{c} | \\ | \\ \text{---} \\ | \\ | \\ | \end{array} + z^2 w^2 \begin{array}{c} | \\ | \\ \text{---} \\ | \\ | \\ | \end{array} + \dots \\ &= \frac{qrwz}{(1 - zC(q, z))(1 - wC(q, w))} \end{aligned} \quad (\text{D.31})$$

where the variable z counts the number of TL sites on the left and w counts the number of TL sites on the right. One can think of $\mathcal{G}(z, w)$ as a two-point “propagator” with $k = 0$ and $\mathcal{J}_0(r, z, w)$ as the source which increases k by 1. For example, using these elements we can write down the two-variable

generating function for two-sided diagrams

$$\mathcal{Y}_0 = \mathcal{G} + \mathcal{J}_0 + \mathcal{J}_0 \mathcal{G} \mathcal{J}_0 + \dots \quad (\text{D.32})$$

or in algebraic form

$$\begin{aligned} \mathcal{Y}_0(r, z, w) &= \mathcal{G}(z, w) (1 + \mathcal{G}(z, w)\mathcal{J}_0(r, z, w) + \mathcal{G}(z, w)^2\mathcal{J}_0(r, z, w)^2 + \dots) \\ &= \frac{\mathcal{G}(z, w)}{1 - \mathcal{G}(z, w)\mathcal{J}_0(r, z, w)} \end{aligned} \quad (\text{D.33})$$

To write down the generating for leading diagrams in $\langle x | D(h) | y \rangle$, we introduce additional $c(\cdot)$ -weighted source functions $\mathcal{J}_1(z, w)$ and $\mathcal{J}_2(r, z, w)$, defined by

$$\begin{aligned} \mathcal{J}_1 &= zw \text{ (diagram)} + z^2w \text{ (diagram)} + zw^2 \text{ (diagram)} + \dots \\ &= \left(z \text{ (diagram)} + z^2 \text{ (diagram)} + \dots \right) \left(w \text{ (diagram)} + w^2 \text{ (diagram)} + \dots \right) \end{aligned} \quad (\text{D.34})$$

$$\begin{aligned} \mathcal{J}_2 &= r \left(z^2w^2 \text{ (diagram)} + 2z^2w^3 \text{ (diagram)} + 2z^3w^2 \text{ (diagram)} + \dots \right) \\ &= qr \left(z^2 \text{ (diagram)} + 2z^3 \text{ (diagram)} + \dots \right) \left(w^2 \text{ (diagram)} + 2w^3 \text{ (diagram)} + \dots \right) \end{aligned} \quad (\text{D.35})$$

where we weight each diagram by product of the number of outer strands on each sides (marked by red crosses above). Algebraically these equations read

$$\mathcal{J}_1(z, w) = \frac{qz}{1 - zC(q, z)} \frac{qw}{1 - wC(q, w)} = H(q, 0, z)H(q, 0, w) \quad (\text{D.36})$$

$$\mathcal{J}_2(r, z, w) = qr \frac{z^2C(q, z)}{(1 - zC(q, z))^2} \frac{w^2C(q, w)}{(1 - wC(q, w))^2} \quad (\text{D.37})$$

Finally we can form the generating function for $\langle x | D(h) | y \rangle$ using

$$\mathcal{Y}_1 = \begin{array}{c} \text{---} \\ | \\ \boxed{\mathcal{Y}_1} \\ | \\ \text{---} \end{array} = \begin{array}{c} \boxed{\mathcal{G}} \\ | \\ \boxed{\mathcal{J}_1} \\ | \\ \boxed{\mathcal{G}} \end{array} + 2 \begin{array}{c} \boxed{\mathcal{G}} \\ | \\ \boxed{\mathcal{J}_1} \\ | \\ \boxed{\mathcal{G}} \\ | \\ \boxed{\mathcal{J}_0} \\ | \\ \boxed{\mathcal{G}} \end{array} + 3 \begin{array}{c} \boxed{\mathcal{G}} \\ | \\ \boxed{\mathcal{J}_1} \\ | \\ \boxed{\mathcal{G}} \\ | \\ \boxed{\mathcal{J}_0} \\ | \\ \boxed{\mathcal{G}} \\ | \\ \boxed{\mathcal{J}_0} \\ | \\ \boxed{\mathcal{G}} \end{array} + \dots \quad (\text{D.38})$$

and similarly for \mathcal{J}_2 . Algebraically this equation is

$$\mathcal{Y}_i(r, w, z) = \frac{\mathcal{J}_i(r, w, z)\mathcal{G}(w, z)^2}{(1 - \mathcal{J}_0(r, w, z)\mathcal{G}(w, z))^2}, \quad i = 1, 2 \quad (\text{D.39})$$

The reason we separate the weighted generating function into \mathcal{Y}_1 and \mathcal{Y}_2 is that after the indicated surgery is performed, the number of loops in diagrams of type \mathcal{J}_1 *decreases* by 1 (this is the only case for $k = 0$); whereas diagrams of type \mathcal{J}_2 *increases* by 1. Denote the triple expansion coefficient of $\mathcal{Y}_i(r, z, w)$ by

$$\mathcal{Y}_i(q, r, w, z) = \sum_{\mu, \nu, k=0}^{\infty} y_{\mu\nu k}^{(i)}(q) z^\mu w^\nu r^k \quad (\text{D.40})$$

This allows us to write down

$$\begin{aligned} q^{-k} \left\langle v_k^{(m)}(q) \middle| \Delta M_k^{(m)}(q') \middle| v_k^{(m)}(q) \right\rangle \\ \approx \left(q' y_{m/2, m/2, k}^{(1)}((qq')^{-1}) + q'^{-1} y_{m/2, m/2, k}^{(2)}((qq')^{-1}) \right) \chi^{m-2k-1} + O(\chi^{m-2k-2}) \end{aligned} \quad (\text{D.41})$$

The first order correction to $\lambda_{M_k^{(m)}}$ from subleading diagrams is thus

$$\Delta_2 \lambda_{M_k^{(m)}} \approx \left((q_A + q_B) y_{m/2, m/2, k}^{(1)}(q_{AB}^{-1}) + (q_A^{-1} + q_B^{-1}) y_{m/2, m/2, k}^{(2)}(q_{AB}^{-1}) \right) \chi^{m-2k-1} \quad (\text{D.42})$$

Although it is not immediately apparent, Eq. (D.29) can be recovered by taking $k = 0$.

- sector mixing

We now give a brief argument that the correction to the degenerate zero eigenvalues in each sector vanish to the first order. In short, we need to find the first order corrections to the null states of the product matrix $M_k^{(m)}(q_A)M_k^{(m)}(q_B)$. We need to apply first order degenerate perturbation theory. Denote

$$\Pi_k^{(m)} = \text{id} - \frac{|v_k^{(m)}(q_A)\rangle \langle v_k^{(m)}(q_B)|}{\langle v_k^{(m)}(q_A) | v_k^{(m)}(q_B) \rangle} \quad (\text{D.43})$$

to be the projector onto the left and right null spaces. To find the perturbation one needs to diagonalize the following matrix

$$\Pi_k^{(m)} \left(\Delta M_k^{(m)}(q_A)(M_0)_k^{(m)}(q_B) + (M_0)_k^{(m)}(q_A)\Delta M_k^{(m)}(q_B) \right) \Pi_k^{(m)} = 0, \quad (\text{D.44})$$

since $(M_0)_k^{(m)}(q)$ is annihilated by the projector $\Pi_k^{(m)}$. Therefore the order $O(\chi^{-1})$ corrections to the zero eigenvalues vanish and the degeneracy is not removed.

The degeneracy is only broken at $O(\chi^{-2})$. At the next order one has the second order contribu-

tion of $\Delta M_k^{(m)}(q_A)(M_0)_k^{(m)}(q_B) + (M_0)_k^{(m)}(q_A)\Delta M_k^{(m)}(q_B)$ as well as the first order contribution of $\Delta M_k^{(m)}(q_A)\Delta M_k^{(m)}(q_B)$, and all other contribution is annihilated by the projector. While the detailed effect of sector mixing is interesting on its own in that there seems to be an additional hierarchy structure from our TL numerics, its effect on the reflected entropy is to the order $O(\chi^{-2})$ which is outside our main interest here.

D.2.3 Explicit form for $k = 0$ and $k = 1$

Here we will perform explicit analytic continuation $m \rightarrow 1$ to find the leading order corrections to the spectral eigenvalue λ_0 and λ_1 . Together they determine the leading corrections to the reflected entropy in powers of χ .

- $k = 0$

The generating function for $\Delta_1\lambda$ can be written as

$$\frac{\chi}{q_A + q_B} G_1(r = 0, z) = \frac{-1 + (1 + q_{AB})\chi z}{2q_{AB}^2\chi^2 z^2} + \frac{1 - 2(1 + q_{AB})\chi z + (1 + q_{AB}^2)\chi^2 z^2}{2q_{AB}\chi^2 z^2 \sqrt{(1 + \chi z(q_{AB} - 1))^2 - 4q_{AB}\chi z}} \quad (\text{D.45})$$

As in the case of main text there is a branch cut induced by the square root. To perform the analytic continuation via contour integral, we chose our contour to wrap around the branch cut. Additional poles at $z = 0$ does not contribute to the integral. To set up our notation, define

$$D_n(q) \equiv -\frac{1}{\pi} \text{Im} \int_{z_-}^{z_+} \frac{dz}{z^n \sqrt{(1 + z(q - 1))^2 - 4qz}} \quad (\text{D.46})$$

$$= \begin{cases} {}_2F_1(1 - n, 1 - n; 1; q), & q \leq 1, \\ q^{n-1} {}_2F_1(1 - n, 1 - n; 1; q^{-1}), & q > 1 \end{cases} \quad (\text{D.47})$$

as the analytic continuation for the series coefficients of $z/\sqrt{(1 + z(q - 1))^2 - 4qz}$. An contour integral gives the expression for $\delta g_{1/2,0}$:

$$\begin{aligned} \delta g_{1/2,0}(q_A, q_B) &= -\frac{1}{\pi} \text{Im} \int_{z_-/\chi}^{z_+/\chi} G_1(0, z) z^{-3/2} dz \\ &= \frac{(q_A + q_B)}{2q_{AB}\sqrt{\chi}} ((1 + q_{AB}^2)D_{3/2}(q_{AB}) - 2(1 + q_{AB})D_{5/2}(q_{AB}) + D_{7/2}(q_{AB})) \end{aligned} \quad (\text{D.48})$$

and

$$\begin{aligned} \Delta_1\lambda_0 &= \frac{2q_{AB}}{\sqrt{\chi}} g_{1/2,0}(q_{AB}^{-1}) g_{1/2,0}^{(1)}(q_A^{-1}, q_B^{-1}) \\ &= \frac{(q_A^{-1} + q_B^{-1})}{\chi} C_{1/2}(q_{AB}^{-1}) ((1 + q_{AB}^{-2})D_{3/2}(q_{AB}^{-1}) - 2(1 + q_{AB}^{-1})D_{5/2}(q_{AB}^{-1}) + D_{7/2}(q_{AB}^{-1})) \end{aligned} \quad (\text{D.49})$$

The expression for $\Delta_2\lambda_0$ is also easy to write down. We work with the single variable generating function Eq. (D.26) here. Use Eq. (5.72) one arrives at

$$Y(q, z) = \left(\frac{1}{z} - q\right) C(q, z) - \frac{1}{z} \quad (\text{D.50})$$

which gives

$$\begin{aligned}\Delta_2\lambda_0 &= \frac{q_{AB}(q_A + q_B)}{\chi} \left(\frac{1}{\pi} \text{Im} \int_{z^-}^{z^+} Y(q_{AB}^{-1}, z) z^{-3/2} dz \right)^2 \\ &= \frac{q_{AB}(q_A + q_B)}{\chi} (C_{3/2}(q_{AB}^{-1}) - q_{AB}^{-1} C_{1/2}(q_{AB}^{-1}))^2\end{aligned}\quad (\text{D.51})$$

and the first order correction is

$$\Delta\lambda_0 = \Delta_1\lambda_0 + \Delta_2\lambda_0 \quad (\text{D.52})$$

- $k = 1$

Extracting the linear r order coefficient of the generating functions we get

$$\begin{aligned}\frac{\chi^2}{q_A + q_B} \frac{\partial G_1(r, z)}{\partial r} \Big|_{r=0} &= \frac{-1 + (q_{AB} + 1)\chi z + q_{AB}^2 z^2 - (q_{AB}^2 - q_{AB})^2 \chi^3 z^3}{2q_{AB}^2 \chi^3 z^3} \\ &+ \frac{1 - 2(q_{AB} + 1)\chi z + \chi^2 z^2 + 2q_{AB}^3 \chi^3 z^3 - (q_{AB}^2 - q_{AB})^2 \chi^4 z^4}{2q_{AB}^2 \chi^3 z^3 \sqrt{(1 + \chi z(q_{AB} - 1))^2 - 4q_{AB}\chi z}}\end{aligned}\quad (\text{D.53})$$

The first term on RHS is irrelevant for determining the contour integral. We have

$$\begin{aligned}g_{1/2,1}^{(1)}(q_A, q_B) &= -\frac{1}{\pi} \text{Im} \int_{z^-/\chi}^{z^+/\chi} \partial_r G_1(0, z) z^{-3/2} dz \\ &= \frac{q_A + q_B}{2\chi^{3/2}} \left(-(q_{AB} - 1)^2 D_{1/2}(q_{AB}) + 2q_{AB} D_{3/2}(q_{AB}) + q_{AB}^{-2} D_{5/2}(q_{AB}) \right. \\ &\quad \left. - 2(q_{AB}^{-2} + q_{AB}^{-1}) D_{7/2}(q_{AB}) + q_{AB}^{-2} D_{9/2}(q_{AB}) \right)\end{aligned}\quad (\text{D.54})$$

and

$$\begin{aligned}\Delta_1\lambda_1 &= \frac{2}{\chi^{3/2}} g_{1/2,1}(q_{AB}^{-1}) g_{1/2,1}^{(1)}(q_A^{-1}, q_B^{-1}) \\ &= \frac{(q_A^{-1} + q_B^{-1})}{\chi^3} (-C_{1/2}(q_{AB}^{-1}) + q_{AB} C_{3/2}(q_{AB}^{-1})) \\ &\quad \times \left((-q_{AB}^{-1} - 1)^2 D_{1/2}(q_{AB}^{-1}) + 2q_{AB}^{-1} D_{3/2}(q_{AB}^{-1}) + q_{AB}^2 D_{5/2}(q_{AB}^{-1}) \right. \\ &\quad \left. - 2(q_{AB}^2 + q_{AB}) D_{7/2}(q_{AB}^{-1}) + q_{AB}^2 D_{9/2}(q_{AB}^{-1}) \right)\end{aligned}\quad (\text{D.55})$$

The two variable generating function $\mathcal{Y}_i(q, r, z, w)$ factorizes when expanded as a series of r . We are interested in terms linear to r here, which is

$$\begin{aligned}\frac{\partial \mathcal{Y}_2(q, r, z, w)}{\partial r} \Big|_{r=0} &= \frac{qz^2 w^2 C(q, z)^3 C(q, w)^3}{(1 - zC(q, z))^2 (1 - wC(q, w))^2}, \\ \frac{\partial \mathcal{Y}_1(q, r, z, w)}{\partial r} \Big|_{r=0} &= 2q^2 \frac{\partial \mathcal{Y}_2(q, r, z, w)}{\partial r} \Big|_{r=0}\end{aligned}\quad (\text{D.56})$$

Using Eq. (5.72) we can write the individual factors as

$$\hat{Y}(q, z) \equiv \frac{z^2 C(q, z)^2}{(1 - zC(q, z))^2} = \frac{-1 + (1 + q)z}{q^2 z^2} + \frac{1 - (2q + 1)z + q^2 z^2}{q^2 z^2} C(q, z) \quad (\text{D.57})$$

$\hat{Y}(q, z)$ has the following contour integral

$$-\frac{1}{\pi} \text{Im} \int_{z_-}^{z_+} \frac{dz}{z^{3/2}} \hat{Y}(q, z) = C_{1/2}(q) - (2q^{-1} + q^{-2})C_{3/2}(q) + q^{-2}C_{5/2}(q) \quad (\text{D.58})$$

which gives the following analytic continuation for the expansion coefficient

$$\begin{aligned} y_{1/2,1/2,1}^{(2)}(q) &= q (C_{1/2}(q) - (2q^{-1} + q^{-2})C_{3/2}(q) + q^{-2}C_{5/2}(q))^2, \\ y_{1/2,1/2,1}^{(1)}(q) &= 2q^2 y_{1/2,1/2,1}^{(2)}(q) \end{aligned} \quad (\text{D.59})$$

and

$$\Delta_2 \lambda_1 = \frac{3(q_A^{-1} + q_B^{-1})}{\chi^3} (C_{1/2}(q_{AB}^{-1}) - (2q_{AB} + q_{AB}^2)C_{3/2}(q_{AB}^{-1}) + q_{AB}^2 C_{5/2}(q_{AB}^{-1}))^2 \quad (\text{D.60})$$

The first order correction to the leading eigenvalue in $k = 2$ sector is given by

$$\Delta \lambda_1 = \Delta_1 \lambda_1 + \Delta_2 \lambda_1 \quad (\text{D.61})$$

D.3 Asymptotic behavior of $p_k(s)$

The purpose of this Appendix is to study the asymptotic behavior of the function $p_k(s)$, which arises in the calculation of the modular flowed reflected entropy in the 2TN model as the classical probability associated to the super-selection sectors. By studying this function in detail, one can prove that the entropy increases without bound as $s \rightarrow \infty$ and as an evidence that there is an emergent type-II₁ von Neumann algebra.

The function of interest can be expressed as a simple contour integral

$$p_k(q, s) = q^{1-k} g_{1/2+is,k}(q^{-1}) g_{1/2-is,k}(q^{-1}), \quad (\text{D.62})$$

$$g_{m,k}(q) = \frac{1}{2\pi i} \oint \frac{dz}{z^{m+1}} C(q, z) (C(q, z) - 1)^k q^{-k} \quad (\text{D.63})$$

where

$$C(q, z) = \frac{1 - z(q-1) + |q-1| \sqrt{z-z_+} \sqrt{z-z_-}}{2z}, \quad z_{\pm} = \frac{1}{(1 \mp \sqrt{q})^2} \quad (\text{D.64})$$

is the generating function of the q-Catalan numbers. $C(q, z)$ has a branch cut running from (z_-, z_+) and the contour of integration is chosen to encircle this branch cut. For a given integer k , one can express p_k in terms of a linear combination over (analytically continued) q-Catalan numbers. For example,

$$g_{m,0}(q) = C_m(q), \quad g_{m,1}(q) = q^{-1} C_{m+1}(q) - C_m(q), \quad \dots \quad (\text{D.65})$$

At large k the expression becomes really complicated and is not useful for determining an asymptotic expression. Instead I will work with the integral expression Eq. (D.62) directly. We will be using saddle point approximation and related methods to extract the large s, k behavior of this integral.

To have a better idea of how the function p_k for typical k looks like, we include an exemplary plot for $p_k(q, s)$ in Fig. (D.5): We can roughly classify the behavior with respect to s into four different regimes, which is characterized by a single number $s^* \equiv k|1 - q|/(2\sqrt{q})$.

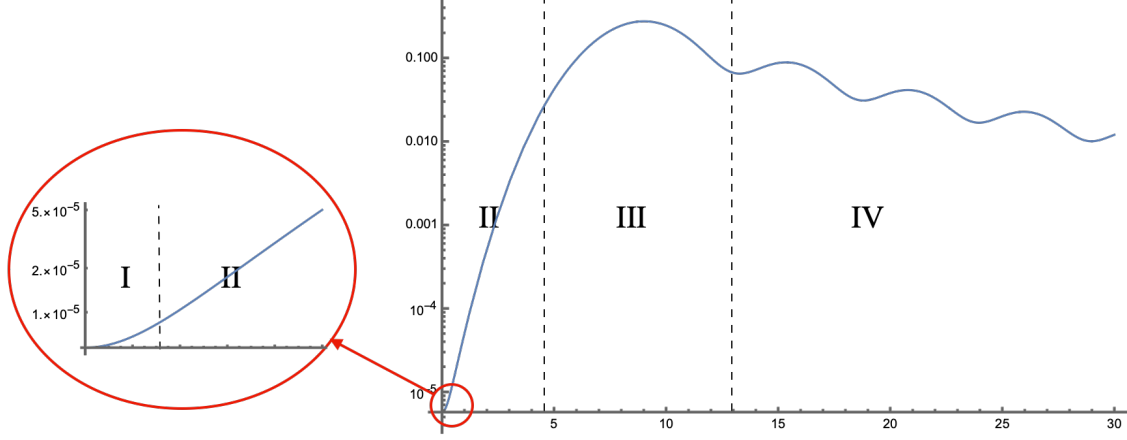


Figure D.5: A plot of $p_k(q, s)$ for $k = 5$ and $q = 10$. The four different regimes are also labeled.

- (I) $s \ll q^{-1}$ (if $q < 1$), or $s \ll q$ (if $q > 1$):

This is not really the limit we are interested in, since in this regime $s \sim O(k^0)$. Nevertheless one can directly expand the integrand of Eq. (D.62) in powers of q and show that under this limit

$$p_k(q, s) \approx \begin{cases} \frac{\Gamma(-\frac{1}{2} + k - is)\Gamma(-\frac{1}{2} + k + is)}{\pi\Gamma(k)^2} q^{1-k} \cosh(\pi s), & q \gg 1 \\ \frac{\Gamma(-\frac{1}{2} + k - is)\Gamma(-\frac{1}{2} + k + is)}{4k^2\pi\Gamma(k)^2} q^k \cosh(\pi s), & q \ll 1 \end{cases} \quad (\text{D.66})$$

which is a simple modification of the asymptotics we found in Sec. (5.4.3). This formula actually still applies in regime II as long as $q \ll s/k$ or $q \gg s/k$.

- (II) $s \ll s^*$ but not of order $q(q^{-1})$:

p_k is growing exponentially in this regime. Using saddle point approximation one can show that

$$p_k(q, s) \underset{s \ll s^*}{\approx} \begin{cases} \frac{1}{2\pi k} q^{-2-k} (q-1)^3 e^{\pi s}, & q > 1 \\ \frac{1}{2\pi k^3} q^k (1-q) s^2 e^{\pi s}, & q < 1 \end{cases} \quad (\text{D.67})$$

- (III) $s \simeq s^*$:

This is the most interesting regime, as p_k attains its maximum here. However naive saddle point approximation breaks down here and using uniform asymptotic expansion one can show that to the leading order in k and when $|\log q| \gg 1$,

$$p_k(q, s) \underset{k \gg 1, s \approx s^*}{\approx} \begin{cases} \frac{2^{8/3}}{k^{2/3}} \text{Ai}^2 \left(-\frac{2^{4/3}}{k^{1/3}} \left(\frac{s}{\sqrt{q}} - \frac{k}{2} \right) \right), & q \gg 1 \\ \frac{2^{8/3}}{k^{2/3}} \text{Ai}^2 \left(-\frac{2^{4/3}}{k^{1/3}} \left(s\sqrt{q} - \frac{k}{2} \right) \right), & q \ll 1 \end{cases} \quad (\text{D.68})$$

For a more detailed expression which is valid for all q and a first order correction please see the analysis part. This region is where the prominent contribution of p_k comes from (when viewed as a function of k , fixing s). Using the formula above one can easily argue that this region contributes to $\sim O(1)$ of the total probability, and its contribution to the reflected entropy scales as $O(s)$.

(IV) $s \gg s^*$: This is a “ringdown” regime for p_k where it starts oscillate and decay. A stationary phase analysis in this regime shows that the decay rate is $\sim s^{-3}$ and the oscillation frequency is $2 \log \left| \frac{\sqrt{q}-1}{\sqrt{q}+1} \right|$, independent of k .

$$p_k(q, s) \underset{s \gg s^*}{\approx} \frac{q^{-3/2} k^2}{4\pi s^3} \left| i(-)^k (\sqrt{q}-1)^3 |\sqrt{q}-1|^{2is} + (\sqrt{q}+1)^3 |\sqrt{q}+1|^{2is} \right|^2 \quad (\text{D.69})$$

Asymptotic analysis

Our main tool for obtaining the asymptotic behavior for g_k (and hence p_k) would be saddle point approximation. We begin by rewriting the integral for g_k as

$$g_{1/2+is, k}(q, s) = \frac{1}{2\pi i} \oint dz \frac{C(q, z)}{z^{3/2}} e^{-kf(q, z)}, \quad f(q, z) = -\log \left(\frac{C(q, z) - 1}{qz^{i\sigma}} \right) \quad (\text{D.70})$$

where $\sigma \equiv s/k$ is a $O(1)$ variable. At large k the integral is dominated by the saddle points of $f(q, z)$ in the complex plane of z . They are given by the expression

$$\zeta_{\pm} = \frac{(q+1)\sigma \pm \sqrt{4q\sigma^2 - (q-1)^2}}{(q-1)^2\sigma} = \zeta^* \pm \frac{\sqrt{(\sigma/\sigma^*)^2 - 1}}{|q-1|\sigma} \quad (\text{D.71})$$

where we define

$$\zeta^* = \frac{q+1}{(q-1)^2}, \quad \sigma^* = \frac{|q-1|}{2\sqrt{q}} \quad (\text{D.72})$$

The behavior of the saddles depends on whether σ is larger or smaller than σ^* . When $\sigma > \sigma^*$, both ζ_+ and ζ_- are real and valid saddles for the $f(q, z)$. When $\sigma < \sigma^*$, ζ_{\pm} becomes complex. Moreover ζ_- ceases to be a saddle and only ζ_+ remains on the principal branch. We summarize the movement of ζ_{\pm} with respect to σ in Fig. (D.6).

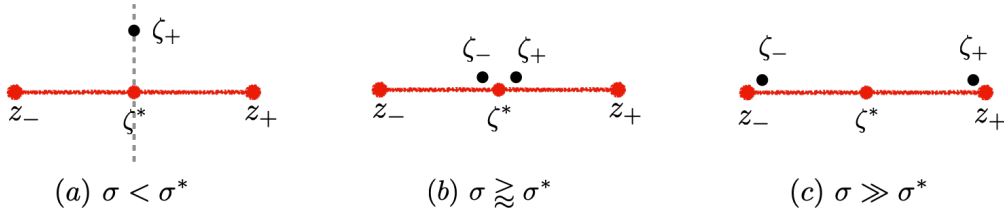


Figure D.6: The location of the saddle points ζ_{\pm} with respect to the flow parameter σ . The red line indicates the branch cut of the function $f(q, z)$. (a) when $\sigma < \sigma^*$, there is only one saddle ζ_+ with $\Im(\zeta_+) > 0$. (b) when $\sigma \approx \sigma^*$ but $\sigma > \sigma^*$, there are two saddles very close to each other. As $\sigma \rightarrow \sigma^*$, the two saddles coalesce at ζ^* . (c) when $\sigma \gg \sigma^*$, the two saddles ζ_{\pm} approaches two branch points of the square root.

We have to treat these three different scenarios as separate cases. In both cases of (a) and (c) a regular saddle point analysis will do the job for us. However for case (b) where the two saddles are coalescing, the naive saddle point approximation fails and we need to resort to the method of *uniform asymptotic expansions*.

- case (a)

We will assume that $\sigma \ll \sigma^*$. This choice corresponds to regime II in Fig. (D.5). Under this limit the

saddle point can be approximated by

$$\zeta_+ \underset{\sigma \ll \sigma^*}{\approx} \frac{i}{|q-1|\sigma} + \zeta^* + O(\sigma) \quad (\text{D.73})$$

Saddle point approximation then gives ⁴

$$g_{1/2+is,k}(q, s) \approx \frac{C(q, \zeta_+)}{\zeta_+^{3/2}} \sqrt{\frac{1}{2\pi k f''(\zeta_+)}} e^{-kf(q, \zeta_+)} \quad (\text{D.74})$$

$$\underset{\sigma \ll \sigma^*}{\approx} \begin{cases} (2\pi k)^{-1/2} (1-q)^{3/2} (-i\sigma(1-q))^{is}, & q < 1 \\ i\sigma(2\pi k)^{-1/2} (q-1)^{1/2} q^{-k} (-i\sigma(q-1))^{is}, & q > 1 \end{cases}$$

Note that as $\sigma \rightarrow -\sigma$, the function satisfies $g_{1/2+is} \rightarrow \bar{g}_{1/2-is}$. And since $p_k \sim g_{1/2+is}g_{1/2-is}$, it is guaranteed to be real and only depends on the modulus of g . After a bit of arithmetic we get

$$p_k(q, s) \underset{k \gg 1, s \ll s^*}{\approx} \begin{cases} \frac{1}{2\pi k} q^{-2-k} (q-1)^3 e^{\pi s}, & q > 1 \\ \frac{1}{2\pi k^3} q^k (1-q) s^2 e^{\pi s}, & q < 1 \end{cases} \quad (\text{D.75})$$

- case (c)

This case corresponds to regime IV in Fig. (D.5). We have two real saddles here, and in the limit $\sigma \gg \sigma^*$ they move close to the two branch points $\{z_+, z_-\}$.

$$\zeta_{\pm} = \frac{1}{(1 \mp \sqrt{q})^2} \mp \frac{1}{4\sqrt{q}\sigma^2} + O(\sigma^{-3}) \quad (\text{D.76})$$

The saddle point approximation now has two terms

$$g_{1/2+is,k}(q, s) \approx \frac{C(q, \zeta_+)}{\zeta_+^{3/2}} \sqrt{\frac{1}{2\pi k f''(\zeta_+)}} e^{-kf(q, \zeta_+)} + \frac{C(q, \zeta_-)}{\zeta_-^{3/2}} \sqrt{\frac{1}{2\pi k f''(\zeta_-)}} e^{-kf(q, \zeta_-)}$$

$$\approx \sqrt{\frac{1}{4\pi k \sigma^3}} q^{-k/2-1/4} \left((-)^k (1-\sqrt{q})^3 e^{\pi i/4} |1-\sqrt{q}|^{2is} + (1+\sqrt{q})^3 e^{-\pi i/4} |1+\sqrt{q}|^{2is} \right) \quad (\text{D.77})$$

Hence

$$p_k(q, s) = q^{1-k} g_{1/2+is,k}(q^{-1}, s) g_{1/2-is,k}(q^{-1}, s) \quad (\text{D.78})$$

$$\underset{k \gg 1, s \gg s^*}{\approx} \frac{q^{-3/2} k^2}{4\pi s^3} \left| i(-)^k (\sqrt{q}-1)^3 |\sqrt{q}-1|^{2is} + (\sqrt{q}+1)^3 |\sqrt{q}+1|^{2is} \right|^2$$

Thus we find that at late time p_k decays as $\sim s^{-3}$. The angular frequency of oscillation can be estimated to be

$$\omega = 2 \log \left| \frac{\sqrt{q}-1}{\sqrt{q}+1} \right| \approx \begin{cases} \frac{4}{\sqrt{q}}, & q \gg 1 \\ 4\sqrt{q}, & q \ll 1 \end{cases} \quad (\text{D.79})$$

⁴Up to a factor of $-i$ which we ignore since p_k only depends on the modulus of $g_{m,k}$.

which is independent of k . We plot the asymptotics we found under case (a) and (c) and compare with the actual function in Fig. (D.7)

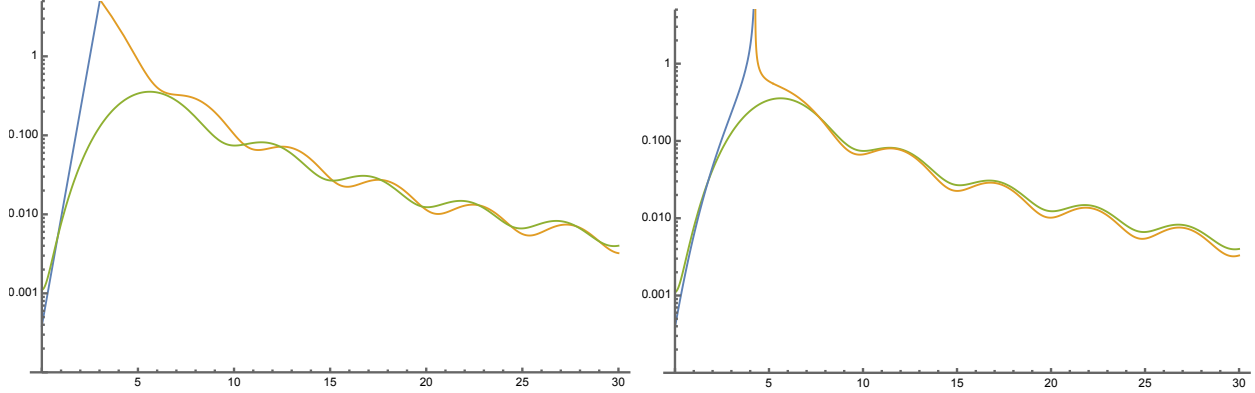


Figure D.7: (left) The asymptotics obtained so far (eq. (D.75) and (D.78)) as blue and orange, versus the actual p_k , as green. We pick $k = 3$ and $q = 10$ here. (right) More accurate asymptotics are available if we do not take the limit $s \gg s^*$ (or $s \ll s^*$) when formulating the saddle point approximations. This way the expressions are much more complicated but captures the original function a lot better. However it is clear that we need a new approximation formula in the crossover region.

- case (b)

This case corresponds to regime III in Fig. (D.5). As $\sigma \rightarrow \sigma^*$ the second derivative $f''(\zeta)$ becomes degenerate and the approximation breaks down, as seen in Fig. (D.7). In general, to deal with these kind of problems of coalescing saddle points one needs to use the method of *uniform asymptotic approximations*. The basic idea here is to find a one-to-one map $u(z)$ near the vicinity of ζ^* that takes the function $f(z, \sigma)$ to a cubic polynomial

$$f(z, \sigma) \rightarrow f(u, \sigma) = \frac{1}{3}u^3 - B^2(\sigma)u + \eta(\sigma), \quad (\text{D.80})$$

which is always possible since the third derivative $f'''(\zeta)$ is always non-degenerate near σ^* . Having done so the original expression can then be integrated repeatedly to a series in terms of Airy functions $\text{Ai}(z)$ and $\text{Ai}'(z)$:

$$\frac{e^{k\eta}}{2\pi i} \int h(z)e^{-kf(z,\sigma)} dz = \frac{\text{Ai}(k^{2/3}B^2)}{k^{1/3}} \left(\sum_{m=0}^{\infty} \frac{a_m}{k^m} \right) + \frac{\text{Ai}'(k^{2/3}B^2)}{k^{2/3}} \left(\sum_{m=0}^{\infty} \frac{b_m}{k^m} \right) \quad (\text{D.81})$$

where the lowest order coefficients are

$$B = \left(\frac{3}{4}[f(\zeta_-, \sigma) - f(\zeta_+, \sigma)] \right)^{1/3}, \quad \eta = \frac{1}{2}[f(\zeta_-, \sigma) + f(\zeta_+, \sigma)], \quad (\text{D.82})$$

$$a_0 = \frac{1}{2}(\phi_+ + \phi_-), \quad b_0 = \frac{1}{2B}(\phi_+ - \phi_-), \quad \phi_{\pm} = h(z) \sqrt{\frac{\pm 2B}{f''(z)}} \Big|_{z=\zeta_{\pm}}$$

For more detailed treatment please refer to standard references on this subject, e.g. [203].

For the present case we are mainly interested in the behavior near $\sigma \simeq \sigma^*$, where the saddles has an

expansion in $\Delta\sigma \equiv \sigma - \sigma^*$ as

$$\zeta_{\pm} \simeq \zeta^* \pm \frac{4q^{3/4}}{|q-1|^{5/2}} \sqrt{\Delta\sigma} \equiv \zeta^* \pm \zeta_0 \sqrt{\Delta\sigma} \quad (\text{D.83})$$

and we have, up to leading order in $\Delta\sigma$,

$$B \approx i \left(\frac{4q^{3/4}}{(q+1)\sqrt{|q-1|}} \right)^{1/3} \sqrt{\Delta\sigma} \equiv B_0 \sqrt{\Delta\sigma}, \quad e^{-\eta} \approx e^{-f(\zeta^*, \sigma^*)} = \frac{i|q-1| - 2\sqrt{q}}{\sqrt{q}(q+1)(\zeta^*)^{i\sigma^*}} \quad (\text{D.84})$$

$$a_0 \approx h(\zeta^*) \sqrt{\frac{2B_0}{\zeta_0 f^{(3)}(\zeta^*)}} = -\frac{2^{4/3} (i\sqrt{q}(q-1)^3 + q|q-1|^3)}{(q+1)^{13/6} |q-1|^{4/3}} \quad (\text{D.85})$$

$$\begin{aligned} b_0 &\approx \frac{1}{\sqrt{2B_0}} \left(\frac{2\zeta_0 h'(\zeta^*)}{\sqrt{\zeta_0 f^{(3)}(\zeta^*)}} - \frac{h(\zeta^*)}{(\zeta_0 f^{(3)}(\zeta^*))^{3/2}} \left(\frac{(\zeta_0)^2 f^{(4)}(\zeta^*)}{2} + \left. \frac{\partial f(z)}{\partial s} \right|_{\zeta^*} \right) \right) \\ &= -\frac{2^{5/3} q(q-1)^3 (4i\sqrt{q}(q-1)^5 + (q-3)|q-1|^5)}{(q+1)^{17/6} |q-1|^{20/3}} \end{aligned} \quad (\text{D.86})$$

We include an example plot for this asymptotic expansion given by these parameters in Fig. (D.8).

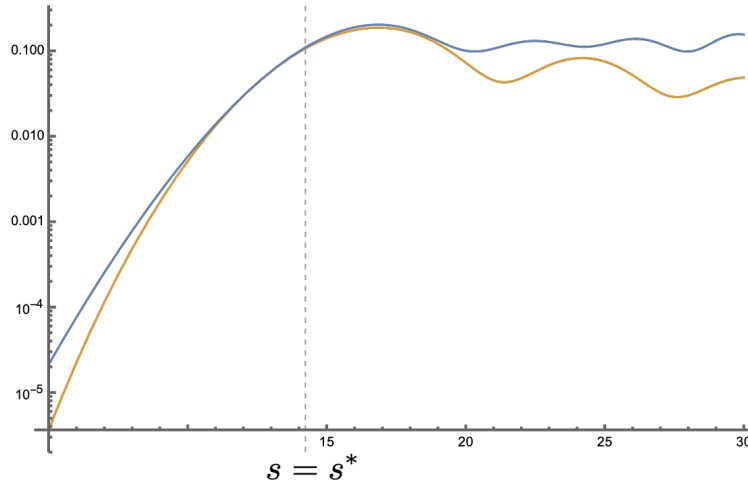


Figure D.8: The asymptotic expansion given by the coefficients Eq. (D.84)-(D.86) (blue), plotted against the actual $p_k(q, s)$ (orange). The parameters chosen in this plot are $q = 10, k = 10$. The blue asymptote is obtained as an approximate formula near $s = s^*$, shown as the gray dashed curve. Like in the previous case a more accurate formula can be obtained if one uses directly the definition (Eq. (D.82)). For $k = 10$ it almost directly lies on the orange curve so we did not include it here.

If we only keep the leading k term then one has ⁵

$$g_{1/2+is, k}(q, s) \underset{k \gg 1, s \gtrsim s^*}{\approx} e^{-k\eta} a_0 \frac{\text{Ai}(k^{2/3} B^2)}{k^{1/3}} + O(k^{-3/2}) \quad (\text{D.87})$$

$$\underset{k \gg 1, s \approx s^*}{\approx} \begin{cases} \frac{q^{-k/2}}{k^{1/3}} (2^{4/3} \sqrt{q}) \text{Ai} \left(-\frac{2^{4/3} (s\sqrt{q} - \frac{k}{2})}{k^{1/3}} \right), & q \ll 1 \\ \frac{q^{-k/2}}{k^{1/3}} (2^{4/3} \sqrt{q}) \text{Ai} \left(-\frac{2^{4/3} (\frac{s}{\sqrt{q}} - \frac{k}{2})}{\sqrt{q} k^{1/3}} \right), & q \gg 1 \end{cases} \quad (\text{D.88})$$

⁵Up to a phase.

and

$$p_k(q, s) \underset{k \gg 1, s \approx s^*}{\approx} \begin{cases} \frac{2^{8/3}}{k^{2/3}} \text{Ai}^2 \left(-\frac{2^{4/3}}{k^{1/3}} \left(\frac{s}{\sqrt{q}} - \frac{k}{2} \right) \right), & q \gg 1 \\ \frac{2^{8/3}}{k^{2/3}} \text{Ai}^2 \left(-\frac{2^{4/3}}{k^{1/3}} (s\sqrt{q} - \frac{k}{2}) \right), & q \ll 1 \end{cases} \quad (\text{D.89})$$

p_k attains its maximum at the first saddle of the Airy function, which occurs at

$$k^{2/3} B^2 \approx -\frac{2^{4/3} (s\sqrt{q} - \frac{k}{2})}{k^{1/3}} = -1.019 \dots, \quad q < = \min(q, q^{-1}) \quad (\text{D.90})$$

or

$$s \approx \frac{1}{\sqrt{q <}} \left(\frac{k}{2} + (0.404 \dots) k^{1/3} \right) \quad (\text{D.91})$$

with a maximum value of

$$\max_s p_k(q, s) \approx \frac{2^{8/3}}{k^{2/3}} |\text{Ai}(-1.019 \dots)|^2 = \frac{1.822 \dots}{k^{2/3}} \quad (\text{D.92})$$

Since $s^* \sim k/(2\sqrt{q <})$, this suggests that the maximum occurs at not too far from s^* . The maximum of the peak scales as $k^{-2/3}$, and the width of the peak scales as $k^{1/3}$. When fixing s and viewed as a function of k , the location, height and width of the peak is roughly $(k^* + O((k^*)^{1/3}), (k^*)^{-2/3}, (k^*)^{1/3})$ respectively, where $k^* \sim 2s\sqrt{q <}$.

The total probability under this peak can be estimated by an integral bounded by the first zero of the Airy function, which can be shown to approach a constant as $s \rightarrow \infty$. On the other hand, the reflected entropy is given by the approximate integral

$$S_R \approx \log \chi^2 \int_0^\infty k p_k(q, s) dk \quad (\text{D.93})$$

which can be easily shown to diverge as $O(k^*) \sim O(s\sqrt{q <})$ as $s \rightarrow \infty$.

D.4 Proofs

D.4.1 Proof of Proposition 5.1

Proof. For given m we have a series of unknowns $d_k^{(m)}$ where $k = 0, 1, \dots, m/2$. We pick $m/2$ elements $t_i \in \text{TL}_m$ such that the trace conditions $\text{Tr}_{\text{TL}_m} t_i = \sum_k d_k^{(m)} \text{tr}(\pi_k^{(m)}(t_i))$ give rise to $m/2$ linear equations for which we check that the proposed solutions $d_k^{(m)} = [2k + 1]_q$ satisfy. We pick:

$$\{t_i\} = \left\{ \begin{array}{c} \begin{array}{|c|} \hline \hline \hline \hline \hline \\ \hline \vdots \\ \hline \end{array}, \begin{array}{|c|} \hline \hline \hline \hline \hline \\ \hline \vdots \\ \hline \end{array}, \begin{array}{|c|} \hline \hline \hline \hline \hline \\ \hline \vdots \\ \hline \end{array}, \dots \end{array} \right\} \quad (\text{D.94})$$

or in terms of generators of TL_m :

$$\{t_i\} = \{\text{id}, e_1, e_1 e_3, e_1 e_3 e_5, \dots\} \quad (\text{D.95})$$

The element e_1 maps to the identity matrix in every submodule, so the trace condition for it is simply

$$\sum_{k=0}^{m/2} d_k^{(m)} |\mathcal{V}_k^{(m)}| = \chi^m \quad (\text{D.96})$$

The element e_1 annihilates the module $\mathcal{V}_{m/2}^{(m)}$ since the action of e_1 on any link state will always contain at least 2 closed strands. Next, to calculate $\text{tr}(\pi_k^{(m)}(e_1))$ we must find all elements $v_j \in \mathcal{V}_k^{(m)}$ such that $\pi_k^{(m)}(e_1)v_j \propto v_j$. Such a link state must have a closed strand connecting first two sites, but can otherwise have arbitrary connections in the remaining $m-2$ sites since e_1 act on these sites just as identity. The closed loop after concatenation contribute a single χ for all $\pi_k^{(m)}(e_1)v_j$ and the trace condition for e_2 is thus

$$\sum_{k=0}^{m/2-1} d_k^{(m)} |\mathcal{V}_k^{(m)}| = \chi^{m-2} \quad (\text{D.97})$$

For other elements in the list a similar argument also works as one simply consider link states with progressively more closed strands connecting adjacent pair of sites when constructing the eigenvector of $\pi_k^{(m)}(t_i)$. The trace condition for t_i is

$$\sum_{k=0}^{m/2-i+1} d_k^{(m)} |\mathcal{V}_k^{(m)}| = \chi^{m-2i+2} \quad (\text{D.98})$$

We observe that all the trace conditions have the same form – in fact for any given m only the t_1 condition is new and the remaining $m/2-1$ conditions coincide with the conditions of the $m-1$ module. This means a solution for $d_k^{(m)}$ automatically solves the equations of $d_k^{(m-1)}$. Thus we conclude that $d_k^{(m)}$ is independent of m . As a result, we will drop the m superscript in the remainder of this proof.

Let us reorganize the d_k equations we obtained. Introducing the variable q which satisfies $\chi = q + q^{-1}$ and rewriting $|\mathcal{V}_k^{(m)}|$ using Lemma B.3 we have an infinite set of conditions

$$\sum_{k=0}^{m/2} d_k \# \text{SYT}(m/2+k, m/2-k) = (q + q^{-1})^m, \quad \forall m \in 2\mathbb{Z}_+ \quad (\text{D.99})$$

We now claim $d_k = [2k+1] = q^{-2k} + q^{-2k+2} + \dots + q^{2k}$ solves this equation for every even m . Plug in d_k and match coefficients with the same power of q we find

$$\sum_{k=0}^n \# \text{SYT}(m/2+k, m/2-k) \stackrel{?}{=} \binom{m}{m/2-n} \quad (\text{D.100})$$

Or equivalently

$$\# \text{SYT}(m/2+n, m/2-n) \stackrel{?}{=} \binom{m}{m/2-n} - \binom{m}{m/2-n-1} \quad (\text{D.101})$$

which one can check by explicit computation

$$\begin{aligned} \# \text{SYT}(m/2+n, m/2-n) &= \binom{m}{m/2-n} - \binom{m}{m/2-n-1} \\ &= \frac{m!(2n+1)}{(m/2+n+1)!(m/2-n)!} \end{aligned} \quad (\text{D.102})$$

To show that the matrix trace $\text{tr} = \sum_k d_k \text{tr}_k$ on $\mathcal{V}^{(m)}$ coincides with Tr_{TL_m} for all elements in $\mathcal{V}^{(m)}$, it suffices to check that Eq. (B.16) is true. We have $\text{tr}(\pi^{(m)}(\text{id})) = \chi^m$ by construction, and $\forall h \in \text{TL}_{m-1} \subset \text{TL}_m$ we have

$$\text{tr}(\pi^{(m)}(he_{m-1})) = \text{tr}(\pi^{(m)}(e_{m-1}h)) = \sum_k d_k \text{tr}(\pi_k^{(m)}(e_{m-1}h)) \quad (\text{D.103})$$

To evaluate this trace we must find all links states $v \in \mathcal{B}_k^{(m)}$ such that $e_{m-1}hv \propto v$. We can classify v 's by the contraction pattern of the last two sites. We denote v_1 to be the set such that the last two sites are connected through a closed strand and v_2 to be the remaining ones. Schematically,

$$v_1 = \left[\begin{array}{c} \text{---} \\ \text{---} \\ \text{---} \\ \text{---} \end{array} \right] \begin{array}{c} \text{---} \\ \text{---} \\ \text{---} \\ \text{---} \end{array} \left[\begin{array}{c} \text{---} \\ \text{---} \\ \text{---} \\ \text{---} \end{array} \right] , \quad v_2 = \left[\begin{array}{c} \text{---} \\ \text{---} \\ \text{---} \\ \text{---} \end{array} \right] \begin{array}{c} \text{---} \\ \text{---} \\ \text{---} \\ \text{---} \end{array} \left[\begin{array}{c} \text{---} \\ \text{---} \\ \text{---} \\ \text{---} \end{array} \right] \quad (\text{D.104})$$

where we used colored block to represent arbitrary connections. It is easy to check that

$$e_{m-1}hv = \left[\begin{array}{c} \text{---} \\ \text{---} \\ \text{---} \\ \text{---} \end{array} \right] \begin{array}{c} \text{---} \\ \text{---} \\ \text{---} \\ \text{---} \end{array} \left[\begin{array}{c} \text{---} \\ \text{---} \\ \text{---} \\ \text{---} \end{array} \right] \begin{array}{c} \text{---} \\ \text{---} \\ \text{---} \\ \text{---} \end{array} \left[\begin{array}{c} \text{---} \\ \text{---} \\ \text{---} \\ \text{---} \end{array} \right] \propto \left[\begin{array}{c} \text{---} \\ \text{---} \\ \text{---} \\ \text{---} \end{array} \right] \begin{array}{c} \text{---} \\ \text{---} \\ \text{---} \\ \text{---} \end{array} \left[\begin{array}{c} \text{---} \\ \text{---} \\ \text{---} \\ \text{---} \end{array} \right] , \quad (\text{D.105})$$

and thus $he_{m-1}v_2 \not\propto hv_2$ so they do not contribute to the trace. For v_1 , note that

$$e_{m-1}hv_1 = \left[\begin{array}{c} \text{---} \\ \text{---} \\ \text{---} \\ \text{---} \end{array} \right] \begin{array}{c} \text{---} \\ \text{---} \\ \text{---} \\ \text{---} \end{array} \left[\begin{array}{c} \text{---} \\ \text{---} \\ \text{---} \\ \text{---} \end{array} \right] \begin{array}{c} \text{---} \\ \text{---} \\ \text{---} \\ \text{---} \end{array} \left[\begin{array}{c} \text{---} \\ \text{---} \\ \text{---} \\ \text{---} \end{array} \right] \propto v_1 \iff \left[\begin{array}{c} \text{---} \\ \text{---} \\ \text{---} \\ \text{---} \end{array} \right] \begin{array}{c} \text{---} \\ \text{---} \\ \text{---} \\ \text{---} \end{array} \left[\begin{array}{c} \text{---} \\ \text{---} \\ \text{---} \\ \text{---} \end{array} \right] \propto \left[\begin{array}{c} \text{---} \\ \text{---} \\ \text{---} \\ \text{---} \end{array} \right] \begin{array}{c} \text{---} \\ \text{---} \\ \text{---} \\ \text{---} \end{array} \left[\begin{array}{c} \text{---} \\ \text{---} \\ \text{---} \\ \text{---} \end{array} \right] . \quad (\text{D.106})$$

But this is only possible if in the diagram of h there is a path connecting the $(m-1)$ -th site on the left to the $(m-1)$ -th site on the right, otherwise either the RHS of Eq. (D.106) vanishes or it is not possible to reproduce the connection pattern of v_1 . Also,

$$hv_1 = \left[\begin{array}{c} \text{---} \\ \text{---} \\ \text{---} \\ \text{---} \end{array} \right] \begin{array}{c} \text{---} \\ \text{---} \\ \text{---} \\ \text{---} \end{array} \left[\begin{array}{c} \text{---} \\ \text{---} \\ \text{---} \\ \text{---} \end{array} \right] \begin{array}{c} \text{---} \\ \text{---} \\ \text{---} \\ \text{---} \end{array} \left[\begin{array}{c} \text{---} \\ \text{---} \\ \text{---} \\ \text{---} \end{array} \right] \propto \left[\begin{array}{c} \text{---} \\ \text{---} \\ \text{---} \\ \text{---} \end{array} \right] \begin{array}{c} \text{---} \\ \text{---} \\ \text{---} \\ \text{---} \end{array} \left[\begin{array}{c} \text{---} \\ \text{---} \\ \text{---} \\ \text{---} \end{array} \right] \quad (\text{D.107})$$

is only possible for the same subset of h that Eq. (D.106) is true for a similar reason. For such h the contraction in the RHS of Eq. (D.106) produces an extra factor of χ , but is otherwise identical to Eq. (D.107). Hence we find that $hv = av \iff e_{m-1}hv = \chi av$ for some $a \in \mathbb{C}$ and thus $\text{tr}(h) = \chi \text{tr}(he_{m-1})$. This result naturally generalizes to all sequential inclusions of algebras in the list $\text{TL}_1 \subset \dots \subset \text{TL}_{m-1} \subset \text{TL}_m$. Using Lemma B.2 we conclude that the trace function we constructed on $\mathcal{V}^{(m)}$ is indeed the same as Tr_{TL_m} . \square

D.4.2 Proof of Proposition 5.2

Proof. The generating function $G(q, r, z)$ is defined as an infinite sum over diagrams

$$\begin{aligned}
 G(q, r, z) = & \left| \begin{array}{l} +z \text{ (circle)} + z^2 \left(\text{(loop)} + \text{(two circles)} \right) + \dots \\ +zr \text{ (C-shape)} + z^2r \left(\text{(loop)} + \text{(C-shape)} + \text{(S-shape)} \right) \\ +z^2r^2 \text{ (S-shape)} \end{array} \right. \quad (D.108)
 \end{aligned}$$

where the power of z counts (half) the number of elements $m/2$ and power of r counts (half) the number of defects k . Each diagram is evaluated in a similar fashion as the definition of linear functional f_q in Eq. (5.52) – for every closed loop in diagram assign a (positive rather than negative) power of q to the result. Also introduce 1PI generating function $H(q, r, z)$ defined as the sum over all connected diagrams:

$$\begin{aligned}
 H(q, r, z) = & \left| \begin{array}{l} z \text{ (circle)} + z^2 \text{ (loop)} + z^3 \left(\text{(loop)} + \text{(two circles)} \right) + \dots \\ +zr \text{ (C-shape)} + z^2r \text{ (S-shape)} + z^3r \left(\text{(S-shape)} + \text{(two circles)} \right) \end{array} \right. \quad (D.109)
 \end{aligned}$$

The form of H allows us to reorganize it as

$$\begin{aligned}
 H(q, r, z) = & \left| \begin{array}{l} z \text{ (circle)} + z^2 \text{ (loop with dot)} + z^3 \text{ (two circles with dots)} + \dots \\ +zr \text{ (C-shape)} + z^2r \text{ (S-shape with dot)} + z^3r \text{ (S-shape with two dots)} \end{array} \right. \quad (D.110)
 \end{aligned}$$

or

$$\begin{aligned}
 H(q, r, z) &= z(q+r)(1 + zC(q, z) + z^2C^2(q, z) + \dots) \\
 &= \frac{z(q+r)}{1 - zC(q, z)} \quad (D.111)
 \end{aligned}$$

G and H are related by

$$\begin{aligned} G(q, r, z) &= 1 + H(q, r, z) + H^2(q, r, z) + \cdots = \frac{1}{1 - H(q, r, z)} \\ &= \frac{1 - zC(q, z)}{1 - z(q + r) - zC(q, z)} \end{aligned} \quad (\text{D.112})$$

The function $C(q, z)$ is the generating function of link states with no defects:

$$\begin{aligned} C(q, z) &= \left| \begin{array}{c} +z \text{ (circle)} \\ +z^2 \left(\text{(\text{S})} + \text{(\text{8})} \right) \\ + \cdots \end{array} \right. \\ &= G(q, r = 0, z) \end{aligned} \quad (\text{D.113})$$

$C(q, z)$ is also known under the name of the generating function of q -Catalan numbers.

$$C(q, z) = \frac{1 - z(q - 1) - \sqrt{(1 + z(q - 1))^2 - 4qz}}{2z} \quad (\text{D.114})$$

For a derivation of $C(q, z)$ please refer to the proof of Lemma B.1. □

D.4.3 Proof of Proposition 5.4

Proof. Define $\tilde{C}(q, z) = C(q, z) - 1$. It satisfies a different quadratic equation

$$\tilde{C}(q, z) + (q + 1 - \frac{1}{z})\tilde{C}(q, z) + q = 0 \quad (\text{D.115})$$

Consider the generating function of $\tilde{C}^k(q, z)$:

$$\begin{aligned} X(q, z, t) &= \sum_{k=0}^{\infty} \tilde{C}^k(q, z) t^k \\ &= (\frac{1}{z} - q - 1) \sum_{k=2}^{\infty} \tilde{C}^{k-1} t^k - q \sum_{k=2}^{\infty} \tilde{C}^{k-2} t^k + \tilde{C}(q, z) t + 1 \\ &= (\frac{1}{z} - q - 1) t (X(q, z, t) - 1) - q t^2 X(q, z, t) + \tilde{C}(q, z) t + 1 \end{aligned} \quad (\text{D.116})$$

Solving for X gives

$$\begin{aligned} X(q, z, t) &= \frac{\tilde{C}(q, z) t + (q + 1 - \frac{1}{z}) t + 1}{q t^2 + (q + 1 - \frac{1}{z}) t + 1} \\ &= \frac{C(q, z) t + (q - \frac{1}{z}) t + 1}{q t^2 + (q + 1 - \frac{1}{z}) t + 1} \end{aligned} \quad (\text{D.117})$$

Now we can write $G(q, r, z)$ as

$$\begin{aligned} G(q, r, z) &= C(q, z)X(q, z, r/q) \\ &= \frac{(r+q)C(q, z) - \frac{r}{z}}{r^2 + (q+1 - \frac{1}{z})r + q} \end{aligned} \tag{D.118}$$

where we have again used Eq. (5.72) to swap out $C^2(q, z)$.

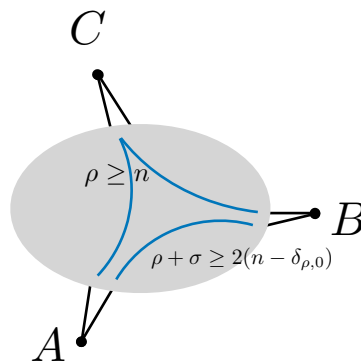
□

Appendix E

Supplement to Chapter 6

E.1 Proof of Lemma 6.18: Structure of optimal ρ, σ

For quick reference we sketch the integer program, Definition 6.5, we are trying to solve:



plus the additional even condition on paths $A \rightarrow B$ (see the original definition.)

Let us introduce some notation. For a path L , not necessarily edge disjoint, define:

$$f(L) = \sum_{e \in L} f(e) \tag{E.1}$$

for some function of the edges $f : E \rightarrow \mathbb{R}$. This is slightly different (but consistent with) the notation introduced previously, because of the possibility that paths L intersect an edge more than once. We sum each edge in the sequence defining L , which then includes such multiplicities.

Definition E.1. We say e is ρ -binding if either $\rho(e) = 0$ or, when $\rho(e) > 0$, there exists a path $L \in \mathcal{P}_{AB,C}$ with $e \in L$ such that $\rho(L) = n$.

For the constraint involving the σ variable Eq. (6.28) we need a refined notion:

Definition E.2. An edge e is called σ -binding within E' for some $E' \subset E$ if either $\sigma(e) = 0$ or, when $\sigma(e) > 0$, then there exists a path $L \in \mathcal{P}_{A,B}$ with $e \in L$ and $L \subset E'$ for which $\sigma(L) + \rho(L) = 2(n - \delta_{\rho(L),0})$. We say that e is *simply* σ -binding for the case $E' = E$.

Given some function ρ on the edges E , we define the graph distance induced by ρ as:

$$d_\rho(x, y) = \min_{L \in \mathcal{P}_{x,y}} \rho(L) \quad (\text{E.2})$$

and similarly for the distances between subsets of V . We define the distance to be ∞ should there be no such path L in the minimization. Given some ρ , define the region:

$$(AB)_0 = \{x \in V : d_\rho(x, AB) = 0\} \quad (\text{E.3})$$

and similarly define

$$E_0 = \{\{x, y\} \in E : x \in (AB)_0 \text{ and } y \in (AB)_0\} \quad (\text{E.4})$$

to be the edges that lie entirely within $(AB)_0$ ¹.

We will construct an optimal pair (ρ, σ) with some nice properties and such that $V' = (AB)_0$ will be our choice for V' in Lemma 6.18. We note however, at this point there is no obvious reason for $\rho(e) = 0$ for all edges within $(AB)_0$.

Lemma E.1. *Given some feasible (ρ, σ) , consider an edge $e \in E_0$, then we have the estimate:*

$$\forall L \in \mathcal{P}_{AB,C} : e \in L \implies \rho(L) - \rho(e) \geq n \quad (\text{E.5})$$

Proof. For all paths $L \in \mathcal{P}_{AB,C}$ passing through $e = \{x, y\}$ in the order $AB \rightarrow x \rightarrow y \rightarrow C$ we note that $\rho(L) \geq \rho(L_{y,C}) + \rho(e)$ where $L_{y,C} \in \mathcal{P}_{y,C}$, after dropping the $AB \rightarrow x$ portion of the path. But since $y \in (AB)_0$ there is some path $L_{AB,y}^*$ from AB to y with $\rho(L_{AB,y}^*) = 0$. We can combine the two paths, denoted as $L_{AB,y}^* \cup L_{y,C} \in \mathcal{P}_{AB,C}$, and use this to estimate:

$$\rho(L) \geq \rho(L_{y,C}) + \rho(e) = \rho(L_{AB,y}^* \cup L_{y,C}) + \rho(e) \geq n + \rho(e) \quad (\text{E.6})$$

by feasibility of ρ . □

Corollary E.2. *For a feasible (ρ, σ) an edge $e \in E_0$ is ρ -binding iff $\rho(e) = 0$.*

Proof. The if statement is obvious from the definition of ρ -binding.

Now for the only if statement: Assume the edge e is ρ -binding. Then either $\rho(e) = 0$ or $\exists L \in \mathcal{P}_{AB,C}$ containing e such that $\rho(L) = n$. If $\rho(e) = 0$ then we are done. Assuming that it is the other case, we use Eq. (E.5) to obtain

$$n - \rho(e) \geq n \implies \rho(e) = 0 \quad (\text{E.7})$$

which is a contradiction. So we must have $\rho(e) = 0$. □

This motivates introducing:

$$\hat{E}_0 = \{e \in E_0 : \rho(e) = 0\} \quad (\text{E.8})$$

as the ρ -binding edges in E_0 . Note that $\hat{E}_0 \subset E_0$.

Remark. One might have expected that for an optimal solution there are simply no edges that are not ρ -binding, otherwise one could get a smaller free energy by making ρ smaller. One cannot directly do this because one has to consider the other constraint for paths $\mathcal{P}_{A,B}$ that also involves ρ . We will eventually show

¹Note that E_0 is not the same as $E[(AB)_0]$, which is the set of edges that have *some* vertex in $(AB)_0$.

this is possible. That is we will prove that $E_0 = \hat{E}_0$, but we cannot do this before we prove some results on the behavior of σ , our next goal.

Define the two σ distance measures for paths within $(AB)_0$:

$$d_\sigma^0(x, y) = \min_{L \in \mathcal{P}_{x, y}: L \subset E_0} \sigma(L), \quad \hat{d}_\sigma^0(x, y) = \min_{L \in \mathcal{P}_{x, y}: L \subset \hat{E}_0} \sigma(L) \quad (\text{E.9})$$

which can be thought of a distance measures on truncated graphs. We continue to define the distance to be ∞ should the set of such paths above be empty.

The next lemma pertains to the region $(AB)_0$ and edges E_0 and \hat{E}_0 :

Lemma E.3. *Given any optimal solution (ρ', σ') , there exists an optimal solution (ρ, σ) such that $\rho + \sigma = \rho' + \sigma'$ and it satisfies the following properties that we prove sequentially:*

(a) *For all $e \in \hat{E}_0$ then e is σ -binding within \hat{E}_0 .*

(b) *There exists a function $k : (AB)_0 \rightarrow \mathbb{Z}$ with $0 \leq k(x) \leq 2(n-1)$ such that $\sigma(e) = |k(x) - k(y)|$ for all $e = \{x, y\} \in E_0$ and where:*

$$k(x) = \begin{cases} \hat{d}_\sigma^0(x, A), & \hat{d}_\sigma^0(x, A) < \infty \\ 2(n-1), & \hat{d}_\sigma^0(x, A) = \infty \end{cases} \quad (\text{E.10})$$

and

$$k(x) = \begin{cases} 2(n-1) - \hat{d}_\sigma^0(x, B), & \hat{d}_\sigma^0(x, B) < \infty \\ 0, & \hat{d}_\sigma^0(x, B) = \infty \end{cases} \quad (\text{E.11})$$

If $L \in \mathcal{P}_{A, B}$ is non-empty, then for all $e \in E_0 \setminus \hat{E}_0$ we have $\rho(e) \in 2 + 2\mathbb{Z}_{\geq 0}$.

(c) *All edges $e \in E_0$ are ρ -binding. In other words $E_0 = \hat{E}_0$. This implies that \hat{d}_σ^0 can be replaced by d_σ^0 in Eq. (E.10) and Eq. (E.11).*

Proof. (a) Consider some optimal (ρ', σ') . We use the notation $(AB)'_0$ and E'_0 for the region as in Eq. (E.3), defined with respect to $d_{\rho'}$, and $\hat{E}'_0 \subset E'_0$ as the set of edges inside $(AB)'_0$ with $\rho'(e) = 0$. Define E_{fail} as the edges $e \in \hat{E}'_0$ which are not σ' -binding within \hat{E}'_0 . Then set

$$(\rho(e), \sigma(e)) = \begin{cases} (\rho'(e) + \sigma'(e), 0), & e \in E_{\text{fail}} \\ (\rho'(e), \sigma'(e)), & \text{otherwise} \end{cases} \quad (\text{E.12})$$

Note that $(AB)_0 \subset (AB)'_0$ since $\rho(e) \geq \rho'(e)$. Also $E_0 \subset E'_0$ and $\hat{E}_0 \subset \hat{E}'_0$ for the same reason. And $\hat{E}_0 \cap E_{\text{fail}} = \emptyset$ since $\rho(e) = (\rho' + \sigma')(e) > 0 \forall e \in E_{\text{fail}}$.

We aim to show that (ρ, σ) is (i) feasible, (ii) optimal and (iii) satisfies the statement under investigation in (a). We start with (iii): Consider any edge $e \in \hat{E}_0$ with $\sigma(e) \neq 0$. Note that $\sigma(e) = \sigma'(e)$ since only edges in E_{fail} are changed. Since this edge is σ' -binding within \hat{E}'_0 , there is a path $L \in \mathcal{P}_{A, B}$ intersecting e such that $L \subset \hat{E}'_0$ and $\sigma'(L) = 2(n-1)$. We just need to show that $L \subset \hat{E}_0$ so that e is σ -binding inside \hat{E}_0 . Note that $L \cap E_{\text{fail}} = \emptyset$ since this would otherwise contradict the definition of E_{fail} (L being a saturating path). Thus $\rho(L) = \rho'(L)$ since these edges are not changed, and $\rho'(L) = 0$ since $L \subset \hat{E}'_0$. This implies that $\rho(e) = 0$ for all $e \in L$ implying that $L \subset \hat{E}_0$, and we are done. For later use, we note that we just proved:

$$\forall L \in \mathcal{P}_{A, B} : L \subset \hat{E}'_0 \text{ then } L \cap E_{\text{fail}} = \emptyset \implies \rho(L) = 0 \quad (\text{E.13})$$

(i) Since $\rho \geq \rho'$ any $L \in \mathcal{P}_{AB,C}$ is clearly still feasible for ρ . Also since $(\sigma' + \rho')(e) = (\sigma + \rho)(e)$ for all edges, we need only check paths $L \in \mathcal{P}_{A,B}$ such that $\delta_{\rho'(L),0} = 1$ and $\delta_{\rho(L),0} = 0$. The condition $\rho'(L) = 0$ implies that $L \subset \hat{E}'_0$, but then the converse of Eq. (E.13) implies that $\rho(L) \neq 0 \implies L \cap E_{\text{fail}} \neq \emptyset$ and thus $\sigma'(L) > 2(n-1)$ by the failure of binding. Recall that the failure of saturating for the $\mathcal{P}_{A,B}$ paths costs $+2$ in the definition of the integer program, so actually $\sigma'(L) \geq 2n$. Thus $(\sigma + \rho)(L) = \sigma'(L) \geq 2n = 2(n - \delta_{\rho(L),0})$ as required. (ii) Optimality is obvious since $(\rho + \sigma)(e) = (\rho' + \sigma')(e)$.

(b) We start with an optimal (ρ', σ') satisfying (a). Note that any point $x \in (AB)'_0$ has at least one path to either A or B contained in \hat{E}'_0 by the definition of these regions. Assume that that $\hat{d}_{\sigma'}^0(x, A) < \infty$, or in other words, assume there is some path from x to A inside \hat{E}'_0 , and define:

$$k(x) = \hat{d}_{\sigma'}^0(x, A) \quad (\text{E.14})$$

where we recall the definition of this hatted distances uses paths inside \hat{E}'_0 . We now aim to find a consistent set of equations Eq. (E.10) and Eq. (E.11) (with σ replaced by σ' for now).

We note that if $\hat{d}_{\sigma'}^0(x, B) = \infty$ then we must have $k(x) = 0$ or otherwise we will violate (a) with some non σ' -binding edge along the path from x to A . Furthermore if $\hat{d}_{\sigma'}^0(x, B) < \infty$ then consider the edge e with $\sigma'(e) \neq 0$ along the piecewise minimal path $L : A \rightarrow x \rightarrow B$ that is closest to x (either towards A or towards B)

$$2(n-1) \leq \sigma'(L) = \hat{d}_{\sigma'}^0(A, x) + \hat{d}_{\sigma'}^0(x, B) \leq \sigma'(L') = 2(n-1) \quad (\text{E.15})$$

where L' is a saturating path for e that exists by (a). The first inequality is feasibility and the second comes from deforming the minimal paths in the distance functions to the path L' (see Fig. (E.1)). Thus:

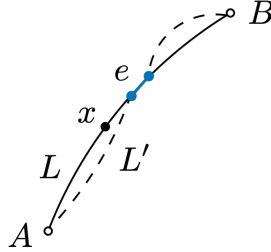


Figure E.1: We deform a piecewise minimal path L (solid line) containing the edge e with $\sigma'(e) \neq 0$ and the vertex x to a saturating path L' (dashed line) containing e , which is guaranteed to exist by the conditions in (a).

$$k(x) = 2(n-1) - \hat{d}_{\sigma'}^0(x, B) \quad (\text{E.16})$$

The only case we have not covered for Eq. (E.10) and Eq. (E.11) is when $\hat{d}_{\sigma'}^0(x, A) = \infty$. In this case we set $k(x) = 2(n-1)$ and this is consistent with Eq. (E.16) since $\hat{d}_{\sigma'}^0(x, B) = 0$ is again necessary in order to not violate (a).

For edges $e = \{x, y\} \in \hat{E}'_0$ we now aim to compute:

$$|k(x) - k(y)| \quad (\text{E.17})$$

There are three cases. Either (i) both $\{x, y\}$ have infinite distance to B , or (ii) both $\{x, y\}$ have infinite

distance to A or (iii) all distances are finite. In the first two cases we have $k(x) = k(y)$. We also have $\sigma'(e) = 0$ for these cases due to (a).

In the last case we can estimate using the triangle inequality:

$$|k(x) - k(y)| \leq \sigma'(e) \quad (\text{E.18})$$

If $\sigma'(e) = 0$ then $k(x) = k(y)$, however if $\sigma'(e) > 0$, then (a) implies the existence of a saturating path L such that:

$$2(n-1) = \sigma'(L) \geq \hat{d}_{\sigma'}^0(A, x) + \sigma'(e) + \hat{d}_{\sigma'}^0(y, B) \quad (\text{E.19})$$

where $e = \{x, y\}$ and the saturating path behaves as $L : A \rightarrow x \rightarrow y \rightarrow B$. Thus:

$$\sigma'(e) \leq k(y) - k(x) \leq |k(y) - k(x)| \quad (\text{E.20})$$

which combining with Eq. (E.18) proves equality. We have now established equality $\sigma'(e) = |k(x) - k(y)|$ for all three cases above (i-iii).

We now consider edges $e = \{x, y\} \in E'_0$ that are not in \hat{E}'_0 . We construct a new (ρ, σ) that differs from the original ones on these edges:

$$(\rho(e), \sigma(e)) = \begin{cases} (\rho'(e) + \sigma'(e) - |k(x) - k(y)|, |k(x) - k(y)|), & e \in E'_0 \setminus \hat{E}'_0 \\ (\rho'(e), \sigma'(e)), & \text{otherwise} \end{cases} \quad (\text{E.21})$$

We need to show that (ρ, σ) is (i) feasible (ii) optimal and (iii) satisfies the requirements in both (a) and (b).

For (i) we first establish that $\rho(e) > 0$ for edges $e = \{x, y\} \in E'_0 \setminus \hat{E}'_0$. There are several cases to deal with depending on whether the $\hat{d}_{\sigma'}$ distances are finite or not. See Fig. (E.2).

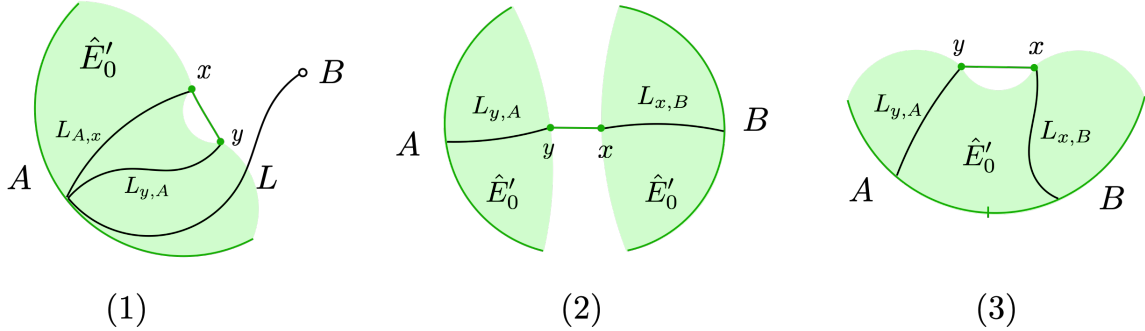


Figure E.2: We construct a path from $A \rightarrow B$ containing $e = \{x, y\}$ using minimal paths within \hat{E}'_0 and use it to prove $\rho(e) \in 2 + 2\mathbb{Z}_{\geq 0}$. There are three different cases depending on whether the $\hat{d}_{\sigma'}$ distances of x, y to the boundary vertices A, B are finite or not. The three cases are treated differently as shown here.

1. If x, y have infinite $\hat{d}_{\sigma'}^0$ -distance both to A or both to B then $|k(x) - k(y)| = 0$ and $\rho(e) > 0$ since $\rho'(e) > 0$ on such an edge. We will need to improve this bound for later use when establishing the statement in (b): Suppose that the $\hat{d}_{\sigma'}$ distances to B is infinite. If there is any path $L \in \mathcal{P}_{A,B}$ then we can combine the minimal paths $L_{A,x} \subset \hat{E}'_0$ and $L_{y,A} \subset \hat{E}'_0$, that are used to compute the respective distances $\hat{d}_{\sigma'}(A, x) = \hat{d}_{\sigma'}(A, y) = 0$, to form a path $L_{A,x} \cup e \cup L_{y,A} \cup L \in \mathcal{P}_{A,B}$ giving the estimate:

$$(\rho' + \sigma')(L_{A,x} \cup e \cup L_{y,A} \cup L) = \rho'(e) + \sigma'(e) + (\rho' + \sigma')(L) \in 2\mathbb{Z}_{\geq 0} \quad (\text{E.22})$$

since ρ' and σ' vanish on these minimal paths. Feasibility gives the even condition. But $(\rho' + \sigma')(L) \in 2\mathbb{Z}_{\geq 0}$ also by feasibility, thus $\rho(e) \in 2 + 2\mathbb{Z}_{\geq 0}$. The other case where $\hat{d}_{\sigma'}^0(x, A) = \hat{d}_{\sigma'}^0(y, A) = \infty$ follows in a similar way.

2. If x has infinite $\hat{d}_{\sigma'}^0$ -distance to A and y has infinite $\hat{d}_{\sigma'}^0$ -distance to B then we can construct a new path $L : A \rightarrow y \rightarrow x \rightarrow B$ using the minimal paths from $A \rightarrow y$ and the minimal path from $x \rightarrow B$ both contained in \hat{E}'_0 . Since these two minimal $\hat{d}_{\sigma'}^0$ -distances vanishes for this new path we must have:

$$2n + 2\mathbb{Z}_{\geq 0} \ni \sigma'(L) + \rho'(L) = \sigma'(e) + \rho'(e) \quad (\text{E.23})$$

where we used feasibility of (ρ', σ') with the fact that $\rho'(e) > 0$. In this case we have $|k(x) - k(y)| = 2(n - 1)$, implying that $\rho(e) \in 2 + 2\mathbb{Z}_{\geq 0}$.

3. If both x, y have finite $\hat{d}_{\sigma'}^0$ -distances to A and B then, picking $k(y) \leq k(x)$, we can construct a path $L : A \rightarrow y \rightarrow x \rightarrow B$, as above, and feasibility now implies that:

$$2n + 2\mathbb{Z}_{\geq 0} \leq \sigma'(L) + \rho'(L) = \sigma'(e) + \rho'(e) + k(y) + 2(n - 1) - k(x) \quad (\text{E.24})$$

$$= \sigma'(e) + \rho'(e) + 2(n - 1) - |k(x) - k(y)| \quad (\text{E.25})$$

or $\rho(e) \in 2 + 2\mathbb{Z}_{\geq 0}$.

We have covered all possibilities and established that $\rho(e) > 0$ for such edges, and furthermore we have established the final condition in (b). A corollary is that $(AB)_0 = (AB)'_0$ (since this only depends on the pattern of zeros in $\rho(e)$) and thus $E_0 = E'_0$ and $\hat{E}_0 = \hat{E}'_0$.

We now prove the rest of feasibility (i). Assume by contradiction that there is a path $L \in \mathcal{P}_{AB,C}$ such that $\rho(L) < n$, then this path must pass through at least one edge e with $e \in E'_0 \setminus \hat{E}'_0$ because ρ' was feasible so L must go through one of the edges where ρ is changed. Consider the first such edge e on the journey from $C \rightarrow AB$. It is possible to use this path to construct a new path L' that uses L from $C \rightarrow e$ and then follows $e \rightarrow AB$ through $\hat{E}_0 = \hat{E}'_0$ (since both vertices in e are in $(AB)'_0$ this is always possible). Thus this path new path L' only intersects one edge with $e \in E'_0 \setminus \hat{E}'_0$. Then:

$$\rho(L') \leq \rho(L) < n \quad (\text{E.26})$$

is still not-feasible for ρ . We use Lemma E.1 which states that for such an edge e and feasible ρ' :

$$\rho(L') > \rho'(L') - \rho'(e) \geq n \quad (\text{E.27})$$

which is a contradiction. The first inequality in Eq. (E.27) follows from $\rho(e) > 0$, and the fact that this is the only edge that is changed relative to ρ' along the path. For paths $L \in \mathcal{P}_{A,B}$ all paths that pass through a deformed edge we maintain $\delta_{\rho(L),0} = \delta_{\rho'(L),0} = 0$ and $\sigma + \rho = \sigma' + \rho'$ so feasibility for these paths is clear. Optimality (ii) is also clear.

Now we show (iii) that the new (ρ, σ) satisfies conditions (a) and (b) of the Lemma. (a) is clear since $\hat{E}_0 = \hat{E}'_0$ and we have not changed any $\sigma(e)$ inside \hat{E}_0 . For (b) we firstly note that $\sigma(e) = |k(x) - k(y)|$ for all $e = \{x, y\} \in E_0$ by construction. Also $\hat{d}_{\sigma}^0(x, y) = \hat{d}_{\sigma'}^0(x, y)$ since $\hat{E}'_0 = \hat{E}_0$ and $\sigma' = \sigma$ on these edges. We are done with (b).

(c) We consider an optimal (ρ, σ) satisfying the properties in (a) and (b). We work by contradiction. That

is we assume there is at least one edge $e \in E'_0 \setminus \hat{E}'_0$ and prove a contradiction. Consider any one of these edges and call it e_* . Construct a new solution:

$$(\rho'(e), \sigma'(e)) = \begin{cases} (0, \sigma(e)), & e = e_* \\ (\rho(e), \sigma(e)), & \text{otherwise} \end{cases} \quad (\text{E.28})$$

This clearly has a smaller objective, so if we can show that (ρ', σ') is feasible we prove a contradiction since (ρ, σ) is optimal. For paths $L \in \mathcal{P}_{AB,C}$ that intersect e_* – without loss of generality we may consider paths that intersect e_* only once. We then use Lemma E.1 which becomes $\rho'(L) \geq n$ as required.

Now consider paths $L \in \mathcal{P}_{A,B}$ with $e_* \in L$. If there are no such paths, then there is nothing more to prove. If there is at least one such path we know from (b) that $\rho(e_*) \in 2\mathbb{Z}_+$ and this implies that the even condition in Eq. (6.28) is preserved for (ρ', σ') . Thus we now consider only the inequality implied in Eq. (6.28). We set $e_* = \{x, y\}$ and pick these vertices so that $L : A \rightarrow x \rightarrow y \rightarrow B$. Define the subpaths as $L_{A,x}$ and $L_{y,B}$ so that $L = L_{A,x} \cup e_* \cup L_{y,B}$. We must consider four cases depending on whether the distances $\hat{d}_\sigma^0(x, B)$ or $\hat{d}_\sigma^0(y, A)$ are finite:

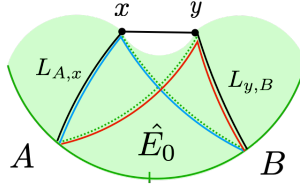


Figure E.3: Starting from the path $L = L_{A,x} \cup e_* \cup L_{y,B} \in \mathcal{P}_{A,B}$ (black solid) we construct two new paths in $\mathcal{P}_{A,B}$ (red and blue solid) using minimal paths (green dashed) that are contained entirely in \hat{E}_0 .

1. If $\hat{d}_\sigma^0(x, B) < \infty$ and $\hat{d}_\sigma^0(y, A) < \infty$ then construct two new paths that by-pass e_* as follows. Consider the minimal paths for these finite distances: from $A \rightarrow y$ and $x \rightarrow B$. Join these, respectively, to $L_{y,B}$ and $L_{A,x}$ (see Fig. (E.3)). These minimal paths are contained in \hat{E}_0 (so ρ vanishes on them). We apply feasibility for (ρ, σ) to these two new paths:

$$\hat{d}_\sigma^0(A, y) + (\rho + \sigma)(L_{y,B}) \geq 2(n - \delta_{\rho(L_{y,B}),0}) \quad (\text{E.29})$$

$$(\rho + \sigma)(L_{A,x}) + \hat{d}_\sigma^0(x, B) \geq 2(n - \delta_{\rho(L_{A,x}),0}) \quad (\text{E.30})$$

adding these two bounds together and using the distance function $k(x)$ we have:

$$(\rho' + \sigma)(L) - \sigma(e_*) + k(y) - k(x) \geq 2(n + 1 - \delta_{\rho(L_{y,B}),0} - \delta_{\rho(L_{A,x}),0}) \quad (\text{E.31})$$

then $\sigma(e_*) = |k(y) - k(x)| \geq k(y) - k(x)$ (by condition (b)) and:

$$1 - \delta_{\rho(L_{y,B}),0} - \delta_{\rho(L_{A,x}),0} \geq -\delta_{\rho(L_{y,B}),0}\delta_{\rho(L_{A,x}),0} = -\delta_{\rho'(L),0} \quad (\text{E.32})$$

combines to give:

$$(\rho' + \sigma)(L) \geq 2(n - \delta_{\rho'(L),0}) \quad (\text{E.33})$$

the required feasibility statement.

2. If $\hat{d}_\sigma^0(x, B) = \infty$ and $\hat{d}_\sigma^0(y, A) = \infty$ then the form of the function $k(x)$ from (b) requires that $k(x) = 0$

and $k(y) = 2(n - 1)$. This implies $\sigma(e_\star) = 2(n - 1)$. Then we note the bound:

$$(\rho + \sigma)(L) \geq (\rho + \sigma)(e_\star) + 2(1 - \delta_{\rho(L_{y,B}),0} \delta_{\rho(L_{A,x}),0}) \quad (\text{E.34})$$

$$= \rho(e_\star) + 2(n - \delta_{\rho'(L),0}) \quad (\text{E.35})$$

which follows by dropping all contributions from the path $L_{y,B}$ and $L_{A,x}$ except for a crude estimate counting a minimal contribution if either $\rho(L_{y,B})$ or $\rho(L_{A,x})$ is non-zero. The bound that we get from this minimal contribution must be even, since $(\rho + \sigma)(e_\star)$ is even, and $(\rho + \sigma)(L)$ is even by feasibility. So any gap between them must be even. So again we get Eq. (E.33).

3. If $\hat{d}_\sigma^0(x, B) < \infty$ and $\hat{d}_\sigma^0(y, A) = \infty$ (the reverse case follows a similar argument) then we must have $k(y) = 2(n - 1)$. We also must have $\hat{d}_\sigma^0(x, A) = \infty$ since otherwise we could construct a path $A \rightarrow x \rightarrow B \rightarrow y$ inside \hat{E}_0 and this would violate the condition $\hat{d}_\sigma^0(y, A) = \infty$. So $k(x) = 2(n - 1)$ and hence $\hat{d}_\sigma^0(x, B) = 0$ and $\sigma(e_\star) = 0$. We estimate:

$$(\rho + \sigma)(L) \geq (\rho + \sigma)(L_{A,x}) + \rho(e_\star) + 2(1 - \delta_{\rho(L_{y,B}),0}) \quad (\text{E.36})$$

where we again crudely dropped all contributions from $L_{y,B}$ except if $\rho(L_{y,B})$ is non-zero. Evenness also demands the gap in the bound is 2. We also consider a combined path that bypasses e_\star using $L_{A,x}$ and the minimal \hat{d}_σ^0 -distance path from y to B inside E_0 and apply feasibility:

$$(\rho + \sigma)(L_{A,x}) + \hat{d}_\sigma^0(x, B) \geq 2(n - \delta_{\rho(L_{A,x}),0}) \quad (\text{E.37})$$

Combining Eq. (E.36) and Eq. (E.37) gives:

$$(\rho' + \sigma)(L) \geq 2(n + 1 - \delta_{\rho(L_{y,B}),0} - \delta_{\rho(L_{A,x}),0}) \geq 2(n - \delta_{\rho'(L),0}) \quad (\text{E.38})$$

as required.

We have now established feasibility for all possible cases and so we find the desired contradiction. We conclude that there are no such edges and $E_0 = \hat{E}_0$. \square

We now move on to prove Lemma 6.18. We use the optimal (ρ, σ) constructed in Lemma E.3. We set $V' = (AB)_0$ and $E' = E_0$. The above result establishes that ρ vanishes on E' where only σ is non-zero. We now use this as an input to the following half integer program that lives on the complementary reduced graph defined as:

$$G^c = (V^c, E^c) \quad V^c = (V \setminus V') \cup (AB)' \quad E^c = E \setminus E' \quad (\text{E.39})$$

with $(AB)' = V \cap \mu_G(V')$.

Lemma E.4. *Given an optimal (ρ, σ) satisfying the properties in Lemma E.3, then*

$$\varrho(e) = (\rho(e) + \sigma(e))|_{E^c} - \mathbf{1}_{\mu(V')}(e) \quad (\text{E.40})$$

is feasible for the following half integer program on the graph $G^c = (V^c, E^c)$:

$$M \equiv \min_{\varrho} \sum_{e \in E^c} w(e) \varrho(e) \quad (\text{E.41})$$

$$\text{subject to } \forall L \in \mathcal{P}_{\Gamma_k, \Gamma_{k'}} : \varrho(L) \in |k - k'| + \mathbb{Z}_{\geq 0} \quad (\text{E.42})$$

$$\text{and } \forall L \in \mathcal{P}_{\Gamma_k, C} : \varrho(L) \in (n - 1) + \mathbb{Z}_{\geq 0} \quad (\text{E.43})$$

$$\text{for all } k, k' = 0, \dots, 2(n - 1) \quad (\text{E.44})$$

where $\varrho(e) \in \mathbb{Z}_{\geq 0}/2$ and $\Gamma_k = \{x \in (AB)' : k(x) = k\}$ and C , are boundary vertices on the reduced graph. Thus:

$$I \geq M + w(\mu(V')) + \sum_{e=\{x,y\} \in E'} w(e) |k(x) - k(y)| \quad (\text{E.45})$$

Proof. We firstly check feasibility for paths $\mathcal{P}_{\Gamma_k, \Gamma_{k'}}$. We start by picking a subset of such paths (possibly empty) $\tilde{\mathcal{P}}_{\Gamma_k, \Gamma_{k'}}$ for all k, k' , with the extra condition that the path only intersects the boundary edges $\mu(V')$ twice (this need not always be the case for all paths, even ones that are edge disjoint).

Let $k' < k$ (the case $k' = k$ is trivial) and consider $\tilde{L} \in \tilde{\mathcal{P}}_{\Gamma_k, \Gamma_{k'}}$. We can construct a path in $\mathcal{P}_{A,B}$ by attaching minimal curves for the distance d_{σ}^0 through E' . We consider such curves from $A \rightarrow \Gamma_{k'}$ and $\Gamma_k \rightarrow B$. We apply feasibility to the combination:

$$(\sigma + \rho)(\tilde{L}) + (k' - k) + 2(n - 1) \geq 2n \quad (\text{E.46})$$

Using $\mathbf{1}_{\mu(V')}(\tilde{L}) = 2$ for such curves gives

$$\varrho(\tilde{L}) \geq |k - k'| \quad (\text{E.47})$$

Now any curve $L \in \mathcal{P}_{\Gamma_k, \Gamma_{k'}}$ can be constructed as a sequence of these restricted \tilde{L} curves from $\Gamma_k \rightarrow \Gamma_{k_1} \rightarrow \dots \Gamma_{k_N} \rightarrow \Gamma_{k'}$ for arbitrary $k_i : i = 1 \dots N$. Thus:

$$\varrho(L) \geq |k - k_1| + |k_1 - k_2| + \dots |k_N - k'| \geq |k - k'| \quad (\text{E.48})$$

by the triangle inequality and Eq. (E.47). That concludes feasibility for $\mathcal{P}_{\Gamma_k, \Gamma_{k'}}$.

For a paths $\mathcal{P}_{\Gamma_k, C}$ we again have to deal with possible multiple intersections with $\mu(V')$. We again restrict to $\tilde{\mathcal{P}}_{\Gamma_k, C}$ such that these paths intersect $\mu(V')$ only once. Consider $\tilde{L} \in \tilde{\mathcal{P}}_{\Gamma_k, C}$ and attach a minimal curve to AB in the E' graph. Then:

$$\varrho(\tilde{L}) = \rho(\tilde{L}) + \sigma(\tilde{L}) - 1 \geq \rho(\tilde{L}) - 1 \geq n - 1 \quad (\text{E.49})$$

where in the first inequality we simply dropped the σ contribution and in the second we used feasibility for the combined curve $\in \mathcal{P}_{AB, C}$ (the minimal curve part sits in the region with $\rho = 0$.) Again any curve in the more general set $L \in \mathcal{P}_{\Gamma_k, C}$ can always be written as a combination of curves $\Gamma_k \rightarrow \Gamma_{k_1} \rightarrow \dots \Gamma_{k_N} \rightarrow C$. Thus we have:

$$\varrho(L) \geq |k - k_1| + \dots + |k_{N-1} - k_N| + n - 1 \geq n - 1 \quad (\text{E.50})$$

as required. We conclude that ϱ is feasible for this intersecting cut problem. The estimate Eq. (E.45) now follows by plugging in Eq. (E.40) to Eq. (E.41) and finally using the form of σ implied by Lemma E.3 on the rest of the edges E' . \square

Remark. The half integer relaxation for this program is convenient in the next section. The above feasible ϱ

is integer valued, but the optimal solution might be half integral. However this does not bother us, since at this stage we only strive for an inequality. Also once the chain of Theorem 6.4 collapses the optimal solution will be integral.

We have now proven Lemma 6.18, as can be seen by picking and choosing results from Lemma E.3 and Lemma E.4.

E.2 Proof of Lemma 6.19: An intersecting cut problem

We now study the ℓ -intersecting cut problem defined in Definition 6.8. We will solve this problem by a

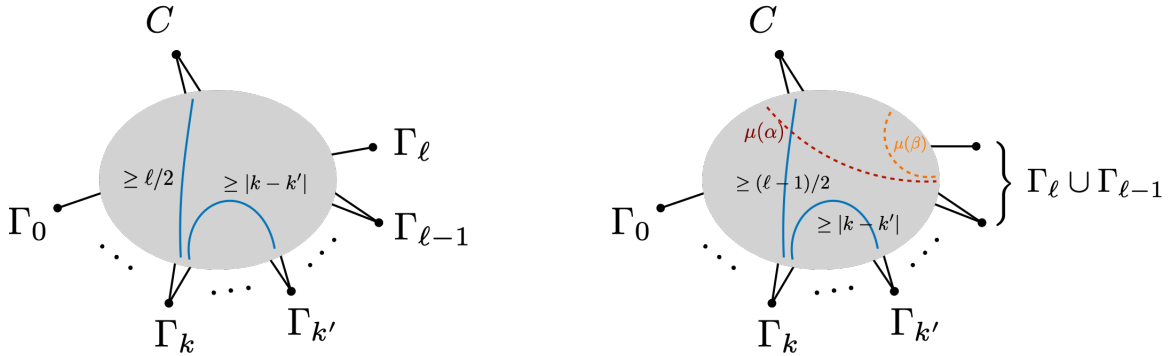


Figure E.4: (left) A sketch of a ℓ -intersection problem defined in Definition 6.8. (right) The reduction of the ℓ -intersection cut problem to the $\ell - 1$ -intersection cut problem.

recursive reduction of the ℓ -intersection cut problem to the $\ell - 1$ -intersection cut problem, as described below in Lemma E.5. We will use a feasible solution to the ℓ -intersection cut problem to construct a feasible solution to the $\ell - 1$ -intersection cut problem. See Fig. (E.4).

Lemma E.5. *Given an feasible ϱ for the ℓ -intersecting cut problem with $\{\Gamma_0, \Gamma_1, \dots, \Gamma_\ell\}$ then there exists a cut, α , for $(\Gamma_0 \cup \Gamma_1 \cup \dots \cup \Gamma_{\ell-1}) : (\Gamma_\ell \cup C)$ and a cut, β , for $\Gamma_\ell : (\Gamma_0 \cup \Gamma_1 \cup \dots \cup \Gamma_{\ell-1} \cup C)$ where β is disjoint to α such that:*

- for $\ell > 1$ there is a feasible ϱ' for the $\ell - 1$ -intersecting cut problem for $\{\Gamma_0, \Gamma_1, \dots, \Gamma_{\ell-1} \cup \Gamma_\ell\}$ with:

$$M(\varrho) = M(\varrho') + \frac{1}{2} (w(\mu(\alpha)) + w(\mu(\beta))) \quad (\text{E.51})$$

- for $\ell = 1$ we simply have the bound:

$$M(\varrho) \geq \frac{1}{2} (w(\mu(\alpha)) + w(\mu(\beta))) \quad (\text{E.52})$$

Before we present a proof, we use the above result to prove Lemma 6.19.

Proof of Lemma 6.19. Starting from an optimal solution ϱ for the ℓ -intersecting cut problem $M(\varrho)$, we apply Lemma E.5 repeatedly to arrive at

$$M(\varrho) \geq \frac{1}{2} \sum_{k=0}^{\ell-1} (w(\mu(\alpha_k)) + w(\mu(\beta_k))) \quad (\text{E.53})$$

where α_k is a cut for $(\Gamma_0 \cup \dots \Gamma_k) : (\Gamma_{k+1} \cup \dots \Gamma_\ell \cup C)$ and β_k is a cut for $(\Gamma_{k+1} \cap \dots \Gamma_\ell) : (\Gamma_0 \cup \dots \Gamma_k \cup C)$. Minimizing over the all such cuts α_k and β_k then gives

$$M(\varrho) \geq \frac{1}{2} \sum_{k=0}^{\ell-1} (w(\mu(\alpha'_k)) + w(\mu(\beta'_k))) \quad (\text{E.54})$$

where α'_k and β'_k are the minimal cuts. We now use them to construct a new ϱ' , defined by

$$\varrho'(e) = \frac{1}{2} \sum_{k=0}^{\ell-1} (\mathbf{1}_{\mu(\alpha'_k)} + \mathbf{1}_{\mu(\beta'_k)})(e) \quad (\text{E.55})$$

It is clear that ϱ' is feasible from the topology of the cuts (see Fig. (E.5)) so $M(\varrho) \geq M(\varrho')$. Also,

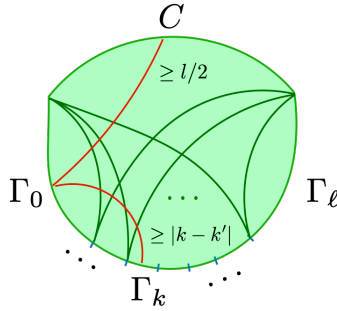


Figure E.5: An example configuration to the solution of $M(\varrho')$. The green solid lines represent minimal cuts α_k and β_k . Consider a path in $L \in \mathcal{P}_{\Gamma_k, C}$ (depicted as red line). It is clear that it must cross at least ℓ minimal surfaces in order to reach C so $w(L) \geq \ell/2$. Similarly, for a path in $L' \in \mathcal{P}_{\Gamma_k, \Gamma_{k'}}$ it must cross at least $2|k - k'|$ minimal surfaces so $w(L') \geq |k - k'|$.

$$M(\varrho') = \frac{1}{2} \sum_{e \in E} w(e) \sum_{k=0}^{\ell-1} (\mathbf{1}_{\mu(\alpha'_k)} + \mathbf{1}_{\mu(\beta'_k)})(e) = \frac{1}{2} \sum_{k=0}^{\ell-1} (w(\mu(\alpha'_k)) + w(\mu(\beta'_k))) \quad (\text{E.56})$$

so $M(\varrho') \geq M(\varrho)$ since α'_k and β'_k are minimal cuts. Thus we have inequalities in both ways and it must be that

$$M = M(\varrho) = M(\varrho') = \frac{1}{2} \sum_{k=0}^{\ell-1} (w(\mu(\alpha'_k)) + w(\mu(\beta'_k))) \quad (\text{E.57})$$

□

Proof. We first consider the region β . Define this as:

$$\beta = \{x \in V : d_\varrho(x, \Gamma_\ell) = 0\} \quad (\text{E.58})$$

It is clear that this satisfies the cut properties stated in the Lemma. It is also clear that $\tilde{\varrho}(e) := \varrho(e) -$

$(1/2)\mathbf{1}_{\mu(\beta)}(e) \geq 0$. We show that $\tilde{\varrho}$ is feasible for the following 1/2 integer program:

$$\tilde{M} \equiv \min_{\tilde{\varrho}} \tilde{M}(\tilde{\varrho}), \quad \tilde{M}(\tilde{\varrho}) = \sum_{e \in E} w(e)\tilde{\varrho}(e) \quad (\text{E.59})$$

$$\text{subject to} \quad \forall L \in \mathcal{P}_{\Gamma_k, \Gamma_{k'}} : \tilde{\varrho}(L) \in |k - k'| + \mathbb{Z}_{\geq 0} \quad (\text{E.60})$$

$$\text{and} \quad \forall L \in \mathcal{P}_{\Gamma_k, C} : \tilde{\varrho}(L) \in \ell/2 + \mathbb{Z}_{\geq 0} \quad (\text{E.61})$$

$$\text{subject to} \quad \forall L \in \mathcal{P}_{\Gamma_k, \Gamma_\ell} : \tilde{\varrho}(L) \in (\ell - k - 1/2) + \mathbb{Z}_{\geq 0} \quad (\text{E.62})$$

$$\text{and} \quad \forall L \in \mathcal{P}_{\Gamma_\ell, C} : \tilde{\varrho}(L) \in (\ell - 1)/2 + \mathbb{Z}_{\geq 0} \quad (\text{E.63})$$

for all $k, k' = 0, \dots, \ell - 1$.

This program is defined for $\ell \geq 1$. The last constraint is trivial if $\ell = 1$. We sketch this program in Fig. (E.6).

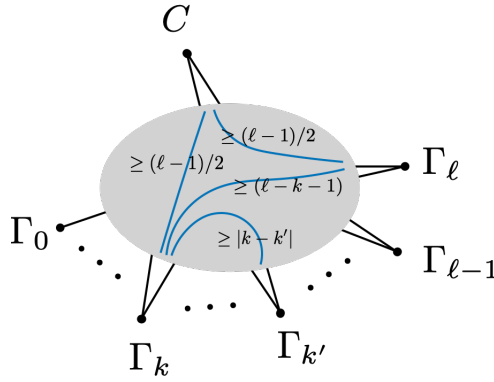


Figure E.6: The intermediate half integer program described in Eq. (E.59).

Feasibility is clear for paths that intersect $\mu(\beta)$ the minimal number of times, that is the subset of paths defined below:

$$\text{(I)} \quad \tilde{\mathcal{P}}_{\Gamma_k, \Gamma_{k'}} = \{L \in \mathcal{P}_{\Gamma_k, \Gamma_{k'}} : \mathbf{1}_{\mu(\beta)}(L) = 0\} \geq |k - k'| \quad (\text{E.64})$$

$$\text{(II)} \quad \tilde{\mathcal{P}}_{C, \Gamma_k} = \{L \in \mathcal{P}_{C, \Gamma_k} : \mathbf{1}_{\mu(\beta)}(L) = 0\} \geq \ell/2 \quad (\text{E.65})$$

$$\text{(III)} \quad \tilde{\mathcal{P}}_{\Gamma_k, \Gamma_\ell} = \{L \in \mathcal{P}_{\Gamma_k, \Gamma_\ell} : \mathbf{1}_{\mu(\beta)}(L) = 1\} \geq (\ell - k - 1/2) \quad (\text{E.66})$$

$$\text{(IV)} \quad \tilde{\mathcal{P}}_{C, \Gamma_\ell} = \{L \in \mathcal{P}_{C, \Gamma_\ell} : \mathbf{1}_{\mu(\beta)}(L) = 1\} \geq (\ell - 1)/2, \quad (\text{E.67})$$

for all $k, k' = 0, \dots, \ell - 1$. We have listed the constraints for the ϱ' problem on the right and on the left we have given labels to the various cases of paths. It is also clear we maintain the integer condition for $\tilde{\varrho}$ in Eq. (E.59) due to the topology of the paths, so we need only consider the inequalities below. Any other path not in this class can be decomposed using these paths. There are four different cases to consider (see Fig. (E.7)):

(I) If $L \in \mathcal{P}_{\Gamma_k, \Gamma_{k'}}$ with $0 \leq k < k' \leq \ell - 1$ we can bound these paths via:

$$\begin{aligned} \tilde{\varrho}(L) + \tilde{\varrho}(L_{x, \Gamma_\ell}) + \tilde{\varrho}(L_{x', \Gamma_\ell}) &\geq \tilde{\varrho}(\tilde{L}_{\Gamma_\ell, \Gamma_k}) + \tilde{\varrho}(\tilde{L}_{\Gamma_\ell, \Gamma_{k'}}) \\ &\geq (\ell - k - 1/2) + (\ell - k' - 1/2) \geq (k' - k) + 1 \end{aligned} \quad (\text{E.68})$$

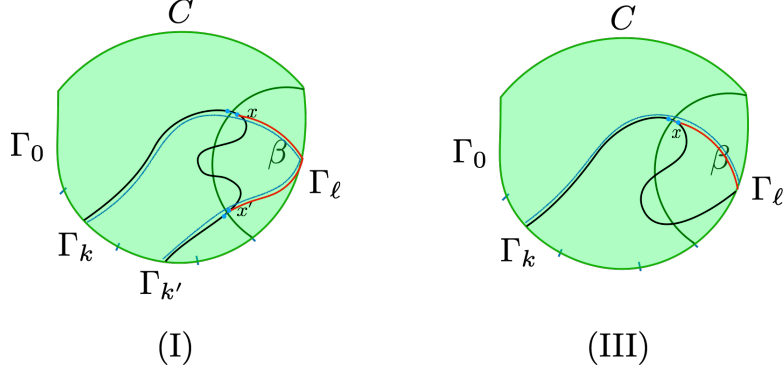


Figure E.7: We perform surgery on a path L (black solid) at point x and x' using minimal paths (red solid) and reduce L to the union of paths (blue solid) and use it to bound $\tilde{\varrho}(L)$. The procedure prescribed for type-I and type-III paths are depicted here. The procedure for type-II and type-IV paths are similar.

where x and x' are the first and last points inside β where the path L enters and leaves. We have sewn on paths L_{x, Γ_ℓ} and L_{x', Γ_ℓ} to these points, where we can pick these paths as the ones minimizing the distance $d_\varrho(x, \Gamma_\ell) = 0$ and $d_\varrho(x', \Gamma_\ell) = 0$. In particular for these paths $\tilde{\varrho}(P_{x, \Gamma_\ell}) = \varrho(P_{x, \Gamma_\ell}) = 0$ and similarly for x' . The first inequality in Eq. (E.68) drops the mid portion of the curve and applies the bound Eq. (E.66) for a curve that intersects $\mu(\beta)$ once, that is $\tilde{L}_{\Gamma_\ell, \Gamma_k}$ and $\tilde{L}_{\Gamma_\ell, \Gamma_{k'}}$.

(II) If $L \in \mathcal{P}_{C, \Gamma_k}$ for $0 \leq k \leq \ell - 1$ we can, in a similar manner as above, split this into two and show:

$$\tilde{\varrho}(L) \geq (\ell - k - 1/2) + (\ell - 1)/2 \geq \ell/2 \quad (\text{E.69})$$

where we applied Eq. (E.66) and Eq. (E.67).

(III) If $L \in \mathcal{P}_{\Gamma_k, \Gamma_\ell}$ for $0 \leq k \leq \ell - 1$, then we simply drop the portion of the path after the first intersection with $x \in \beta$ along the path $\Gamma_k \rightarrow x \rightarrow \Gamma_\ell$. Adding the curve $\tilde{\varrho}(L_{x, \Gamma_\ell}) = 0$ gives the estimate:

$$\tilde{\varrho}(L) \geq (\ell - k - 1/2) \quad (\text{E.70})$$

where we applied Eq. (E.66).

(IV) If $L \in \tilde{\mathcal{P}}_{C, \Gamma_\ell}$ we do the same and drop the portion of the path after the first intersection to give:

$$\tilde{\varrho}(L) \geq (\ell - 1)/2 \quad (\text{E.71})$$

where we again applied Eq. (E.67).

This completes the proof that $\tilde{\varrho}$ is feasible for Eq. (E.59).

We now introduce the region:

$$\alpha^c = \{x : d_{\tilde{\varrho}}(x, \Gamma_\ell) + d_{\tilde{\varrho}}(x, C) = (\ell - 1)/2\} \cup \{x : d_{\tilde{\varrho}}(x, \Gamma_\ell) = 0\} \cup \{x : d_{\tilde{\varrho}}(x, C) = 0\} \quad (\text{E.72})$$

We check that it satisfies the cut properties. It is clear that $C \cup \Gamma_\ell \subset \alpha^c$ by definition. Assume that $\Gamma_k \in \alpha^c$ for some $0 \leq k \leq \ell - 1$. Thus either:

$$(\ell - 1)/2 = d_{\tilde{\varrho}}(\Gamma_k, \Gamma_\ell) + d_{\tilde{\varrho}}(\Gamma_k, C) \geq (\ell - k - 1/2) + \ell/2 \geq (\ell + 1)/2 \quad (\text{E.73})$$

which is not possible. Or $d_{\tilde{\rho}}(\Gamma_k, \Gamma_\ell) \geq (\ell - k - 1/2)$ which is not possible or $d_{\tilde{\rho}}(\Gamma_k, C) \geq \ell/2$ which is also not possible. Thus we have a contradiction and $\Gamma_k \in \alpha$. This establishes the cut properties stated.

We now define:

$$\varrho'(e) = \tilde{\varrho}(e) - \frac{1}{2} \mathbf{1}_{\mu(\alpha)}(e) \quad (\text{E.74})$$

We aim to show that $\varrho'(e) \geq 0$. Consider an edge $e = \{x, y\} \in \mu(\alpha)$ with $x \in \alpha^c$ and $y \in \alpha$. The triangle inequality to C states that:

$$\tilde{\varrho}(e) = d_{\tilde{\rho}}(x, y) \geq (d_{\tilde{\rho}}(y, C) - d_{\tilde{\rho}}(x, C)) \quad (\text{E.75})$$

So if $d_{\tilde{\rho}}(x, C) = 0$ then $\tilde{\varrho}(e) \geq d_{\tilde{\rho}}(y, C) > 0$ since $y \in \alpha$ and so must have this strictly greater than 0. Similarly for Γ_ℓ :

$$\tilde{\varrho}(e) \geq d_{\tilde{\rho}}(x, y) = (d_{\tilde{\rho}}(y, \Gamma_\ell) - d_{\tilde{\rho}}(x, \Gamma_\ell)) \quad (\text{E.76})$$

So $d_{\tilde{\rho}}(x, \Gamma_\ell) = 0$ then $\tilde{\varrho}(e) > 0$. Finally if $d_{\tilde{\rho}}(x, \Gamma_\ell) + d_{\tilde{\rho}}(x, C) = (\ell - 1)/2$ we add the two inequality above to show that:

$$2\tilde{\varrho}(e) \geq d_{\tilde{\rho}}(y, C) + d_{\tilde{\rho}}(y, \Gamma_\ell) > 0 \quad (\text{E.77})$$

Thus in all case we have $\tilde{\varrho}(e) \geq 1/2$, by the integrality gap. Indeed $\varrho'(e) \geq 0$.

We thus have:

$$M(\varrho) = M(\varrho') + \frac{1}{2} (w(\mu(\alpha)) + w(\mu(\beta))) \quad (\text{E.78})$$

as required. For $\ell = 1$ we simply bound $M(\varrho') \geq 0$ and we are done. For $\ell > 1$ we need to check feasibility of ϱ' for the $\ell - 1$ -intersecting cut program. Paths that cross $\mu(\alpha)$ a minimal number of times are clearly feasible:

$$\text{(I)} \quad \tilde{\mathcal{P}}_{C, \Gamma_\ell} = \{L \in \mathcal{P}_{C, \Gamma_\ell} : \mathbf{1}_{\mu(\alpha)}(L) = 0\} \geq (\ell - 1)/2 \quad (\text{E.79})$$

$$\text{(II)} \quad \tilde{\mathcal{P}}_{C, \Gamma_k} = \{L \in \mathcal{P}_{C, \Gamma_k} : \mathbf{1}_{\mu(\alpha)}(L) = 1\} \geq (\ell - 1)/2 \quad (\text{E.80})$$

$$\text{(III)} \quad \tilde{\mathcal{P}}_{\Gamma_k, \Gamma_\ell} = \{L \in \mathcal{P}_{\Gamma_k, \Gamma_\ell} : \mathbf{1}_{\mu(\alpha)}(L) = 1\} \geq (\ell - k - 1) \quad (\text{E.81})$$

$$\text{(IV)} \quad \tilde{\mathcal{P}}_{\Gamma_k, \Gamma_{k'}} = \{L \in \mathcal{P}_{\Gamma_k, \Gamma_{k'}} : \mathbf{1}_{\mu(\alpha)}(L) = 0\} \geq |k - k'| \quad (\text{E.82})$$

for all $k, k' = 0, \dots, \ell - 1$, where we have listed the constraints for the ϱ' problem on the right and on the left we have given labels to the various cases of paths.

We now prove a basic result that will seed the rest of our discussion. We consider a path $L \in \mathcal{P}_{C, \Gamma_\ell}$ but now with $\mathbf{1}_{\mu(\alpha)}(L) \geq 2$, see Fig. (E.8). Consider the first edge e in $\mu(\alpha)$ the path crosses (starting at C .) Let

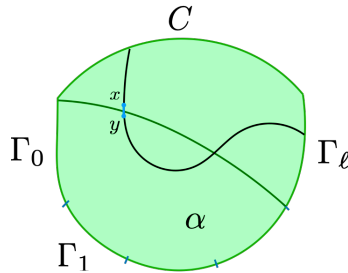


Figure E.8: We consider a path from C to Γ_ℓ that intersect the cut surface $\mu(\alpha)$ at least twice and we denote $e = \{x, y\}$ to be the first edge in the path that crosses $\mu(\alpha)$ (shown as the green solid line).

$e = \{x, y\}$ with $x \in \alpha^c$ and $y \in \alpha$. We know that:

$$d_{\tilde{\rho}}(y, C) + d_{\tilde{\rho}}(y, \Gamma_\ell) > (\ell - 1)/2 \quad (\text{E.83})$$

Using the minimality of these paths and comparing these to the two segments of L split at y we find:

$$\tilde{\rho}(L) > (\ell - 1)/2 \implies \tilde{\rho}(L) \geq (\ell - 1)/2 + 1 \quad (\text{E.84})$$

where we used the fact that the gap for such paths is 1 (see Eq. (E.63)). If this curve had only two intersections with α ($\mathbf{1}_{\mu(\alpha)}(L) = 2$) we would be done since then we have shown that $\rho'(L) \geq (\ell - 1)/2$.

Another obvious bound applies to any path L :

$$\tilde{\rho}(L) \geq \frac{1}{2} \mathbf{1}_{\mu(\alpha)}(L) \quad (\text{E.85})$$

since we know $\tilde{\rho}$ on these edges. This bound is too crude to be used on its own, but we will still make use of it below when we start performing surgery on the paths and we find paths that start and end on the same boundary region. In this later case the bound we just derived can be tight.

We now address the four types of paths:

- (I) Consider a path $L \in \mathcal{P}_{C, \Gamma_\ell}$ intersecting N times with $\mu(\alpha)$, where $N \geq 2$ is even. We aim to show that $\tilde{\rho}(L) \geq (\ell - 1)/2 + N/2$. We do this by induction. We have proved the case $N = 2$ in Eq. (E.84). We assume it is true for $N - 2$ and prove it for N . Consider the second edge $e = \{x, y\}$ that intersects $\mu(\alpha)$ along the path $C \rightarrow y \rightarrow x \rightarrow \Gamma_\ell$, where $x \in \alpha^c$. There are now three cases (a,b,c) to consider depending on which set x belongs to in Eq. (E.72).

- (a) If $d_{\tilde{\rho}}(x, C) + d_{\tilde{\rho}}(x, \Gamma_\ell) = (\ell - 1)/2$ then consider the minimal paths $L_{x,C}, L_{x,\Gamma_\ell}$ defining these two distances. We show that both of these curves $L_{x,C}, L_{x,\Gamma_\ell}$ lie entirely inside α^c . If not there would be some $y \in \alpha$ (the first vertex where either $L_{x,C}, L_{x,\Gamma_\ell}$ leaves α^c) with $d_{\tilde{\rho}}(y, C) + d_{\tilde{\rho}}(y, \Gamma_\ell) = (\ell - 1)/2$ and this is a contradiction. We use $L_{x,C}, L_{x,\Gamma_\ell}$ to perform surgery on L as in the first figure shown in Fig. (E.9). That is we start with L and $L_{x,C} \cup L_{x,\Gamma_\ell}$ and end up with two paths in $\mathcal{P}_{C, \Gamma_\ell}$. These later

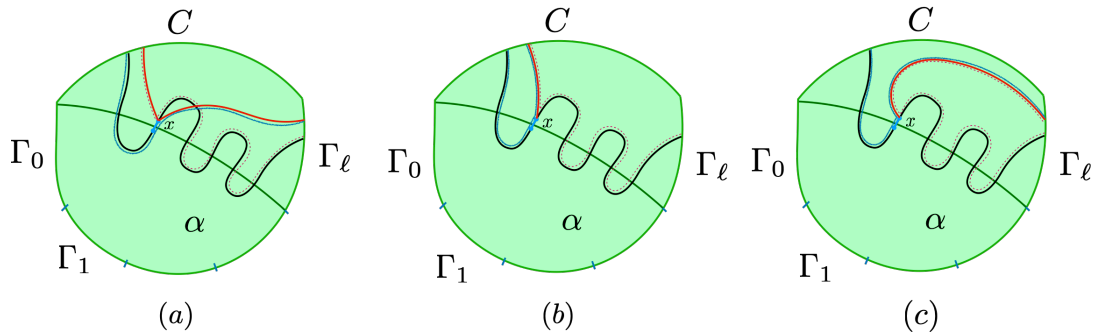


Figure E.9: We perform surgeries on the N -intersecting path $L \in \mathcal{P}_{C, \Gamma_\ell}$ (black solid lines) at the point x using various minimal paths (red solid lines) and reduce L to two paths – the blue solid lines, which intersect $\mu(\alpha)$ two times, and red dashed lines, which intersect $\mu(\alpha)$ $N - 2$ times.

curves intersect $\mu(\alpha)$ two times and $N - 2$ times respectively. Thus:

$$\tilde{q}(L) + (\ell - 1)/2 = \tilde{q}(L) + \tilde{q}(L_{x,C} \cup L_{x,\Gamma_\ell}) \quad (\text{E.86})$$

$$\geq ((\ell - 1)/2 + 1) + ((\ell - 1)/2 + (N - 2)/2) \quad (\text{E.87})$$

Thus $\tilde{q}(P) \geq (\ell - 1)/2 + N/2$ as required.

(b) If $d_{\tilde{q}}(x, C) = 0$, we instead perform surgery with two copies of this minimal path. It is clear this path remains inside α^c . These paths do not cost anything. See the second figure in Fig. (E.9) for the pattern. In particular we find, after surgery, a curve that starts and ends in C and that intersects $\mu(\alpha)$ twice, and a curve in $\mathcal{P}_{C,\Gamma_\ell}$ intersecting $N - 2$ times. For the former curve we use the estimate Eq. (E.85) and find:

$$\tilde{q}(P) \geq (1) + ((\ell - 1)/2 + (N - 2)/2) = (\ell - 1)/2 + N/2 \quad (\text{E.88})$$

as required.

(c) If $d_{\tilde{q}}(x, \Gamma_\ell) = 0$ then we again use two copies of this minimal path to perform surgery: see the third figure in Fig. (E.9) for the pattern.

The right hand side is now a path $\mathcal{P}_{C,\Gamma_\ell}$ with two intersections and a path from $\mathcal{P}_{\Gamma_\ell,\Gamma_\ell}$ with $N - 2$ intersections. Thus:

$$\tilde{q}(L) \geq ((\ell - 1)/2 + 1) + ((N - 2)/2) = (\ell - 1)/2 + N/2 \quad (\text{E.89})$$

where we used Eq. (E.84) and Eq. (E.85). We have completed the induction step.

(II) Consider a path $L \in \mathcal{P}_{C,\Gamma_k}$ for some $0 \leq k \leq \ell - 1$ and intersecting N times with $\mu(\alpha)$, where $N \geq 3$ is odd. We aim to show that $\tilde{q}(L) \geq (\ell - 1)/2 + N/2$. Consider the *last* edge $e = \{x, y\}$ that intersects $\mu(\alpha)$ along the path $C \rightarrow y \rightarrow x \rightarrow \Gamma_k$, where $x \in \alpha^c$. There are again three cases (a,b,c) to consider:

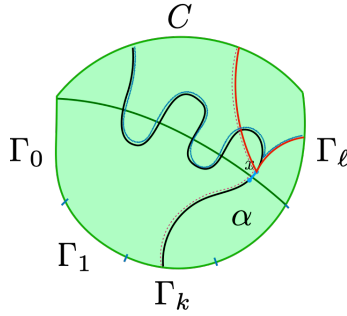


Figure E.10: We perform a surgery that turns a path $L \in \mathcal{P}_{C,\Gamma_k}$ of type-II (a) (black solid curve) to a type-I path in $\mathcal{P}_{C,\Gamma_\ell}$ (blue solid) and a path in $\tilde{\mathcal{P}}_{C,\Gamma_k}$ (red dashed) that only intersects $\mu(\alpha)$ one time.

(a) If $d_{\tilde{q}}(x, C) + d_{\tilde{q}}(x, \Gamma_\ell) = (\ell - 1)/2$, we again perform surgery as shown in Fig. (E.10). from which we arrive at a path in $\mathcal{P}_{C,\Gamma_\ell}$ intersecting $N - 1$ times and a path in \mathcal{P}_{C,Γ_k} with one intersection. We dealt with the later path at the start and the former we have already bounded in (I) above. Thus:

$$\tilde{q}(L) + (\ell - 1)/2 \geq ((\ell - 1)/2 + (N - 1)/2) + (\ell/2) \quad (\text{E.90})$$

implying $\tilde{q}(L) \geq (\ell - 1)/2 + N/2$.

(b) If $d_{\tilde{\varrho}}(x, C) = 0$, we take these minimal paths and join in the obvious way to find a path in $\mathcal{P}_{C, C}$ with $N - 1$ intersections and one in $\mathcal{P}_{C, \Gamma_k}$ with one intersection. Thus:

$$\tilde{\varrho}(L) \geq ((N - 1)/2) + (\ell/2) = (\ell - 1)/2 + N/2 \quad (\text{E.91})$$

(c) If $d_{\tilde{\varrho}}(x, \Gamma_\ell) = 0$ we use these minimal paths to construct a path in $\mathcal{P}_{\Gamma_k, \Gamma_\ell}$ with one intersection and one in $\mathcal{P}_{C, \Gamma_\ell}$ with $N - 1$ intersections. Hence:

$$\tilde{\varrho}(L) \geq (\ell - k - 1/2) + ((\ell - 1)/2 + (N - 1)/2) \geq (\ell - 1)/2 + N/2 \quad (\text{E.92})$$

where we used $\ell - k - 1 \geq 0$. And we claim victory for these paths.

(III) Consider a path $L \in \mathcal{P}_{\Gamma_k, \Gamma_\ell}$ for some $0 \leq k \leq \ell - 1$ and intersecting N times with $\mu(\alpha)$, where $N \geq 3$ is odd. We consider now the second edge $e = \{x, y\}$ along the path from $L : \Gamma_k \rightarrow x \rightarrow y \rightarrow \Gamma_\ell$ with $x \in \alpha^c$. As usual there are three cases:

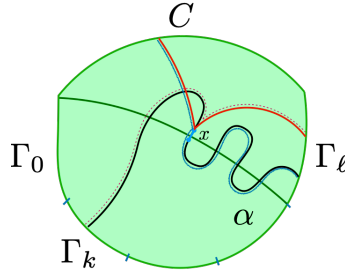


Figure E.11: We perform a surgery that turns a path $L \in \mathcal{P}_{\Gamma_k, \Gamma_\ell}$ of type-III (a) (black solid curve) to a type-II path in $\mathcal{P}_{C, \Gamma_\ell}$ (blue solid) and a path in $\tilde{\mathcal{P}}_{\Gamma_k, \Gamma_\ell}$ (red dashed) that only intersects $\mu(\alpha)$ one time.

(a) If $d_{\tilde{\varrho}}(x, C) + d_{\tilde{\varrho}}(x, \Gamma_\ell) = (\ell - 1)/2$, we again perform surgery as shown in Fig. (E.11). The resulting paths are in $\mathcal{P}_{\Gamma_k, \Gamma_\ell}$ with one intersections and and in $\mathcal{P}_{C, \Gamma_\ell}$ with $(N - 1)$ intersections. Thus:

$$\tilde{\varrho}(L) + (\ell - 1)/2 \geq (\ell - k - 1/2) + ((\ell - 1)/2 + (N - 1)/2) \quad (\text{E.93})$$

Or $\tilde{\varrho}(L) \geq (\ell - k - 1) + N/2$ as required.

(b) Now if $d_{\tilde{\varrho}}(x, C) = 0$, our surgery results in a path in $\mathcal{P}_{C, \Gamma_k}$ with one intersection and a path in $\mathcal{P}_{C, \Gamma_\ell}$ with $N - 1$ intersections. Hence:

$$\tilde{\varrho}(L) \geq (\ell/2) + ((\ell - 1)/2 + (N - 1)/2) = \ell - 1 + N/2 \geq (\ell - k - 1) + N/2 \quad (\text{E.94})$$

(c) Now if $d_{\tilde{\varrho}}(x, \Gamma_\ell) = 0$, our surgery results in a path in $\mathcal{P}_{\Gamma_k, \Gamma_\ell}$ with one intersection and a path in $\mathcal{P}_{\Gamma_\ell, \Gamma_\ell}$ with $N - 1$ intersections. Hence:

$$\tilde{\varrho}(L) \geq (\ell - k - 1/2) + ((N - 1)/2) = (\ell - k - 1) + N/2 \quad (\text{E.95})$$

(IV) Consider a path $L \in \mathcal{P}_{\Gamma_k, \Gamma_{k'}}$ for some $0 \leq k < k' \leq \ell - 1$ and intersecting N times with $\mu(\alpha)$, where $N \geq 2$ is even. We consider now the second edge $e = \{x, y\}$ along the path from $L : \Gamma_k \rightarrow x \rightarrow y \rightarrow \Gamma_{k'}$ with $x \in \alpha^c$. As usual there are three cases:

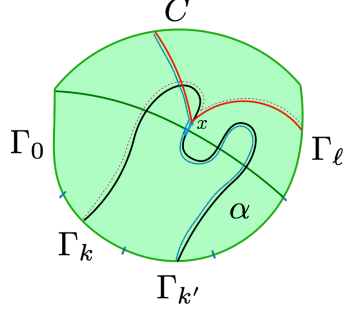


Figure E.12: We perform a surgery that turns a path $L \in \mathcal{P}_{k, \Gamma'_k}$ of type-IV (a) (black solid curve) to a type-II path in $\mathcal{P}_{C, \Gamma'_k}$ (blue solid) and a path in $\tilde{\mathcal{P}}_{\Gamma_k, \Gamma'_k}$ (red dashed) that only intersects $\mu(\alpha)$ one time.

(a) If $d_{\tilde{\rho}}(x, C) + d_{\tilde{\rho}}(x, \Gamma_\ell) = (\ell - 1)/2$, surgery results in a path in $\mathcal{P}_{\Gamma_k, \Gamma_\ell}$ with one intersection and another path in $\mathcal{P}_{C, \Gamma_{k'}}$ with $N - 1$ intersections, see Fig. (E.12). Thus, using (II) we have:

$$\tilde{\varrho}(L) + (\ell - 1)/2 \geq (\ell - k - 1/2) + ((\ell - 1)/2 + (N - 1)/2) \quad (\text{E.96})$$

implying $\tilde{\varrho}(L) \geq (\ell - k - 1) + N/2 \geq (k' - k) + N/2$ where we used $\ell - 1 \geq k'$. This is the required bound.

(b) Now if $d_{\tilde{\rho}}(x, C) = 0$, our surgery results in a path in $\mathcal{P}_{\Gamma_k, C}$ with one intersection and a path in $\mathcal{P}_{\Gamma_{k'}, C}$ with $(N - 1)$ intersections. Thus:

$$\tilde{\varrho}(L) \geq (\ell/2) + ((\ell - 1)/2 + (N - 1)/2) = \ell - 1 + N/2 \geq (k' - k) + N/2 \quad (\text{E.97})$$

where we again used (II).

(c) Now if $d_{\tilde{\rho}}(x, \Gamma_\ell) = 0$, our surgery results in a path in $\mathcal{P}_{\Gamma_k, \Gamma_\ell}$ with one intersection and a path in $\mathcal{P}_{\Gamma_\ell, \Gamma_{k'}}$ with $N - 1$ intersections. Hence:

$$\tilde{\varrho}(L) \geq (\ell - k - 1/2) + (\ell - k' - 1 + (N - 1)/2) \geq (k' - k) + N/2 \quad (\text{E.98})$$

where we used (III) and $\ell - k' - 1 \geq -(\ell - k' - 1)$. And we are done.

The above bound establish feasibility of ϱ' for the $\ell - 1$ intersecting cut problem. (The integer gap conditions are again all automatic because the even/oddness of the number of intersections is fixed by the topology of the path.) \square

E.3 Proof of Lemma 6.25: Probabilistic convergence for S_R

Consider the renormalized operator:

$$\hat{\mathcal{O}} = (\varrho \otimes \varrho) \chi^{2n\mathcal{A}(AB:C)} \quad (\text{E.99})$$

and define the renormalized measure:

$$d\hat{\mu}_\Psi(\hat{\lambda}) = \chi^{2(n-1)\mathcal{A}(A:B:C) - 2n\mathcal{A}(AB:C)} \sum_i |\langle \Psi | v_i \rangle|^2 \delta(\hat{\lambda} - \hat{\lambda}_i) d\hat{\lambda} \quad (\text{E.100})$$

where $\hat{\lambda} = \lambda \chi^{2n\mathcal{A}(AB:C)}$. We know that new measure satisfies

$$\lim_{\chi \rightarrow \infty} \overline{\int_0^\infty d\hat{\mu}_\Psi(\hat{\lambda}) \hat{\lambda}^{m/2}} = 1 \quad (\text{E.101})$$

for $m/2 \in \mathbb{Z}_{\geq 1}$. Note that we do not know the zeroth moment of $\hat{\lambda}$.

Pick some cut-off $\Lambda > 1$ and define

$$\Delta_{m/2} = \overline{\int d\hat{\mu}_\Psi(\hat{\lambda}) \hat{\lambda}^{m/2} \theta(\hat{\lambda} - \Lambda)} \leq \Lambda^{-m/2} \overline{\int d\hat{\mu}_\Psi(\hat{\lambda}) \hat{\lambda}^m \theta(\hat{\lambda} - \Lambda)} \leq \Lambda^{-m/2} \overline{\int d\hat{\mu}_\Psi(\hat{\lambda}) \hat{\lambda}^m} \quad (\text{E.102})$$

From now on we will set $\Lambda = 2$. Then we have:

$$\lim_{\chi \rightarrow \infty} \Delta_{m/2} \leq \lim_{\chi \rightarrow \infty} \Delta_{m'/2} \leq 2^{-m'/2} \quad (\text{E.103})$$

for all $m' \in \mathbb{Z}$ and $m' \geq m \geq 1$. Taking $m' \rightarrow \infty$ proves that that $\lim_{\chi \rightarrow \infty} \Delta_{m/2} = 0$ for $m \in \mathbb{Z}_{\geq 1}$. In particular, for any polynomial function $f(\hat{\lambda})$ we have that

$$\overline{\int_2^\infty d\hat{\mu}_\Psi(\hat{\lambda}) f(\hat{\lambda})} = \sum_{k \in \mathbb{N}} \frac{f^{(k)}(0)}{k!} \Delta_k \xrightarrow{\chi \rightarrow \infty} 0 \quad (\text{E.104})$$

In other words, the measure $\hat{\mu}_\Psi(\hat{\lambda})$ is highly concentrated in the interval $[0, 2]$ and it suffices to only consider test functions with compact support on the interval.

Let us approximate the square root function on $[0, 2]$ as:

$$p_M(x) \equiv \sum_{\mu=1}^M \sqrt{\frac{2\mu}{M}} b_{\mu,M}(x/2) \quad (\text{E.105})$$

where $b_{\mu,M}(x)$ are the Bernstein polynomials of degree M . Since only $b_{0,M}(x)$ has the constant monomial in it, we only need the higher moments. For all $\delta > 0$ there exists some integer M such that

$$\|\sqrt{x} - p_M(x)\|_{L^\infty[0,2]} < \delta \quad (\text{E.106})$$

Now we write

$$\begin{aligned} \left| \left(\overline{\int_0^\infty d\hat{\mu}_\Psi(\hat{\lambda}) \hat{\lambda}^{1/2}} \right) - 1 \right| &\leq \underbrace{\overline{\int_2^\infty d\hat{\mu}_\Psi(\hat{\lambda}) \hat{\lambda}^{1/2}}}_{C_1} + \underbrace{\left| \left(\overline{\int_0^2 d\hat{\mu}_\Psi(\hat{\lambda}) p_M(\hat{\lambda})} \right) - 1 \right|}_{C_2} \\ &\quad + \underbrace{\left| \overline{\int_0^2 d\hat{\mu}_\Psi(\hat{\lambda}) (\hat{\lambda}^{1/2} - p_M(\hat{\lambda}))} \right|}_{C_3} \end{aligned} \quad (\text{E.107})$$

Using Markov inequality along with Eq. (E.103) we can show that for any integer m ,

$$\Pr(C_1 \geq \epsilon) \leq \frac{\Delta_m}{\epsilon} \xrightarrow{\chi \rightarrow \infty} 0 \quad (\text{E.108})$$

For C_2 we consider:

$$C_2 \leq \left| \left(\int_0^2 d\hat{\mu}_\Psi(\hat{\lambda}) p_M(\hat{\lambda}) \right) - \overline{\left(\int_0^2 d\hat{\mu}_\Psi(\hat{\lambda}) p_M(\hat{\lambda}) \right)} \right| + \left| \overline{\left(\int_0^2 d\hat{\mu}_\Psi(\hat{\lambda}) p_M(\hat{\lambda}) \right)} - 1 \right| \quad (\text{E.109})$$

We can bound the first term using Chebyshev's inequality:

$$\Pr(C_2^{\text{first}} \geq \epsilon) \leq \frac{\sigma^2}{\epsilon^2} \quad (\text{E.110})$$

where

$$\sigma^2 = \text{Var}(C_2^{\text{first}}) \cong \text{Var} \left(\int_0^\infty d\hat{\mu}_\Psi(\hat{\lambda}) p_M(\hat{\lambda}) \right) = \sum_{m=1}^M p_m \text{Var} \left(\int_0^\infty d\hat{\mu}_\Psi(\hat{\lambda}) \hat{\lambda}^m \right) \quad (\text{E.111})$$

where p_m are Taylor coefficients of $p_M(\lambda)$. Note that we have extended the integration limit in Eq. (E.111). The error from doing so can be shown to vanish in the limit $\chi \rightarrow \infty$ by application of Eq. (E.104). The expectation values of the double moments are related to

$$\overline{\left(\int_0^\infty d\hat{\mu}_\Psi(\hat{\lambda}) \hat{\lambda}^m \right)^2} = \chi^{(4n-1)\mathcal{A}(A:B:C) - 4n\mathcal{A}(AB:C)} \overline{\langle \Psi |^{\otimes 2} \hat{O}^m \otimes \hat{O}^m | \Psi \rangle^{\otimes 2}} \quad (\text{E.112})$$

which can be computed by a different symmetry group optimization problem defined on G . We now minimize over $g \in S_{2mn}$ in this graph such that the boundary conditions are $\tilde{g}_A \equiv g_A^{(1)} g_A^{(2)}$, $\tilde{g}_B \equiv g_B^{(1)} g_B^{(2)}$ and $\tilde{g}_C = \text{id}$, where $g_{A,B}^{(1)}$ permutes the first mn replicas and leaving the second mn copies invariant; whereas $g_{A,B}^{(2)}$ permutes the second mn replicas and leaving the first invariant. Our analysis in Sec. (6.4) largely carries over. The main difference is that we must now coarse-grain using the new element $\tilde{X} \equiv \tilde{g}_A \wedge \tilde{g}_B = X^{(1)} X^{(2)}$ with $X^{(i)}$ defined similarly as above. We need the following generalization of Lemma 6.10:

Lemma E.6. *For any $q \in P_{4n}$ we have*

$$d(\tilde{q}_A, q) + d(\tilde{q}_B, q) \geq d(\tilde{q}_A, \tilde{q}_B) + 2(1 - \delta_{\#_1^{(1)}(q), 0}) + 2(1 - \delta_{\#_1^{(2)}(q), 0}) + 2\delta_{q \vee \tau, \mathbb{Z}_{4n}} \quad (\text{E.113})$$

where $\tilde{q}_{A,B} = q_{\tilde{X}}(\tilde{g}_{A,B})$, $\#_1^{(1,2)}(\cdot)$ counts the number of singlets in the first (second) sets of $2n$ elements, and $\tau = \{\mathbb{Z}_{2n}, \mathbb{Z}_{2n}\}$ is the maximal element in P_{4n} that is disconnected between the two sets of $2n$ elements.

Proof. If $q \in P_{2n} \times P_{2n}$ then $\delta_{q \vee \tau, \mathbb{Z}_{4n}} = 0$ and we can simply break down the problem into two smaller problems on disconnected copies of $2n$ elements. Applying Lemma 6.10 on each copy proves the result.

Now suppose that $q \in P_{4n} \setminus P_{2n} \times P_{2n}$. Then there must exist some $u_{ij} \in P_{4n} \setminus P_{2n} \times P_{2n}$ such that $p \vee u_{ij} = p$, where u_{ij} is the unique partition with a doublet connecting element i from the first copy to element j in the second copy and singlets at every other position. We write

$$\begin{aligned} d(\tilde{q}_A, p) &= d(\tilde{q}_A, p \vee u_{ij}) = \#(\tilde{q}_A) + \#(p \vee u_{ij}) - 2\#(\tilde{q}_A \vee p \vee u_{ij}) \\ &= 1 + \#(\tilde{q}_A \vee u_{ij}) + \#(p \vee u_{ij}) - 2\#(\tilde{q}_A \vee p \vee u_{ij}) \\ &= d(\tilde{q}_A \vee u_{ij}, p) + 1 \end{aligned} \quad (\text{E.114})$$

and similarly for $d(\tilde{q}_B, p)$. Thus

$$\begin{aligned} d(\tilde{q}_A, p) + d(p, \tilde{q}_B) &= d(\tilde{q}_A \vee u_{ij}, p) + d(p, \tilde{q}_B \vee u_{ij}) + 2 \\ &\geq d(\tilde{q}_A \vee u_{ij}, \tilde{q}_B \vee u_{ij}) + 2 \end{aligned} \quad (\text{E.115})$$

by triangle inequality. This bound can be strengthened in a similar fashion as the proof in Lemma 6.10. The bipartite graph of $\tilde{q}_A \vee u_{ij}$ and $\tilde{q}_B \vee u_{ij}$ is now connected with two cycles, each corresponding to a $2n$ -element copy. A singlet in the first copy will break the first cycle and leads to an enhancement of the bound by 2, and likewise for a singlet in the second copy. Since $d(\tilde{q}_A \vee u_{ij}, \tilde{q}_B \vee u_{ij}) = d(\tilde{q}_A, \tilde{q}_B)$ we obtain

$$d(\tilde{q}_A, p) + d(p, \tilde{q}_B) \geq d(\tilde{q}_A, \tilde{q}_B) + 2(1 - \delta_{\#_1^{(1)}(q), 0}) + 2(1 - \delta_{\#_1^{(2)}(q), 0}) + 2 \quad (\text{E.116})$$

And this completes the proof. \square

Using Lemma E.6 we see that we may restrict to the disconnected elements $q \in P_{2n} \times P_{2n}$ (and hence $g \in S_{mn} \times S_{mn}$ as the coarse-graining retains this information) in the optimization problems, since for any path $L \in \mathcal{P}_{A:B}$ and vertex v in the path, any $q(v) \in P_{4n} \setminus P_{2n} \times P_{2n}$ will lead to a stricter bound in the integer program. Thus we find that the optimal value of our problem is simply twice of that in the original problem:

$$\overline{\left(\int d\mu_\Psi(\lambda) \lambda^{m/2} \right)^2} = \chi^{-4(n-1)\mathcal{A}(A:B:C) + 2n(m-2)\mathcal{A}(AB:C)} (1 + O(1/\chi)) \quad (\text{E.117})$$

And we have that $\sigma^2 = O(1/\chi)$ and $C_2^{\text{first}} \xrightarrow{\text{Pr}} 0$ as $\chi \rightarrow \infty$. For the second term we have

$$\begin{aligned} C_2^{\text{second}} &\leq \left| \overline{\left(\int_0^\infty d\hat{\mu}_\Psi(\hat{\lambda}) p_M(\hat{\lambda}) \right)} - 1 \right| + \left| \overline{\left(\int_2^\infty d\hat{\mu}_\Psi(\hat{\lambda}) p_M(\hat{\lambda}) \right)} \right| \\ &\xrightarrow{\chi \rightarrow \infty} |p_M(1) - 1| \leq \delta \end{aligned} \quad (\text{E.118})$$

where we have used Eq. (E.101) to rewrite the moment integrals in the first line, and the bound $|p_M(1) - 1| \leq \|p_M(x) - \sqrt{x}\|_{L^\infty[0,2]} = \delta$. The second term in the first line vanishes by Eq. (E.104) in the $\chi \rightarrow \infty$ limit.

For C_3 we write

$$\begin{aligned} C_3 &\leq \int_0^2 d\hat{\mu}_\Psi(\hat{\lambda}) \left| \hat{\lambda}^{1/2} - p_M(\hat{\lambda}) \right| \\ &\leq \int_0^2 d\hat{\mu}_\Psi(\hat{\lambda}) \hat{\lambda}^{1/2} f(\ln \hat{\lambda}) + \int_0^2 d\hat{\mu}_\Psi(\hat{\lambda}) (1 - f(\ln \hat{\lambda})) \left| \hat{\lambda}^{1/2} - p_M(\hat{\lambda}) \right| \\ &\leq \int_0^2 d\hat{\mu}_\Psi(\hat{\lambda}) \hat{\lambda}^{1/2} f(\ln \hat{\lambda}) + \delta \int_0^2 d\hat{\mu}_\Psi(\hat{\lambda}) (1 - f(\ln \hat{\lambda})) \end{aligned} \quad (\text{E.119})$$

where passing from the first line to second we used the fact that $p_M(x)$ approaches \sqrt{x} from below, which follows from the positivity of $p_M(x)$. We have also introduced a function f with $f(x) = 0$ for $x \geq 0$ and whose other properties we will enumerate below. For the second term, we suppose that:

$$\|(1 - f(x))e^{-x}\theta(\ln 2 - x)\|_{L^\infty} \equiv f_1 < \infty \quad (\text{E.120})$$

For the first term we write this out:

$$\begin{aligned}
& C_3^{\text{first}} \chi^{-2(n-1)\mathcal{A}(A:B:C)+n\mathcal{A}(AB:C)} \\
&= \langle 1_{AB}^{\otimes n} | \Sigma_A^\dagger (\varrho^{1/2} \otimes 1) f(\ln(\varrho \otimes \varrho) + 2n\mathcal{A}(AB:C) \ln \chi) (1 \otimes \varrho^{1/2}) \Sigma_A | 1_{AB}^{\otimes n} \rangle \\
&\leq \|\tilde{f}'\|_{L^1} \|\varrho \otimes \varrho - \pi/\chi^{2n\mathcal{A}(AB:C)}\|_1 \|(1 \otimes \varrho^{1/2}) \Sigma_A | 1_{AB}^{\otimes n} \rangle\| \|(\varrho^{1/2} \otimes 1) \Sigma_A | 1_{AB}^{\otimes n} \rangle\|
\end{aligned}$$

where we have applied Eq. (6.157) in the second line. Or, setting $f_2 \equiv \|\tilde{f}'\|_{L^1}$:

$$\begin{aligned}
C_3 &\leq f_1 \delta + f_2 \|\varrho \otimes \varrho - \pi/\chi^{2n\mathcal{A}(AB:C)}\|_1 \times \int_0^\infty d\hat{\mu}_\Psi(\hat{\lambda}) \hat{\lambda}^{1/2} \\
&\leq f_1 \delta + f_2 \|\varrho \otimes \varrho - \pi/\chi^{2n\mathcal{A}(AB:C)}\|_1 \left(1 + \left| \left(\int_0^\infty d\hat{\mu}_\Psi(\hat{\lambda}) \hat{\lambda}^{1/2} \right) - 1 \right| \right)
\end{aligned} \tag{E.121}$$

Since the same quantity appears on the left hand side of Eq. (E.107) we should subtract and write:

$$\left| \left(\int_0^\infty d\hat{\mu}_\Psi(\hat{\lambda}) \hat{\lambda}^{1/2} \right) - 1 \right| \left(1 - f_2 \|\varrho \otimes \varrho - \pi/\chi^{2n\mathcal{A}(AB:C)}\|_1 \right) \leq C_1 + C_2 + C'_3 \tag{E.122}$$

with

$$C'_3 \leq f_1 \delta + f_2 \|\varrho \otimes \varrho - \pi/\chi^{2n\mathcal{A}(AB:C)}\|_1 \xrightarrow{\chi \rightarrow \infty} f_1 \delta \tag{E.123}$$

where we have used Eq. (6.158) in the limit. Now suppose that $0 < f_2 < 1/2$ then using the fact that the trace distance is bounded by 2:

$$\left| \left(\int_0^\infty d\hat{\mu}_\Psi(\hat{\lambda}) \hat{\lambda}^{1/2} \right) - 1 \right| \leq \frac{C_1 + C_2 + C'_3}{1 - 2f_2} \tag{E.124}$$

Since δ can be made arbitrarily small, we have $C_1 \xrightarrow{Pr} 0$ by Eq. (E.108), $C_2 \xrightarrow{Pr} 0$ by Chebyshev's inequality and the vanishing of the variance of moments and Eq. (E.118), and $C'_3 \xrightarrow{Pr} 0$ by Eq. (E.123). The rest of the proof is fairly standard and we find:

$$\chi^{2(n-1)\mathcal{A}(A:B:C)-n\mathcal{A}(AB:C)} \text{Tr}(\rho_{AA^*}^{(1/2)})^n = \left(\int_0^\infty d\hat{\mu}_\Psi(\hat{\lambda}) \hat{\lambda}^{1/2} \right) \xrightarrow{Pr} 1 \tag{E.125}$$

The map $x \rightarrow -\frac{1}{n-1} \ln x$ is continuous for $x > 0$, which is where the random variable is defined so, so by the continuous mapping theorem we prove Eq. (6.169).

We have imposed various properties on f in the above proof. To finish we must show there exists a function with these properties. We desire:

1. f is real with $f \in C^\infty(\mathbb{R})$ with $f(x) = 0$ for $x \geq 0$. Also $f' \in \mathcal{S}(\mathbb{R})$.
2. $f_1 < \infty$ where:

$$f_1 = \sup_{x \leq 0} |(1 - f(x))e^{-x}| \tag{E.126}$$

3. $f_2 < 1/2$ where:

$$f_2 = \|\mathfrak{F}(f')\|_{L^1} \tag{E.127}$$

There is an easy way to achieve this. We need smooth function $\sigma \geq 0$ compactly supported between

$-L < x < 0$. Then set:

$$f(x) = \int_x^0 dx \sigma(x) \quad (\text{E.128})$$

The requirements become: 1. is satisfied. 2 requires:

$$\int_{-L}^0 dx \sigma(x) = 1 \quad \implies \quad \|\sigma\|_{L^1} = 1 \quad (\text{E.129})$$

which implies that:

$$f_1 = \sup_{-L \leq x \leq 0} \left| \int_{-L}^x dx \sigma(x) \exp(-x) \right| < \infty \quad (\text{E.130})$$

We need:

$$f_2 = \|\mathfrak{F}(\sigma)\|_{L^1} < 1/2 \quad (\text{E.131})$$

Or, ignoring the normalization, we seek a bump function, where:

$$\frac{\|\mathfrak{F}(\sigma)\|_{L^1}}{\|\sigma\|_{L^1}} < \frac{1}{2} \quad (\text{E.132})$$

Consider a bump function $b(x)$ defined inside $-1 \leq x \leq 0$, and independent of L , then set:

$$\sigma(x) = b(x/L) \quad (\text{E.133})$$

Then:

$$\frac{\|\mathfrak{F}(\sigma)\|_{L^1}}{\|\sigma\|_{L^1}} = \frac{\int ds \left| \int dx e^{ixs} b(x/L) \right|}{\int dx |b(x/L)|} = L^{-1} \frac{\|\mathfrak{F}(b)\|_{L^1}}{\|b\|_{L^1}} \quad (\text{E.134})$$

So we need to choose:

$$L > \frac{2\|\mathfrak{F}(b)\|_{L^1}}{\|b\|_{L^1}} \quad (\text{E.135})$$

In summary our function that does the job is:

$$f(x) = \frac{1}{L\|b\|_{L^1}} \int_x^0 dx b(x/L) \quad (\text{E.136})$$

Double checking:

$$\|\mathfrak{F}(f')\|_{L^1} = \frac{1}{L\|b\|_{L^1}} \int ds \left| \int dx e^{ixs} b(x/L) \right| = \frac{\|\mathfrak{F}(b)\|_{L^1}}{L\|b\|_{L^1}} < 1/2 \quad (\text{E.137})$$

as required. Notice also that:

$$f(x) = 1 \quad x < -L \quad (\text{E.138})$$

which is required for f_1 to be finite. Thus completing the proof.

E.4 Proof of Eq. (6.166)

Proof of Eq. (6.166):

$$is\mathfrak{F}(f_a)(s) = \mathfrak{F}(f'_a)(s) = \mathfrak{F}(f'w_a)(s) + \mathfrak{F}(fw'_a)(s) \quad (\text{E.139})$$

We have two remainder terms to analyze:

$$\|s\mathfrak{F}(f_a)(s)\|_{L_1} - \|\mathfrak{F}(f')\|_{L_1} \leq \|\mathfrak{F}(f'w_a)\|_{L_1} + \|\mathfrak{F}(f'(1-w_a))\|_{L_1} \quad (\text{E.140})$$

For the second term:

$$\begin{aligned} \|\mathfrak{F}(f'(1-w_a))\|_{L_1} &\leq \|(1+s^2)^{-1}\|_{L_1} \|(1+s^2)\mathfrak{F}(f'(1-w_a))(s)\|_{L_\infty} \\ &\leq \pi(\|f'(1-w_a)\|_{L_1} + \|(f'(1-w_a))''\|_{L_1}) \\ &\leq \pi\left(\sup_{x \leq -a} |(1+x^2)f'(x)| + \sup_{x \leq -a} |(1+x^2)f'''(x)|\right) \\ &\quad + 2\pi\|f''\|_{L_1}\|w'_a\|_{L_\infty} + \pi\|f'\|_{L_1}\|w''_a\|_{L_\infty} \end{aligned} \quad (\text{E.141})$$

where in the first line we use the Hausdorff-Young inequality. But $\|w'_a\|_{L_\infty} = (1/a)\|w'\|_{L_\infty} \rightarrow 0$ and similarly $\|w''_a\|_{L_\infty} = (1/a^2)\|w''\|_{L_\infty} \rightarrow 0$ as $a \rightarrow \infty$ and also:

$$\sup_{x \leq -a} |(1+x^2)f'(x)| < a^{-2} \sup_{x \leq -a} |x^2(1+x^2)f'(x)| < a^{-2}\|x^2(1+x^2)f'(x)\|_{L_\infty} \rightarrow 0 \quad (\text{E.142})$$

For the first term use:

$$\begin{aligned} \mathfrak{F}(fw'_a)(s) &= \mathfrak{F}((f-f_a)w'_a)(s) + f_a \int_{-\infty}^{\infty} dx e^{ixs} w'_a(x) \\ &= \mathfrak{F}((f-f_a)w'_a)(s) + f_a \int_{-\infty}^{\infty} dx e^{ixsa} w'(x) \\ &= \mathfrak{F}((f-f_a)w'_a)(s) + f_a \mathfrak{F}(w')(sa) \end{aligned} \quad (\text{E.143})$$

where for some constant f_a . We pick $f_a = \inf_{x < -a} f(x)$ then:

$$\begin{aligned} \|\mathfrak{F}((f-f_a)w'_a)\|_{L_1} &\leq \|(f-f_a)w'_a\|_{L_1} + \|((f-f_a)w'_a)''\|_{L_1} \\ &\leq \left(\sup_{x < -a} |f(x) - f_a|\right)\|w'_a\|_{L_1} + \|(f-f_a)\|_{L_\infty}\|w'''_a\|_{L_1} \\ &\quad + \|f''\|_{L_1}\|w'_a\|_{L_\infty} + 2\|f'\|_{L_1}\|w''_a\|_{L_\infty} \end{aligned} \quad (\text{E.144})$$

the last two terms are dealt with as above. Note that:

$$\begin{aligned} \|f - C\|_{L_\infty} &\leq \|f\|_{L_\infty} + C = C + \sup_x |f(b) + \int_b^x dy f'(y)| \\ &\leq C + |f(b)| + \sup_x \int_b^x dy |f'(y)| \leq C + |f(b)| + \|f'\|_{L_1} \end{aligned} \quad (\text{E.145})$$

which is clearly finite. This analysis implies that f_a is finite and $\|f - f_a\|_{L_\infty}$ is finite. Thus we need to compute:

$$\|w'_a\|_{L_1} = \|w'\|_{L_1} \quad \|w'''_a\|_{L_1} = \frac{1}{a^2}\|w'''\|_{L_1} \quad (\text{E.146})$$

the later of which vanishes. Since the first term does not vanish we instead note that:

$$\begin{aligned}
\sup_{x < -a} |f(x) - f_a| &= \sup_{x < -a} f(x) - \inf_{x < -a} f(x) \approx f(x_s) - f(x_i) \\
&= \int_{x_s}^{x_i} dx f'(x) \leq \int_{x_s}^{x_i} dx |f'(x)| \leq \int_{-\infty}^a dx |f'(x)| \\
&\leq a^{-2} \int_{-\infty}^a dx x^2 |f'(x)| \leq a^{-2} \|x^2 f'(x)\|_{L_1} \rightarrow 0
\end{aligned} \tag{E.147}$$

where x_i and x_s approximate the location of the inf and sup respectively. This approximation is what we mean by \approx and this can be removed after taking limits.

All that is left to do is to compute:

$$\|\mathfrak{F}(w')(a \cdot)\|_{L_1} = \int_{-\infty}^{\infty} ds |\mathfrak{F}(w')(as)| = a^{-1} \|\mathfrak{F}(w')\|_{L_1} \rightarrow 0 \tag{E.148}$$

Thus establishing the limit Eq. (6.166).

Appendix F

Supplement to Chapter 7

F.1 Non-maximally entangled RTNs

In a standard RTN, the edges are projected onto maximally entangled states. These RTN states can be deformed to nearby states by simply changing the entanglement spectrum on the edges. One may then ask whether we can prove $E_P = EW$ for a larger class of states by considering such a deformation, and attempting to enlarge the parameter space where the inequality in Theorem 7.2 is saturated. It turns out the answer is no, and we give an example in this section to highlight the basic issue.

Consider the 1TN model of Sec. (7.2.1) with a non-maximally entangled leg for subregion C . This state, for a specific choice of spectrum, is identical to that of the PSSY model, an evaporating black hole in JT gravity coupled to end-of-the-world branes with flavour indices entangled with a radiation system [15]. Here, we will not restrict to the PSSY spectrum, and find more generally how this deformation affects the phase diagram of reflected entropy.

For generality, consider the state $|\rho_{AB}^{m/2}\rangle$, a one parameter generalization of the canonical purification. We have computed the entanglement spectrum of ρ_{AA^*} for this state in Chapter 4. It consists of two features: a single pole of weight $p_d(m)$ and a mound of $\min(d_A^2 - 1, d_B^2 - 1)$ eigenvalues with weight $p_c(m)$. The weights are given by

$$p_d(m) = \frac{\text{tr}(\rho_{AB}^{m/2})^2}{d_A d_B \text{tr}(\rho_{AB}^m)} \quad (\text{F.1})$$

$$p_c(m) = 1 - p_d(m). \quad (\text{F.2})$$

Now, we would like to compare the phase diagram of this model with the standard 1TN with maximally entangled legs. First note that the transition between e and X in the 1TN phase diagram in Fig. (7.2) is dictated by the location of the entanglement wedge phase transition, which we hold fixed to compare the two models. Then the remaining question is where the transition from X to g_A/g_B happens.

Consider the region of the phase diagram where $d_A > d_B$. The transition happens in the connected sector. Thus, we have $p_c(m) \approx 1$ and the spectrum of ρ_{AB} is well approximated by the spectrum on the C leg. Using this, we find that the location of the transition for $S_R^{(2)}$ is given by

$$p_d(m) = \frac{1}{d_B}. \quad (\text{F.3})$$

Using Eq. (F.1), we then have

$$(2 - m)S_{m/2} - (1 - m)S_m = \log d_A, \quad (\text{F.4})$$

where S_n is the n th Renyi entropy of the non-maximal spectrum on the C leg.

Then it is clear that at $m = 1$, the location of the phase transition is $x_A = \frac{S_{1/2}}{S_1} \geq 1$. The standard 1TN has a flat spectrum, i.e, $S_n = S_1$ and the transition is at $x_A = 1$. Thus, the shaded region where we cannot prove $E_P = EW$ is larger after deforming the RTN to add non-maximally entangled legs.

As a side note, we would like to mention what happens for $m \geq 2$ where one can use the usual RTN calculation of domain walls with tensions modified by the entanglement spectrum, thus introducing an m dependence [47, 110]. For $m \geq 2$, we have $x_A = \frac{S_{m/2}}{S_1} - (m - 1) \frac{S_{m/2} - S_m}{S_1} \leq 1$ since $S_m \leq S_{m/2} \leq S_1$. Thus, the X region shrinks for $m \geq 2$ after deforming the spectrum on the legs. However, as demonstrated above for $m = 1$, the naive analytic continuation of the result at $m \geq 2$ fails.

References

- [1] A. Kitaev and J. Preskill, “Topological entanglement entropy,” *Phys. Rev. Lett.*, vol. 96, p. 110 404, 2006. DOI: [10.1103/PhysRevLett.96.110404](https://doi.org/10.1103/PhysRevLett.96.110404). arXiv: [hep-th/0510092](https://arxiv.org/abs/hep-th/0510092).
- [2] M. Levin and X.-G. Wen, “Detecting Topological Order in a Ground State Wave Function,” *Phys. Rev. Lett.*, vol. 96, no. 11, 110405, p. 110 405, Mar. 2006. DOI: [10.1103/PhysRevLett.96.110405](https://doi.org/10.1103/PhysRevLett.96.110405). arXiv: [cond-mat/0510613](https://arxiv.org/abs/cond-mat/0510613) [[cond-mat.str-el](#)].
- [3] H. Li and F. D. M. Haldane, “Entanglement Spectrum as a Generalization of Entanglement Entropy: Identification of Topological Order in Non-Abelian Fractional Quantum Hall Effect States,” *Phys. Rev. Lett.*, vol. 101, no. 1, 010504, p. 010 504, Jul. 2008. DOI: [10.1103/PhysRevLett.101.010504](https://doi.org/10.1103/PhysRevLett.101.010504). arXiv: [0805.0332](https://arxiv.org/abs/0805.0332) [[cond-mat.mes-hall](#)].
- [4] S. R. White, “Density-matrix algorithms for quantum renormalization groups,” *Phys. Rev. B*, vol. 48, pp. 10 345–10 356, 1993. DOI: [10.1103/PhysRevB.48.10345](https://doi.org/10.1103/PhysRevB.48.10345).
- [5] G. Vidal, “Class of Quantum Many-Body States That Can Be Efficiently Simulated,” *Phys. Rev. Lett.*, vol. 101, p. 110 501, 2008. DOI: [10.1103/PhysRevLett.101.110501](https://doi.org/10.1103/PhysRevLett.101.110501). arXiv: [quant-ph/0610099](https://arxiv.org/abs/quant-ph/0610099).
- [6] H. Casini and M. Huerta, “A Finite entanglement entropy and the c-theorem,” *Phys. Lett. B*, vol. 600, pp. 142–150, 2004. DOI: [10.1016/j.physletb.2004.08.072](https://doi.org/10.1016/j.physletb.2004.08.072). arXiv: [hep-th/0405111](https://arxiv.org/abs/hep-th/0405111).
- [7] H. Casini and M. Huerta, “On the RG running of the entanglement entropy of a circle,” *Phys. Rev. D*, vol. 85, p. 125 016, 2012. DOI: [10.1103/PhysRevD.85.125016](https://doi.org/10.1103/PhysRevD.85.125016). arXiv: [1202.5650](https://arxiv.org/abs/1202.5650) [[hep-th](#)].
- [8] H. Casini, E. Testé, and G. Torroba, “Markov Property of the Conformal Field Theory Vacuum and the a Theorem,” *Phys. Rev. Lett.*, vol. 118, no. 26, p. 261 602, 2017. DOI: [10.1103/PhysRevLett.118.261602](https://doi.org/10.1103/PhysRevLett.118.261602). arXiv: [1704.01870](https://arxiv.org/abs/1704.01870) [[hep-th](#)].
- [9] T. Faulkner, R. G. Leigh, O. Parrikar, and H. Wang, “Modular Hamiltonians for Deformed Half-Spaces and the Averaged Null Energy Condition,” *JHEP*, vol. 09, p. 038, 2016. DOI: [10.1007/JHEP09\(2016\)038](https://doi.org/10.1007/JHEP09(2016)038). arXiv: [1605.08072](https://arxiv.org/abs/1605.08072) [[hep-th](#)].
- [10] S. Balakrishnan, T. Faulkner, Z. U. Khandker, and H. Wang, “A General Proof of the Quantum Null Energy Condition,” *JHEP*, vol. 09, p. 020, 2019. DOI: [10.1007/JHEP09\(2019\)020](https://doi.org/10.1007/JHEP09(2019)020). arXiv: [1706.09432](https://arxiv.org/abs/1706.09432) [[hep-th](#)].
- [11] S. W. Hawking, “Particle Creation by Black Holes,” *Commun. Math. Phys.*, vol. 43, pp. 199–220, 1975, [[167\(1975\)](#)]. DOI: [10.1007/BF02345020](https://doi.org/10.1007/BF02345020), [10.1007/BF01608497](https://doi.org/10.1007/BF01608497).
- [12] J. D. Bekenstein, “Black holes and entropy,” *Phys. Rev. D*, vol. 7, pp. 2333–2346, 1973. DOI: [10.1103/PhysRevD.7.2333](https://doi.org/10.1103/PhysRevD.7.2333).

- [13] A. Almheiri, R. Mahajan, J. Maldacena, and Y. Zhao, “The Page curve of Hawking radiation from semiclassical geometry,” 2019. arXiv: [1908.10996 \[hep-th\]](#).
- [14] A. Almheiri, T. Hartman, J. Maldacena, E. Shaghoulian, and A. Tajdini, “Replica Wormholes and the Entropy of Hawking Radiation,” 2019. arXiv: [1911.12333 \[hep-th\]](#).
- [15] G. Penington, S. H. Shenker, D. Stanford, and Z. Yang, “Replica wormholes and the black hole interior,” 2019. arXiv: [1911.11977 \[hep-th\]](#).
- [16] S. S. Gubser, I. R. Klebanov, and A. M. Polyakov, “Gauge theory correlators from noncritical string theory,” *Phys. Lett. B*, vol. 428, pp. 105–114, 1998. DOI: [10.1016/S0370-2693\(98\)00377-3](#). arXiv: [hep-th/9802109](#).
- [17] E. Witten, “Anti-de Sitter space and holography,” *Adv. Theor. Math. Phys.*, vol. 2, pp. 253–291, 1998. DOI: [10.4310/ATMP.1998.v2.n2.a2](#). arXiv: [hep-th/9802150](#).
- [18] J. M. Maldacena, “The Large N limit of superconformal field theories and supergravity,” *Int. J. Theor. Phys.*, vol. 38, pp. 1113–1133, 1999, [Adv. Theor. Math. Phys.2,231(1998)]. DOI: [10.1023/A:1026654312961](#), [10.4310/ATMP.1998.v2.n2.a1](#). arXiv: [hep-th/9711200 \[hep-th\]](#).
- [19] J. M. Maldacena, “Wilson loops in large N field theories,” *Phys. Rev. Lett.*, vol. 80, pp. 4859–4862, 1998. DOI: [10.1103/PhysRevLett.80.4859](#). arXiv: [hep-th/9803002](#).
- [20] G. ’t Hooft, “Dimensional reduction in quantum gravity,” *Conf. Proc. C*, vol. 930308, pp. 284–296, 1993. arXiv: [gr-qc/9310026](#).
- [21] L. Susskind, “The World as a hologram,” *J. Math. Phys.*, vol. 36, pp. 6377–6396, 1995. DOI: [10.1063/1.531249](#). arXiv: [hep-th/9409089](#).
- [22] S. Sachdev, “Holographic metals and the fractionalized Fermi liquid,” *Phys. Rev. Lett.*, vol. 105, p. 151 602, 2010. DOI: [10.1103/PhysRevLett.105.151602](#). arXiv: [1006.3794 \[hep-th\]](#).
- [23] J. Maldacena and D. Stanford, “Remarks on the Sachdev-Ye-Kitaev model,” *Phys. Rev.*, vol. D94, no. 10, p. 106 002, 2016. DOI: [10.1103/PhysRevD.94.106002](#). arXiv: [1604.07818 \[hep-th\]](#).
- [24] A. Almheiri, X. Dong, and D. Harlow, “Bulk Locality and Quantum Error Correction in AdS/CFT,” *JHEP*, vol. 04, p. 163, 2015. DOI: [10.1007/JHEP04\(2015\)163](#). arXiv: [1411.7041 \[hep-th\]](#).
- [25] P. Saad, S. H. Shenker, and D. Stanford, “JT gravity as a matrix integral,” Mar. 2019. arXiv: [1903.11115 \[hep-th\]](#).
- [26] S. Ryu and T. Takayanagi, “Holographic derivation of entanglement entropy from AdS/CFT,” *Phys. Rev. Lett.*, vol. 96, p. 181 602, 2006. DOI: [10.1103/PhysRevLett.96.181602](#). arXiv: [hep-th/0603001](#).
- [27] S. Ryu and T. Takayanagi, “Aspects of Holographic Entanglement Entropy,” *JHEP*, vol. 08, p. 045, 2006. DOI: [10.1088/1126-6708/2006/08/045](#). arXiv: [hep-th/0605073](#).
- [28] V. E. Hubeny, M. Rangamani, and T. Takayanagi, “A Covariant holographic entanglement entropy proposal,” *JHEP*, vol. 07, p. 062, 2007. DOI: [10.1088/1126-6708/2007/07/062](#). arXiv: [0705.0016 \[hep-th\]](#).
- [29] T. Faulkner, A. Lewkowycz, and J. Maldacena, “Quantum corrections to holographic entanglement entropy,” *JHEP*, vol. 11, p. 074, 2013. DOI: [10.1007/JHEP11\(2013\)074](#). arXiv: [1307.2892 \[hep-th\]](#).
- [30] N. Engelhardt and A. C. Wall, “Quantum Extremal Surfaces: Holographic Entanglement Entropy beyond the Classical Regime,” *JHEP*, vol. 01, p. 073, 2015. DOI: [10.1007/JHEP01\(2015\)073](#). arXiv: [1408.3203 \[hep-th\]](#).

- [31] T. Faulkner, M. Guica, T. Hartman, R. C. Myers, and M. Van Raamsdonk, “Gravitation from Entanglement in Holographic CFTs,” *JHEP*, vol. 03, p. 051, 2014. DOI: [10.1007/JHEP03\(2014\)051](https://doi.org/10.1007/JHEP03(2014)051). arXiv: [1312.7856](https://arxiv.org/abs/1312.7856) [[hep-th](#)].
- [32] T. Faulkner, F. M. Haehl, E. Hijano, O. Parrikar, C. Rabideau, and M. Van Raamsdonk, “Nonlinear Gravity from Entanglement in Conformal Field Theories,” *JHEP*, vol. 08, p. 057, 2017. DOI: [10.1007/JHEP08\(2017\)057](https://doi.org/10.1007/JHEP08(2017)057). arXiv: [1705.03026](https://arxiv.org/abs/1705.03026) [[hep-th](#)].
- [33] T. Takayanagi and K. Umemoto, “Entanglement of purification through holographic duality,” *Nature Phys.*, vol. 14, no. 6, pp. 573–577, 2018. DOI: [10.1038/s41567-018-0075-2](https://doi.org/10.1038/s41567-018-0075-2). arXiv: [1708.09393](https://arxiv.org/abs/1708.09393) [[hep-th](#)].
- [34] B. Czech, J. L. Karczmarek, F. Nogueira, and M. Van Raamsdonk, “The Gravity Dual of a Density Matrix,” *Class. Quant. Grav.*, vol. 29, p. 155 009, 2012. DOI: [10.1088/0264-9381/29/15/155009](https://doi.org/10.1088/0264-9381/29/15/155009). arXiv: [1204.1330](https://arxiv.org/abs/1204.1330) [[hep-th](#)].
- [35] A. C. Wall, “Maximin Surfaces, and the Strong Subadditivity of the Covariant Holographic Entanglement Entropy,” *Class. Quant. Grav.*, vol. 31, no. 22, p. 225 007, 2014. DOI: [10.1088/0264-9381/31/22/225007](https://doi.org/10.1088/0264-9381/31/22/225007). arXiv: [1211.3494](https://arxiv.org/abs/1211.3494) [[hep-th](#)].
- [36] X. Dong, D. Harlow, and A. C. Wall, “Reconstruction of Bulk Operators within the Entanglement Wedge in Gauge-Gravity Duality,” *Phys. Rev. Lett.*, vol. 117, no. 2, p. 021 601, 2016. DOI: [10.1103/PhysRevLett.117.021601](https://doi.org/10.1103/PhysRevLett.117.021601). arXiv: [1601.05416](https://arxiv.org/abs/1601.05416) [[hep-th](#)].
- [37] D. Harlow, “The Ryu–Takayanagi Formula from Quantum Error Correction,” *Commun. Math. Phys.*, vol. 354, no. 3, pp. 865–912, 2017. DOI: [10.1007/s00220-017-2904-z](https://doi.org/10.1007/s00220-017-2904-z). arXiv: [1607.03901](https://arxiv.org/abs/1607.03901) [[hep-th](#)].
- [38] B. Swingle, “Entanglement Renormalization and Holography,” *Phys. Rev. D*, vol. 86, p. 065 007, 2012. DOI: [10.1103/PhysRevD.86.065007](https://doi.org/10.1103/PhysRevD.86.065007). arXiv: [0905.1317](https://arxiv.org/abs/0905.1317) [[cond-mat.str-el](#)].
- [39] F. Pastawski, B. Yoshida, D. Harlow, and J. Preskill, “Holographic quantum error-correcting codes: Toy models for the bulk/boundary correspondence,” *JHEP*, vol. 06, p. 149, 2015. DOI: [10.1007/JHEP06\(2015\)149](https://doi.org/10.1007/JHEP06(2015)149). arXiv: [1503.06237](https://arxiv.org/abs/1503.06237) [[hep-th](#)].
- [40] P. Hayden, S. Nezami, X.-L. Qi, N. Thomas, M. Walter, and Z. Yang, “Holographic duality from random tensor networks,” *JHEP*, vol. 11, p. 009, 2016. DOI: [10.1007/JHEP11\(2016\)009](https://doi.org/10.1007/JHEP11(2016)009). arXiv: [1601.01694](https://arxiv.org/abs/1601.01694) [[hep-th](#)].
- [41] R. Orus, “A Practical Introduction to Tensor Networks: Matrix Product States and Projected Entangled Pair States,” *Annals Phys.*, vol. 349, pp. 117–158, 2014. DOI: [10.1016/j.aop.2014.06.013](https://doi.org/10.1016/j.aop.2014.06.013). arXiv: [1306.2164](https://arxiv.org/abs/1306.2164) [[cond-mat.str-el](#)].
- [42] J. Biamonte, “Lectures on Quantum Tensor Networks,” *arXiv e-prints*, arXiv:1912.10049, arXiv:1912.10049, Dec. 2019. DOI: [10.48550/arXiv.1912.10049](https://doi.org/10.48550/arXiv.1912.10049). arXiv: [1912.10049](https://arxiv.org/abs/1912.10049) [[quant-ph](#)].
- [43] Z. Yang, P. Hayden, and X.-L. Qi, “Bidirectional holographic codes and sub-AdS locality,” *JHEP*, vol. 01, p. 175, 2016. DOI: [10.1007/JHEP01\(2016\)175](https://doi.org/10.1007/JHEP01(2016)175). arXiv: [1510.03784](https://arxiv.org/abs/1510.03784) [[hep-th](#)].
- [44] B. Swingle, “Constructing holographic spacetimes using entanglement renormalization,” Sep. 2012. arXiv: [1209.3304](https://arxiv.org/abs/1209.3304) [[hep-th](#)].
- [45] P. Hayden and G. Penington, “Learning the Alpha-bits of Black Holes,” *JHEP*, vol. 12, p. 007, 2019. DOI: [10.1007/JHEP12\(2019\)007](https://doi.org/10.1007/JHEP12(2019)007). arXiv: [1807.06041](https://arxiv.org/abs/1807.06041) [[hep-th](#)].

- [46] C. Akers and G. Penington, “Leading order corrections to the quantum extremal surface prescription,” *JHEP*, vol. 04, p. 062, 2021. DOI: [10.1007/JHEP04\(2021\)062](https://doi.org/10.1007/JHEP04(2021)062). arXiv: [2008.03319](https://arxiv.org/abs/2008.03319) [[hep-th](#)].
- [47] X. Dong, X.-L. Qi, and M. Walter, “Holographic entanglement negativity and replica symmetry breaking,” *JHEP*, vol. 06, p. 024, 2021. DOI: [10.1007/JHEP06\(2021\)024](https://doi.org/10.1007/JHEP06(2021)024). arXiv: [2101.11029](https://arxiv.org/abs/2101.11029) [[hep-th](#)].
- [48] C. Akers, T. Faulkner, S. Lin, and P. Rath, “Reflected entropy in random tensor networks,” *JHEP*, vol. 05, p. 162, 2022. DOI: [10.1007/JHEP05\(2022\)162](https://doi.org/10.1007/JHEP05(2022)162). arXiv: [2112.09122](https://arxiv.org/abs/2112.09122) [[hep-th](#)].
- [49] M. Walter, D. Gross, and J. Eisert, *Multi-partite entanglement*, 2017. arXiv: [1612.02437](https://arxiv.org/abs/1612.02437) [[quant-ph](#)].
- [50] S. Hollands and K. Sanders, “Entanglement measures and their properties in quantum field theory,” Feb. 2017. arXiv: [1702.04924](https://arxiv.org/abs/1702.04924) [[quant-ph](#)].
- [51] E. Witten, “APS Medal for Exceptional Achievement in Research: Invited article on entanglement properties of quantum field theory,” *Rev. Mod. Phys.*, vol. 90, no. 4, p. 045003, 2018. DOI: [10.1103/RevModPhys.90.045003](https://doi.org/10.1103/RevModPhys.90.045003). arXiv: [1803.04993](https://arxiv.org/abs/1803.04993) [[hep-th](#)].
- [52] H. Araki, “Type of von Neumann Algebra Associated with Free Field,” *Progress of Theoretical Physics*, vol. 32, no. 6, pp. 956–965, Dec. 1964, ISSN: 0033-068X. DOI: [10.1143/PTP.32.956](https://doi.org/10.1143/PTP.32.956). eprint: <https://academic.oup.com/ptp/article-pdf/32/6/956/5311286/32-6-956.pdf>. [Online]. Available: <https://doi.org/10.1143/PTP.32.956>.
- [53] K. Fredenhagen, “On the Modular Structure of Local Algebras of Observables,” *Commun. Math. Phys.*, vol. 97, p. 79, 1985. DOI: [10.1007/BF01206179](https://doi.org/10.1007/BF01206179).
- [54] J. Yngvason, “The role of type iii factors in quantum field theory,” *Reports on Mathematical Physics*, vol. 55, no. 1, pp. 135–147, 2005, ISSN: 0034-4877. DOI: [https://doi.org/10.1016/S0034-4877\(05\)80009-6](https://doi.org/10.1016/S0034-4877(05)80009-6). [Online]. Available: <https://www.sciencedirect.com/science/article/pii/S0034487705800096>.
- [55] E. Witten, “Why Does Quantum Field Theory In Curved Spacetime Make Sense? And What Happens To The Algebra of Observables In The Thermodynamic Limit?,” Dec. 2021. arXiv: [2112.11614](https://arxiv.org/abs/2112.11614) [[hep-th](#)].
- [56] S. Dutta and T. Faulkner, “A canonical purification for the entanglement wedge cross-section,” 2019. arXiv: [1905.00577](https://arxiv.org/abs/1905.00577) [[hep-th](#)].
- [57] Y. Zou, K. Siva, T. Soejima, R. S. K. Mong, and M. P. Zaletel, “Universal tripartite entanglement in one-dimensional many-body systems,” *Phys. Rev. Lett.*, vol. 126, no. 12, p. 120501, 2021. DOI: [10.1103/PhysRevLett.126.120501](https://doi.org/10.1103/PhysRevLett.126.120501). arXiv: [2011.11864](https://arxiv.org/abs/2011.11864) [[quant-ph](#)].
- [58] C. Akers and P. Rath, “Entanglement Wedge Cross Sections Require Tripartite Entanglement,” 2019. arXiv: [1911.07852](https://arxiv.org/abs/1911.07852) [[hep-th](#)].
- [59] S. X. Cui, P. Hayden, T. He, M. Headrick, B. Stoica, and M. Walter, “Bit Threads and Holographic Monogamy,” *Commun. Math. Phys.*, vol. 376, no. 1, pp. 609–648, 2019. DOI: [10.1007/s00220-019-03510-8](https://doi.org/10.1007/s00220-019-03510-8). arXiv: [1808.05234](https://arxiv.org/abs/1808.05234) [[hep-th](#)].
- [60] S. Nezami and M. Walter, “Multipartite Entanglement in Stabilizer Tensor Networks,” *Phys. Rev. Lett.*, vol. 125, p. 241602, 2020. DOI: [10.1103/PhysRevLett.125.241602](https://doi.org/10.1103/PhysRevLett.125.241602). arXiv: [1608.02595](https://arxiv.org/abs/1608.02595) [[quant-ph](#)].
- [61] D. N. Page, “Average entropy of a subsystem,” *Phys. Rev. Lett.*, vol. 71, pp. 1291–1294, 1993. DOI: [10.1103/PhysRevLett.71.1291](https://doi.org/10.1103/PhysRevLett.71.1291). arXiv: [gr-qc/9305007](https://arxiv.org/abs/gr-qc/9305007) [[gr-qc](#)].

- [62] D. Marolf, S. Wang, and Z. Wang, “Probing phase transitions of holographic entanglement entropy with fixed area states,” *JHEP*, vol. 12, p. 084, 2020. DOI: [10.1007/JHEP12\(2020\)084](https://doi.org/10.1007/JHEP12(2020)084). arXiv: [2006.10089](https://arxiv.org/abs/2006.10089) [[hep-th](#)].
- [63] X. Dong and H. Wang, “Enhanced corrections near holographic entanglement transitions: a chaotic case study,” *JHEP*, vol. 11, p. 007, 2020. DOI: [10.1007/JHEP11\(2020\)007](https://doi.org/10.1007/JHEP11(2020)007). arXiv: [2006.10051](https://arxiv.org/abs/2006.10051) [[hep-th](#)].
- [64] A. Schrijver, *Theory of Linear and Integer Programming*. USA: John Wiley & Sons, Inc., 1986, ISBN: 0471908541.
- [65] M. Freedman and M. Headrick, “Bit threads and holographic entanglement,” *Commun. Math. Phys.*, vol. 352, no. 1, pp. 407–438, 2017. DOI: [10.1007/s00220-016-2796-3](https://doi.org/10.1007/s00220-016-2796-3). arXiv: [1604.00354](https://arxiv.org/abs/1604.00354) [[hep-th](#)].
- [66] M. Headrick and V. E. Hubeny, “Covariant bit threads,” Aug. 2022. arXiv: [2208.10507](https://arxiv.org/abs/2208.10507) [[hep-th](#)].
- [67] C. Akers, T. Faulkner, S. Lin, and P. Rath, “The Page curve for reflected entropy,” *JHEP*, vol. 06, p. 089, 2022. DOI: [10.1007/JHEP06\(2022\)089](https://doi.org/10.1007/JHEP06(2022)089). arXiv: [2201.11730](https://arxiv.org/abs/2201.11730) [[hep-th](#)].
- [68] C. Akers, T. Faulkner, S. Lin, and P. Rath, “Reflected entropy in random tensor networks. Part II. A topological index from canonical purification,” *JHEP*, vol. 01, p. 067, 2023. DOI: [10.1007/JHEP01\(2023\)067](https://doi.org/10.1007/JHEP01(2023)067). arXiv: [2210.15006](https://arxiv.org/abs/2210.15006) [[hep-th](#)].
- [69] C. Akers, T. Faulkner, S. Lin, and P. Rath, “Entanglement of Purification in Random Tensor Networks,” Jun. 2023. arXiv: [2306.06163](https://arxiv.org/abs/2306.06163) [[hep-th](#)].
- [70] C. Akers, T. Faulkner, S. Lin, and P. Rath, “Reflected Entropy in Random Tensor Networks III: Triway Cuts,” eprint: [toappear](https://arxiv.org/abs/2306.06163).
- [71] S. F. Edwards and P. W. Anderson, “Theory of spin glasses,” *Journal of Physics F: Metal Physics*, vol. 5, no. 5, p. 965, May 1975. DOI: [10.1088/0305-4608/5/5/017](https://doi.org/10.1088/0305-4608/5/5/017). [Online]. Available: <https://dx.doi.org/10.1088/0305-4608/5/5/017>.
- [72] M. Natsuume, *AdS/CFT Duality User Guide*. 2015, vol. 903, ISBN: 978-4-431-55441-7, 978-4-431-55440-0. DOI: [10.1007/978-4-431-55441-7](https://doi.org/10.1007/978-4-431-55441-7). arXiv: [1409.3575](https://arxiv.org/abs/1409.3575) [[hep-th](#)].
- [73] M. Ammon and J. Erdmenger, *Gauge/gravity duality: Foundations and applications*. Cambridge: Cambridge University Press, Apr. 2015, ISBN: 978-1-107-01034-5, 978-1-316-23594-2.
- [74] H. Nastase, “Introduction to AdS-CFT,” Dec. 2007. arXiv: [0712.0689](https://arxiv.org/abs/0712.0689) [[hep-th](#)].
- [75] J. Kaplan, *Lectures on ads/cft from the bottom up*, 2016. [Online]. Available: <https://sites.krieger.jhu.edu/jared-kaplan/files/2016/05/AdSCFTCourseNotesCurrentPublic.pdf>.
- [76] M. Rangamani and T. Takayanagi, *Holographic Entanglement Entropy*. Springer, 2017, vol. 931. DOI: [10.1007/978-3-319-52573-0](https://doi.org/10.1007/978-3-319-52573-0). arXiv: [1609.01287](https://arxiv.org/abs/1609.01287) [[hep-th](#)].
- [77] M. Headrick, “Lectures on entanglement entropy in field theory and holography,” Jul. 2019. arXiv: [1907.08126](https://arxiv.org/abs/1907.08126) [[hep-th](#)].
- [78] D. Harlow, “TASI Lectures on the Emergence of Bulk Physics in AdS/CFT,” *PoS*, vol. TASI2017, p. 002, 2018. DOI: [10.22323/1.305.0002](https://doi.org/10.22323/1.305.0002). arXiv: [1802.01040](https://arxiv.org/abs/1802.01040) [[hep-th](#)].
- [79] J. D. Brown and M. Henneaux, “Central Charges in the Canonical Realization of Asymptotic Symmetries: An Example from Three-Dimensional Gravity,” *Commun. Math. Phys.*, vol. 104, pp. 207–226, 1986. DOI: [10.1007/BF01211590](https://doi.org/10.1007/BF01211590).

- [80] T. Banks, M. R. Douglas, G. T. Horowitz, and E. J. Martinec, “AdS dynamics from conformal field theory,” Aug. 1998. arXiv: [hep-th/9808016](#).
- [81] N. Seiberg and E. Witten, “The D1 / D5 system and singular CFT,” *JHEP*, vol. 04, p. 017, 1999. DOI: [10.1088/1126-6708/1999/04/017](#). arXiv: [hep-th/9903224](#).
- [82] S. Sachdev and J. Ye, “Gapless spin-fluid ground state in a random quantum Heisenberg magnet,” *Phys. Rev. Lett.*, vol. 70, no. 21, pp. 3339–3342, May 1993. DOI: [10.1103/PhysRevLett.70.3339](#). arXiv: [cond-mat/9212030 \[cond-mat\]](#).
- [83] A. Kitaev, “A simple model of quantum holography,” *In KITP strings seminar*, vol. 12, 2015.
- [84] J. S. Cotler *et al.*, “Black Holes and Random Matrices,” *JHEP*, vol. 05, p. 118, 2017, [Erratum: *JHEP* 09, 002 (2018)]. DOI: [10.1007/JHEP05\(2017\)118](#). arXiv: [1611.04650 \[hep-th\]](#).
- [85] M. Berkooz, P. Narayan, and J. Simon, “Chord diagrams, exact correlators in spin glasses and black hole bulk reconstruction,” *JHEP*, vol. 08, p. 192, 2018. DOI: [10.1007/JHEP08\(2018\)192](#). arXiv: [1806.04380 \[hep-th\]](#).
- [86] H. W. Lin, “The bulk Hilbert space of double scaled SYK,” Aug. 2022. arXiv: [2208.07032 \[hep-th\]](#).
- [87] S. W. Hawking, “Breakdown of Predictability in Gravitational Collapse,” *Phys. Rev. D*, vol. 14, pp. 2460–2473, 1976. DOI: [10.1103/PhysRevD.14.2460](#).
- [88] J. de Boer, E. P. Verlinde, and H. L. Verlinde, “On the holographic renormalization group,” *JHEP*, vol. 08, p. 003, 2000. DOI: [10.1088/1126-6708/2000/08/003](#). arXiv: [hep-th/9912012](#).
- [89] J. de Boer, “The Holographic renormalization group,” *Fortsch. Phys.*, vol. 49, E. A. Bergshoeff, A. Ceresole, C. Kounnas, D. Lust, and A. Sevrin, Eds., pp. 339–358, 2001. DOI: [10.1002/1521-3978\(200105\)49:4/6<339::AID-PR0P339>3.0.CO;2-A](#). arXiv: [hep-th/0101026](#).
- [90] I. Heemskerk and J. Polchinski, “Holographic and Wilsonian Renormalization Groups,” *JHEP*, vol. 06, p. 031, 2011. DOI: [10.1007/JHEP06\(2011\)031](#). arXiv: [1010.1264 \[hep-th\]](#).
- [91] T. Faulkner, H. Liu, and M. Rangamani, “Integrating out geometry: Holographic Wilsonian RG and the membrane paradigm,” *JHEP*, vol. 08, p. 051, 2011. DOI: [10.1007/JHEP08\(2011\)051](#). arXiv: [1010.4036 \[hep-th\]](#).
- [92] P. Calabrese and J. Cardy, “Entanglement entropy and conformal field theory,” *J. Phys. A*, vol. 42, p. 504005, 2009. DOI: [10.1088/1751-8113/42/50/504005](#). arXiv: [0905.4013 \[cond-mat.stat-mech\]](#).
- [93] E. Witten, “Gravity and the crossed product,” *JHEP*, vol. 10, p. 008, 2022. DOI: [10.1007/JHEP10\(2022\)008](#). arXiv: [2112.12828 \[hep-th\]](#).
- [94] V. Chandrasekaran, R. Longo, G. Penington, and E. Witten, “An algebra of observables for de Sitter space,” *JHEP*, vol. 02, p. 082, 2023. DOI: [10.1007/JHEP02\(2023\)082](#). arXiv: [2206.10780 \[hep-th\]](#).
- [95] G. Penington and E. Witten, “Algebras and States in JT Gravity,” Jan. 2023. arXiv: [2301.07257 \[hep-th\]](#).
- [96] X. Dong, D. Harlow, and D. Marolf, “Flat entanglement spectra in fixed-area states of quantum gravity,” *JHEP*, vol. 10, p. 240, 2019. DOI: [10.1007/JHEP10\(2019\)240](#). arXiv: [1811.05382 \[hep-th\]](#).
- [97] C. Akers and P. Rath, “Holographic Renyi Entropy from Quantum Error Correction,” *JHEP*, vol. 05, p. 052, 2019. DOI: [10.1007/JHEP05\(2019\)052](#). arXiv: [1811.05171 \[hep-th\]](#).

- [98] X. Dong and D. Marolf, “One-loop universality of holographic codes,” *JHEP*, vol. 03, p. 191, 2020. DOI: [10.1007/JHEP03\(2020\)191](https://doi.org/10.1007/JHEP03(2020)191). arXiv: [1910.06329](https://arxiv.org/abs/1910.06329) [hep-th].
- [99] R. Haag, N. M. Hugenholtz, and M. Winnink, “On the equilibrium states in quantum statistical mechanics,” *Communications in Mathematical Physics*, vol. 5, no. 3, pp. 215–236, 1967.
- [100] J. M. Maldacena, “Eternal black holes in anti-de Sitter,” *JHEP*, vol. 04, p. 021, 2003. DOI: [10.1088/1126-6708/2003/04/021](https://doi.org/10.1088/1126-6708/2003/04/021). arXiv: [hep-th/0106112](https://arxiv.org/abs/hep-th/0106112) [hep-th].
- [101] P. Hayden, O. Parrikar, and J. Sorce, “The Markov gap for geometric reflected entropy,” Jun. 2021. arXiv: [2107.00009](https://arxiv.org/abs/2107.00009) [hep-th].
- [102] C. Akers, N. Engelhardt, G. Penington, and M. Usatyuk, “Quantum Maximin Surfaces,” 2019. arXiv: [1912.02799](https://arxiv.org/abs/1912.02799) [hep-th].
- [103] V. Chandrasekaran, M. Miyaji, and P. Rath, “Including contributions from entanglement islands to the reflected entropy,” *Phys. Rev. D*, vol. 102, no. 8, p. 086 009, 2020. DOI: [10.1103/PhysRevD.102.086009](https://doi.org/10.1103/PhysRevD.102.086009). arXiv: [2006.10754](https://arxiv.org/abs/2006.10754) [hep-th].
- [104] M. Afrasiar, H. Chourasiya, V. Raj, and G. Sengupta, “Covariant holographic reflected entropy in AdS3/CFT2,” *Phys. Lett. B*, vol. 835, p. 137 590, 2022. DOI: [10.1016/j.physletb.2022.137590](https://doi.org/10.1016/j.physletb.2022.137590). arXiv: [2209.02654](https://arxiv.org/abs/2209.02654) [hep-th].
- [105] N. Bao and N. Cheng, “Multipartite Reflected Entropy,” *JHEP*, vol. 10, p. 102, 2019. DOI: [10.1007/JHEP10\(2019\)102](https://doi.org/10.1007/JHEP10(2019)102). arXiv: [1909.03154](https://arxiv.org/abs/1909.03154) [hep-th].
- [106] P. Hayden, M. Lemm, and J. Sorce, “Reflected entropy is not a correlation measure,” Feb. 2023. arXiv: [2302.10208](https://arxiv.org/abs/2302.10208) [hep-th].
- [107] B. Collins, I. Nechita, and K. Zyczkowski, “Random graph states, maximal flow and Fuss-Catalan distributions,” *J. Phys. A*, vol. 43, p. 275 303, 2010. DOI: [10.1088/1751-8113/43/27/275303](https://doi.org/10.1088/1751-8113/43/27/275303). arXiv: [1003.3075](https://arxiv.org/abs/1003.3075) [quant-ph].
- [108] B. Collins, I. Nechita, and K. Zyczkowski, “Area law for random graph states,” *J. Phys. A*, vol. 46, p. 305 302, 2013. DOI: [10.1088/1751-8113/46/30/305302](https://doi.org/10.1088/1751-8113/46/30/305302). arXiv: [1302.0709](https://arxiv.org/abs/1302.0709) [math-ph].
- [109] X.-L. Qi, “Emergent bulk gauge field in random tensor networks,” Sep. 2022. arXiv: [2209.02940](https://arxiv.org/abs/2209.02940) [hep-th].
- [110] N. Cheng, C. Lancien, G. Penington, M. Walter, and F. Witteveen, “Random tensor networks with nontrivial links,” Jun. 2022. arXiv: [2206.10482](https://arxiv.org/abs/2206.10482) [quant-ph].
- [111] A. W. Harrow, *The church of the symmetric subspace*, 2013. arXiv: [1308.6595](https://arxiv.org/abs/1308.6595) [quant-ph].
- [112] Z. Bai and J. W. Silverstein, *Spectral Analysis of Large Dimensional Random Matrices*. Springer New York, 2010. DOI: [10.1007/978-1-4419-0661-8](https://doi.org/10.1007/978-1-4419-0661-8). [Online]. Available: <https://doi.org/10.1007/978-1-4419-0661-8>.
- [113] N. Engelhardt and A. C. Wall, “Decoding the Apparent Horizon: Coarse-Grained Holographic Entropy,” *Phys. Rev. Lett.*, vol. 121, no. 21, p. 211 301, 2018. DOI: [10.1103/PhysRevLett.121.211301](https://doi.org/10.1103/PhysRevLett.121.211301). arXiv: [1706.02038](https://arxiv.org/abs/1706.02038) [hep-th].
- [114] N. Engelhardt and A. C. Wall, “Coarse Graining Holographic Black Holes,” *JHEP*, vol. 05, p. 160, 2019. DOI: [10.1007/JHEP05\(2019\)160](https://doi.org/10.1007/JHEP05(2019)160). arXiv: [1806.01281](https://arxiv.org/abs/1806.01281) [hep-th].

- [115] D. Marolf, “CFT sewing as the dual of AdS cut-and-paste,” *JHEP*, vol. 02, p. 152, 2020. DOI: [10.1007/JHEP02\(2020\)152](https://doi.org/10.1007/JHEP02(2020)152). arXiv: [1909.09330](https://arxiv.org/abs/1909.09330) [hep-th].
- [116] A. Lewkowycz and J. Maldacena, “Generalized gravitational entropy,” *JHEP*, vol. 08, p. 090, 2013. DOI: [10.1007/JHEP08\(2013\)090](https://doi.org/10.1007/JHEP08(2013)090). arXiv: [1304.4926](https://arxiv.org/abs/1304.4926) [hep-th].
- [117] Y. Kusuki and K. Tamaoka, “Entanglement Wedge Cross Section from CFT: Dynamics of Local Operator Quench,” 2019. arXiv: [1909.06790](https://arxiv.org/abs/1909.06790) [hep-th].
- [118] H. Shapourian, S. Liu, J. Kudler-Flam, and A. Vishwanath, “Entanglement negativity spectrum of random mixed states: A diagrammatic approach,” Nov. 2020. arXiv: [2011.01277](https://arxiv.org/abs/2011.01277) [cond-mat.str-el].
- [119] X. Dong, S. McBride, and W. W. Weng, “Replica Wormholes and Holographic Entanglement Negativity,” Oct. 2021. arXiv: [2110.11947](https://arxiv.org/abs/2110.11947) [hep-th].
- [120] S. Vardhan, J. Kudler-Flam, H. Shapourian, and H. Liu, “Bound Entanglement in Thermalized States and Black Hole Radiation,” *Phys. Rev. Lett.*, vol. 129, no. 6, p. 061602, 2022. DOI: [10.1103/PhysRevLett.129.061602](https://doi.org/10.1103/PhysRevLett.129.061602). arXiv: [2110.02959](https://arxiv.org/abs/2110.02959) [hep-th].
- [121] S. Fischetti and D. Marolf, “Complex Entangling Surfaces for AdS and Lifshitz Black Holes?” *Class. Quant. Grav.*, vol. 31, no. 21, p. 214005, 2014. DOI: [10.1088/0264-9381/31/21/214005](https://doi.org/10.1088/0264-9381/31/21/214005). arXiv: [1407.2900](https://arxiv.org/abs/1407.2900) [hep-th].
- [122] V. Balasubramanian, P. Hayden, A. Maloney, D. Marolf, and S. F. Ross, “Multiboundary Wormholes and Holographic Entanglement,” *Class. Quant. Grav.*, vol. 31, p. 185015, 2014. DOI: [10.1088/0264-9381/31/18/185015](https://doi.org/10.1088/0264-9381/31/18/185015). arXiv: [1406.2663](https://arxiv.org/abs/1406.2663) [hep-th].
- [123] S. H. Shenker and D. Stanford, “Multiple Shocks,” *JHEP*, vol. 12, p. 046, 2014. DOI: [10.1007/JHEP12\(2014\)046](https://doi.org/10.1007/JHEP12(2014)046). arXiv: [1312.3296](https://arxiv.org/abs/1312.3296) [hep-th].
- [124] M. Fannes, “A continuity property of the entropy density for spin lattice systems,” *Communications in Mathematical Physics*, vol. 31, no. 4, pp. 291–294, 1973.
- [125] K. M. Audenaert, “A sharp fannes-type inequality for the von neumann entropy,” *arXiv preprint quant-ph/0610146*, 2006.
- [126] A. E. Rastegin, “Some general properties of unified entropies,” *Journal of Statistical Physics*, vol. 143, no. 6, pp. 1120–1135, 2011.
- [127] E. Lubkin, “Entropy of an n-system from its correlation with ak-reservoir,” *Journal of Mathematical Physics*, vol. 19, no. 5, pp. 1028–1031, 1978.
- [128] Z.-W. Liu, S. Lloyd, E. Y. Zhu, and H. Zhu, “Entanglement, quantum randomness, and complexity beyond scrambling,” *JHEP*, vol. 07, p. 041, 2018. DOI: [10.1007/JHEP07\(2018\)041](https://doi.org/10.1007/JHEP07(2018)041). arXiv: [1703.08104](https://arxiv.org/abs/1703.08104) [quant-ph].
- [129] J. Jurkiewicz, G. Lukaszewski, and M. Nowak, “Diagrammatic approach to fluctuations in the wishart ensemble,” *Acta Physica Polonica B - ACTA PHYS POL B*, vol. 39, Apr. 2008.
- [130] E. Brézin and A. Zee, “Universality of the correlations between eigenvalues of large random matrices,” *Nuclear Physics B*, vol. 402, no. 3, pp. 613–627, 1993, ISSN: 0550-3213. DOI: [https://doi.org/10.1016/0550-3213\(93\)90121-5](https://doi.org/10.1016/0550-3213(93)90121-5). [Online]. Available: <https://www.sciencedirect.com/science/article/pii/0550321393901215>.

- [131] E. Brézin and A. Zee, “Universal relation between green functions in random matrix theory,” *Nuclear Physics B*, vol. 453, no. 3, pp. 531–551, 1995, ISSN: 0550-3213. DOI: [https://doi.org/10.1016/0550-3213\(95\)00446-Y](https://doi.org/10.1016/0550-3213(95)00446-Y). [Online]. Available: <https://www.sciencedirect.com/science/article/pii/S055032139500446Y>.
- [132] J. Kudler-Flam, V. Narovlansky, and S. Ryu, “Negativity Spectra in Random Tensor Networks and Holography,” Sep. 2021. arXiv: [2109.02649](https://arxiv.org/abs/2109.02649) [hep-th].
- [133] N. Bao, G. Penington, J. Sorce, and A. C. Wall, “Beyond Toy Models: Distilling Tensor Networks in Full AdS/CFT,” *JHEP*, vol. 11, p. 069, 2019. DOI: [10.1007/JHEP11\(2019\)069](https://doi.org/10.1007/JHEP11(2019)069). arXiv: [1812.01171](https://arxiv.org/abs/1812.01171) [hep-th].
- [134] X.-L. Qi, Z. Yang, and Y.-Z. You, “Holographic coherent states from random tensor networks,” *JHEP*, vol. 08, p. 060, 2017. DOI: [10.1007/JHEP08\(2017\)060](https://doi.org/10.1007/JHEP08(2017)060). arXiv: [1703.06533](https://arxiv.org/abs/1703.06533) [hep-th].
- [135] A. Almheiri, X. Dong, and B. Swingle, “Linearity of Holographic Entanglement Entropy,” *JHEP*, vol. 02, p. 074, 2017. DOI: [10.1007/JHEP02\(2017\)074](https://doi.org/10.1007/JHEP02(2017)074). arXiv: [1606.04537](https://arxiv.org/abs/1606.04537) [hep-th].
- [136] T. Faulkner, “The holographic map as a conditional expectation,” Aug. 2020. arXiv: [2008.04810](https://arxiv.org/abs/2008.04810) [hep-th].
- [137] E. Shaghoulian, “Emergent gravity from Eguchi-Kawai reduction,” *JHEP*, vol. 03, p. 011, 2017. DOI: [10.1007/JHEP03\(2017\)011](https://doi.org/10.1007/JHEP03(2017)011). arXiv: [1611.04189](https://arxiv.org/abs/1611.04189) [hep-th].
- [138] W. Donnelly, B. Michel, D. Marolf, and J. Wien, “Living on the Edge: A Toy Model for Holographic Reconstruction of Algebras with Centers,” *JHEP*, vol. 04, p. 093, 2017. DOI: [10.1007/JHEP04\(2017\)093](https://doi.org/10.1007/JHEP04(2017)093). arXiv: [1611.05841](https://arxiv.org/abs/1611.05841) [hep-th].
- [139] L. Vidmar and M. Rigol, “Entanglement Entropy of Eigenstates of Quantum Chaotic Hamiltonians,” *Phys. Rev. Lett.*, vol. 119, no. 22, p. 220603, 2017. DOI: [10.1103/PhysRevLett.119.220603](https://doi.org/10.1103/PhysRevLett.119.220603). arXiv: [1708.08453](https://arxiv.org/abs/1708.08453) [cond-mat.stat-mech].
- [140] C. Murthy and M. Srednicki, “Structure of chaotic eigenstates and their entanglement entropy,” *Phys. Rev. E*, vol. 100, no. 2, p. 022131, 2019. DOI: [10.1103/PhysRevE.100.022131](https://doi.org/10.1103/PhysRevE.100.022131). arXiv: [1906.04295](https://arxiv.org/abs/1906.04295) [cond-mat.stat-mech].
- [141] N. Engelhardt and Å. Folkestad, “Canonical purification of evaporating black holes,” *Phys. Rev. D*, vol. 105, no. 8, p. 086010, 2022. DOI: [10.1103/PhysRevD.105.086010](https://doi.org/10.1103/PhysRevD.105.086010). arXiv: [2201.08395](https://arxiv.org/abs/2201.08395) [hep-th].
- [142] X. Dong, “The Gravity Dual of Renyi Entropy,” *Nature Commun.*, vol. 7, p. 12472, 2016. DOI: [10.1038/ncomms12472](https://doi.org/10.1038/ncomms12472). arXiv: [1601.06788](https://arxiv.org/abs/1601.06788) [hep-th].
- [143] J. Cotler, P. Hayden, G. Penington, G. Salton, B. Swingle, and M. Walter, “Entanglement Wedge Reconstruction via Universal Recovery Channels,” *Phys. Rev. X*, vol. 9, no. 3, p. 031011, 2019. DOI: [10.1103/PhysRevX.9.031011](https://doi.org/10.1103/PhysRevX.9.031011). arXiv: [1704.05839](https://arxiv.org/abs/1704.05839) [hep-th].
- [144] C.-F. Chen, G. Penington, and G. Salton, “Entanglement Wedge Reconstruction using the Petz Map,” *JHEP*, vol. 01, p. 168, 2020. DOI: [10.1007/JHEP01\(2020\)168](https://doi.org/10.1007/JHEP01(2020)168). arXiv: [1902.02844](https://arxiv.org/abs/1902.02844) [hep-th].
- [145] H. Liu and S. Vardhan, “Entanglement entropies of equilibrated pure states in quantum many-body systems and gravity,” *PRX Quantum*, vol. 2, p. 010344, 2021. DOI: [10.1103/PRXQuantum.2.010344](https://doi.org/10.1103/PRXQuantum.2.010344). arXiv: [2008.01089](https://arxiv.org/abs/2008.01089) [hep-th].

- [146] S. Vardhan, J. Kudler-Flam, H. Shapourian, and H. Liu, “Mixed-state entanglement and information recovery in thermalized states and evaporating black holes,” *JHEP*, vol. 01, p. 064, 2023. DOI: [10.1007/JHEP01\(2023\)064](https://doi.org/10.1007/JHEP01(2023)064). arXiv: [2112.00020 \[hep-th\]](https://arxiv.org/abs/2112.00020).
- [147] H. N. V. Temperley and E. H. Lieb, “Relations between the ‘percolation’ and ‘colouring’ problem and other graph-theoretical problems associated with regular planar lattices: some exact results for the ‘percolation’ problem,” *Proc. Roy. Soc. Lond. A*, vol. 322, pp. 251–280, 1971. DOI: [10.1098/rspa.1971.0067](https://doi.org/10.1098/rspa.1971.0067).
- [148] D. R. Brill, “Multi - black hole geometries in (2+1)-dimensional gravity,” *Phys. Rev. D*, vol. 53, pp. 4133–4176, 1996. DOI: [10.1103/PhysRevD.53.R4133](https://doi.org/10.1103/PhysRevD.53.R4133). arXiv: [gr-qc/9511022](https://arxiv.org/abs/gr-qc/9511022).
- [149] K. Krasnov, “Holography and Riemann surfaces,” *Adv. Theor. Math. Phys.*, vol. 4, pp. 929–979, 2000. DOI: [10.4310/ATMP.2000.v4.n4.a5](https://doi.org/10.4310/ATMP.2000.v4.n4.a5). arXiv: [hep-th/0005106](https://arxiv.org/abs/hep-th/0005106).
- [150] K. Skenderis and B. C. van Rees, “Holography and wormholes in 2+1 dimensions,” *Commun. Math. Phys.*, vol. 301, pp. 583–626, 2011. DOI: [10.1007/s00220-010-1163-z](https://doi.org/10.1007/s00220-010-1163-z). arXiv: [0912.2090 \[hep-th\]](https://arxiv.org/abs/0912.2090).
- [151] X. Yin, “On Non-handlebody Instantons in 3D Gravity,” *JHEP*, vol. 09, p. 120, 2008. DOI: [10.1088/1126-6708/2008/09/120](https://doi.org/10.1088/1126-6708/2008/09/120). arXiv: [0711.2803 \[hep-th\]](https://arxiv.org/abs/0711.2803).
- [152] H. Maxfield, S. Ross, and B. Way, “Holographic partition functions and phases for higher genus Riemann surfaces,” *Class. Quant. Grav.*, vol. 33, no. 12, p. 125018, 2016. DOI: [10.1088/0264-9381/33/12/125018](https://doi.org/10.1088/0264-9381/33/12/125018). arXiv: [1601.00980 \[hep-th\]](https://arxiv.org/abs/1601.00980).
- [153] D. Harlow and H. Ooguri, “Symmetries in quantum field theory and quantum gravity,” *Commun. Math. Phys.*, vol. 383, no. 3, pp. 1669–1804, 2021. DOI: [10.1007/s00220-021-04040-y](https://doi.org/10.1007/s00220-021-04040-y). arXiv: [1810.05338 \[hep-th\]](https://arxiv.org/abs/1810.05338).
- [154] X. Dong, D. Marolf, P. Rath, A. Tajdini, and Z. Wang, “The spacetime geometry of fixed-area states in gravitational systems,” *JHEP*, vol. 08, p. 158, 2022. DOI: [10.1007/JHEP08\(2022\)158](https://doi.org/10.1007/JHEP08(2022)158). arXiv: [2203.04973 \[hep-th\]](https://arxiv.org/abs/2203.04973).
- [155] D. Ridout and Y. Saint-Aubin, “Standard modules, induction and the structure of the Temperley-Lieb algebra,” *Adv. Theor. Math. Phys.*, vol. 18, no. 5, pp. 957–1041, 2014. DOI: [10.4310/ATMP.2014.v18.n5.a1](https://doi.org/10.4310/ATMP.2014.v18.n5.a1). arXiv: [1204.4505 \[math-ph\]](https://arxiv.org/abs/1204.4505).
- [156] T. Dupic and I. Pérez Castillo, “Spectral density of products of Wishart dilute random matrices. Part I: the dense case,” *arXiv e-prints*, arXiv:1401.7802, arXiv:1401.7802, Jan. 2014. arXiv: [1401.7802 \[cond-mat.dis-nn\]](https://arxiv.org/abs/1401.7802).
- [157] W. Młotkowski, M. A. Nowak, K. A. Penson, and K. Życzkowski, “Spectral density of generalized wishart matrices and free multiplicative convolution,” *Phys. Rev. E*, vol. 92, p. 012121, 1 Jul. 2015. DOI: [10.1103/PhysRevE.92.012121](https://doi.org/10.1103/PhysRevE.92.012121). [Online]. Available: <https://link.aps.org/doi/10.1103/PhysRevE.92.012121>.
- [158] J. A. Mingo and R. Speicher, *Free Probability and Random Matrices*. Springer New York, 2017. DOI: [10.1007/978-1-4939-6942-5](https://doi.org/10.1007/978-1-4939-6942-5). [Online]. Available: <https://doi.org/10.1007/978-1-4939-6942-5>.
- [159] V. A. Marčenko and L. A. Pastur, “Distribution of eigenvalues for some sets of random matrices,” *Mathematics of the USSR-Sbornik*, vol. 1, no. 4, pp. 457–483, Apr. 1967. DOI: [10.1070/sm1967v001n04abeh001994](https://doi.org/10.1070/sm1967v001n04abeh001994). [Online]. Available: <https://doi.org/10.1070/sm1967v001n04abeh001994>.

- [160] J. Wang, “Beyond islands: A free probabilistic approach,” Sep. 2022. arXiv: [2209.10546 \[hep-th\]](#).
- [161] R. Bousso, V. Chandrasekaran, P. Rath, and A. Shahbazi-Moghaddam, “Gravity dual of Connes cocycle flow,” *Phys. Rev. D*, vol. 102, no. 6, p. 066 008, 2020. DOI: [10.1103/PhysRevD.102.066008](#). arXiv: [2007.00230 \[hep-th\]](#).
- [162] M. Kaplan and D. Marolf, “The action of HRT-areas as operators in semiclassical gravity,” *JHEP*, vol. 08, p. 102, 2022. DOI: [10.1007/JHEP08\(2022\)102](#). arXiv: [2203.04270 \[hep-th\]](#).
- [163] X. Dong, D. Marolf, and P. Rath, “Geometric entropies and their geometric flow: the power of Lorentzian methods,” eprint: [toappear](#).
- [164] J. Held, M. Kaplan, D. Marolf, and J.-q. Wu, “A Geodesic Network in Classical AdS3 Gravity from the Entanglement Wedge Cross Section,” eprint: [toappear](#).
- [165] V. Jones, “Index for subfactors.,” *Inventiones mathematicae*, vol. 72, pp. 1–26, 1983. [Online]. Available: <http://eudml.org/doc/143011>.
- [166] S. Leutheusser and H. Liu, “Causal connectability between quantum systems and the black hole interior in holographic duality,” Oct. 2021. arXiv: [2110.05497 \[hep-th\]](#).
- [167] M. Berkooz, M. Isachenkov, V. Narovlansky, and G. Torrents, “Towards a full solution of the large N double-scaled SYK model,” *JHEP*, vol. 03, p. 079, 2019. DOI: [10.1007/JHEP03\(2019\)079](#). arXiv: [1811.02584 \[hep-th\]](#).
- [168] L. Susskind, “Computational Complexity and Black Hole Horizons,” *Fortsch. Phys.*, vol. 64, pp. 24–43, 2016, [Addendum: *Fortsch.Phys.* 64, 44–48 (2016)]. DOI: [10.1002/prop.201500092](#). arXiv: [1403.5695 \[hep-th\]](#).
- [169] A. R. Brown, D. A. Roberts, L. Susskind, B. Swingle, and Y. Zhao, “Holographic Complexity Equals Bulk Action?” *Phys. Rev. Lett.*, vol. 116, no. 19, p. 191 301, 2016. DOI: [10.1103/PhysRevLett.116.191301](#). arXiv: [1509.07876 \[hep-th\]](#).
- [170] E. Dahlhaus, D. S. Johnson, C. H. Papadimitriou, P. D. Seymour, and M. Yannakakis, “The complexity of multiterminal cuts,” *SIAM Journal on Computing*, vol. 23, no. 4, pp. 864–894, 1994. DOI: [10.1137/S0097539792225297](#). [Online]. Available: <https://doi.org/10.1137/S0097539792225297>.
- [171] P. Nguyen, T. Devakul, M. G. Halbasch, M. P. Zaletel, and B. Swingle, “Entanglement of purification: from spin chains to holography,” *JHEP*, vol. 01, p. 098, 2018. DOI: [10.1007/JHEP01\(2018\)098](#). arXiv: [1709.07424 \[hep-th\]](#).
- [172] S. Chopra and M. R. Rao, “On the multiway cut polyhedron,” *Networks*, vol. 21, no. 1, pp. 51–89, 1991. DOI: <https://doi.org/10.1002/net.3230210106>. [Online]. Available: <https://onlinelibrary.wiley.com/doi/abs/10.1002/net.3230210106>.
- [173] B. Monjardet, “Metrics on partially ordered sets—a survey,” *Discrete Mathematics*, vol. 35, no. 1, pp. 173–184, 1981, Special Volume on Ordered Sets, ISSN: 0012-365X. DOI: [https://doi.org/10.1016/0012-365X\(81\)90206-5](https://doi.org/10.1016/0012-365X(81)90206-5). [Online]. Available: <https://www.sciencedirect.com/science/article/pii/0012365X81902065>.
- [174] A. Gadde, V. Krishna, and T. Sharma, “New multipartite entanglement measure and its holographic dual,” *Phys. Rev. D*, vol. 106, no. 12, p. 126 001, 2022. DOI: [10.1103/PhysRevD.106.126001](#). arXiv: [2206.09723 \[hep-th\]](#).

- [175] G. Penington, M. Walter, and F. Witteveen, “Fun with replicas: tripartitions in tensor networks and gravity,” *JHEP*, vol. 05, p. 008, 2023. DOI: [10.1007/JHEP05\(2023\)008](https://doi.org/10.1007/JHEP05(2023)008). arXiv: [2211.16045](https://arxiv.org/abs/2211.16045) [hep-th].
- [176] A. Gadde, V. Krishna, and T. Sharma, “Towards classification of holographic multi-partite entanglement measures,” Apr. 2023. arXiv: [2304.06082](https://arxiv.org/abs/2304.06082) [hep-th].
- [177] M. Hutchings, F. Morgan, M. Ritoré, and A. Ros, “Proof of the double bubble conjecture,” *Annals of Mathematics*, vol. 155, no. 2, pp. 459–489, 2002, ISSN: 0003486X. [Online]. Available: <http://www.jstor.org/stable/3062123>.
- [178] A. Cotton and D. Freeman, “The double bubble problem in spherical and hyperbolic space,” *International Journal of Mathematics and Mathematical Sciences*, vol. 32, p. 189 517, 2002. DOI: [10.1155/S0161171202207188](https://doi.org/10.1155/S0161171202207188). [Online]. Available: <https://doi.org/10.1155/S0161171202207188>.
- [179] B. W. Reichardt, “Proof of the double bubble conjecture in \mathbb{R}^n ,” *Journal of Geometric Analysis*, vol. 18, no. 1, pp. 172–191, 2008. DOI: [10.1007/s12220-007-9002-y](https://doi.org/10.1007/s12220-007-9002-y). [Online]. Available: <https://doi.org/10.1007/s12220-007-9002-y>.
- [180] G. R. Lawlor, “Double bubbles for immiscible fluids in \mathbb{R}^n ,” *Journal of Geometric Analysis*, vol. 24, no. 1, pp. 190–204, 2014. DOI: [10.1007/s12220-012-9333-1](https://doi.org/10.1007/s12220-012-9333-1). [Online]. Available: <https://doi.org/10.1007/s12220-012-9333-1>.
- [181] J. Harper, “Hyperthreads in holographic spacetimes,” *JHEP*, vol. 09, p. 118, 2021. DOI: [10.1007/JHEP09\(2021\)118](https://doi.org/10.1007/JHEP09(2021)118). arXiv: [2107.10276](https://arxiv.org/abs/2107.10276) [hep-th].
- [182] J. Harper and M. Headrick, “Bit threads and holographic entanglement of purification,” *JHEP*, vol. 08, p. 101, 2019. DOI: [10.1007/JHEP08\(2019\)101](https://doi.org/10.1007/JHEP08(2019)101). arXiv: [1906.05970](https://arxiv.org/abs/1906.05970) [hep-th].
- [183] A. Klappenecker and M. Rotteler, “Mutually unbiased bases are complex projective 2-designs,” in *Proceedings. International Symposium on Information Theory, 2005. ISIT 2005.*, IEEE, 2005, pp. 1740–1744.
- [184] D. Gross, K. Audenaert, and J. Eisert, “Evenly distributed unitaries: On the structure of unitary designs,” *Journal of mathematical physics*, vol. 48, no. 5, p. 052 104, 2007.
- [185] Z. Webb, “The clifford group forms a unitary 3-design,” *arXiv preprint arXiv:1510.02769*, 2015.
- [186] H. Zhu, “Multiqubit clifford groups are unitary 3-designs,” *Physical Review A*, vol. 96, no. 6, p. 062 336, 2017.
- [187] N. Bao, N. Cheng, S. Hernández-Cuenca, and V. P. Su, “The Quantum Entropy Cone of Hypergraphs,” *SciPost Phys.*, vol. 9, no. 5, p. 5, 2020. DOI: [10.21468/SciPostPhys.9.5.067](https://doi.org/10.21468/SciPostPhys.9.5.067). arXiv: [2002.05317](https://arxiv.org/abs/2002.05317) [quant-ph].
- [188] M. Walter and F. Witteveen, “Hypergraph min-cuts from quantum entropies,” *J. Math. Phys.*, vol. 62, no. 9, p. 092 203, 2021. DOI: [10.1063/5.0043993](https://doi.org/10.1063/5.0043993). arXiv: [2002.12397](https://arxiv.org/abs/2002.12397) [quant-ph].
- [189] C. Yin and Z. Liu, “Universal Entanglement and Correlation Measure in Two-Dimensional Conformal Field Theories,” *Phys. Rev. Lett.*, vol. 130, no. 13, p. 131 601, 2023. DOI: [10.1103/PhysRevLett.130.131601](https://doi.org/10.1103/PhysRevLett.130.131601). arXiv: [2211.11952](https://arxiv.org/abs/2211.11952) [cond-mat.stat-mech].
- [190] A. Milekhin, P. Rath, and W. Weng, “Computable Cross Norm in Tensor Networks and Holography,” Dec. 2022. arXiv: [2212.11978](https://arxiv.org/abs/2212.11978) [hep-th].
- [191] B. M. Terhal, M. Horodecki, D. W. Leung, and D. P. DiVincenzo, “The entanglement of purification,” *Journal of Mathematical Physics*, vol. 43, no. 9, pp. 4286–4298, 2002.

- [192] J. Hauschild, E. Leviatan, J. H. Bardarson, E. Altman, M. P. Zaletel, and F. Pollmann, “Finding purifications with minimal entanglement,” *Physical Review B*, vol. 98, no. 23, p. 235 163, 2018.
- [193] T. Faulkner, M. Li, and H. Wang, “A modular toolkit for bulk reconstruction,” *JHEP*, vol. 04, p. 119, 2019. DOI: [10.1007/JHEP04\(2019\)119](https://doi.org/10.1007/JHEP04(2019)119). arXiv: [1806.10560](https://arxiv.org/abs/1806.10560) [hep-th].
- [194] S. Leutheusser and H. Liu, “Emergent times in holographic duality,” Dec. 2021. arXiv: [2112.12156](https://arxiv.org/abs/2112.12156) [hep-th].
- [195] P. Biane, “Some properties of crossings and partitions,” *Discret. Math.*, vol. 175, no. 1-3, pp. 41–53, 1997. DOI: [10.1016/S0012-365X\(96\)00139-2](https://doi.org/10.1016/S0012-365X(96)00139-2). [Online]. Available: [https://doi.org/10.1016/S0012-365X\(96\)00139-2](https://doi.org/10.1016/S0012-365X(96)00139-2).
- [196] G. Birkhoff, *Lattice Theory*, 3rd. Providence: American Mathematical Society, 1967.
- [197] J. S. Kim, S. Seo, and H. Shin, “Annular noncrossing permutations and minimal transitive factorizations,” *Journal of Combinatorial Theory Series A*, vol. 124, Jan. 2012. DOI: [10.1016/j.jcta.2014.02.005](https://doi.org/10.1016/j.jcta.2014.02.005).
- [198] V. F. R. Jones, “Hecke algebra representations of braid groups and link polynomials,” *Annals of Mathematics*, vol. 126, no. 2, pp. 335–388, 1987, ISSN: 0003486X. [Online]. Available: <http://www.jstor.org/stable/1971403>.
- [199] A. Ram, “Seminormal Representations of Weyl Groups and Iwahori-Hecke Algebras,” *Proceedings of the London Mathematical Society*, vol. 75, no. 1, pp. 99–133, Jul. 1997, ISSN: 0024-6115. DOI: [10.1112/S0024611597000282](https://doi.org/10.1112/S0024611597000282). [Online]. Available: <https://doi.org/10.1112/S0024611597000282>.
- [200] B. Westbury, “The representation theory of the temperley-lieb algebras,” *Mathematische Zeitschrift*, vol. 219, no. 4, pp. 539–566, 1995. [Online]. Available: <http://eudml.org/doc/174788>.
- [201] J. J. Graham and G. I. Lehrer, “Cellular algebras,” *Inventiones mathematicae*, vol. 123, no. 1, pp. 1–34, 1996. DOI: [10.1007/BF01232365](https://doi.org/10.1007/BF01232365). [Online]. Available: <https://doi.org/10.1007/BF01232365>.
- [202] C. Akers, N. Engelhardt, and D. Harlow, “Simple holographic models of black hole evaporation,” Oct. 2019. arXiv: [1910.00972](https://arxiv.org/abs/1910.00972) [hep-th].
- [203] R. Wong, *Asymptotic Approximations of Integrals*. Society for Industrial and Applied Mathematics, 2001. DOI: [10.1137/1.9780898719260](https://doi.org/10.1137/1.9780898719260). eprint: <https://epubs.siam.org/doi/pdf/10.1137/1.9780898719260>. [Online]. Available: <https://epubs.siam.org/doi/abs/10.1137/1.9780898719260>.